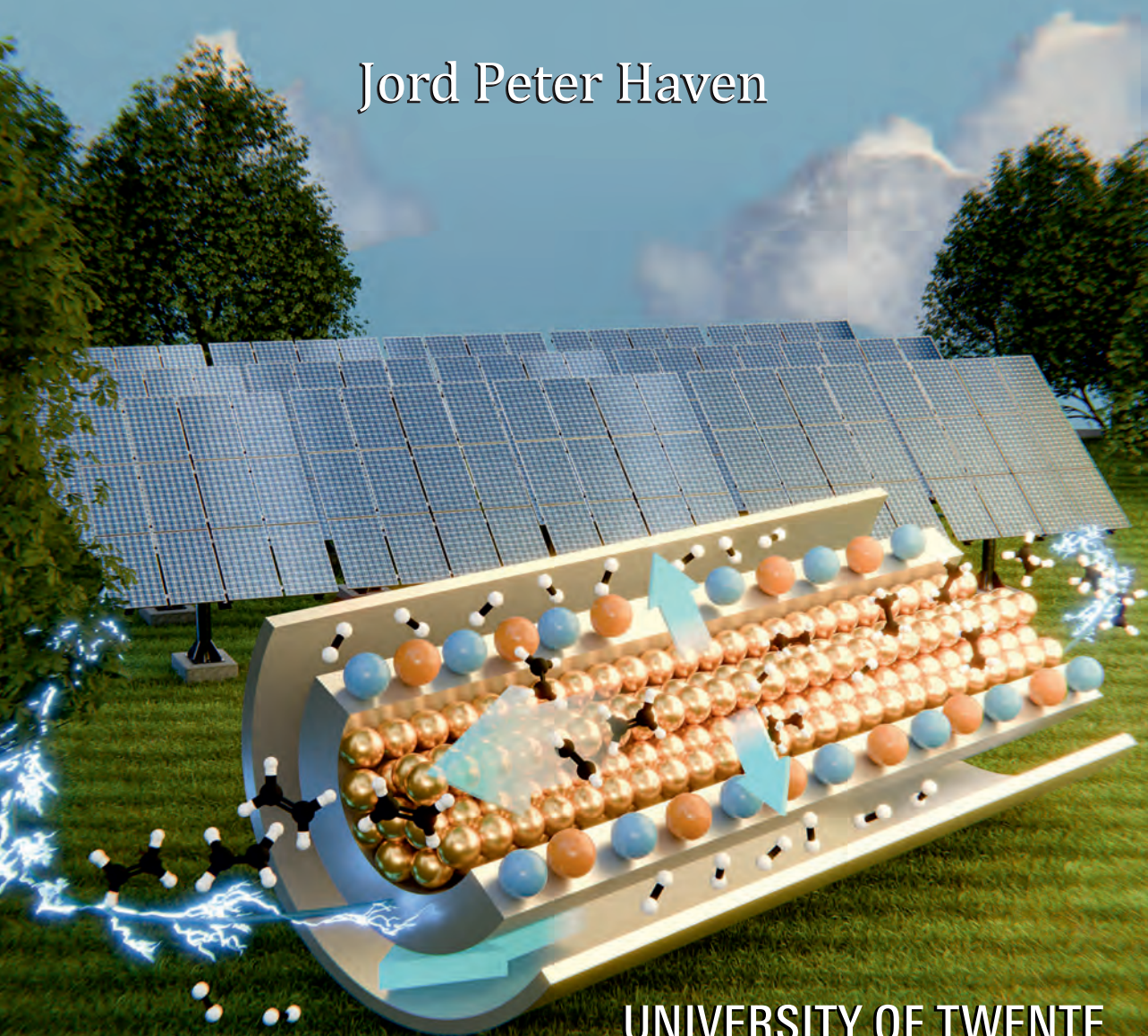# NON-OXIDATIVE DEHYDROGENATION OF LIGHT ALKANES USING CERAMIC MEMBRANES

A TECHNOLOGICAL AND TECHNO-ECONOMIC ASSESSMENT

Jord Peter Haven

UNIVERSITY OF TWENTE.

NON-OXIDATIVE DEHYDROGENATION OF LIGHT ALKANES USING CERAMIC MEMBRANES

A TECHNOLOGICAL AND TECHNO-ECONOMIC ASSESSMENT

Jord Peter Haven

NON-OXIDATIVE DEHYDROGENATION OF LIGHT ALKANES USING CERAMIC MEMBRANES

A TECHNOLOGICAL AND TECHNO-ECONOMIC ASSESSMENT

PROEFSCHRIFT

ter verkrijging van
de graad van doctor aan de Universiteit Twente,
op gezag van de rector magnificus,
prof. dr. ir. A. Veldkamp,
volgens besluit van het College voor Promoties
in het openbaar te verdedigen
op vrijdag 16 mei 2025 om 14.45 uur

door

Jord Peter Haven
geboren op 7 juli 1996
te Oldenzaal, Nederland

Dit proefschrift is goedgekeurd door:

Promotoren

prof.dr.ir. L. Lefferts

prof.dr. J.A. Faria Albanese

PROMOTIECOMMISSIE:

Voorzitter / secretaris: prof.dr. J.L. Herek

Promotoren: prof.dr.ir. L. Lefferts
Universiteit Twente, TNW, Catalytic Processes and Materials

prof.dr. J.A. Faria Albanese
Universiteit Twente, TNW, Catalytic Processes and Materials

Leden: prof.dr. J.M. Serra-Alfaro
Universitat Politècnica de València

prof.dr. F. Gallucci
Eindhoven University of Technology

dr. J. Xie
Rijksuniversiteit Groningen

prof.dr.ing. M.B. Franke
Universiteit Twente, TNW, Sustainable Process Technology

prof.dr.ir. A. Nijmeijer
Universiteit Twente, TNW, Inorganic Membranes

Contents

Chapter 1

Membrane-assisted light alkane dehydrogenation: A sustainable olefin production route?

Summary

Light olefins are widely used as building blocks for plastics, oxygenates, and chemical intermediates, even though conventional olefin production processes, like steam cracking and fluid catalytic cracking, are highly energy and carbon intensive. The direct non-oxidative dehydrogenation (NODH) of C2-C3 alkanes to olefins represents a more direct alternative production pathway. However, light alkane NODH is limited by thermodynamic equilibrium, requiring high temperatures (500-700 °C) for restricted olefin yields (30-40%). Dense ceramic hydrogen permeable membranes can potentially be used to shift the equilibrium toward the olefin side. The use of membranes could thereby substantially reduce the required energy input and carbon footprint of olefin production processes. However, before potentially industrializing this technology the challenges related to the performance of the required dehydrogenation catalyst under membrane reactor conditions and the potential techno-economic benefits and hurdles of membrane-assisted light alkane NODH need to be identified and quantified, which is the aim of this dissertation.

1.1 Motivation

The growing world population and global wealth have pushed the worldwide demand for material goods to unprecedented levels [1]. To satisfy this increasing demand, chemical production processes have massively expanded in the last decades [2]. As a result, the chemical industry is nowadays the largest contributor to the total industrial energy usage [3,4]. A major part of the required energy is generated using non-renewable resources, making the chemical industry highly carbon intensive [5]. However, chemical processes have to be modified drastically in the near future, as global greenhouse gas emissions need to be reduced by 45% in 2030 compared to 2019 [6], and should reach net zero in 2050 [7], following the Paris Agreement. To achieve these emission targets, the main pillars for the chemical industry are (i) to strongly increase the energy efficiency of existing processes, (ii) to replace current high-temperature processes by renewably electrified (e.g. wind, solar) processes, and (iii) to replace oil and gas material resources by green carbon feedstocks, such as CO_2, biomass, or recycled carbon [8,9].

Approximately 80% of the products of the chemical industry comprises of polymers and plastics [10]. More than 50% of these plastic materials are currently produced from light olefins, like ethylene and propylene [11]. These light olefins are further applied to the production of oxygenates (ethylene glycol, acetaldehyde, acetone and ethylene/propylene oxides), and chemical intermediates (ethylbenzene, propionaldehyde) [11], and are therefore crucial chemical building blocks. The demand for light olefins is ever-increasing and is expected to grow substantially in the coming decade (**Figure 1.1**). Current ethylene and propylene production is primarily based on highly energy-intensive steam cracking and fluid catalytic cracking of petroleum-derived resources [11,12]. Next to dwindling petroleum reserves, the high energy demand in combination with limited olefin yields (ca. 50%) are major drawbacks of these conventional olefin production processes [13,14].
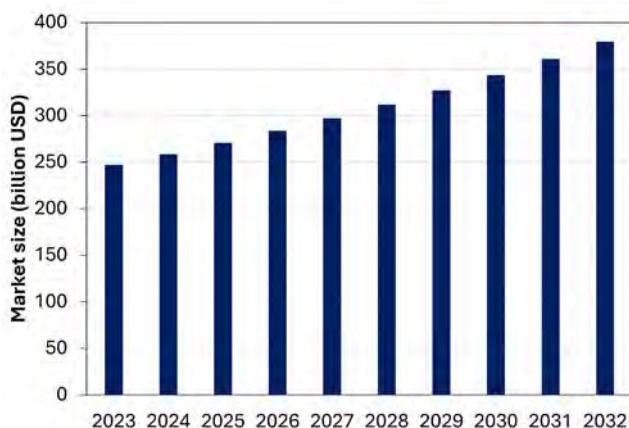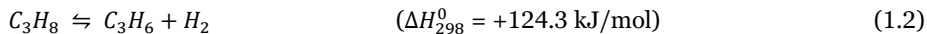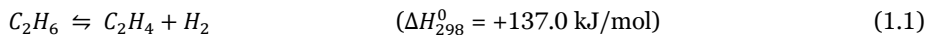

Figure 1.1: Forecasted global light olefin (ethylene + propylene) market size. Data retrieved from Precedence Research [15,16].

Possible alternative routes to produce light olefins comprise (i) alkane dehydrogenation, (ii) methanol-to-olefins, and (iii) olefin metathesis [12]. Considering the currently achievable reaction performances of these three processes, alkane dehydrogenation is financially the most attractive option [12]. Alkane dehydrogenation can be operated either under oxidative or non-oxidative conditions. Oxidative dehydrogenation (ODH) is energetically attractive, as it allows for operation at mild temperatures (300-500 °C), due to the exothermic nature of this reaction [14,17]. Moreover, ODH is not limited by thermodynamic equilibrium [14,17]. However, the combination of oxidants and hydrocarbons provides a risk for explosive atmospheres and complicates safe control of side and consecutive oxidation reactions, thereby limiting olefin selectivity [14,18]. Industrialization of light alkane ODH processes is still hampered by the limited olefin yields [14,17]. In contrast to alkane ODH, the non-oxidative dehydrogenation (NODH) of light alkanes is endothermic, therefore intrinsically more energy intensive, and limited by a thermodynamic equilibrium (**Equation 1.1** and **1.2**) [14,17]. Alkane NODH requires higher temperatures (>500 °C) relative to alkane ODH, resulting in a higher risk for catalyst deactivation due to coke formation [14,17]. Nevertheless, the olefin selectivity can be extremely high (>95%) at moderate alkane conversion level (20-50%) [14], which makes alkane NODH the preferred industrial alternative.

Alkane NODH has been commercialized already since the 1940s for the butane to butadiene reaction, and more recently also for the propane to propylene reaction (**Equation 1.2**) [19]. The alkane feedstock is commonly obtained from natural gas processing [14]. As a more sustainable alternative, the alkane reactant could be retrieved e.g. as a byproduct from the production of sustainable aviation fuel [20] or from electrically heated plastic pyrolysis [21]. Five different processes are currently operated in industry for light alkane NODH: (i) Lummus/CB&I CATOFIN, (ii) UOP/Honeywell Oleflex, (iii) Uhde/Thyssenkrupp STeam Active Reforming (STAR), (iv) Snamprogetti Yarsintez Fluidized Bed Dehydrogenation (FBD), and (v) Linde-BASF propane dehydrogenation (PDH) [22,23]. All these processes utilize a multistage reactor approach to cope with the endothermicity of the dehydrogenation reaction [22,23]. Besides, they all apply either parallel or serial configured reactors to allow for continuous operation [22,23], while removing carbon deposits upon catalyst regeneration [17]. Moreover, all these processes are commonly operated between 500 to 700 °C [19]. The catalysts that are used in these processes are typically PtSn or CrO_x-based, despite the high costs of Pt and the environmental concerns for industrial usage of chromium [14,17].

In contrast to propane and butane NODH, ethane NODH (**Equation 1.1**) has not been commercialized, due to the more stringent thermodynamic equilibrium limitation. Ethane NODH intrinsically requires extremely high temperatures (>700 °C) to achieve significant conversion levels (ca. 40%) [24], which is industrially undesired in terms of energy input and carbon deposition. Ethylene and propylene production via ethane NODH (**Equation 1.1**) and propane NODH (**Equation 1.2**), respectively, is favored at high temperatures

and reduced pressures [17]. They are both enthalpic uphill reactions and are, hence, driven by entropy maximization.

$$C_2H_6 \leftrightharpoons C_2H_4 + H_2 \qquad (\Delta H^0_{298} = +137.0 \text{ kJ/mol}) \qquad (1.1)$$

$$C_3H_8 \leftrightharpoons C_3H_6 + H_2 \qquad (\Delta H^0_{298} = +124.3 \text{ kJ/mol}) \qquad (1.2)$$

Light alkane NODH processes are highly energy and carbon intensive, due to the elevated temperatures required. Shifting the thermodynamic equilibrium (**Equation 1.1** and **1.2**) toward the olefin side by withdrawing the produced hydrogen from the reaction zone presents a promising strategy to drastically reduce the energy and carbon intensity. This can be accomplished either by selectively combusting the produced hydrogen or by selectively removing the hydrogen from the reaction zone using membranes [14]. The use of membranes is the preferred industrial option, because of the risk of possible hydrocarbon oxidation in the selective hydrogen combustion route.

Dense ceramic and dense metallic membranes can be applied to remove hydrogen from high temperature (500-700 °C) gas phase reactions [25,26]. Dense metallic membranes have a ca. five times higher hydrogen permeability than dense ceramic membranes [26,27]. However, metallic membranes suffer from poor thermochemical stability under hydrocarbon-rich conditions [28]. Dense ceramic membranes are therefore the more propitious option when targeting integration of these membranes into alkane dehydrogenation processes.

Dense ceramic membranes can be classified into (i) mixed proton-electron conducting (MPEC), and (ii) proton-conducting electrolysis cell (PCEC) membranes [25]. In MPECs, protons and electrons are both transported through the membrane and hydrogen permeation is fully driven by a gradient in hydrogen chemical potential [29]. A gradient in operational pressure between membrane feed and permeate side is commonly used to facilitate hydrogen permeation through MPECs [29]. Besides, either a sweep gas or a vacuum is needed on the permeate side to minimize H_2 chemical potential and thereby maximize the hydrogen permeation flux [25].

In contrast to MPECs, only protons are transported through PCEC membranes, whilst the electrons are directed via an external circuit by applying a voltage [25]. Hydrogen permeation through PCECs is driven by a gradient in hydrogen electrochemical potential, i.e. a combination of a gradient in hydrogen chemical potential and a gradient in electrostatic potential [25]. PCECs are typically operated between 200-800 mV [30,31], at which the electrostatic potential gradient is dominating the driving force for permeation. In that situation, hydrogen can be transported in a direction opposing the H_2 partial pressure gradient, allowing for the generation of a purified and pressurized H_2 product stream on the permeate side.

The most evident advantage of integrating hydrogen permeable ceramic membranes into alkane NODH processes is the possible shift of the thermodynamic equilibrium, allowing

for increased olefin yields at a given temperature. **Figure 1.2** schematically shows the principle of such a membrane-assisted alkane NODH process for a packed bed membrane reactor operating the ethane NODH reaction. The hydrogen product is removed from the reaction zone via permeation through the ceramic membrane (**Figure 1.2**). The resulting reduced H_2 partial pressure thermodynamically allows for further conversion of ethane to ethylene (**Equation 1.1**).
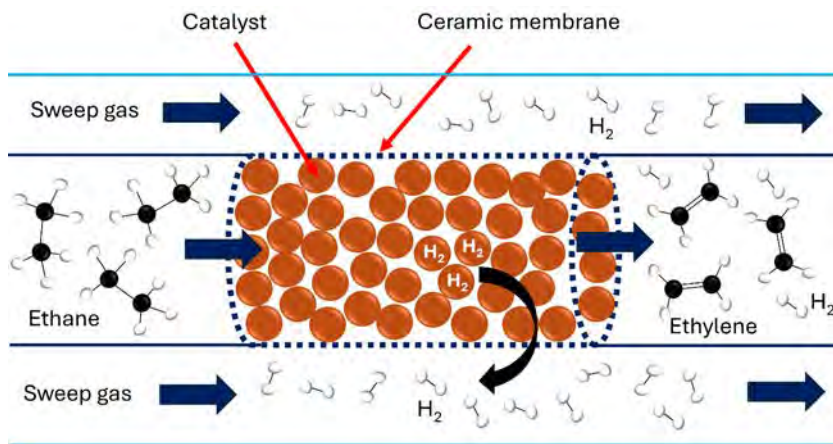
Figure 1.2: Schematic representation of a tube-in-tube membrane reactor where the membrane represents the wall between the tubes and in which a pure ethane feed is supplied on the inner tube, whilst a cocurrent sweep gas flow is used in the outer tube to sweep away the hydrogen.

Applying membranes in light alkane NODH processes also offers several benefits on a process scale. For example, integration of energy-intensive dehydrogenation and separation steps in a membrane reactor could substantially reduce the investment costs and energy demand of the overall process. Furthermore, a valuable hydrogen byproduct stream is generated upon isolation of the hydrogen in membrane reactors. An additional advantage of PCECs is that hydrogen transport is driven electrically via the applied voltage, thereby allowing for the use of renewable electricity to operate these chemical reactors. Moreover, resistive Joule heat is generated inside the PCEC membrane reactor, due to the electrical resistance of the membrane, which can directly be integrated for operating the endothermic dehydrogenation reaction. Also, the applied potential allows for hydrogen transport in a direction opposing the hydrogen partial pressure gradient and enables hydrogen compression *in situ* with reactor operation and hydrogen separation. As a result, a pressurized and purified hydrogen product stream can be obtained in PCEC systems.

The energy usage and related greenhouse gas emissions of ceramic membrane-assisted alkane NODH processes are potentially much lower compared to conventional cracking technologies for light olefin production, due to the combination of the thermodynamic shift toward olefins, the integration of reaction, separation, and hydrogen compression,

and the usage of renewable electricity. The concept of integrating hydrogen permeable dense ceramic membranes into alkane dehydrogenation processes could thereby contribute to (i) increase the energy efficiency of existing olefin production processes, and to (ii) electrify the chemical industry, in the aim for reaching the Paris Agreement goals. It should be noted that the required alkane reactants need to be obtained from e.g. polymer recycling or green electrified plastic pyrolysis, instead of from conventional petroleum or natural gas reserves, to establish a circular economy for olefin production.

1.2   Alkane dehydrogenation catalysts

Suitable alkane NODH catalysts are either based on Pt or CrO_x [14,19]. These catalysts are extremely selective (>95%) in dehydrogenating alkanes, without consecutively converting the intrinsically more reactive olefin. The most common side reactions that can occur are: (i) hydrogenolysis, (ii) cracking, (iii) hydrogenation, and (iv) coking [12,14]. As an example, these side reactions are presented in **Equation 1.3-1.6** for the propane dehydrogenation reaction, where it is assumed that the produced coke species is pure carbon. Generally, Pt-based catalysts show a higher intrinsic dehydrogenation activity, a lower activation barrier for dehydrogenation, and a better stability compared to CrO_x catalysts [14]. The focus is therefore on Pt-based catalysts in this dissertation.

Propane cracking: $C_3H_8 \rightarrow C_2H_4 + CH_4$ (1.3)

Propane hydrogenolysis: $C_3H_8 + H_2 \rightarrow C_2H_6 + CH_4$ (1.4)

Ethylene hydrogenation: $C_2H_4 + H_2 \leftrightharpoons C_2H_6$ (1.5)

Propane coking: $C_3H_8 \leftrightharpoons 3C + 4H_2$ (1.6)
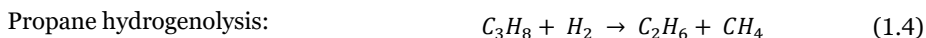
1.2.1   Role of platinum

Pt is preferred to other noble metals as dehydrogenation catalyst, since it is superior in cleaving C-H bonds and inferior in cleaving C-C bonds [14]. The Pt active sites that are responsible for dehydrogenating alkanes differ from the ones that accelerate side reactions. For example, alkane hydrogenolysis, alkane cracking, and olefin isomerization primarily take place on large Pt ensembles, whilst alkane dehydrogenation is structure insensitive [14]. For this reason, small Pt clusters, and hence high Pt dispersions, favor light paraffin dehydrogenation [17,32,33]. Moreover, only low Pt loadings (<4%) are required, as Pt is intrinsically highly active for light alkane conversion [17]. The use of small Pt clusters leads to a relatively large number of low coordinated Pt sites compared to Pt flat surfaces. Since low coordinated sites are generally more reactive than flat surfaces, the drawback of applying small Pt clusters is that coke formation is boosted [14].

1.2.2   Role of promoters

The highly active Pt needs to be modified with promoters to improve the olefin selectivity and catalyst stability [17]. Commonly applied promoters are Zn, Co, Fe, Ga [34], In, and

Sn [35]. Particularly, Sn promotion has led to substantial improvements in catalyst stability and olefin selectivity [36]. Even though Pt-Sn catalysts have been developed and industrially applied for decades, the exact working principle of Sn promotion is still under debate. In general, tin promotion is claimed to enhance olefin selectivity and catalyst stability by either (i) suppressing hydrogenolysis and isomerization side reactions [34], (ii) neutralizing support acidity [37,38], (iii) minimizing Pt sintering, and/or (iv) facilitating migration of coke species and hydrogen from Pt active sites to the support [14].

The effects of Sn promotion are generally attributed to either geometrical or electronic causes induced by the Sn. Geometrically, Sn could (i) selectively cover low coordination Pt sites (e.g. step, corner, or edge sites), and/or (ii) ensure the formation of a PtSn alloy [33]. Suppression of the activity of low coordination Pt sites anticipatedly minimizes coke formation and, thus, improves catalyst stability. Besides, by the formation of a PtSn alloy the number of neighboring Pt sites is reduced. In other words, Sn acts as a spacer between adjacent Pt sites and thereby ensures the formation of small Pt ensembles, which favor olefin formation at the expense of side products [33,38].

The commonly claimed electronic explanation for the beneficial effect of Sn promotion follows from the formation of a PtSn alloy. This alloy formation is believed to lead to a transfer of electron density from Sn to Pt [33,37,39]. Consequently, Sn weakens the attraction between Pt and hydrocarbons, and thereby limits the formation of strongly-bound coke-inducing alkylidyne surface species [33,37]. Furthermore, the weakened Pt-hydrocarbon interaction allows for enhanced migration of coke precursors from PtSn sites toward the support [37,38]. Analogously, the Pt-hydrogen bond is also weakened upon Sn promotion. This enhances hydrogen migration across the surface, which in turn helps in diminishing coke formation as well [38]. The reduction in Pt-hydrocarbon bond strength induced by the Sn negatively affects the intrinsic activity of the Pt. However, the presence of Sn reduces the desorption barrier, and thereby averts the occurrence of consecutive reactions (e.g. coking, deep dehydrogenation, cracking) for the benefit of a higher olefin selectivity and an improved catalyst stability [14].

1.2.3   Role of the support

Alumina is often used as catalyst support material for Pt-based catalysts. However, the most common types of alumina are either too acidic (γ-Al$_2$O$_3$) or have too low surface areas (θ-Al$_2$O$_3$ and α-Al$_2$O$_3$) to be applied in alkane dehydrogenation systems. The acid sites in γ-Al$_2$O$_3$ boost cracking reactions at the cost of olefin formation [14]. These acid sites on the support can be poisoned by introducing alkaline metals like Li, Na, or K into its structure [17]. Instead of using alkaline dopants, related alternative aluminates like magnesium aluminate (MgAl$_2$O$_4$) or zinc aluminate (ZnAl$_2$O$_4$) can be used [40]. ZnAl$_2$O$_4$ and MgAl$_2$O$_4$ have a less acidic and thermally more stable spinel structure compared to γ-Al$_2$O$_3$ [40–42]. Besides, in these spinels Zn and Mg have strong interactions with Pt active sites, which thereby helps to avoid Pt sintering [42]. Nevertheless, the specific surface area of these spinel structures is typically a factor three to four lower compared to γ-Al$_2$O$_3$ (ca.

50 m^2/g vs. 150-200 m^2/g) [42]. The ZnAl$_2$O$_4$ spinel support is industrially applied in the Uhde/Thyssenkrupp STAR process, particularly because of its high stability and resistance to coke [14].

1.2.4 Catalyst deactivation

The activity of PtSn-based dehydrogenation catalysts deteriorates over time, which can be caused by either Pt sintering or carbon deposition [14]. Pt sintering originates from a combination of high temperature operation, the presence of air (in regeneration cycles), and weak Pt-support interactions. This type of deactivation is partly reversible, as Pt can be redispersed again by treating the catalyst with low amounts of oxygen and chlorine [14]. Carbon deposits on the surface of PtSn catalysts are believed to originate from olefin oligomerization [14]. Deactivation due to coke formation is commonly counteracted (i) by reducing the operational temperature if possible [37], and/or (ii) by cofeeding components like H$_2$, H$_2$O, CO$_2$, or CO [14]. These light gases typically suppress consecutive surface reactions by boosting olefin desorption. Despite the efforts aimed at minimizing coke formation, periodic catalyst regeneration through coke removal is still a prerequisite in industry [14], as catalyst deactivation due to coke formation is ubiquitous for alkane dehydrogenation processes [33]. The catalyst is commonly regenerated in a stream containing air and steam [19]. The air oxidizes the coke deposits, whereas the steam is cofed for heat dilution [43]. The amount of energy generated during the regeneration runs is typically integrated as a heat supply for the endothermic alkane dehydrogenation reactors [19].

1.2.5 Reaction mechanism

The reaction mechanism of light alkane NODH on Pt catalysts has been primarily studied in the past for propane NODH [33,44–51] and isobutane NODH [36,42,48,52–54]. Reaction rate expressions based on exponential or Langmuir-Hinshelwood-Hougen-Watson (LHHW) kinetics have shown good agreement with experimental results. Despite all these efforts, there is still considerable debate about the mechanism of light paraffin NODH on Pt catalysts. The main discrepancies are related to the rate-determining step (RDS) and the type of surface species. The RDS is generally claimed to be a C-H cleavage step, either in the form of dissociative adsorption of the alkane [44,50] or in the form of a surface C-H bond cleavage after adsorption [33,48,55,56]. Besides, the surface coverage distribution is either claimed to be dominated by the olefin [47,51], or by the alkane and the olefin [33], or by hydrogen and the olefin [44], or by a range of possible products and side products formed [45,50,56]. These reaction mechanisms are typically based on catalytic data that is obtained within a narrow window of alkane, alkene, and H$_2$ partial pressures, complicating the extrapolation of these models outside this operational window. In hydrogen removing membrane reactors, the hydrogen and olefin concentrations are anticipated to vary greatly along the reactor length, as hydrogen is removed to increase olefin yields. The effect of variations in hydrogen and olefin partial

pressures on the reaction rate and mechanism of light alkane NODH on Pt catalysts is, therefore, investigated in this dissertation.

1.3   Dense ceramic membranes

Dense ceramic membranes can be classified into (i) mixed proton-electron conducting (MPEC) membranes, and (ii) proton-conducting electrolysis cell (PCEC) membranes. In MPECs, protons and electrons are both transported through the membrane and hydrogen permeation is fully driven by a gradient in hydrogen chemical potential (**Figure 1.3**) [29]. On the contrary, only protons are transported through PCEC membranes, whilst the electrons are directed via an external circuit by applying a voltage (**Figure 1.3**) [25]. Hydrogen permeation through PCECs is driven by a gradient in hydrogen electrochemical potential, i.e. a combination of a gradient in hydrogen chemical potential and a gradient in electrostatic potential [25]. PCECs are typically operated at high voltages, such that the electrostatic potential gradient is dominating the driving force for permeation.
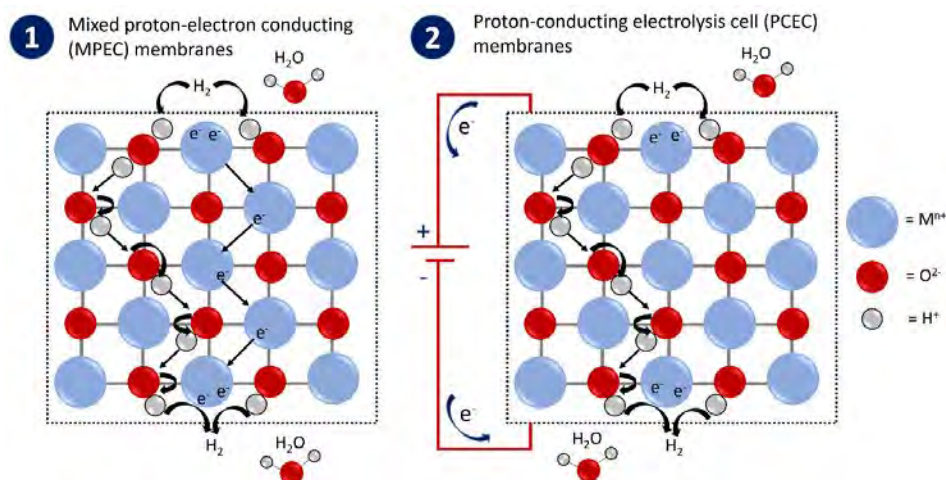
Figure 1.3: Transport mechanisms of hydrogen permeation through (1) mixed proton-electron conducting (MPEC) membranes, and (2) proton-conducting electrolysis cell (PCEC) membranes.

Hydrogen transport through ceramics primarily takes place via proton migration between adjacent oxygens (**Figure 1.3**), following the Grotthuss mechanism, and requiring reorientations of hydroxide ions [27,57]. Although protons are the most mobile species in ceramic materials and oxygens are mostly localized on their crystallographic positions [57], proton transport can also partly take place through OH^- migration instead of proton migration, where the involved oxygen-ions move into the positions of adjacent oxygen vacancies [29].

Suitable MPEC materials require good ambipolar (protonic and electronic) conductivity [29], as both protons and electrons are transported through MPEC membranes (**Figure 1.3**). By contrast, PCEC materials primarily need to possess a good protonic conductivity, as electrons are directed via an external circuit in PCECs. Potential PCEC materials are perovskite-type strontium ($SrCeO_3$ and $SrZrO_3$) [58] and barium ($BaCeO_3$ and $BaZrO_3$) oxides, which all possess high proton conductivities [25]. These metal oxides are often substituted with acceptor cations, such as Y, Sc, Eu, or Gd [27,57]. These acceptor cations are lower valent cations (e.g. Y^{3+} or Sc^{3+} as a replacement of Zr^{4+} or Ce^{4+}) aimed to provide electronic space for the incorporation of protons [29,57]. The substitution ions should match size and acid/base characteristics with the original transition metal ions of the ceramic material to maintain structural stability [57].

Acceptor substituted strontium and barium oxides are unsuitable MPEC materials, because of their limited electronic conductivity [29]. Possible alternatives encompass transition metal oxides, which are highly reducible materials. For this reason, recent MPEC research has among others focused on the use of titanates, tungstates, and sesquioxides (e.g. Nd_2O_3 or Tb_2O_3) [59]. As an example, Chen and coworkers [60] showed that niobium and molybdenum substituted lanthanum tungstates exhibit a high ambipolar conductivity in combination with a good stability under harsh operational conditions (i.e. in presence of H_2S and various salts) [25,29,60]. The tungsten in lanthanum tungstates is typically replaced by lower valent molybdenum or niobium acceptor cations to boost the electronic conductivity, while leaving the protonic conductivity unaffected [60,61]. Lanthanum tungstate membranes are limited by electronic conductivity at temperatures relevant to industrial light alkane dehydrogenation processes (ca. 500-700 °C) and are limited by protonic conductivity at higher temperatures [61].

Dense ceramic membranes are usually applied in asymmetric membrane configurations comprising a dense separation layer on top of a porous support layer [62,63]. The thin ceramic separation layer (ca. 5-50 μm) maximizes the hydrogen permeation flux, assuming that bulk diffusion is limiting hydrogen transport, following Fick's first law of diffusion [25]. By contrast, the significantly thicker porous support layer (ca. 300-700 μm) ensures the required mechanical stability [25]. The challenge of using asymmetric ceramic membranes is that the thermal expansion coefficients of the support and separation layers need to match to avoid bending, delamination, and thermal cracking of the membrane upon temperature variations [29]. For this reason, it is often preferred to utilize similar ceramic materials as support and separation layers.

Dense ceramic membranes are known to function optimally in the presence of steam (**Figure 1.3**), facilitating hydrogen incorporation and recombination through the generation of surface hydroxyls [64]. In hydrogen removing membrane reactors equipped with ceramic membranes the Pt catalyst will therefore inevitably be exposed to moistened atmospheres. The influence of cofeeding steam on the reaction rate, reaction mechanism, and catalytic performance of alkane NODH on Pt-based catalysts is currently poorly understood and is, therefore, researched in this dissertation.

1.4 Membrane-assisted alkane dehydrogenation

1.4.1 Membrane reactor configurations

In this dissertation, a distinction is made between (i) systems in which the catalyst is physically separated from the membrane, as e.g. in packed bed membrane reactors (PBMRs, **Figure 1.4a**) or fluidized bed membrane reactors, and (ii) systems in which the catalyst is in direct contact with the membrane material (**Figure 1.4b**). In PBMRs, the Pt-based catalyst particles or pellets are surrounded by a tubular membrane wall (**Figure 1.4a**). In such a system, radial gas transport is often limited due to the dominant axial convective transport. Radial mass transport limitations particularly start to play a role in membrane reactors containing extremely thin (<5 μm) dense membranes, as those systems are limited the least by bulk membrane diffusion [27]. Moreover, in PBMRs hydrogen needs to desorb from the catalyst particles and readsorb and dissociate on the membrane material to allow for hydrogen to permeate.

An alternative reactor configuration is the catalyst-functionalized membrane reactor, where the Pt dehydrogenation catalyst is deposited directly onto the proton-conducting membrane (**Figure 1.4b**). This can be accomplished using asymmetric membranes, in which the porous layer is functionalized with the catalyst, whilst the dense layer functions as the actual hydrogen separation layer (**Figure 1.4b**). In such a catalyst-functionalized membrane reactor, limitations in the mass transport of the hydrogen from the catalyst to the membrane are minimized. Moreover, hydrogen could spillover from the catalyst active phase onto the membrane material, thereby avoiding desorption, readsorption, and incorporation steps. It is currently unclear how proton-conducting supports affect the performance of Pt-based dehydrogenation catalysts. In this dissertation, the Pt catalyst is deposited onto an MPEC and onto a PCEC material to investigate how proton-conducting support properties influence the dehydrogenation performance of Pt.
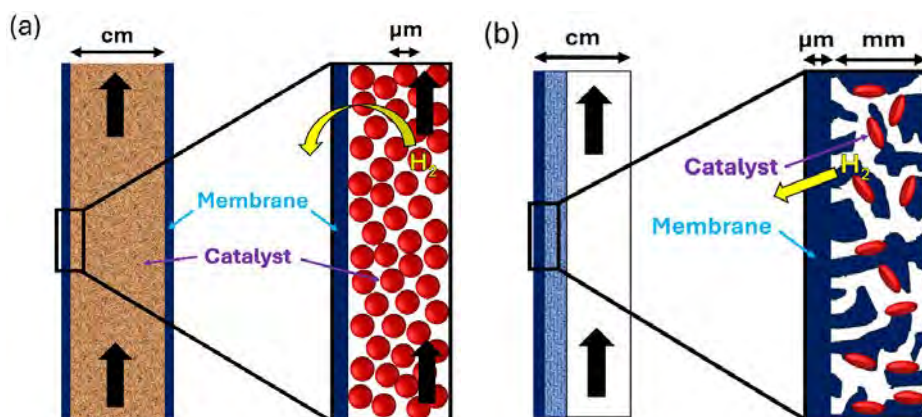
Figure 1.4: Schematic representation of (a) a packed bed membrane reactor (PBMR), and (b) a catalyst-functionalized membrane reactor.

1.4.2 State-of-art membrane reactors

The concept of H_2 removal in membrane reactors to shift the alkane dehydrogenation equilibrium toward the olefin side has been demonstrated for ethane [24,65–68], propane [45,69–73] and isobutane [74,75] dehydrogenation. Dense ceramic [66–68] as well as dense metallic [45,69–72,74,75] membranes were successfully applied to accomplish this equilibrium shift, as both membrane types are fully permselective to H_2. The research on dense metallic membranes focused primarily on Pd and Pd alloy-based materials [45,69–72,74,75]. On the contrary, the applied ceramic membranes were mainly based on barium zirconates and cerates [66–68].

The H_2 permeation flux through dense metallic membranes is typically about five times higher than through dense ceramic membranes [27]. Nonetheless, the focus in this dissertation is on dense ceramic membranes, as dense ceramics are chemically and thermally more stable at high temperatures in hydrocarbon-rich atmospheres [28,76], making them better suited for integration with high temperature gas phase reactions, like the alkane dehydrogenation reaction. Dense metallic membrane reactors for hydrogen permeation are typically operated between 300 and 700 °C [27]. By contrast, MPEC-based dense ceramic membranes often require even higher temperatures (600-900 °C), as proton transport through metal oxides is a strongly thermally activated process [29]. However, when an external voltage is applied to enhance proton migration as in PCECs, more moderate operating temperatures in the range between 400-600 °C can be used [67,68].

The removal of H_2 from reaction systems containing hydrocarbons typically leads to more carbon deposition on the surface of the membrane and/or the applied catalyst [71–73]. Consequently, olefin yields above equilibrium level are generally only attained during the first couple of hours of membrane reactor operation [73,77]. Carbon formation can be minimized by operating at lower temperatures [71], which has the inherent disadvantages of a lower dehydrogenation activity and a lower hydrogen permeation flux, if the applied voltage is not increased. Alternatively, light gases like H_2, H_2O, CO_2, or CO can be cosupplied with the alkane on the reaction side of the membrane to suppress coke formation [14]. Furthermore, the co-ionic properties of proton-conducting ceramics can be used to optimize membrane stability. For instance, Morejudo et al. [77] showed that the cotransport of O^{2-} ions in the direction opposing the direction of proton transport through PCECs leads to the distributed injection of oxygen to the reaction zone, which facilitates coke removal.

Most of the membrane reactor research into alkane dehydrogenation was carried out in packed bed membrane reactors (PBMRs, **Figure 1.4a**) [65,69,70,73,74]. PBMRs usually have a tube-in-tube configuration, where the catalyst can be packed either on the inner tube or on the shell side. To increase the available membrane surface area per reactor volume, a multi-tubular design can be used, in which the catalyst is stacked on the shell side [27]. Disadvantages of the PBMR design are the pressure drop along the reactor and the complex heat management, especially for highly endothermic reactions, like the alkane

dehydrogenation reaction [27,78]. These drawbacks are avoided in fluidized bed membrane reactors (FBMRs) [27,78]. However, FBMRs suffer from attrition of catalyst particles and erosion of reactor internals, caused by the harsh fluidization conditions [78].

More recently, the catalyst-functionalized membrane reactor design (**Figure 1.4b**) has been applied to electrically driven hydrogen permeation systems (e.g. PCECs, **Figure 1.3b**) [67,68,79]. These systems resembled traditional solid oxide fuel cells, in which tubular [79] and planar [66–68] cells were considered. Tubular systems were concluded to be more suitable than planar systems for PCEC applications in which H_2 is electrochemically compressed upon separation and purification, as tubular systems can mechanically better withstand pressure differences across the membrane [80–82].

1.4.3 Industrial perspective

Steam cracking and fluid catalytic cracking are the main conventional processes for the production of light olefins [14,19]. As alternative route, light alkane NODH has been industrialized for propane and isobutane NODH without the use of membranes [19]. On the contrary, ethane NODH is hitherto not commercialized, because of the more stringent thermodynamic equilibrium limitation as compared to propane and isobutane NODH. Membrane-assisted alkane NODH processes need to be competitive in terms of capital investment, profitability, energy efficiency, and carbon footprint with the conventional production routes to ever become industrially attractive alternatives for light olefin production. This is a challenging undertaking, particularly due to the large scale in which light olefins are globally produced (ethylene: ca. 130 billion USD in 2022 [16,83], propylene: ca. 105 billion USD in 2022 [15,84]). Prior to large scale industrial implementation of innovative approaches, like membrane-assisted alkane NODH to produce light olefins, it is therefore essential to assess the techno-economic advantages and disadvantages of the emerged technology. This issue is therefore addressed in detail in this dissertation.

1.5 Scope and outline

Light olefin production via non-oxidative dehydrogenation (NODH) of light alkanes is researched in this thesis under conditions relevant to membrane reactor applications. Besides, the techno-economics of membrane-assisted light alkane NODH processes are investigated and compared to conventional light olefin production routes. The questions central to this dissertation are:

- Which technological hurdles need to be overcome to operate ceramic membrane reactors for light alkane NODH?
- Is ceramic membrane-assisted alkane NODH a feasible industrial alternative to produce ethylene and propylene?

1.5.1 Technological challenges

The reaction mechanism of light alkane NODH under varying conditions relevant to membrane reactor application needs to be fully understood. To this end, the influence of varying ethane, ethylene, and hydrogen partial pressures on the reaction kinetics of the ethane NODH reaction on a Pt-Sn/ZnAl$_2$O$_4$ catalyst is investigated in **Chapter 2**. This chapter also proposes a reaction model that can describe the ethane NODH reaction across a wide range of concentrations. Since dense ceramic membranes are known to function optimally in the presence of steam [64], the alkane NODH catalysts will inevitably be exposed to moistened gas phase atmospheres inside membrane reactors equipped with these membranes. For this reason, the effect of steam on the structure and the performance of Pt-based catalysts in the ethane NODH reaction is investigated in **Chapter 3**. A possible membrane reactor strategy is to deposit the alkane NODH catalyst directly onto the ceramic membrane material (**Figure 1.4b**). In that configuration, mass transfer from the catalyst to the membrane is optimized and it is ensured that the alkane NODH reaction takes place in the immediate vicinity of the membrane. To assess the potential of this strategy, Pt catalyst active phases are deposited on a promising MPEC material (i.e. LWMO, lanthanum tungsten molybdenum oxide) and a promising PCEC material (i.e. BZCY, barium zirconium cerium yttrium oxide). The performance of Pt/LWO and Pt/BZCY catalyst powders are benchmarked against conventional Pt/ZnAl$_2$O$_4$ in **Chapter 4**.

1.5.2 Techno-economic assessment

In addition to the technological challenges related to the catalyst and membrane formulations, the potential impact of ceramic membrane-assisted alkane NODH on a process level needs to be quantified to assess the viability of this technology. Moreover, there is currently no clear understanding of the main bottlenecks that could prevent industrial implementation of dense ceramic membranes. Whether membrane-assisted propane NODH could be a feasible alternative for commercialized on-purpose propylene production processes is investigated in **Chapter 5**. This is done by conducting an exhaustive analysis of the process economics, energy usage, and carbon dioxide emissions of propane NODH processes equipped with (i) MPEC and (ii) PCEC membranes. For this purpose, we benchmarked these alternatives against the Honeywell/UOP Oleflex process. Herein, the different process cases are either heated by natural gas combustion or by using electricity, in which a distinction is made between the use of green and fossil electricity. An analogous techno-economic study is conducted in **Chapter 6** for a membrane-assisted ethane NODH process, which is a process that is not yet industrialized. The aim of this chapter is to examine if the use of dense ceramic membranes could make ethane NODH processes commercially attractive. To this end, the potential impact of using dense ceramic membranes is evaluated by comparing a membrane-driven ethane NODH process to a conventional ethane steam cracking process.

1.5.3 Evaluation of ceramic membrane-assisted alkane dehydrogenation

The key insights gained in this dissertation are summarized in **Chapter 7**. Besides, an outlook on the future of the membrane-assisted light alkane NODH technology is provided, including the main benefits and remaining challenges. Moreover, it offers directions for future research areas that need to be explored to further demonstrate the viability of this technology.

References

1.   Stephan, D. On-purpose propylene: the rise of on-purpose propylene: How to supply the world's hunger for plastic. https://www.process-worldwide.com/the-rise-of-on-purpose-propylene-how-to-supply-the-worlds-hunger-for-plastic-a-499478/ (accessed September 2020).

2.   Statista Research Department. Total revenue of the chemical industry worldwide from 2005 to 2022. https://www.statista.com/statistics/302081/revenue-of-global-chemical-industry/ (accessed October 2024).

3.   Odyssee Mure. Energy consumption trend by industrial branch. https://www.odyssee-mure.eu/publications/efficiency-by-sector/industry/energy-consumption-trend-industrial-branch-eu.html (accessed November 2023).

4.   Statista Research Department. Energy consumption in the manufacturing industries in the United States as of 2018, by type. https://www.statista.com/statistics/1011858/us-manufacturing-sectors-energy-consumption-by-industry/ (accessed April 2023).

5.   Statista Research Department. Energy consumption distribution of the chemical industry in the European Union (EU-27) in 2022, by source. https://www.statista.com/statistics/1307323/eu-chemical-industry-energy-consumption-share-by-source/ (accessed February 2025).

6.   United Nations Framework Convention on Climate Change. New analysis of national climate plans: insufficient progress made, COP28 must set stage for immediate action. https://unfccc.int/news/new-analysis-of-national-climate-plans-insufficient-progress-made-cop28-must-set-stage-for-immediate (accessed February 2024).

7.   United Nations. For a livable climate: Net-zero commitments must be backed by credible action. https://www.un.org/en/climatechange/net-zero-coalition (accessed December 2024).

8.   Netherlands Ministry of Economic Affairs. Energierapport - transitie naar duurzaam. https://www.rijksoverheid.nl/documenten/rapporten/2016/01/18/energierapport-transitie-naar-duurzaam (accessed November 2023).

9.   United States Department of Energy. Industrial decarbonization roadmap. https://www.energy.gov/industrial-technologies/doe-industrial-decarbonization-roadmap (accessed March 2024).

10. Investopedia. Who are the consumers of the chemicals sector? https://www.investopedia.com/ask/answers/042015/what-types-industries-are-main-consumers-products-chemicals-sector.asp (accessed June 2024).

11. Rabenhorst, R. On-purpose: what's driving new propane dehydrogenation projects in North America? https://rbnenergy.com/on-purpose-whats-driving-new-propane-dehydrogenation-projects-in-north-america (accessed June 2020).

12. Agarwal, A., Sengupta, D. & El-halwagi, M. Sustainable process design approach for on-purpose propylene production and intensification. *ACS Sustain. Chem. Eng.* **6**, 2407–2421 (2018).

13. Zimmermann, H. & Walzl, R. Ethylene. in *Ullmann's Encyclopedia of Industrial Chemistry* (Wiley-VCH Verlag GmbH & Co. KGaA, Weinheim, Germany, 2009). doi:https://doi.org/10.1002/14356007.a10_045.pub3.

14. Sattler, J. J. H. B., Ruiz-Martinez, J., Santillan-Jimenez, E. & Weckhuysen, B. M. Catalytic dehydrogenation of light alkanes on metals and metal oxides. *Chem. Rev.* **114**, 10613–10653 (2014).

15. Bidwai, S. Propylene market. https://www.precedenceresearch.com/propylene-market (accessed October 2023).

16. Bidwai, S. Ethylene market. https://www.precedenceresearch.com/ethylene-market (accessed October 2024).

17. Bhasin, M. M., Mccain, J. H., Vora, B. V., Imai, T. & Pujad, P. R. Dehydrogenation and oxydehydrogenation of paraffins to olefins. *Appl. Catal. A: Gen.* **221**, 397–419 (2001).

18. Grasselli, R. K., Stern, D. L. & Tsikoyiannis, J. G. Catalytic dehydrogenation (DH) of light paraffins combined with selective hydrogen combustion (SHC) I . DH → SHC → DH catalysts in series (co-fed process mode). *Appl. Catal. A: Gen.* **189**, 1–8 (1999).

19. Nawaz, Z. Light alkane dehydrogenation to light olefin technologies: A comprehensive review. *Rev. Chem. Eng.* **31**, 413–436 (2015).

20. Baldwin, R. M., Nimlos, M. R. & Zhang, Y. Techno-economic, feasibility, and life cycle analysis of renewable propane - final report. (2022) doi:https://doi.org/10.2172/1891468.

21. Pal, S., Kumar, A., Sharma, A. K., Ghodke, P. K., Pandey, S. & Patel, A. Recent advances in catalytic pyrolysis of municipal plastic waste for the production of hydrocarbon fuels. *Processes* **10**, 1497 (2022).

22.   Maddah, H. A. A comparative study between propane dehydrogenation (PDH) technologies and plants in Saudi Arabia. *American Scientific Research Journal for Engineering, Technology, and Sciences (ASRJETS)* **45**, 49–63 (2018).

23.   Bai, P., Liu, D., Wu, P. & Yan, Z. Catalytic dehydrogenation of propane to propene: Catalyst development, mechanistic aspects and reactor design. *Rev. Adv. Sci. Eng*. **3**, 180–195 (2014).

24.   Champagnie, A. M., Tsotsis, T. T., Minet, R. G. & Wagner, E. The study of ethane dehydrogenation in a catalytic membrane reactor. *J. Catal*. **134**, 713–730 (1992).

25.   Deibert, W., Ivanova, M. E., Baumann, S. & Guillon, O. Ion-conducting ceramic membrane reactors for high-temperature applications. *J. Membr. Sci*. **543**, 79–97 (2017).

26.   Gallucci, F., Medrano, J. A., Fernandez, E., Melendez, J., van Sint Annaland, M. & Pacheco-Tanaka, D. A. Advances on high temperature Pd-based membranes and membrane reactors for hydrogen purification and production. *J. Membr. Sci. Res*. **3**, 142–156 (2017).

27.   Gallucci, F., Fernandez, E., Corengia, P. & Sint, M. Van. Recent advances on membranes and membrane reactors for hydrogen production. *Chem. Eng. Sci*. **92**, 40–66 (2013).

28.   Polfus, J. M., Xing, W., Fontaine, M. L., Denonville, C., Henriksen, P. P. & Bredesen, R. Hydrogen separation membranes based on dense ceramic composites in the La27W5O55.5-LaCrO3 system. *J. Membr. Sci*. **479**, 39–45 (2015).

29.   Norby, T. & Haugsrud, R. Dense ceramic membranes for hydrogen separation. in *Nonporous Inorganic Membranes: for Chemical Processing* (eds. Sammells, A. F. & Mundschau, M. V.) 1–48 (Wiley-VCH Verlag GmbH & Co. KGaA, 2006).

30.   Malerød-fjeld, H., Clark, D., Yuste-tirados, I., Zanón, R., Catalán-martinez, D., Beeaff, D., Morejudo, S. H., Vestre, P. K., Norby, T., Haugsrud, R., Serra, J. M. & Kjølseth, C. Thermo-electrochemical production of compressed hydrogen from methane with near-zero energy loss. *Nat. Energy* **2**, 923–931 (2017).

31.   Clark, D., Malerød-Fjeld, H., Budd, M., Yuste-Tirados, I., Beeaff, D., Aamodt, S., Nguyen, K., Ansaloni, L., Peters, T., Vestre, P. K., Pappas, D. K., Valls, M. I., Remiro-Buenamañana, S., Norby, T., Bjørheim, T. S., Serra, J. M. & Kjølseth, C. Single-step hydrogen production from NH3, CH4, and biogas in stacked proton ceramic reactors. *Science* **376**, 390–393 (2022).

32.   Srinivasan, B. R. & Davis, B. H. The structure of platinum-tin reforming catalysts. *Platin. Met. Rev*. **36**, 151–163 (1992).

33. Gómez-Quero, S., Tsoufis, T., Rudolf, P., Makkee, M., Kapteijn, F. & Rothenberg, G. Kinetics of propane dehydrogenation over Pt-Sn/Al2O3. *Catal. Sci. Technol.* **3**, 962–971 (2013).

34. Jablonski, E. L., Castro, A. A., Scelza, O. A. & Miguel, S. R. De. Effect of Ga addition to Pt/Al2O3 on the activity, selectivity and deactivation in the propane dehydrogenation. *Appl. Catal. A: Gen.* **183**, 189–198 (1999).

35. Sun, M., Zhai, S., Weng, C., Wang, H. & Yuan, Z. Y. Pt-based catalysts for direct propane dehydrogenation: Mechanisms revelation, advanced design, and challenges. *Mol. Catal.* **558**, 114029 (2024).

36. Cortright, R. D., Hill, J. M. & Dumesic, J. A. Selective dehydrogenation of isobutane over supported Pt/Sn catalysts. *Catal. Today* **55**, 213–223 (2000).

37. Larsson, M., Hult, M., Blekkan, E. A. & Andersson, B. The effect of reaction conditions and time on stream on the coke formed during propane dehydrogenation. *J. Catal.* **53**, 44–53 (1996).

38. Barias, O. A., Holmen, A. & Blekkan, E. A. Propane dehydrogenation over supported Pt and Pt–Sn catalysts: catalyst preparation, characterization, and activity measurements. *J. Catal.* **158**, 1–12 (1996).

39. Aguilar-rios, G., Salas, P., Valenzuela, M. A., Armendariz, H., Wang, J. A. & Salmones, J. Propane dehydrogenation activity of Pt and Pt–Sn catalysts supported on magnesium aluminate: Influence of steam and hydrogen. *Catal. Letters* **60**, 21–25 (1999).

40. Lai, Y., He, S., Li, X., Sun, C. & Seshan, K. Dehydrogenation of n-dodecane over PtSn/MgAlO catalysts: Investigating the catalyst performance while monitoring the products. *Appl. Catal. A: Gen.* **469**, 74–80 (2014).

41. Pakhomov, N. A., Buyanov, R. A., Moroz, E. M., Kotelnikov, G. R. & Patanov, V. A. Medium effect in thermal pretreatment on the state and catalytic properties of platinum supported on zinc-aluminium spinel. *React. Kinet. Catal. Lett.* **9**, 257–263 (1978).

42. Aguilar-rios, G., Valenzuela, M. A., Salas, P., Armendariz, H., Bosch, P., Del Toro, G., Silva, R., Bertín, V., Castillo, S., Ramírez-Solís, A. & Schifter, I. Hydrogen interactions and catalytic properties of platinum-tin supported on zinc aluminate. *Appl. Catal. A: Gen.* **127**, 65–75 (1995).

43. Heynderickx, G. J., Schools, E. M. & Marin, G. B. Optimization of the decoking procedure of an ethane cracker with a steam/air mixture. *Ind. Eng. Chem. Res.* **45**, 7520–7529 (2006).

44. Li, Q., Sui, Z., Zhou, X. & Chen, D. Kinetics of propane dehydrogenation over Pt–Sn/Al2O3 catalyst. *Appl. Catal. A: Gen.* **398**, 18–26 (2011).

45.   Ricca, A., Montella, F., Iaquaniello, G., Palo, E. & Salladini, A. Membrane assisted propane dehydrogenation: Experimental investigation and mathematical modelling of catalytic reactions. *Catal. Today* **331**, 43–52 (2019).

46.   van Sint Annaland, M., Kuipers, J. A. M. & van Swaaij, W. P. M. A kinetic rate expression for the time-dependent coke formation rate during propane dehydrogenation over a platinum alumina monolithic catalyst. *Catal. Today* **66**, 427–436 (2001).

47.   Lobera, M. P., Téllez, C., Herguido, J. & Menéndez, M. Transient kinetic modelling of propane dehydrogenation over a Pt–Sn–K/Al2O3 catalyst. *Appl. Catal. A: Gen.* **349**, 156–164 (2008).

48.   Rashidi, M., Nikazar, M. & Rahmani, M. Kinetic modeling of simultaneous dehydrogenation of propane and isobutane on Pt-Sn-K/Al2O3 catalyst. *Chem. Eng. Res. Des.* **95**, 239–247 (2014).

49.   Larsson, M., Henriksson, N. & Andersson, B. Investigation of the kinetics of a deactivating system by transient experiments. *Appl. Catal. A: Gen.* **166**, 9–19 (1998).

50.   Farjoo, A., Khorasheh, F., Niknaddaf, S. & Soltani, M. Kinetic modeling of side reactions in propane dehydrogenation over Pt-Sn/y-Al2O3 catalyst. *Scientia Iranica* **18**, 458–464 (2011).

51.   Sheintuch, M., Liron, O., Ricca, A. & Palma, V. Propane dehydrogenation kinetics on supported Pt catalyst. *Appl. Catal. A: Gen.* **516**, 17–29 (2016).

52.   Cortright, R. D. & Dumesic, J. A. Effects of potassium on silica-supported Pt and Pt/Sn catalysts for isobutane dehydrogenation. *J. Catal.* **157**, 576–583 (1995).

53.   Cortright, R. D., Levin, P. E. & Dumesic, J. A. Kinetic studies of isobutane dehydrogenation and isobutene hydrogenation over Pt/Sn-based catalysts. *Ind. Eng. Chem. Res.* **37**, 1717–1723 (1998).

54.   Natal-Santiago, M. A., Podkolzin, S. G., Cortright, R. D. & Dumesic, J. A. Microcalorimetric studies of interactions of ethene, isobutene, and isobutane with silica-supported Pd, Pt, and PtSn. *Catal. Letters.* **45**, 155–163 (1997).

55.   Biloen, P., Dautzenberg, F. M. & Sachtler, W. M. H. Catalytic dehydrogenation of propane to propene over platinum and platinum-gold alloys. *J. Catal.* **50**, 77–86 (1977).

56.   Barghi, B., Fattahi, M. & Khorasheh, F. Kinetic modeling of propane dehydrogenation over an industrial catalyst in the presence of oxygenated compounds. *React. Kinet. Mech. Catal.* **107**, 141–155 (2012).

57. Kreuer, K. D. Aspects of the formation and mobility of protonic charge carriers and the stability of perovskite-type oxides. *Solid State Ion.* **125**, 285–302 (1999).

58. Iwahara, H., Esaka, T., Uchida, H. & Maeda, N. Proton conduction in sintered oxides and its application to steam electrolysis for hydrogen production. *Solid State Ion.* **3–4**, 359–363 (1981).

59. Haugsrud, R., Larring, Y. & Norby, T. Proton conductivity of Ca-doped Tb2O3. *Solid State Ion.* **176**, 2957–2961 (2005).

60. Chen, Y., Cheng, S., Chen, L., Wei, Y., Ashman, P. J. & Wang, H. Niobium and molybdenum co-doped La5.5WO11.25-d membrane with improved hydrogen permeability. *J. Membr. Sci.* **510**, 155–163 (2016).

61. Amsif, M., Magrasó, A., Marrero-López, D., Ruiz-Morales, J. C., Canales-Vázquez, J. & Núñez, P. Mo-substituted lanthanum tungstate La28-yW4+yO54+δ: A competitive mixed electron-proton conductor for gas separation membrane applications. *Chem. Mat.* **24**, 3868–3877 (2012).

62. Zhu, Z., Hou, J., He, W. & Liu, W. High-performance Ba(Zr0.1Ce0.7Y0.2)O3-δ asymmetrical ceramic membrane with external short circuit for hydrogen separation. *J. Alloy. Comp.* **660**, 231–234 (2016).

63. Deibert, W., Ivanova, M. E., Meulenberg, W. A., Vaßen, R. & Guillon, O. Preparation and sintering behaviour of La5.4WO12-δ asymmetric membranes with optimised microstructure for hydrogen separation. *J. Membr. Sci.* **492**, 439–451 (2015).

64. Meng, Y., Gao, J., Zhao, Z., Amoroso, J., Tong, J. & Brinkman, K. S. Review : recent progress in low-temperature proton-conducting ceramics. *J. Mater. Sci.* 9291–9312 (2019).

65. Galuszka, J., Giddings, T. & Clelland, I. Catalytic dehydrogenation of ethane in hydrogen membrane reactor. in *Inorganic Membranes for Energy and Environmental Applications* (Springer Science + Business Media, LLC, 2009).

66. Shi, Z., Luo, J., Wang, S., Sanger, A. R. & Chuang, K. T. Protonic membrane for fuel cell for co-generation of power and ethylene. *J. Power Sources* **176**, 122–127 (2008).

67. Ding, D., Zhang, Y., Wu, W., Chen, D., Liu, M. & He, T. A novel low-thermal-budget approach for the co-production of ethylene and hydrogen via the electrochemical non-oxidative deprotonation of ethane. *Energy Environ. Sci.* **11**, 1710–1716 (2018).

68. Wu, W., Wang, L. C., Hu, H., Bian, W., Gomez, J. Y., Orme, C. J., Ding, H., Dong, Y., He, T., Li, J. & Ding, D. Electrochemically engineered, highly energy-efficient

conversion of ethane to ethylene and hydrogen below 550 °C in a protonic ceramic electrochemical cell. *ACS Catal.* **11**, 12194–12202 (2021).

69.   Weyten, H., Luyten, J., Keizer, K., Willems, L. & Leysen, R. Membrane performance: The key issues for dehydrogenation reactions in a catalytic membrane reactor. *Catal. Today* **56**, 3–11 (2000).

70.   Gbenedio, E., Wu, Z., Hatim, I., Kingsbury, B. F. K. & Li, K. A multifunctional Pd/alumina hollow fibre membrane reactor for propane dehydrogenation. *Catal. Today* **156**, 93–99 (2010).

71.   Peters, T. A., Liron, O., Tschentscher, R., Sheintuch, M. & Bredesen, R. Investigation of Pd-based membranes in propane dehydrogenation (PDH) processes. *Chem. Eng. J.* **305**, 191–200 (2016).

72.   Gimeno, M. P., Wu, Z. T., Soler, J., Herguido, J., Li, K. & Menéndez, M. Combination of a two-zone fluidized bed reactor with a Pd hollow fibre membrane for catalytic alkane dehydrogenation. *Chem. Eng. J.* **155**, 298–303 (2009).

73.   Schäfer, R., Noack, M., Kölsch, P., Stöhr, M. & Caro, J. Comparison of different catalysts in the membrane-supported dehydrogenation of propane. *Catal. Today* **82**, 15–23 (2003).

74.   Matsuda, T., Koike, I., Kubo, N., Kikuchi, E. & Kikuchi, E. Dehydrogenation of isobutane to isobutene in a palladium membrane reactor. *Appl. Catal. A: Gen.* **96**, 3–13 (1993).

75.   Shu, J., Grandjean, B. P. A., Kaliaguine, S., Ciavarella, P., Giroir-Fendler, A. & Dalmon, J. -A. Gas permeation and isobutane dehydrogenation over very thin Pd/ceramic membranes. *Can. J. Chem. Eng.* **75**, 712–720 (1997).

76.   Babita, K., Sridhar, S. & Raghavan, K. V. Membrane reactors for fuel cell quality hydrogen through WGSR – Review of their status, challenges and opportunities. *Int. J. Hydrog. Energy* **36**, 6671–6688 (2011).

77.   Morejudo, S. H., Zanón, R., Escolástico, S., Yuste-Tirados, I., Malerød-Fjeld, H., Vestre, P. K., Coors, W. G., Martínez, A., Norby, T., Serra, J. M. & Kjølseth, C. Direct conversion of methane to aromatics in a catalytic co-ionic membrane reactor. *Science* **353**, 563–566 (2016).

78.   Deshmukh, S. A. R. K., Heinrich, S., Mörl, L., van Sint Annaland, M. & Kuipers, J. A. M. Membrane assisted fluidized bed reactors: Potentials and hurdles. *Chem. Eng. Sci.* **62**, 416–436 (2007).

79.   Liu, L., Bhowmick, A., Cheng, S., Blazquez, B. H., Pan, Y., Zhang, J., Zhang, Y., Shu, Y., Tran, D. T., Luo, Y., Ierapetritou, M., Zhang, C. & Liu, D. Alkane

dehydrogenation in scalable and electrifiable carbon membrane reactor. *Cell Rep. Phys. Sci.* **4**, 101692 (2023).

80. Special Power Sources. A comprehensive comparison of planar and tubular solid oxide fuel cells. https://spsources.com/a-comprehensive-comparison-of-planar-and-tubular-solid-oxide-fuel-cells/ (accessed September 2024).

81. Heinz, M. V. F., Graeber, G., Landmann, D. & Battaglia, C. Pressure management and cell design in solid-electrolyte batteries, at the example of a sodium-nickel chloride battery. *J. Power Sources* **465**, 228268 (2020).

82. Community Research and Development Information Service. Final report summary - ELECTRA (high temperature electrolyser with novel proton ceramic tubular modules of superior efficiency, robustness, and lifetime economy). https://cordis.europa.eu/project/id/621244/reporting (accessed September 2024).

83. Skyquest. Global Ethylene Market Insights. https://www.skyquestt.com/report/ethylene-market (accessed October 2023).

84. The Business Research Company. Propylene Global Market Report 2023. https://www.thebusinessresearchcompany.com/report/propylene-global-market-report (accessed October 2023).

Chapter 2

Deviations from ideal Langmuir adsorption govern surface coverages in ethane dehydrogenation on Pt-Sn/ZnAl$_2$O$_4$

Summary

Non-oxidative dehydrogenation (NODH) of light alkanes over Pt-based catalysts has been primarily studied at low alkane, H$_2$, and olefin partial pressures, resulting in Langmuir-Hinshelwood-based reaction mechanisms involving coverage independent adsorption thermodynamics. Here, we have combined detailed reaction kinetics and transition state treatments to demonstrate that ethane NODH on a Pt-Sn/ZnAl$_2$O$_4$ catalyst is strongly affected by the hydrogen and ethylene surface coverages. We found that high hydrogen and ethylene surface coverages lead to important deviations from ideal Langmuir adsorption. For hydrogen adsorption, this was attributed to a combination of lateral interactions and reduced hydrogen surface mobility at high surface coverages. By contrast, for ethylene the deviation from Langmuir adsorption was ascribed to a stronger ethylene adsorption configuration existing for low surface coverages. Exploring the impact of large changes in hydrogen and ethylene partial pressures on this reaction is highly relevant when integrating this reaction in a membrane reactor where large concentration gradients, and thus gradients in the surface coverage distribution, are expected along the reactor bed.

2.1. Introduction

Light olefins are essential building blocks to produce plastics, oxygenates, and important chemical intermediates [1]. The demand for these light alkenes is ever-increasing and forecasted to remain high in the coming decades, due to growing world population and global wealth [2,3]. Conventionally, light olefins, such as ethylene and propylene, are produced via steam cracking and fluid catalytic cracking [1,4]. Unfortunately, these cracking processes are petroleum-based and highly energy and carbon intensive [5]. Despite these shortcomings, new ethane cracking plants are currently under construction in Europe, Asia, and the U.S. to cope with the increasing demand [6–12].

Developing alternative processes for olefin production is a challenging undertaking, because of the sheer scale of the ethylene (ca. 130 billion USD in 2022 [13,14]) and propylene markets (ca. 105 billion USD in 2022 [15,16]), which requires scalable technologies that can compete with existing ones in terms of energy efficiency, carbon footprint, and production costs. Broadly speaking, the main alternative olefin production routes are based on (i) alkane dehydrogenation, (ii) olefin metathesis, and (iii) methanol to olefins processes. Considering the market prices of reactants and products of these processes, alkane dehydrogenation represents the most attractive option [4]. Non-oxidative dehydrogenation (NODH) is generally preferred to oxidative dehydrogenation (ODH) for industrial applications, as the formation of consecutive oxidation products in ODH reduces olefin selectivity [5]. Ethylene and propylene can be produced via NODH of ethane and propane, respectively, as presented in **Equation 2.1** and **2.2**.

$$C_2H_6 \leftrightharpoons C_2H_4 + H_2 \qquad (\Delta H^0_{298} = +137.0 \text{ kJ/mol}) \qquad (2.1)$$

$$C_3H_8 \leftrightharpoons C_3H_6 + H_2 \qquad (\Delta H^0_{298} = +124.3 \text{ kJ/mol}) \qquad (2.2)$$
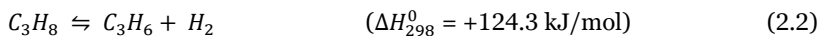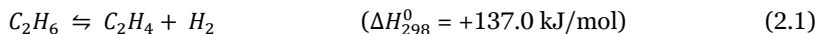
Light alkane NODH is endothermic, i.e. high temperatures are required, and it is limited by thermodynamic equilibrium (**Equation 2.1** and **2.2**). Propane NODH is industrially operated between 500-650 °C with single-pass olefin yields of about 40% [17]. Ethane NODH is not industrialized, because achievable single-pass yields are even lower compared to propane NODH, due to stringent thermodynamic equilibrium limitations (i.e. 28% ethylene yield at 650 °C). Instead, ethane steam cracking is preferred for the production of ethylene [18].

The prototypical catalyst for light alkane NODH is based on platinum and platinum-tin alloys supported on metal oxides. Here, the Pt is intrinsically highly active for hydrocarbon conversion, readily leading to deep dehydrogenation toward carbon-rich surface species like coke. This in turn inhibits catalyst selectivity and activity. For this reason, Pt catalysts are often modified with promoters like Zn, Ga, Ge, Ag, and Sn [19,20]. Particularly, Sn promotion has led to enhanced catalyst stability and olefin selectivity [21]. A basic $ZnAl_2O_4$ spinel-type support material is preferred to more standard and more acidic alumina

catalyst support materials, because the acid sites on the support enhance undesirable cracking and carbon deposition reactions [22,23].

In contrast to propane [23–31] and isobutane [21,27,32–35] NODH the literature on ethane NODH reaction kinetics on Pt is rather scarce. In the case of C3-C4 alkanes, exponential or Langmuir-Hinshelwood-Hougen-Watson (LHHW) kinetics have shown good agreement with experimental results. Despite all these efforts, there is still considerable debate about the mechanism of light paraffin NODH on Pt catalysts. The main discrepancies are related to the rate-determining step (RDS) and the type of surface species. The RDS is generally claimed to be a C-H cleavage step, either in the form of dissociative adsorption of the alkane [24,29] or in the form of a surface C-H bond cleavage after adsorption [27,30,36,37]. Besides, the type of surface species included in the LHHW denominator range from only the olefin [23,31], the alkane and the olefin [30], hydrogen and the olefin [24], to all possible products and byproducts formed [23,29,37]. These reaction mechanisms are typically based on catalytic data that is obtained within a narrow window of alkane, alkene, and H_2 partial pressures, complicating the extrapolation of these models outside this operational window. Understanding the impact of varying hydrogen and olefin partial pressures on the alkane NODH reaction mechanism is particularly relevant, because one of the most promising strategies to increase the conversion in alkane NODH is to shift the reaction equilibrium toward olefins by *in situ* hydrogen removal.

The selective separation of hydrogen from a propane NODH reaction mixture has been demonstrated for dense metallic [38] and dense ceramic [39,40] membranes. Hydrogen transport through dense metallics is governed by a gradient in H_2 chemical potential. The same holds for dense ceramic mixed proton-electron conducting (MPEC) membranes. By contrast, dense ceramic proton-conducting electrolysis cell (PCEC) membranes can be driven electrochemically as the H_2 transport is driven by a gradient in H_2 electrochemical potential. The additional advantage of PCECs is that it enables the electrification of the process while increasing olefin yields. In this strategy, olefin partial pressures will be much higher and H_2 partial pressures will be much lower in comparison to typical catalytic testing conditions, which might lead to changes in the surface coverage distribution and/or the RDS of the reaction. In this contribution, we carefully assessed this issue by interrogating the reaction mechanism of ethane NODH on a Pt-Sn/ZnAl$_2$O$_4$ catalyst using rigorous reaction kinetics in combination with kinetic modeling and catalyst characterization.

2.2. Experimental

2.2.1.   Materials and instrumentation

The ZnAl$_2$O$_4$ catalyst support was synthesized using Zn(NO$_3$)$_2$•6H$_2$O (98%, extra pure, Acros Organics) and Al(NO$_3$)$_3$•9H$_2$O (99+%, for analysis, Acros Organics). In addition, the following precursors were used for wet impregnation of the support: H$_2$PtCl$_6$•6H$_2$O (99.95%, Alfa Aesar) and SnCl$_4$•5H$_2$O (98%, Alfa Aesar). Also, hydrochloric acid (HCl,

fuming, 37%, for analysis, EMSURE®, Merck KGaA) and ammonium hydroxide solution (25% NH_3 basis, Sigma-Aldrich) were used as pH-adjusting agents in the catalyst synthesis. For the catalytic ethane NODH tests, ethane 2.5 (≥99.5%, Linde plc) was used as feedstock.

Nitrogen physisorption was carried out using a Micromeritics TriStar Surface Area and Porosity Analyzer. A degassing temperature of 300 °C was applied. The Brunauer-Emmett-Teller (BET) adsorption theory for multilayer adsorption was fitted to the obtained adsorption data. Besides, CO chemisorption was performed in a Micromeritics ChemiSorb 2750 pulse chemisorption system. Before chemisorbing CO, the catalyst samples were pretreated in a stream of H_2 at elevated temperature (400 °C, 1 h, heating rate: 10 °C/min).

X-ray fluorescence (XRF) was performed using a Bruker s8 Tiger Series WDXRF spectrometer. Fused bead analysis was performed to determine the Zn, Al, and Sn contents, where fused beads of the concerned samples were prepared using an xrFuse2 fusion machine of XRF Scientific in a 1/8 sample/flux ratio (flux = 66% lithium tetraborate, 34% lithium metaborate, 0.2% lithium bromide). The Pt loading was determined via powder-based XRF analysis. X-ray diffraction (XRD) was applied using a Bruker D2 PHASER XRD system, in which the spectra were obtained between 10° and 90° 2θ diffraction angles, using a total scanning time of 35 minutes with one second per step.

Scanning transmission electron microscopy high-angle annular dark-field (STEM-HAADF) analysis was applied to identify the size and shape of the catalyst active sites. Herein, energy dispersive X-ray spectroscopy (EDS) was used to determine the elemental composition and distribution of the active sites. The catalyst samples were reduced *ex situ* in a stream of H_2 (10 ml/min STP) at 550 °C for 1 h. After cooling down in a stream of inert N_2 (80 ml/min), the catalyst samples were temporarily exposed to ambient air before conducting the STEM-HAADF analysis. STEM imaging was carried out in a probe-corrected Titan (Thermo Fisher Scientific, formerly FEI) operated at 300 kV and equipped with a high brightness X-FEG and a spherical aberration Cs-corrector (CEOS) for the condenser system to provide sub-Ångström probe size. Besides, EDS was performed with an Ultim Max detector (Oxford Instruments).

Lastly, X-ray photoelectron spectroscopy (XPS) was performed to determine the surface composition and surface charge of fresh and pre-activated Pt-Sn/$ZnAl_2O_4$. The pre-activation step was performed in a pre-treatment chamber of the XPS apparatus right before performing the XPS analysis, without intermediate exposure to air. The pre-activation step was performed in a gas stream containing 10% of H_2 and 90% of N_2 at 550 °C for 1 h (heating rate: 10 °C/min). The XPS measurements were conducted in a SPECS spectrometer equipped with a PHOIBOS 150 MCD analyzer working at fixed pass energy of 35 eV and 0.1 eV resolution for the studied zones. The XPS spectra were obtained at room temperature under ultra-high vacuum (10^{-10} mbar(a)) using Al Kα radiation at 250 W and 12.5 kV. Prior to analysis, every sample was pressed into a disk. The Al 2p peak was

fixed at 74.3 eV in the binding energy correction. All spectra were analyzed using CasaXPS software. High resolution spectra of the regions corresponding to Al 2p + Pt 4f, Pt 4d, Sn 3d + O 2s, Zn 2p, O 1s and C 1s levels were acquired and quantified.

2.2.2.   Catalyst synthesis and activation

2.2.2.1.   Catalyst support preparation: coprecipitation

The ZnAl$_2$O$_4$ catalyst support was prepared via known methods based on coprecipitation of Zn(NO$_3$)$_2$•6H$_2$O and Al(NO$_3$)$_3$•9H$_2$O precursors from an aqueous solution [32,41–47]. Ammonium hydroxide solution was added dropwise to a pH of 7.5 while stirring. The atomic Al/Zn ratio supplied in the support synthesis was about 2.3, as an excess of aluminum is needed to ensure spinel formation. After adding ammonium hydroxide, the system was heated to 50 °C while stirring to obtain a gel. Subsequently, the gel was washed three times with Milli-Q water to remove traces of ammonia. Then, the gel was filtered using a Büchner funnel under vacuum conditions to collect a white precipitate. This precipitate was then dried in an oven (105 °C) overnight. Afterward, the solids were mortared into particles before calcination in a stream of air at 800 °C for 8 h (heating rate: 5 °C/min).

2.2.2.2.   Catalyst support functionalization: sequential wet impregnation

The prepared ZnAl$_2$O$_4$ support material was functionalized with Pt-Sn catalyst active phases via known methods based on sequential wet impregnation using SnCl$_4$ and H$_2$PtCl$_6$ precursors [32,41,42,48,49]. First, the ZnAl$_2$O$_4$ support was impregnated with Sn using an acidified solution of SnCl$_4$ in ethanol (ca. 100 mM HCl in ethanol). The impregnated solids were aged for 30 minutes and then dried for 15 minutes at 60 °C under vacuum conditions in a rotary evaporator. Afterward, the Sn-impregnated solids were impregnated with Pt using a non-acidified solution of H$_2$PtCl$_6$ in ethanol. The impregnated solids were again aged for 30 minutes and then dried for 15 minutes at 60 °C under vacuum conditions in a rotary evaporator. In the following step, the catalyst particles were calcined at 550 °C (heating rate: 2 °C/min) for 4 h in the presence of air. Subsequently, the particles were mortared and sieved into the following particle size fractions: <45 μm, 45-125 μm, and 125-250 μm. Solely the fraction below 45 μm was used in the catalytic tests, as internal mass transfer limitations were excluded for this particle size fraction (**Supporting Information 2.C1**). Prior to catalytic testing, the catalyst was activated in a stream of H$_2$ (10 ml/min STP) at 550 °C for 1 h inside the catalytic testing setup.

2.2.3.   Catalytic testing

The catalytic tests were performed using a continuous flow fixed bed reactor setup. The prepared Pt-Sn/ZnAl$_2$O$_4$ catalyst was diluted with quartz particles (quartz, fine granular, SiO$_2$, Merck KGaA, 125-250 μm) in approximately a 1/19 mass-based dilution to ensure isothermal catalyst bed operation. The catalyst bed was mounted in between pieces of

quartz wool into a quartz reactor tube (*I.D.* = 4 mm, *O.D.* = 6 mm, *L* = 450 mm) containing a constriction halfway the tube (ca. 2 mm). The latter constriction ensured that the catalyst bed was situated in the same position during all tests. A thermocouple was located on the inner side of the tubular furnace in the immediate vicinity of the catalyst bed to control the reaction temperature. A schematic flow diagram of the used experimental setup is available as **Supporting Information 2.A**. The setup was equipped with ethane, ethylene, and H_2 gas lines to be able to vary partial pressures. Besides, N_2 was used as a balancing gas. The reactor effluent stream was analyzed using an on-line gas chromatograph (GC, Varian Chrompack CP-3800), equipped with an Agilent GS-GasPro GC column (60 m x 0.32 mm *I.D.*), and a flame ionization detector (FID). The additional specifications of the GC-FID were: FID temperature: 250 °C, injection temperature: 220 °C, He flow rate: 1.5 ml/min, temperature ramp column: 40-140 °C.

The ethane flow was started immediately after catalyst activation. Reactions were carried out at atmospheric pressure and at temperatures ranging from 475 °C to 550 °C. The ethane feed partial pressure was varied between 5-500 mbar(a), the H_2 feed partial pressure between 40-125 mbar(a), and the ethylene feed partial pressure between 0-25 mbar(a). Flows were controlled using Brooks mass flow controllers. The total flow rate was constant in all tests around 95 ml/min STP. Ethane conversion (χ_{eth}) and product selectivity (S_i) and yield (Y_i) were calculated as follows in this work:

$$\chi_{eth} = 1 - \frac{p_{eth}}{p_{eth,0}} \tag{2.3}$$

$$S_i = \frac{p_i}{p_{eth,0} - p_{eth}} \tag{2.4}$$

$$Y_i = \frac{p_i}{p_{eth.0}} \tag{2.5}$$

Here, the ethane partial pressure (p_{eth}) and ethane feed partial pressure ($p_{eth,0}$) were determined using a GC calibration curve for ethane. The only detected products were ethylene and methane. The ethylene partial pressure ($p_{i=ethylene}$) was determined using a calibration curve for ethylene, whilst the methane partial pressure ($p_{i=methane}$) was determined using the ethane calibration curve in combination with an FID response factor of 1.25 for methane relative to ethane [50]. Note that the total gas flow rate was considered constant along the reactor length, as the ethane concentration in most tests was below 4 vol% and the ethane conversion was below 15%. The quartz reactor tube was assumed to behave like a plug flow reactor. The relation between the mass based ethylene formation rate ($R_{m,C2H4}$, in $mol_{C2H4}/kg_{cat} \cdot s$), the experimentally measured ethylene yield (Y_{C2H4}, **Equation 2.5**), and the apparent turnover frequency of ethylene formation ($TOF_{app,C2H4}$, in $mol_{C2H4}/mol_{Pt,s} \cdot s$) is given by **Equation 2.6** (see **Supporting Information 2.L**).

$$R_{m,C2H4} = \frac{F_{C2H6,0} Y_{C2H4}}{m_{cat}} = \frac{TOF_{app,C2H4} \sigma_{Pt} \beta_{Pt}}{M_{W,Pt}} \tag{2.6}$$

In **Equation 2.6**, $F_{C2H6,0}$ represents the ethane molar feed flow rate (in mol/s), m_{cat} the mass of catalyst in the bed (in kg_{cat}), σ_{Pt} the Pt loading of the catalyst (in kg_{Pt}/kg_{cat}), β_{Pt} the Pt dispersion (in $mol_{Pt,s}/mol_{Pt}$), as determined using CO chemisorption, and $M_{W,Pt}$ the molar weight of Pt (in kg_{Pt}/mol_{Pt}). Herein, $mol_{Pt,s}$ indicates the number of moles of Pt exposed to the surface. We define an apparent TOF here, because the experimentally determined TOF is not necessarily equal to the true TOF, as it might be influenced by e.g. adsorption, concentration, and thermodynamic equilibrium effects.

2.3. Results and discussion

2.3.1. Catalyst synthesis and characterization

Detailed physicochemical characterization was conducted on the bare support ($ZnAl_2O_4$), Pt-, Sn-, and Pt-Sn containing catalysts (see **Table 2.1**) to determine the porous structure and concentration of active sites. The surface area and pore volume of the prepared $ZnAl_2O_4$ support are in line with values reported in literature for $ZnAl_2O_4$ supports prepared via coprecipitation methods [32,41,42,44,47]. The number-based Pt cluster size resulting from STEM-HAADF analysis differed from the CO chemisorption result. This is attributed to the existence of a limited number of large particles (>10 nm, see **Supporting Information 2.B**) that are not captured significantly by the number-based average particle size as determined using STEM-HAADF.

Table 2.1: Properties of the fresh catalyst samples. Surface area and pore volume were determined with N_2 physisorption, Pt and Sn loadings with XRF.

Characteristic:	$ZnAl_2O_4$	$Sn/ZnAl_2O_4$	$Pt/ZnAl_2O_4$	$Pt-Sn/ZnAl_2O_4$
Surface area (m^2/g)	76.3	71.4	71.3	66.0
Pore volume (cm^3/g)	0.165	0.157	0.146	0.138
Pt loading (wt.%)	-	-	3.6	4.0
Sn loading (wt.%)	-	2.5	-	1.6
Pt cluster size (nm)[1]	-	-	9.4	9.4*
Pt cluster size (nm)[2], number-based	-	-	1.6	3.8

*[1]Pt cluster size as determined using CO chemisorption, [2]Pt cluster size as determined using STEM-HAADF using a minimum of 200 particles. *Active Pt cluster size was determined assuming that only Pt adsorbs CO.*

X-ray diffraction (XRD) patterns were gathered after the different stages of impregnation, calcination, and activation of the catalyst to investigate possible structural changes (see

Supporting Information 2.B). The bare $ZnAl_2O_4$ support showed all characteristic $ZnAl_2O_4$ spinel peaks [47,51]. Sn addition did not lead to new XRD peaks, whilst calcined Pt-impregnated $ZnAl_2O_4$ showed a Pt metal phase in the XRD spectrum. Freshly calcined Pt-Sn/$ZnAl_2O_4$ also contained Pt metal phases, whilst pre-activated Pt-Sn/$ZnAl_2O_4$ showed Pt-Sn alloy XRD peaks, confirming the formation of a PtSn alloy under reducing atmospheres, which is in line with previous research on PtSn-based catalysts [30,52,53]. The XPS characterization revealed the reduction of oxidized Pt species to primarily metallic Pt^0 after reduction (see **Supporting Information 2.B**). By contrast, no clear indications of changes in the oxidation state of Sn, Zn, Al, nor O were identified. Furthermore, five different Pt species were discerned, related to the presence of Pt^{4+}, Pt^{2+}, Pt^0, platinum hydroxide, and hydrogen adsorbed Pt-H.
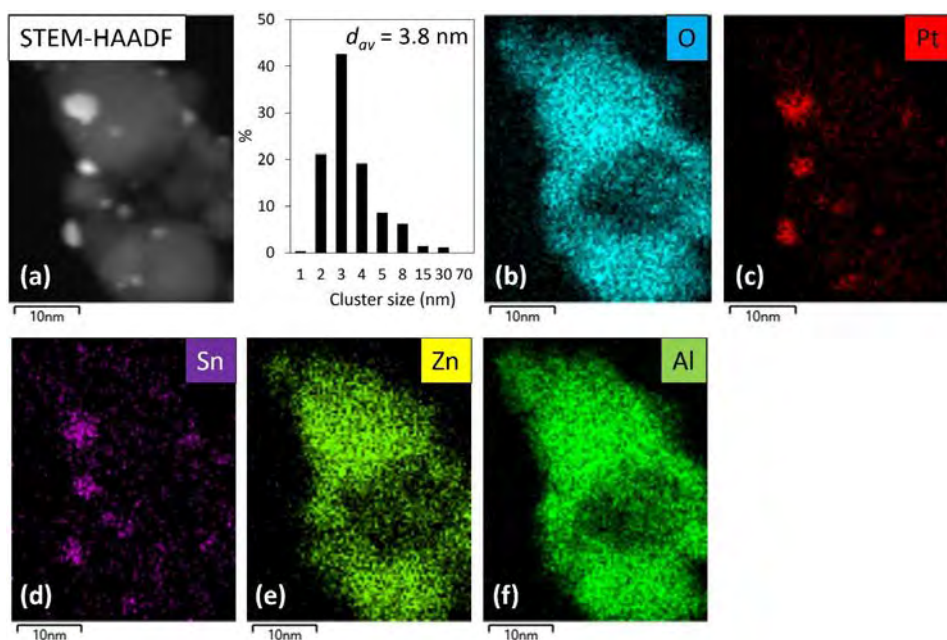
Figure 2.1: (a) STEM-HAADF image of fresh Pt-Sn/$ZnAl_2O_4$, including particle size distribution, and EDS elemental maps of (b) oxygen, (c) platinum, (d) tin, (e) zinc, and (f) aluminum.

To further investigate the distribution of Pt and Sn in the Pt-Sn/$ZnAl_2O_4$ catalyst, we conducted scanning transmission electron microscopy high-angle annular dark-field (STEM-HAADF) imaging, in combination with energy dispersive X-ray spectroscopy (EDS). The EDS elemental mapping of the STEM-HAADF images indicated metal particles containing Pt and Sn in the near vicinity of each other on top of a homogeneous support (see **Figure 2.1**). The close vicinity of Pt and Sn suggests the formation of a PtSn alloy. At the same time, the Sn was spread over an area larger than that of the Pt clusters, possibly indicating the presence of an oxidized tin phase near the PtSn.

2.3.2. Catalytic ethane dehydrogenation

Prior to the kinetic study, internal and external mass transfer limitations were experimentally excluded (see **Supporting Information 2.C1** and **2.C2**). We confirmed that a kinetic regime was attained when operating with Pt-Sn/ZnAl$_2$O$_4$ catalyst particles in the range 0-45 μm. Furthermore, we identified that the reactor is operating within a differential regime for catalyst-to-feed ratios (W/F_{ethane}) below 100 kg$_{cat}$•s/kg$_{ethane}$ (**Supporting Information 2.C5**). Since the ethane dehydrogenation reaction is limited by thermodynamic equilibrium (see **Supporting Information 2.C3**), the reversibility of the reaction was included in the evaluation of the reaction kinetics. Moreover, the kinetic tests were carried out within two different conversion regimes. In the first regime, the tests were performed at 40-60% of the thermodynamically attainable conversion level. In the second regime, the tests were performed at 70-90% of the thermodynamic maximum conversion to see the influence of the reaction reversibility on the reaction kinetics. The exact conditions used and the corresponding conversion levels and approaches to equilibrium are summarized in **Supporting Information 2.P**. In all tests, the Pt-Sn/ZnAl$_2$O$_4$ catalyst was diluted with inert quartz particles to ensure isothermal operation and to control the conversion level, as Pt is intrinsically highly active for hydrocarbon conversion. The used dilution fraction was about 0.95 (i.e. 95 wt.% bed diluent, 5 wt.% catalyst), which was sufficient to avoid channeling through the bed, following a relation proposed by Berger et al. [54] on the impact of bed dilution on the observed conversion level (see **Supporting Information 2.C4**). Lastly, the catalysts were tested in the steady state with minimum deactivation (see **Supporting Information 2.D**). Only in case of high cofed ethylene partial pressures, an extrapolation to initial activity was employed to estimate the reaction rate in absence of deactivation.

2.3.2.1. Kinetic testing

Throughout our investigations, the selectivity to ethylene was above 95% regardless of the temperature and partial pressures employed. Methane was detected as a byproduct. Apparent reaction orders in ethane, hydrogen, and ethylene were obtained by determining the influence of the respective partial pressures on the apparent turnover frequency of ethylene formation ($TOF_{app,ethylene}$).

The apparent ethane and hydrogen reaction orders on Pt-Sn/ZnAl$_2$O$_4$ were determined in the range of 40-60% of the theoretically attainable maximum conversion (see **Supporting Information 2.P**) and at temperatures ranging from 475 °C to 550 °C (**Figure 2.2a** and **2.2b**). The apparent ethane reaction order was about one for every temperature investigated. This is in line with alkane reaction orders previously reported for propane and isobutane kinetic studies [22,24,30,34,36]**.**
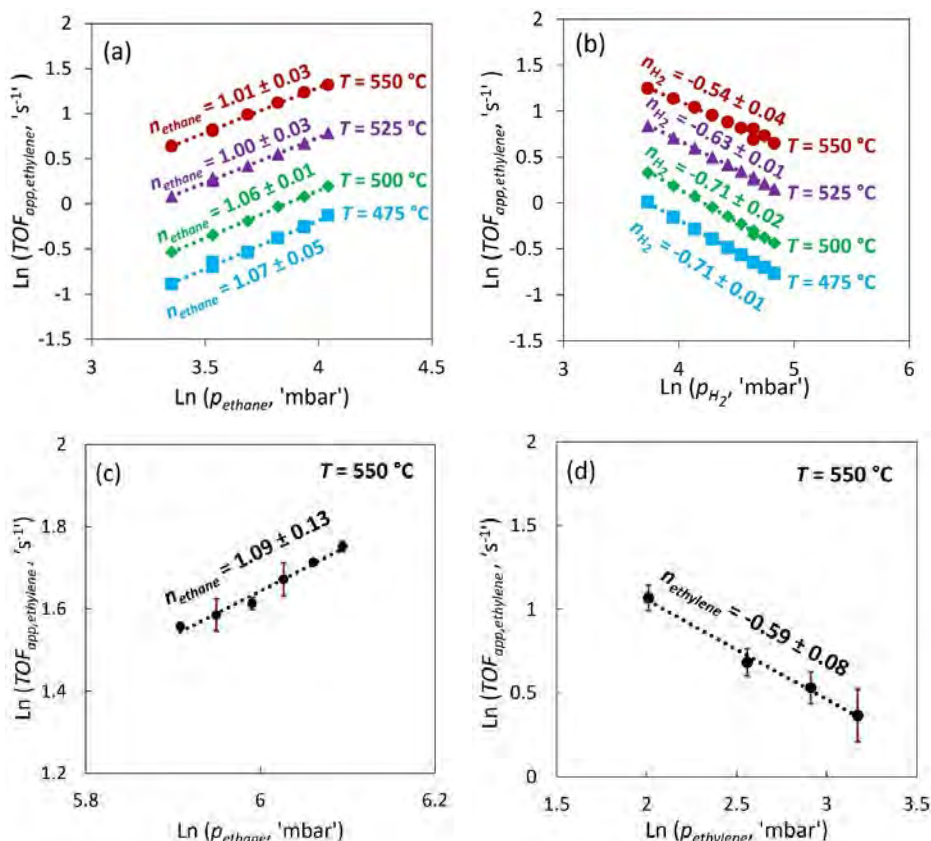
Figure 2.2: Apparent (a) ethane and (b) H_2 reaction orders along the temperature range 475-550 °C on Pt-Sn/ZnAl$_2$O$_4$. Conditions for (a): p_{ethane} = 20-60 mbar(a), p_{H2} = 105 mbar(a). Conditions for (b): p_{ethane} = 35 mbar(a), p_{H2} = 40-120 mbar(a). (c) Apparent ethane reaction order for high ethane partial pressures (360-450 mbar(a)), T = 550 °C, p_{H2} = 410 mbar(a). (d) Apparent ethylene reaction order at 550 °C, p_{ethane} = 150 mbar(a), p_{H2} = 75 mbar(a), $p_{ethylene}$ = 5-25 mbar(a).

The apparent hydrogen reaction order was negative at all temperatures (**Figure 2.2b**), indicating competitive adsorption of hydrogen with the reacting alkane. Moreover, the apparent hydrogen reaction order was about -0.5 at 550 °C and became more negative with lowering the temperature. As desorption is favored at higher temperatures, the rate inhibiting effect of the hydrogen was somewhat mitigated when increasing the temperature. This is in correspondence with the work by Cortright et al. on isobutane dehydrogenation [34]. Moreover, the existence of hydrogen covered Pt species is in line with the presence of Pt-H in Pt-Sn/ZnAl$_2$O$_4$ exposed to reductive atmospheres, as observed using XPS (**Supporting Information 2.B**).

In addition to the determination of the apparent ethane reaction order under low ethane partial pressure conditions (20-60 mbar(a), **Figure 2.2a**), the apparent ethane reaction order was also determined for much higher ethane partial pressures (360-450 mbar(a)) at 550 °C, as shown in **Figure 2.2c**. Similar to the low ethane partial pressure case, the apparent ethane reaction order was about one, which indicates that the surface coverage of ethane is low even for high ethane partial pressures. Lastly, the apparent ethylene reaction order was determined at 550 °C in the ethylene partial pressure range of 5-25 mbar(a). The result is shown in **Figure 2.2d**, where the y-axis represents the rate of ethylene formation, i.e. the detected amount of ethylene excluding the amount of ethylene supplied to the system. Here, the apparent ethylene reaction order was negative. This could indicate competitive adsorption between ethylene and the reacting alkane and/or an enhancement of the reverse reaction at higher ethylene concentrations. Note that the ethylene partial pressures used in identifying the differential regime of the reactor (**Supporting Information 2.C5**) and in the ethane and hydrogen reaction order tests (**Figure 2.2a** and **2.2b**) were considerably lower (<3 mbar(a)) than the ethylene concentrations used in determining the apparent ethylene reaction order (5-25 mbar(a), **Figure 2.2d**). The inhibiting effect of the produced ethylene, as illustrated in **Figure 2.2d**, should therefore not affect the ethane and hydrogen reaction orders.

The apparent activation barrier for typical conditions used in these catalytic tests was around 80-85 kJ/mol (see **Figure 2.3**), which is in line with typical apparent barriers for light alkane activation on Pt (70-130 kJ/mol) [25,27,34,36].
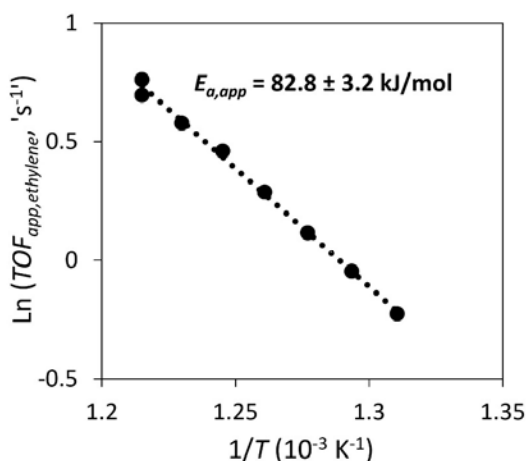
Figure 2.3: Arrhenius curve for ethylene formation on Pt-Sn/ZnAl$_2$O$_4$, T = 490-550 °C, p_{ethane} = 34 mbar(a), p_{H2} = 105 mbar(a).

The apparent experimental turnover frequency was consistently lower at higher conversion (70-90% of the equilibrium conversion, **Supporting Information 2.N**), indicating the possible impact of the ethylene surface coverage and/or the reaction reversibility on the kinetics of the forward ethane NODH reaction. However, the apparent

activation barrier and ethane and hydrogen reaction orders were similar at much higher conversion levels (**Supporting Information 2.M**). Despite rate inhibition at higher conversion, the reaction mechanism is, thus, similar to that observed at lower conversion.

2.3.2.2. Reaction mechanism

To interrogate the reaction mechanism we combined the reaction data with Langmuir-Hinshelwood-Hougen-Watson (LHHW) kinetic modeling, which is the most suitable model for describing alkane NODH [23–25,27,29–31,37,55]. In the LHHW model, it is assumed that (i) all components adsorb onto the same catalyst active site, (ii) only monolayer adsorption takes place, (iii) all active sites are energetically uniform, and (iv) there are no lateral interactions between adsorbed and adsorbing molecules. In this model, one or more rate-determining steps can control the observed reaction rate, whilst all other elementary steps are in quasi-equilibrium. Here, a different mechanism is discriminated either if one of the elementary steps changes or if the rate-determining step changes.

Inspired by previous work on C_2+ alkane dehydrogenation [24,25,27,29–31,34,37] one can distinguish various possible reaction pathways. First, the reacting alkane can adsorb dissociatively [24,25,29,31,34,37] or molecularly on PtSn [27,30] (**Figure 2.4**). For pure Pt catalysts, microcalorimetry showed that light alkanes and light alkenes primarily adsorb dissociatively, whereas dissociation was suppressed for PtSn catalysts [35]. Afterward, atomic hydrogen is abstracted on the surface of the PtSn catalyst. Lastly, the produced olefin desorbs either immediately after being formed or via desorption of chemisorbed ethylene, depending on whether the ethylene adsorption equilibrium lies at the desorption side or at the adsorption side (**Figure 2.4**). Note that only dissociative adsorption of H_2 is considered, since H_2 is generally accepted to adsorb dissociatively on Pt [56–59].
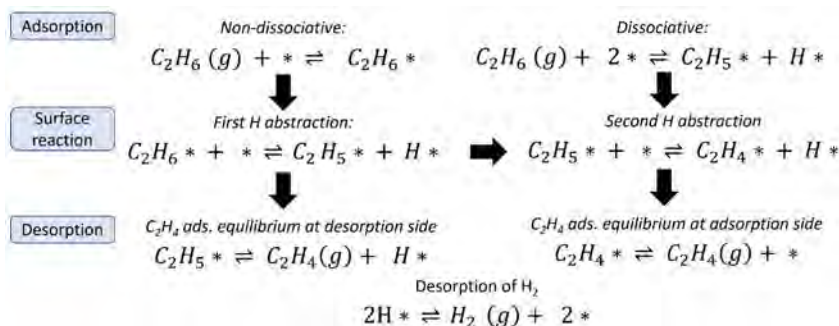
Figure 2.4: Possible reaction pathways for ethane NODH on Pt-based catalysts.

In short, the possible reaction mechanisms thus depend on the rate-determining step (RDS) and the way in which ethane adsorbs and ethylene desorbs. A matrix of fourteen possible reaction mechanisms was generated when considering that only a single RDS controls the rate (**Table 2.2**).

Table 2.2: Matrix of possible reaction mechanisms considering a single rate-determining step.

		Matrix of possible reaction mechanisms	
#	C$_2$H$_6$ adsorption	C$_2$H$_4$ ads. equilibrium	Rate-determining step
1	Non-dissociative	Adsorption side	1st H removal
2	Non-dissociative	Desorption side	1st H removal
3	Dissociative	Adsorption side	Dissociative adsorption
4	Dissociative	Desorption side	Dissociative adsorption
5	Non-dissociative	Adsorption side	2nd H removal
6	Non-dissociative	Desorption side	2nd H removal
7	Dissociative	Adsorption side	2nd H removal
8	Dissociative	Desorption side	2nd H removal
9	Non-dissociative	Adsorption side	C$_2$H$_4$ desorption
10	Dissociative	Adsorption side	C$_2$H$_4$ desorption
11	Dissociative	Adsorption side	H$_2$ desorption
12	Dissociative	Desorption side	H$_2$ desorption
13	Non-dissociative	Adsorption side	H$_2$ desorption
14	Non-dissociative	Desorption side	H$_2$ desorption

*Note: the associated fourteen possible different reaction mechanisms are available in **Supporting Information 2.E**.*

A LHHW reaction rate expression was derived for every individual mechanism (see **Supporting Information 2.G**). As an example, the full derivation of mechanism 3 is available in **Supporting Information 2.F**. The derivation of the LHHW rate expressions of all other mechanisms is broadly analogous to that of mechanism 3. The apparent reaction orders that one would obtain for H$_2$, ethane, and ethylene differ per mechanism and depend on the relative respective partial pressures. To discriminate between the different reaction mechanisms, one can inspect the possible reaction orders that are theoretically obtained at the extreme pressures. The theoretical reaction orders of all mechanisms are tabulated in **Supporting Information 2.H** for three different situations: (i) excess p_{C2H6}, (ii) excess p_{C2H4}, and (iii) excess p_{H2}. This simple analysis facilitates the identification of reaction mechanisms that fail to explain the apparent reaction orders experimentally observed with the caveat that kinetic data must cover said extremes.

The first main observation from **Section 2.3.2.1** was that the ethane reaction order was one for low and high ethane partial pressures (**Figure 2.2a** and **2.2c**). This indicates that ethane is not molecularly occupying surface sites and, thus, that ethane adsorbs dissociatively on Pt-Sn/ZnAl$_2$O$_4$. The second main observation was that the ethylene and hydrogen reaction orders were negative (**Figure 2.2b** and **2.2d**), indicating competitive

adsorption of the ethylene and the hydrogen with the reacting alkane on the metal active centers. The latter implies that the ethylene and hydrogen adsorption equilibria are located at the adsorption side. These experimental observations exclude all possible reaction mechanisms in which (i) ethane adsorbed non-dissociatively, and/or (ii) the ethylene adsorption equilibrium was located at the desorption side. From this analysis, only mechanisms 3, 7, 10, and 11 could potentially explain our observations (see **Table 2.2**). These four mechanisms comply with the following four elementary steps and each mechanism considers a different step as RDS (**Equations 2.7-2.10**).

1 $\quad C_2H_6\,(g) +\ 2* \ \leftrightharpoons\ C_2H_5*+H*$ $\hfill$ (2.7)

3 $\quad C_2H_5*+* \qquad \leftrightharpoons\ C_2H_4*+H*$ $\hfill$ (2.8)

4 $\quad C_2H_4* \qquad\qquad \leftrightharpoons\ C_2H_4\,(g) +*$ $\hfill$ (2.9)

5 $\quad 2H* \qquad\qquad\ \leftrightharpoons\ H_2\,(g) + 2*$ $\hfill$ (2.10)

Detailed inspection of the resulting reaction rate expressions of mechanisms 7, 10, and 11 (**Supporting Information 2.G**) revealed that ethane reaction orders between -1 and 0 should be observed at high ethane partial pressures (**Supporting Information 2.H**) as an ethane partial pressure term would appear in the denominator. This contradicts the experimentally found ethane reaction order of 1 (**Figure 2.2a** and **2.2c**). In this scenario, only mechanism 3 in which dissociative ethane adsorption (**Equation 2.7**) is the RDS could predict our experimental observations.

Using mechanism 3 one can derive the LHHW rate expression shown in **Equation 2.11** (see **Supporting Information 2.F** for the detailed derivation).

$$TOF_{app,model} = \frac{k_1\left(p_{C2H6} - \dfrac{p_{C2H4}p_{H2}}{K_{eq}}\right)}{\left(1 + \dfrac{K_4\sqrt{K_5}}{K_3}\,p_{C2H4}\sqrt{p_{H2}} + K_4\,p_{C2H4} + \sqrt{K_5 p_{H2}}\right)^2} \qquad (2.11)$$

The denominator in **Equation 2.11** contains respective surface coverage terms for vacant sites and for adsorbed ethyl (C_2H_5*), ethylene (C_2H_4*), and hydrogen ($H*$). A previous study from Cortright et al. [34] showed that for isobutane dehydrogenation on PtSn-based catalysts the isobutyl (C_4H_9*) surface intermediate occupancy is negligible. This isobutyl (C_4H_9*) reaction intermediate is analogous to the ethyl (C_2H_5*) intermediate in ethane dehydrogenation, hence the ethyl (C_2H_5*) surface species is expected to be a short-lived intermediate that is readily converted to C_2H_4*, which reduces **Equation 2.11** to **Equation 2.12**.

$$TOF_{app,model} = \frac{k_1\left(p_{C2H6} - \dfrac{p_{C2H4}p_{H2}}{K_{eq}}\right)}{\left(1 + K_4\,p_{C2H4} + \sqrt{K_5 p_{H2}}\right)^2} \qquad (2.12)$$

The kinetic regression was conducted using **Equation 2.12**, following the thermodynamic consistency criteria proposed by Vannice [60], which considers that:

a) Gibbs free energies of adsorption ($\Delta G_{ads,i}$) must increase or become less negative with increasing temperature, as desorption is favored at higher temperatures.
b) Gibbs free energies of transition states ($\Delta G_i^{\neq}$) must decrease with increasing temperatures, as thermal activation enhances chemical conversions.
c) The enthalpy of adsorption of a species i is always negative ($\Delta H_{ads,i} < 0$) [60].
d) The entropy of adsorption of a species i is always negative ($\Delta S_{ads,i} < 0$) [60], since the number of degrees of freedom of an adsorbed species is lower than that of the same species in the gas phase.
e) The decrease in entropy of a species i upon adsorption cannot be larger than the corresponding gas phase entropy of that species ($|\Delta S_{ads,i}| < S_{g,i}$) [60].

The proposed LHHW reaction rate expression (**Equation 2.12**) contains a reaction rate constant (k_1) and three equilibrium constants. The ethane dehydrogenation reaction equilibrium constant (K_{eq}) was fixed in the kinetic regression using a thermodynamic equilibrium description for the ethane NODH reaction obtained from Champagnie et al. [61]. On the contrary, the equilibrium constants describing the adsorption of ethylene (K_4) and hydrogen (K_5) were, together with the reaction rate constant, included as adjustable parameters in the kinetic regression.

The temperature dependence of the reaction rate constant can be determined using transition state treatments of the rate using **Equation 2.13**, where k_b represents the Boltzmann constant, h the Planck constant, and $\Delta G_i^{\ddagger}$, $\Delta H_i^{\ddagger}$, and $\Delta S_i^{\ddagger}$ the Gibbs free energy, enthalpy, and entropy of the corresponding transition state, respectively.

$$k_i = \frac{k_b T}{h} * \exp\left(\frac{-\Delta G_i^{\ddagger}}{RT}\right) = \frac{k_b T}{h} * \exp\left(\frac{-\Delta H_i^{\ddagger}}{RT}\right) * \exp\left(\frac{\Delta S_i^{\ddagger}}{R}\right) \qquad (2.13)$$

Similarly, one can express the adsorption equilibrium constants using the Van 't Hoff equation (**Equation 2.14**), where ΔG_j, ΔH_j, and ΔS_j represent the Gibbs free energy, enthalpy, and entropy of the concerning adsorption equilibrium.

$$K_j = \exp\left(\frac{-\Delta G_j}{RT}\right) = \exp\left(\frac{-\Delta H_j}{RT}\right) * \exp\left(\frac{\Delta S_j}{R}\right) \qquad (2.14)$$

Each adjustable parameter in **Equation 2.12** is defined by the corresponding Gibbs free energy, which in turn consists of an enthalpic and entropic contribution. To limit the number of adjustable parameters in the kinetic regression, only the Gibbs free energies were varied. As initial guess for the Gibbs free energy of the transition state ($\Delta G_i^{\ddagger}$) the experimentally determined apparent activation barrier was taken (82.8 kJ/mol, **Figure 2.3**). The initial estimations for the Gibbs free energy of the adsorption equilibria were

derived by using a procedure for thermodynamic approximations as proposed by Gao et al. [62]. In this procedure, equilibrium constants were quantified by approximating the enthalpy and entropy of gas phase and adsorbed surface species under reaction conditions, as further explained in **Supporting Information 2.J**.

The kinetic and adsorption equilibrium constants of reaction mechanism 3 (**Equation 2.12**) were regressed using a combination of the experimental ethane and hydrogen reaction order data obtained at low conversion (**Figure 2.2a** and **2.2b**) and the corresponding reaction order data obtained at high conversion (**Figure 2.M1a** and **2.M1b**). The regression was performed per reaction temperature by minimizing the sum of least-square residuals (S_r), the latter being defined as the difference between the apparent experimental turnover frequency for ethylene formation ($TOF_{app,exp}$) and the corresponding apparent TOF for ethylene formation as predicted by the concerning rate expression ($TOF_{app,model}$), following **Equation 2.15**. In this equation, i represents a specific data point and n the total number of data points for a given reaction temperature. The regression was first conducted for the data obtained at the lowest temperature investigated (i.e. 475 °C), after which the regression outcomes were applied as thermodynamic constraints (**a-e**) for the next temperature (500 °C), and so on to the highest temperature of 550 °C.

$$S_r = \sum_{i=1}^{n} r_i^2 = \sum_{i=1}^{n} (TOF_{app,exp,i} - TOF_{app,model,i})^2 \tag{2.15}$$

An additional criterion that can be used to select a statistically preferred model is the Akaike Information Criterion (*AIC*, **Equation 2.16**) [63], which penalizes for over-fitting, where n_a is the number of adjustable parameters included in the kinetic regression and n the number of measurements.

$$AIC = 2\,n_a + n \ln (S_r) \tag{2.16}$$

Surprisingly, when enforcing thermodynamic consistency by applying the specified Langmuir kinetics rules (**a-e**) listed above, reaction model 3 overpredicts the experimental rates, particularly at higher temperatures (see **Figure 2.5a**). In other words, reaction model 3 misses a characteristic that inhibits the experimental rate, especially when increasing the temperature.
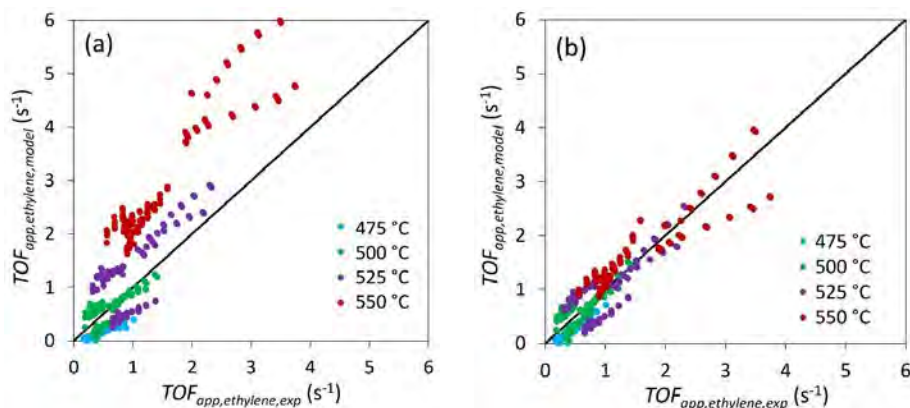
Figure 2.5: Parity plots of the kinetic regression outcomes for mechanism 3 (a) when applying all thermodynamic constraints related to Langmuir reaction kinetics, and (b) when removing the coverage independency of $\Delta G_{ads,H2}$ and $\Delta G_{ads,C2H4}$.

A possible explanation for the finding that reaction model 3, which satisfies the observed experimental reaction orders, fails to describe the observed reaction rates, could be that one of the thermodynamic consistency criteria proposed by Vannice [60] (**a-e**) does not hold under the kinetic testing conditions. LHHW kinetics assume that all catalyst active sites are equal and that possible lateral interactions can be disregarded. Consequently, the enthalpy and entropy of adsorption of all species are independent of surface coverage. However, García-Diéguez et al. [64] showed for H_2 adsorption on Pt/Al_2O_3 that $\Delta H_{ads,H2}$ and $\Delta S_{ads,H2}$ change with the hydrogen surface coverage. They claimed that undercoordinated Pt sites bind hydrogen the strongest (-60 to -50 kJ/mol) at low coverage and are, therefore, the first ones to be saturated. For higher coverages, planar Pt sites bind hydrogen weaker (-50 to -35 kJ/mol). Moreover, when almost full surface saturation is attained, $\Delta H_{ads,H2}$ reduces even further (-35 to -20 kJ/mol), as acting lateral interactions hinder further hydrogen adsorption. Also, García-Diéguez et al. [64] reported that the entropy of hydrogen adsorption becomes more negative with increasing hydrogen surface coverage on Pt/Al_2O_3. This was attributed to the fact that surface hydrogen becomes less mobile when monolayer coverage is approached. Desorption is normally favored at higher temperatures, leading to lower surface coverages. Following the results of García-Diéguez et al. [64], upon reducing hydrogen surface coverage, the enthalpy of adsorption will become more negative, whereas the entropy of adsorption becomes less negative. Consequently, the Gibbs free energy of hydrogen adsorption would become more negative with decreasing surface coverage and, thus, with increasing temperature. This violates the thermodynamic consistency criterion (**a**) as listed by Vannice [60].

Ethylene can adsorb on PtSn clusters in three different configurations, namely (i) as π-bonded ethylene, (ii) as di-σ-bonded ethylene, and (iii) as ethylidyne species (**Figure 2.6**) [65]. The adsorption strength generally increases from the π-bonded to the ethylidyne to the di-σ-bonded type of ethylene adsorbate on Pt and PtSn [65]. The contribution of more

strongly bound di-σ-bonded can change with the surface coverage distribution and thereby with temperature [66]. Possibly, ethylene adsorbs to a larger extent as π-bonded ethylene for higher surface coverages and primarily as di-σ-bonded ethylene for lower surface coverages. This could possibly violate again thermodynamic criterion (**a**) as proposed by Vannice [60].
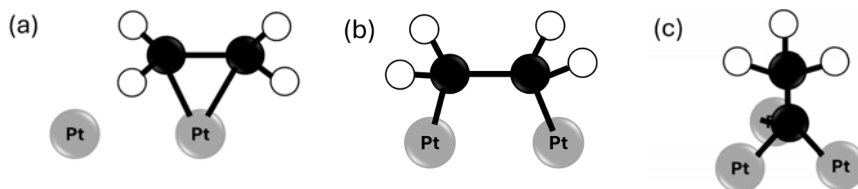
Figure 2.6: Schematic representation of (a) π-bonded ethylene, (b) di-σ-bonded ethylene, and (c) ethylidyne adsorbed on Pt, based on Watwe et al. [65].

To account for these effects one could allow the $\Delta G_{ads,H2}$ and $\Delta G_{ads,C2H4}$ to vary with surface coverage, which are ultimately a function of the temperature. The experimental data used in the kinetic regression were gathered under steady state conditions where the surface of the catalyst was covered by hydrogen and hydrocarbons. The regression result, therefore, does not yield adsorption enthalpies and entropies corresponding to a clean PtSn surface, especially since Pt-based catalysts are known to be covered by an ethylidyne-rich carbon layer in presence of hydrocarbons [66–68]. Instead, the kinetic regression yields adsorption thermodynamics related to the first next respective molecule adsorbing onto that covered PtSn surface. The possible variation in $\Delta G_{ads,H2}$ and $\Delta G_{ads,C2H4}$ with temperature was included by removing the thermodynamic consistency criterion (**a**) for hydrogen and ethylene adsorption.

Table 2.3: Akaike Information Criterion (*AIC*) of mechanism 3 (i) when enforcing thermodynamic consistency and (ii) after allowing for coverage dependent hydrogen and ethylene adsorption.

T = 475 °C	T = 500 °C	T = 525 °C	T = 550 °C
AIC when enforcing thermodynamic consistency:			
1501.1	1382.2	1756.7	2243.1
AIC after allowing for coverage dependent hydrogen and ethylene adsorption:			
1168.2	1399.5	1609.1	1815.6

The elimination of the temperature constraints of $\Delta G_{ads,H2}$ and $\Delta G_{ads,C2H4}$ in the kinetic regression leads to a fundamental change in the quality of the parity plot for mechanism 3 (see **Figure 2.5b**). Here, one can note that after this modification the proposed reaction model provides a substantially better prediction of the rates at all temperatures. This is

confirmed by the results in **Table 2.3**, showing that the lowest *AIC* values were generally obtained after allowing for coverage dependent hydrogen and ethylene adsorption.

The thermodynamic outcomes of the kinetic regression using mechanism 3, including coverage dependent hydrogen and ethylene adsorption, were quantified using the Arrhenius and Van 't Hoff relations in **Equation 2.13** and **2.14** (**Table 2.4** and **Supporting Information 2.K**). The results in **Table 2.4** indicate that a good agreement between model 3 and experiments was only obtained when hydrogen and ethylene adsorption become both less favorable at lower temperatures. For both components, this is attributed to changing surface coverages with temperature. For hydrogen adsorption, this could be caused by a combination of lateral interactions and decreased hydrogen surface mobility for near saturated Pt surfaces at reduced temperatures, as pointed out by García-Diéguez et al. [64]. On the contrary, for ethylene adsorption this could be caused by a higher surface concentration of stronger σ-bonded ethylene species for lower surface coverages at higher temperature relative to π-bonded ethylene.

Table 2.4: Thermodynamic outcomes of the kinetic regression using mechanism 3, including temperature and coverage dependent hydrogen and ethylene adsorption.

| T (°C) | k_1 | K_4 ($= K_{C2H4}$) | K_5 ($= K_{H2}$) |
	$\Delta G_1^{\ddagger}$ (kJ/mol)	$\Delta G_{4,ads}$ (kJ/mol)	$\Delta G_{5,ads}$ (kJ/mol)
475	48.7 ± 0.3	-95.6 ± 0.4	-133.1 ± 0.6
500	48.6 ± 0.3	-97.5 ± 0.4	-138.0 ± 0.6
525	48.4 ± 0.3	-97.8 ± 0.4	-140.0 ± 0.6
550	47.3 ± 0.3	-99.6 ± 0.4	-143.0 ± 0.6

Instead of releasing the thermodynamic equilibrium constraints for hydrogen and ethylene adsorption, one could also consider the possible existence of dual rate-determining steps (RDS), particularly since the results presented here indicated that the hydrogen and ethylene surface coverages are strongly impacting the rate. We addressed this issue by estimating the degree of rate control (DRC), as introduced to the field of catalysis by Charles Campbell [69,70], under varying gas phase atmospheres (see **Supporting Information 2.Q**). Herein, we compared the rate control distribution (i) between the dissociative ethane adsorption and the hydrogen desorption step, and (ii) between the dissociative ethane adsorption and the ethylene desorption step. The results indicated that the hydrogen desorption step only became colimiting for a combination of extremely low hydrogen and ethylene partial pressures, which is an unrealistic scenario for membrane reactor applications aiming at ethylene yield maximization (**Supporting Information 2.Q1**). On the contrary, the colimiting ethylene desorption analysis indicated that upon increasing ethylene yield by removing H_2 from the reaction zone, the

reaction pathway will shift from one in which the dissociative ethane adsorption is governing the rate to one in which ethylene desorption becomes controlling the rate (**Supporting Information 2.Q2**). However, it needs to be emphasized here that one needs to be careful with the interpretation of these outcomes, as these DRC results were extrapolated far outside the experimentally applied range. Nevertheless, the resulting trends demonstrate that the reaction pathway can change when removing hydrogen to maximize olefin yields.

In this work, we further focus on the single RDS mechanism that considers dissociative ethane adsorption as the only RDS (mechanism 3), with the inclusion of coverage dependent hydrogen and ethylene adsorption. The kinetic regression using mechanism 3 (**Figure 2.5a** and **2.5b**) was performed using a combination of relatively low conversion data, gathered at 40-60% of the theoretically attainable maximum conversion, and relatively high conversion data, obtained at 70-90% of the equilibrium conversion (see **Supporting Information 2.P**). The apparent experimental turnover frequency for ethylene formation ($TOF_{app,ethylene,exp}$) was found to be significantly lower under high conversion conditions (70-90% of theoretical maximum) compared to the low conversion data for equal ethane and hydrogen partial pressures (see **Supporting Information 2.N**). A higher ethylene partial pressure at higher conversion leads to a larger reaction reversibility term and a higher ethylene surface coverage, both negatively impacting the rate (**Equation 2.12**).

The regressed thermodynamic outcomes of mechanism 3 (**Table 2.4**) were used to plot the surface coverage distributions under varying temperatures and gas phase compositions, as used in the catalytic tests (see **Figure 2.6**). The catalytic activity was enhanced at higher temperatures (**Figure 2.3**), leading to higher ethylene partial pressures. At the same time, our regression results (**Table 2.4**) indicated that the ethylene and the hydrogen adsorption both become intrinsically stronger with lower surface coverages, and hence with increasing temperatures. Ultimately, the ethylene coverage was found to increase, while the hydrogen coverage was found to decrease with increasing temperature (**Figure 2.6a**). This explains why the inhibiting effect of the hydrogen on the dehydrogenation rate becomes less pronounced at higher temperatures, as experimentally observed by means of less negative hydrogen reaction orders at higher temperatures (**Figure 2.2b**).

Upon increasing the ethane partial pressure at a given temperature and hydrogen partial pressure, the ethylene formation rate was enhanced (**Figure 2.2a**). This results in a higher ethylene surface coverage at the expense of the hydrogen coverage (**Figure 2.6b**). Analogously, upon increasing the hydrogen partial pressure for a constant temperature and ethane partial pressure, the hydrogen surface coverage was boosted (**Figure 2.6c**). Lastly, the surface coverage became dominated by ethylene for the experiments in which ethylene was cosupplied (**Figure 2.6d**). It should be noted that under the conditions used for constructing **Figure 2.6d** the PtSn catalyst deactivated experimentally. This

emphasizes that the PtSn catalyst primarily deactivates in case of ethylene covered surfaces. One needs to be careful with the interpretation of the surface coverage distribution in **Figure 2.6d**, as they were constructed using extrapolated regression outcomes.
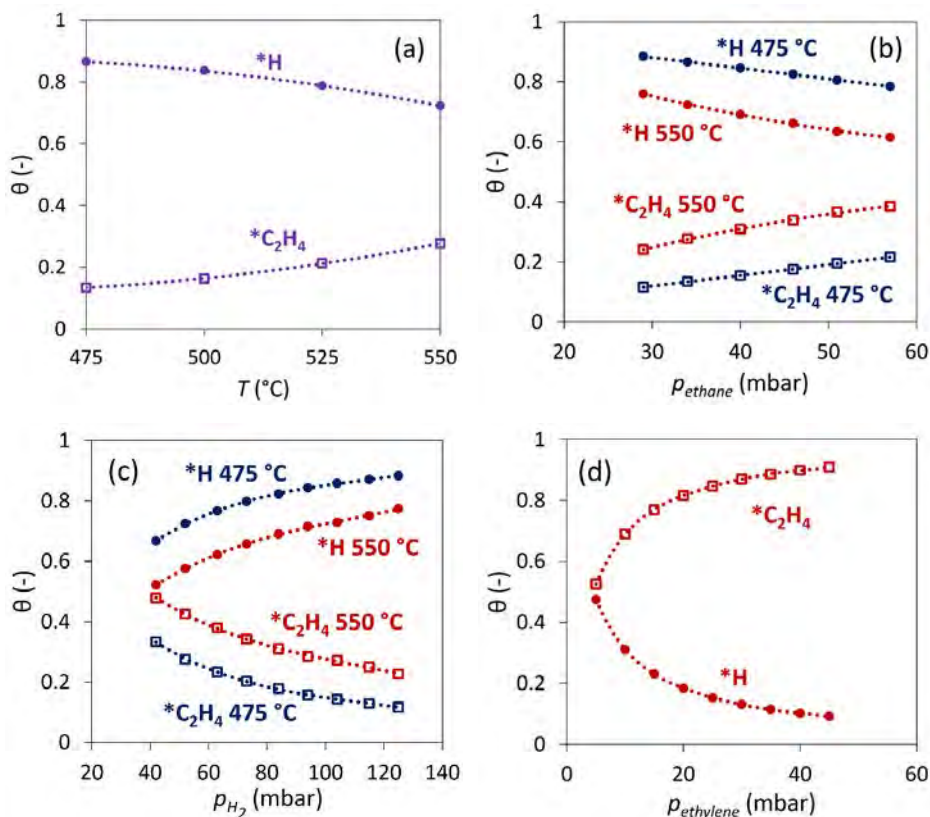
Figure 2.6: Surface coverage distribution (a) as a function of temperature (p_{ethane} = 34 mbar(a), p_{H2} = 104 mbar(a)), (b) as a function of ethane partial pressure (p_{H2} = 104 mbar(a)), (c) as a function of H_2 partial pressure (p_{ethane} = 34 mbar(a)), and (d) as a function of ethylene partial pressure (p_{ethane} = 150 mbar(a), p_{H2} = 75 mbar(a), T = 550 °C).

Figure 2.6 showed the surface coverage distributions under the conditions used in the kinetic study. The kinetic regression was performed using a dataset comprising of a wide range of temperatures and ethane, hydrogen, and ethylene partial pressures. Consequently, the resulting kinetic model enables the prediction of the ethane NODH reaction for wide variations in gas phase atmospheres. This is particularly relevant for membrane-driven ethane NODH, which is an important strategy to potentially industrialize ethane NODH. In that situation, ethylene yields will be much higher and hydrogen and ethylene concentration gradients along the reactor will be much larger as compared to typical kinetic testing conditions. Reaction model 3, as developed in this

work, was therefore used to predict the surface coverage distribution under realistic membrane reactor conditions. In hydrogen removing membrane reactors the PtSn active centers are expected to be occupied primarily by ethylene (**Supporting Information 2.O**). Traditional alkane dehydrogenation catalysts are operated in the presence of coke suppressing agents like H_2 and H_2O, facilitating olefin desorption [17]. Developing catalysts that are sufficiently stable in hydrogen-poor atmospheres should therefore be a key focus for further development of membrane-driven alkane NODH.

In this chapter, the plug flow reactor data was treated differentially by considering a constant dehydrogenation rate along the catalytic bed. This is a valid approach when the concentrations of all species involved in the reaction barely change throughout the bed. For the concentrations of the ethane reactant and the cosupplied hydrogen it is reasonable to assume that they are constant for the applied conversion level (<12%). Despite the low ethylene concentrations used in these tests, due to the low conversion level, the Pt-based catalyst located close to the reactor outlet will be exposed to higher ethylene concentrations than the Pt-based catalyst situated at the reactor inlet. It is therefore contestable if it is fair to assume a constant ethylene concentration along the bed. For this reason, we are investigating in ongoing kinetic regressions if the regressed kinetic and thermodynamic parameters would significantly change when considering the PFR as an integral reactor in which the dehydrogenation rate is allowed to vary in axial direction, due to changes in gas phase composition, instead of averaged along the bed.

2.4. Conclusion

This work presents a kinetic study of non-oxidative ethane dehydrogenation on Pt-Sn/ZnAl$_2$O$_4$ obtained in a wide range of alkane, hydrogen, and olefin partial pressures. We showed that a good agreement between reaction model and experimental data could only be obtained for coverage dependent hydrogen and ethylene adsorption thermodynamics. Consequently, the hydrogen and ethylene adsorption in this catalyst system deviate from ideal Langmuir adsorption. For hydrogen adsorption, this discrepancy was attributed to lateral interactions and reduced hydrogen surface mobility for high surface coverages. By contrast, for ethylene adsorption this deviation from Langmuir adsorption could be caused by a stronger ethylene adsorption configuration existing for low surface coverages. These results are particularly relevant for membrane reactor applications, in which Pt-based catalysts are integrated with hydrogen removing membranes, which presents a promising strategy to shift alkane NODH equilibria toward olefins. Upon increasing the ethylene concentration by reducing the hydrogen partial pressure, the surface coverage distribution will be strongly modified, which in turn will lead to changes in the adsorption phenomena, the corresponding reaction pathway, and thereby the related dehydrogenation rate on the Pt-Sn/ZnAl$_2$O$_4$ catalyst.

References

1. Rabenhorst, R. On-purpose: what's driving new propane dehydrogenation projects in North America? https://rbnenergy.com/on-purpose-whats-driving-new-propane-dehydrogenation-projects-in-north-america (accessed June 2020).

2. Data Bridge Market Research. Global ethylene market - industry trends and forecast to 2028. https://www.databridgemarketresearch.com/reports/global-ethylene-market (accessed September 2022).

3. Data Bridge Market Research. Global propylene market - industry trends and forecast to 2032. https://www.databridgemarketresearch.com/reports/global-propylene-market (accessed January 2025).

4. Agarwal, A., Sengupta, D. & El-halwagi, M. Sustainable process design approach for on-purpose propylene production and intensification. *ACS Sustain. Chem. Eng.* **6**, 2407–2421 (2018).

5. Sattler, J. J. H. B., Ruiz-Martinez, J., Santillan-Jimenez, E. & Weckhuysen, B. M. Catalytic dehydrogenation of light alkanes on metals and metal oxides. *Chem. Rev.* **114**, 10613–10653 (2014).

6. INEOS - Project ONE. Construction ethane cracker INEOS Project One kicks off with sheet piling. https://project-one.ineos.com/en/news/construction-ethane-cracker-ineos-project-one-kicks-off-with-sheet-piling/ (accessed October 2023).

7. TotalEnergies. United States: TotalEnergies announces the start-up of new ethane cracker in Port Arthur. https://totalenergies.com/media/news/press-releases/united-states-totalenergies-announces-start-new-ethane-cracker-port (accessed October 2023).

8. Carr, H. Building the perfect beast - Shell's new ethane-consuming steam cracker in the home stretch. https://rbnenergy.com/building-the-perfect-beast-shells-new-ethane-consuming-steam-cracker-in-the-home-stretch (accessed October 2023).

9. Hays, K. Enterprise planning new 2 mil mt/year steam cracker in Texas: documents. https://www.spglobal.com/commodityinsights/en/market-insights/latest-news/petrochemicals/061522-enterprise-planning-new-2-mil-mtyear-steam-cracker-in-texas-documents (accessed October 2023).

10. Narayan, M. GAIL plans $4.9 billion ethane cracker in West India- sources. https://www.reuters.com/world/india/gail-plans-49-billion-ethane-cracker-west-india-sources-2023-05-10/ (accessed October 2023).

11. Offshore Technology. QatarEnergy and CPChem announce $4.4bn financing for petrochemicals facility. https://www.offshore-technology.com/news/qatarenergy-cpchem-petrochem-facility/?cf-view (accessed October 2023).

12. Saudi Aramco. South Korean president and Aramco CEO attend S-OIL's $7bn Shaheen groundbreaking. https://www.aramco.com/en/news-media/news/2023/south-korean-president-and-aramco-ceo-attend-shaheen-groundbreaking (accessed October 2023).

13. Skyquest. Global ethylene market insights. https://www.skyquestt.com/report/ethylene-market (accessed October 2023).

14. Bidwai, S. Ethylene market. https://www.precedenceresearch.com/ethylene-market (accessed October 2024).

15. The Business Research Company. Propylene global market report 2023. https://www.thebusinessresearchcompany.com/report/propylene-global-market-report (accessed October 2023).

16. Bidwai, S. Propylene market. https://www.precedenceresearch.com/propylene-market (accessed October 2023).

17. Nawaz, Z. Light alkane dehydrogenation to light olefin technologies: A comprehensive review. *Rev. Chem. Eng.* **31**, 413–436 (2015).

18. Zimmermann, H. & Walzl, R. Ethylene. in *Ullmann's Encyclopedia of Industrial Chemistry* (Wiley-VCH Verlag GmbH & Co. KGaA, Weinheim, Germany, 2009). doi:https://doi.org/10.1002/14356007.a10_045.pub3.

19. Jablonski, E. L., Castro, A. A., Scelza, O. A. & Miguel, S. R. De. Effect of Ga addition to Pt/Al2O3 on the activity, selectivity and deactivation in the propane dehydrogenation. *Appl. Catal. A: Gen.* **183**, 189–198 (1999).

20. Sun, M., Zhai, S., Weng, C., Wang, H. & Yuan, Z. Y. Pt-based catalysts for direct propane dehydrogenation: Mechanisms revelation, advanced design, and challenges. *Mol. Catal.* **558**, 114029 (2024).

21. Cortright, R. D., Hill, J. M. & Dumesic, J. A. Selective dehydrogenation of isobutane over supported Pt/Sn catalysts. *Catal. Today* **55**, 213–223 (2000).

22. Galvita, V., Siddiqi, G., Sun, P. & Bell, A. T. Ethane dehydrogenation on Pt/Mg(Al)O and PtSn/Mg(Al)O catalysts. *J. Catal.* **271**, 209–219 (2010).

23. Sheintuch, M., Liron, O., Ricca, A. & Palma, V. Propane dehydrogenation kinetics on supported Pt catalyst. *Appl. Catal. A: Gen.* **516**, 17–29 (2016).

24. Li, Q., Sui, Z., Zhou, X. & Chen, D. Kinetics of propane dehydrogenation over Pt–Sn/Al2O3 catalyst. *Appl. Catal. A: Gen.* **398**, 18–26 (2011).

25. Ricca, A., Montella, F., Iaquaniello, G., Palo, E. & Salladini, A. Membrane assisted propane dehydrogenation: Experimental investigation and mathematical modelling of catalytic reactions. *Catal. Today* **331**, 43–52 (2019).

26. van Sint Annaland, M., Kuipers, J. A. M. & van Swaaij, W. P. M. A kinetic rate expression for the time-dependent coke formation rate during propane dehydrogenation over a platinum alumina monolithic catalyst. *Catal. Today* **66**, 427–436 (2001).

27. Rashidi, M., Nikazar, M. & Rahmani, M. Kinetic modeling of simultaneous dehydrogenation of propane and isobutane on Pt-Sn-K/Al2O3 catalyst. *Chem. Eng. Res. Des.* **95**, 239–247 (2014).

28. Larsson, M., Henriksson, N. & Andersson, B. Investigation of the kinetics of a deactivating system by transient experiments. *Appl. Catal. A: Gen.* **166**, 9–19 (1998).

29. Farjoo, A., Khorasheh, F., Niknaddaf, S. & Soltani, M. Kinetic modeling of side reactions in propane dehydrogenation over Pt-Sn/y-Al2O3 catalyst. *Scientia Iranica* **18**, 458–464 (2011).

30. Gómez-Quero, S., Tsoufis, T., Rudolf, P., Makkee, M., Kapteijn, F. & Rothenberg, G. Kinetics of propane dehydrogenation over Pt-Sn/Al2O3. *Catal. Sci. Technol.* **3**, 962–971 (2013).

31. Lobera, M. P., Téllez, C., Herguido, J. & Menéndez, M. Transient kinetic modelling of propane dehydrogenation over a Pt–Sn–K/Al2O3 catalyst. *Appl. Catal. A: Gen.* **349**, 156–164 (2008).

32. Aguilar-rios, G., Valenzuela, M. A., Salas, P., Armendariz, H., Bosch, P., Del Toro, G., Silva, R., Bertín, V., Castillo, S., Ramírez-Solís, A. & Schifter, I. Hydrogen interactions and catalytic properties of platinum-tin supported on zinc aluminate. *Appl. Catal. A: Gen.* **127**, 65–75 (1995).

33. Cortright, R. D. & Dumesic, J. A. Effects of potassium on silica-supported Pt and Pt/Sn catalysts for isobutane dehydrogenation. *J. Catal.* **157**, 576–583 (1995).

34. Cortright, R. D., Levin, P. E. & Dumesic, J. A. Kinetic studies of isobutane dehydrogenation and isobutene hydrogenation over Pt/Sn-based catalysts. *Ind. Eng. Chem. Res.* **37**, 1717–1723 (1998).

35. Natal-Santiago, M. A., Podkolzin, S. G., Cortright, R. D. & Dumesic, J. A. Microcalorimetric studies of interactions of ethene, isobutene, and isobutane with silica-supported Pd, Pt, and PtSn. *Catal. Letters.* **45**, 155–163 (1997).

36. Biloen, P., Dautzenberg, F. M. & Sachtler, W. M. H. Catalytic dehydrogenation of propane to propene over platinum and platinum-gold alloys. *J. Catal.* **50**, 77–86 (1977).

37. Barghi, B., Fattahi, M. & Khorasheh, F. Kinetic modeling of propane dehydrogenation over an industrial catalyst in the presence of oxygenated compounds. *React. Kinet. Mech. Catal.* **107**, 141–155 (2012).

38. Brencio, C., Di Felice, L. & Gallucci, F. Fluidized bed membrane reactor for the direct dehydrogenation of propane: proof of concept. *Membranes* **12**, 1211 (2022).

39. Morejudo, S. H., Zanón, R., Escolástico, S., Yuste-Tirados, I., Malerød-Fjeld, H., Vestre, P. K., Coors, W. G., Martínez, A., Norby, T., Serra, J. M. & Kjølseth, C. Direct conversion of methane to aromatics in a catalytic co-ionic membrane reactor. *Science* **353**, 563–566 (2016).

40. Clark, D., Malerød-Fjeld, H., Budd, M., Yuste-Tirados, I., Beeaff, D., Aamodt, S., Nguyen, K., Ansaloni, L., Peters, T., Vestre, P. K., Pappas, D. K., Valls, M. I., Remiro-Buenamañana, S., Norby, T., Bjørheim, T. S., Serra, J. M. & Kjølseth, C. Single-step hydrogen production from NH3, CH4, and biogas in stacked proton ceramic reactors. *Science* **376**, 390–393 (2022).

41. Aguilar-rios, G., Valenzuela, M. A., Armendariz, H., Salas, P., Dominguez, J. M., Acosta, D. R. & Schifter, I. Metal-support effects and catalytic properties of platinum supported on zinc aluminate. *Appl. Catal. A: Gen.* **90**, 25–34 (1992).

42. Bosch, P., Valenzuela, M. A., Zapata, B., Acosta, D., Aguilar-rios, G., Maldonado, C. & Schifter, I. High temperature treated Pt/Sn-ZnAl2O4 catalysts. *J. Mol. Catal.* **93**, 67–78 (1994).

43. Valenzuela, M. A., Jacobs, J.-P., Bosch, P., Reijne, S., Zapata, B. & Brongersma, H. H. The influence of the preparation method on the surface structure of ZnAl2O4. *Appl. Catal. A: Gen.* **148**, 315–324 (1997).

44. Valenzuela, M. A., Bosch, P., Zapata, B., Aguilar-Rios, G., Lara, V. H., García-Figueroa, E. & Schifter, I. Effects of hydrogen at high temperature on ZnAl2O4 and Sn-ZnAl204. *J. Therm. Anal.* **44**, 639–653 (1995).

45. Pakhomov, N. A., Buyanov, R. A., Moroz, E. M., Kotelnikov, G. R. & Patanov, V. A. Medium effect in thermal pretreatment on the state and catalytic properties of platinum supported on zinc-aluminium spinel. *React. Kinet. Catal. Lett.* **9**, 257–263 (1978).

46. van der Laag, N. J., Snel, M. D., Magusin, P. C. M. M. & de With, G. Structural, elastic, thermophysical and dielectric properties of zinc aluminate (ZnAl2O4). *J. Eur. Ceram. Soc.* **24**, 2417–2424 (2004).

47.   Ballarini, A. D., Miguel, S. R. De, Castro, A. A. & Scelza, O. A. n-Decane dehydrogenation on Pt, PtSn and PtGe supported on spinels prepared by different methods of synthesis. *Appl. Catal. A: Gen.* **467**, 235–245 (2013).

48.   Aguilar-rios, G., Salas, P., Valenzuela, M. A., Armendariz, H., Wang, J. A. & Salmones, J. Propane dehydrogenation activity of Pt and Pt–Sn catalysts supported on magnesium aluminate: Influence of steam and hydrogen. *Catal. Letters* **60**, 21–25 (1999).

49.   Salmones, J., Wang, J., Galicia, J. A. & Aguilar-rios, g. H2 reduction behaviors and catalytic performance of bimetallic tin-modified platinum catalysts for propane dehydrogenation. *J. Mol. Catal. A: Chem.* **184**, 203–213 (2002).

50.   J.U.M. Engineering GmbH. Response Factors. http://www.jum-aerosol.com/images/E-Fakt-02.pdf (accessed October 2023).

51.   de Macedo, H. P., Bezerra de Araújo Medeiros, R. L. B., de Medeiros, A. L., Silva de Oliveira, Â. A. de, de Figueredo, G. P., Antônio, M., de Freitas Melo, M. A. & de Araújo Melo, D. M. Characterization of ZnAl2O4 spinel obtained by hydrothermal and microwave assisted combustion method: A comparative study. *Mater. Res.* **20**, 29–33 (2017).

52.   Iglesias-Juez, A., Beale, A. M., Maaijen, K., Weng, T. C., Glatzel, P. & Weckhuysen, B. M. A combined in situ time-resolved UV-Vis, Raman and high-energy resolution X-ray absorption spectroscopy study on the deactivation behavior of Pt and PtSn propane dehydrogenation catalysts under industrial reaction conditions. *J. Catal.* **276**, 268–279 (2010).

53.   Deng, L., Shishido, T., Teramura, K. & Tanaka, T. Effect of reduction method on the activity of Pt-Sn/SiO2 for dehydrogenation of propane. *Catal. Today* **232**, 33–39 (2014).

54.   Berger, R. J., Pérez-Ramírez, J., Kapteijn, F. & Moulijn, J. A. Catalyst performance testing: Bed dilution revisited. *Chem. Eng. Sci.* **57**, 4921–4932 (2002).

55.   Sheintuch, M. & Simakov, D. S. A. Alkanes Dehydrogenation. in *Membrane Reactors for Hydrogen Production Processes* 183–200 (2011). doi:10.1007/978-0-85729-151-6.

56.   Luntz, A. C., Brown, J. K. & Williams, D. Molecular beam studies of H2 and D2 dissociative chemisorption on Pt (111). *J. Chem. Phys.* **93**, 5240–5246 (1990).

57.   Salomonsson, A., Eriksson, M. & Dannetun, H. Hydrogen interaction with platinum and palladium metal-insulator- semiconductor devices. *J. Appl. Phys.* **98**, 014505 (2005).

58.   Koverga, A. A., Flórez, E., Jimenez-orozco, C. & Rodriguez, J. A. Spot the difference: hydrogen adsorption and dissociation on unsupported platinum and

platinum-coated transition metal carbides. *Phys. Chem. Chem. Phys.* **23**, 20255–20267 (2021).

59. Oudenhuijzen, M. K., Bitter, J. H. & Koningsberger, D. C. The nature of the Pt-H bonding for strongly and weakly bonded hydrogen on platinum. A XAFS spectroscopy study of the Pt-H antibonding shaperesonance and Pt-H EXAFS. *J. Phys. Chem. B* **105**, 4616–4622 (2001).

60. Vannice, M. A. Evaluation of parameter consistency in rate expressions for ideal surfaces. in *Kinetics of Catalytic Reactions* 134–140 (Springer Science+Business Media, Inc., 2005).

61. Champagnie, A. M., Tsotsis, T. T., Minet, R. G. & Wagner, E. The study of ethane dehydrogenation in a catalytic membrane reactor. *J. Catal.* **134**, 713–730 (1992).

62. Gao, X., Heyden, A., Abdelrahman, O. A. & Bond, J. Q. Microkinetic analysis of acetone hydrogenation over Pt/SiO2. *J. Catal.* **374**, 183–198 (2019).

63. Akaike, H. A new look at the statistical model identification. *IEEE Trans. Automat. Contr.* **19**, 716–723 (1974).

64. García-Diéguez, M., Hibbitts, D. D. & Iglesia, E. Hydrogen chemisorption isotherms on platinum particles at catalytic temperatures: Langmuir and two-dimensional gas models revisited. *J. Phys. Chem. C* **123**, 8447–8462 (2019).

65. Watwe, R. M., Cortright, R. D., Mavrikakis, M., Nørskov, J. K. & Dumesic, J. A. Density functional theory studies of the adsorption of ethylene and oxygen on Pt(111) and Pt3Sn(111). *J. Chem. Phys.* **114**, 4663–4668 (2001).

66. Zaera, F. Outstanding mechanistic questions in heterogeneous catalysis. *J. Phys. Chem. B* **106**, 4043–4052 (2002).

67. Zaera, F. On the mechanism for the hydrogenation of olefins on transition-metal surfaces: The chemistry of ethylene on Pt(111). *Langmuir* **12**, 88–94 (1996).

68. Öfner, H. & Zaera, F. Ethylene adsorption on platinum: Kinetics, bonding, and relevance to catalysis. *JACS* **124**, 10982–10983 (2002).

69. Campbell, C. T. The degree of rate control: A powerful tool for catalysis research. *ACS Catal.* **7**, 2770–2779 (2017).

70. Campbell, C. T. & Mao, Z. Analysis and prediction of reaction kinetics using the degree of rate control. *J. Catal.* **404**, 647–660 (2021).

71. Serrano-Ruiz, J. C., Huber, G. W., Sánchez-Castillo, M. A., Dumesic, J. A., Rodríguez-Reinoso, F. & Sepúlveda-Escribano, A. Effect of Sn addition to Pt/CeO2-Al2O3 and Pt/Al2O3 catalysts: An XPS, 119Sn Mössbauer and microcalorimetry study. *J. Catal.* **241**, 378–388 (2006).

72. National Institute of Standards and Technology. Ethane. https://webbook.nist.gov/cgi/cbook.cgi?ID=C74840&Mask=1 (accessed March 2023).

73. The Engineering ToolBox. Standard enthalpy of formation, Gibbs energy of formation, entropy and molar heat capacity of organic substances. https://www.engineeringtoolbox.com/standard-enthalpy-formation-value-Gibbs-free-energy-entropy-heat-capacity-organic-d_1979.html (accessed March 2023).

74. National Institute of Standards and Technology. Ethylene. https://webbook.nist.gov/cgi/cbook.cgi?ID=C74851&Mask=1 (accessed March 2023).

75. Chemistry LibreTexts. Homolytic C-H bond dissociation energies of organic molecules. https://chem.libretexts.org/Bookshelves/Organic_Chemistry/Supplemental_Modules_(Organic_Chemistry)/Fundamentals/Homolytic_C-H_Bond_Dissociation_Energies_of_Organic_Molecules (accessed March 2023).

76. Xu, L., Stangland, E. E., Dumesic, J. A. & Mavrikakis, M. Hydrodechlorination of 1,2-dichloroethane on platinum catalysts: insights from reaction kinetics experiments, density functional theory, and microkinetic modeling. *ACS Catal.* **11**, 7890–7905 (2021).

Supporting Information

2.A. Catalytic testing setup
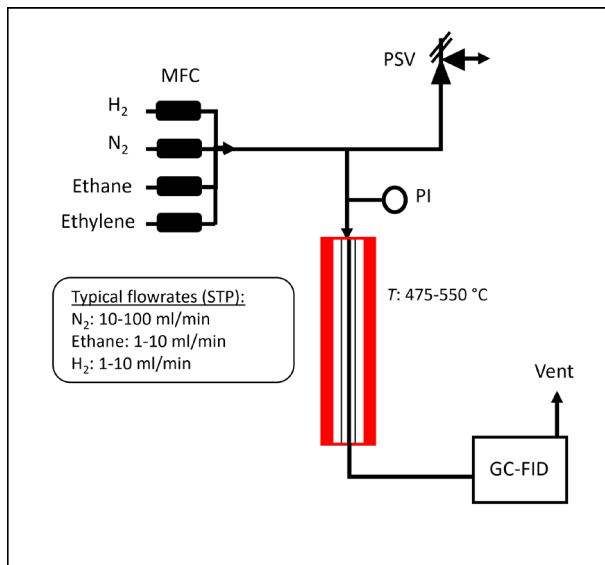
Figure 2.A1: Flow diagram of catalytic testing setup. GC-FID = Gas Chromatograph (GC), equipped with a Flame Ionization Detector (FID).

2.B. Catalyst characterization

The characteristics of $ZnAl_2O_4$, $Sn/ZnAl_2O_4$, $Pt/ZnAl_2O_4$, and $Pt-Sn/ZnAl_2O_4$ and the corresponding packed beds used during catalytic testing are summarized in **Table 2.B1**.

Table 2.B1: Characteristics of $ZnAl_2O_4$, $Sn/ZnAl_2O_4$, $Pt/ZnAl_2O_4$, and $Pt-Sn/ZnAl_2O_4$ and the corresponding packed beds.

Characteristic:	$ZnAl_2O_4$	Sn/ $ZnAl_2O_4$	Pt/ $ZnAl_2O_4$	Pt-Sn/ $ZnAl_2O_4$
BET area (m^2/g)	76.3	71.4	71.3	66.0
Pore volume (cm^3/g)	0.165	0.157	0.148	0.138
Pt loading (wt.%)	-	-	3.6	4.0
Sn loading (wt.%)	-	2.5	-	1.6
Pt cluster size (nm)[1]	-	-	9.4	9.4*
Pt cluster size (nm)[2]	-	-	1.6	3.8
Catalyst particle size (μm)	-	-	0-45	0-45

Quartz bed diluent particle (μm)	-	-	125-250	125-250
Catalyst fraction in bed (-)	-	-	ca. 0.05	ca. 0.05

[1]*Pt cluster size as determined using CO chemisorption, [2]Pt cluster size as determined using STEM-HAADF using a minimum of 200 particles. *Active Pt cluster size was determined assuming that only Pt adsorbs CO.*

X-ray diffraction (XRD) patterns were gathered after the different stages of impregnation, calcination, and activation of the catalyst to investigate possible structural changes (see **Figure 2.B1**). The bare $ZnAl_2O_4$ support showed all characteristic $ZnAl_2O_4$ spinel peaks [47,51]. After impregnation with Sn, no additional peaks were observed. Impregnating the $ZnAl_2O_4$ support with only Pt led to the formation of a Pt metal phase in addition to the $ZnAl_2O_4$ phase (**Figure 2.B1**). These same Pt peaks were observed for fresh Pt-Sn/$ZnAl_2O_4$ but to a lesser extent as compared to Pt/$ZnAl_2O_4$. Remarkably, no Pt phases but PtSn alloy phases were observed for Pt-Sn/$ZnAl_2O_4$ pre-activated in a stream of H_2 at 550 °C for 1 h, confirming the formation of a PtSn alloy under reducing atmospheres, which is in line with previous research on PtSn-based catalysts [30,52,53].
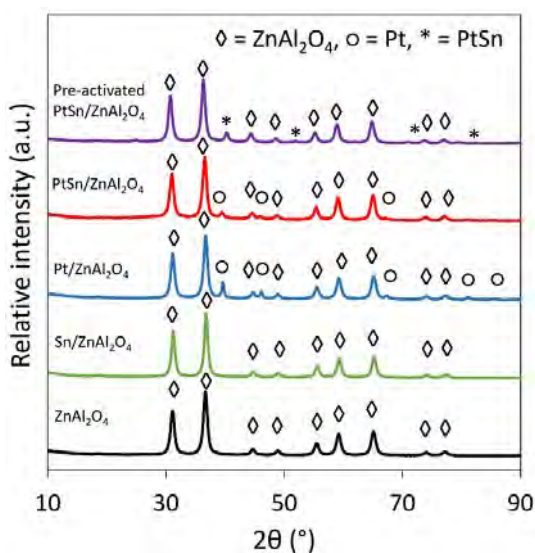
Figure 2.B1: XRD spectra of freshly calcined $ZnAl_2O_4$, Sn/$ZnAl_2O_4$, Pt/$ZnAl_2O_4$, and Pt-Sn/$ZnAl_2O_4$, and pre-activated PtSn/$ZnAl_2O_4$.

X-ray photoelectron spectroscopy (XPS) was performed to determine the surface concentrations and oxidation states of Pt and Sn in fresh and pre-activated bimetallic Pt-Sn/$ZnAl_2O_4$ catalysts. The most intense Pt photoelectrons corresponded to the electrons released from the Pt 4f levels. However, these photoemission lines overlapped with the Al 2p peaks. For this reason, the Pt XPS analysis focused on the Pt 4d peaks. On traditional

Al_2O_3 supports, metallic Pt^0 $4d_{5/2}$ electrons commonly have a binding energy of about 313.0 eV [30,71], whilst Pt $4d_{5/2}$ electrons in Pt^{2+} and Pt^{4+} typically have binding energies of ca. 315 eV and ca. 319 eV, respectively [71]. Compared to traditional Al_2O_3 supports, the metal-support interactions are stronger in case Pt is functionalized onto $ZnAl_2O_4$ or $MgAl_2O_4$ spinel-type supports [32]. Electron binding strengths of Pt 4d electrons are therefore expected to be somewhat greater in $Pt/ZnAl_2O_4$ catalysts as compared to the prescribed binding energy values of Pt/Al_2O_3 systems, due to a lower electron density around Pt in $Pt/ZnAl_2O_4$. Supposedly, Pt^{2+} (ca. 317 eV) and Pt^{4+} (ca. 322 eV) in freshly calcined Pt-Sn/ZnAl$_2O_4$ were reduced to primarily Pt^0 after H_2 treatment (**Figure 2.B2**).
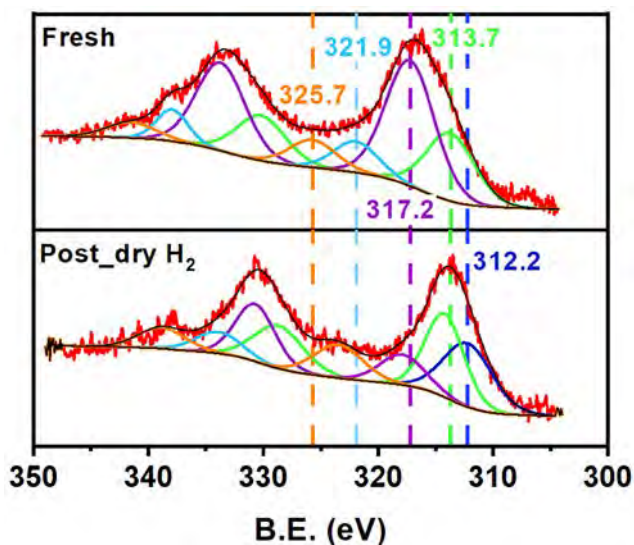
Figure 2.B2: X-ray photoelectron spectroscopy (XPS) results of the Pt 4d photoemission lines of fresh and reduced Pt-Sn/ZnAl$_2O_4$. The reduced sample is exposed to a stream of H_2 (10 ml/min STP) at 550 °C for 1 h.

After deconvoluting the Pt 4d XPS spectrum, five different Pt types can be discerned (see **Figure 2.B2**). Each Pt type was composed of a $4d_{3/2}$ and a $4d_{5/2}$ spin state electron and the ratio of these spin states should be 2:3 for Pt 4d electrons. Besides, the distance between the $4d_{3/2}$ and $4d_{5/2}$ spin states should be about 17 eV and the full width at half maximum (FWHM) of both states needed to be equal. These Pt 4d electron requirements were imposed in the deconvolution. The Pt $4d_{5/2}$ photoemission lines in **Figure 2.B2** around 313.7 eV, 317.2 eV, and 321.9 eV can be ascribed to the presence of Pt^0, Pt^{2+}, and Pt^{4+}, respectively. The Pt $4d_{5/2}$ electrons at even higher binding energy can possibly be attributed to higher oxidized Pt or Pt hydroxide species, e.g. Pt(OH)$_4$. Besides, the Pt $4d_{5/2}$ photoemission line around 312 eV can supposedly be assigned to hydrogen covered Pt-H species. The latter peak only appeared in the H_2 treated Pt-Sn/ZnAl$_2O_4$ sample and could originate from electron donation from the hydrogen to the Pt upon adsorption.

The atomic and mass composition of fresh and reduced Pt-Sn/ZnAl$_2$O$_4$, as shown in **Table 2.B2**, suggest that Zn was somewhat enriched on the surface relative to the bulk, which is possible indication of strong metal-support interactions in the reduced sample. The reduction in Pt and C surface concentration after H$_2$ treatment could be caused by slight Pt sintering and hydrogenation of carbon deposits, respectively.

Table 2.B2: Atomic and mass-based surface composition of Pt-Sn/ZnAl$_2$O$_4$, as determined using X-ray photoelectron spectroscopy (XPS).

	O 1s	Zn 2p	Al 2p	Pt 4d	Sn 3d	C 1s
Pt-Sn/ZnAl$_2$O$_4$ fresh						
At.%	49.4	20.4	25.7	1.2	0.7	2.6
Wt.%	25.0	42.1	21.9	7.4	2.6	1.0
Pt-Sn/ZnAl$_2$O$_4$ post dry H$_2$						
At.%	48.1	21.2	27.6	0.8	0.7	1.5
Wt.%	24.4	43.9	23.6	4.9	2.6	0.6

In contrast to the Pt 4d photoemission lines, no clear changes in the electron binding energies of the Sn 4d electrons can be identified after reducing the Pt-Sn/ZnAl$_2$O$_4$ sample (see **Figure 2.B3**). Possible shifts toward lower binding energies of the Sn 4d electrons, related to the formation of a PtSn alloy, could be hidden by the overlapping O 2s peaks.
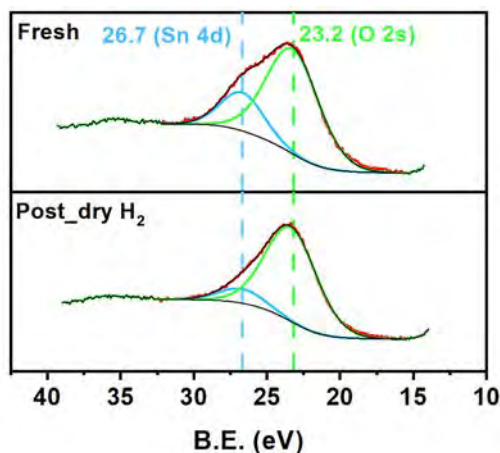
Figure 2.B3: X-ray photoelectron spectroscopy (XPS) results of the Sn 4d photoemission lines of fresh and reduced Pt-Sn/ZnAl$_2$O$_4$. The reduced sample is exposed to a stream of H$_2$ (10 ml/min STP) at 550 °C for 1 h.

An example of a STEM-HAADF image of the Pt-Sn/ZnAl$_2$O$_4$ catalyst sample is presented in **Figure 2.B4**. This figure illustrates the presence of a limited number of large metal particles in addition to a large number of small metal particles.
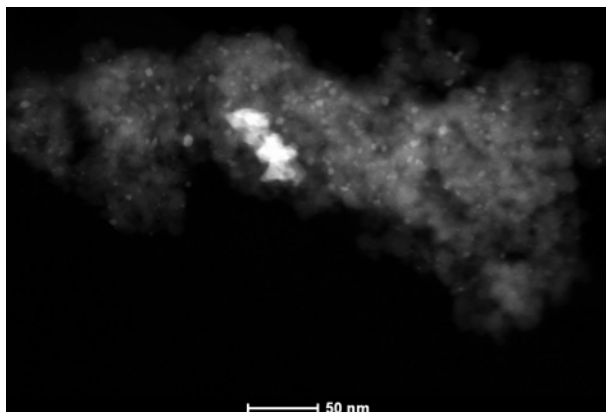
Figure 2.B4: STEM-HAADF image of Pt-Sn/ZnAl$_2$O$_4$, indicating the presence of a limited number of large metal particles in addition to a large number of small ones.

2.C. Kinetic regime checks

2.C1. Internal mass transfer limitations check

Internal mass transfer limitations were excluded by varying catalyst particle sizes for catalyst-to-feed ratios (W/F_{ethane}) of ca. 8.6 and ca. 17.1 kg$_{cat}$•s/kg$_{ethane}$. **Table 2.C1** confirms that internal mass transfer limitations start to play a role for 125 μm catalyst particles and bigger. The kinetic tests were performed using the <45 μm particle size fraction to ensure operation in a regime free of internal mass transfer limitations.

Table 2.C1: Internal mass transfer limitations check, T = 650 °C, p_{ethane} = 40 mbar(a), p_{H2} = 120 mbar(a), 0.01 g of Pt-Sn/ZnAl$_2$O$_4$ catalyst in bed.

W/F_{ethane} (kg_{cat}•s/kg_{ethane})	Ethane conversion (%)		
	<45 μm	45-125 μm	125-250 μm
8.6-8.7	17.4 ± 0.6	18.8 ± 0.4	14.0 ± 0.4
17.0-17.2	26.4 ± 0.4	27.3 ± 1.1	22.7 ± 0.3

2.C2. External mass transfer limitations check

External mass transfer limitations were checked for catalyst particles between 45-125 μm by varying catalyst amounts and flow rates accordingly, i.e. by keeping W/F_{ethane} constant at ca. 8.6 kg$_{cat}$•s/kg$_{ethane}$. The results confirm that the conversion is not affected by changes in the flow profile along the catalyst particles in the packed bed (see **Figure 2.C2**).
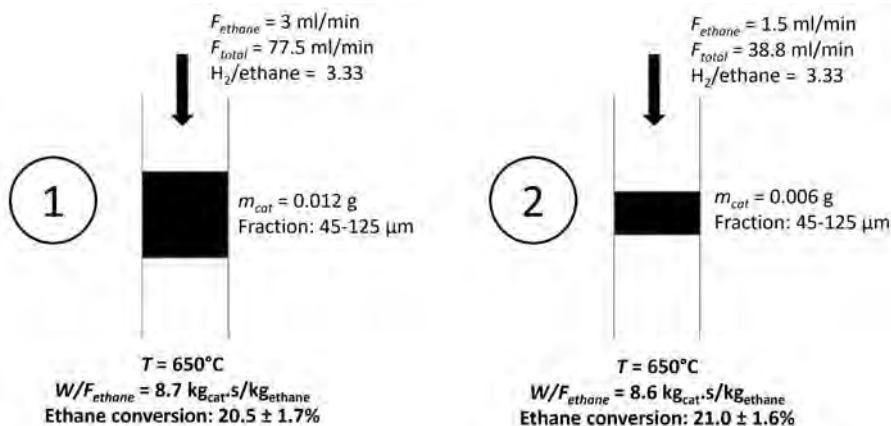
Figure 2.C2: Conditions and outcomes of external mass transfer limitations check.

2.C3. Thermodynamic equilibrium check

The kinetic tests were performed for two different conversion levels, corresponding to situations relatively close (i.e. 70-90%) and further away (i.e. 40-60%) of the thermodynamically attainable equilibrium conversion (**Supporting Information 2.P**). In the hydrogen reaction order testing, the hydrogen partial pressure was varied between 40-105 mbar(a) for a constant ethane partial pressure of 35 mbar(a). The equilibrium conversion is lower when cosupplying more hydrogen (see **Figure 2.C3**).
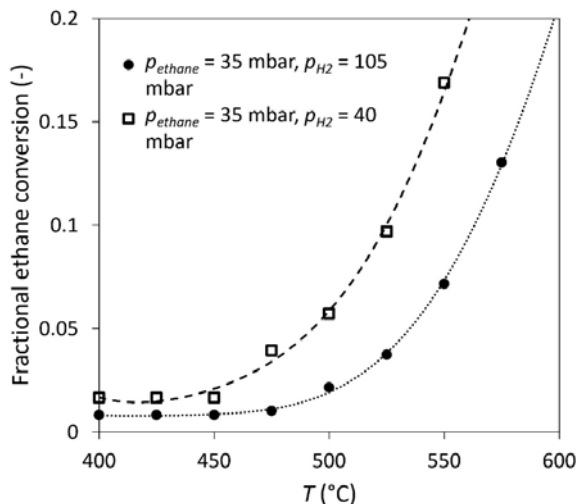
Figure 2.C3: Fractional equilibrium conversion of ethane NODH, based on the thermodynamic data from Champagnie et al. [61] and a total pressure of 1 bar(a).

2.C4. Catalyst bed dilution check

The Pt catalyst was diluted with inert quartz (SiO_2) particles to ensure isothermal operation and to control the conversion level. For reactions dealing with positive reaction orders in reactants, the fraction of catalyst in the bed should be such that it is low enough to stay away from equilibrium but at the same time high enough to avoid channeling of gas through the bed. Berger et al. [54] developed a relation between the reduction in conversion caused by bed dilution and the corresponding catalyst bed parameters (e.g. dilution fraction, conversion level, particle diameter, bed height) for a first-order reaction. In this work, the used dilution fraction was about 0.95 (i.e. 95 wt.% bed diluent, 5 wt.% catalyst) [34]. This leads to a deviation between actual conversion and the corresponding conversion in a homogeneous bed (no bed diluent) of less than 1%, following the relation proposed by Berger et al. [54]. This marginal deviation is caused by a relatively low conversion level (ca. 10%), a relatively small bed diluent and catalyst particle size (<250 µm), and a relatively long bed (ca. 2-3 cm). Hence, channeling is minimal under these conditions and its influence on the conversion level can be neglected.

2.C5. Differential character of the reactor

The catalyst-to-feed ratio (W/F_{ethane}) was varied by changing the amount of catalyst to identify under which conditions the reactor operates in a differential regime. At W/F_{ethane} values below ca. 100 $kg_{cat} \cdot s/kg_{ethane}$, the ethylene yield increases linearly with increasing W/F_{ethane} (**Figure 2.C4**). Within this regime, the ethylene formation rate does not change with varying catalyst amounts and, hence, effectively along the reactor length. The ethane and hydrogen reaction order tests were, therefore, conducted at W/F_{ethane} values below 100 $kg_{cat} \cdot s/kg_{ethane}$. At higher W/F_{ethane} values, the thermodynamic equilibrium sets in, which hinders further ethylene formation.
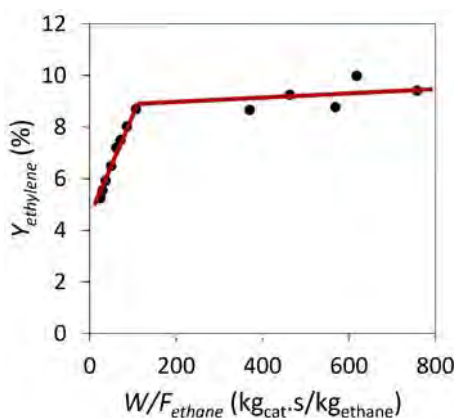
Figure 2.C4: Influence of the catalyst-to-feed ratio (W/F_{ethane}) on the ethylene yield for a feed stream containing 34 mbar(a) ethane, 104 mbar(a) H_2, balanced with N_2, T = 550 °C.

2.D. Catalyst stability

The Pt-Sn/ZnAl$_2$O$_4$ catalyst was stable during the activation barrier and ethane and H$_2$ reaction order determination, allowing for the use of a single bed per temperature condition investigated. This is illustrated in **Figure 2.D1a** for the H$_2$ reaction order test performed at 550 °C at 70-90% of the thermodynamic equilibrium conversion. Upon stepwise reducing the H$_2$ partial pressure over time, the conversion increases, while keeping the ethane partial pressure constant. At the end of the test, the conditions were returned to the initial testing conditions (see **Figure 2.D1a**). Using this procedure, the catalytic activity at the end of the test was found to be equal to the initial activity for all activation barrier, ethane reaction order, and H$_2$ reaction order tests, thereby excluding possible influences of catalyst deactivation on the obtained kinetic data.
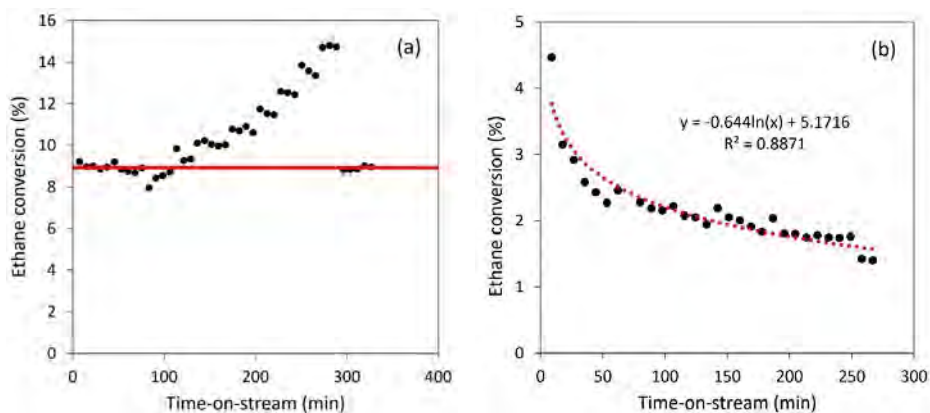
Figure 2.D1: Ethane conversion vs. time-on-stream (a) for catalytic tests without ethylene cosupply, where the catalyst was stable throughout the day (initial and final conditions are equal) and where in this case stepwise reduction in H$_2$ partial pressure during the day resulted in increased ethane conversion levels (T = 550 °C, p_{ethane} = 35 mbar(a), p_{H2} = 40-125 mbar(a)), and (b) for catalytic tests in which ethylene was cosupplied, leading to rapid deactivation, requiring extrapolation to retrieve initial activities (T = 550 °C, p_{ethane} = 155 mbar(a), p_{H2} = 77 mbar(a), $p_{ethylene}$ = 18 mbar(a)).

In contrast to the ethane and H$_2$ reaction order data, the catalyst did deactivate over time for the ethylene reaction order investigations. For this reason, a single catalyst bed was used per ethylene partial pressure condition investigated. Besides, time-on-stream data needed to be extrapolated to time t = 0 to obtain initial ethylene formation activities. This is illustrated in **Figure 2.D1b** for the test in which 18 mbar(a) of ethylene was cosupplied with 155 mbar(a) of ethane and 77 mbar(a) of H$_2$. A logarithmic fit was found to best describe the experimental catalytic decay over time for all ethylene reaction order tests. The sensitivity of the initial activity values determined via this procedure to the location of the first data point time-on-stream was included in the error margin calculation of the ethylene reaction order data points (**Figure 2.2d**).

2.E. Possible reaction mechanisms

Note: for the possible reaction mechanisms proposed in this section, the same number is consistently assigned to equal reaction steps for convenience, i.e. ethylene desorption is always step 4, H_2 desorption is always step 5, etc. Moreover, different mechanisms are discriminated if either one of the elementary steps or the rate-determining step changes.

<u>Mechanism 1:</u>
- **Non-dissociative** adsorption of ethane
- Ethylene adsorption equilibrium on the **adsorption** side
- **RDS = 1st H abstraction (step 2)**

1. $C_2H_6\,(g) + \quad * \quad \leftrightharpoons C_2H_6\, *$
2. $C_2H_6\, * + \; * \quad \rightarrow \quad C_2H_5\, * + H\, *$
3. $\;C_2H_5\, * + * \quad \leftrightharpoons \; C_2H_4\, * + H\, *$
4. $\;C_2H_4\, * \quad\quad\quad \leftrightharpoons \; C_2H_4\,(g) + *$
5. $\;\;2H\, * \quad\quad\quad\; \leftrightharpoons \; H_2\,(g) + 2\, *$
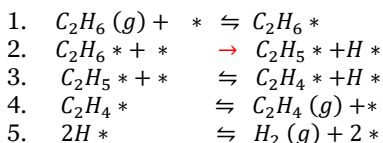
<u>Mechanism 2:</u>
- **Non-dissociative** adsorption of ethane
- Ethylene adsorption equilibrium on the **desorption** side
- **RDS = 1st H abstraction (step 2)**

1. $C_2H_6\,(g) + \quad * \quad \leftrightharpoons C_2H_6\, *$
2. $C_2H_6\, * + * \quad\quad \rightarrow \quad C_2H_5\, * + H\, *$
3. $\;C_2H_5\, * \quad\quad\quad \leftrightharpoons \; C_2H_4\,(g) + H\, *$
4.
5. $\;\;2H\, * \quad\quad\quad\; \leftrightharpoons \; H_2\,(g) + 2\, *$
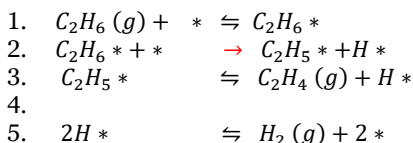
<u>Mechanism 3:</u>
- **Dissociative adsorption** of ethane
- Ethylene adsorption equilibrium on the **adsorption** side
- **RDS = dissociative adsorption (step 1)**

1. $C_2H_6\,(g) + \; 2\, * \quad \rightarrow \; C_2H_5\, * + H\, *$
2.
3. $\;C_2H_5\, * \; + \; * \quad \leftrightharpoons \; C_2H_4\, * + H\, *$
4. $\;C_2H_4\, * \quad\quad\quad \leftrightharpoons \; C_2H_4\,(g) + \; *$
5. $\;\;2H\, * \quad\quad\quad\; \leftrightharpoons \; H_2\,(g) + 2\, *$
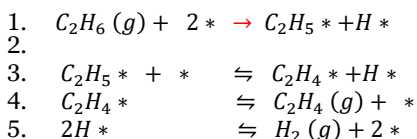
<u>Mechanism 4:</u>
- **Dissociative** adsorption of ethane
- Ethylene adsorption equilibrium on the **desorption** side
- **RDS = dissociative adsorption (step 1)**

1. $C_2H_6\,(g) + \; 2\, * \rightarrow \; C_2H_5\, * + H\, *$
2.
3.
4. $\;C_2H_5\, * \quad\quad\quad \leftrightharpoons \; C_2H_4\,(g) + H\, *$
5. $\;\;2H\, * \quad\quad\quad\; \leftrightharpoons \; H_2\,(g) + 2\, *$
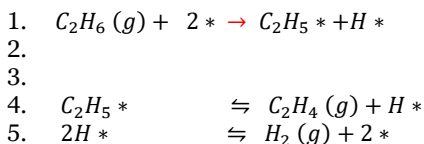
Mechanism 5:
- **Non-dissociative** adsorption of ethane
- Ethylene adsorption equilibrium on the **adsorption** side
- **RDS = 2nd H abstraction (step 3)**

1. $C_2H_6\,(g) + \quad * \quad \leftrightharpoons C_2H_6 *$
2. $C_2H_6 * + * \quad \leftrightharpoons C_2H_5 * + H *$
3. $C_2H_5 * + * \quad \rightarrow C_2H_4 * + H *$
4. $C_2H_4 * \qquad \leftrightharpoons C_2H_4\,(g) + \quad *$
5. $2H * \qquad \leftrightharpoons H_2\,(g) + 2 *$
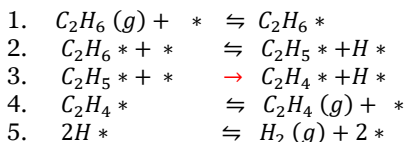
Mechanism 6:
- **Non-dissociative** adsorption of ethane
- Ethylene adsorption equilibrium on the **desorption** side
- **RDS = 2nd H abstraction (step 3)**

1. $C_2H_6\,(g) + \quad * \quad \leftrightharpoons C_2H_6 *$
2. $C_2H_6 * + * \quad \leftrightharpoons C_2H_5 * + H *$
3. $C_2H_5 * \qquad \rightarrow C_2H_4\,(g) + H *$
4.
5. $2H * \qquad \leftrightharpoons H_2\,(g) + 2 *$
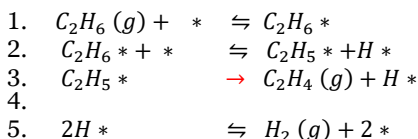
Mechanism 7:
- **Dissociative** adsorption of ethane
- Ethylene adsorption equilibrium on the **adsorption** side
- **RDS = 2nd H abstraction (step 3)**

1. $C_2H_6\,(g) + \quad 2 * \leftrightharpoons C_2H_5 * + H *$
2.
3. $C_2H_5 * + * \quad \rightarrow C_2H_4 * + H *$
4. $C_2H_4 * \qquad \leftrightharpoons C_2H_4\,(g) + \quad *$
5. $2H * \qquad \leftrightharpoons H_2\,(g) + 2 *$
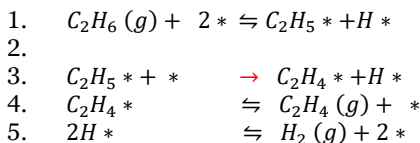
Mechanism 8:
- **Dissociative** adsorption of ethane
- Ethylene adsorption equilibrium on the **desorption** side
- **RDS = 2nd H abstraction (step 4)**

1. $C_2H_6\,(g) + \quad 2 * \quad \leftrightharpoons C_2H_5 * + H *$
2.
3.
4. $C_2H_5 * \qquad \rightarrow C_2H_4\,(g) + H *$
5. $2H * \qquad \leftrightharpoons H_2\,(g) + 2 *$
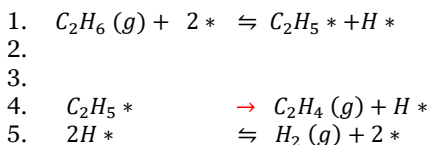
Mechanism 9:
- **Non-dissociative** adsorption of ethane
- Ethylene adsorption equilibrium on the **adsorption** side
- **RDS = ethylene desorption (step 4)**

1. $C_2H_6\,(g) + \quad * \quad \leftrightharpoons C_2H_6 *$
2. $C_2H_6 * + * \quad \leftrightharpoons C_2H_5 * + H *$
3. $C_2H_5 * + * \quad \leftrightharpoons C_2H_4 * + H *$
4. $C_2H_4 * \qquad \rightarrow C_2H_4\,(g) + \quad *$
5. $2H * \qquad \leftrightharpoons H_2\,(g) + 2 *$
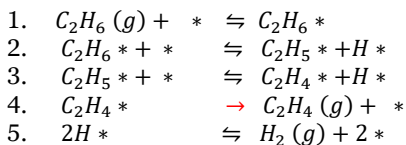
Mechanism 10:
- **Dissociative** adsorption of ethane
- Ethylene adsorption equilibrium on the **adsorption** side
- **RDS = ethylene desorption (step 4)**

1. $C_2H_6 (g) + 2* \leftrightarrows C_2H_5* + H*$
2.
3. $C_2H_5* + * \leftrightarrows C_2H_4* + H*$
4. $C_2H_4* \rightarrow C_2H_4 (g) + *$
5. $2H* \leftrightarrows H_2 (g) + 2*$
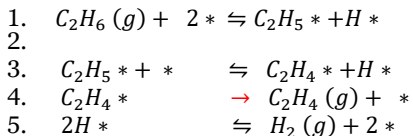
Mechanism 11:
- **Dissociative** adsorption of ethane
- Ethylene adsorption equilibrium on the **adsorption** side
- **RDS = H$_2$ desorption (step 5)**

1. $C_2H_6 (g) + 2* \leftrightarrows C_2H_5* + H*$
2.
3. $C_2H_5* + * \leftrightarrows C_2H_4* + H*$
4. $C_2H_4* \leftrightarrows C_2H_4 (g) + *$
5. $2H* \rightarrow H_2 (g) + 2*$
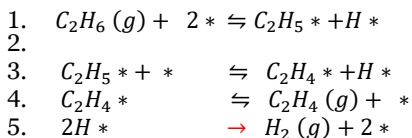
Mechanism 12:
- **Dissociative** adsorption of ethane
- Ethylene adsorption equilibrium on the **desorption** side
- **RDS = H$_2$ desorption (step 5)**

1. $C_2H_6 (g) + 2* \leftrightarrows C_2H_5* + H*$
2.
3.
4. $C_2H_5* \leftrightarrows C_2H_4 (g) + H*$
5. $2H* \rightarrow H_2 (g) + 2*$
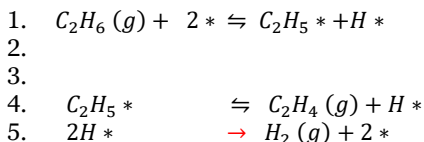
Mechanism 13:
- **Non-dissociative** adsorption of ethane
- Ethylene adsorption equilibrium on the **adsorption** side
- **RDS = H$_2$ desorption (step 5)**

1. $C_2H_6 (g) + * \leftrightarrows C_2H_6*$
2. $C_2H_6* + * \leftrightarrows C_2H_5* + H*$
3. $C_2H_5* + * \leftrightarrows C_2H_4* + H*$
4. $C_2H_4* \leftrightarrows C_2H_4 (g) + *$
5. $2H* \rightarrow H_2 (g) + 2*$
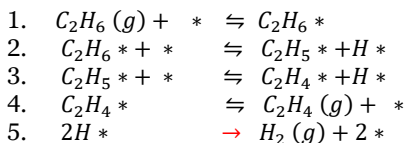
Mechanism 14:
- **Non-dissociative** adsorption of ethane
- Ethylene adsorption equilibrium on the **desorption** side
- **RDS = H$_2$ desorption (step 5)**

1. $C_2H_6 (g) + * \leftrightarrows C_2H_6*$
2. $C_2H_6* + * \leftrightarrows C_2H_5* + H*$
3. $C_2H_5* \leftrightarrows C_2H_4 (g) + H*$
4.
5. $2H* \rightarrow H_2 (g) + 2*$
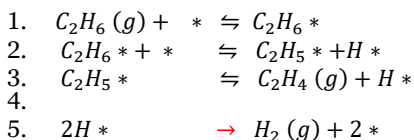
2.F. Derivation of LHHW expression of mechanism 3

<u>Mechanism 3:</u>

1	$C_2H_6\,(g) +\ 2*$	$\rightarrow$	$C_2H_5 * + H *$
3	$C_2H_5 * + *$	$\leftrightharpoons$	$C_2H_4 * + H *$
4	$C_2H_4 *$	$\leftrightharpoons$	$C_2H_4\,(g) + *$
5	$2H *$	$\leftrightharpoons$	$H_2\,(g) + 2 *$
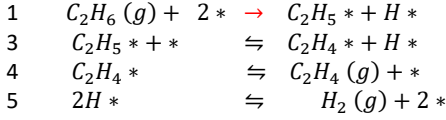
From (4): $\qquad K_{eq,4} = \frac{\theta_{C2H4*}}{p_{C2H4}\theta_V} \rightarrow \theta_{C2H4*} = K_{eq,4} p_{C2H4}\theta_V$

From (5): $\qquad K_{eq,5} = \frac{\theta_{H*}^2}{p_{H2}\theta_V^2} \rightarrow \theta_{H*} = K_{eq,5}^{1/2} p_{H2}^{1/2}\theta_V$

From (3): $\qquad K_{eq,3} = \frac{\theta_{C2H4*}\theta_{H*}}{\theta_{C2H5*}\theta_V} \rightarrow \theta_{C2H5*} = \frac{\theta_{C2H4*}\theta_{H*}}{K_{eq,3}\theta_V} = \frac{K_{eq,4}p_{C2H4}\theta_V K_{eq,5}^{1/2}p_{H2}^{1/2}\theta_V}{K_{eq,3}\theta_V} = \frac{K_{eq,4}p_{C2H4}K_{eq,5}^{1/2}p_{H2}^{1/2}\theta_V}{K_{eq,3}}$

Site balance: $\qquad \theta_{total} = \theta_V + \theta_{C2H4*} + \theta_{H*} + \theta_{C2H5*} = 1$

Leads to: $\qquad \theta_{total} = \theta_V + K_{eq,4}p_{C2H4}\theta_V + K_{eq,5}^{1/2}p_{H2}^{1/2}\theta_V + \frac{K_{eq,4}p_{C2H4}K_{eq,5}^{1/2}p_{H2}^{1/2}\theta_V}{K_{eq,3}} = 1$

Equals: $\qquad \theta_{total} = \theta_V \left(1 + K_{eq,4}p_{C2H4} + K_{eq,5}^{\frac{1}{2}}p_{H2}^{\frac{1}{2}} + \frac{K_{eq,4}p_{C2H4}K_{eq,5}^{\frac{1}{2}}p_{H2}^{\frac{1}{2}}}{K_{eq,3}}\right) = 1$

Leads to: $\qquad \theta_V = \dfrac{1}{\left(1 + K_{eq,4}p_{C2H4} + K_{eq,5}^{\frac{1}{2}}p_{H2}^{\frac{1}{2}} + \frac{K_{eq,4}p_{C2H4}K_{eq,5}^{\frac{1}{2}}p_{H2}^{\frac{1}{2}}}{K_{eq,3}}\right)}$

$$TOF = k_1\,p_{C2H6}\theta_V^2$$

$$TOF = \frac{k_1\,p_{C2H6}}{\left(1 + \frac{K_{eq,4}K_{eq,5}^{\frac{1}{2}}}{K_{eq,3}}p_{C2H4}p_{H2}^{\frac{1}{2}} + K_{eq,4}p_{C2H4} + K_{eq,5}^{\frac{1}{2}}p_{H2}^{\frac{1}{2}}\right)^2}$$

In this rate expression, the four different denominator terms account for the respective surface occupancy of (i) empty sites, (ii) C_2H_5*, (iii) C_2H_4*, and (iv) $H*$. The ethyl (C_2H_5*) surface occupancy is expected to be negligible, similar to the isobutyl surface occupancy in isobutane dehydrogenation [34], which simplifies the LHHW rate expression to:

$$TOF = \frac{k_1\,p_{C2H6}}{\left(1 + K_{eq,4}p_{C2H4} + K_{eq,5}^{\frac{1}{2}}p_{H2}^{\frac{1}{2}}\right)^2}$$

Including reversibility term of the ethane dehydrogenation reaction leads to:

$$TOF = \frac{k_1\left(p_{C2H6} - \frac{p_{C2H4}p_{H2}}{K_{eq}}\right)}{\left(1 + K_{eq,4}p_{C2H4} + K_{eq,5}^{\frac{1}{2}}p_{H2}^{\frac{1}{2}}\right)^2}$$

2.G. LHHW rate expressions of the different possible mechanisms

**Characteristics and LHHW rate expression**

1   Non-dissociative C_2H_6 adsorption, C_2H_4 at adsorption side, RDS = 1st H removal

$$TOF = \frac{k_2 \, K_1 \left(p_{C2H6} - \frac{p_{C2H4}p_{H2}}{K_{eq}} \right)}{\left(1 + K_1 p_{C2H6} + \frac{K_4 \, K_5^{0.5}}{K_3} \, p_{C2H4} \, p_{H2}^{0.5} + K_4 \, p_{C2H4} + K_5^{0.5}p_{H2}^{0.5} \right)^2}$$

2   Non-dissociative C_2H_6 adsorption, C_2H_4 at desorption side, RDS = 1st H removal

$$TOF = \frac{k_2 \, K_1 \left(p_{C2H6} - \frac{p_{C2H4}p_{H2}}{K_{eq}} \right)}{\left(1 + K_1 p_{C2H6} + \frac{K_4 \, K_5^{0.5}}{K_3} \, p_{C2H4} \, p_{H2}^{0.5} + K_5^{0.5}p_{H2}^{0.5} \right)^2}$$

3   Dissociative C_2H_6 adsorption, C_2H_4 at adsorption side, RDS = dissociative adsorption

$$TOF = \frac{k_1 \left(p_{C2H6} - \frac{p_{C2H4}p_{H2}}{K_{eq}} \right)}{\left(1 + \frac{K_4 \, K_5^{0.5}}{K_3} \, p_{C2H4} \, p_{H2}^{0.5} + K_4 \, p_{C2H4} + K_5^{0.5}p_{H2}^{0.5} \right)^2}$$

4   Dissociative C_2H_6 adsorption, C_2H_4 at desorption side, RDS = dissociative adsorption

$$TOF = \frac{k_1 (p_{C2H6} - \frac{p_{C2H4}p_{H2}}{K_{eq}})}{\left(1 + \frac{K_5^{0.5}}{K_4} \, p_{C2H4} \, p_{H2}^{0.5} + K_5^{0.5}p_{H2}^{0.5} \right)^2}$$

5   Non-dissociative C_2H_6 adsorption, C_2H_4 at adsorption side, RDS = 2nd H removal

$$TOF = \frac{\frac{k_3 K_2 K_1}{K_5^{0.5}p_{H2}^{0.5}} \left(p_{C2H6} - \frac{p_{C2H4}p_{H2}}{K_{eq}} \right)}{\left(1 + K_1 p_{C2H6} + \frac{K_2 \, K_1}{K_5^{0.5}} \, \frac{p_{C2H6}}{p_{H2}^{0.5}} + K_4 \, p_{C2H4} + K_5^{0.5}p_{H2}^{0.5} \right)^2}$$

6   Non-dissociative C_2H_6 adsorption, C_2H_4 at desorption side, RDS = 2nd H removal

$$TOF = \frac{\frac{k_3 K_2 K_1}{K_5^{0.5}p_{H2}^{0.5}} \left(p_{C2H6} - \frac{p_{C2H4}p_{H2}}{K_{eq}} \right)}{\left(1 + K_1 p_{C2H6} + \frac{K_2 \, K_1}{K_5^{0.5}} \, \frac{p_{C2H6}}{p_{H2}^{0.5}} + K_5^{0.5}p_{H2}^{0.5} \right)}$$

7   Dissociative C_2H_6 adsorption, C_2H_4 at adsorption side, RDS = 2nd H removal

$$TOF = \frac{\frac{k_3 K_1}{K_5^{0.5}p_{H2}^{0.5}} \left(p_{C2H6} - \frac{p_{C2H4}p_{H2}}{K_{eq}} \right)}{\left(1 + \frac{K_1}{K_5^{0.5}} \, \frac{p_{C2H6}}{p_{H2}^{0.5}} + K_4 \, p_{C2H4} + K_5^{0.5}p_{H2}^{0.5} \right)^2}$$

8   Dissociative C_2H_6 adsorption, C_2H_4 at desorption side, RDS = 2nd H removal

$$TOF = \frac{\dfrac{k_3 K_1}{K_5^{0.5} p_{H2}^{0.5}}\left(p_{C2H6} - \dfrac{p_{C2H4} p_{H2}}{K_{eq}}\right)}{\left(1 + \dfrac{K_1}{K_5^{0.5}}\ \dfrac{p_{C2H6}}{p_{H2}^{0.5}} + K_5^{0.5} p_{H2}^{0.5}\right)}$$

9   Non-dissociative C_2H_6 adsorption, C_2H_4 at adsorption side, RDS = C_2H_4 desorption

$$TOF = \frac{\dfrac{k_4 K_3 K_2 K_1}{K_5 p_{H2}}(p_{C2H6} - \dfrac{p_{C2H4} p_{H2}}{K_{eq}})}{\left(1 + K_1 p_{C2H6} + \dfrac{K_2 K_1 p_{C2H6}}{K_5^{0.5} p_{H2}^{0.5}} + \dfrac{K_3 K_2 K_1 p_{C2H6}}{K_5 p_{H2}} + K_5^{0.5} p_{H2}^{0.5}\right)}$$

10   Dissociative C_2H_6 adsorption, C_2H_4 at adsorption side, RDS = C_2H_4 desorption

$$TOF = \frac{\dfrac{k_4 K_3 K_1}{K_5 p_{H2}}\left(p_{C2H6} - \dfrac{p_{C2H4} p_{H2}}{K_{eq}}\right)}{\left(1 + \dfrac{K_1 p_{C2H6}}{K_5^{0.5} p_{H2}^{0.5}} + \dfrac{K_3 K_1 p_{C2H6}}{K_5 p_{H2}} + K_5^{0.5} p_{H2}^{0.5}\right)}$$

11   Dissociative C_2H_6 adsorption, C_2H_4 at adsorption side, RDS = H_2 desorption

$$TOF = \frac{k_5 \dfrac{K_1 K_3}{K_4 p_{C2H4}}\left(p_{C2H6} - \dfrac{p_{C2H4} p_{H2}}{K_{eq}}\right)}{\left(1 + \dfrac{K_1^{0.5} K_3^{0.5} p_{C2H6}^{0.5}}{K_3^{0.5} p_{C2H4}^{0.5}} + K_4 p_{C2H4} + \dfrac{K_1^{0.5} K_4^{0.5} p_{C2H6}^{0.5} p_{C2H4}^{0.5}}{K_3^{0.5}}\right)^2}$$

12   Dissociative C_2H_6 adsorption, C_2H_4 at desorption side, RDS = H_2 desorption

$$TOF = \frac{k_5 \dfrac{K_1 K_4}{p_{C2H4}}\left(p_{C2H6} - \dfrac{p_{C2H4} p_{H2}}{K_{eq}}\right)}{\left(1 + \dfrac{K_1^{0.5} p_{C2H6}^{0.5} p_{C2H4}^{0.5}}{K_4^{0.5}} + \dfrac{K_1^{0.5} K_4^{0.5} p_{C2H6}^{0.5}}{p_{C2H4}^{0.5}}\right)^2}$$

13   Non-dissociative C_2H_6 adsorption, C_2H_4 at adsorption side, RDS = H_2 desorption

$$TOF = \frac{k_5 \dfrac{K_3 K_2 K_1}{K_4 p_{C2H4}}\left(p_{C2H6} - \dfrac{p_{C2H4} p_{H2}}{K_{eq}}\right)}{\left(1 + K_1 p_{C2H6} + \dfrac{K_1^{0.5} K_2^{0.5} K_4^{0.5} p_{C2H6}^{0.5} p_{C2H4}^{0.5}}{K_3^{0.5}} + K_4 p_{C2H4} + \dfrac{K_3^{0.5} K_2^{0.5} K_1^{0.5} p_{C2H6}^{0.5}}{K_4^{0.5} p_{C2H4}^{0.5}}\right)^2}$$

14   Non-dissociative C_2H_6 adsorption, C_2H_4 at desorption side, RDS = H_2 desorption

$$TOF = \frac{k_5 \dfrac{K_1 K_2}{K_3 p_{C2H4}}\left(p_{C2H6} - \dfrac{p_{C2H4} p_{H2}}{K_{eq}}\right)}{\left(1 + K_1 p_{C2H6} + K_3^{0.5} K_2^{0.5} K_1^{0.5} p_{C2H6}^{0.5} p_{C2H4}^{0.5} + \dfrac{K_1^{0.5} K_2^{0.5} p_{C2H6}^{0.5}}{K_3^{0.5} p_{C2H4}^{0.5}}\right)^2}$$

2.H. Theoretical C$_2$H$_6$, C$_2$H$_4$, and H$_2$ reaction orders

Table 2.H1: Theoretical reaction orders for the different reaction mechanisms for extreme cases in which an excess of p_{C2H6}, p_{H2}, and p_{C2H4} is applied, respectively.

#	Condition	n_{C2H6}	n_{H2}	n_{C2H4}
1	$p_{C2H6} >> p_{C2H4} \approx p_{H2}$	-1	0	0
	$p_{H2} >> p_{C2H6} \approx p_{C2H4}$	1	-1	-2 to 0
	$p_{C2H4} >> p_{C2H6} \approx p_{H2}$	1	-1 to 0	-2
2	$p_{C2H6} >> p_{C2H4} \approx p_{H2}$	-1	0	0
	$p_{H2} >> p_{C2H6} \approx p_{C2H4}$	1	-1	-2 to 0
	$p_{C2H4} >> p_{C2H6} \approx p_{H2}$	1	-1 to 0	-2 t0 0
3	$p_{C2H6} >> p_{C2H4} \approx p_{H2}$	1	0	0
	$p_{H2} >> p_{C2H6} \approx p_{C2H4}$	1	-1	-2 to 0
	$p_{C2H4} >> p_{C2H6} \approx p_{H2}$	1	-1 to 0	-2
4	$p_{C2H6} >> p_{C2H4} \approx p_{H2}$	1	0	0
	$p_{H2} >> p_{C2H6} \approx p_{C2H4}$	1	-1	-2 to 0
	$p_{C2H4} >> p_{C2H6} \approx p_{H2}$	1	-1 to 0	-2 to 0
5	$p_{C2H6} >> p_{C2H4} \approx p_{H2}$	-1	-0.5 to 0.5	0
	$p_{H2} >> p_{C2H6} \approx p_{C2H4}$	-1 to 1	-1.5 to 0.5	0
	$p_{C2H4} >> p_{C2H6} \approx p_{H2}$	1	-0.5	-2
6	$p_{C2H6} >> p_{C2H4} \approx p_{H2}$	0	-0.5 to 0	0
	$p_{H2} >> p_{C2H6} \approx p_{C2H4}$	0 to 1	-1 to 0	0
	$p_{C2H4} >> p_{C2H6} \approx p_{H2}$	1	-0.5	0
7	$p_{C2H6} >> p_{C2H4} \approx p_{H2}$	-1	0.5	0
	$p_{H2} >> p_{C2H6} \approx p_{C2H4}$	1	-1.5	0
	$p_{C2H4} >> p_{C2H6} \approx p_{H2}$	1	-0.5	-2
8	$p_{C2H6} >> p_{C2H4} \approx p_{H2}$	0	0	0
	$p_{H2} >> p_{C2H6} \approx p_{C2H4}$	1	-0.5 to 0	0
	$p_{C2H4} >> p_{C2H6} \approx p_{H2}$	1	-0.5	0
9	$p_{C2H6} >> p_{C2H4} \approx p_{H2}$	0	-1 to 0	0
	$p_{H2} >> p_{C2H6} \approx p_{C2H4}$	1	-1.5 to -1	0
	$p_{C2H4} >> p_{C2H6} \approx p_{H2}$	1	-1	0
10	$p_{C2H6} >> p_{C2H4} \approx p_{H2}$	0	-0.5 to 0	0
	$p_{H2} >> p_{C2H6} \approx p_{C2H4}$	1	-1.5 to -1	0
	$p_{C2H4} >> p_{C2H6} \approx p_{H2}$	1	-1	0
11	$p_{C2H6} >> p_{C2H4} \approx p_{H2}$	0	0	-2 to 0
	$p_{H2} >> p_{C2H6} \approx p_{C2H4}$	1	0	-1
	$p_{C2H4} >> p_{C2H6} \approx p_{H2}$	0 to 1	0	-3 to -2
12	$p_{C2H6} >> p_{C2H4} \approx p_{H2}$	0	0	-2 to 0
	$p_{H2} >> p_{C2H6} \approx p_{C2H4}$	1	0	-1
	$p_{C2H4} >> p_{C2H6} \approx p_{H2}$	0 to 1	0	-2 to 0
13	$p_{C2H6} >> p_{C2H4} \approx p_{H2}$	-1 to 0	0	-2 to 0
	$p_{H2} >> p_{C2H6} \approx p_{C2H4}$	1	0	-1
	$p_{C2H4} >> p_{C2H6} \approx p_{H2}$	0 to 1	0	-3 to -2
14	$p_{C2H6} >> p_{C2H4} \approx p_{H2}$	-1 to 0	0	-2 to 0
	$p_{H2} >> p_{C2H6} \approx p_{C2H4}$	1	0	-1
	$p_{C2H4} >> p_{C2H6} \approx p_{H2}$	0 to 1	0	-2 to -1

2.J. Initial estimate approximation of thermodynamic parameters

The initial estimations of the Gibbs free energy of the adsorption equilibria were derived by using a procedure for thermodynamic approximations as proposed by Gao et al. [62]. In this procedure, equilibrium constants were quantified by approximating the enthalpy and entropy of gas phase and adsorbed surface species under reaction conditions.

2.J1. Gas phase species approximation

The reaction order data were obtained at four different temperatures (i.e. 475, 500, 525, and 550 °C). The initial approximations therefore also had to be computed at these four temperatures. The standard gas phase thermodynamic data of the species involved in the elementary steps of the various proposed reaction mechanisms are tabulated in **Table 2.J1**.

Table 2.J1: Standard gas phase thermodynamic data, T = 298 K, P = 1 atm.

Species	$\Delta_f H_i^0$ (kJ/mol)	S_i^0 (J/mol.K)	$C_{P,i}$ (J/mol.K)	Ref.
Ethane (C_2H_6)	-84.0	229.2	52.49	[72,73]
Ethylene (C_2H_4)	52.4	219.3	42.90	[73,74]
H_2	0	130.7	28.84	[62]
H	218.0	114.7	20.79	[62]
C_2H_5	121.0	224.5	47.70	

Since C_2H_5 is a non-existing, unstable gas phase species, its thermodynamic properties could not be retrieved from data tables. As the gas phase degrees of freedom and the thermal properties of C_2H_5 are supposedly comparable to C_2H_6 and C_2H_4, the averages of the standard molar entropy and heat capacity of C_2H_6 and C_2H_4 were assumed to be representative for C_2H_5. The enthalpy of C_2H_5 formation was calculated based on the C-H bond dissociation energy and the gas phase formation enthalpies of C_2H_6 and H:

$$\Delta_f H_{C2H5}^0 = \Delta_f H_{C2H6}^0 + BDE_{CH} - \Delta_f H_H^0 \tag{2.J1}$$

Equation 2.J1 was based on the fact that gas phase C_2H_5 can effectively be formed via C-H bond dissociation from C_2H_6, yielding gas phase H as a fictive coproduct:

$$C_2H_6\ (g) \leftrightarrow C_2H_5\ (g) + H\ (g) \tag{2.J2}$$

The bond dissociation energy of an ethyl C-H bond is 423 kJ/mol [75]. Using this value and the standard gas phase enthalpies of C_2H_6 and H, the standard enthalpy of formation of C_2H_5 was computed to be 121 kJ/mol using **Equation 2.J1**. The temperature dependency of the gas phase enthalpy and entropy of the various species was calculated using **Equation 2.J3** and **2.J4**.

$$\Delta_f H_i\,(T) = \Delta_f H_i^0 + C_{P,i}(T - T^0) \tag{2.J3}$$

$$S_i(T) = S_i^0 + C_{P,i}\ln\left(\frac{T}{T^0}\right) \tag{2.J4}$$

Herein, the heat capacity was assumed to be independent of temperature. The resulting gas phase thermodynamic data for the different temperatures used in the kinetic tests (475, 500, 525, and 550 °C) were calculated using **Equation 2.J3** and **2.J4** with the data from **Table 2.J1**. The results are shown in **Table 2.J2**.

Table 2.J2: Gas phase thermodynamic data for the different reaction temperatures, $P = 1$ atm.

Species	475 °C		500 °C		525 °C		550 °C	
	H_i kJ/mol	S_i J/mol.K	H_i kJ/mol	S_i J/mol.K	H_i kJ/mol	S_i J/mol.K	H_i kJ/mol	S_i J/mol.K
Ethane (C_2H_6)	-60.4	277.9	-59.1	279.6	-57.8	281.3	-56.4	282.9
Ethylene (C_2H_4)	71.7	258.8	72.8	260.2	73.9	261.6	74.9	262.9
H_2	13.0	157.2	13.7	158.2	14.4	159.1	15.1	160.0
H	227.4	133.8	227.9	134.5	228.4	135.2	228.9	135.8
C_2H_5	142.5	268.3	143.7	269.9	144.8	271.4	146.0	272.9

2.J2. Adsorbed surface species approximation

The enthalpies of the surface-bound species were estimated as the difference between the gas phase enthalpy of a concerning species for a given temperature and the binding energy of that species:

$$H_{i,x}\,(T) = H_i\,(T) - BE_{i,x} \tag{2.J5}$$

Where the x subscript indicates an adsorbed state. The binding energies of the different species were considered to be independent of temperature and surface coverage. The results are shown in **Table 2.J3**. It should be noted that the extent to which ethane adsorbs dissociatively on PtSn depends on Sn content and the nature of the PtSn sites [35]. Thus, for other relative Pt and Sn loadings and for differently shaped PtSn clusters, ethane adsorption might take place differently.

Table 2.J3: Adsorbed surface species enthalpy data at ambient temperature and at the different reaction temperatures, P = 1 atm. Binding energies (BE_i) were retrieved from Xu et al. [76].

Species	BE_i (kJ/mol)	25 °C $H_{i,x}$ (kJ/mol)	475 °C $H_{i,x}$ (kJ/mol)	500 °C $H_{i,x}$ (kJ/mol)	525 °C $H_{i,x}$ (kJ/mol)	550 °C $H_{i,x}$ (kJ/mol)
Ethane (C_2H_6)	31.8	-115.8	-92.2	-90.9	-89.6	-88.3
Ethylene (C_2H_4)	164.0	-111.6	-92.3	-91.3	-90.2	-89.1
H	276.9	-58.9	-49.6	-49.1	-48.5	-48.0
C_2H_5	226.8	-105.8	-84.3	-83.1	-81.9	-80.7

In the determination of the entropy of surface-bound species it was assumed that the gas-phase translational movement disappears upon adsorption, whilst gas-phase rotational and vibrational movements were retained. The entropy of surface-bound species was considered to be equal to the summation of the local gas phase entropy and the diffusional entropy:

$$S_{i,x} = S_{i,loc} + 2 \cdot S_{i,diff,1D} \tag{2.J6}$$

Where a surface species was assumed to have diffusional freedom in two dimensions (planar directions). The diffusional entropy can be defined as follows:

$$S_{i,diff,1D} = R \cdot \left(\left(\frac{X_i}{\exp(X_i) - 1} \right) - \ln(1 - exp(-X_i)) \right) \tag{2.J7}$$

Where:

$$X_i = \frac{h\nu_{i,diff}}{k_b T} \tag{2.J8}$$

The frequency of the diffusional movement ($\nu_{i,diff}$) in Hz of a single molecule is defined as:

$$\nu_{i,diff} = \sqrt{\frac{0.12 \cdot BE_{i,x}}{2l^2 m_i}} \tag{2.J9}$$

In which the diffusion barrier (in J) of species i was approximated as 12% of its binding energy. Besides, l represents the unit cell edge length (in m), which was assumed to be $3.0 \cdot 10^{-10}$ m for Pt [62], and m_i is the molar weight of a single molecule in kg/particle. Considering the assumption that the gas-phase translational movement disappears upon

adsorption, the 'local gas-phase' entropy of surface-bound species can be approximated as:

$$S_{i,loc} = S_i - S_{i,tran}^{3D} - S_{i,elec} \qquad (2.J10)$$

Where the three-dimensional translational entropy is defined as:

$$S_{i,tran}^{3D} = R \bullet \left(\ln \left(\left(\frac{2\pi m_i k_b T}{h^2} \right)^{\frac{3}{2}} \bullet \frac{k_b T}{P_0} \right) + \frac{5}{2} \right) \qquad (2.J11)$$

The electronic entropy ($S_{i,elec}$) depends on the degeneracy of the electronic ground state (g_i):

$$S_{i,elec} = R \bullet \ln (g_i) \qquad (2.J12)$$

The degeneracy of the electronic species is typically 1 if that species does not have unpaired electrons, which is the case for ethane and ethylene. For species that do contain an unpaired electron, like atomic hydrogen and C_2H_5 on the surface, g_i equals 2.

By using **Equation 2.J6** to **2.J12**, the entropy of the surface species ($S_{i,x}$) was calculated at different temperatures. The results are shown in **Table 2.J4**.

Table 2.J4: Adsorbed surface species entropy data at ambient temperature and at the different reaction temperatures, P = 1 atm.

Species	25 °C	475 °C	500 °C	525 °C	550 °C
	$S_{i,x}$ (J/mol.K)	$S_{i,x}$ (J/mol.K)	$S_{i,x}$ (J/mol.K)	$S_{i,x}$ (J/mol.K)	$S_{i,x}$ (J/mol.K)
Ethane (C_2H_6)	128.2	172.7	174.3	175.8	177.3
Ethylene (C_2H_4)	104.6	140.2	141.5	142.7	143.9
H	6.6	19.5	20.0	20.5	21.0
C_2H_5	101.2	141.2	142.6	144.0	145.4

2.J3. Approximation of adsorption and surface equilibrium thermodynamic parameters

From the difference between gas phase and surface-based thermodynamic data, the enthalpy and entropy of adsorption of the various species can be calculated using **Equation 2.J13** and **2.J14**.

$$\Delta H_{ads} = H_{i,x} (T) - H_i (T) \qquad (2.J13)$$

$$\Delta S_{ads} = S_{i,x} (T) - S_i (T) \qquad (2.J14)$$

The resulting enthalpies and entropies of adsorption are represented in **Table 2.J5** and **Table 2.J6**, respectively. Note that the enthalpy of adsorption is independent of temperature for all species, since the binding energy was assumed to be constant with temperature (**Equation 2.J5**). The entropy of adsorption becomes more negative with increasing temperature, since the difference in degrees of freedom of the species between gas phase and adsorbed phase increases with increasing temperature.

Table 2.J5: Estimated enthalpies of adsorption at ambient temperature and at the different reaction temperatures, $P = 1$ atm.

Species	25 °C ΔH_{ads} (kJ/mol)	475 °C ΔH_{ads} (kJ/mol)	500 °C ΔH_{ads} (kJ/mol)	525 °C ΔH_{ads} (kJ/mol)	550 °C ΔH_{ads} (kJ/mol)
Ethane (C_2H_6)	-31.8	-31.8	-31.8	-31.8	-31.8
Ethylene (C_2H_4)	-164.0	-164.0	-164.0	-164.0	-164.0
H	-276.9	-276.9	-276.9	-276.9	-276.9
C_2H_5	-226.8	-226.8	-226.8	-226.8	-226.8

Table 2.J6: Estimated entropies of adsorption at ambient temperature and at the different reaction temperatures, $P = 1$ atm.

Species	25 °C ΔS_{ads} (J/mol.K)	475 °C ΔS_{ads} (J/mol.K)	500 °C ΔS_{ads} (J/mol.K)	525 °C ΔS_{ads} (J/mol.K)	550 °C ΔS_{ads} (J/mol.K)
Ethane (C_2H_6)	-101.4	-105.2	-105.4	-105.5	-105.6
Ethylene (C_2H_4)	-114.7	-118.6	-118.7	-118.8	-119.0
H	-108.1	-114.3	-114.5	-114.7	-114.8
C_2H_5	-123.4	-127.2	-127.3	-127.4	-127.6

From the enthalpy and entropy of adsorption, the Gibbs free energy of adsorption could be computed (**Equation 2.J15**), as tabulated in **Table 2.J7**. These values increase with increasing temperature, as desorption is favored at higher temperatures.

$$\Delta G_{ads} = \Delta H_{ads} - T * \Delta S_{ads} \qquad (2.J15)$$

Table 2.J7: Estimated Gibbs free energies of adsorption at ambient temperature and at the different reaction temperatures, P = 1 atm.

Species	25 °C ΔG_{ads} (kJ/mol)	475 °C ΔG_{ads} (kJ/mol)	500 °C ΔG_{ads} (kJ/mol)	525 °C ΔG_{ads} (kJ/mol)	550 °C ΔG_{ads} (kJ/mol)
Ethane (C_2H_6)	-1.6	46.9	49.6	52.3	55.1
Ethylene (C_2H_4)	-129.9	-75.4	-72.3	-69.2	-66.1
H	-244.7	-191.4	-188.4	-185.4	-182.4
C_2H_5	-190.0	-131.6	-128.4	-125.1	-121.8

Interestingly, the negative Gibbs free energies of adsorption of ethylene, hydrogen, and the ethyl (*C_2H_5) group indicate surface adsorption of these species under reaction conditions. On the contrary, ethane does not bind to the catalyst surface under reaction conditions according to these theoretical estimations. This is in line with the experimental observation that ethane binds dissociatively on Pt-Sn/$ZnAl_2O_4$. The Gibbs free energies of adsorption of ethylene and hydrogen in **Table 2.J7** were used as initial estimates in the kinetic regression. The C_2H_5 to C_2H_4 surface equilibrium is not an adsorption equilibrium but a surface reaction equilibrium. The corresponding initial estimate therefore had to be determined in an alternative manner. The thermodynamics of the surface equilibrium reaction can be defined as:

$$\Delta H_{eq} = \left(H_{C2H4,x} + H_{H,x}\right) - H_{C2H5,x} \tag{2.J16}$$

And:

$$\Delta S_{eq} = \left(S_{C2H4,x} + S_{H,x}\right) - S_{C2H5,x} \tag{2.J17}$$

And from **Equation 2.J16** and **2.J17**:

$$\Delta G_{eq} = \Delta H_{eq} - T\Delta S_{eq} \tag{2.J18}$$

The resulting thermodynamic initial estimates for the surface equilibrium reaction are presented in **Table 2.J8**. This surface equilibrium step represents a dehydrogenation step, which is typically favored at higher temperatures, as illustrated by the temperature dependency of the Gibbs free energy of the surface equilibrium shown in **Table 2.J8**.

Table 2.J8: Estimated thermodynamic parameters of the $*C_2H_5$ to $*C_2H_4$ surface equilibrium at ambient temperature and at the different reaction temperatures, $P = 1$ atm.

	25 °C	475 °C	500 °C	525 °C	550 °C
ΔH_{eq} (kJ/mol)	-64.8	-57.6	-57.2	-56.8	-56.4
ΔS_{eq} (J/mol.K)	10.0	18.5	18.9	19.2	19.6
ΔG_{eq} (kJ/mol)	-67.8	-71.5	-71.8	-72.2	-72.5

2.K. Thermodynamic parameters of reaction mechanism 3

The thermodynamic outcomes of the kinetic regression are presented in **Table 2.K1**.

Table 2.K1: Thermodynamic outcomes of the kinetic regression using mechanism 3, including the temperature and related coverage dependency of hydrogen and ethylene adsorption.

T (°C)	k_1		$K_4 = K_{C2H4,ads}$		$K_5 = K_{H2,ads}$	
	$\Delta H_1^{\ddagger}$ (kJ/mol)	$\Delta S_1^{\ddagger}$ (J/mol.K)	$\Delta H_{4,ads}$ (kJ/mol)	$\Delta S_{4,ads}$ (J/mol.K)	$\Delta H_{5,ads}$ (kJ/mol)	$\Delta S_{5,ads}$ (J/mol.K)
475	67.7	24.8	-58.9	49.4	-38.6	127.2
500	67.7	24.8	-58.9	49.4	-38.6	127.2
525	67.7	24.8	-58.9	49.4	-38.6	127.2
550	67.7	24.8	-58.9	49.4	-38.6	127.2

2.L. Plug flow reactor balance

The tubular reactor used for catalytic testing (*I.D.* = 4 mm, L = 450 mm) was considered to satisfy the plug flow reactor model (**Figure 2.L1**).
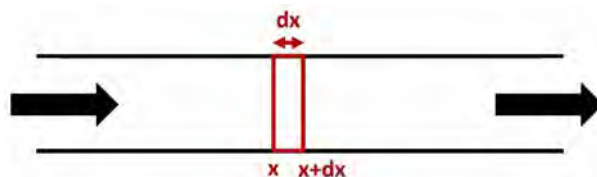
Figure 2.L1: Plug flow reactor.

The mass balance of species i across a single reactor slice with length dx (**Figure 2.L1**) is:

$$\frac{dm_i}{dt} = \emptyset_m w_i|_x - \emptyset_m w_i|_{x+dx} + R_{V,i} M_i S dx \qquad \text{(in kg/s)} \qquad (2.L1)$$

Where w_i represents the weight fraction of i, $\emptyset_m$ the total mass flow rate (in kg/s), $R_{V,i}$ the volumetric conversion/formation rate of species i (in $mol_i/m^3 \cdot s$), M_i the molar weight of i (in kg/mol), and S the cross-sectional area of the reactor (in m^2). In case of steady state operation (i.e. $\frac{dm_i}{dt} = 0$), **Equation 2.L1** reduces to **Equation 2.L2**.

$$\emptyset_m w_i|_{x+dx} - \emptyset_m w_i|_x = R_{V,i} M_i S dx \qquad \text{(in kg/s)} \qquad (2.L2)$$

By realizing that w_i is a function of the concentration of i (c_i, in mol/m^3) and the total stream density (ρ_{tot}, in kg/m^3) via $w_i = \frac{M_i c_i}{\rho_{tot}}$ and $\emptyset_m$ is a function of the volumetric gas flow rate ($\emptyset_V$, in m^3/s) and ρ_{tot} via $\emptyset_m = \emptyset_V \rho_{tot}$, **Equation 2.L2** can be rewritten to:

$$\emptyset_V c_i|_{x+dx} - \emptyset_V c_i|_x = R_{V,i} S dx \qquad \text{(in mol/s)} \qquad (2.L3)$$

In **Equation 2.L3**, the volume-based reaction rate can be rewritten into a reaction rate per catalyst mass (R_m, in $mol_i/kg_{cat} \cdot s$) using the catalyst density (ρ_{cat}, in $kg_{cat}/m^3_{reactor}$):

$$\emptyset_V c_i|_{x+dx} - \emptyset_V c_i|_x = R_{m,i} \rho_{cat} S dx \qquad \text{(in mol/s)} \qquad (2.L4)$$

When considering an infinitesimally small reactor slice, **Equation 2.L4** reduces to **Equation 2.L5**.

$$\lim_{dx \to 0} \frac{\emptyset_V c_i|_{x+dx} - \emptyset_V c_i|_x}{dx} = \frac{\delta(\emptyset_V c_i)}{\delta x} = R_{m,i} \rho_{cat} S \qquad \text{(in mol/s)} \qquad (2.L5)$$

The vast majority of the kinetic tests were performed using low ethane concentrations (1-10 vol%) and low conversion levels (1-10%). The volumetric expansion caused by the ethane NODH reaction is therefore negligible for those tests, which reduces **Equation 2.L5** into **Equation 2.L6**.

$$\frac{\emptyset_V}{\rho_{cat} S} \frac{\delta c_i}{\delta x} = R_{m,i} \qquad \text{(in mol/s)} \qquad (2.L6)$$

Equation 2.L6 is still based on the mass-based reaction rate $R_{m,i}$, which can be rewritten into an analogous equation containing the apparent turnover frequency of the formation of species i ($TOF_{app,i}$), as shown in **Equation 2.L7**, by using the catalyst loading ($\sigma_{Pt} = 0.04$ kg_{Pt}/kg_{cat}), the Pt molar weight ($M_{W,Pt} = 0.195$ kg_{Pt}/mol_{Pt}), and the Pt dispersion ($\beta_{Pt} = 0.12$ $mol_{Pt,s}/mol_{Pt}$), according to **Equation 2.L8**, where $mol_{Pt,s}$ indicates the number of moles of Pt exposed to the surface.

$$\frac{\emptyset_V}{\rho_{cat} S} \frac{\delta c_i}{\delta x} = \frac{TOF_{app,i} \sigma_{Pt} \beta_{Pt}}{M_{W,Pt}} = R_{m,i} \qquad \text{(in mol/s)} \qquad (2.L7)$$

$$TOF_{app,i} = \frac{R_{m,i}M_{W,Pt}}{\sigma_{Pt}\beta_{Pt}}$$ (2.L8)

As an example, the mass-based ethylene formation rate ($R_{m,C2H4}$) was defined in this work as in **Equation 2.L9**.

$$R_{m,C2H4} = \frac{F_{C2H6,0}Y_{C2H4}}{m_{cat}}$$ (in mol$_{C2H4}$/kg$_{cat}$•s) (2.L9)

In which $F_{C2H6,0}$ represents the ethane molar feed flow rate (in mol/s), Y_{C2H4} the ethylene yield, as defined by **Equation 2.5**, and m_{cat} the mass of catalyst in the bed (in kg).

2.M. High conversion catalytic testing data
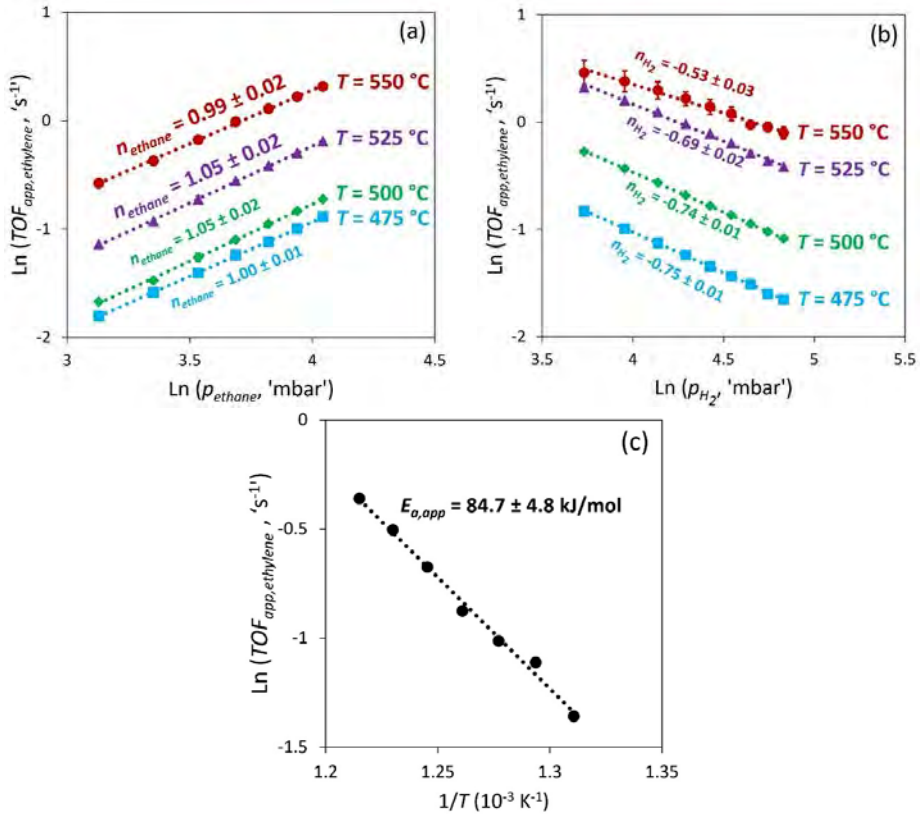
Figure 2.M1: (a) Ethane and (b) H$_2$ reaction orders along the temperature range 475-550 °C. Conditions for (a): p_{ethane} = 20-60 mbar(a), p_{H2} = 105 mbar(a). Conditions for (b): p_{ethane} = 35 mbar(a), p_{H2} = 40-120 mbar(a). (c) Arrhenius curve for ethylene formation on Pt-Sn/ZnAl$_2$O$_4$. T = 490-550 °C, p_{ethane} = 34 mbar(a), p_{H2} = 105 mbar(a). Data gathered at 70-90% of the theoretically maximum attainable conversion level.

2.N. Apparent TOF of ethylene formation at high and low conversion
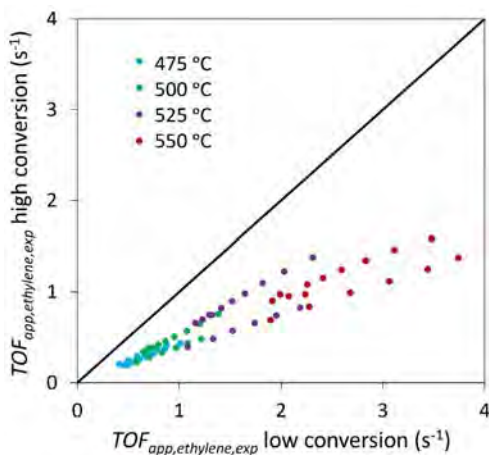
Figure 2.N1: Apparent experimental turnover frequency of ethylene formation ($TOF_{app,ethylene,exp}$) obtained within the high conversion range (i.e. 70-90% of theoretically attainable maximum) plotted against the related $TOF_{app,ethylene,exp}$ values gathered within the low conversion range (i.e. 40-60% of the theoretical maximum). The conditions used and the corresponding conversion levels and approaches to equilibrium are summarized in **Supporting Information 2.P**.

2.O. Influence of H_2 removal on the surface coverage distribution

The outcomes of the kinetic regression (**Table 2.4**) were used to construct the surface coverage distributions as a function of the fraction of hydrogen removal (**Figure 2.O1**). Herein, a distinction was made between hydrogen removal from a system operating under conditions in line with the conditions used in the catalytic tests (**Figure 2.O1a**) and hydrogen removal inside a potential membrane reactor (**Figure 2.O1b**). By doing so, it was implicitly assumed that the thermodynamic adsorption parameters, as determined in this work for hydrogen adsorption onto hydrogen-rich surfaces, were extrapolatable to potentially more ethylene-rich surfaces encountered inside membrane reactors. **Figure 2.O1** illustrates that the surface coverage of ethylene inside potential membrane reactors will be considerably higher than under the conditions used in the catalytic tests, regardless of the fraction of hydrogen removed. Moreover, even for representative catalytic testing conditions the surface becomes readily dominated by ethylene instead of hydrogen when removing only marginal fractions of hydrogen from the reaction zone (**Figure 2.O1a**).
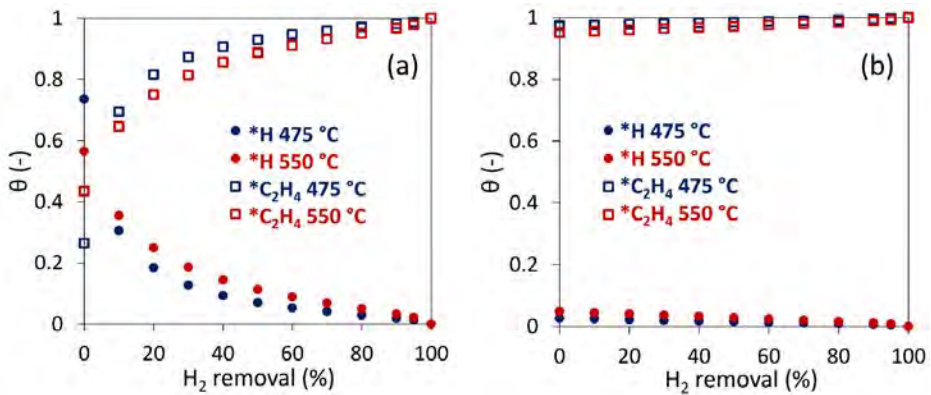
Figure 2.O1: Predicted surface coverage distributions as a function of the percentage of hydrogen removal (a) for catalytic testing conditions as used in this work (feed: 40 mbar(a) ethane, 100 mbar(a) hydrogen, $Y_{ethylene}$: 5%), and (b) for realistic membrane reactors conditions (feed: pure ethane, P: 1 atm, $Y_{ethylene}$: 11%).

2.P. Summarizing table of the used conditions and the applied conversion levels

Table 2.P1: Summary of the applied conditions and the corresponding applied conversion and thermodynamic equilibrium conversion level (X_{ethane}).

T (°C)	p_{ethane} (mbar)	p_{H2} (mbar)	Applied X_{ethane} (%)	Max. $p_{ethylene}$ (mbar)	Equilibrium X_{ethane} (%)	Approach to equilibrium (-)
Low conversion range data:						
Ethane reaction order testing						
475	28.6	104.5	1.3	0.37	2.6	0.50
475	34.2	104.4	1.3	0.44	2.6	0.50
475	39.9	104.4	1.3	0.52	2.6	0.50
475	45.6	104.3	1.3	0.61	2.6	0.50
475	51.3	104.3	1.3	0.69	2.6	0.50
475	57.0	104.2	1.4	0.78	2.6	0.54
500	28.6	104.5	2.0	0.56	3.1	0.65
500	34.2	104.4	2.0	0.68	3.1	0.65
500	39.9	104.4	2.0	0.80	3.1	0.65
500	45.6	104.3	2.0	0.93	3.1	0.65
500	51.3	104.3	2.0	1.04	3.1	0.65
500	57.0	104.2	2.1	1.17	3.1	0.68
525	28.6	104.5	3.4	0.96	5.5	0.62
525	34.2	104.4	3.5	1.19	5.5	0.64
525	39.9	104.4	3.4	1.35	5.5	0.62
525	45.6	104.3	3.4	1.55	5.5	0.62

525	51.3	104.3	3.4	1.73	5.5	0.62
525	57.0	104.2	3.4	1.94	5.5	0.62
550	28.6	104.5	5.9	1.69	9.7	0.61
550	34.2	104.4	5.9	2.03	9.7	0.61
550	39.9	104.4	6.0	2.38	9.7	0.62
550	45.6	104.3	6.0	2.72	9.7	0.62
550	51.3	104.3	6.0	3.06	9.7	0.62
550	57.0	104.2	5.9	3.35	9.7	0.61
Hydrogen reaction order testing						
475	34.2	41.8	2.6	0.90	5.2	0.50
475	34.2	52.2	2.2	0.76	4.3	0.51
475	34.2	62.6	2.0	0.67	3.7	0.54
475	34.2	73.1	1.7	0.60	3.3	0.52
475	34.2	83.5	1.6	0.54	2.8	0.57
475	34.2	94.0	1.5	0.50	2.6	0.58
475	34.2	104.4	1.4	0.47	2.6	0.54
475	34.3	114.9	1.3	0.44	2.1	0.62
475	34.3	125.3	1.2	0.41	2.0	0.60
500	34.2	41.8	3.9	1.34	6.1	0.64
500	34.2	52.2	3.4	1.16	5.3	0.64
500	34.2	62.6	3.0	1.04	4.8	0.63
500	34.2	73.1	2.7	0.92	4.3	0.63
500	34.2	83.5	2.4	0.83	3.8	0.63
500	34.2	94.0	2.2	0.77	3.4	0.65
500	34.2	104.4	2.0	0.68	3.1	0.54
500	34.3	114.9	1.9	0.66	2.6	0.73
500	34.3	125.3	1.8	0.62	2.4	0.75
525	34.2	41.8	6.0	2.06	11.6	0.52
525	34.2	52.2	5.3	1.81	9.9	0.54
525	34.2	62.6	4.7	1.62	8.7	0.54
525	34.2	73.1	4.3	1.46	7.7	0.56
525	34.2	83.5	4.0	1.35	7.0	0.57
525	34.2	94.0	3.7	1.26	6.4	0.58
525	34.2	104.4	3.4	1.15	5.5	0.62
525	34.3	114.9	3.2	1.09	5.0	0.64
525	34.3	125.3	3.0	1.03	4.4	0.68
550	34.2	41.8	9.0	3.10	19.0	0.47
550	34.2	52.2	8.1	2.77	16.8	0.48
550	34.2	62.6	7.4	2.52	15.2	0.49
550	34.2	73.1	6.7	2.31	12.8	0.52
550	34.2	83.5	6.3	2.15	11.6	0.54

550	34.2	94.0	5.9	2.01	10.6	0.56
550	34.2	104.4	5.8	1.99	9.7	0.60
550	34.3	114.9	5.4	1.85	9.0	0.60
550	34.3	125.3	5.0	1.70	8.4	0.60

High conversion range data:

Ethane reaction order testing

475	22.8	104.5	2.2	0.51	2.6	0.85
475	28.6	104.5	2.2	0.64	2.6	0.85
475	34.2	104.4	2.2	0.77	2.6	0.85
475	39.9	104.4	2.3	0.90	2.6	0.88
475	45.6	104.3	2.2	1.02	2.6	0.85
475	51.3	104.3	2.2	1.15	2.6	0.85
475	57.0	104.2	2.2	1.28	2.6	0.85
500	22.8	104.5	2.5	0.57	3.1	0.81
500	28.6	104.5	2.4	0.70	3.1	0.77
500	34.2	104.4	2.4	0.81	3.1	0.77
500	39.9	104.4	2.5	1.01	3.1	0.81
500	45.6	104.3	2.6	1.17	3.1	0.84
500	51.3	104.3	2.6	1.32	3.1	0.84
500	57.0	104.2	2.6	1.47	3.1	0.84
525	22.8	104.5	4.7	1.08	5.5	0.85
525	28.6	104.5	4.7	1.33	5.5	0.85
525	34.2	104.4	4.6	1.57	5.5	0.84
525	39.9	104.4	4.8	1.93	5.5	0.87
525	45.6	104.3	4.9	2.22	5.5	0.89
525	51.3	104.3	4.9	2.50	5.5	0.89
525	57.0	104.2	4.9	2.79	5.5	0.89
550	22.8	104.5	8.8	2.02	9.7	0.91
550	28.6	104.5	8.7	2.48	9.7	0.90
550	34.2	104.4	8.7	2.98	9.7	0.90
550	39.9	104.4	8.9	3.56	9.7	0.92
550	45.6	104.3	8.8	4.01	9.7	0.91
550	51.3	104.3	8.7	4.48	9.7	0.90
550	57.0	104.2	8.6	4.93	9.7	0.89

Hydrogen reaction order testing

475	34.2	41.8	3.9	1.32	5.2	0.75
475	34.2	52.2	3.3	1.13	4.3	0.77
475	34.2	62.6	2.9	0.98	3.7	0.78
475	34.2	73.1	2.6	0.88	3.3	0.79
475	34.2	83.5	2.3	0.79	2.8	0.82
475	34.2	94.0	2.1	0.72	2.6	0.81

475	34.2	104.4	1.9	0.66	2.6	0.73
475	34.3	114.9	1.8	0.61	2.1	0.86
475	34.3	125.3	1.7	0.58	2.0	0.85
500	34.2	41.8	6.1	2.42	6.1	1.00
500	34.2	52.2	5.0	2.07	5.3	0.94
500	34.2	62.6	4.3	1.82	4.8	0.90
500	34.2	73.1	3.7	1.61	4.3	0.86
500	34.2	83.5	3.3	1.46	3.8	0.87
500	34.2	94.0	2.9	1.34	3.4	0.85
500	34.2	104.4	2.5	1.24	3.1	0.81
500	34.3	114.9	2.4	1.15	2.6	0.92
500	34.3	125.3	2.1	1.08	2.4	0.88
525	34.2	41.8	10.9	4.40	11.6	0.94
525	34.2	52.2	9.4	3.90	9.9	0.95
525	34.2	62.6	8.2	3.50	8.7	0.94
525	34.2	73.1	7.1	3.13	7.7	0.92
525	34.2	83.5	6.4	2.86	7.0	0.91
525	34.2	94.0	5.6	2.62	6.4	0.88
525	34.2	104.4	4.9	2.35	5.5	0.89
525	34.3	114.9	4.5	2.22	5.0	0.90
525	34.3	125.3	4.1	2.10	4.4	0.93
550	34.2	41.8	14.7	5.05	19.0	0.77
550	34.2	52.2	13.6	4.65	16.8	0.81
550	34.2	62.6	12.5	4.28	15.2	0.82
550	34.2	73.1	11.6	3.96	12.8	0.91
550	34.2	83.5	10.7	3.68	11.6	0.92
550	34.2	94.0	10.1	3.45	10.6	0.95
550	34.2	104.4	9.5	3.24	9.7	0.98
550	34.3	114.9	8.9	3.04	9.0	0.99
550	34.3	125.3	8.4	2.88	8.4	1.00

2.Q. Dual rate-determining step mechanisms

The proposed reaction model developed in this work (model 3) considers dissociative ethane adsorption as the the rate-determining step (RDS). This proposed mechanism was proven to be valid across a wide range of temperatures and hydrocarbon and hydrogen partial pressures (see **Figure 2.5b**). However, an important strategy to potentially industrialize ethane NODH is based on the use of hydrogen permeable membranes to shift the ethane dehydrogenation equilibrium toward the ethylene side, potentially leading to even more extreme hydrogen and hydrocarbon concentrations. Under those extreme atmospheres, the RDS could be different than the dissociative ethane adsorption step,

particularly since the results in this work indicate that hydrogen and ethylene adsorption are strongly affecting the reaction mechanism.

We addressed this issue by checking the degree of rate control (DRC), as introduced by Charles Campbell [69,70], under varying gas phase atmospheres. Herein, we compared the rate control distribution (i) between the dissociative ethane adsorption and the hydrogen desorption step, and (ii) between the dissociative ethane adsorption and the ethylene desorption step. The starting point in this analysis was the set of elementary steps that complied with the experimentally obtained reaction orders (**Equation 2.7-2.10**).

2.Q1. Colimiting dissociative ethane adsorption and hydrogen desorption

The elementary steps for the reaction mechanism in which the dissociative ethane adsorption step and the hydrogen desorption step are colimiting, are as follows:

1. $C_2H_6\,(g) +\ 2* \ \rightarrow C_2H_5* + H*$
2.
3. $C_2H_5* \ + \ * \ \leftrightharpoons C_2H_4* + H*$
4. $C_2H_4* \qquad \leftrightharpoons C_2H_4\,(g) + \ *$
5. $2H* \qquad\quad \rightarrow H_2\,(g) + 2*$
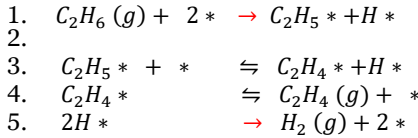
Which leads to the following rate expression:

$$TOF = \frac{k_1\left(p_{C2H6} - \frac{p_{C2H4}p_{H2}}{K_{eq}}\right)}{\left(1 + K_4 p_{C2H4} + \sqrt{\frac{k_1 p_{C2H6} + k_{-5} p_{H2}}{k_5}}\right)^2} \tag{2.Q1}$$

In **Equation 2.Q1**, $k_1 p_{C2H6}$ is the amount of surface hydrogens generated via dissociative ethane adsorption, $k_{-5} p_{H2}$ the amount generated via hydrogen adsorption, and k_5 the amount of hydrogen released via desorption. **Equation 2.Q1** is rewritten to **Equation 2.Q2** using the Arrhenius and Van 't Hoff equations (**Equation 2.13** and **2.14**).

$$TOF = \frac{\frac{k_b T}{h}\exp\left(\frac{-\Delta G_1}{RT}\right)\left(p_{C2H6} - \frac{p_{C2H4}p_{H2}}{K_{eq}}\right)}{\left(1 + \exp\left(\frac{-\Delta G_4}{RT}\right)p_{C2H4} + \sqrt{\frac{\frac{k_b T}{h}\exp\left(\frac{-\Delta G_1}{RT}\right)p_{C2H6} + \frac{k_b T}{h}\exp\left(\frac{-\Delta G_{-5}}{RT}\right)p_{H2}}{\frac{k_b T}{h}\exp\left(\frac{-\Delta G_5}{RT}\right)}}\right)^2} \tag{2.Q2}$$

Equation 2.Q2 simplifies to **Equation 2.Q3** by defining $\frac{-\Delta G_i}{RT}$ as g_i.

$$TOF = \frac{\frac{k_b T}{h}\exp(g_1)\left(p_{C2H6} - \frac{p_{C2H4}p_{H2}}{K_{eq}}\right)}{\left(1 + \exp(g_2)\,p_{C2H4} + \sqrt{\frac{\frac{k_b T}{h}\exp(g_1)\,p_{C2H6} + \frac{k_b T}{h}\exp(g_3)\,p_{H2}}{\frac{k_b T}{h}\exp(g_4)}}\right)^2} \tag{2.Q3}$$

The definition of the degree of rate control (DRC = $X_{RC,i}$) is as follows [69,70]:

$$X_{RC,i} = \frac{k_i}{r}\left(\frac{\delta TOF}{\delta k_i}\right)_{k_{j\neq i},K_i} = \left(\frac{\delta \ln (TOF)}{\delta \ln (k_i)}\right)_{k_{j\neq i},K_i} = \left(\frac{\delta \ln (TOF)}{\delta \left(\frac{-\Delta G_i}{RT}\right)}\right)_{\Delta G_{j\neq i}} \tag{2.Q4}$$

Taking the natural logarithm of **Equation 2.Q3** gives:

$$\ln(TOF) = \ln\left(\frac{\left(\frac{k_b T}{h}\right)\exp(g_1)\left(p_{C2H6} - \frac{p_{C2H4}p_{H2}}{K_{eq}}\right)}{\left(\left(1 + \exp(g_2)\,p_{C2H4} + \sqrt{\frac{\exp(g_1)\,p_{C2H6} + \exp(g_3)\,p_{H2}}{\exp(g_4)}}\right)^2\right)}\right) \tag{2.Q5}$$

Which can be simplified to:

$$\ln(TOF) = \ln\left(\left(\frac{k_b T}{h}\right)\exp(g_1)\,(p_{C2H6} - \frac{p_{C2H4}p_{H2}}{K_{eq}})\right) \tag{2.Q6}$$

$$- 2\ln\left(1 + \exp(g_2)\,p_{C2H4} + \sqrt{\frac{\exp(g_1)\,p_{C2H6} + \exp(g_3)\,p_{H2}}{\exp(g_4)}}\right)$$

To evaluate the DRC of the dissociative ethane adsorption step, the derivative of **Equation 2.Q6** needs to be taken with respect to g_1:

$$\frac{\delta \ln(TOF)}{\delta g_1} \tag{2.Q7}$$
$$= 1$$
$$- \frac{p_{C2H6}\exp(g_1)}{\exp(g_4)\sqrt{\frac{\exp(g_3)\,p_{H2} + p_{C2H6}\exp(g_1)}{\exp(g_4)}}\left(\exp(g_2)\,p_{C2H4} + \sqrt{\frac{\exp(g_3)\,p_{H2} + p_{C2H6}\exp(g_1)}{\exp(g_4)} + 1}\right)}$$

Analogously, to determine the DRC of the hydrogen desorption step, the derivative of **Equation 2.Q6** needs to be taken with respect to g_4:

$$\frac{\delta \ln(TOF)}{\delta g_4} = \frac{\sqrt{\exp(g_3)\,p_{H2} + p_{C2H6}\exp(g_1)\,\exp(-g_4)}}{\exp(g_2)\,p_{C2H4} + \sqrt{\exp(g_3)\,p_{H2} + p_{C2H6}\exp(g_1)\,\exp(-g_4) + 1}} \tag{2.Q8}$$

The DRC results indicated that the hydrogen desorption step only became colimiting at extremely low hydrogen and ethylene partial pressures (**Figure 2.Q1**). In that case, dissociative ethane adsorption is comparably fast, due to the low Pt surface occupancy. In other words, the formation of adsorbed hydrogen (θ_{H*}) via dissociative ethane adsorption (**Equation 2.Q1**) is faster than the disappearance of θ_{H*} via hydrogen desorption. On the contrary, in case of significant hydrogen partial pressures, the amount of surface

hydrogens is controlled by the hydrogen adsorption equilibrium and not by the amount of hydrogen generated via dissociative ethane adsorption (**Equation 2.Q1**), because of the substantial barrier for C-H cleavage. Under steady state membrane reactor conditions, the ethylene and hydrogen surface coverages will be significant and the rate will not be controlled by the hydrogen desorption step. The DRC only changes to hydrogen desorption for membrane reactor startup conditions, where limited amounts of ethylene are formed and where the initial amount of H_2 formed has been removed from the reaction zone.
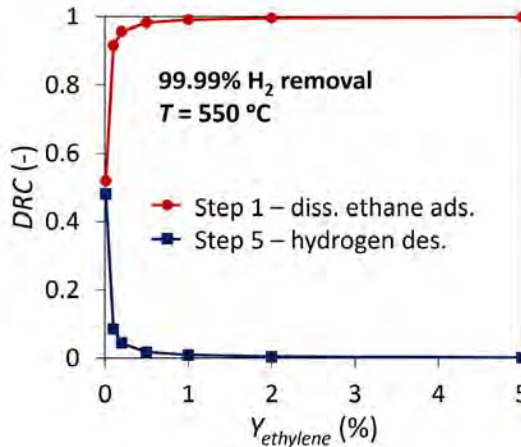
Figure 2.Q1: Degree of rate control (DRC) between (i) dissociative ethane adsorption and (ii) hydrogen desorption as a function of the ethylene yield ($Y_{ethylene}$) for a situation of 99.99% H_2 removal at 550 °C, in combination with a pure ethane feed.

2.Q2. Colimiting dissociative ethane adsorption and ethylene desorption

The following elementary steps correspond to the mechanism in which dissociative ethane adsorption and ethylene desorption are colimiting the dehydrogenation rate:

1. $C_2H_6\,(g) +\ 2* \quad \rightarrow\ C_2H_5*+H*$
2.
3. $C_2H_5*\ +\ * \quad \leftrightarrows\ C_2H_4*+H*$
4. $C_2H_4* \qquad\quad \rightarrow\ C_2H_4\,(g) +\ *$
5. $2H* \qquad\qquad \leftrightarrows\ H_2\,(g) + 2*$
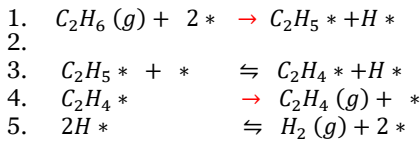
Equation 2.Q9 shows the corresponding rate expression:

$$TOF = \frac{k_1(p_{C2H6} - \frac{p_{C2H4}p_{H2}}{K_{eq}})}{\left(1 + K_5^{0.5}p_{H2}^{0.5} + \frac{k_{-4}p_{C2H4}}{k_4 - 1}\right)^2} \qquad (2.Q9)$$

Considering the Arrhenius and Van 't Hoff equations (**Equation 2.13** and **2.14**), **Equation 2.Q9** can be rewritten to:

$$TOF = \frac{\left(\frac{k_bT}{h}\right)\exp\left(\frac{-\Delta G_1}{RT}\right)\left(p_{C2H6} - \frac{p_{C2H4}p_{H2}}{K_{eq}}\right)}{\left(1 + \exp\left(\frac{-\Delta G_2}{RT}\right)^{0.5} p_{H2}^{0.5} + \frac{\left(\frac{k_bT}{h}\right)\exp\left(\frac{-\Delta G_{-4}}{RT}\right)p_{C2H4}}{\left(\frac{k_bT}{h}\right)\exp\left(\frac{-\Delta G_4}{RT}\right) - 1}\right)^2} \tag{2.Q10}$$

Which is transformed into **Equation 2.Q11** when defining g_i as $\frac{\Delta G_i}{RT}$.

$$TOF = \frac{\left(\frac{k_bT}{h}\right)\exp(g_1)\left(p_{C2H6} - \frac{p_{C2H4}p_{H2}}{K_{eq}}\right)}{\left(1 + \exp(g_2)^{0.5}p_{H2}^{0.5} + \frac{\left(\frac{k_bT}{h}\right)\exp(g_3)p_{C2H4}}{\left(\frac{k_bT}{h}\right)\exp(g_4) - 1}\right)^2} \tag{2.Q11}$$

When taking the natural logarithm of **Equation 2.Q11**, this gives:

$$\ln(TOF) = \ln\left(\frac{\left(\frac{k_bT}{h}\right)\exp(g_1)\left(p_{C2H6} - \frac{p_{C2H4}p_{H2}}{K_{eq}}\right)}{\left(1 + \exp(g_2)^{0.5}p_{H2}^{0.5} + \frac{\left(\frac{k_bT}{h}\right)\exp(g_3)p_{C2H4}}{\left(\frac{k_bT}{h}\right)\exp(g_4) - 1}\right)^2}\right) \tag{2.Q12}$$

Which can be rewritten to:

$$\ln(TOF) = \ln\left(\left(\frac{k_bT}{h}\right)\exp(g_1)\left(p_{C2H6} - \frac{p_{C2H4}p_{H2}}{K_{eq}}\right)\right) \tag{2.Q13}$$

$$- 2\ln\left(1 + \exp(g_2)^{0.5}p_{H2}^{0.5} + \frac{\left(\frac{k_bT}{h}\right)\exp(g_3)p_{C2H4}}{\left(\frac{k_bT}{h}\right)\exp(g_4) - 1}\right)$$

The DRC of the dissociative ethane adsorption step was quantified by taking the derivative of **Equation 2.Q13** with respect to g_1:

$$\frac{\delta \ln(TOF)}{\delta g_1} = 1 \tag{2.Q14}$$

The fact that the derivative in **Equation 2.Q14** equals 1 indicates that the DRC of the dissociative ethane adsorption step in this case equals 1 when all other reaction rate and adsorption equilibrium constants are unchanged, according to the definition of the DRC in **Equation 2.Q4**. Analogous to **Equation 2.Q14**, to determine the DRC of the ethylene desorption step, the derivative of **Equation 2.Q13** needs to be taken with respect to g_4:

$$\frac{\delta \ln(TOF)}{\delta g_4} = \frac{2\left(\frac{k_bT}{h}\right)^2 \exp(g_3)p_{C2H4}\exp(g_4)}{\left(\left(\frac{k_bT}{h}\right)\exp(g_4)-1\right)^2 (\exp(g_2)^{0.5}p_{H2}^{0.5})} \tag{2.Q15}$$

However, **Equation 2.Q15** shows that if the reaction rate constant corresponding to the ethylene desorption step is changed, the DRC distribution is effectively changed. In this regime of colimiting dissociative ethane adsorption and ethylene desorption the DRC of the dissociative ethane adsorption step was, therefore, calculated by subtracting the DRC of the ethylene desorption from 1, i.e. the result of the dissociative ethane adsorption derivative in **Equation 2.Q14**.

The results were evaluated for two different extents of H_2 removal from the reaction zone, i.e. 50% and 99.99% H_2 removal (**Figure 2.Q2**). At 50% H_2 removal, there was a colimiting regime between dissociative ethane adsorption and ethylene desorption for significant ethylene yields (>1%, **Figure 2.Q2a**). Under those conditions, there was still a substantial amount of hydrogen present, implying that the ethylene desorption term ($k_{-4}p_{C2H4}$ in **Equation 2.Q2**) was not fully controlling the rate denominator. On the contrary, when effectively all hydrogen was removed from the reaction zone (99.99% H_2 removal) the degree of rate control shifted entirely to the ethylene desorption step (**Figure 2.Q2b**). The results in **Figure 2.Q2** thereby indicate that upon increasing ethylene yield by removing H_2 from the reaction zone, the reaction pathway shifts from one in which the dissociative ethane adsorption is governing the rate to one in which ethylene desorption becomes controlling the rate. Nevertheless, care needs to be taken with the interpretation of the results in **Figure 2.Q2**, as these graphs were constructed by extrapolating the kinetic regression outcomes far outside the experimental range investigated in this study.
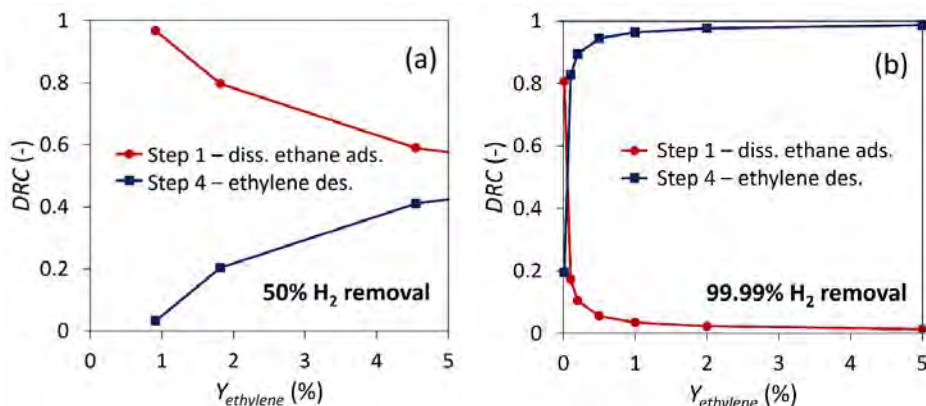
Figure 2.Q2: Degree of rate control (DRC) between (i) dissociative ethane adsorption and (ii) ethylene desorption as a function of the ethylene yield ($Y_{ethylene}$) for (a) 50%, and (b) 99.99% H_2 removal. Figures are constructed at 550 °C with a pure ethane feed.

Chapter 3

Steam impacts catalyst chemistry and enhances product desorption in ethane dehydrogenation over Pt catalysts

Summary

Hydrogen permeable dense ceramic membranes represent a promising strategy to increase olefin yields in alkane dehydrogenation processes. These ceramic membranes function optimally in the presence of steam. In integrated packed bed membrane reactors, the prototypical Pt-based dehydrogenation catalyst will therefore inevitably be exposed to moistened gas phase atmospheres. In this chapter, we demonstrate that the presence of steam enhances the ethylene formation rate in the non-oxidative dehydrogenation (NODH) of ethane using $Pt/ZnAl_2O_4$ and $Pt-Sn/ZnAl_2O_4$ catalysts. Since the $Pt/ZnAl_2O_4$ catalyst was not physicochemically modified under wet atmospheres, the corresponding performance improvement was attributed to an enhancement in product removal from the Pt sites, either via product desorption or spillover. On the contrary, the $Pt-Sn/ZnAl_2O_4$ was found to be physicochemically modified in the presence of steam by means of PtSn dealloying and the existence of more oxidized Pt states after steam exposure. Consequently, the performance improvement of the $Pt-Sn/ZnAl_2O_4$ catalyst under wet conditions was ascribed to stronger hydrocarbon surface binding and thereby enhanced ethane dissociation relative to dry conditions.

3.1. Introduction

Non-oxidative dehydrogenation (NODH) of ethane (**Equation 3.1**) is a non-commercialized process, because it is severely limited by thermodynamic equilibrium. On the contrary, related propane and isobutane are more easily dehydrogenated, as propane and isobutane are less stable molecules than ethane. Accordingly, propane and isobutane NODH are commercialized technologies in which platinum and platinum-tin alloys supported on metal oxides are the prototypical catalysts [1].

$$C_2H_6 \leftrightharpoons C_2H_4 + H_2 \qquad (\Delta H^0_{298} = +137.0 \text{ kJ/mol}) \qquad (3.1)$$
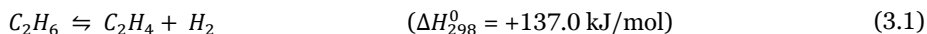
The reaction mechanism of light alkane NODH on Pt-based catalysts has been researched in the past primarily for propane [2–10] and isobutane NODH [5,11–15]. In most of these kinetic studies the rate-determining step of the proposed mechanism consisted of a C-H bond scission step, either in the form of dissociative adsorption of the alkane [2,10] or in the form of a C-H bond scission on the Pt surface after molecular adsorption [5,9,16,17]. Besides, the olefin and hydrogen products are generally believed to be in competition with the reacting alkane for the Pt active sites [2,3,7–10,17]. In **Chapter 2**, we demonstrated that ethylene and hydrogen are indeed inhibiting the rate of the ethane NODH reaction. Moreover, we showed that hydrogen and ethylene adsorption on Pt-Sn/ZnAl₂O₄ deviate from ideal Langmuir adsorption. For hydrogen adsorption, this was attributed to lateral interactions and reduced hydrogen surface mobility at higher surface coverages. By contrast, the deviation from Langmuir adsorption for ethylene was ascribed to a stronger ethylene adsorption configuration at lower surface coverages. Knowledge on the coverage dependency of hydrogen and olefin adsorption and the concomitant effects on the reaction mechanism is particularly relevant for membrane reactor applications, where the olefin yield of thermodynamically hindered alkane NODH (**Equation 3.1**) processes can be increased by *in situ* hydrogen removal.

The selective separation of hydrogen from alkane NODH reaction mixtures has been demonstrated for dense metallic [18] and dense ceramic [19,20] membranes. Dense ceramic membranes are typically preferred to dense metallic membranes for high temperature applications ($T > 400$ °C), because of their better thermal and chemical stability [21,22], even though the hydrogen permeation flux through dense metallics is typically a factor five times the hydrogen flux through dense ceramics [23]. A cosupply of steam is required on both sides of dense ceramic membranes to facilitate hydrogen permeation, as surface hydroxyl groups are essential for hydrogen incorporation and recombination [24]. When integrating dense ceramic membranes with Pt-based catalysts in packed bed membrane reactors, the Pt catalyst will therefore inevitably be exposed to steam-rich gas phase atmospheres. For this reason, it is key to understand the influence of steam on the performance and stability of Pt-based catalysts in the alkane NODH reaction.

In general, cofeeding light gases like H_2, CO_2, or steam leads to a reduction in carbon deposition [10,25,26]. In the commercial Uhde STeam Active Reforming (STAR) process®, steam is cosupplied with the paraffinic feed to suppress coke formation [1]. Also, steam dilutes the paraffinic feed in the Uhde STAR process®, allowing for higher paraffin conversions [1]. In addition to eliminating carbon deposits, cosupplied light gases like CO_2 and steam are also known to facilitate olefin product desorption [27]. Despite the prior knowledge on the effect of steam on inhibiting carbon deposition, the effect of steam on the catalyst physicochemical properties and on the alkane NODH reaction mechanism on Pt-based catalysts are still poorly understood. This chapter therefore addresses the role of steam via a kinetic study of ethane NODH on $Pt/ZnAl_2O_4$ and $Pt-Sn/ZnAl_2O_4$ catalysts under dry and wet gas phase atmospheres, in combination with detailed catalyst characterization. The gained insights will be key to understand the functionality of integrated packed bed membrane reactors for alkane NODH applications in the aim to minimize the energy and carbon intensity of olefin production processes.

3.2. Experimental

3.2.1. Materials and instrumentation

The $ZnAl_2O_4$ support was prepared using zinc nitrate ($Zn(NO_3)_2 \cdot 6H_2O$, 98%, extra pure, Acros Organics) and aluminum nitrate ($Al(NO_3)_3 \cdot 9H_2O$, 99+%, Acros Organics). Besides, the support was functionalized via wet impregnation using tin chloride ($SnCl_4 \cdot 5H_2O$, 98%, Alfa Aesar) and chloroplatinic acid ($H_2PtCl_6 \cdot 6H_2O$, 99.95%, Alfa Aesar) precursors. Ammonium hydroxide (25% NH_3 basis, Sigma-Aldrich) was used as precipitating agent in the support synthesis and hydrochloric acid (HCl, fuming, 37%, Merck KGaA) was applied as acidifying agent in the impregnation of the support with the Sn precursor. The catalytic tests were carried out using ethane 2.5 (≥99.5%, Linde plc).

A Bruker s8 Tiger Series WDXRF spectrometer was used for X-ray fluorescence (XRF) to determine the elemental composition of the catalyst. A powder based measurement was performed to quantify the Pt loading, whilst a fused bead measurement was conducted to determine the Zn, Al, and Sn bulk concentrations. An XRF Scientific xrFuse2 fusion machine generated the fused beads comprising of a 1/8 catalyst/flux ratio, where the flux compound contained 66% lithium tetraborate, 34% lithium metaborate, and 0.2% lithium bromide. Besides, a Bruker D2 PHASER XRD was applied for X-ray diffraction (XRD). The XRD spectra were gathered of the freshly calcined, reduced, and steam treated $ZnAl_2O_4$, $Sn/ZnAl_2O_4$, $Pt/ZnAl_2O_4$, and $Pt-Sn/ZnAl_2O_4$ samples and were retrieved between diffraction angles of 10° and 90°. In the steam treatment, the samples were *ex situ* exposed to moistened reductive atmospheres using a gas stream containing 3 vol% of H_2O and 10 vol% of H_2, balanced with N_2 at 550 °C for 3 hours. All samples were temporarily exposed to ambient air upon transportation to the XRD spectrometer. A Micromeritics TriStar Surface Area and Porosity Analyzer was applied for nitrogen physisorption, in which a degassing temperature of 300 °C was used. Before performing CO chemisorption,

the catalyst samples were exposed to a stream of H_2 at 400 °C for 1 hour (heating rate: 10 °C/min). A Micromeritics ChemiSorb 2750 pulse chemisorption system was used for CO chemisorption.

The size, shape, and elemental distribution of the catalyst active centers were analyzed using scanning transmission electron microscopy with high-angle annular dark-field (STEM-HAADF) imaging, in combination with energy dispersive X-ray spectroscopy (EDS). Before performing STEM-HAADF analysis, the catalyst samples were *ex situ* exposed to H_2 (10 ml/min STP) at 550 °C for 1 hour (heating rate: 10 °C/min), then cooled down in inert N_2, and temporarily exposed to ambient air upon transportation to the STEM-HAADF system. STEM imaging was conducted in a probe-corrected Titan from Thermo Fisher Scientific (300 kV), equipped with a high brightness X-FEG and a spherical aberration Cs-corrector (CEOS) for the condenser system to provide sub-Ångström probe size. An Ultim Max detector system (Oxford Instruments) was used for EDS mapping.

The surface composition and oxidation states of reduced and steam treated $Pt/ZnAl_2O_4$ and $Pt-Sn/ZnAl_2O_4$ were determined using X-ray photoelectron spectroscopy (XPS). The $Pt/ZnAl_2O_4$ and $Pt-Sn/ZnAl_2O_4$ samples were exposed to reducing (10 vol% H_2, 90 vol% N_2, 550 °C, heating rate: 10 °C/min, 1 h) and wet reducing (10 vol% H_2, 1.4 vol% H_2O, 88.6 vol% N_2, 550 °C, heating rate: 10 °C/min, 3 h) gas phase atmospheres in a pre-treatment chamber of the XPS machine, without intermediate exposure to air. XPS analysis was performed in a SPECS spectrometer equipped with a PHOIBOS 150 MCD analyzer working at fixed pass energy of 35 eV and 0.1 eV resolution for the studied zones. Prior to analysis, every sample was pressed into a disk. The XPS spectra were acquired at ambient temperature under ultra-high vacuum (10^{-10} mbar) using Al Kα radiation at 250 W and 12.5 kV and were analyzed using CasaXPS software. High resolution spectra of the regions corresponding to Pt 4d, Sn 4d + O 2s, Zn 2p, O 1s, Al 2s, and C 1s levels were obtained and quantified. All binding energies were corrected using the stable Al 2p photoemission line at 74.3 eV as reference.

3.2.2.   Catalyst synthesis and activation

The $Pt-Sn/ZnAl_2O_4$ catalyst was prepared following procedures described in detail in **Chapter 2**. In short, the $ZnAl_2O_4$ support was synthesized via coprecipitation of zinc nitrate and aluminum nitrate [11,28–31]. The $Pt-Sn/ZnAl_2O_4$ catalyst was then prepared by impregnating the $ZnAl_2O_4$ sequentially with Sn and Pt precursor solutions in ethanol [11,28,32,33], in which the Sn precursor solution was acidified with 100 mM HCl. By contrast, the $Pt/ZnAl_2O_4$ catalyst was prepared by impregnating the $ZnAl_2O_4$ support only with the Pt precursor solution in ethanol. After impregnation, the catalysts were calcined in a stream of air at 550 °C (heating rate: 2 °C/min) for 4 hours, before mortaring into particles with the following size fractions: 0-45 μm, 45-125 μm, 125-250 μm, and 250-600 μm. Only the 0-45 μm particle size fraction was used in the catalytic tests, as internal mass transfer limitations were excluded for this fraction (see **Chapter 2**). Prior to catalytic

testing, the catalysts were pre-activated in a stream of H_2 (10 ml/min STP) at 550 °C for 1 hour inside the catalytic testing setup.

3.2.3. Catalytic testing

The catalyst particles were diluted with quartz (fine granular, Merck KGaA, 125-250 μm) particles in a 1/19 catalyst-to-diluent ratio for isothermal operation of the catalyst packed bed. The bed was mounted inside a quartz reactor tube (*I.D.* = 4 mm, *O.D.* = 6 mm, *L* = 450 mm) with pieces of quartz wool. The reactor tube was positioned inside a tubular furnace, where the reaction temperature was controlled using a thermocouple on the inner wall of the furnace positioned in the immediate vicinity of the catalyst bed. A continuous flow fixed bed reactor setup was used for conducting the catalytic tests (see **Supporting Information 3.A**). This setup contained ethane, ethylene, and H_2 gas lines to vary the partial pressures, whilst N_2 was used as balancing gas. Mass flow controllers from Brooks were used to control the gas flows. Besides, an ISCO 500D syringe pump was used to cosupply water to the catalyst bed. The water was introduced into a flowing gas stream in a preheating zone operated at 110 °C and comprised of a metal cylinder (*I.D.* = ca. 8 mm) filled with quartz wool to allow for pulse-free evaporation of the water. An on-line gas chromatograph (GC, Varian Chrompack CP-3800), equipped with an Agilent GS-GasPro GC column (60m x 0.32 mm *I.D.*), and a flame ionization detector (FID), was used to analyze the reactor effluent stream. The line between the reactor outlet and the GC-FID inlet was continuously heated to 120 °C while testing to avoid steam condensation. Immediately after catalyst activation, the water flow was started and stabilized for about 15 minutes, while maintaining a continuous N_2 flow, to ensure moistened conditions throughout the setup before starting the experiment. Subsequently, the ethane flow was started and possible H_2 and ethylene cofeed flows were specified. The catalytic tests were conducted at atmospheric pressure and with temperatures ranging from 475 °C to 550 °C.

Ethane conversion (χ_{eth}) and product selectivity (S_i) and yield (Y_i) were calculated as follows in this work:

$$\chi_{eth} = 1 - \frac{p_{eth}}{p_{eth,0}} \tag{3.2}$$

$$S_i = \frac{p_i}{p_{eth,0} - p_{eth}} \tag{3.3}$$

$$Y_i = \frac{p_i}{p_{eth.0}} \tag{3.4}$$

Where $p_{eth,0}$ and p_{eth} represent the inlet and outlet ethane partial pressures, respectively, and p_i is the partial pressure in the outlet stream of component i. The values of $p_{eth,0}$ and p_{eth} were determined using a calibration curve for ethane. Analogously, the ethylene partial pressure ($p_{i=ethylene}$) was calculated using a calibration curve for ethylene. Note that the

total gas flow rate was considered constant along the reactor length, as the ethane concentration in most tests was below 4 vol% and the ethane conversion was below 15%.

Similar to **Equation 2.6** in **Chapter 2**, the relation between the experimentally obtained ethylene yield (Y_{C2H4}), the mass-based ethylene formation rate ($R_{m,C2H4}$, in $mol_{C2H4}/kg_{cat}•s$), and the apparent turnover frequency of ethylene formation ($TOF_{app,C2H4}$, in $mol_{C2H4}/mol_{Pt,s}•s$) is given by **Equation 3.5**.

$$R_{m,C2H4} = \frac{F_{C2H6,0}Y_{C2H4}}{m_{cat}} = \frac{TOF_{app,C2H4}\sigma_{Pt}\beta_{Pt}}{M_{W,Pt}} \tag{3.5}$$

Where $F_{C2H6,0}$ indicates the molar flow rate of ethane in the feed (in mol/s), m_{cat} the mass of catalyst in the bed (in kg_{cat}), σ_{Pt} the Pt loading of the catalyst (in kg_{Pt}/kg_{cat}), β_{Pt} the Pt dispersion (in $mol_{Pt,s}/mol_{Pt}$), as determined using CO chemisorption, and $M_{W,Pt}$ the molar weight of Pt (in kg_{Pt}/mol_{Pt}). Furthermore, in the unit of $TOF_{app,C2H4}$, $mol_{Pt,s}$ indicates the number of moles of Pt exposed to the surface. An apparent turnover frequency was used again in this chapter, as **Chapter 2** demonstrated that effects related to non-ideal adsorption and the reversibility of the reaction impact the experimentally observed dehydrogenation rate.

3.3. Results and discussion

3.3.1. Characterization of fresh catalysts

The Pt/ZnAl₂O₄ and Pt-Sn/ZnAl₂O₄ catalysts synthesized and tested in this work are the same as used in **Chapter 2** and have therefore equal physicochemical properties (**Supporting Information 3.B**). The BET surface area of both catalysts is about 70 m²/g, the Pt loading of Pt/ZnAl₂O₄ is 3.6 wt.%, and the Pt and Sn loadings of Pt-Sn/ZnAl₂O₄ are 4.0 wt.% and 1.6 wt.%, respectively.

3.3.2. Catalytic ethane dehydrogenation

Internal mass transfer limitations were excluded under dry ethane NODH conditions for Pt-Sn/ZnAl₂O₄ catalyst particles smaller than 45 μm (see **Chapter 2**). Besides, external mass transfer limitations were excluded and operation in a differential regime was ensured for catalyst-to-feed ratios (*W/F_ethane*) below 100 kg_cat•s/kg_ethane under dry ethane NODH conditions (see **Chapter 2**). Isothermal operation of the packed bed was guaranteed by diluting the Pt-Sn/ZnAl₂O₄ catalyst with inert quartz bed diluent particles. The used dilution fraction of 0.95 (i.e. 5 wt.% of catalyst and 95 wt.% of bed diluent) suffices to avoid channeling through the bed, according to a relation on the influence of bed dilution on the conversion level of packed bed systems, as developed by Berger et al. [34] (see **Chapter 2** for more details). Furthermore, the kinetic tests were conducted under steady state

conditions with minimum deactivation (**Supporting Information 3.C**) and at 40-60% of the theoretically attainable conversion level (see **Chapter 2**).

Ethylene was the main product in all ethane NODH performance tests using Pt/ZnAl$_2$O$_4$ and Pt-Sn/ZnAl$_2$O$_4$ catalysts with a selectivity above 90%. Methane was detected as a byproduct from ethane cracking (0-10% selectivity), and the remaining mass could be attributed to the formation of carbon monoxide, carbon dioxide, or coke. The ethylene selectivity was typically somewhat higher under dry ethane NODH conditions (95-100%) as compared to wet ethane NODH conditions (90-95%), due to a slightly higher methane selectivity under wet conditions (**Table 3.1**). Notably, the apparent turnover frequency of ethylene formation ($TOF_{app,ethylene}$) was slightly higher for Pt/ZnAl$_2$O$_4$ compared to Pt-Sn/ZnAl$_2$O$_4$ under dry and moistened atmospheres (**Table 3.1**). This is attributed to the high intrinsic activity of Pt for converting alkanes [1]. While the possible olefin selectivity enhancing effect of Sn was insignificantly captured in our tests (**Table 3.1**), the Sn addition did lead to a reduction in activity, allegedly by increasing the electron density around the Pt, thereby weakening the adsorbate-metal bond [9,25].

Table 3.1: Apparent turnover frequency of ethylene formation ($TOF_{app,ethylene}$) and the ethylene selectivity ($S_{ethylene}$) for Pt/ZnAl$_2$O$_4$ and Pt-Sn/ZnAl$_2$O$_4$ under dry and wet conditions. Dry conditions: p_{ethane} = 35 mbar(a), p_{H2} = 105 mbar(a), T = 550 °C. Wet conditions: p_{ethane} = 35 mbar(a), p_{H2} = 105 mbar(a), p_{H2O} = 15 mbar(a), T = 550 °C.

	Dry		*Wet*	
	$TOF_{app,ethylene}$ (mol/mol$_{Pt,s}$•s)	$S_{ethylene}$ (%)	$TOF_{app,ethylene}$ (mol/mol$_{Pt,s}$•s)	$S_{ethylene}$ (%)
Pt/ZnAl$_2$O$_4$	0.98 ± 0.01	94.8 ± 2.0	1.55 ± 0.05	90.8 ± 1.1
Pt-Sn/ZnAl$_2$O$_4$	0.71 ± 0.07	96.1 ± 3.6	1.28 ± 0.02	91.3 ± 2.3

Surprisingly, the apparent activation barrier for ethylene formation under dry conditions was lower for PtSn (**Figure 3.1b**) as compared to Pt (**Figure 3.1a**), while addition of Sn decreased the apparent ethylene formation rate (**Table 3.1**). In **Chapter 2** we showed that the hydrogen and ethylene surface coverages are both inhibiting the ethane dehydrogenation rate on Pt-based catalysts. Although the intrinsic ethane dissociation could be faster on Pt compared to PtSn because of its stronger interaction with hydrocarbons, we anticipate that high hydrogen and ethylene surface coverages on Pt relative to PtSn cause the higher apparent barrier for ethylene formation.
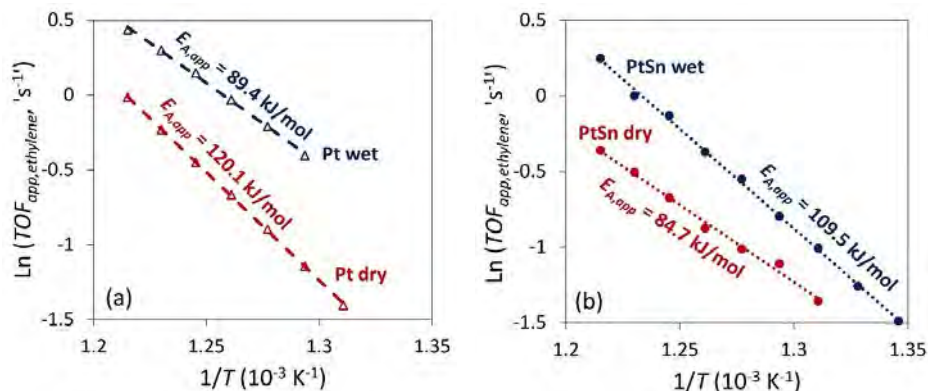
Figure 3.1: Arrhenius plots for (a) Pt/ZnAl$_2$O$_4$ and (b) Pt-Sn/ZnAl$_2$O$_4$ under dry and wet conditions. Dry conditions: p_{ethane} = 35 mbar(a), p_{H2} = 105 mbar(a), T = 460-550 °C. Wet conditions: p_{ethane} = 35 mbar(a), p_{H2} = 105 mbar(a), p_{H2O} = 15 mbar(a), T = 460-550 °C.

To further investigate possible coverage effects on the catalytic performance, we determined the ethane and hydrogen reaction orders of the ethane NODH reaction on Pt/ZnAl$_2$O$_4$ and Pt-Sn/ZnAl$_2$O$_4$ under dry and moistened conditions. The ethane reaction order was found to be about 1 on Pt and PtSn and under dry as well as wet conditions (see **Supporting Information 3.G**). This indicates that the ethane surface coverage is low under the catalytic testing conditions applied in the different dry and wet cases. On the contrary, the hydrogen reaction order on Pt/ZnAl$_2$O$_4$ and Pt-Sn/ZnAl$_2$O$_4$ was different under dry and moistened atmospheres, as shown in **Figure 3.2**. Under dry conditions, the hydrogen reaction order was more negative for Pt/ZnAl$_2$O$_4$ as compared to Pt-Sn/ZnAl$_2$O$_4$ (**Figure 3.2**). This supports the reasoning that the hydrogen surface coverage was higher on Pt relative to PtSn, leading to a higher apparent activation barrier under dry conditions (**Figure 3.1**).
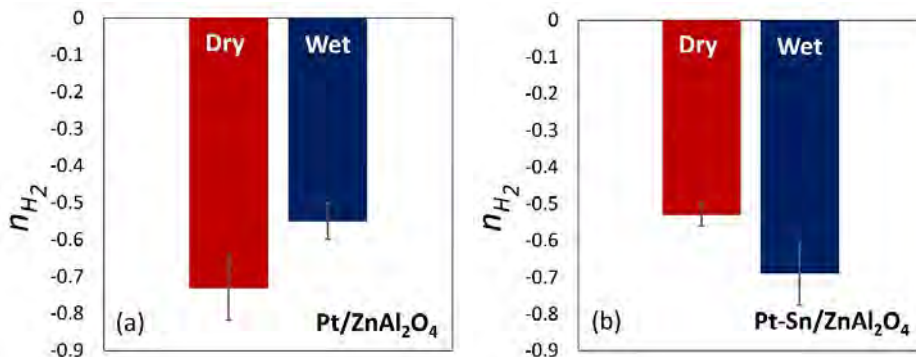
Figure 3.2: H$_2$ reaction orders for (a) Pt/ZnAl$_2$O$_4$ and (b) Pt-Sn/ZnAl$_2$O$_4$ under dry and wet conditions. Dry conditions: p_{ethane} = 35 mbar(a), p_{H2} = 105 mbar(a), T = 550 °C. Wet conditions: p_{ethane} = 35 mbar(a), p_{H2} = 105 mbar(a), p_{H2O} = 15 mbar(a), T = 550 °C.

Cofeeding steam strongly impacted the performance of Pt/ZnAl$_2$O$_4$ and Pt-Sn/ZnAl$_2$O$_4$ in the ethane NODH reaction. Notably, the apparent ethylene formation rates were considerably higher under wet conditions compared to dry conditions for both Pt/ZnAl$_2$O$_4$ and Pt-Sn/ZnAl$_2$O$_4$ (see **Table 3.1**). Also, the apparent activation barriers to ethane NODH on both catalysts differ for dry and wet conditions, as shown in **Figure 3.1**. Interestingly, the apparent barrier for Pt-Sn/ZnAl$_2$O$_4$ was higher in wet than in dry conditions (109.5 vs. 84.7 kJ/mol), whilst the opposite holds for Pt/ZnAl$_2$O$_4$ (89.4 vs. 120.1 kJ/mol). Analogously, opposite hydrogen reaction order trends were observed between Pt and PtSn when changing from dry to wet conditions, as the hydrogen reaction order became less negative for Pt/ZnAl$_2$O$_4$ and more negative for Pt-Sn/ZnAl$_2$O$_4$ under moistened atmospheres (**Figure 3.2**).

To investigate the role of steam in the ethane NODH reaction mechanism, we (i) determined the reaction order with respect to H$_2$O, and (ii) performed kinetic isotope labeling experiments with D$_2$O instead of H$_2$O. The H$_2$O reaction order was close to zero for Pt/ZnAl$_2$O$_4$ and Pt-Sn/ZnAl$_2$O$_4$ across the temperature range investigated (475-550 °C, see **Figure 3.3**). This suggests that the H$_2$O surface coverage was negligible in both catalyst systems. Moreover, kinetic isotope investigations in which the ethylene formation rate in the presence of H$_2$O was compared to the rate in the presence of D$_2$O did not show any significant kinetic isotope effect (**Supporting Information 3.F**), indicating that the H$_2$O is not involved in the rate-determining step of the reaction mechanism.
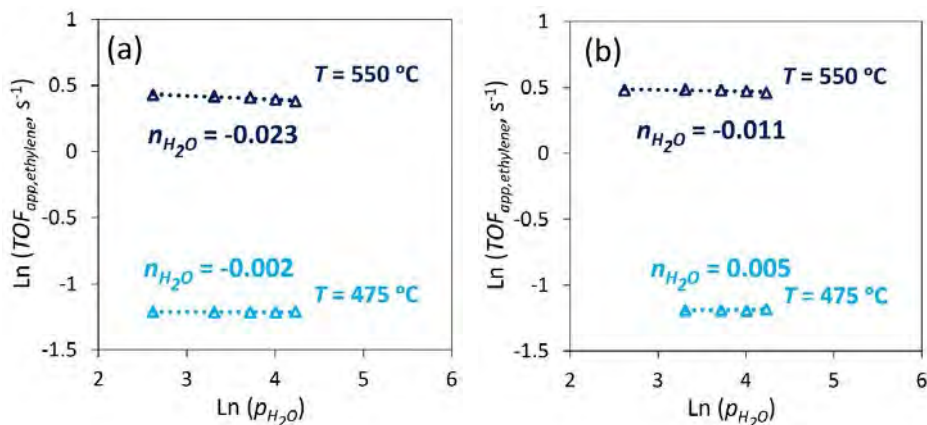
Figure 3.3: Reaction order of H$_2$O in the apparent turnover frequency of ethylene formation ($TOF_{app,ethylene}$) for (a) Pt/ZnAl$_2$O$_4$ and (b) Pt-Sn/ZnAl$_2$O$_4$ at 475 and 550 °C.

The difference in performance between Pt/ZnAl$_2$O$_4$ and Pt-Sn/ZnAl$_2$O$_4$ under dry and wet conditions could either be caused by mechanistic effects or by physicochemical modifications of the catalyst active centers induced by the steam. To understand the nature of the catalyst active sites under dry and wet atmospheres, detailed catalyst characterization was conducted on dry and wet treated Pt/ZnAl$_2$O$_4$ and Pt-Sn/ZnAl$_2$O$_4$.

3.3.3.   Characterization of treated and tested catalysts

X-ray diffraction spectra of the fresh catalyst samples were collected after each impregnation, calcination, and reduction step (**Figure 3.4**, see **Supporting Information 3.B** for the full XRD spectra). The calcined $ZnAl_2O_4$ support showed all characteristic $ZnAl_2O_4$ spinel peaks [31,35]. Impregnation with Sn did not lead to additional diffraction peaks nor to shifts of the $ZnAl_2O_4$ spinel peaks. On the contrary, impregnation with Pt resulted in the formation of a metallic Pt phase, following the appearance of characteristic metallic Pt XRD peaks for calcined $Pt/ZnAl_2O_4$ around 39.6º and 46.1º (**Figure 3.4**) [36]. Notably, the $ZnAl_2O_4$ and Pt crystalline phases in $Pt/ZnAl_2O_4$ did not change upon reduction and H_2O treatment (**Figure 3.4** and **Supporting Information 3.B**), confirming the crystallographic stability of $Pt/ZnAl_2O_4$.
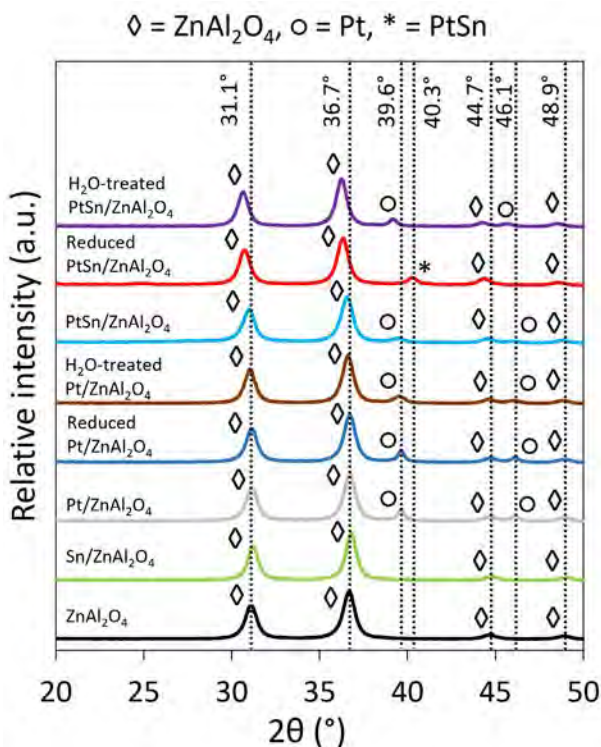
Figure 3.4: XRD spectra of fresh, calcined $ZnAl_2O_4$, $Sn/ZnAl_2O_4$, $Pt/ZnAl_2O_4$, and Pt-$Sn/ZnAl_2O_4$, reduced $Pt/ZnAl_2O_4$ and Pt-$Sn/ZnAl_2O_4$, and H_2O-treated $Pt/ZnAl_2O_4$ and Pt-$Sn/ZnAl_2O_4$.

A metallic Pt phase was also observed in the calcined Pt-$Sn/ZnAl_2O_4$ sample (**Figure 3.4**) but to a lesser extent as compared to $Pt/ZnAl_2O_4$. Remarkably, no Pt phases but PtSn alloy phases were observed for Pt-$Sn/ZnAl_2O_4$ reduced at 550 °C for 1 hour (**Figure 3.4** and **Supporting Information 3.B**) [37]. This indicates the formation of a PtSn alloy under

reductive atmospheres, which is in line with previous research on PtSn-based catalysts [9,38,39]. Moreover, a shift of the $ZnAl_2O_4$ spinel peaks toward lower diffraction angles ($\Delta 2\theta$ = ca. 0.3-0.4°) was observed after reducing the Pt and Sn containing sample (**Figure 3.4** and **Supporting Information 3.B**). This indicates an expansion of the $ZnAl_2O_4$ lattice after reducing the sequentially impregnated catalyst.

The XRD patterns of $ZnAl_2O_4$, $Sn/ZnAl_2O_4$, $Pt/ZnAl_2O_4$, and $Pt-Sn/ZnAl_2O_4$ were also gathered after exposure to moistened reducing conditions using a gas stream containing 3 vol% H_2O and 10 vol% H_2, balanced with N_2 at 550 °C for 3 hours. This steam treatment step was applied to the samples that were already reduced under dry conditions. The steam treatment did not affect the crystalline structure of $ZnAl_2O_4$, $Sn/ZnAl_2O_4$, and $Pt/ZnAl_2O_4$ (see **Figure 3.4** and **Supporting Information 3.B**). By contrast, the steam did change the crystal structure of the reduced $Pt-Sn/ZnAl_2O_4$ (**Figure 3.4** and **Supporting Information 3.B**), as the H_2O-treated $Pt-Sn/ZnAl_2O_4$ contained metallic Pt phases instead of the PtSn alloy phase that was present in the reduced $Pt-Sn/ZnAl_2O_4$. This indicates dealloying of the PtSn in the presence of steam. Moreover, the expansion of the $ZnAl_2O_4$ structure in the presence of Pt and Sn still existed after H_2O exposure (**Figure 3.4** and **Supporting Information 3.B**).

The XPS results of $Pt/ZnAl_2O_4$ and $Pt-Sn/ZnAl_2O_4$ showed that the electronic states of zinc, aluminum, and oxygen did not change upon exposure to dry or wet reducing conditions (**Supporting Information 3.D**). Besides, no clear changes in the electron binding energy of the Sn 4d electrons could be identified after reducing $Pt-Sn/ZnAl_2O_4$ under dry and moistened conditions. However, possible shifts toward lower binding energy of the Sn 4d electrons, related to the possible formation of a PtSn alloy, could be hidden overlapping O 2s photoemission lines (see **Supporting Information 3.D**).

The most intense Pt photoemission lines corresponded to the electrons released from the Pt 4f levels. However, these photoemission lines overlapped with the Al 2p electron binding energies. For this reason, the Pt XPS analysis focuses here on the Pt 4d peaks. When comparing the bare XPS spectra of $Pt/ZnAl_2O_4$ freshly calcined, exposed to dry reducing conditions, and exposed to wet reducing conditions (**Figure 3.5a** to **3.5c**), it becomes clear that the binding energy of the Pt 4d electrons reduced similarly for dry and wet reductive atmospheres. Also, the binding energy of the Pt 4d electrons of the Pt-Sn/$ZnAl_2O_4$ catalyst reduced in a similar fashion after exposure to dry reducing atmospheres (**Figure 3.5e**) as compared to the corresponding freshly calcined sample (**Figure 3.5d**). On the contrary, part of the Pt content of $Pt-Sn/ZnAl_2O_4$ remained more oxidized after exposure to wet reductive conditions, which is illustrated by the XPS peaks around 340 eV in **Figure 3.5f**.

To identify the different types of platinum species existing in $Pt/ZnAl_2O_4$ and Pt-Sn/$ZnAl_2O_4$ under dry and wet atmospheres, we deconvoluted the XPS results in **Figure 3.5**. In the applied deconvolution procedure, several requirements related to Pt 4d photoelectrons were imposed. Firstly, each Pt type was composed of a $4d_{3/2}$ and a $4d_{5/2}$

spin state electron in a ratio of 2:3. Besides, the distance between the $4d_{3/2}$ and $4d_{5/2}$ spin states should be about 17 eV. Also, the full width at half maximum (FWHM) of both states needed to be equal. On traditional Al_2O_3 supports, metallic Pt^0 $4d_{5/2}$ electrons commonly have a binding energy of about 313.0 eV [9,40], while Pt $4d_{5/2}$ electrons in Pt^{2+} and Pt^{4+} typically have binding energies of ca. 315 eV and ca. 319 eV, respectively [40]. Compared to traditional Al_2O_3 supports, the metal-support interactions are stronger in case Pt is functionalized onto $ZnAl_2O_4$ or $MgAl_2O_4$ spinel-type supports [11]. This could be an explanation why the electron binding strengths of the Pt 4d electrons, as obtained in this work (**Figure 3.5**), were somewhat greater as compared to the prescribed binding energy values of Pt/Al_2O_3 systems. The $ZnAl_2O_4$ support could withdraw electrons from the Pt, thereby lowering the electron density around Pt in $Pt/ZnAl_2O_4$ and $Pt-Sn/ZnAl_2O_4$.

After deconvoluting the XPS results, five different types of platinum were discerned, corresponding to Pt $4d_{5/2}$ binding energies around 312 eV, 314 eV, 318 eV, 321 eV, and 325 eV (see **Figure 3.5**). The specific Pt peaks around 314 eV, 318 eV, and 321 eV can be attributed to the presence of Pt^0, Pt^{2+}, and Pt^{4+} [9,40]. The more oxidized Pt species with an electron binding energy of ca. 325 eV possibly indicated the existence of $Pt(OH)_4$, particularly since this peak is prevalent in the steam treated $Pt-Sn/ZnAl_2O_4$ sample. Hydroxyl complexes surrounding Pt can substantially increase the binding strength of Pt electrons [41]. The concerning hydroxyl groups withdraw electron density from the Pt, which results in a greater binding strength of the remaining Pt 4d electrons. An additional type of Pt species with a relatively low binding energy of about 312 eV existed in dry and wet reduced $Pt/ZnAl_2O_4$ and in dry reduced $Pt-Sn/ZnAl_2O_4$ (**Figure 3.5**). The latter type of platinum could correspond to hydrogen-covered platinum, as the binding strength of Pt $4d_{5/2}$ electrons can reduce with increasing hydrogen coverage [42]. Electron donation from the hydrogen to the Pt upon adsorption could lead to weakly bound Pt 4d electrons.

Two main conclusions can be drawn from the results in **Figure 3.5**. Firstly, the peaks with an Pt $4d_{3/2}$ electron binding strength around 340 eV in **Figure 3.5f** indicate that part of the Pt remained more oxidized in steam treated $Pt-Sn/ZnAl_2O_4$ as compared to steam treated $Pt/ZnAl_2O_4$ (**Figure 3.5c**) and the corresponding dry reduced samples (**Figure 3.5b** and **3.5e**). This suggests that a higher concentration of $Pt(OH)_4$ and Pt^{4+} exists in steam treated $Pt-Sn/ZnAl_2O_4$. The second conclusion is related to the more weakly bound electrons around 312 eV, as attributed to hydrogen-covered Pt-H species. The concentration of this species was low in freshly calcined $Pt/ZnAl_2O_4$ and $Pt-Sn/ZnAl_2O_4$ (see **Figure 3.5a** and **3.5d**). The contribution of this type of platinum increased significantly for dry and wet reduced $Pt/ZnAl_2O_4$ (**Figure 3.5b** and **3.5c**) and for dry reduced $Pt-Sn/ZnAl_2O_4$ (**Figure 3.5e**) but it remained minor for wet reduced $Pt-Sn/ZnAl_2O_4$ (**Figure 3.5f**). This suggests that the Pt-H concentration was lower for the steam treated $Pt-Sn/ZnAl_2O_4$ catalyst as compared to steam treated $Pt/ZnAl_2O_4$ and the concerning dry reduced samples.
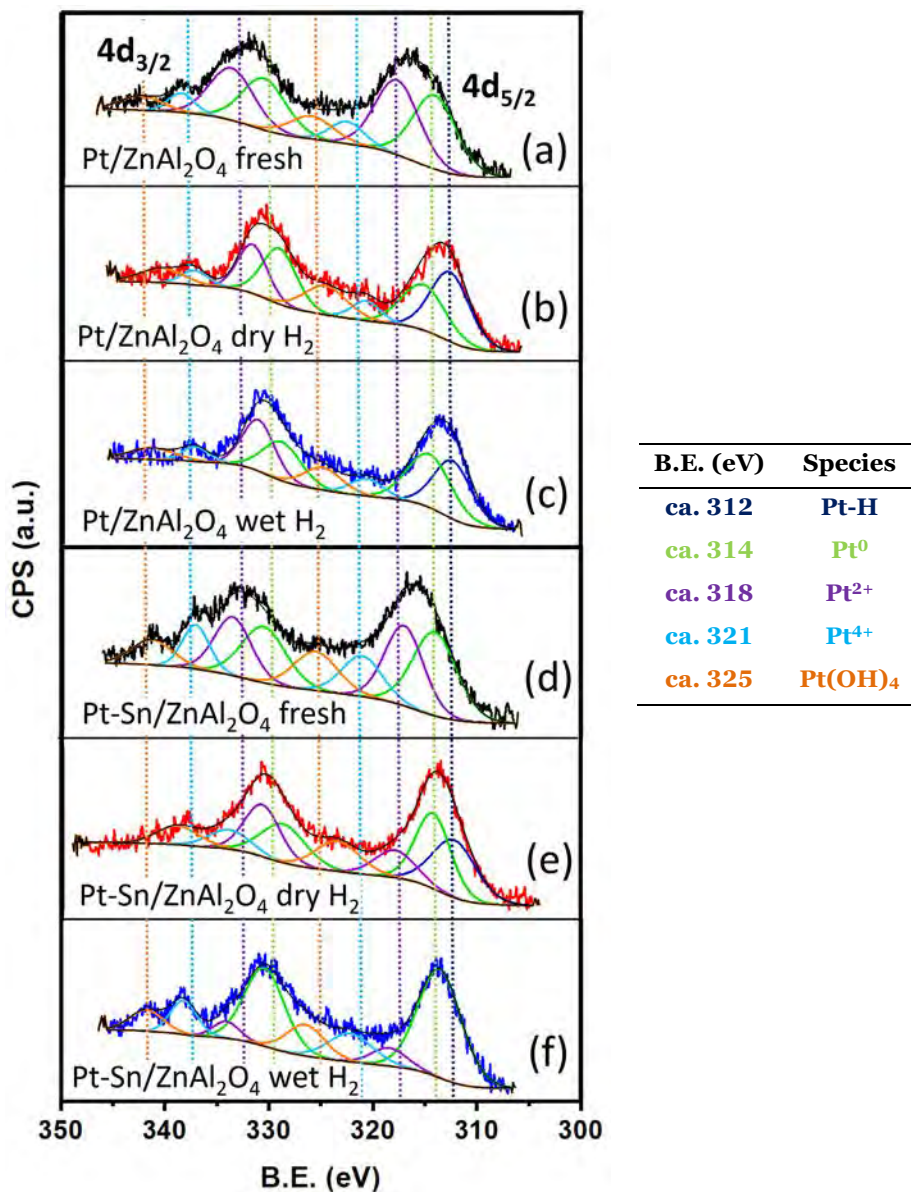
Figure 3.5: X-ray photoelectron spectra of the Pt 4d photoemission lines of $Pt/ZnAl_2O_4$ (a) freshly calcined, (b) after dry H_2 treatment, and (c) after wet H_2 treatment, and for Pt-$Sn/ZnAl_2O_4$ (d) freshly calcined, (e) after dry H_2 treatment, and (f) after wet H_2 treatment. Conditions for dry H_2 treatment: 10 vol% H_2, 90 vol% N_2, 550 °C, 1 h, conditions for wet H_2 treatment: 10 vol% H_2, 1.4 vol% H_2O, 88.6 vol% N_2, 550 °C, 3 h.

The STEM-HAADF results indicated some degree of Pt sintering during catalytic testing in dry conditions for $Pt/ZnAl_2O_4$ (**Figure 3.E1a-b**) and Pt-$Sn/ZnAl_2O_4$ (**Figure 3.E1e-**

f). This sintering process was suppressed for both catalysts in the presence of steam (**Figure 3.E1c-d** and **Figure 3.E1g-h**). The influence of possible Pt sintering on the calculated apparent turnover frequency of ethylene formation was disregarded here.

3.3.4. Discussion

3.3.4.1. Pt/ZnAl$_2$O$_4$

The XRD and XPS spectra of Pt/ZnAl$_2$O$_4$ after dry and wet reduction were comparatively similar to each other (**Figure 3.4** and **3.5b-c**). This indicates that the steam did not modify the crystal structure and electronic state of the catalyst support material nor the metal active site. The substantial difference in observed performance of Pt/ZnAl$_2$O$_4$ tested under dry and wet atmospheres (**Figure 3.1a** and **3.2a,** and **Table 3.1**) can therefore only be explained by a mechanistic effect of the steam. Supposedly, the steam enhances product desorption [27], which is supported by the hydrogen reaction orders in **Figure 3.2a**, showing that under wet conditions hydrogen is less inhibiting the ethylene formation than under dry conditions. In addition, ethylene desorption could be boosted under moistened conditions, as ethylene is known to adsorb as relatively weak π-bonded ethylene on oxygen-covered Pt surfaces, while it adsorbs in a more strongly bound di-σ-bonded configuration on oxygen-free Pt surfaces [43].

In **Chapter 2**, we showed that hydrogen and ethylene are inhibiting the formation of ethylene in ethane NODH on Pt-based catalysts and that the hydrogen and ethylene surface coverages strongly influence the reaction rate. A possible enhancement in product desorption induced by steam could therefore lead to a reduction in apparent activation energy and an increment in ethylene formation rate. Considering that the H$_2$O reaction order is zero for Pt/ZnAl$_2$O$_4$ (**Figure 3.3a**), steam does seemingly not occupy surface sites. It has been demonstrated in the past that Pt hydroxylation and dehydroxylation are highly dynamic processes, such that surface hydroxyl groups do not irreversibly block Pt active sites [44]. Possibly, steam is functioning as a cleaning agent by enhancing hydrogen and ethylene desorption from Pt sites, or by enhancing hydrogen and carbon spillover from Pt sites to the support material, both leading to lower product coverages on Pt.

3.3.4.2. Pt-Sn/ZnAl$_2$O$_4$

In dry reductive atmospheres, the Pt in Pt-Sn/ZnAl$_2$O$_4$ was reduced in a similar fashion as the Pt reduction in Pt/ZnAl$_2$O$_4$ under dry and wet reductive atmospheres (**Figure 3.5e** vs. **3.5b-c**). However, under wet reducing conditions the Pt in Pt-Sn/ZnAl$_2$O$_4$ remained significantly more oxidized compared to the Pt in Pt/ZnAl$_2$O$_4$, as indicated by the Pt XPS peaks around 340 eV in **Figure 3.5f**. Moreover, the XRD results indicated that the PtSn dealloys upon exposure to H$_2$O (**Figure 3.4** and **3.B3**). This dealloying in presence of steam was not confirmed by the XPS results, since possible shifts in binding energy of the Sn 4d electrons after H$_2$O treatment could be hidden by overlapping O 2s photoemission lines (see **Supporting Information 3.D**). Nevertheless, for Pt-Sn/ZnAl$_2$O$_4$ the observed

difference in catalytic performance under dry and wet conditions (**Figure 3.1b** and **3.2b**, and **Table 3.1**) could be caused by modifications of the catalyst induced by the steam, in addition to possible mechanistic effects.

The more oxidized Pt in Pt-Sn/ZnAl$_2$O$_4$ exposed to moistened conditions was ascribed to Pt(OH)$_4$ (**Figure 3.5f**), whilst this type of Pt was not detected for steam treated Pt/ZnAl$_2$O$_4$ (**Figure 3.5c**). Sn is generally much more prone to oxidation in the presence of H$_2$O than the noble Pt. Possibly, the Pt in Pt-Sn/ZnAl$_2$O$_4$ is electronically influenced by neighboring tin hydroxide complexes, analogous to the influence of oxide supports on the properties of Pt. Most of the Pt is metallic in both Pt/ZnAl$_2$O$_4$ and Pt-Sn/ZnAl$_2$O$_4$, as the major contributor to the XPS spectra of the wet reduced samples is still Pt^0 (see **Figure 3.5c** and **3.5f**). Besides, Pt surfaces can be prone to hydroxylation, even for modest H$_2$O pressures (< 1 mbar(a)) [44]. Hydroxyl complexes surrounding Pt can substantially increase the binding strength of Pt electrons [41]. Similar to Pt/ZnAl$_2$O$_4$, the reaction order in H$_2$O was about zero for Pt-Sn/ZnAl$_2$O$_4$ (**Figure 3.3b**), as surface hydroxyl groups do not irreversibly block catalyst active centers in Pt/ZnAl$_2$O$_4$ nor in Pt-Sn/ZnAl$_2$O$_4$.

The more oxidized Pt existing in steam treated Pt-Sn/ZnAl$_2$O$_4$ possibly attracts the hydrogen and hydrocarbons more strongly as compared to Pt-Sn/ZnAl$_2$O$_4$ exposed to dry conditions. Stronger ethane adsorption under wet conditions facilitates ethyl C-H bond dissociation but stronger hydrogen and ethylene adsorption increases the apparent activation barrier, as these reaction products are hard to remove from the catalyst surface. The latter is confirmed by the hydrogen reaction order results in **Figure 3.2b**, showing that hydrogen has a more inhibiting effect on the reaction rate under wet conditions than under dry conditions. Thus, even if the steam would be similarly enhancing product desorption for Pt-Sn/ZnAl$_2$O$_4$ as it does for Pt/ZnAl$_2$O$_4$ this effect could be overcompensated by the influence of electronic modifications of the Pt in Pt-Sn/ZnAl$_2$O$_4$.

3.3.4.3.   Future perspective

In packed bed membrane reactors equipped with dense ceramic membranes to remove hydrogen, the applied catalyst bed will inevitably be exposed to wet conditions, as these ceramic membranes function optimally in the presence of steam [24]. Moreover, cofeeding steam assists in minimizing carbon deposition in alkane NODH systems [10,25,26]. A steam cosupply is expected to be a key feature for membrane reactors in which hydrogen is removed from hydrocarbons, as those systems are operating under hydrogen-poor atmospheres, which are prone to coking [25]. Here, we demonstrated that PtSn-based catalysts were physicochemically modified by steam, whilst catalysts containing only Pt remained unaffected. This suggests that tin-free catalysts are preferred in ceramic membrane systems, particularly since our results indicated that steam enhances ethylene formation by facilitating product desorption. Nevertheless, a Pt-Sn/ZnAl$_2$O$_4$ catalyst is employed in the commercialized Uhde STAR® process [1]. This commercial catalyst contains calcium-magnesium aluminate as a binder [1], which possibly avoids Sn leaching

or PtSn dealloying. Adaptations to the Pt-Sn/ZnAl$_2$O$_4$ catalyst employed could, therefore, be considered to improve the stability of PtSn catalysts in wet atmospheres.

The differences in apparent activation barrier (**Figure 3.1**) and hydrogen reaction order (**Figure 3.2**) between Pt/ZnAl$_2$O$_4$ and Pt-Sn/ZnAl$_2$O$_4$ and between dry and wet conditions were explained by means of modifications of the catalyst active phases and by differences in the hydrogen and ethylene surface coverages. Herein, it was implicitly assumed that the reaction mechanism and the rate-determining step were similar in all systems investigated. In case the reaction mechanism would be different in one of the systems, then this would distort the interpretation of the results in **Figure 3.1** and **3.2**. Ideally, one would compare the activation barrier between the various cases for equal ethane, ethylene, and hydrogen reaction orders to be as certain as possible about the uniformity of the reaction mechanism. In that case, it would be valuable to quantify the actual activation barrier and the enthalpies and entropies of ethylene and hydrogen adsorption under moistened conditions and compare the outcomes to the kinetic and thermodynamic parameters retrieved under dry conditions, as e.g. reported in **Chapter 2**. This could allow for a quantitative assessment of possible mechanistic effects induced by the steam for both catalysts.

3.4.   Conclusion

In this chapter, we showed that cofeeding 3 vol% of steam enhanced the ethane dehydrogenation rate for Pt/ZnAl$_2$O$_4$ and Pt-Sn/ZnAl$_2$O$_4$ catalysts. Detailed characterization revealed that the Pt/ZnAl$_2$O$_4$ was not physicochemically modified by the steam. The concerning performance improvement was therefore ascribed to mechanistic effects induced by the steam for Pt/ZnAl$_2$O$_4$. It was postulated that steam functions as a cleaning agent either by enhancing product desorption from Pt sites, or by enhancing hydrogen and carbon spillover from Pt sites to the support material, both leading to lower coverages on Pt. In contrast to Pt/ZnAl$_2$O$_4$, the Pt-Sn/ZnAl$_2$O$_4$ catalyst was physicochemically modified by steam, as the XRD results indicated dealloying of PtSn and the XPS results showed that the Pt in Pt-Sn/ZnAl$_2$O$_4$ remained more oxidized after steam treatment. More oxidized Pt anticipatedly binds hydrocarbons and hydrogen more strongly. Consequently, ethane dissociation and product adsorption are enhanced under wet atmospheres. Thus, even if steam would be similarly enhancing product desorption for Pt-Sn/ZnAl$_2$O$_4$ as it did for Pt/ZnAl$_2$O$_4$ this effect could be overcompensated by electronic modifications of the Pt. This knowledge on the effect of steam on the performance of Pt-based catalysts in the ethane NODH reaction is pivotal for promising membrane strategies in which hydrogen permeable dense ceramic membranes, which function optimally under moistened conditions, are used to increase ethylene yields.

References

1. Sattler, J. J. H. B., Ruiz-Martinez, J., Santillan-Jimenez, E. & Weckhuysen, B. M. Catalytic dehydrogenation of light alkanes on metals and metal oxides. *Chem. Rev.* **114**, 10613–10653 (2014).

2. Farjoo, A., Khorasheh, F., Niknaddaf, S. & Soltani, M. Kinetic modeling of side reactions in propane dehydrogenation over Pt-Sn/y-Al2O3 catalyst. *Scientia Iranica* **18**, 458–464 (2011).

3. Ricca, A., Montella, F., Iaquaniello, G., Palo, E. & Salladini, A. Membrane assisted propane dehydrogenation: Experimental investigation and mathematical modelling of catalytic reactions. *Catal. Today* **331**, 43–52 (2019).

4. van Sint Annaland, M., Kuipers, J. A. M. & van Swaaij, W. P. M. A kinetic rate expression for the time-dependent coke formation rate during propane dehydrogenation over a platinum alumina monolithic catalyst. *Catal. Today* **66**, 427–436 (2001).

5. Rashidi, M., Nikazar, M. & Rahmani, M. Chemical Engineering Research and Design Kinetic modeling of simultaneous dehydrogenation of propane and isobutane on Pt-Sn-K / Al 2 O 3 catalyst. *Chemical Engineering Research and Design* **95**, 239–247 (2014).

6. Larsson, M., Henriksson, N. & Andersson, B. Investigation of the kinetics of a deactivating system by transient experiments. *Appl. Catal. A: Gen.* **166**, 9–19 (1998).

7. Lobera, M. P., Téllez, C., Herguido, J. & Menéndez, M. Transient kinetic modelling of propane dehydrogenation over a Pt–Sn–K/Al2O3 catalyst. *Appl. Catal. A: Gen.* **349**, 156–164 (2008).

8. Sheintuch, M., Liron, O., Ricca, A. & Palma, V. Propane dehydrogenation kinetics on supported Pt catalyst. *Appl. Catal. A: Gen.* **516**, 17–29 (2016).

9. Gómez-Quero, S., Tsoufis, T., Rudolf, P., Makkee, M., Kapteijn, F. & Rothenberg, G. Kinetics of propane dehydrogenation over Pt-Sn/Al2O3. *Catal. Sci. Technol.* **3**, 962–971 (2013).

10. Li, Q., Sui, Z., Zhou, X. & Chen, D. Kinetics of propane dehydrogenation over Pt–Sn/Al2O3 catalyst. *Appl. Catal. A: Gen.* **398**, 18–26 (2011).

11. Aguilar-rios, G., Valenzuela, M. A., Salas, P., Armendariz, H., Bosch, P., Del Toro, G., Silva, R., Bertín, V., Castillo, S., Ramírez-Solís, A. & Schifter, I. Hydrogen interactions and catalytic properties of platinum-tin supported on zinc aluminate. *Appl. Catal. A: Gen.* **127**, 65–75 (1995).

12. Cortright, R. D. & Dumesic, J. A. Effects of potassium on silica-supported Pt and Pt/Sn catalysts for isobutane dehydrogenation. *J. Catal.* **157**, 576–583 (1995).

13. Cortright, R. D., Hill, J. M. & Dumesic, J. A. Selective dehydrogenation of isobutane over supported Pt/Sn catalysts. *Catal. Today* **55**, 213–223 (2000).

14. Cortright, R. D., Levin, P. E. & Dumesic, J. A. Kinetic studies of isobutane dehydrogenation and isobutene hydrogenation over Pt/Sn-based catalysts. *Ind. Eng. Chem. Res.* **37**, 1717–1723 (1998).

15. Natal-Santiago, M. A., Podkolzin, S. G., Cortright, R. D. & Dumesic, J. A. Microcalorimetric studies of interactions of ethene, isobutene, and isobutane with silica-supported Pd, Pt, and PtSn. *Catal. Letters.* **45**, 155–163 (1997).

16. Biloen, P., Dautzenberg, F. M. & Sachtler, W. M. H. Catalytic dehydrogenation of propane to propene over platinum and platinum-gold alloys. *J. Catal.* **50**, 77–86 (1977).

17. Barghi, B., Fattahi, M. & Khorasheh, F. Kinetic modeling of propane dehydrogenation over an industrial catalyst in the presence of oxygenated compounds. *React. Kinet. Mech. Catal.* **107**, 141–155 (2012).

18. Brencio, C., Di Felice, L. & Gallucci, F. Fluidized bed membrane reactor for the direct dehydrogenation of propane: proof of concept. *Membranes* **12**, 1211 (2022).

19. Morejudo, S. H., Zanón, R., Escolástico, S., Yuste-Tirados, I., Malerød-Fjeld, H., Vestre, P. K., Coors, W. G., Martínez, A., Norby, T., Serra, J. M. & Kjølseth, C. Direct conversion of methane to aromatics in a catalytic co-ionic membrane reactor. *Science* **353**, 563–566 (2016).

20. Clark, D., Malerød-Fjeld, H., Budd, M., Yuste-Tirados, I., Beeaff, D., Aamodt, S., Nguyen, K., Ansaloni, L., Peters, T., Vestre, P. K., Pappas, D. K., Valls, M. I., Remiro-Buenamañana, S., Norby, T., Bjørheim, T. S., Serra, J. M. & Kjølseth, C. Single-step hydrogen production from NH3, CH4, and biogas in stacked proton ceramic reactors. *Science* **376**, 390–393 (2022).

21. Babita, K., Sridhar, S. & Raghavan, K. V. Membrane reactors for fuel cell quality hydrogen through WGSR – Review of their status, challenges and opportunities. *Int. J. Hydrog. Energy* **36**, 6671–6688 (2011).

22. Polfus, J. M., Xing, W., Fontaine, M. L., Denonville, C., Henriksen, P. P. & Bredesen, R. Hydrogen separation membranes based on dense ceramic composites in the La27W5O55.5-LaCrO3 system. *J. Membr. Sci.* **479**, 39–45 (2015).

23. Gallucci, F., Fernandez, E., Corengia, P. & Sint, M. Van. Recent advances on membranes and membrane reactors for hydrogen production. *Chem. Eng. Sci.* **92**, 40–66 (2013).

24. Meng, Y., Gao, J., Zhao, Z., Amoroso, J., Tong, J. & Brinkman, K. S. Review : recent progress in low-temperature proton-conducting ceramics. *J. Mater. Sci.* 9291–9312 (2019).

25. Larsson, M., Hult, M., Blekkan, E. A. & Andersson, B. The Effect of Reaction Conditions and Time on Stream on the Coke Formed during Propane Dehydrogenation. *J. Catal.* **53**, 44–53 (1996).

26. Sattler, J. J. H. B., Beale, A. M. & Weckhuysen, B. M. Operando Raman spectroscopy study on the deactivation of Pt/Al2O3 and Pt-Sn/Al2O3 propane dehydrogenation catalysts. *Phys. Chem. Chem. Phys.* **15**, 12095–12103 (2013).

27. Nakagawa, K., Kajita, C., Okumura, K., Ikenaga, N., Nishitani-Gamo, M., Ando, T., Kobayashi, T. & Suzuki, T. Role of carbon dioxide in the dehydrogenation of ethane over gallium-loaded catalysts. *J. Catal.* **203**, 87–93 (2001).

28. Bosch, P., Valenzuela, M. A., Zapata, B., Acosta, D., Aguilar-rios, G., Maldonado, C. & Schifter, I. High temperature treated Pt/Sn-ZnAl2O4 catalysts. *J. Mol. Catal.* **93**, 67–78 (1994).

29. Valenzuela, M. A., Jacobs, J.-P., Bosch, P., Reijne, S., Zapata, B. & Brongersma, H. H. The influence of the preparation method on the surface structure of ZnAl2O4. *Appl Catal A Gen* **148**, 315–324 (1997).

30. Laag, N. J. Van Der, Snel, M. D., Magusin, P. C. M. M. & With, G. De. Structural, elastic, thermophysical and dielectric properties of zinc aluminate (ZnAl2O4). *J. Eur. Ceram. Soc.* **24**, 2417–2424 (2004).

31. Ballarini, A. D., Miguel, S. R. De, Castro, A. A. & Scelza, O. A. n-Decane dehydrogenation on Pt, PtSn and PtGe supported on spinels prepared by different methods of synthesis. *Appl. Catal. A: Gen.* **467**, 235–245 (2013).

32. Aguilar-rios, G., Salas, P., Valenzuela, M. A., Armendariz, H., Wang, J. A. & Salmones, J. Propane dehydrogenation activity of Pt and Pt–Sn catalysts supported on magnesium aluminate: Influence of steam and hydrogen. *Catal. Letters* **60**, 21–25 (1999).

33. Salmones, J., Wang, J., Galicia, J. A. & Aguilar-rios, G. H2 reduction behaviors and catalytic performance of bimetallic tin-modified platinum catalysts for propane dehydrogenation. *J. Mol. Catal. A: Chem.* **184**, 203–213 (2002).

34. Berger, R. J., Pérez-Ramírez, J., Kapteijn, F. & Moulijn, J. A. Catalyst performance testing: Bed dilution revisited. *Chem. Eng. Sci.* **57**, 4921–4932 (2002).

35.   de Macedo, H. P., Bezerra de Araújo Medeiros, R. L. B., de Medeiros, A. L., Silva de Oliveira, Â. A. de, de Figueredo, G. P., Antônio, M., de Freitas Melo, M. A. & de Araújo Melo, D. M. Characterization of ZnAl2O4 spinel obtained by hydrothermal and microwave assisted combustion method: A comparative study. *Mater. Res.* **20**, 29–33 (2017).

36.   Svintsitskiy, D. A., Slavinskaya, E. M., Stonkus, O. A., Romanenko, A. V., Stadnichenko, A. I., Kibis, L. S., Derevyannikova, E. A., Evtushkova, A. A. & Boronin, A. I. The state of platinum and structural features of Pt/Al2O3 catalysts in the reaction of NH3 oxidation. *J. Struct. Chem.* **60**, 919–931 (2019).

37.   Llorca, J., Homs, N., Fierro, J.-L. G., Sales, J. & Ramírez de la Piscina, P. Platinum-tin catalysts supported on silica highly selective for n-hexane dehydrogenation. *J. Catal.* **166**, 44–52 (1997).

38.   Iglesias-Juez, A., Beale, A. M., Maaijen, K., Weng, T. C., Glatzel, P. & Weckhuysen, B. M. A combined in situ time-resolved UV-Vis, Raman and high-energy resolution X-ray absorption spectroscopy study on the deactivation behavior of Pt and PtSn propane dehydrogenation catalysts under industrial reaction conditions. *J. Catal.* **276**, 268–279 (2010).

39.   Deng, L., Shishido, T., Teramura, K. & Tanaka, T. Effect of reduction method on the activity of Pt-Sn/SiO2 for dehydrogenation of propane. *Catal. Today* **232**, 33–39 (2014).

40.   Serrano-Ruiz, J. C., Huber, G. W., Sánchez-Castillo, M. A., Dumesic, J. A., Rodríguez-Reinoso, F. & Sepúlveda-Escribano, A. Effect of Sn addition to Pt/CeO2-Al2O3 and Pt/Al2O3 catalysts: An XPS, 119Sn Mössbauer and microcalorimetry study. *J. Catal.* **241**, 378–388 (2006).

41.   Kalinkin, A. V., Smirnov, M. Yu., Nizovskii, A. I. & Bukhtiyarov, V. I. X-ray photoelectron spectra of platinum compounds excited with monochromatic AgLα irradiation. *J. Electron Spectrosc. Relat. Phenom.* **177**, 15–18 (2010).

42.   Huizinga, T., van 'T Blik, H. F. J., Vis, J. C. & Prins, R. XPS investigations of Pt and Rh supported on γ-Al2O3 and TiO2. *Surf. Sci.* **135**, 580–596 (1983).

43.   Stuve, E. M. & Madix, R. J. Use of the .pi..sigma. parameter for characterization of rehybridization upon adsorption on metal surfaces. *J. Phys. Chem.* **89**, 3183–3185 (1985).

44.   Mom, R. V. & Knop-Gericke, A. Hydroxylation of platinum surface oxides induced by water vapor. *J. Phys. Chem. Lett.* **13**, 879–883 (2022).

45.   Aguilar-rios, G., Valenzuela, M. A., Armendariz, H., Salas, P., Dominguez, J. M., Acosta, D. R. & Schifter, I. Metal-support effects and catalytic properties of platinum supported on zinc aluminate. *Appl. Catal. A: Gen.* **90**, 25–34 (1992).

46. Valenzuela, M. A., Bosch, P., Zapata, B., Aguilar-Rios, G., Lara, V. H., García-Figueroa, E. & Schifter, I. Effects of hydrogen at high temperature on ZnAl2O4 and Sn-ZnAl204. *J. Therm. Anal.* **44**, 639–653 (1995).

Supporting Information

3.A. Catalytic testing setup
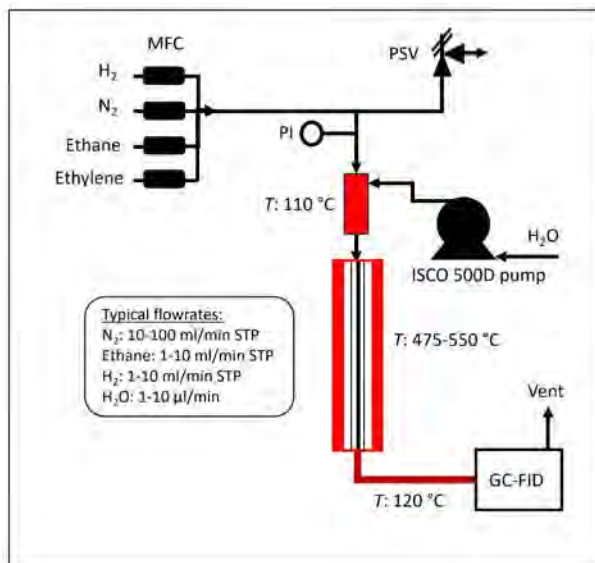
Figure 3.A1: Process flow diagram of the catalytic testing setup.

3.B. Physicochemical properties of Pt/ZnAl$_2$O$_4$ and Pt-Sn/ZnAl$_2$O$_4$

Detailed physicochemical characterization was conducted on the bare support (ZnAl$_2$O$_4$), Pt-, Sn-, and Pt-Sn containing catalysts (see **Table 3.B1**). The surface areas and pore volumes of the prepared ZnAl$_2$O$_4$ support are in line with values reported in literature for ZnAl$_2$O$_4$ supports prepared via coprecipitation methods [11,28,31,45,46]. The difference between the cluster size determined using CO chemisorption and the number-based Pt cluster size resulting from STEM-HAADF analysis is attributed to the existence of a limited number of large particles (>10 nm, see **Figure 3.B1**) that are not captured significantly by the number-based STEM-HAADF average.

Table 3.B1: Properties of fresh catalysts. Surface area and pore volume were determined with N_2 physisorption, Pt and Sn loadings with XRF, and Pt cluster size using CO chemisorption and STEM-HAADF.

Characteristic:	$ZnAl_2O_4$	$Sn/ZnAl_2O_4$	$Pt/ZnAl_2O_4$	$Pt-Sn/ZnAl_2O_4$
Surface area (m²/g)	76.3	71.4	71.3	66.0
Pore volume (cm³/g)	0.165	0.157	0.146	0.138
Pt loading (wt.%)	-	-	3.6	4.0
Sn loading (wt.%)	-	2.5	-	1.6
Pt cluster size (nm)[1]	-	-	9.4	9.4*
Pt cluster size (nm)[2], number-based	-	-	1.6	3.8

[1]Pt cluster size as determined using CO chemisorption, [2]Pt cluster size as determined using STEM-HAADF using a minimum of 200 particles, *Active Pt cluster size was determined assuming that only Pt adsorbs CO.

An example of a STEM-HAADF image of the $Pt-Sn/ZnAl_2O_4$ catalyst sample is presented in **Figure 3.B1**, which illustrates the presence of a limited number of large metal particles in addition to a large number of small metal particles.
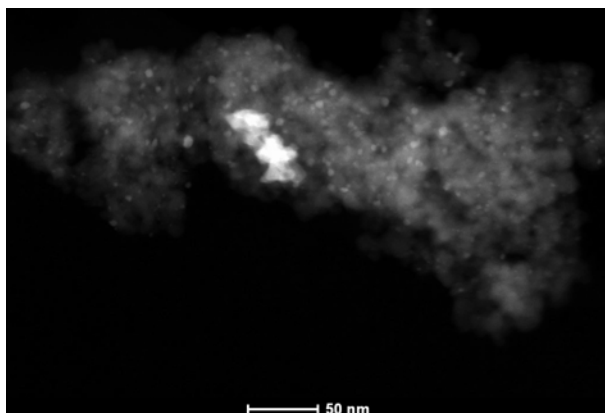
Figure 3.B1: STEM-HAADF image of $Pt-Sn/ZnAl_2O_4$, indicating the presence of a limited number of large metal particles in addition to a large number of small metal particles.

The full XRD spectra of the $ZnAl_2O_4$, $Sn/ZnAl_2O_4$, $Pt/ZnAl_2O_4$, and $Pt-Sn/ZnAl_2O_4$ samples treated under dry and wet reducing gas phase atmospheres are presented in **Figure 3.B2**. Besides, zoom-in representations of the XRD spectra focusing on the shift of the $ZnAl_2O_4$ spinel peaks, and on the location of the Pt and PtSn peaks are available in **Figure 3.B3**.
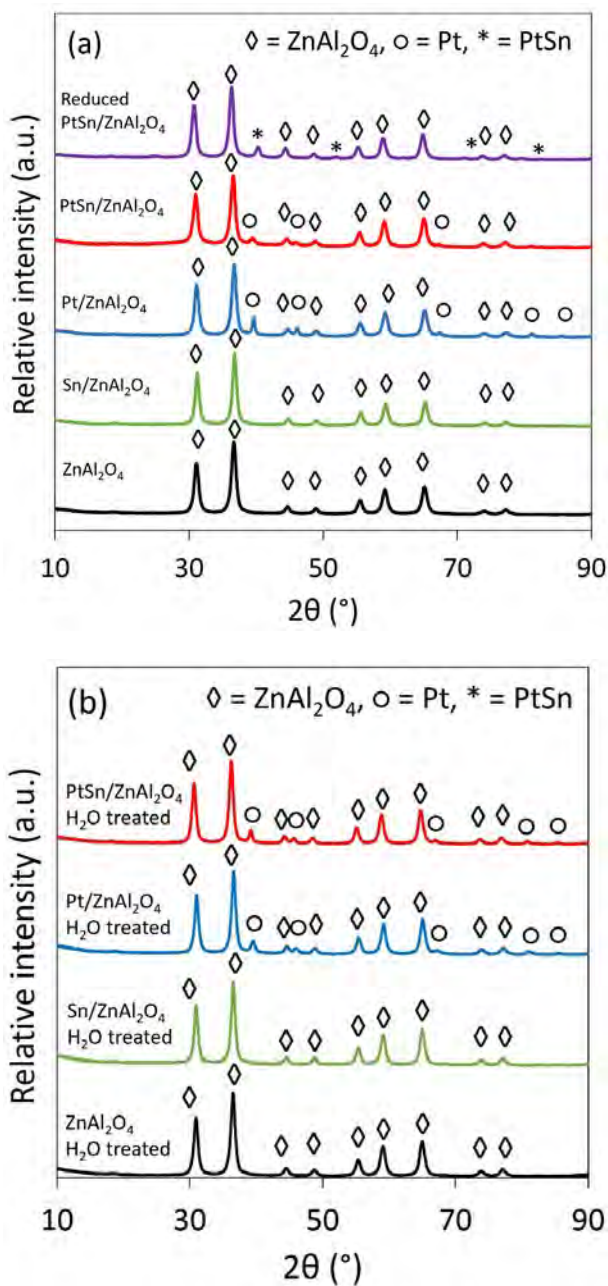
Figure 3.B2: (a) XRD spectra of fresh, calcined ZnAl₂O₄, Sn/ZnAl₂O₄, Pt/ZnAl₂O₄, Pt-Sn/ZnAl₂O₄, and reduced Pt-Sn/ZnAl₂O₄ and (b) XRD spectra of H₂O-treated ZnAl₂O₄, Sn/ZnAl₂O₄, Pt/ZnAl₂O₄, and Pt-Sn/ZnAl₂O₄.
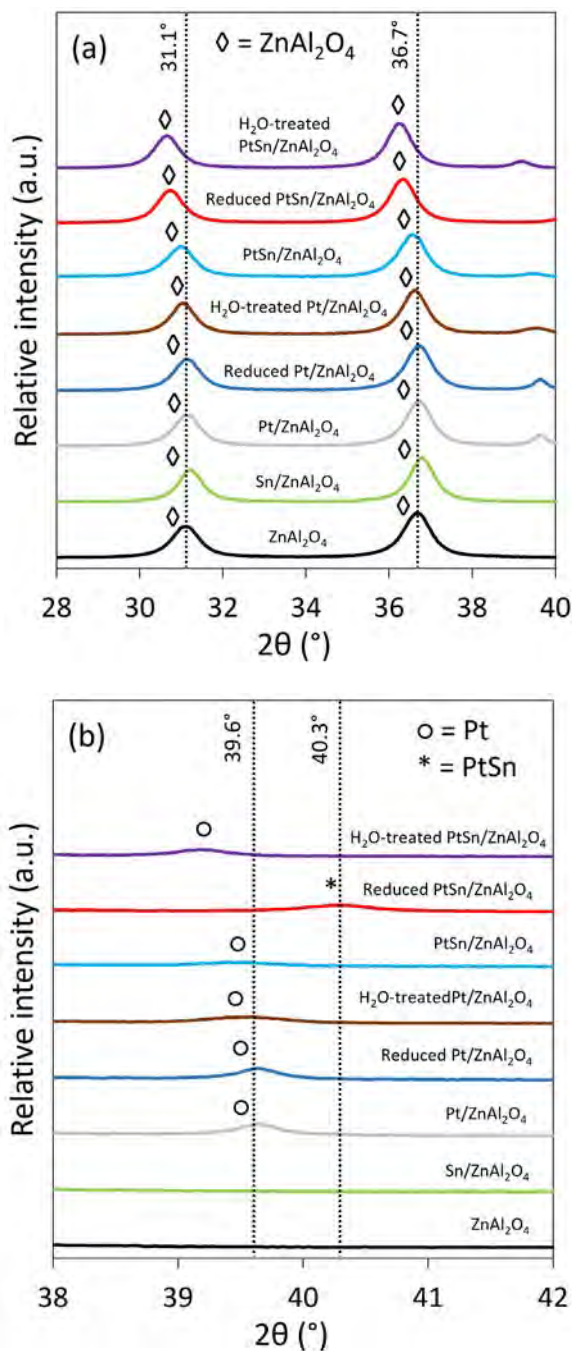
Figure 3.B3: Zoom-in of XRD spectra of (a) the shift of $ZnAl_2O_4$ spinel peaks, and (b) the location of Pt and PtSn peaks.

The size of the $ZnAl_2O_4$, Pt, and PtSn crystalline domains (τ) of the various catalysts were determined from the XRD results (**Figure 3.4** and **Figure 3.B2**) using the Scherrer equation (**Equation 3.B1**). The outcomes are presented in **Table 3.B2**.

$$\tau = \frac{\kappa \lambda}{\beta \cos(\theta)} \tag{3.B1}$$

In **Equation 3.B1**, κ represents the shape factor, assumed to be 0.9 in this analysis, λ the X-ray wavelength (0.154 nm), β the full width at half maximum of the concerning XRD peak (in radians), and θ the Bragg angle (in radians).

Table 3.B2: Outcomes of the crystallite size determination from the XRD results, using the Scherrer equation.

	$ZnAl_2O_4$ peak (ca. 36.7°)		Pt peak (ca. 39.6°) or PtSn peak (ca. 40.3°)	
	Bragg angle 2θ (°)	τ (nm)	Bragg angle 2θ (°)	τ (nm)
$ZnAl_2O_4$	36.66	11.9	-	-
$ZnAl_2O_4$ H_2O-treated	36.52	11.8	-	-
$Sn/ZnAl_2O_4$	36.80	12.9	-	-
$Sn/ZnAl_2O_4$ H_2O-treated	36.55	13.3	-	-
$Pt/ZnAl_2O_4$	36.68	11.4	39.65	26.0
$Pt/ZnAl_2O_4$ reduced	36.70	11.2	39.72	22.8
$Pt/ZnAl_2O_4$ H_2O-treated	36.63	12.1	39.59	13.4
$Pt-Sn/ZnAl_2O_4$	36.60	11.4	39.40	14.8
$Pt-Sn/ZnAl_2O_4$ reduced	36.33	11.8	40.30*	13.9
$Pt-Sn/ZnAl_2O_4$ H_2O-treated	36.22	12.5	39.16	13.9

PtSn peak.

3.C. Catalyst stability

The catalytic tests employed in this work lasted for ca. 3-6 hours on-stream. The $Pt/ZnAl_2O_4$ and $Pt-Sn/ZnAl_2O_4$ catalysts did not deactivate significantly during this testing period under dry as well as wet gas phase atmospheres. The concentration of the olefin, which is generally believed to be the precursor for coke formation [4], was low in all tests, due to the low ethane partial pressures (ca. 40 mbar(a)) and low conversion levels (<15%) used. Furthermore, the steam that was cosupplied in the moistened tests is known to suppress carbon deposition [9,25–27].

The stability of the different catalysts is illustrated in **Figure 3.C1** for the hydrogen reaction order tests on $Pt/ZnAl_2O_4$ and $Pt-Sn/ZnAl_2O_4$ performed under dry and wet

conditions at 550 °C. The conversion increases upon reducing the hydrogen partial pressure, while maintaining a constant ethane partial pressure. The catalyst stability was checked by returning to the same experimental conditions at the end of the test as employed in the beginning of the test (**Figure 3.C1**). For most catalytic testing data reported in this work, the difference in conversion level between starting and ending conditions was insignificant, thereby excluding any possible influence of the deactivation of the Pt/ZnAl$_2$O$_4$ and Pt-Sn/ZnAl$_2$O$_4$ catalysts on the obtained kinetic data. The only exception was the case in which Pt-Sn/ZnAl$_2$O$_4$ was exposed to moistened conditions, as characterization of that spent catalyst indicated PtSn dealloying and more oxidized Pt states after steam treatment.
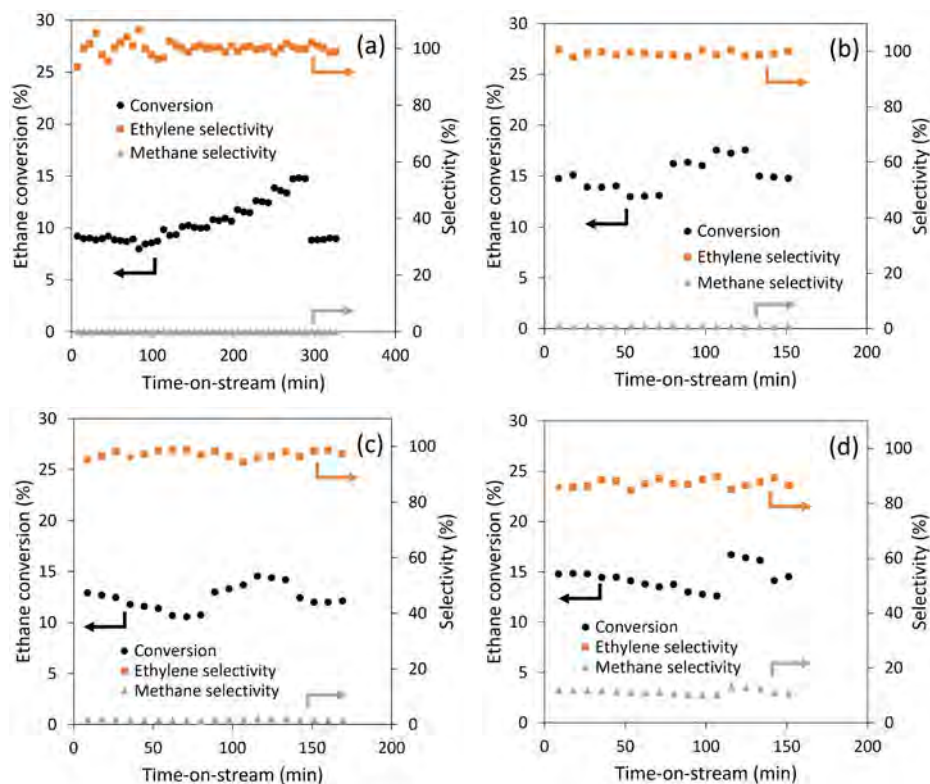
Figure 3.C1: Ethane conversion as a function of time-on-stream for the hydrogen reaction order tests on (a) Pt-Sn/ZnAl$_2$O$_4$ and (b) Pt/ZnAl$_2$O$_4$ under dry conditions, and on (c) Pt-Sn/ZnAl$_2$O$_4$ and (d) Pt/ZnAl$_2$O$_4$ under wet conditions at 550 °C. Stepwise reductions in the hydrogen partial pressure led to increments in the ethane conversion, p_{ethane} = 34 mbar(a).

3.D. X-ray photoelectron spectroscopy results

3.D1. XPS spectra of Zn, Al, O, and Sn
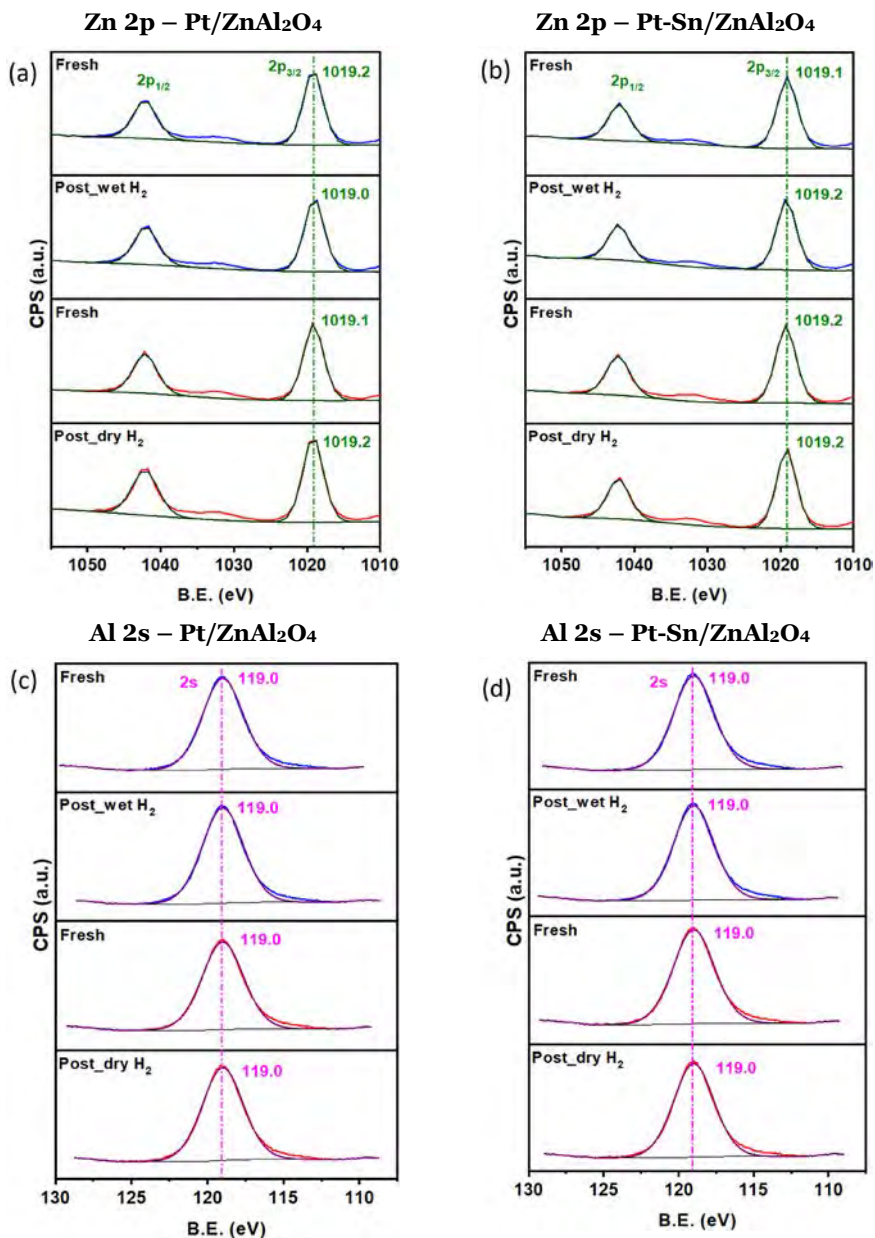
Figure 3.D1: X-ray photoelectron spectra of (a-b) Zn 2p, and (c-d) Al 2s electrons of Pt/ZnAl$_2$O$_4$ and Pt-Sn/ZnAl$_2$O$_4$, before treatment, after treatment in dry H$_2$ (10 vol% H$_2$, 90 vol% N$_2$, 1 h) and wet H$_2$ (10 vol% H$_2$, 1.4 vol% H$_2$O, 88.6 vol% N$_2$, 3 h) at 550 °C.

O 1s – Pt/ZnAl₂O₄

O 1s – Pt-Sn/ZnAl₂O₄

Sn 4d + O 2s – Pt-Sn/ZnAl₂O₄
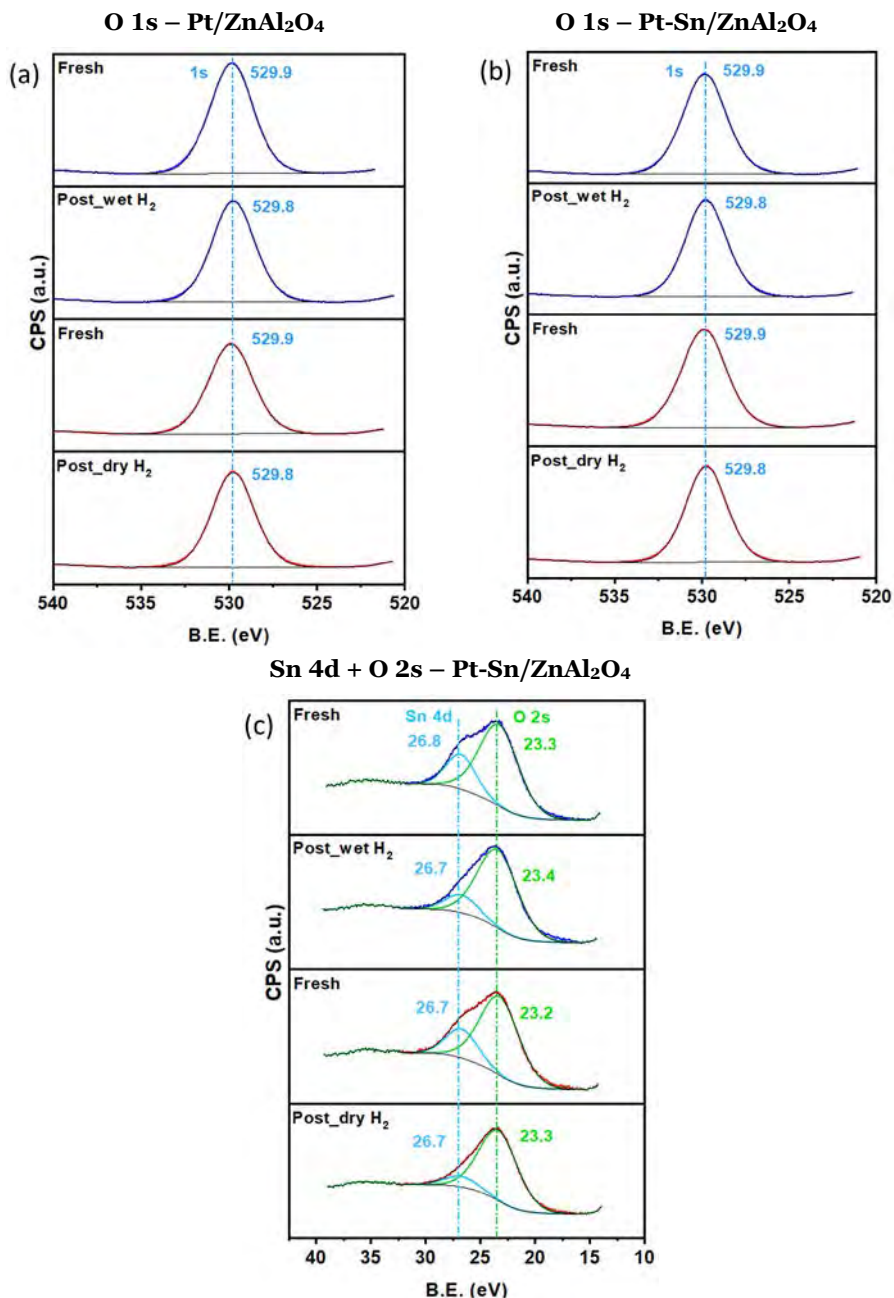
Figure 3.D2: X-ray photoelectron spectra of (a-b) O 1s, and (c) Sn 4d + O 2s electrons of Pt/ZnAl₂O₄ and Pt-Sn/ZnAl₂O₄, before treatment, after treatment in dry H₂ (10 vol% H₂, 90 vol% N₂, 1 h) and wet H₂ (10 vol% H₂, 1.4 vol% H₂O, 88.6 vol% N₂, 3 h) at 550 °C.

3.D2. Surface concentrations

Table 3.D1: Elemental surface concentrations, as obtained using XPS.

At.%	Freshly calcined	Exposed to dry H_2	Exposed to wet H_2
Pt/ZnAl$_2$O$_4$			
Zn 2p	22.2	22.7	20.8
O 1s	49.0	48.5	49.5
C 1s	3.0	1.2	1.2
Pt 4d	0.6	0.5	0.5
Al 2s	25.2	27.1	28.0
Pt-Sn/ZnAl$_2$O$_4$			
Zn 2p	20.4	21.2	19.0
O 1s	49.4	48.1	49.6
C 1s	2.6	1.5	1.6
Sn 3d	0.7	0.7	0.9
Pt 4d	1.2	0.8	0.7
Al 2s	25.7	27.6	28.3

3.E. Particle size distributions of Pt/ZnAl$_2$O$_4$ and Pt-Sn/ZnAl$_2$O$_4$

The particle size distributions of the dry and wet reduced Pt/ZnAl$_2$O$_4$ and Pt-Sn/ZnAl$_2$O$_4$ samples and the related samples tested in the ethane NODH reaction under dry and wet conditions were determined using *ex situ* STEM-HAADF (**Figure 3.E1**). Each distribution was created using 200-300 particles in total from 4-6 different STEM images.
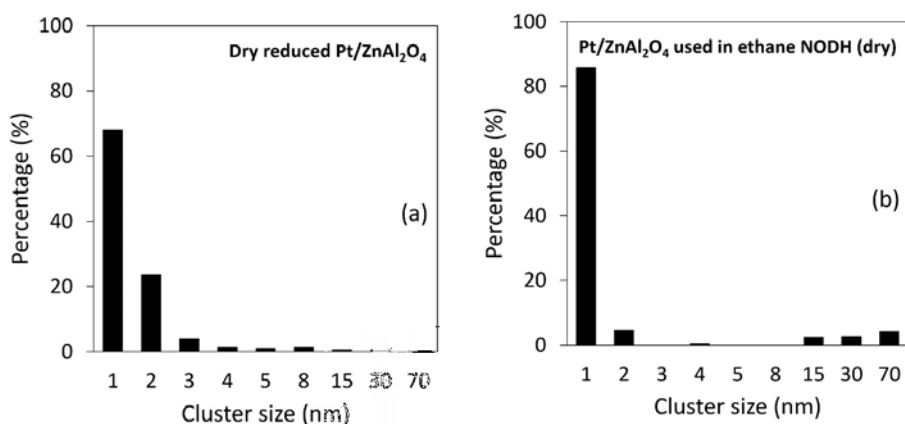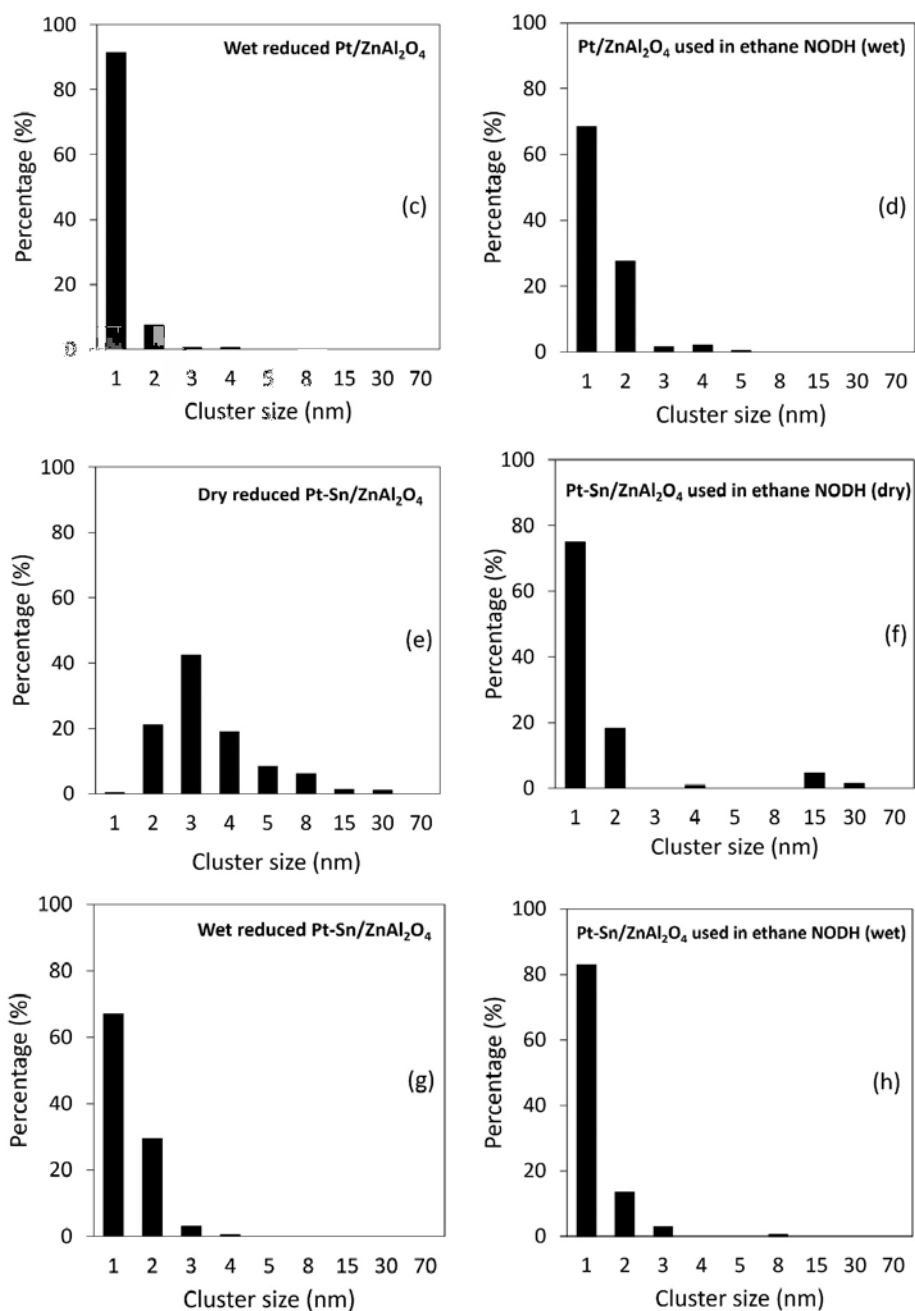
Figure 3.E1: Particle size distribution of (a-d) Pt/ZnAl$_2$O$_4$ and (e-h) Pt-Sn/ZnAl$_2$O$_4$, (a+e) reduced in dry H$_2$, (b+f) tested in ethane NODH under dry conditions, (c+g) reduced under wet H$_2$ conditions, and (d+h) tested in ethane NODH under wet conditions.

3.F. Kinetic isotope effect

In the kinetic isotope effect (*KIE*) investigation, the cosupplied H_2O was replaced by D_2O, and the *KIE* was defined as the ratio between the observed reaction rate in the presence of H_2O divided by the observed rate in the presence of D_2O. The results are shown in **Figure 3.F1** for Pt/ZnAl$_2$O$_4$ and Pt-Sn/ZnAl$_2$O$_4$ with varying temperature.
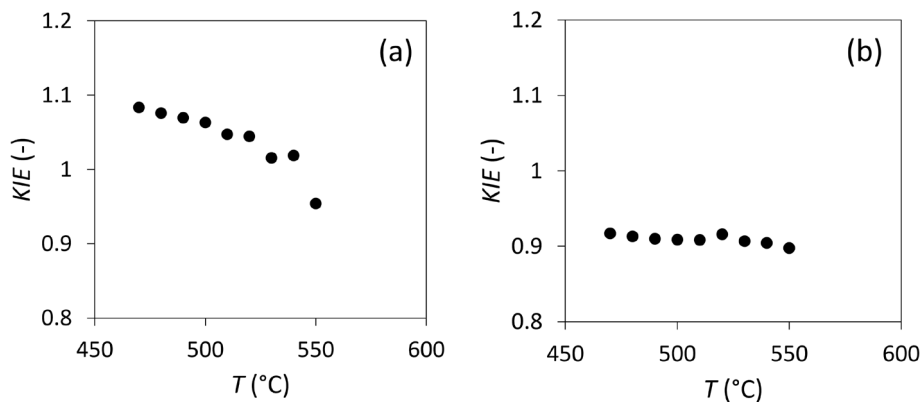
Figure 3.F1: Kinetic isotope effect (*KIE*) as a function of temperature for (a) Pt/ZnAl$_2$O$_4$ and (b) Pt-Sn/ZnAl$_2$O$_4$. Conditions: p_{ethane} = 39 mbar(a), p_{H2} = 103 mbar(a), p_{H2O} or p_{D2O} = 14 mbar(a).

3.G. Ethane reaction orders

The ethane reaction orders of the ethane NODH reaction on $Pt/ZnAl_2O_4$ and Pt-$Sn/ZnAl_2O_4$ under dry and wet conditions are presented in **Figure 3.G1**.
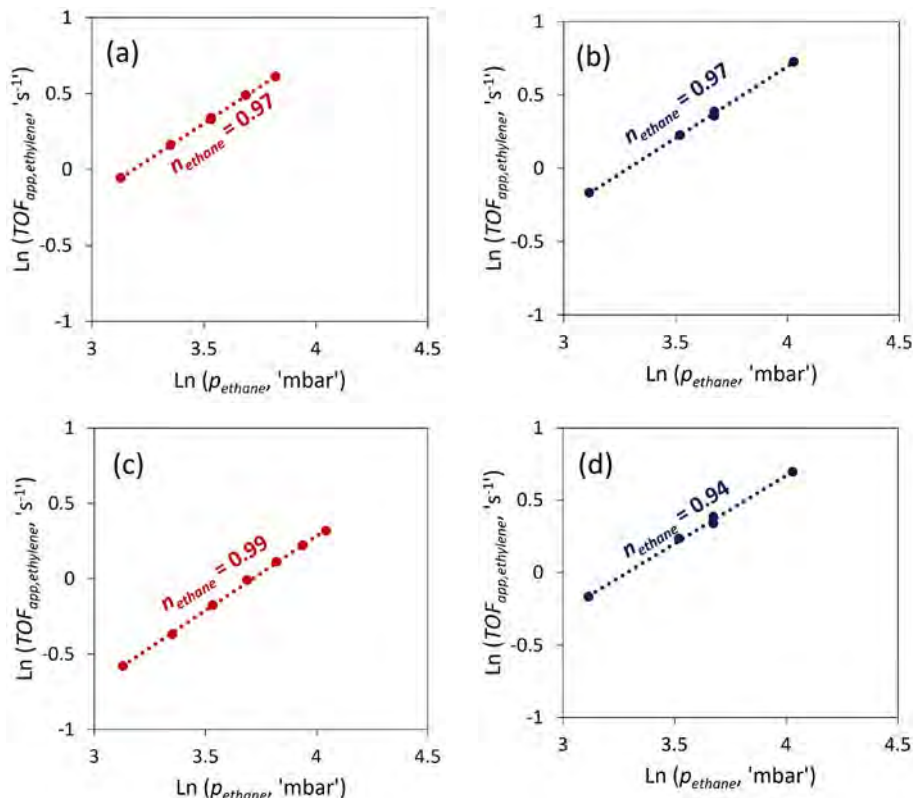
Figure 3.G1: Ethane reaction order in the ethane NODH reaction on $Pt/ZnAl_2O_4$ under (a) dry and (b) wet conditions, and on Pt-$Sn/ZnAl_2O_4$ under (c) dry and (d) wet conditions. Dry conditions: p_{ethane} = 20-50 mbar(a), p_{H2} = 105 mbar(a), T = 550 °C, wet conditions: p_{ethane} = 20-60 mbar(a), p_{H2} = 105 mbar(a), p_{H2O} = 15 mbar(a), T = 550 °C.

Chapter 4

Proton-conducting supports for Pt-catalyzed ethane dehydrogenation

Summary

Olefin formation via non-oxidative dehydrogenation of light alkanes is limited by thermodynamic equilibrium. A possible strategy to increase olefin yields in this reaction is by removing H_2 from the reaction zone using proton-conducting membranes to shift the equilibrium toward the olefin side. For efficient removal of the H_2, the dehydrogenation catalyst needs to be deposited directly onto the proton-conducting material. In this context, a Pt dehydrogenation catalyst was deposited onto typical proton conductor materials, such as lanthanum tungstate (LWO) and barium zirconium cerium yttrium (BZCY) oxide. The performance of Pt/LWO and Pt/BZCY was compared to a conventional $Pt/ZnAl_2O_4$ dehydrogenation catalyst in the non-oxidative dehydrogenation of ethane. The ethylene selectivity on Pt/LWO and Pt/BZCY was found to be much lower than for $Pt/ZnAl_2O_4$, at the cost of a higher methane selectivity. Methane formation is possibly boosted by C-C cleavage on Lewis acid sites of the LWO and BZCY supports. These acid sites originate from the presence of oxygen vacancies in LWO and BZCY. Additionally, Pt/LWO was found to deactivate rapidly in dry atmospheres, due to Pt sintering. This sintering, however, was suppressed when cofeeding steam. The Pt/BZCY system was comparably stable relative to Pt/LWO, which was attributed to relatively strong interactions between Pt and the Ba in the support, resulting in a lesser extent of Pt sintering in Pt/BZCY.

4.1. Introduction

Non-oxidative dehydrogenation (NODH) of ethane (**Equation 4.1**) is a highly endothermic reaction and strongly limited by thermodynamic equilibrium. Consequently, it is currently not an industrial attractive route to produce ethylene. By contrast, alkane NODH processes are already commercialized for decades using propane and butanes as feedstocks to produce propylene and isobutylene or butadiene [1]. The latter reactions suffer less from thermodynamic equilibrium limitations as ethane NODH, as ethane is a considerably more stable molecule than propane and butane.

$$C_2H_6 \leftrightharpoons C_2H_4 + H_2 \qquad (\Delta H_{298}^0 = +137.0 \text{ kJ/mol}) \qquad (4.1)$$
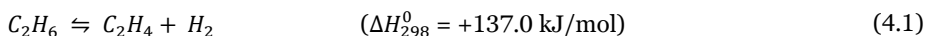
A platinum-based catalyst on a metal oxide support is often used in industrial propane and isobutane NODH processes, as platinum is highly active in converting alkanes [2]. Promoters like Cu, Ga [3], Ni, Mn, In, and Sn are commonly added to the Pt-based catalyst composition to further boost the olefin selectivity [4]. Furthermore, relatively basic spinel-type $MgAl_2O_4$ and $ZnAl_2O_4$ supports are generally more suitable for alkane NODH than traditional Al_2O_3 supports [5−7]. The reason for this is that the acid sites of Al_2O_3 typically enhance side reactions like alkane cracking and carbon deposition [2].

The focus in this dissertation is on the use of dense ceramic membranes for hydrogen removal to shift alkane NODH equilibria, like the ethane NODH equilibrium (**Equation 4.1**), toward the olefin side. Dense ceramic membranes for hydrogen permeation can be categorized into mixed proton-electron conducting (MPEC) and proton-conducting electrolysis cell (PCEC) membranes. In MPECs, protons and electrons are both transported through the metal oxide structure. On the contrary, only protons are transported through the metal oxide structure in PCECs, as the electrons are directed via an external circuit by applying a voltage. Hydrogen transport through MPEC membranes is fully driven by a gradient in H_2 chemical potential, which translates into a gradient in H_2 partial pressure under ideal gas conditions. By contrast, the driving force for hydrogen permeation through PCEC membranes is a gradient in H_2 electrochemical potential, i.e. a combination of a gradient in H_2 chemical potential and a gradient in electrostatic potential.

PCECs are commonly operated at high voltages, such that the electrostatic potential gradient dominates the driving force for hydrogen permeation. Under those conditions, hydrogen can be transported in a direction opposing the H_2 partial pressure gradient, which allows for generation of a purified and pressurized H_2 stream while performing the alkane NODH reaction. Besides, PCEC operation allows for electrification of chemical processes using renewable electricity (e.g. solar, wind). Moreover, resistive Joule heat is generated inside the PCEC membrane reactor, due to the electrical resistance across the PCEC membrane, which can be efficiently integrated with the endothermic alkane dehydrogenation reaction. The combination of (i) the shift in thermodynamic equilibrium toward olefins, (ii) the integration of reaction, *in situ* hydrogen removal, and hydrogen compression, and (iii) the possibility of green process electrification coupled with resistive

heating, marks the potential of membrane-assisted alkane NODH in the aim for reducing the energy usage and carbon footprint of alkane NODH processes.

The material requirements of MPEC and PCEC membranes are somewhat different. MPEC membrane materials need to possess a good ambipolar (proton and electron) conductivity. Molybdenum-substituted lanthanum tungstate (LWMO) has a high ambipolar conductivity in combination with a good stability in harsh conditions (CO_2, H_2S, various salts) and is therefore a suitable MPEC material [8–12]. In contrast to MPECs, suitable PCEC materials primarily need to possess a high proton conductivity. Barium zirconium cerium yttrium (BZCY) oxide-based systems are known for their outstanding proton conductivity properties in combination with good stability in hydrocarbon atmospheres [13,14]. BZCY-based electrolytes are therefore favorable PCEC materials.

In packed bed membrane reactors for hydrogen extraction, where packed bed catalyst particles are surrounded by a tubular membrane wall (**Figure 4.1a**), radial hydrogen diffusion can be limited by axial convective transport. To avoid possible limitations in the mass transport of hydrogen from the catalyst to the membrane, the Pt catalyst could be deposited directly onto the proton-conducting membrane. This can be accomplished in a catalyst-functionalized membrane reactor, based on an asymmetric membrane configuration (**Figure 4.1b**). In the latter system, a porous layer that provides the required mechanical stability is functionalized with the catalyst active phase, whilst a dense layer functions as the actual hydrogen separation layer. Herein, hydrogen removal occurs in the immediate vicinity of the alkane NODH reaction. Consequently, the hydrogen that is generated in the alkane NODH reaction does not necessarily have to desorb from and readsorb onto the membrane material, as it could possibly spillover from the catalyst active phase onto the contacting membrane.
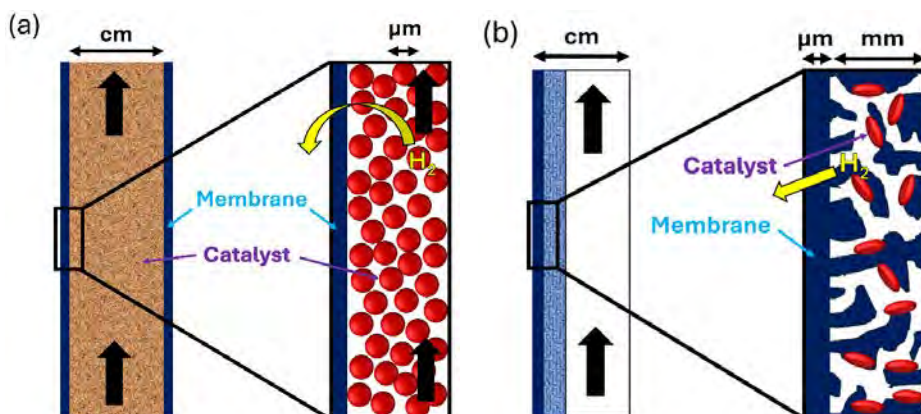
Figure 4.1: Schematic representation of (a) a packed bed membrane reactor, and (b) a catalyst-functionalized membrane reactor.

To our knowledge, the influence of using proton-conducting supports on the performance of Pt-based catalysts in the alkane NODH reaction has not been studied before. Here, we

therefore compared the performance of a traditional $Pt/ZnAl_2O_4$ dehydrogenation catalyst to the performance of a Pt-catalyst supported onto a suitable MPEC material (Pt/LWO) and a suitable PCEC material (Pt/BZCY) in the ethane NODH reaction.

4.2. Experimental

4.2.1. Materials and instrumentation

For the synthesis of the $ZnAl_2O_4$ support, zinc nitrate ($Zn(NO_3)_2 \cdot 6H_2O$, 98%, extra pure, Acros Organics) and aluminum nitrate ($Al(NO_3)_3 \cdot 9H_2O$, 99+%, Acros Organics) were used. Besides, ammonium hydroxide (25% NH_3 basis, Sigma-Aldrich) was used as precipitating agent in the $ZnAl_2O_4$ support synthesis. The lanthanum tungstate (LWO) support was synthesized using lanthanum nitrate hexahydrate ($La(NO_3)_3 \cdot 6H_2O$, 99.99%, Sigma-Aldrich) and ammonium tungstate ($(NH_4)_{10}H_2(W_2O_7)_6$ >99.99%, Sigma-Aldrich) precursors. Besides, ethylenediaminetetraacetic acid (EDTA, $(HOCCH_2)_2NCH_2CH_2N(CH_2CO_2H)_2$, ≥98.5%, Sigma-Aldrich) and citric acid ($HOC(COOH)(CH_2COOH)_2$, ≥99%, Sigma-Aldrich) were used as complexing agents in the LWO synthesis. Furthermore, ammonium hydroxide (NH_4OH, 28-30%, Sigma-Aldrich) and ammonium nitrate (NH_4NO_3, ≥99.5%, Sigma-Aldrich) were applied as pH adjusting agent and as fuel for auto-combustion in the LWO synthesis, respectively. Commercially available barium cerium yttrium zirconate ($BaZr_{0.7}Ce_{0.2}Y_{0.1}O_3$, >99%, CerPoTech) was used as BZCY support in this work [15]. Besides, chloroplatinic acid ($H_2PtCl_6 \cdot 6H_2O$, 99.95%, Alfa Aesar) was applied as catalyst precursor for functionalizing the three different support materials with Pt active phases. Lastly, the catalytic tests were conducted using ethane 2.5 (≥99.5%, Linde plc).

X-ray fluorescence (XRF) was applied using a Bruker s8 Tiger Series WDXRF spectrometer to check the elemental composition of the different supports and to quantify the Pt loading. The support compositions were determined using fused bead measurements, in which the fused beads were made in an xrFuse2 fusion machine from XRF Scientific. The fused beads were shaped by mixing the catalyst with a flux matrix compound (66% lithium tetraborate, 34% lithium metaborate, 0.2% lithium bromide) in a 1/8 catalyst/flux ratio. Besides, powder-based XRF measurements were applied to quantify the Pt loading in the different catalyst systems. X-ray diffraction (XRD) patterns were gathered of the non-functionalized and Pt-functionalized supports between 10º and 90º Bragg angles using a Bruker D2 PHASER XRD system. In this analysis, a total scanning time of 35 minutes was applied using a step size of one second per step.

Nitrogen physisorption was performed using a Micromeritics TriStar Surface Area and Porosity Analyzer, using a degassing temperature of 300 °C. Besides, CO chemisorption was conducted for all three catalysts using a Micromeritics ChemiSorb 2750 pulse chemisorption system. Prior to chemisorbing CO, the catalyst samples were reduced in a stream of H_2 at 400 °C for 1 h (heating rate: 10 °C/min).

Scanning transmission electron microscopy with high-angle annular dark-field (STEM-HAADF) imaging, combined with energy dispersive X-ray spectroscopy (EDS), was carried out to analyze the size and shape of the fresh and spent catalyst samples. A probe-corrected Titan from Thermo Fisher Scientific (300 kV), equipped with a high brightness X-FEG and a spherical aberration Cs-corrector (CEOS) for the condenser system to provide sub-Ångström probe size, was used for STEM-HAADF analysis. EDS mapping was performed using an Ultim Max detector system from Oxford Instruments. Prior to STEM-HAADF analysis, the catalyst samples were reduced *ex situ* in a stream of H_2 (10 ml/min STP) at 550 °C for 1 h (heating rate: 10 °C/min), cooled down in inert N_2, and temporarily exposed to ambient air upon transportation to the STEM-HAADF system.

We further employed ammonia (NH_3) temperature programmed desorption (TPD) using an AutoChem II 2920 instrument to quantify the relative number of surface acid sites of the different catalysts. Before performing the NH_3-TPD characterization, ca. 0.15 g of the sample was degassed in Ar for 30 minutes at 550 °C, followed by reduction in H_2 for 1 h at 550 °C. Then, the system was cooled to 50 °C and subsequently exposed to NH_3 for 30 minutes. Afterward, the temperature was raised to 700 °C in the presence of a He flow using a ramping rate of 10 °C/min. A thermal conductivity detector (TCD) was used to analyze the product stream.

4.2.2. Catalyst synthesis and activation

4.2.2.1. Support preparation

The $ZnAl_2O_4$ support was synthesized via known methods [7,16–21], based on coprecipitation of zinc nitrate and aluminum nitrate under dropwise addition of ammonium hydroxide, as described in detail in **Chapter 2**. Besides, the used BZCY support was commercially available [15]. The LWO support was synthesized using a modified Pechini method, which is a widely used method for the synthesis of LWO [18,22–24]. In this method, the two aqueous metal precursor solutions (lanthanum nitrate and ammonium tungstate) were prepared separately. The first solution contained 21.0 g of lanthanum nitrate hexahydrate, 14.2 g of EDTA, and 14.0 g of citric acid in 150 ml of demineralized water. The pH of this solution was adjusted to 8.5 at 80 °C by dropwise adding an ammonium hydroxide solution. The second solution contained 2.3 g of ammonium tungstate, 2.6 g of EDTA, and 2.6 g of citric acid in 100 ml of demineralized water. The pH of this second solution was adjusted to 9.5 at 80 °C by adding an ammonium hydroxide solution. The abovementioned masses and conditions give ca. 10 g of lanthanum tungstate with a La/W ratio of about 5.4. Once the precursors were fully dissolved, both precursor solutions were mixed and 56.2 g of ammonium nitrate was added as fuel for the auto-combustion. The pH of the resulting solution was adjusted to 9.5 using an ammonium hydroxide solution. Then, the solution was stirred at 80 °C until a gel was formed. This gel was then poured into a metal cylinder, which was heated to 300 °C to burn off all organic constituents. The resulting powder was then calcined at 1200 °C

for 12 h (heating rate: 3 °C/min). Afterward, the powder was ball milled in ethanol for ca. 24 h. The dried powder was then sintered at 1200 °C for 12 h (heating rate: 2 °C/min).

4.2.2.2. Support functionalization

The three different supports were functionalized with Pt active phases using wet impregnation. Herein, a platinic acid (H_2PtCl_6) precursor was dissolved in ethanol. The platinic acid concentration of this precursor solution was adjusted to the available specific surface area of the concerning support, aiming at equal Pt concentrations per m^2 of support surface. Each support was exposed to the platinic acid precursor solution for 30 minutes, before drying for 15 minutes at 60 °C under vacuum in a rotary evaporator. Subsequently, the resulting catalysts were calcined at 550 °C (heating rate: 2 °C/min) for 4 h in a stream of air. Then, the particles were mortared and sieved into particle sizes <50 µm, 50-125 µm, 125-250 µm, and >250 µm. Only the smallest fraction (<50 µm) was applied in the catalytic tests, as internal mass transfer limitations were excluded for this fraction (see **Chapter 2**). The catalysts were pre-activated in a stream of H_2 (10 ml/min STP) at 550 °C for 1 h before starting the catalyst performance tests.

4.2.3. Catalytic testing

A continuous flow fixed bed reactor was used for the catalytic tests (**Supporting Information 4.A**). The ethane feed flow was balanced with N_2, while a cofeed of H_2 was used to mitigate catalyst deactivation. Mass flow controllers (Brooks) were used to control the gas flow rates. The catalyst performance tests were carried out in the absence and in the presence of steam. The H_2O was supplied in liquid form using an ISCO 500D syringe pump and was evaporated in a preheating zone at 110 °C. This preheating zone consisted of a metal cylinder (*I.D.* = ca. 8 mm) filled with quartz wool to ensure pulse-free evaporation of the water. All catalysts were diluted with quartz particles (SiO_2, fine granular, Merck KGaA, 125-250 µm) to ensure isothermal operation of the packed bed. The dilution fraction (catalyst/diluent) differed per support material: 1/19 for Pt/$ZnAl_2O_4$, 1/6 for Pt/BZCY, and 1/1.2 for Pt/LWO. This difference was applied to ensure equal amounts of Pt inside the reactor to allow for a reliable performance comparison between the three different catalysts. The catalyst bed was mounted in between pieces of quartz wool inside a quartz reactor tube (*I.D.* = 4 mm, *O.D.* = 6 mm, *L* = 450 mm). A thermocouple positioned near the catalyst bed on the inner wall of a tubular furnace ensured good control over the reaction temperature. The product distribution was determined using an on-line gas chromatograph (GC, Varian Chrompack CP-3800), equipped with an Agilent GS-GasPro column (*L* = 60 m x *I.D.* = 0.32 mm) and a flame ionization detector (FID). Additional specifications of the GC system were: He carrier gas flow rate: 1.5 ml/min STP, sample injection temperature: 220 °C, temperature ramp GC column: 40-140 °C, FID temperature: 250 °C.

In case of dry reaction conditions, the ethane feed flow was started immediately after the catalyst pre-activation step. By contrast, in case of moistened reaction conditions the water

flow was started immediately after catalyst activation, while maintaining a continuous N_2 flow. The system was then allowed to stabilize for about 15 minutes to ensure moistened conditions throughout the setup before starting the experiment. Subsequently, the ethane flow was started and possible H_2 and ethylene cofeed flows were specified. When operating under moistened atmospheres, the line between the reactor outlet and the GC-FID inlet was continuously heated to 120 °C to avoid possible steam condensation.

The catalyst performance tests were conducted at atmospheric pressure and at a temperature of 550 °C. The ethane conversion (χ_{eth}), and selectivity (S_i) and yield (Y_i) toward product i were calculated using **Equation 4.2-4.4**.

$$\chi_{eth} = 1 - \frac{p_{eth}}{p_{eth,0}} \tag{4.2}$$

$$S_i = \frac{p_i}{p_{eth,0} - p_{eth}} \tag{4.3}$$

$$Y_i = \frac{p_i}{p_{eth,0}} \tag{4.4}$$

In which $p_{eth,0}$ and p_{eth} represent the ethane partial pressure in the reactor feed and effluent, respectively, as determined using a GC calibration curve for ethane. The products detected with the GC-FID were ethylene and methane. The ethylene partial pressure ($p_{i=ethylene}$) was quantified using a GC calibration curve for ethylene, whilst the methane partial pressure ($p_{i=methane}$) was determined using the ethane calibration curve corrected with an FID response factor of 1.25 for methane relative to ethane [25]. Note that the total gas flow rate was considered constant along the reactor length, as the ethane concentration in most tests was below 4 vol% and the ethane conversion was below 15%.

Similar to **Chapter 2** and **3**, the relation between the experimentally obtained ethylene yield (Y_{C2H4}), the mass-based ethylene formation rate ($R_{m,C2H4}$, in molC2H4/kgcat•s), and the apparent turnover frequency of ethylene formation ($TOF_{app,C2H4}$, in molC2H4/molPt,s•s) is given by:

$$R_{m,C2H4} = \frac{F_{C2H6,0}Y_{C2H4}}{m_{cat}} = \frac{TOF_{app,C2H4}\sigma_{Pt}\beta_{Pt}}{M_{W,Pt}} \tag{4.5}$$

Where $F_{C2H6,0}$ indicates the molar flow rate of ethane in the feed (in mol/s), m_{cat} the mass of catalyst in the bed (in kgcat), σ_{Pt} the Pt loading of the catalyst (in kgPt/kgcat), β_{Pt} the Pt dispersion (in molPt,s/molPt), as determined using CO chemisorption, and $M_{W,Pt}$ the molar weight of Pt (in kgPt/molPt). Furthermore, in the unit of $TOF_{app,C2H4}$, molPt,s indicates the number of moles of Pt exposed to the surface.

4.3. Results and discussion

4.3.1. Characterization results – fresh catalysts

The bare support materials and the functionalized catalysts were characterized to examine the porosity and crystallinity of the supports and to determine the concentration of active sites (**Table 4.1**). The XRD spectra of the synthesized $ZnAl_2O_4$ and LWO supports showed the characteristic $ZnAl_2O_4$ spinel and cubic single phase LWO peaks, respectively (**Supporting Information 4.B**). Besides, the commercial BZCY support contained the crystalline phase that characterizes the proton-conducting $BaZr_{0.7}Ce_{0.2}Y_{0.1}$ phase. From this analysis it can be concluded that the bare support materials satisfied the targeted phase structures. Additionally, the specific surface area of the $ZnAl_2O_4$ support (**Table 4.1**) was in line with other $ZnAl_2O_4$ supports synthesized via coprecipitation methods, as reported in literature [7,20,21,26]. Besides, the specific surface area of the LWO and BZCY materials, which are conventionally applied as dense ceramic membrane materials, were significantly lower than the $ZnAl_2O_4$ surface area (**Table 4.1**). The Pt loadings were adjusted accordingly with the specific surface areas to obtain similar Pt cluster sizes for all three catalysts (**Table 4.1**). The Pt cluster size resulting from STEM-HAADF analysis, as reported in **Table 4.1**, differed from the CO chemisorption result for all three catalysts. This is attributed to the existence of a limited number of large particles (>10 nm, see **Chapter 2**) that are insignificantly captured by the number-based average particle size as determined using STEM-HAADF.

Table 4.1: Properties of the fresh support materials and Pt-functionalized catalysts.

Characteristic:	$ZnAl_2O_4$	$Pt/ZnAl_2O_4$	LWO	Pt/LWO	BZCY	Pt/BZCY
BET area (m^2/g)	76.3	71.3	5.5	5.5	21.8	21.1
Pt loading (wt.%)	-	3.6	-	0.4	-	1.3
Pt cluster size (nm)[1]	-	9.4	-	8.3	-	9.6
Pt cluster size (nm)[2]	-	1.6	-	1.2	-	1.9

LWO = lanthanum tungstate, BZCY = barium cerium yttrium zirconate, [1]Pt cluster size as determined using CO chemisorption, [2]Pt cluster size as determined using STEM-HAADF using a minimum of 100 particles from at least four representative images.

4.3.2. Catalytic testing results

Internal mass transfer limitations were excluded in dry ethane NODH conditions for Pt-Sn/$ZnAl_2O_4$ catalyst particles smaller than 45 μm (see **Chapter 2**). Internal mass transfer limitations are less likely to play a role for LWO and BZCY, since the $ZnAl_2O_4$ support is substantially more porous than LWO and BZCY (see **Table 4.1**). Besides, external mass transfer limitations were excluded and operation in a differential regime was ensured for catalyst-to-feed ratios (*W/F*$_{ethane}$) below 100 kg$_{cat}$•s/kg$_{ethane}$ under dry ethane NODH

conditions (see **Chapter 2**). Isothermal operation of the packed bed was guaranteed by diluting the Pt-Sn/ZnAl$_2$O$_4$ catalyst with inert quartz bed diluent particles. The used dilution fraction for the Pt/ZnAl$_2$O$_4$ catalyst of 0.95 (i.e. 5 wt.% of catalyst and 95 wt.% of bed diluent) suffices to avoid channeling through the bed, according to a relation on the influence of bed dilution on the conversion level of packed bed systems, as developed by Berger et al. [27] (see **Chapter 2** for more details). The dilution fractions of the Pt/LWO (catalyst/diluent = 1/1.2) and Pt/BZCY (catalyst/diluent = 1/6) systems were significantly less extreme compared to the Pt/ZnAl$_2$O$_4$ packed bed (catalyst/diluent = 1/19). The influence of bed dilution on the conversion level can therefore also be ignored for the Pt/LWO and Pt/BZCY packed beds.

The catalytic performance of Pt/ZnAl$_2$O$_4$, Pt/LWO, and Pt/BZCY in the ethane NODH reaction was compared for similar Pt cluster sizes (see **Table 4.1**) and equal amounts of Pt in the packed bed (ca. 0.2 mg of Pt). The use of equal Pt amounts for the different support materials was accomplished by using different catalyst bed dilution fractions (catalyst/diluent) for each support material: 1/19 for Pt/ZnAl$_2$O$_4$, 1/6 for Pt/BZCY, and 1/1.2 for Pt/LWO. The only byproduct detected with the GC-FID was methane. The apparent turnover frequency of ethylene formation and methane formation on the three different types of catalysts are compared to each other in **Figure 4.2**. The ethane conversion under dry conditions in all these tests was between 3-7%, while the ethane conversion in wet conditions was between 3-7% for Pt/LWO and Pt/BZCY and around 10% for Pt/ZnAl$_2$O$_4$.

The traditional Pt/ZnAl$_2$O$_4$ dehydrogenation catalyst was highly active and stable in the formation of ethylene in dry and wet conditions (**Figure 4.2a**). As demonstrated in **Chapter 3**, ethylene formation is boosted on Pt/ZnAl$_2$O$_4$ in wet conditions, as the steam supposedly enhances product desorption. Besides, the formation of methane was found to be negligible in dry atmospheres (**Figure 4.2b**). On the contrary, methane formation on Pt/ZnAl$_2$O$_4$ was observed under moistened conditions but the concerning methane formation sites deactivated quickly over time. Ultimately, the ethylene selectivity was consistently above 95% on Pt/ZnAl$_2$O$_4$ in dry as well as in wet conditions.
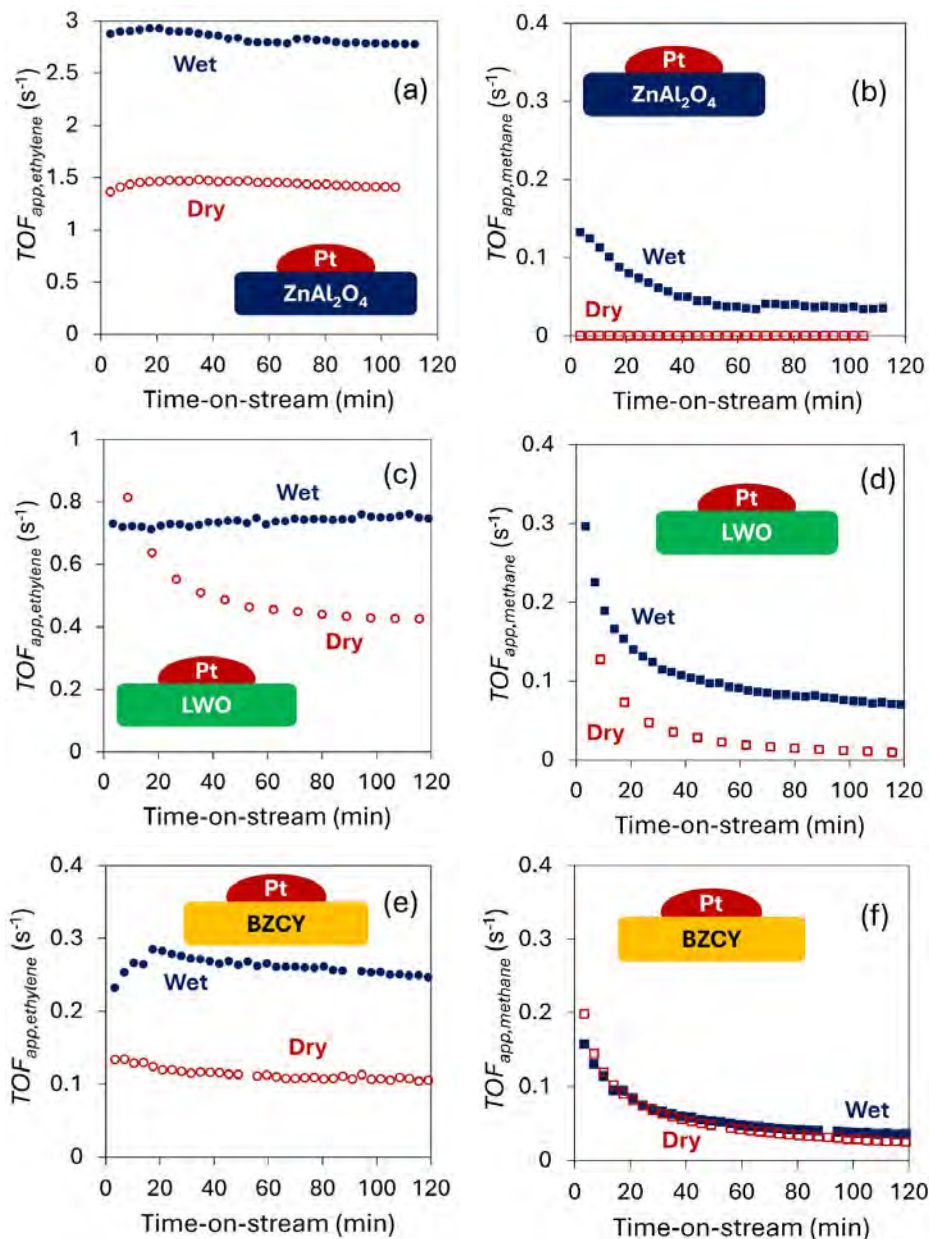
Figure 4.2: Apparent turnover frequency of ethylene and methane formation in dry and wet conditions at 550 °C of (a-b) Pt/ZnAl$_2$O$_4$, (c-d) Pt/LWO, and (e-f) Pt/BZCY. Dry conditions: p_{ethane} = 34 mbar(a), p_{H2} = 104 mbar(a). Wet conditions: p_{ethane} = 40 mbar(a), p_{H2} = 104 mbar(a), p_{H2O} = 14 mbar(a). Amount of Pt in bed: 0.2 mg. The ethane conversion in dry conditions was between 3-7%, while the ethane conversion in wet conditions was between 3-7% for Pt/LWO and Pt/BZCY and around 10% for Pt/ZnAl$_2$O$_4$.

Compared to $Pt/ZnAl_2O_4$, the Pt/LWO catalyst was considerably less active in the formation of ethylene, and significantly more active in the formation of methane in dry and wet conditions (**Figure 4.2c** and **4.2d**). Consequently, the ethylene selectivity was much lower for Pt/LWO relative to $Pt/ZnAl_2O_4$ in dry (ca. 90% vs. >99%) and moistened atmospheres (70-90% vs. 95-99%). Interestingly, the ethylene formation sites of Pt/LWO rapidly deactivated in dry atmospheres, whilst a stable ethylene formation rate was attained when cosupplying steam (**Figure 4.2c**). At the same time, the methane formation sites deactivated under dry as well as under wet atmospheres (**Figure 4.2d**). Moreover, methane formation was enhanced in the presence of steam, while the decay in methane formation over time was comparable for dry and wet conditions (**Figure 4.2d**).

Relative to $Pt/ZnAl_2O_4$ and Pt/LWO, the intrinsic activity for the formation of ethylene was more limited for Pt/BZCY (**Figure 4.2e**). Similar to $Pt/ZnAl_2O_4$, the ethylene formation was enhanced in wet conditions (**Figure 4.2e**), which can possibly be attributed to an analogous enhancement in product desorption induced by the steam. Furthermore, the Pt/BZCY catalyst was comparably stable in the formation of ethylene under dry conditions relative to Pt/LWO (**Figure 4.2c** and **4.2e**). Compared to the performance of $Pt/ZnAl_2O_4$ and Pt/LWO, substantial amounts of methane were formed when using the Pt/BZCY catalyst. Consequently, the ethylene selectivity was the lowest of the three catalysts for Pt/BZCY in dry (35-75%) as well as in wet atmospheres (65-85%). Nevertheless, it should be noted that the methane formation sites on Pt/BZCY deactivate faster than the ethylene formation sites, implying that the ethylene selectivity on Pt/BZCY increases with time-on-stream.

4.3.3.   Characterization results – spent and treated catalysts

Scanning transmission electron microscopy with high-angle annular dark-field (STEM-HAADF) imaging was used to investigate possible changes in Pt cluster size after exposing the three different catalysts to dry and moistened ethane NODH conditions (**Figure 4.3** and **4.4**). The fresh $Pt/ZnAl_2O_4$ catalyst contained mainly small Pt clusters with an average size of ca. 1.6 nm (**Figure 4.3a**). Notably, part of the Pt clusters in $Pt/ZnAl_2O_4$ sintered to large Pt ensembles (>5 nm), whilst another fraction of the Pt clusters was more dispersed, after testing in dry ethane NODH conditions (**Figure 4.3b** vs. **4.3a**). This Pt sintering was suppressed when exposing the $Pt/ZnAl_2O_4$ catalyst to moistened ethane NODH conditions (**Figure 4.3c** vs. **4.3b**).

The Pt was well dispersed in the fresh Pt/LWO sample (**Figure 4.3d**), possibly due to the low Pt loading in Pt/LWO (**Table 4.1**). However, the Pt in Pt/LWO consistently sintered from ensembles in the range 1-2 nm to ensembles in the range 2-10 nm during testing in dry ethane NODH conditions (**Figure 4.3e** vs. **4.3d**). The Pt appeared to agglomerate particularly along the LWO grain boundaries (**Figure 4.3e** and **4.3f**). Similar to $Pt/ZnAl_2O_4$, cofeeding steam while performing the ethane NODH reaction mitigated the extent of Pt sintering (**Figure 4.3f** vs. **4.3e**).

Pt/ZnAl$_2$O$_4$ fresh

Pt/ZnAl$_2$O$_4$ dry EDH

Pt/ZnAl$_2$O$_4$ wet EDH

Pt/LWO fresh

Pt/LWO dry EDH

Pt/LWO wet EDH
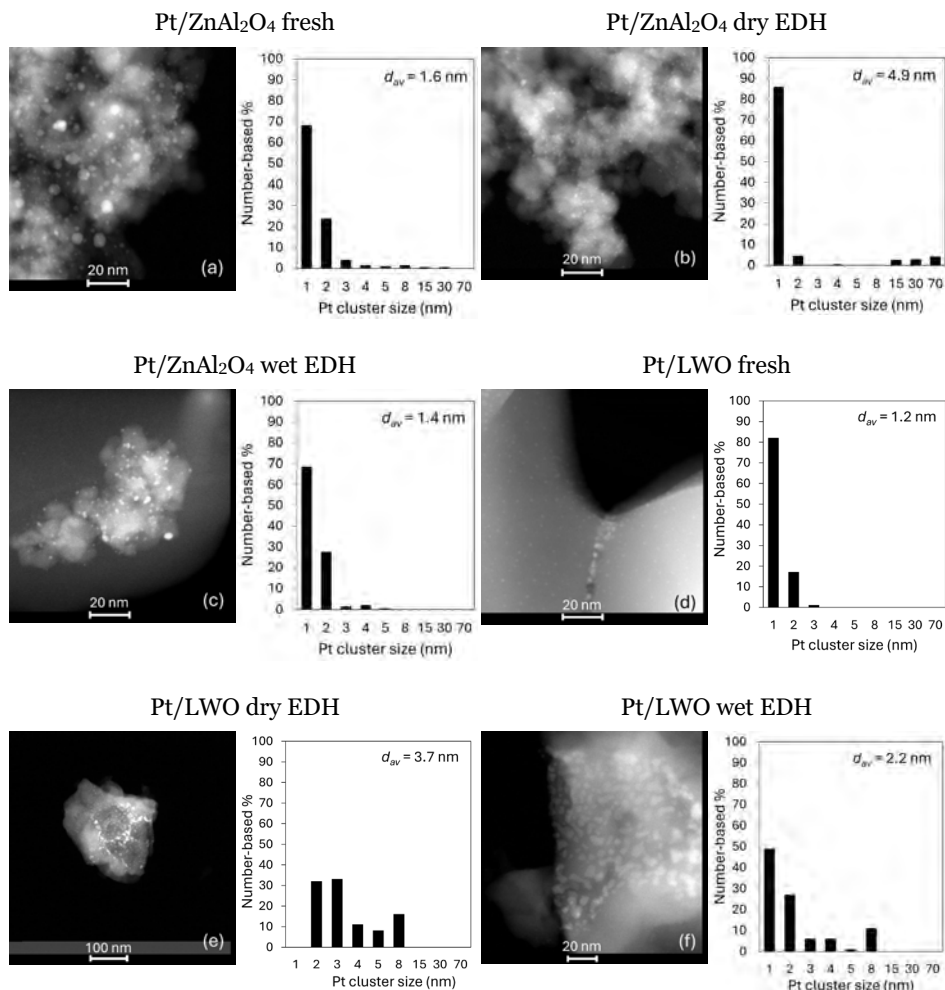
Figure 4.3: Representative STEM-HAADF images and corresponding number-based particle size distributions of (a-c) Pt/ZnAl$_2$O$_4$, and (d-f) Pt/LWO. The fresh samples were reduced in a stream of H$_2$ (10 ml/min STP) at 550 °C for 1 h, the dry EDH samples were exposed to dry non-oxidative ethane dehydrogenation (EDH) conditions at 550 °C for 6 h (p_{ethane} = 34 mbar(a), p_{H2} = 104 mbar(a)), whilst the wet EDH samples were exposed to EDH conditions in the presence of steam at 550 °C for 6 h (p_{ethane} = 40 mbar(a), p_{H2} = 104 mbar(a), p_{H2O} = 14 mbar(a)). The number-based particle size distributions were obtained by including >100 particles from 4-5 representative STEM-HAADF images.

Relative to fresh Pt/ZnAl$_2$O$_4$ and Pt/LWO, the Pt ensembles in fresh Pt/BZCY were somewhat larger with an average size of about 1.9 nm (**Figure 4.4a**). Notably, the Pt cluster size of Pt/BZCY did not significantly change upon exposure to dry and wet EDH conditions (**Figure 4.4a** to **4.4c**). This thereby indicates that Pt sintering occurred to a

lesser extent in Pt/BZCY as compared to Pt/ZnAl$_2$O$_4$ and Pt/LWO when applying it in the ethane NODH reaction under dry and wet conditions. In contrast to Pt/ZnAl$_2$O$_4$ and Pt/LWO, cofeeding steam did not significantly affect the Pt cluster size distribution in Pt/BZCY (**Figure 4.4c** vs. **4.4b**).

Pt/BZCY fresh

Pt/BZCY dry EDH

Pt/BZCY wet EDH
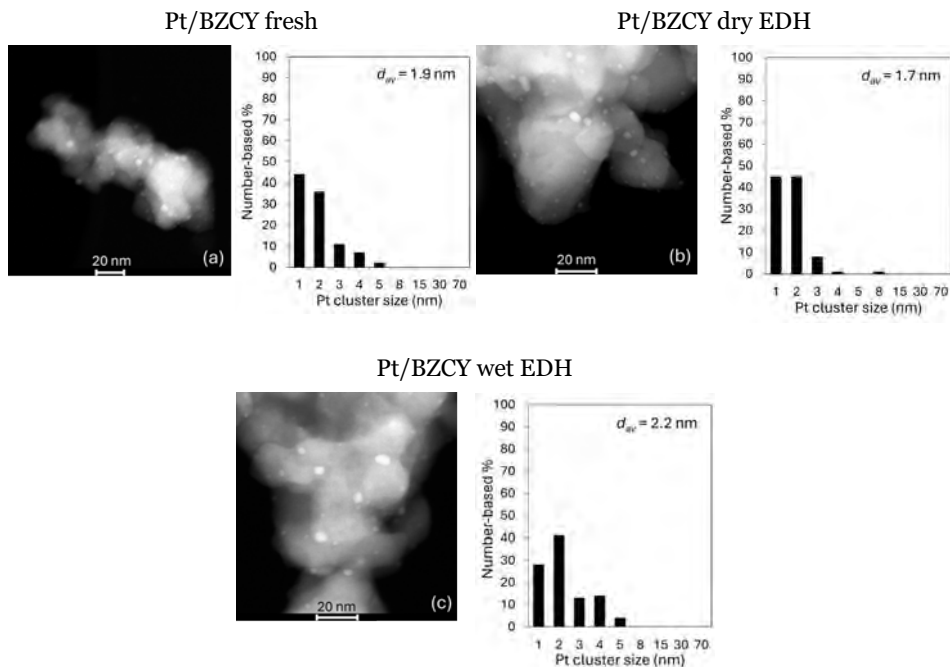
Figure 4.4: Representative STEM-HAADF images and corresponding number-based particle size distributions of (a) Pt/BZCY reduced in a stream of H$_2$ (10 ml/min STP) at 550 °C for 1 h, (b) Pt/BZCY exposed to dry non-oxidative ethane dehydrogenation (EDH) conditions at 550 °C for 6 h (p_{ethane} = 34 mbar(a), p_{H2} = 104 mbar(a)), and (c) Pt/BZCY exposed to wet reducing conditions at 550 °C for 6 h (p_{ethane} = 40 mbar(a), p_{H2} = 104 mbar(a), p_{H2O} = 14 mbar(a)). The number-based particle size distributions were obtained by including >100 particles from 4-5 representative STEM-HAADF images.

The relative number of acid sites of the three different catalysts was quantified using NH$_3$ temperature programmed desorption (TPD, **Figure 4.5**). In this analysis, the relative intensities of the NH$_3$-TPD spectra of the three different catalysts were normalized to their respective specific surface areas and multiplied with different factors to better visualize the peak locations (**Figure 4.5**). The Pt/LWO catalyst surface was considerably more acidic than the surface of Pt/ZnAl$_2$O$_4$ and Pt/BZCY, as indicated by the significantly higher amount of NH$_3$ desorbed per square meter of available surface area. In particular, the conventional Pt/ZnAl$_2$O$_4$ dehydrogenation catalyst had only a limited number of surface acid sites in the typical temperature range for alkane dehydrogenation (500-700 °C) as compared to Pt/LWO and Pt/BZCY.

Four significant NH_3-TPD peaks were discerned in **Figure 4.5**, corresponding to desorption temperatures of about 90 °C, 300 °C, 320 °C, and 450 °C, respectively. The peak at a desorption temperature around 90 °C was considerable for Pt/ZnAl$_2$O$_4$ and Pt/BZCY and existent to a more marginal extent for Pt/LWO. This peak is attributed to NH_3 chemisorbed on weak acid sites [28], possibly related to hydroxylated Brønsted acid sites [29,30]. The NH_3-TPD spectrum of Pt/LWO contained an additional peak around 300 °C (**Figure 4.5**). Oxygen vacancies are known to be created in LWO in the temperature range between 200 to 600 °C [31]. Prior to catalytic testing the catalysts were reduced at 550 °C for 1 h, which means that it is reasonable to assume that the Pt/LWO used in these catalytic tests contained oxygen vacancies. The cations in LWO will be shielded less when neighboring oxygens are missing, leading to the generation of Lewis acid sites in Pt/LWO. The presence of Lewis acid sites could thereby explain the appearance of a wide NH_3-TPD peak around 300 °C for Pt/LWO. For similar reasons, the NH_3-TPD peak around 320 °C in the Pt/BZCY spectrum can be ascribed to Lewis acid sites formed upon the generation of oxygen vacancies, as oxygen vacancies are known to be created in barium zirconium yttrium oxides between 200-400 °C [32]. The NH_3 desorption peak around 450 °C for Pt/BZCY is likely to be attributable to the formation of oxygen vacancies as well.
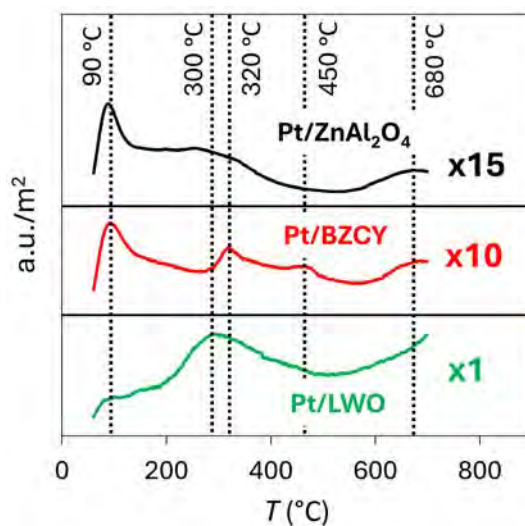
Figure 4.5: NH_3 temperature programmed desorption spectrum of Pt/LWO, Pt/BZCY, and Pt/ZnAl$_2$O$_4$. The desorption intensities were normalized per square meter of available support surface area and the relative intensities of Pt/BZCY and Pt/ZnAl$_2$O$_4$ were multiplied with a factor of 10 and 15, respectively, to better visualize the peak locations.

4.3.4.   Discussion

The traditional Pt/ZnAl$_2$O$_4$ dehydrogenation catalyst was active, selective, and stable in the ethane NODH reaction (**Figure 4.2a** and **4.2b**). By contrast, the Pt/LWO and

Pt/BZCY catalysts showed a worse activity, stability, and/or ethylene selectivity (**Figure 4.2c-4.2f**). The Pt/LWO and Pt/BZCY catalysts were both more active in the formation of methane and considerably less active in the formation of ethylene as compared to Pt/ZnAl$_2$O$_4$ (**Figure 4.2**). The ethylene selectivity was, therefore, significantly lower on Pt/LWO (dry: ca. 90 %, wet: 70-90%) and Pt/BZCY (dry: 35-75%, wet: 65-85%) relative to Pt/ZnAl$_2$O$_4$ (dry: >99%, wet: 95-99%). The higher methane selectivity for Pt/LWO and Pt/BZCY can be attributed to the presence of Lewis acid sites (**Figure 4.5**). The LWO [33] and BZCY [34] supports contain oxygen vacancies under reductive atmospheres. Consequently, the cations in LWO and BZCY are less shielded due to missing neighboring oxygens, leading to the generation of Lewis acid sites in Pt/LWO and Pt/BZCY. Surface acid sites are known to cleave C-C bonds [2], thereby enhancing methane formation. This reasoning suggests the existence of two distinct active sites, namely Pt-based ethylene formation sites and methane producing Lewis acid sites in Pt/LWO and Pt/BZCY.

Figure 4.2d showed that cofeeding steam boosts methane formation on Pt/LWO. Possibly, Brønsted acid sites are generated on Pt/LWO in presence of steam, which further increases methane formation. Besides, the methane and ethylene formation sites of Pt/LWO both deactivated in dry conditions (**Figure 4.2c** and **4.2d**). For ethylene formation, this could be attributed to Pt sintering in dry conditions, as indicated by the STEM-HAADF results in **Figure 4.3d-e**. It is suggested that the Pt did not sinter further after a certain extent of Pt sintering, leading to a new stable ethylene formation rate with time-on-stream (**Figure 4.2c**). Remarkably, the ethylene formation rate was stabilized in moistened atmospheres (**Figure 4.2c**). Steam therefore suppressed Pt sintering in Pt/LWO, as confirmed by the STEM-HAADF results in **Figure 4.3e-f**. Mild oxidizing conditions can ensure Pt redispersion in supported Pt catalysts [1]. It cannot be ruled out that carbon deposition played a role in the catalyst deactivation as well, although this was not quantified. Possibly, the methane formation sites in Pt/LWO deactivated (**Figure 4.2d**) due to the occurrence of carbon deposition on the Lewis acid centers.

The ethylene formation rate on Pt/BZCY was comparably stable in dry conditions relative to Pt/LWO (**Figure 4.2e** vs. **4.2c**). This difference is likely to be associated with the lower extent of Pt sintering in Pt/BZCY in dry atmospheres (**Figure 4.4a-b**) relative to Pt/LWO (**Figure 4.3d-e**). It is postulated that Pt sinters to a lesser extent on BZCY than on LWO, due to relatively strong interactions of the Pt with Ba in the BZCY support. Besides, the decay in activity of methane formation over time on Pt/BZCY (**Figure 4.2f**) is possibly attributable to acid-catalyzed carbon deposition, similar to Pt/LWO.

4.3.5.   Perspective

The results in this chapter indicated that the ethylene selectivity on Pt/LWO and Pt/BZCY was considerably worse as compared to Pt/ZnAl$_2$O$_4$. This was attributed to the existence of Lewis acid sites in Pt/LWO and Pt/BZCY, related to the generation of oxygen vacancies in these catalysts in reductive atmospheres. These acid sites located on the surface of the LWO and BZCY supports catalyze C-C cleavage and thereby boost methane formation.

Additionally, the stability of Pt/LWO and Pt/BZCY was worse than that of Pt/ZnAl$_2$O$_4$, due to Pt sintering. The limited stability and ethylene selectivity of Pt/LWO and Pt/BZCY represent major challenges for applications of the catalyst-functionalized membrane configuration. If the stability and ethylene selectivity of these catalyst-functionalized membrane materials cannot be improved, then the traditional packed bed membrane reactor designs, equipped with conventional alumina-supported Pt catalysts, are recommended for membrane-assisted light alkane NODH.

Several characterization methods are suggested to further investigate the experimental trends observed in this work. First of all, thermogravimetric analysis (TGA) of intensively spent catalysts would allow for identification of possible carbon deposition in the three different catalysts. In this work, the Pt/ZnAl$_2$O$_4$, Pt/LWO, and Pt/BZCY catalysts were all diluted with quartz bed diluent particles, which complicated quantification of coke deposits. Applying packed beds containing only catalyst particles in the ethane NODH reaction for several days, followed by TGA analysis, would help in understanding the role of possible carbon formation on the stability of the catalysts. Additionally, performing X-ray photoelectron spectroscopy (XPS) could provide insights in the generation of oxygen vacancies in the three different supports in dry and wet atmospheres. The creation of oxygen vacancies in reductive atmospheres is expected to lower the oxidation states of the cations. Quantification of cation valence state variations using XPS can therefore help in monitoring oxygen vacancy creation. Lastly, characterization of the spent catalysts using CO chemisorption would provide further information on possible Pt sintering.

4.4. Conclusion

The influence of using proton-conducting supports on the performance of Pt catalysts in the non-oxidative dehydrogenation of ethane was investigated in this chapter. To this end, the performance of a traditional Pt/ZnAl$_2$O$_4$ dehydrogenation catalyst was compared to systems in which Pt was deposited onto the promising mixed proton-electron conducting (MPEC) material lanthanum tungstate (LWO) and onto the promising proton-conducting electrolysis cell (PCEC) material barium zirconium cerium yttrium (BZCY) oxide. The ethylene selectivity on Pt/LWO and Pt/BZCY was substantially lower as compared to Pt/ZnAl$_2$O$_4$ in dry and wet conditions, due to enhanced methane formation on Pt/LWO and Pt/BZCY. This difference was attributed to the more acidic nature of LWO and BZCY supports. The latter supports contain intrinsic oxygen vacancies, which cause the existence of Lewis acid sites in these structures that can accelerate C-C cleavage, resulting in a higher methane selectivity relative to Pt/ZnAl$_2$O$_4$. Besides, the activity of ethylene formation on Pt/LWO decayed rapidly over time in dry atmospheres, due to Pt sintering. This sintering appeared to be suppressed in presence of steam. Pt sintered to a lesser extent on BZCY as compared to LWO, possibly due to stronger interactions of the Pt with the Ba in BZCY. As a result, ethylene formation was comparably stable on Pt/BZCY relative to Pt/LWO.

References

1.   Nawaz, Z. Light alkane dehydrogenation to light olefin technologies: A comprehensive review. *Rev. Chem. Eng.* **31**, 413–436 (2015).

2.   Sattler, J. J. H. B., Ruiz-Martinez, J., Santillan-Jimenez, E. & Weckhuysen, B. M. Catalytic dehydrogenation of light alkanes on metals and metal oxides. *Chem. Rev.* **114**, 10613–10653 (2014).

3.   Jablonski, E. L., Castro, A. A., Scelza, O. A. & Miguel, S. R. De. Effect of Ga addition to Pt/Al2O3 on the activity, selectivity and deactivation in the propane dehydrogenation. *Appl. Catal. A: Gen.* **183**, 189–198 (1999).

4.   Sun, M., Zhai, S., Weng, C., Wang, H. & Yuan, Z. Y. Pt-based catalysts for direct propane dehydrogenation: Mechanisms revelation, advanced design, and challenges. *Mol. Catal.* **558**, 114029 (2024).

5.   Pakhomov, N. A., Buyanov, R. A., Moroz, E. M., Kotelnikov, G. R. & Patanov, V. A. Medium Effect in Thermal Pretreatment on the State and Catalytic Properties of Platinum Supported on Zinc-aluminium Spinel. *React. Kinet. Catal. Lett.* **9**, 257–263 (1978).

6.   Lai, Y., He, S., Li, X., Sun, C. & Seshan, K. Dehydrogenation of n-dodecane over PtSn/MgAlO catalysts: Investigating the catalyst performance while monitoring the products. *Appl. Catal. A: Gen.* **469**, 74–80 (2014).

7.   Aguilar-rios, G., Valenzuela, M. A., Salas, P., Armendariz, H., Bosch, P., Del Toro, G., Silva, R., Bertín, V., Castillo, S., Ramírez-Solís, A. & Schifter, I. Hydrogen interactions and catalytic properties of platinum-tin supported on zinc aluminate. *Appl. Catal. A: Gen.* **127**, 65–75 (1995).

8.   Chen, Y., Cheng, S., Chen, L., Wei, Y., Ashman, P. J. & Wang, H. Niobium and molybdenum co-doped La5.5WO11.25-d membrane with improved hydrogen permeability. *J. Membr. Sci.* **510**, 155–163 (2016).

9.   Magrasó, A. & Haugsrud, R. Effects of the La/W ratio and doping on the structure, defect structure, stability and functional properties of proton-conducting lanthanum tungstate La28-xW4+xO54+δ. A review. *J. Mater. Chem. A* **2**, 12630–12641 (2014).

10.   Amsif, M., Magrasó, A., Marrero-López, D., Ruiz-Morales, J. C., Canales-Vázquez, J. & Núñez, P. Mo-substituted lanthanum tungstate La28-yW4+yO54+δ: A competitive mixed electron-proton conductor for gas separation membrane applications. *Chem. Mat.* **24**, 3868–3877 (2012).

11.   Vøllestad, E., Vigen, C. K., Magrasó, A. & Haugsrud, R. Hydrogen permeation characteristics of La27Mo1.5W3.5O55.5. *J. Membr. Sci.* **461**, 81–88 (2014).

12.   Cao, Y., Xiong, C., Jian, L., Vøllestad, E., Evans, A. & Haugsrud, R. Enhancement of the electron conductivity of La27(W0.85Nb0.15)5O55.5−δ by Mo doping for hydrogen permeation. *J. Electrochem. Soc.* **163**, F1151–F1156 (2016).

13.   Malerød-fjeld, H., Clark, D., Yuste-tirados, I., Zanón, R., Catalán-martinez, D., Beeaff, D., Morejudo, S. H., Vestre, P. K., Norby, T., Haugsrud, R., Serra, J. M. & Kjølseth, C. Thermo-electrochemical production of compressed hydrogen from methane with near-zero energy loss. *Nat. Energy* **2**, 923–931 (2017).

14.   Clark, D., Malerød-Fjeld, H., Budd, M., Yuste-Tirados, I., Beeaff, D., Aamodt, S., Nguyen, K., Ansaloni, L., Peters, T., Vestre, P. K., Pappas, D. K., Valls, M. I., Remiro-Buenamañana, S., Norby, T., Bjørheim, T. S., Serra, J. M. & Kjølseth, C. Single-step hydrogen production from NH3, CH4, and biogas in stacked proton ceramic reactors. *Science* **376**, 390–393 (2022).

15.   CerPoTech. Barium cerium yttrium zirconate, BZCY. https://www.cerpotech.com/products/barium-cerium-yttrium-zirconate-bzcy (accessed August 2023).

16.   Valenzuela, M. A., Bosch, P., Zapata, B., Aguilar-Rios, G., Lara, V. H., García-Figueroa, E. & Schifter, I. Effects of hydrogen at high temperature on ZnAl2O4 and Sn-ZnAl204. *J. Therm. Anal.* **44**, 639–653 (1995).

17.   van der Laag, N. J., Snel, M. D., Magusin, P. C. M. M. & de With, G. Structural, elastic, thermophysical and dielectric properties of zinc aluminate (ZnAl2O4). *J. Eur. Ceram. Soc.* **24**, 2417–2424 (2004).

18.   Ran, K., Deibert, W., Ivanova, M. E., Meulenberg, W. A. & Mayer, J. Crystal structure investigation of La5.4W1−yMoyO12−δ for gas separation by high-resolution transmission electron microscopy. *Sci. Rep.* **9**, 3274 (2019).

19.   Valenzuela, M. A., Jacobs, J.-P., Bosch, P., Reijne, S., Zapata, B. & Brongersma, H. H. The influence of the preparation method on the surface structure of ZnAl2O4. *Appl. Catal. A: Gen.* **148**, 315–324 (1997).

20.   Ballarini, A. D., Miguel, S. R. De, Castro, A. A. & Scelza, O. A. n-Decane dehydrogenation on Pt, PtSn and PtGe supported on spinels prepared by different methods of synthesis. *Appl. Catal. A: Gen.* **467**, 235–245 (2013).

21.   Aguilar-rios, G., Valenzuela, M. A., Armendariz, H., Salas, P., Dominguez, J. M., Acosta, D. R. & Schifter, I. Metal-support effects and catalytic properties of platinum supported on zinc aluminate. *Appl. Catal. A: Gen.* **90**, 25–34 (1992).

22. Escolástico, S., Vert, V. B. & Serra, J. M. Preparation and characterization of nanocrystalline mixed proton–electronic conducting materials based on the system Ln6WO12. *Chem. Mater.* **21**, 3079–3089 (2009).

23. Seeger, J., Ivanova, M. E., Meulenberg, W. A., Sebold, D., Stöver, D., Scherb, T., Schumacher, G., Escolástico, S., Solís, C. & Serra, J. M. Synthesis and characterization of nonsubstituted and substituted proton-conducting La6–xWO12–y. *Inorg. Chem.* **52**, 10375–10386 (2013).

24. Fantin, A., Scherb, T., Seeger, J., Schumacher, G., Gerhards, U., Ivanova, M. E. & Meulenberg, W. A. Crystal structure of Mo-substituted lanthanum by X-ray and neutron diffraction research papers. *J. Appl. Cryst.* **52**, 1043–1053 (2019).

25. J.U.M. Engineering GmbH. Response Factors. http://www.jum-aerosol.com/images/E-Fakt-02.pdf (accessed October 2023).

26. Bosch, P., Valenzuela, M. A., Zapata, B., Acosta, D., Aguilar-rios, G., Maldonado, C. & Schifter, I. High temperature treated Pt/Sn-ZnAl2O4 catalysts. *J. Mol. Catal.* **93**, 67–78 (1994).

27. Berger, R. J., Pérez-Ramírez, J., Kapteijn, F. & Moulijn, J. A. Catalyst performance testing: Bed dilution revisited. *Chem. Eng. Sci.* **57**, 4921–4932 (2002).

28. Wannaborworn, M., Praserthdam, P. & Jongsomjit, B. A comparative study of solvothermal and sol-gel-derived nanocrystalline alumina catalysts for ethanol dehydration. *J. Nanomater.* **2015**, 19425 (2015).

29. Wang, S., Song, L. & Qu, Z. Cu/ZnAl2O4 catalysts prepared by ammonia evaporation method: Improving methanol selectivity in CO2 hydrogenation via regulation of metal-support interaction. *Chem. Eng. J.* **469**, 144008 (2023).

30. Liu, Q., Wang, L., Wang, C., Qu, W., Tian, Z., Ma, H., Wang, D., Wang, B. & Xu, Z. The effect of lanthanum doping on activity of Zn-Al spinel for transesterification. *Appl. Catal. B: Environ.* **136–137**, 210–217 (2013).

31. Chen, Y., Wei, Y., Xie, H., Zhuang, L. & Wang, H. Effect of the La/W ratio in lanthanum tungstate on the structure, stability and hydrogen permeation properties. *J. Membr. Sci.* **542**, 300–306 (2017).

32. Al-Fatesh, A. S., Patel, R., Srivastava, V. K., Ibrahim, A. A., Naeem, M. A., Fakeeha, A. H., Abasaeed, A. E., Alquraini, A. A. & Kumar, R. Barium-promoted yttria–zirconia-supported Ni catalyst for hydrogen production via the dry reforming of methane: role of barium in the phase stabilization of cubic ZrO2. *ACS Omega* **7**, 16468–16483 (2022).

33. Kojo, G., Shono, Y., Ushiyama, H., Oshima, Y. & Otomo, J. Influence of La/W ratio on electrical conductivity of lanthanum tungstate with high La/W ratio. *J. Solid State Chem.* **248**, 1–8 (2017).

34.   Loureiro, F. J. A., Ramasamy, D., Ribeiro, A. F. G., Mendes, A. & Fagg, D. P. Underscoring the transport properties of yttrium-doped barium cerate in nominally dry oxidising conditions. *Electrochim. Acta* **334**, 135625 (2020).

35.   de Macedo, H. P., Bezerra de Araújo Medeiros, R. L. B., de Medeiros, A. L., Silva de Oliveira, Â. A. de, de Figueredo, G. P., Antônio, M., de Freitas Melo, M. A. & de Araújo Melo, D. M. Characterization of ZnAl2O4 spinel obtained by hydrothermal and microwave assisted combustion method: A comparative study. *Mater. Res.* **20**, 29–33 (2017).

36.   Magrasó, A., Frontera, C., Marrero-López, D. & Núñez, P. New crystal structure and characterization of lanthanum tungstate 'La6WO12' prepared by freeze-drying synthesis. *Dalton Trans.* **46**, 10273–10283 (2009).

37.   Castellani, P., Nicollet, C., Quarez, E., Joubert, O. & Le Gal La Salle, A. Synthesis of yttrium doped barium zirconate/cerate electrolyte materials and densification using conventional and cold-sintering processes. *ECS Trans.* **109**, 13–29 (2022).

38.   Sata, N. & Costa, R. Protonic ceramic electrochemical cells in a metal supported architecture: challenges, status and prospects. *Prog. Energy* **6**, 032002 (2024).

Supporting Information

4.A. Catalytic testing setup
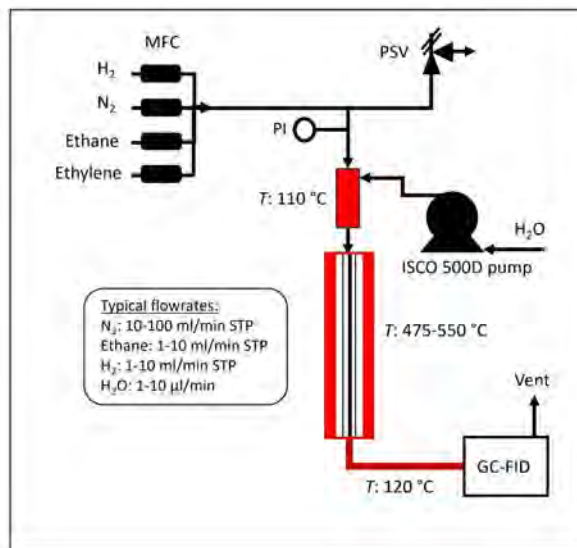
Figure 4.A1: Schematic representation of the continuous flow packed bed reactor setup, used in this work for the catalytic performance testing.

4.B. Characterization results – X-ray diffraction

The X-ray diffraction (XRD) spectra of the bare support materials and the Pt-functionalized catalysts were collected after calcination (**Figure 4.C1**). The synthesized $ZnAl_2O_4$ support showed all characteristic $ZnAl_2O_4$ spinel peaks with Bragg angles around 32°, 37°, 44°, 48°, 55°, 58°, 64°, 73°, and 76° (**Figure 4.C1a**) [20,35]. Besides, the XRD spectrum of the bare lanthanum tungstate (LWO, **Figure 4.C1b**) contained peaks around 28°, 32°, 46°, 55°, 57°, 67°, 74°, 76°, and 85°, which are characteristic for a single cubic LWO phase [31,36]. The additional minor peaks around 26° and 30° are likely to originate from a La_2O_3 impurity phase [31,36]. Barium cerium yttrium zirconates containing a composition that is rich in zirconium (i.e. $BaZr_{0.7}Ce_{0.2}Y_{0.1}$) possess diffraction angles around 30°, 36°, 42°, 52°, 62°, 70°, and 78° [15,37,38], which were all observed for the bare BZCY support (**Figure 4.C1c**). From this analysis it can be concluded that the synthesized $ZnAl_2O_4$ and LWO contain the targeted crystalline phases and that the commercial BZCY support satisfies the crystallinity of the desired $BaZr_{0.7}Ce_{0.2}Y_{0.1}$ phase.
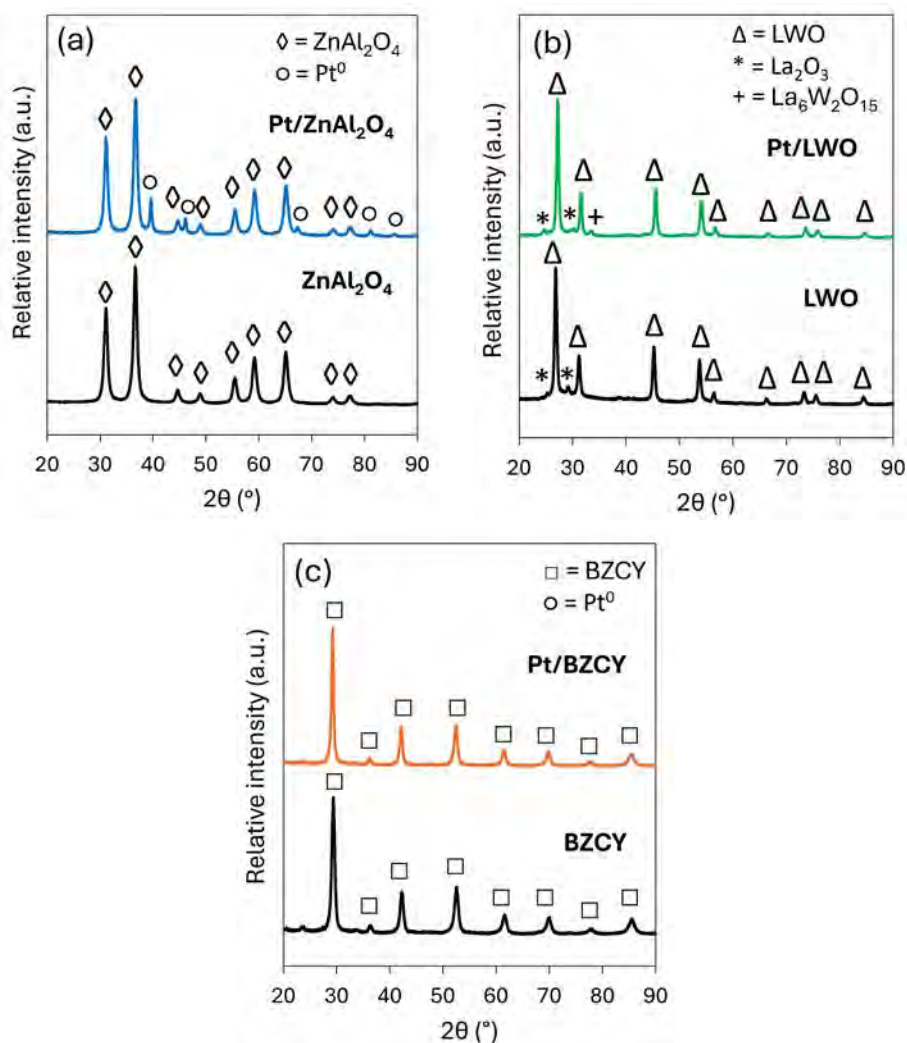
Figure 4.B1: X-ray diffraction (XRD) patterns of (a) calcined ZnAl$_2$O$_4$ and Pt/ZnAl$_2$O$_4$, (b) calcined LWO and Pt/LWO, and (c) calcined BZCY and Pt/BZCY.

The Pt-functionalized ZnAl$_2$O$_4$ catalyst showed the presence of a metallic Pt phase in addition to the ZnAl$_2$O$_4$ phase (**Figure 4.C1a**). This metallic Pt phase was not observed after functionalizing the LWO and BZCY supports with Pt (**Figure 4.C1b** and **4.C1c**). This difference is supposedly caused by the considerably higher Pt loading in Pt/ZnAl$_2$O$_4$ as compared to Pt/LWO and Pt/BZCY (**Table 4.1**). Additionally, upon functionalizing the LWO support with Pt, a minor La$_6$W$_2$O$_{15}$ appeared to be segregated [36], while the bulk ZnAl$_2$O$_4$, LWO, and BZCY phases were unaffected by Pt functionalization (**Figure 4.C1**).

Chapter 5

Leveraging green electricity to drive propylene production in membrane reactors

Summary

This chapter assessed the potential for applying ceramic proton-conducting membranes in propane dehydrogenation processes with the aim of achieving drastic reductions in greenhouse gas emissions. These membranes could shift the dehydrogenation equilibrium toward propylene, thereby significantly increasing the process energy efficiency, and allow the electrification of the propylene production process. The potential of two different membrane reactor systems was explored, consisting of (i) mixed proton-electron conducting (MPEC) membranes and (ii) proton-conducting electrolysis cell (PCEC) membranes. Both membrane-assisted processes were benchmarked against the conventional Honeywell UOP Oleflex process for propylene production, resulting in a comparison between these three processes. Rigorous techno-economic analysis indicated that the MPEC process requires an exceedingly large membrane surface area, making it the least competitive option. In contrast, the electrically heated PCEC process could be an attractive alternative to traditional Oleflex, as it had a 20% lower capital investment and a 30% lower specific energy input than Oleflex. However, this only translated into a lower carbon footprint when fully renewable electricity was utilized and when off-gas streams rich in hydrocarbons were not used for heat integration. Notably, electrification of the Oleflex process led to comparable improvements in carbon dioxide emissions as industrial implementation of PCEC membranes. Moreover, guidelines were established regarding PCEC performance criteria, electricity price and carbon intensity, and the carbon taxation required to stimulate industrialization of electrified PCEC processes.

5.1. Introduction

Propylene is a major bulk chemical with a market size of ca. 105 billion USD in 2022 [1,2]. It is employed primarily to produce plastics (polypropylene) and oxygenates (propylene oxide) [3]. The demand for propylene is ever-expanding, due to increasing world population and improving global wealth [4]. Propylene is conventionally produced via steam cracking and fluid catalytic cracking [5]. The onset of inexpensive shale gas, however, has reduced the propylene yield from these cracking processes, leading to the so-called 'propylene gap' [6]. This has triggered the development of on-purpose propylene production plants [7]. Next to this, the carbon footprint of conventional cracking processes is rather substantial (1.0-2.0 t_{CO2}/t_{olefin}) [8], due to the high temperature (ca. 800 °C) required for the reaction [9]. Developing new technologies that can support the expansion of propylene production in a sustainable manner is therefore essential to reach the climate action sustainable development goal (i.e. SDG13) set by the United Nations [10].

The possible on-purpose propylene production routes are based on either: (i) olefin metathesis [11,12], (ii) methanol conversion [13,14], or (iii) propane dehydrogenation (PDH) [5,15]. Here, one of the most promising strategies is PDH, as this can be profitable using scalable technologies [5]. PDH can be conducted using either oxidative or non-oxidative dehydrogenation routes. While the oxidative reaction can be operated autothermally, due to the exothermicity of the reaction, the endothermic non-oxidative dehydrogenation (NODH) of propane (**Equation 5.1**) is still industrially preferred as a higher propylene selectivity can be achieved (>95%) [16–18].

$$C_3H_8 \leftrightharpoons C_3H_6 + H_2 \qquad (\Delta H^0_{298} = +124.3\ \text{kJ/mol}) \qquad (5.1)$$
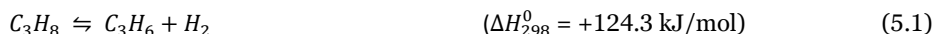
Propylene formation is thermodynamically favored at elevated temperatures and reduced pressures. For this reason, industrial propane NODH is operated at near-ambient pressures and temperatures between 500 to 650 °C. At these conditions, the thermodynamic equilibrium restricts the single-pass propylene yield to about 40% [19].

Next to the challenges associated with the reaction, the propane NODH process is characterized by a large carbon footprint (0.5-1.5 $t_{CO2}/t_{propylene}$) [5]. The corresponding carbon dioxide emissions are related to the fossil heat needed to operate the heaters and endothermic reactors, the generation of electricity for the compressors, and the combustion of carbon deposits formed on the surface of the dehydrogenation catalyst. The use of hydrogen permeable dense membranes represents a promising strategy to reduce the carbon intensity of propane NODH processes, as these membranes offer an excellent opportunity to achieve (i) process electrification coupled with resistive heating, (ii) integration of reaction, *in situ* H_2 separation, and H_2 compression, (iii) smaller process streams and process units as a result of higher single-pass conversions due to a shift in thermodynamic equilibrium toward propylene, and (iv) facile product isolation downstream. Dense ceramic membranes are preferred to dense metallic membranes for

integration with high-temperature (T = 500-700 °C) hydrocarbon-rich reactions, because of their considerably better stability [20], despite the higher H_2 permeation fluxes through metallic membranes [21].

Dense ceramic membranes can be subdivided into mixed proton-electron conducting (MPEC) and proton-conducting electrolysis cell (PCEC) membranes. In MPECs, hydrogen permeates via cotransport of protons and electrons (ambipolar diffusion, **Figure 5.1**), driven by a gradient in H_2 partial pressure between feed and permeate side (**Figure 5.2**). Protons are believed to move via the Grotthuss mechanism in which protons hop between adjacent oxygen-ions, whilst electrons move through the metal-ion network (**Figure 5.1**) [22]. In these MPECs, no external voltage is applied and a vacuum or sweep gas is needed on the permeate side to minimize the H_2 pressure (**Figure 5.2**). On the contrary, in the case of PCECs an electrical potential is applied across the membrane, forcing electron transport through an external circuit, whilst only protons are transported through the dense ceramic membrane (**Figure 5.1**). In this case, hydrogen transport is driven by a gradient in H_2 electrochemical potential, i.e. a combination of a gradient in H_2 chemical potential (yellow arrow in **Figure 5.2**) and a gradient in electrostatic potential (red arrow in **Figure 5.2**). PCECs are commonly operated at high external voltages, such that the electrostatic contribution dominates the driving force, and hydrogen can be transported in a direction opposing the gradient in H_2 pressure (**Figure 5.2**). This leads to the generation of a pure and pressurized hydrogen stream on the permeate side. Malerød-Fjeld et al. [23] showed that hydrogen can be pressurized up to 50 bar(a) using this concept.
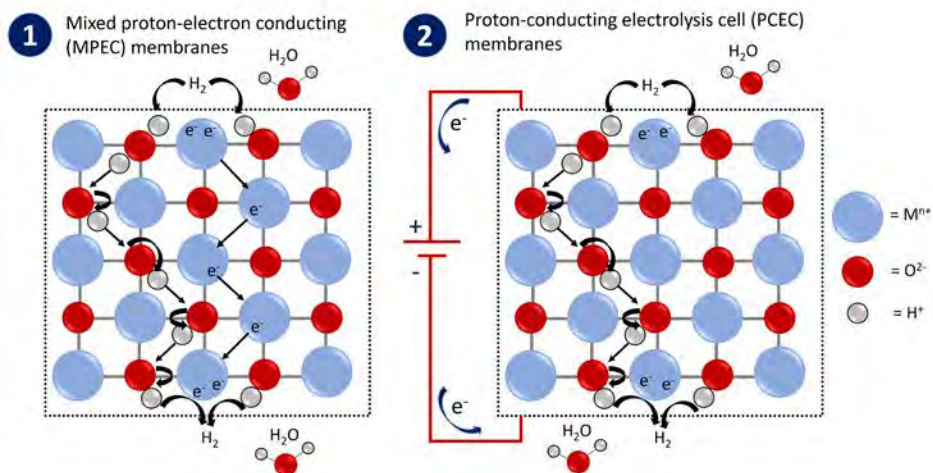
Figure 5.1: Transport mechanism of protons and electrons in (1) mixed proton-electron conducting (MPEC) membranes, and (2) proton-conducting electrolysis cell (PCEC) membranes.

While MPECs offer the opportunity to shift the propane NODH equilibrium toward propylene, the PCEC systems have the additional advantages of possible process electrification and possible tailoring of reaction thermodynamics and kinetics via the applied potential. Moreover, part of the PCEC power consumption is converted into Joule heat, due to the electrical resistance across the PCEC membrane. However, industrial implementation of PCEC systems is expected to be accompanied by more drastic adjustments to existing propylene production facilities as compared to MPEC systems, because of the incorporation of the more complex and electrified PCECs. MPEC and PCEC membranes are both believed to function optimally in the presence of steam on both sides, as this ensures sufficient surface hydroxyl groups that facilitate hydrogen incorporation and recombination [24].
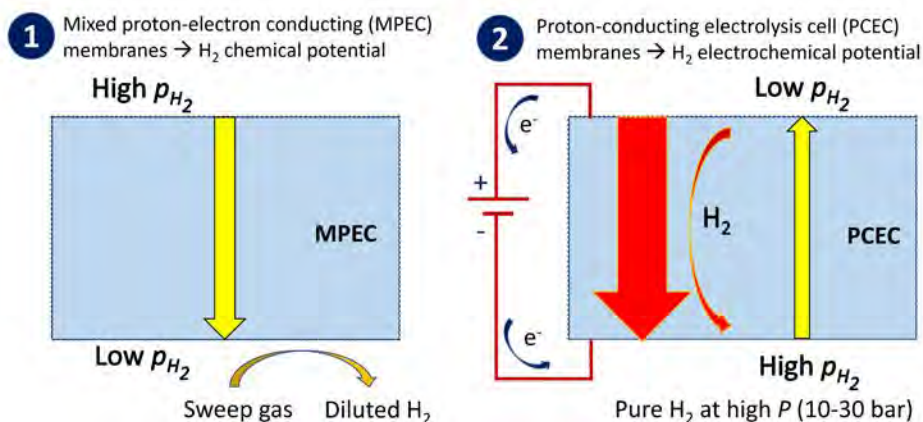
Figure 5.2: Driving force for hydrogen transport through (1) mixed proton-electron conducting (MPEC) membranes, and (2) proton-conducting electrolysis cell (PCEC) membranes. Yellow and red arrows represent the driving forces for H_2 permeation induced by the H_2 partial pressure gradient and electrostatic potential gradient, respectively.

The concept of increasing olefin yields in alkane dehydrogenation processes by applying proton-conducting membranes has been demonstrated at laboratory scale [25,26]. However, it is currently unclear how the energy usage, carbon footprint, and profitability of a propane NODH process equipped with state-of-the-art proton-conducting membranes compares with conventional propylene production routes. To fill this knowledge gap, an exhaustive analysis of the process economics, energy usage, and carbon dioxide emissions was conducted of (i) a conventional Honeywell UOP Oleflex process, (ii) an MPEC-assisted propane NODH process, and (iii) a PCEC-assisted propane NODH process. Herein, the possible impact of industrial implementation of proton-conducting membranes on the climate action sustainable development goal of the United Nations (i.e. SDG13) was evaluated [10] by assessing the potential reductions in energy usage and greenhouse gas emissions of integrating proton-conducting membranes into propylene production plants. Moreover, by performing sensitivity analyses with varying membrane

reactor performances and market conditions several guidelines were set and the main challenges were identified for industrial implementation of this technology.

5.2. Case study

The process flow diagrams of the Honeywell UOP Oleflex, MPEC-assisted, and PCEC-assisted processes are described here to set the stage for the process simulations and the succeeding techno-economic assessment. More detailed process flow diagrams as implemented in Aspen Plus are available in **Supporting Information 5.C**.

5.2.1. Honeywell UOP Oleflex process

The Honeywell UOP Oleflex process, schematically presented in **Figure 5.3**, is industrially applied for propane and butane dehydrogenation [5,19]. In this study, fresh propane was pressurized first from a 5 bar(a) pipeline pressure to a 15 bar(a) depropanizer pressure [5,27]. In the depropanizer column, heavy (i.e. C4+) impurities were removed from the process feed. In the patented cold box technology, autorefrigeration methods were applied to heat the feed and simultaneously cool down the effluent of the dehydrogenation reactors. The cold box was simulated according to patented technology [28] in which subzero temperatures were reached without the need for external refrigeration using a sequence of isentropic expansion, subcooling, and separation steps. The hydrocarbons were liquefied in the cold box, allowing for facile separation from gas phase hydrogen.
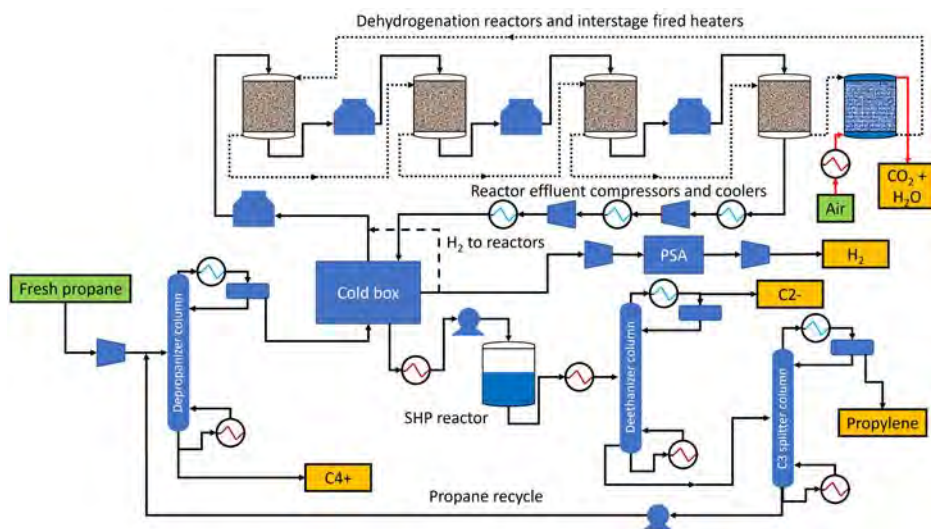
Figure 5.3: Process flow diagram of the Honeywell UOP Oleflex process. Adapted with permission from Agarwal et al. [5]. Copyright 2018 American Chemical Society.

A Pt-Sn-based catalyst was employed in a dehydrogenation reactor system consisting of multiple adiabatic radial flow moving-bed reactors operating in series [18,19,29]. Typical operating conditions are between 1-3 bar(a) and 525-705 °C, where interstage fired heaters represent the major heat source for the endothermic dehydrogenation [18,19]. Here, propane NODH was operated in a sequence of four adiabatic reactors with an inlet temperature of 600 °C. The pressure reduced from 5 bar(a) to 1 bar(a) along the reactor system, meaning 1 bar pressure drop per reactor. The last reactor in series was connected to a regenerator (T = 600 °C, P = 1 bar(a)) where coke deposits were burned off the catalyst using a stream of air and where Pt was redispersed on the catalyst support surface [19]. The total reaction/regeneration cycle in the Oleflex process takes about 5-10 days [18,19]. A propylene selectivity of 90% was taken for moderate total single-pass conversions (ca. 40%), resulting in a 36% single-pass propylene yield [19]. The lifetime of the applied Pt-based catalyst is typically between 1-3 years [19] and was set to two years here.

The dehydrogenation reactor effluent was sent through a sequence of three coolers and two compressors to compress the effluent to ca. 14 bar(a) before sudden expansion inside the cold box. The interstage coolers ensured that the compressor effluent temperature did not exceed ca. 150 °C, above which olefin polymerization could take place [9]. Also, these lower temperatures were preferred to attain higher compression efficiencies [30]. The gas phase hydrogen leaving the cold box was partly obtained as a valuable product and partly recycled to the dehydrogenation reactors. Hydrogen was recycled to these reactors to minimize coke formation and, thus, catalyst deactivation. The hydrogen product fraction was purified using pressure swing adsorption (PSA) [31]. These PSA units are commonly operated isothermally between 10-50 °C [31]. Here, an operating temperature of 40 °C was selected for the PSA. Pressure swings were carried out between elevated pressure (P = 20 bar(a)) and near-ambient pressure (P = 3 bar(a)) [31]. It was assumed that all hydrocarbons desorb at 3 bar(a), whilst hydrogen does not adsorb at all. Hence, hydrogen leaves the PSA at 20 bar(a) and was further pressurized to 50 bar(a).

The liquefied hydrocarbon effluent of the cold box was sent to the selective hydrogenation process (SHP) reactor. In this reactor, double unsaturated hydrocarbons (e.g. propadiene) were selectively hydrogenated to increase the propylene yield. The hydrogen required for this step originated from the incomplete separation of hydrogen after the cold box. Downstream the SHP reactor, the light impurities (C2-) were removed from the C3's in the deethanizer column (P = 38 bar(a), T = 34-86 °C). Lastly, in the C3 splitter (P = 19 bar(a), T = 45-54 °C), the targeted propylene overhead product was separated from the unconverted propane, which in turn was recycled to the process feed. These C3 splitter columns are often wide and extremely tall columns (100-200 stages) with high reflux ratios (10-20), because of the close relative volatility of propane and propylene [32].

5.2.2. MPEC membrane-assisted process

The process flow diagram of the MPEC-assisted propane NODH process was adapted from the Oleflex process design and is shown in **Figure 5.4**. When comparing this design to

the Oleflex process (**Figure 5.3**), one can notice the following differences: (i) steam was cofed to the reactor, (ii) steam was employed as sweep gas, (iii) the serial moving-bed reactors were replaced by parallel fixed-bed membrane reactors, and (iv) the cold box technology was removed. Both membrane-assisted processes were simulated with 95% hydrogen removal, where the hydrogen removal fraction was defined as the ratio between the amount of hydrogen extracted and the amount of hydrogen present. Besides, the single-pass propylene yield was 50% for the MPEC and PCEC processes. This propylene yield is above the Oleflex propylene yield of 36%, thereby mimicking the targeted equilibrium shift by using membranes. A hydrogen removal fraction of 95% was selected, since more than 90% of the hydrogen needs to be removed to substantially shift the propane NODH equilibrium yield (**Supporting Information 5.B**).
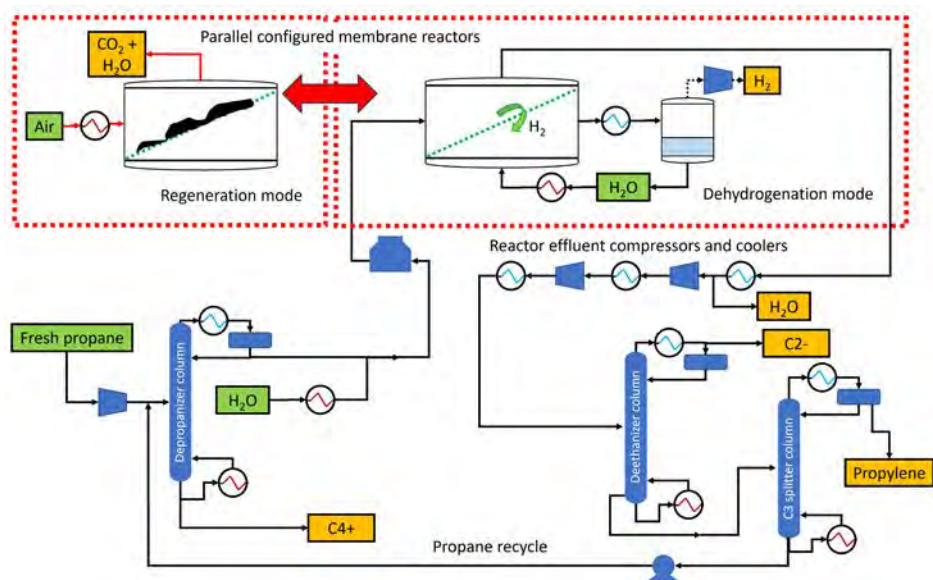
Figure 5.4: Schematic process flow diagram of the MPEC-assisted process.

Molybdenum-substituted lanthanum tungstate (LWMO) was selected as MPEC material in this process. LWMO has a high ambipolar conductivity in combination with a good stability in harsh conditions (CO_2, H_2S, various salts) [33–37]. A steam cosupply is generally needed on both sides of dense ceramic membranes to facilitate hydrogen permeation [24]. In this work, 3 vol% of steam was cosupplied with propane on the feed side of the membrane (**Figure 5.4**), as substituted lanthanum tungstates are known to perform well under wet gas atmospheres containing 2-3 vol% of steam [38,39]. This steam was condensed again in the first cooler downstream the membrane reactors. Cofeeding steam on the membrane feed side expectedly also suppresses coke formation, thereby improving catalyst stability [40]. For both membrane processes, this steam cosupply was assumed to take over the role of the recycled H_2 in the Oleflex process in stabilizing the applied Pt catalyst. Any possible reforming reaction was disregarded as propane reforming

is typically initiated at temperatures above 600 °C [41]. The MPEC membrane reactor had a total pressure of 4 bar(a) on the feed side and a total pressure of 1 bar(a) on the permeate side.

The primary role of the sweep gas was to minimize hydrogen partial pressure on the permeate side to maximize the driving force for hydrogen permeation. In this work, steam was selected as suitable sweep gas, since a cosupply of steam was inevitably needed to facilitate hydrogen permeation. Besides, steam is easily separated from the permeated hydrogen via liquefaction in a flash drum. The steam sweep gas flow was regulated in such a way that the hydrogen partial pressure on the permeate side was below the lowest feed side hydrogen partial pressure, i.e. below the outlet hydrogen partial pressure on the feed side after 95% hydrogen abstraction. The condensed water was heated and evaporated to be reused as sweep gas. It should be noted that dense ceramic materials can also transport O^{2-} ions in addition to protons and electrons. If the oxygen electrochemical potential would be higher on one side of the membrane, then cotransport of O^{2-} ions could take place in a direction opposing the proton transport direction. This could possibly induce oxidation reactions on the feed side of the membrane [42]. For simplicity, the potential oxygen-ion cotransport and possible resulting oxidation reactions were not included in this work.

The MPEC and PCEC membrane reactors were parallel-configured tubular fixed-bed reactors (see **Supporting Information 5.F**). Some of them were operating in dehydrogenation mode and some of them in regeneration mode at any point in time to allow for continuous operation. Each membrane reactor was operating isothermally under dehydrogenation (T = 600 °C, P = 4 bar(a)) and regeneration (T = 600 °C, P = 1 bar(a)) conditions with intermediate flushing runs. Here, it was assumed that the heat generated during regeneration and the heat externally supplied by either burning natural gas, burning off-gas, or using electricity, could be directly integrated in the membrane reactor design.

The MPEC and PCEC membranes were both assumed to be fully permselective. Consequently, the permeate side effluent contains only steam and hydrogen. Upon liquefaction in a flash drum, the hydrogen product was purified to a nearly pure hydrogen stream with only traces of water, thereby exceeding the 98 mol% hydrogen purity specification. Because of the strict requirement of 95% hydrogen removal in both membranes, only marginal amounts of hydrogen ended up in the hydrocarbon effluent. These small amounts of hydrogen were separated as part of the lights (C2-) fraction in the deethanizer column (**Figure 4**), making the cold box technology from the Oleflex process unnecessary.

5.2.3.   PCEC membrane-assisted process

The process flow diagram of the PCEC-assisted process, as shown in **Figure 5.5**, was also adapted from the Oleflex process design. The PCEC system was based on a cathode-supported cell design where an anode layer made of $PrBa_{0.5}Sr_{0.5}Co_{1.5}Fe_{0.5}O_{5+\delta}$ (PBSCF)

was deposited on an electrolyte layer of $BaZr_{0.7}Ce_{0.2}Y_{0.05}Yb_{0.05}O_{3-\delta}$ (BZCYYb), which in turn was applied on top of a NiO/BZCYYb cathode support [25]. An additional barrier layer of Gd-doped ceria (GDC) was needed to avoid any chemical reaction between the PBSCF electrode and the yttrium-containing electrolyte [43]. BZCY-based PCEC systems are known for their outstanding proton conductivity properties in combination with good stability in hydrocarbon atmospheres [23,44].
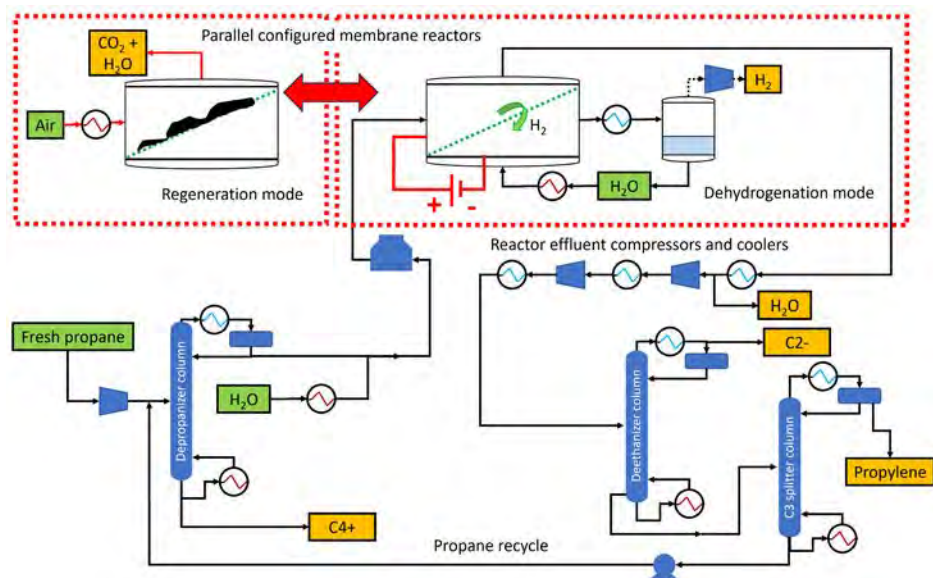
Figure 5.5: Schematic process flow diagram of the PCEC-assisted process.

Similar to the MPEC process, each parallel PCEC fixed-bed reactor was operating isothermally in cycles under dehydrogenation (T = 600 °C, P = 4 bar(a)) and regeneration (T = 600 °C, P = 1 bar(a)) conditions, assuming that regeneration heat, natural gas heat, off-gas heat, or electrical heat can be directly integrated in the PCEC reactors. In contrast to MPEC membranes, an external voltage was applied in the PCEC membrane reactors to drive hydrogen permeation (**Figure 5.5**). It has been demonstrated that hydrogen can be electrochemically compressed to 50 bar(a) in BZCY-based electrochemical cells [23]. However, electrochemical compression is most efficient for light compressions [45]. For this reason, the hydrogen product was electrochemically compressed here to 10 bar(a), followed by mechanical compression up to the 50 bar(a) hydrogen product pressure. Also, for PCEC membranes, 3 vol% of steam was cosupplied on both sides of the membrane to optimize its performance [24], and the water was again separated via downstream condensation. Note that the amount of steam needed for wetting the permeate side of the PCEC membrane (i.e. 3 vol% steam, with 97% permeated hydrogen at 10 bar(a)) was considerably smaller compared to the steam sweep gas amount in the MPEC process.

Again, no cold box technology was required, since 95% of the produced hydrogen was removed and the PCEC membrane was fully permselective.

5.3. Methodology

The three propane NODH processes were simulated in Aspen Plus V12.1 using the Soave-Redlich-Kwong equation of state as the property method. The benchmark Honeywell UOP Oleflex process was simulated based on previous academic studies [5,18,19,46,47] and patents [28].

5.3.1. Process feed and product specifications

The system boundaries of all three processes were maintained the same. The targeted propylene production capacity was 450 ktpa, based on the typical industrial Oleflex production capacity ranging from 450-750 ktpa [48], and the number of operating hours per year was 8,400. The targeted product was polymer grade propylene [47] (≥99.5%, see **Supporting Information 5.A1**) at a pressure of 19 bar(a). Besides, internal combustion fuel grade A hydrogen (≥98.0%) was targeted as valuable byproduct (**Supporting Information 5.A2**) at 50 bar(a) [49]. The fresh propane feed stream was derived from a natural gas processing plant and contained 95% of propane, with 2.5% of ethane and 2.5% of n-butane as impurities at 5 bar(a) [46] (**Supporting Information 5.A3**). Traces of sulfur impurities in the fresh propane stream were considered to be removed in upstream desulfurization units in all three processes and were thereby beyond the scope of this study.

Table 5.1: Feedstock and product prices.

Compound	Price (USD/t)	Reference year	Reference location	Ref.
NG-derived* propane	497 (0.94 USD/gal)	2022	Worldwide	[50]
Polymer grade propylene	997	2022	Worldwide	[51]
Fuel grade A hydrogen	1500	2023	Worldwide	[52,53]

*NG = natural gas.

The prices of the feedstock and product streams, included in the financial evaluation, are listed in **Table 5.1**. Propane and propylene prices were estimated based on global average market prices in 2022 [50,51]. The price of grey hydrogen produced via conventional steam methane reforming of natural gas usually ranges between 1,000-2,000 USD/t [52,53]. The hydrogen produced in the Oleflex and membrane-assisted processes in this work should be economically competitive to these traditional hydrogen production ways. For this reason, a hydrogen selling price of about 1,500 USD/t was selected. The three plants were assumed to be constructed in the U.S. Gulf Coast, because of the close vicinity of relatively cheap and large capacity natural gas resources [54–56].

5.3.2. Utility specifications

The different types of utilities needed, including the corresponding costs, are listed in **Table 5.2**. Cooling water was used for all cooling and condensation steps within the process, as the target temperature of all these cooling steps allowed for the use of cooling water (20 °C [57], 5 bar(a)). A minimum temperature gap of 10 °C with the stream to be cooled was taken. The required energy for operating the endothermic reactors was provided either from fossil or electricity resources. In case of fossil reactor heating, natural gas was used as heating fuel. For all other heating steps within the process, low pressure (i.e. 2 bar(a), 120 °C) steam was used and the heating steps were carried out by using only the latent heat, i.e. only by condensing the steam. The reboiling operations in all distillation columns occurred at temperatures below 100 °C, as they dealt with vaporization of light hydrocarbons. Consequently, low pressure (LP) steam of 2 bar(a) was sufficient for these steps [58]. The LP steam costs were calculated based on a 120 °C water feed stream temperature [59] and natural gas firing costs of 6.11 USD/GJ [55]. Lastly, pumps and compressors in the process required electricity. Two types of electricity were considered in this study: (i) U.S. average grid electricity, and (ii) fully renewable electricity. The two types of electricity were assumed to be equally expensive in the base case analysis.

Table 5.2: Utility types and prices.

Utility type	Cost	Year	Location	Ref.
Cooling water (20 °C)	0.042 USD/m^3	2018	United States	[60]
Low pressure (LP) steam (2 bar(a), 120 °C)	0.014 USD/kg	2023	Worldwide	[59,61]
Natural gas (NG)	22.0 USD/MWh (6.11 USD/GJ)	2022	United States Henry Hub	[55]
Electricity	0.076 USD/kWh (0.021 USD/MJ)	April 2023	United States	[62]

5.3.3. Reactor simulations

The four serial Oleflex moving-bed reactors were simulated in Aspen Plus as four sequential stoichiometric reactors with interstage heaters. The single-pass yields were retrieved from previous studies and were equally distributed among the four sequential reactors: propane dehydrogenation (36%), propane cracking (1.6%), propane hydrogenolysis (0.8%), and propane coking (2%) [5] (**Supporting Information 5.D1).** The MPEC and PCEC membrane reactors were simulated in Aspen Plus by applying a combination of a stoichiometric reactor and a component splitter. The component splitter defined the fraction of hydrogen present in the outlet stream of the stoichiometric reactor that was effectively removed by the membrane. The propane NODH yield at 600 °C could be increased to 88% when removing 95% of the hydrogen (see **Supporting Information 5.B**) [63]. The single-pass propane NODH yield used in the base case MPEC and PCEC

processes was 50%. This value was below the theoretically attainable equilibrium yield after hydrogen extraction (ca. 88%), and well above the Oleflex yield of 36%.

The largest savings in energy input, covering energy requirements for heating, reboiling, and compression, could be achieved when moving from 36% to 50% propylene yield for 95% hydrogen removal (see **Supporting Information 5.S1**), due to a reduction in size of the process streams and process units thanks to a smaller recycle. Further increasing propylene yields only marginally improved the energy input, due to a minimum amount of energy needed for reaction, heating, and mass circulation. Morejudo et al. [42] demonstrated experimentally for the related methane dehydroaromatization reaction that the thermodynamic equilibrium could yet be surpassed for much milder percentages (50%) of hydrogen removal. The side reaction yields were assumed to be equal in the MPEC and PCEC processes and were 1% of propane cracking, 1% of propane hydrogenolysis, and 2% of propane coking. Hydrogen removal was anticipated to enhance coke formation on the catalyst and membrane surfaces but this was not included in the propane coking yield in this work. Instead, a 40% overdesign on the required membrane surface area was applied to include sufficient regeneration capacity (see **Supporting Information 5.F**).

The polycyclic aromatic hydrocarbon coronene, with chemical formula $C_{24}H_{12}$, was employed in this work as coke model compound, as solids are difficult to model in process simulations. Coronene was in the gas phase under reaction conditions ($T = 600$ °C) and therefore easily transported to a separate regeneration unit in the process simulations. In the regenerator, the coronene content was fully combusted to mimic the amount of energy generated by removing coke deposits upon catalyst regeneration. For more information on the simulations of the (membrane) reactors in the different processes, see **Supporting Information 5.D**.

5.3.4.   Equipment design

The dimensions of the moving-bed Oleflex reactors were determined by using a model for radial-flow moving-bed reactors as developed by Bijani et al. [29] for isobutane dehydrogenation (**Supporting Information 5.E**). For the design of the membrane reactors applied in the MPEC and PCEC-assisted propane NODH processes, the tubular ceramic membrane reactor design developed by CoorsTek was used [44,64]. This tubular design was preferred to a planar design for systems dealing with considerable pressure gradients that arise e.g. upon electrochemical compression in PCEC membranes. The CoorsTek design represents a modular approach where the repeating unit is a so-called single engineering unit (SEU) that consists of six tubular ceramic cells. Detailed information regarding the membrane reactor design and the specific multilayer compositions applied in both types of ceramic cells are available in **Supporting Information 5.F**. The design of other process equipment, e.g. compressors, and distillation columns, is available in **Supporting Information 5.G**.

Typical hydrogen permeation fluxes through ca. 30 μm thick MPEC and PCEC membranes are about 0.033 μmol/s.cm^2 and 3.3 μmol/s.cm^2, as reported in previous academic studies for $La_{5.5}W_{0.6}Mo_{0.4}O_{11.25-\delta}$ and $BaZr_{0.8}Ce_{0.1}Y_{0.1}O_{3-\delta}$, respectively [23,65]. Based on these input values, the required membrane surface area for removing 95% of the produced hydrogen from a propane NODH plant with a capacity of 450 ktpa propylene, is ca. 10^6 m^2 for the MPEC process and 10^4 m^2 for the PCEC process, respectively. A 40% overdesign on the membrane area was applied for inclusion of catalyst and membrane regeneration cycles, which is twice the typical Oleflex reactor capacity for regeneration [19]. The PCEC membrane reactor was operated at a current density of 1.0 A/cm^2 and with an area specific resistance of 0.4 Ω.cm^2, estimated based on the work by Malerød-Fjeld et al. [23], resulting in a total electrical power of 42 MW for the 10^4 m^2 membrane area operating in reaction mode. For a current density of about 100 mA/cm^2, hydrogen removal percentages of about 60% have been reached by Morejudo et al. [42]. Based on these data, 95% hydrogen removal was estimated to be possible for 1.0 A/cm^2. It should be noted that part of the electric power consumption generates Joule heat, due to the electrical resistance across the PCEC membrane.

5.3.5.   Process economics, energy usage, and carbon dioxide emissions

The outcomes of the Aspen Plus simulations (e.g. heating and cooling duties, number of distillation column stages, pump and compressor powers) were used for quantification of the capital expenditures (CAPEX), operating expenditures (OPEX), energy usage, and carbon dioxide emissions.

5.3.5.1.   Capital expenditures (CAPEX)

The capital expenditures were estimated based on the factor method proposed by Towler and Sinnott [66]. This method was based on a bottom-up approach, where the capital investment of the overall process was a summation of the capital investment per individual unit operation. The direct investment per unit operation was in turn a function of the purchased equipment costs, a compensation factor as proposed by W.E. Hand [66] for installation of process equipment, a material factor for compensation of possible material constraints, and correction factors for inflation (Chemical Engineering Plant Cost Index, CEPCI) and plant location. The CEPCI was evaluated for April 2023, when the CEPCI value was 803.4 [67]. Besides, the (membrane) reactor equipment was constructed with stainless steel 304, whereas all other process equipment was constructed using carbon steel. The corresponding process equipment costs were evaluated at the U.S. Gulf Coast. For further information on the applied factor method for the CAPEX estimation, see **Supporting Information 5.L**, **5.M**, and **5.N**.

The capital investment of the Oleflex reactors was approximated by the steel costs required to construct the radial-flow moving-bed reactors and regenerator (**Supporting Information 5.E3**). On the contrary, the investment costs of both membrane reactors were estimated using a method proposed by Malerød-Fjeld et al. [23] for cost estimation

of CoorsTek proton-conducting membrane reactors (**Supporting Information 5.F**). In this method, the investment costs were comprised of (i) SEU steel costs, (ii) hot box steel costs, (iii) stack material costs, (iv) tooling costs, and (v) additional costs. The stack material costs contained the bare costs for the electrode and electrolyte materials, as well as costs for gas manifolds, interconnects, weld connectors, and sealing rings. Besides, the tooling costs represented the depreciation of the equipment needed for manufacturing, in which it was assumed that the equipment was fully depreciated over the process units manufactured in the plant. Lastly, the additional costs contained costs for instrumentation, tubing, fittings, etc. [23]. The SEUs and hot box were constructed with stainless steel (grade SS 304), the tooling costs were estimated to be about 290 USD/SEU [23], and the additional costs were estimated as 10% of the total SEU costs (i.e. SEU steel costs + stack material costs). The steel costs of the Oleflex reactors, membrane reactors, and distillation columns were all estimated based on the corresponding process unit dimensions and the required wall thickness (see **Supporting Information 5.H**).

5.3.5.2.   Operating expenditures (OPEX)

The profitability of the process was predicted based on the method proposed by Towler and Sinnott [68] for determining process revenues and operating expenditures (OPEX). The revenues contained contributions from the targeted propylene product as well as the valuable hydrogen byproduct. Moreover, several off-gas streams available within the process (deethanizer lights, depropanizer heavies, and PSA retentate) were sold at fuel value if they were not used for heat integration within the process. The total operating expenditures were the sum of the total variable production costs and the total fixed production costs. The former depended on the plant capacity and contained costs related to (i) raw materials, (ii) utilities, (iii) consumables, (iv) effluent disposal, (v) packaging and shipping, and (vi) carbon taxation. On the contrary, fixed production costs were independent of production capacity and consisted among others of (i) labor costs, (ii) process maintenance costs, (iii) property taxes, and (iv) rent of land.

Regarding the variable production costs, consumables were comprised of catalysts, adsorbents (only Oleflex), and membranes. The catalyst lifetime was estimated to be two years (Oleflex: 1-3 years) [18]. The amount of catalyst needed in the membrane-assisted processes was assumed to be equal to the Oleflex process for equal production capacities. The lifetime of the membrane materials was set equal to the lifetime of the Pt catalyst, such that they could be replaced all at once. It was assumed here that only the membrane stack materials needed to be replaced periodically. Main contributors to the fixed production costs were the costs for maintenance and equipment replacement. The maintenance costs generally include costs for catalyst replacement at the end of the catalyst lifetime. The additional equipment replacement costs included in this work represented the costs for replacing the dense ceramic membrane units, as this is expected to be more costly than catalyst replacement only. The final contributor to the production costs was the carbon tax. This was done in the context of the energy transition as it is expected that the carbon

tax will become a more dominant factor in evaluating the profitability of different process alternatives. In this work, the carbon tax only covered carbon dioxide emissions, and equaled 65 USD/t$_{CO2}$ in the base case [69].

The three different processes were compared to one another in terms of profitability by using the return on investment (*ROI*) and the payback period. The *ROI* was calculated from the net annual profit and the total capital investment, whilst the payback period was computed using the net annual profit and the total depreciable capital. Herein, the difference between the net annual profit and the gross annual profit was the corporate income tax, computed based on an estimated tax rate of 21% for the U.S. Gulf Coast region [70,71]. The gross profit was in turn calculated from the difference between the revenues and operating costs, corrected for a depreciation term based on linear depreciation of the total depreciable capital for a project period of 30 years. The calculations related to the operating expenditures, revenues, and profitability assessment are explained in more detail in **Supporting Information 5.P**.

5.3.5.3. Energy usage and carbon dioxide emissions

The energy usage of the process was quantified in terms of specific energy input, meaning the total energy that needs to be supplied per ton of propylene produced. In this analysis, the total energy equaled a summation of heating, reboiling, compressing, and pumping duties. In the base case, carbon dioxide emissions were comprised of three contributors, including: (i) natural gas burning, (ii) electricity generation, and (iii) coke burning upon catalyst/membrane regeneration. The energy usage and carbon dioxide emissions were computed with integration of (i) Joule heat in the PCEC process, and (ii) catalyst regeneration heat in all three processes, for heating the dehydrogenation reactors. For fossil fuel heated reactors, the resistive Joule heat led to a saving in natural gas utility.

Table 5.3: Resource mix of U.S. average electricity, data valid for 2019 [72].

Coal (%)	Oil (%)	Gas (%)	Nuclear (%)	Hydro (%)	Biomass (%)	Wind (%)	Solar (%)	Geoth. (%)	Other (%)
23.3	0.6	38.4	19.6	6.8	1.6	7.1	1.7	0.4	0.4

The carbon dioxide emission factors related to burning natural gas, utilizing electricity with the U.S. average grid electricity carbon footprint, and utilizing fully renewable electricity are available as **Supporting Information 5.R**. As shown in **Table 5.3**, the resource mix of U.S. average grid electricity was primarily based on fossil resources [72]. As fully renewable electricity, a 50/50 solar/wind electricity mixture was taken and emissions related to the construction of wind turbines and solar panels were included. Possible carbon dioxide emissions related to the generation of low pressure steam used as utility in the process were not included in this analysis. The same holds for the off-gas streams that were sold at fuel value in the case that heat integration measures were not

implemented. After heat integration, parts of the heating utilities were replaced by burning off-gas streams, which was also accompanied by the generation of carbon dioxide. Further information on the carbon footprint calculations is available in **Supporting Information 5.R**.

5.3.6. Process heat integration

Possible ways of heat integration for the propane NODH processes were: (i) off-gas heat recovery, (ii) catalyst regeneration, (iii) Joule heating, and (iv) heat exchange between process streams (**Supporting Information 5.J**). The amounts of heat generated during catalyst regeneration and Joule heating were included in the base case analysis. Off-gas heat recovery represented the amount of energy that was generated by burning off-gas streams like the deethanizer lights, depropanizer heavies, and PSA retentate (Oleflex) streams. Lastly, heat could be integrated within the process by exchanging heat from hot process streams to cold process streams. A thermal pinch analysis was applied to all three processes to estimate the utilities that could be saved via heat exchange between process streams. A full heat exchanger network was not designed. The heat integration analysis is discussed in detail in **Supporting Information 5.J**, while the resistive Joule heating calculations are shown in **Supporting Information 5.K**.

5.4. Results and discussion

5.4.1. Specific energy input

The specific energy input (*SEI*) encompassed the energy duties of heating, reboiling, compressing, and pumping. As shown in **Figure 5.6,** the *SEI* of the Oleflex process was slightly lower than the typical energy requirement of naphtha steam crackers (26-31 MJ/kg$_{olefin}$) [8]. Notably, the total energy consumption of the MPEC process was about 40% higher than conventional Oleflex, due to a significant duty for additional heat employed for heating and evaporating the steam sweep gas (**Supporting Information 5.Q**). On the contrary, the energy usage of the PCEC process was about 30% lower than Oleflex. This was caused by the higher single-pass propylene yield (50% vs. 36% for Oleflex), which leads to a smaller recycle, smaller process streams and smaller process units, ultimately leading to lower heating, reboiling, and compression duties.
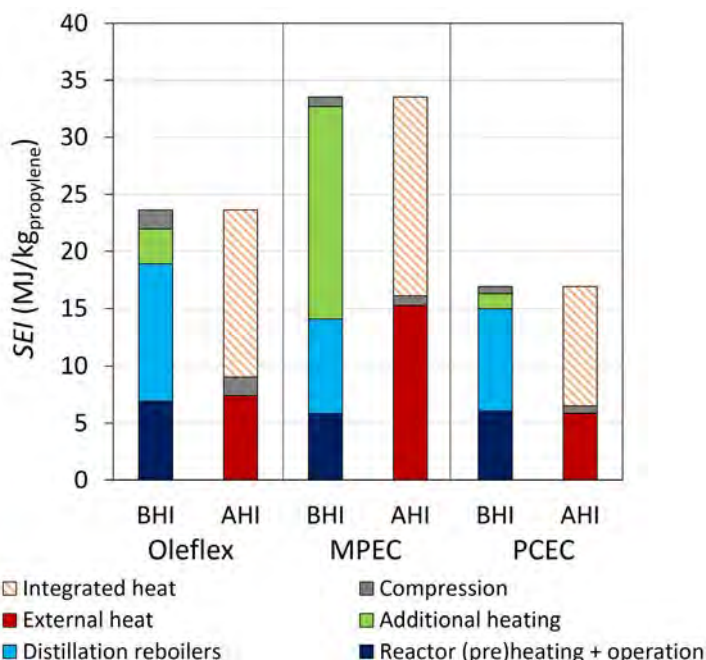
Figure 5.6: Specific energy input (*SEI*) for the three different processes before heat integration (BHI) and after heat integration (AHI).

In the Oleflex process, about 66% of the total energy requirement can be covered by heat integration, i.e. by a combination of off-gas heat and heat exchanged between hot and cold process streams (**Figure 5.6**). The available off-gas heat is more limited for the MPEC and PCEC processes, because of smaller process streams. Also, the amount of heat that can be exchanged within the steam sweep gas cycle is limited, as the concerning steam condensation and water evaporation occur to a large extent around the same temperature range (**Supporting Information 5.J5**). The remaining external energy amount after applying the heat integration measures (i.e. external heat + compression), is the lowest for the PCEC process with 6.5 MJ/kg$_{propylene}$, compared to Oleflex (9.1 MJ/kg$_{propylene}$) and MPEC (16.1 MJ/kg$_{propylene}$).

5.4.2.   Process utilities

For the process utility assessment, two different cases were considered: (i) one in which the reactors were heated in a fossil manner by burning natural gas, and (ii) one in which the reactors were operated using electrical heating. In case of electrical heating, all steps in and around the dehydrogenation reactors were driven electrically. This encompasses the heat needed for the dehydrogenation reaction itself and the heating requirements for pre-heating the hydrocarbon feed, the water/steam cosupply, the steam sweep gas, as well as the air supply to the regenerator. A complete breakdown of the utilities per unit operation is available as **Supporting Information 5.O**.

Figure 5.7 shows that the utility costs were clearly lower after heat integration for all cases. Before heat integration, utility costs were the highest for the MPEC process for both heating methods. This was attributed to the high heating and cooling demand of the steam sweep gas cycle. Notably, before heat integration the electrical heating cases were all more costly than the fossil counterpart, as the considered electricity price (76 USD/MWh) was higher than the natural gas price (22 USD/MWh). The opposite trend was observed after heat integration, when the heat from expensive electricity was replaced by a combination of off-gas heat and internal process heat. For the electrified Oleflex (E-Oleflex) and electrified PCEC (E-PCEC) process cases, the complete electricity demand could be covered by the available off-gas heat and internal process heat upon heat integration (**Figure 5.7**). In conclusion, utility costs were the lowest for the electrically heated PCEC process after heat integration, as the higher single-pass propylene yield results in smaller process streams and energy duties to be covered by utilities as compared to Oleflex.
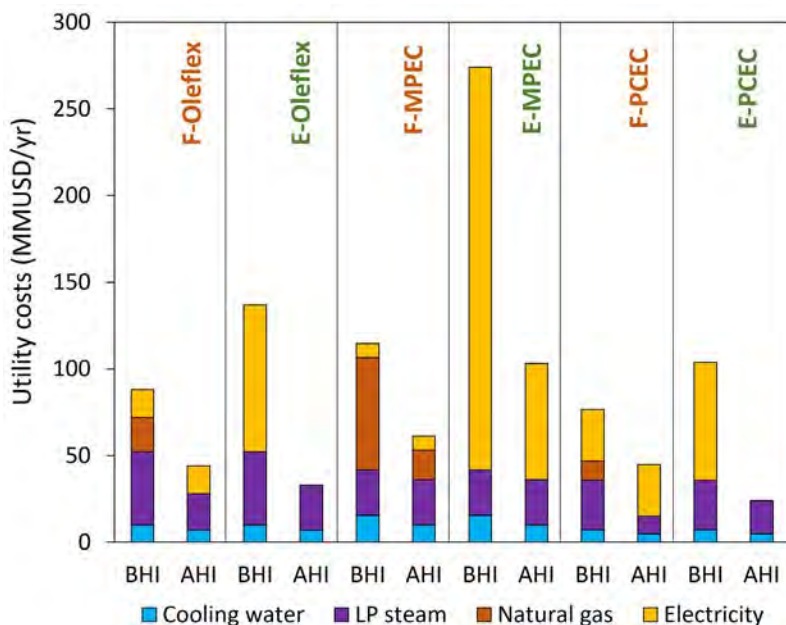
Figure 5.7: Utility costs of the three different processes before heat integration (BHI) and after heat integration (AHI) in case reactors were heated (i) by burning fossil natural gas (F) or (ii) by using electricity (E).

5.4.3. Process carbon dioxide footprint

In the evaluation of the carbon footprint of the different processes, a distinction was made between the usage of U.S. average (fossil) grid electricity (**Figure 5.8**) and fully renewable (green) electricity (**Figure 5.9**). A full breakdown of the carbon footprint outcomes is available in **Supporting Information 5.R2**. The carbon footprint of the traditional

fossil fuel heated Oleflex process as determined in this work (**Figure 5.8**) is in line with previous Oleflex process simulation studies (0.5-1.5 $kg_{CO2}/kg_{propylene}$) [5], and lower than the typical carbon footprint of naphtha crackers (1.8-2.0 $kg_{CO2}/kg_{propylene}$) [8].

In general, total carbon dioxide emissions were higher when U.S. average grid electricity was used (**Figure 5.8**) instead of green electricity (**Figure 5.9**), due to the high carbon intensity of U.S. grid electricity. Interestingly, when U.S. grid electricity was used (**Figure 5.8**), the total carbon footprint before heat integration of both membrane processes (F-MPEC, E-MPEC, F-PCEC, and E-PCEC) was similar or larger than conventional Oleflex (F-Oleflex and E-Oleflex). The cause for the large carbon footprint of the MPEC process was the high natural gas demand for steam sweep gas heating, whilst for the PCEC process the large carbon footprint was caused by the high electricity demand for driving hydrogen permeation. Also, electrification of all studied cases (F to E-case) increased the carbon emissions before heat integration, as direct heating using natural gas was environmentally friendlier than indirect heating with electricity generated using fossil resources.
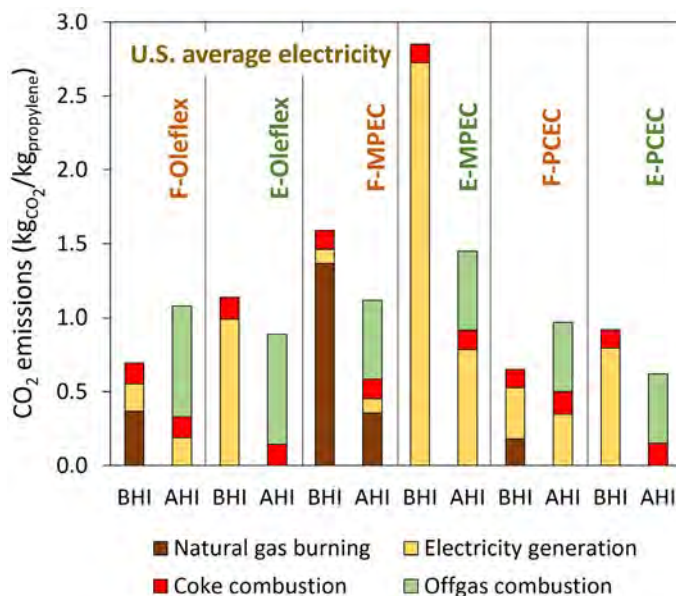
Figure 5.8: Carbon dioxide emissions of the different processes before heat integration (BHI) and after heat integration (AHI) in case reactors were heated (i) by burning fossil natural gas (F) or (ii) by electrical heat (E), considering fossil U.S. average electricity.

When fully renewable electricity was used (**Figure 5.9**), the situation before heat integration (BHI) led to much lower carbon emissions for all three processes. The carbon dioxide emissions before heat integration of the green electrified processes (**Figure 5.9**) were a factor four to eight lower compared to the same process cases electrified with fossil electricity (**Figure 5.8**). This emphasizes that fully renewable electricity needs to be used in membrane-assisted processes to possibly outperform conventional Oleflex in terms of

carbon intensity. The largest improvement in carbon footprint relative to fossil Oleflex as it is currently operated in industry (0.69 $kg_{CO2}/kg_{propylene}$ of F-Oleflex in **Figure 5.8**) was achieved for the green electrified PCEC process (0.23 $kg_{CO2}/kg_{propylene}$ of E-PCEC) BHI in **Figure 5.9** with approximately 65% less carbon dioxide emissions. However, it is remarkable to see that the total carbon footprint of the green electrified PCEC process BHI was about equal to that of the green electrified Oleflex (E-Oleflex) process (**Figure 5.9**), implying that electrifying Oleflex led to the same sustainability improvement as industrial implementation of PCEC membranes.
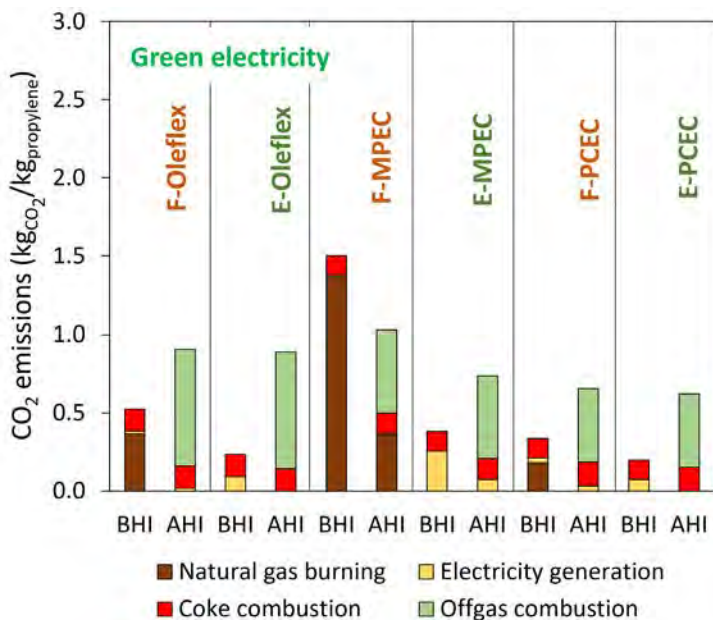
Figure 5.9: Carbon dioxide emissions of the three different processes before heat integration (BHI) and after heat integration (AHI) in case reactors were heated (i) by burning fossil natural gas (F) or (ii) by using electricity (E), considering fully renewable electricity.

The trends in carbon footprint changed after applying the heat integration measures, which included the heat exchanged between hot and cold process streams and the heat generated upon combusting off-gas streams. The MPEC process benefitted from efficient use of off-gas heat and heat exchange between the steam sweep gas stream toward and from the MPEC membrane reactor, leading to a smaller carbon footprint when fossil heat and/or fossil electricity was used. On the contrary, for the Oleflex and PCEC processes, where less heat could be exchanged between process streams (**Supporting Information 5.J**), the carbon footprint after heat integration was predominantly governed by off-gas heat (**Figure 5.9**). The carbon dioxide emissions of the Oleflex and PCEC processes generally increased upon replacing natural gas heat by off-gas heat (F-Oleflex and F-PCEC

in **Figure 5.9**). The amount of energy generated per mole of carbon dioxide was higher for the combustion of methane (0.89 MJ/mol$_{CO2}$) than for the combustion of *n*-butane (0.71 MJ/mol$_{CO2}$) or ethane (0.78 MJ/mol$_{CO2}$) from the depropanizer heavies and deethanizer lights streams, respectively. In other words, more carbon dioxide was emitted when using ethane and/or *n*-butane as fuel to generate the required amount of process energy as compared to methane. Moreover, when renewable electricity was targeted it was environmentally very disadvantageous to use the off-gas energy to cover part of the green electrical heating duty, leading to increased carbon footprints after heat integration for all Oleflex and PCEC cases in **Figure 5.9**. It was, thus, recommendable to sell the off-gas streams at fuel value rather than using them for internal heat integration in order to minimize the process carbon footprint.

5.4.4. Process economics

5.4.4.1. Capital expenditures

To make a fair comparison between the studied process cases before and after heat integration the costs of the heat exchangers required for implementation of the heat integration measures were included. It has been demonstrated by Agarwal et al. [5], while studying heat integration and process intensification of the Oleflex process, that the total capital investment of the Oleflex process did not change after heat integration. This was caused by the fact that the costs for the additional heat exchangers were offset by a reduction in costs for fired heaters and reactor effluent coolers. Since the composite curves of the PCEC process were similar to Oleflex in terms of relative heat to be exchanged (**Supporting Information 5.J**), the capital investment of the PCEC process was also assumed to be the same before and after heat integration. On the contrary, the hot and cold composite curves of the MPEC process showed a larger overlap, implying that a larger fraction of utilities could be saved (**Figure 5.7**) by installing additional heat exchangers.

The total capital investment of the MPEC process was found to be a factor eighteen times the Oleflex process capital investment (**Table 5.4** and **Supporting Information 5.N**). This was attributed to the extremely large membrane area required for the MPEC process, caused by the rather low hydrogen permeability. The costs for e.g. the steel housing, the heating mantles, and the MPEC stack materials all scale with the required membrane area, while also related installation and maintenance costs were traditionally estimated as fractions of the purchase equipment costs. The hydrogen flux through the MPEC membrane was estimated in this study at 0.03 μmol H_2/cm^2.s, which is valid for a ca. 30 μm thick electrolyte [65]. This flux is ca. 100 times lower than the hydrogen flux through PCEC membranes for equal electrolyte thicknesses. Thus, the MPEC membrane performance needs to be considerably improved, either by increasing the intrinsic hydrogen permeability or by improving the mechanical stability of very thin MPEC membranes, to brighten its industrial perspective. Moreover, one needs to realize that the mentioned hydrogen fluxes were experimentally obtained at higher temperatures (700-

900 °C) and in systems where a hydrogen-rich feed stream was supplied [65]. Particularly for MPEC membranes, these hydrogen fluxes are therefore a highly optimistic approximation, as in reality feed side hydrogen partial pressures and, thus, the driving force for permeation will be much lower.

Table 5.4: Capital costs of the Honeywell UOP Oleflex, MPEC-assisted, and PCEC-assisted propane NODH processes, before heat integration (BHI) and after heat integration (AHI).

Equipment type	Capital cost (MMUSD, 2023)			
	Oleflex process	MPEC process		PCEC process
		BHI	AHI	
Reactors	49	7,386	7,386	74
Distillation columns	183	149	149	150
Fired heaters	20	8	8	8
Pumps + compressors + expanders	79	81	81	57
Heat exchangers	109	143	115	76
Total direct investment (=ISBL*)	***440***	***7,768***	***7,739***	***366***
OSBL** costs (=40% of ISBL*)	176	3,107	3,096	146
Engineering + contingency costs (=25% of ISBL* + OSBL**)	154	2,719	2,709	128
Total fixed capital investment	**771**	**13,593**	**13,543**	**641**

*ISBL = Inside battery limits, **OSBL = Outside battery limits.*

The total capital investment of the PCEC process was about 20% lower than Oleflex (**Table 5.4**). This was due to lower investments in distillation columns, fired heaters, pumps, compressors, and heat exchangers. These unit operations and connected process streams were all considerably smaller compared to Oleflex, as a result of a smaller recycle, caused by a higher single-pass propylene yield in the PCEC process (50%) as compared to Oleflex (36%). Also, compressor costs were lower for the PCEC process, because of *in situ* dehydrogenation and hydrogen compression. Interestingly, the PCEC membrane reactor costs were only marginally higher than for conventional Oleflex, as Oleflex reactor investments are also substantial due to the combination of four sequential moving bed reactors and a regeneration unit.

The heat exchanger investment of the MPEC process reduced significantly after heat integration. The costs for the additional steam sweep gas heat exchanger were overcompensated by a reduction in capital investment of the individual steam sweep gas fired heater and cooler. Notwithstanding the reduction in heat exchanger investment after

heat integration, the financial attractiveness of the MPEC process was not improved, as its CAPEX was dominated by the membrane reactor costs.

5.4.4.2. Operating expenditures

The operating expenditures (OPEX) were evaluated for all three processes (**Figure 5.10**) considering a carbon tax that corresponds to the use of fully renewable electricity. The operational costs of the MPEC process were a factor three times the Oleflex and PCEC OPEX (**Figure 5.10**). In particular, the membrane, fixed production, and depreciation costs were all comparably high. This was all attributed to the higher membrane reactor capital investment of the MPEC process. Maintenance and periodic equipment replacement costs, which were part of the fixed production costs, were traditionally estimated as a percentage of the capital investment. Since the MPEC process had a large capital investment (**Table 5.4**), also the fixed production costs were substantial. Moreover, the expensive MPEC membrane equipment depreciates rapidly over time, leading to a high depreciation contribution to the OPEX in **Figure 5.10**. Nevertheless, even without depreciation and fixed production costs the MPEC process was not profitable in any of the cases, following the crossing of the revenues line with the stacked operating costs. Note that the total revenues were higher for all cases before heat integration (BHI) compared to after heat integration (AHI), as the off-gas streams were sold at fuel value in the case that they were not used for heat integration.

In contrast to the MPEC process, the total production costs of the PCEC process were about 5-10% lower than Oleflex in all cases (**Figure 5.10**). This was ascribed to lower raw material costs and lower utility costs (**Figure 5.7**). Raw material costs were lower for the PCEC process than for the Oleflex process due to the fact that a smaller fraction of the propane feed ends up in the off-gas streams for the PCEC process, which is a result of the higher single-pass propylene yield and the integration of the dehydrogenation reaction and hydrogen separation in the PCEC reactor. The Oleflex and PCEC process were profitable in all cases after applying heat integration measures (**Figure 5.10**). It should be noted that an electricity price of 76 USD/MWh was included in the utility costs of all cases studied in **Figure 5.10**, notwithstanding the fact that renewable electricity is generally cheaper [73]. The profitability of electrified Oleflex and PCEC processes with respect to their fossil alternatives would be further enhanced if the electricity price would become lower than the natural gas price per MWh (see **Supporting Information 5.S2**). See **Supporting Information 5.P** for further details on the OPEX calculations.
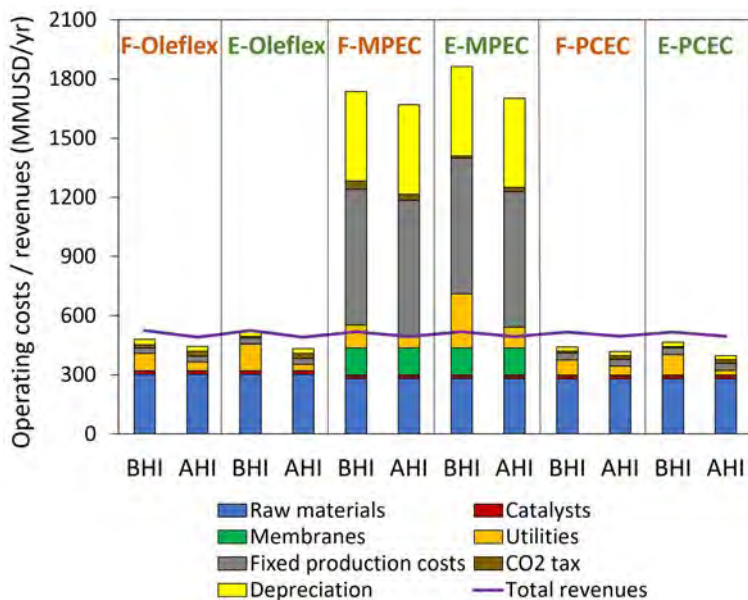
Figure 5.10: Comparison of the operating expenditures and revenues of the Oleflex, MPEC-assisted, and PCEC-assisted propane NODH process before heat integration (BHI) and after heat integration (AHI), in case the heating was performed (i) by burning fossil resources (F), or (ii) by using electricity (E), considering a carbon tax of 65 USD/t$_{CO2}$ and based on green electricity.

The profitability of the Oleflex and PCEC processes was further quantified in terms of payback period and return on investment (*ROI*). The MPEC process was excluded from this analysis, as capital and operating expenditures for this process were too high to ever become a profitable process, as shown in **Table 5.4** and **Figure 5.10**. **Table 5.5** and **5.6** show that the PCEC process was more profitable than conventional Oleflex with shorter payback times and higher returns on investment in case of fossil fuel based reactor heating as well as in case of electrical heating. **Figure 5.10** and **Table 5.6** show that the electrified Oleflex process before heat integration was not financially viable, because of high utility costs. **Table 5.5** and **5.6** also show that the processes based on green electricity were in principle more attractive than the fossil electrified processes, due to lower carbon taxes. However, upon heat integration for the electrically heated Oleflex and PCEC processes, the electricity demand could be fully covered by burning off-gas streams. As a result, the carbon tax became independent of the type of electricity used, leading to equal payback times and *ROI*s in **Table 5.6**. Ultimately, the most profitable process was the electrified and heat integrated PCEC process with a payback period of eight years compared to eighteen for Oleflex (**Table 5.6**). Nonetheless, the use of off-gas heat as a replacement of green electricity in the E-PCEC process led to a substantial increment in carbon dioxide emissions (**Figure 5.9**), which made implementation of off-gas recovery

as heat integration measure environmentally undesired when fully renewable electricity was targeted for heating.

Table 5.5: Profitability of the Oleflex and PCEC process, before heat integration (BHI) and after heat integration (AHI), in case heating was operated by burning fossil natural gas (F), considering either U.S. average electricity or green electricity.

	Fossil fuel heated reactors			
	F-Oleflex		F-PCEC	
	BHI	AHI	BHI	AHI
U.S. average electricity:				
Payback time (yr)	24	25	13	12
ROI (%)	3.6	3.4	6.9	7.1
Green electricity:				
Payback time (yr)	22	22	11	11
ROI (%)	4.0	3.9	7.9	8.1

ROI = return on investment.

Table 5.6: Profitability of the Oleflex and PCEC process, before heat integration (BHI) and after heat integration (AHI), in case heating was operated by using electricity (E), considering either U.S. average electricity or green electricity.

	Electrically heated reactors			
	E-Oleflex		E-PCEC	
	BHI	AHI	BHI	AHI
U.S. average electricity:				
Payback time (yr)	-	18	27	8
ROI (%)	-2.4	4.9	3.2	10.5
Green electricity:				
Payback time (yr)	206	18	16	8
ROI (%)	0.4	4.9	5.4	10.5

ROI = return on investment.

5.4.5.   Industrial perspective and guidelines

The results in this study showed that the MPEC-assisted propane dehydrogenation process could not compete with the Honeywell UOP Oleflex and PCEC processes for propylene production in terms of carbon emissions (**Figure 5.9**) and profitability (**Figure 5.10**). This was particularly caused by the high membrane reactor capital investment and the high sweep gas heating demand, which were both related to the poor hydrogen permeation fluxes through MPEC membranes. To possibly become cost-competitive, the MPEC hydrogen permeation flux should be increased with a factor of ca. 100, meaning from ca. 0.03 µmol/s.cm^2 to the PCEC hydrogen flux of ca. 3 µmol/s.cm^2. This could be achieved by drastically reducing the required MPEC thickness, in combination with modifications of intrinsic MPEC material properties to increase hydrogen permeability. To this end, extremely thin (ca. 1-5 µm) and stable membranes need to be developed, in combination

with efficient surface catalysts capable of matching surface exchange and bulk diffusion rates. Still, MPEC membranes are unfavored for membrane extractor configurations in which hydrogen needs to be removed from the reaction zone, since the driving force for hydrogen permeation decreases upon hydrogen removal.

In contrast to the MPEC-assisted process, the PCEC-assisted process was financially and ecologically competitive to conventional Oleflex, as illustrated in **Figure 5.9** and **Table 5.5** and **5.6**. However, several challenges related to market conditions and technological performance of PCEC reactors need to be addressed before PCEC systems could be implemented industrially. The first challenge is related to the stability of PCEC systems. The potential shift in propane dehydrogenation equilibrium induced by PCEC membranes was mimicked in this study by simulating the PCEC process with a higher single-pass propylene yield (50%) than the Oleflex process (ca. 36%). However, an increment in olefin yield by removing hydrogen is anticipated to boost propylene conversion and coke formation [74], putting a restriction on the stability of PCECs. In this work, a 40% overdesign on the required membrane surface area was yet included to have sufficient regeneration capacity but a larger capacity could be needed in practice. Besides, the lifetime of the PCEC membranes was assumed to be equal to the lifetime of the dehydrogenation catalyst, i.e. two years. A hopeful sign is that a sensitivity analysis revealed that the profitability of the PCEC process remained more or less unaffected even if the membrane replacement frequency needs to be increased from every two years to every two months (see **Supporting Information 5.S3**). Herein, only stack material replacement was considered and a total downtime of ca. 15 days per year was taken into account, irrespective of the replacement frequency. Nevertheless, experimental confirmation of the PCEC stability under hydrogen removal rates and olefin yields needed to industrially outcompete conventional Oleflex is currently missing to justify industrialization of PCEC membranes for alkane dehydrogenation. This study revealed that a propylene yield of 50% in combination with a hydrogen removal fraction of 95% would be a reasonable starting point for future confirming PCEC research. Besides, the steam cosupply that is needed to attain optimal PCEC performance could assist in minimizing coke formation.

Next to the PCEC stability, also the hydrogen permeation flux through PCECs for a given combination of temperature, current density, area specific resistance (*ASR*), and feed-to-permeate side pressure ratio needs to be proven. In this simulation study, the hydrogen permeation flux through the PCEC membrane was estimated to be about 3.3 μmol/s.cm^2, as obtained by Malerød-Fjeld et al. [23] for BZCY-based PCECs at 800 °C for a current density of 0.5 A/cm^2 and an *ASR* of 0.4 Ω.cm^2. This flux value was assumed to be valid here for 600 °C operation with a current density of 1.0 A/cm^2 and the same *ASR*. Experimental evidence of PCEC performance at temperatures suitable for integration with alkane dehydrogenation reactions (i.e. 500-700 °C) is required to confirm the potential of PCEC membranes in this field. An additional advantage of operation at lower temperatures is the thermodynamic mitigation of carbon deposition and, thereby, of coke-induced PCEC

deactivation. However, higher voltages need to be applied across the PCEC membrane when operating at lower temperatures to attain a given hydrogen permeation flux.

Another challenge is related to the large scale propylene production facilities to which PCEC systems have to be implemented. Commercial propane dehydrogenation plants have a typical production capacity between 450 and 750 ktpa [15]. Consequently, PCECs need to become available in substantial amounts to meet the industrial demand. This introduces a restriction to the applicable PCEC compositions. For example, the applied PCEC structures should contain elements that are abundantly available. Furthermore, an additional research field that needs to be explored is related to recycling of the PCECs, as PCEC elements should be sustainably recoverable at the end of lifetime. Ideally, coke removing regeneration methods are sufficient to fully recover catalyst and membrane performance. However, if frequent PCEC replacement appears to be needed, it could be essential to focus on extraction routes to recover individual PCEC elements, similar to e.g. the recovery of catalyst elements in the hydroprocessing industry [75]. Next to the PCEC disposal, the methods for assembling the PCEC systems and for synthesizing the PCEC electrode and electrolyte materials need to be sustainable and scalable.

This study illustrated that fully renewable electricity is required in electrified PCEC-assisted propane dehydrogenation as well as in electrified Oleflex to outcompete conventional fossil fuel heated Oleflex in terms of carbon dioxide emissions (**Figure 5.9** vs. **Figure 5.8**). This implies that renewable electricity needs to be continuously available for operating the propylene production facilities, which presents a challenge if e.g. intermittent wind or solar power are targeted as renewable electricity source. Besides, electricity grids around propylene plants should be capable of meeting the great electricity demand of electrified production processes. These infrastructural prerequisites are essential not only for PCEC integrated chemical processes but for all electrified chemical plants.

Based on the outcomes of this study a set of guidelines can be outlined, related to e.g. electricity price, carbon intensity of electricity, and carbon taxation, where one should adhere to when targeting for industrial PCEC implementation and/or process electrification. To stimulate electrification of the chemical industry, electrical heat should become cheaper than fossil fuel-based heat. This specifically means for this study that the electricity price, which was 76 USD/MWh in the base case scenario, should become cheaper than the natural gas price of 22 USD/MWh to make electrified processes more profitable than their fossil alternatives, as illustrated in **Supporting Information 5.S2**.

Variations in the carbon intensity of the electricity utility, as presented in **Supporting Information 5.S4**, demonstrated that for the electrified Oleflex and PCEC processes the total process carbon footprint was lower after heat integration for an electricity carbon intensity of more than 300 kg_{CO2}/MWh. In that situation, it was enviromentally beneficial to combust the available off-gas streams for heating instead of using relatively fossil electrical heat. By contrast, when the carbon intensity of the electricity became lower than

250 kg$_{CO2}$/MWh the total process carbon footprint was lower before heat integration, such that it was ecologically friendlier to use electrical heat instead of incinerating available off-gas streams. **Supporting Information 5.S4** also showed that the largest reduction in carbon emissions can be achieved for the electrified Oleflex and PCEC processes when operated using wind powered electricity. In that case, the total carbon footprint can be reduced to ca. 0.15 kg$_{CO2}$/kg$_{propylene}$, which is a ca. 75% reduction in carbon emissions as compared to traditional fossil fuel heated Oleflex (ca. 0.69 kg$_{CO2}$/kg$_{propylene}$, **Figure 5.8**).

The influence of changes of the imposed carbon tax on the profitability of the different process cases, as presented in **Supporting Information 5.S5**, showed that all process cases suffered from increased carbon taxation when U.S. average electricity was utilized, as all these cases have significant carbon emissions (**Figure 5.8**). On the contrary, when green electricity was used, then the most profitable process for marginal carbon taxations (<250 USD/t$_{CO2}$) was the electrified PCEC process after heat integration, in which the great and expensive electricity demand was fully covered by incinerating off-gas streams. However, for carbon taxes above 250 USD/t$_{CO2}$ it was financially more attractive to use expensive green electricity for heating instead of the available but now heavily carbon penalized off-gas heat (**Supporting Information 5.S5**). A minimum carbon tax of 250 USD/t$_{CO2}$ is therefore suggested to stimulate electrification of PCEC-assisted propylene production processes.

Since there is a large difference between the cost of electricity (76 USD/MWh) and natural gas (22 USD/MWh) included in this analysis, one could wonder how large the carbon taxation should be to reach parity cost when targeting green electricity. This was estimated using a natural gas emission factor of 1.92 kg$_{CO2}$/m$^3_{NG}$, and a heating value of 31,670 kJ/m$^3_{NG}$. From this calculation, one realizes that a carbon tax of 247 USD/t$_{CO2}$ should be levied to make natural gas heating as expensive as green electricity, which is in line with the profitability assessment. However, green electricity generated via solar photovoltaics (40 USD/MWh) and onshore wind (33 USD/MWh) is yet significantly cheaper than 76 USD/MWh [76]. As a result, when using solely photovoltaics or solely onshore wind for electricity generation, a carbon tax of only 82 USD/t$_{CO2}$ and 50 USD/t$_{CO2}$, respectively, would be needed to make natural gas-based and green electrical heating equally expensive. Costs associated with the intermittency of wind and solar energy are not included in this reasoning.

The viability of PCEC-assisted propane dehydrogenation plants will strongly depend on the local market conditions. In this work, the different processes were considered to be constructed in the U.S. Gulf Coast region, because of the close vicinity of natural gas feedstock. However, the U.S. Gulf Coast is not the geographic location with the most renewable electricity. Currently, only ca. 21% of the electricity originates from renewable sources in the U.S., which is forecasted to grow to ca. 44% in 2050 [77]. In this regard, e.g. Canada, Europe, or the Asia-Pacific region could be more suitable for industrialization of electrified propylene production processes, as electricity grids with average shares of renewables of more than 50% can already be encountered in these regions [78].

Nevertheless, it should be noted that the profitability of propane dehydrogenation processes is also dependent on the difference between local propane and propylene prices and on e.g. the regional prices of steel and utilities. Also, locally imposed carbon taxes can play a pivotal role in deciding the most suitable places for process electrification and PCEC commercialization.

Apart from membrane-assisted propane NODH, the main green alternative routes for producing propylene encompass (i) propane oxidative dehydrogenation (ODH), (ii) methanol-to-propylene, and (iii) electrochemical CO_2 reduction. Propane ODH can be conducted using an oxidant cofeed [16] or via chemical looping systems with redox catalysts [79]. In the presence of an oxidant cosupply, there is a high risk of over-oxidizing the olefin product and of creating explosive atmospheres, which makes this route industrially unattractive [16]. Besides, the chemical looping route suffers from limitations related to the mechanical stability of the redox catalysts and the complexity of the reactor design [79]. The drawback of the methanol-to-propylene route is the limited financial margin between reactant and product prices to develop a profitable process, especially in comparison to e.g. propane dehydrogenation [5]. Electrochemical CO_2 reduction therefore seems to be the most promising alternative for green propylene production, as it has the clear advantage of having CO_2 as feedstock, potentially allowing for net zero emissions. However, electrochemical CO_2 reduction suffers from a low activity and selectivity, in combination with high reactor costs [80,81]. For this reason, significant performance improvements and proof-of-concept studies are needed to confirm the potential of this route. Electrochemical CO_2 reduction is thereby in a similar technological development stage as membrane-assisted propane NODH.

If all challenges related to the market conditions and the PCEC performance could be overcome, then commercializing PCEC systems could make propylene production processes considerably more sustainable. Propylene is a major bulk chemical with a market size of about 105 billion USD in 2022, which corresponds to about 105 million tons of propylene per year for the given propylene price of about 1,000 USD/t. The share of propylene production from on-purpose technologies, like propane NODH, is anticipated to grow to ca. 32% by 2027 [48]. For the current market size, this corresponds to about 34 million ton of propylene produced annually via on-purpose routes. This work showed that the PCEC process consumes about 30% less energy and emits about 65% less carbon dioxide than conventional Oleflex when green electricity is used. This corresponds to 8.6 MJ in energy saving and 0.45 kg of carbon dioxide emission reduction per kg of propylene produced. For 34 million ton of annual propylene production, this leads to yearly savings of approximately 300 petajoule in energy and 15 million tons of carbon dioxide emissions if PCEC membranes would be implemented in all industrial propane NODH plants. To rationalize these values, this corresponds to about 8% of the annual energy usage and about 30% of the yearly carbon dioxide emissions of New York City [82,83]. Green electrification of propane dehydrogenation processes can, therefore, significantly

contribute to the required reduction toward net zero greenhouse gas emissions in 2050, following sustainable development goal 13 on climate action of the United Nations [10].

The calculation methods applied in this study have a couple of limitations. For instance, the accuracy of the capital investment in this type of preliminary feasibility studies in ca. 10-30% [66]. This relatively low accuracy is related to the basic design of equipment and to the limited accuracy of the available cost data. Despite the equipment design efforts made in this work, more detailed design and cost estimations of the different unit operations, including quotation requests, would be needed to ascertain the total capital investment needed. Besides, drastic variations in e.g. steel costs or PCEC material costs could strongly impact the industrialization perspective of the PCEC process in relation to conventional Oleflex. Also, regional changes in raw material, product, and utility prices would greatly affect the profitability of the different processes, as illustrated e.g. by the electricity price sensitivity analysis in **Supporting Information 5.S2**. Even though these latter price changes would impact the payback period and *ROI* values, it is expected to not change the selection between the process alternatives, as the profitability of all processes will be similarly affected by this.

5.5. Conclusion

This work assessed the potential of ceramic proton-conducting membranes for propylene production by comparing the techno-economics of (i) a conventional Honeywell UOP Oleflex process, (ii) a mixed proton-electron conducting (MPEC) membrane-assisted process, and (iii) a proton-conducting electrolysis cell (PCEC) membrane-assisted process. The MPEC process was financially and environmentally not an attractive alternative, due to the extremely low hydrogen permeation fluxes. As a result, the MPEC reactor costs were exceedingly high. Also, the specific energy input of the MPEC process was about 40% higher compared to Oleflex, due to the large heating requirement of the sweep gas. This ultimately led to considerable carbon dioxide emissions, regardless of the usage of natural gas, off-gas, fossil electricity, or green electricity for heating.

In contrast to the MPEC process, the PCEC process could be an attractive alternative to traditional Oleflex. Energy savings were maximal for the PCEC process compared to Oleflex when moving from the 36% Oleflex propylene yield to a 50% propylene yield. The process streams and units were smaller for the PCEC process relative to Oleflex, due to a smaller process recycle, thanks to the higher single-pass propylene yield in the PCEC process. Consequently, the capital investment of the PCEC process was about 20% lower than Oleflex. In addition, the specific energy input of the PCEC process was about 30% lower than conventional Oleflex, because of lower heating, cooling, and reboiling duties. Moreover, the carbon footprint of the electrified PCEC process was the lowest of all cases but only if fully renewable electricity was utilized. Notably, electrification of the Oleflex process led to comparable savings in carbon dioxide emissions as industrial implementation of PCEC membranes.

The most profitable process was the green electrified and heat integrated PCEC process with a payback period of eight years compared to eighteen for Oleflex, due to the lower capital investments and utility costs. However, the use of off-gas heat as a replacement of green electricity in the E-PCEC process led to a substantial increment in carbon dioxide emissions, making implementation of off-gas recovery as a heat integration measure environmentally undesired when fully renewable electricity is targeted for heating. In short, the most profitable process was the electrified PCEC process after heat integration, whilst the processes with the lowest carbon footprint were the green electrified PCEC and Oleflex processes before heat integration. Sensitivity analyses revealed that the carbon intensity of the electricity should become lower than 250 kg_{CO2}/MWh and the carbon tax should become higher than 250 USD/t_{CO2} to discourage off-gas incineration and to stimulate the use of electrical heat.

References

1.   The Business Research Company. Propylene global market report 2023. https://www.thebusinessresearchcompany.com/report/propylene-global-market-report (accessed October 2023).

2.   Bidwai, S. Propylene market. https://www.precedenceresearch.com/propylene-market (accessed October 2023).

3.   Rabenhorst, R. On-purpose: what's driving new propane dehydrogenation projects in North America? https://rbnenergy.com/on-purpose-whats-driving-new-propane-dehydrogenation-projects-in-north-america (accessed June 2020).

4.   Data Bridge Market Research. Global propylene market - industry trends and forecast to 2032. https://www.databridgemarketresearch.com/reports/global-propylene-market (accessed January 2025).

5.   Agarwal, A., Sengupta, D. & El-halwagi, M. Sustainable process design approach for on-purpose propylene production and intensification. *ACS Sustain. Chem. Eng.* **6**, 2407–2421 (2018).

6.   Economic Plant - Business Magazine for Industrial Plant Engineering and Plant Operation. Increasing global demand for on-purpose production of propylene. https://www.economic-plant.com/18-news/70-increasing-global-demand-for-on-purpose-production-of-propylene.html (accessed December 2020).

7.   Boswell, C. On-purpose technologies ready to fill propylene gap. https://www.icis.com/explore/resources/news/2012/04/16/9549968/on-purpose-technologies-ready-to-fill-propylene-gap/ (accessed January 2025).

8.   Ren, T., Patel, M. & Blok, K. Olefins from conventional and heavy feedstocks: Energy use in steam cracking and alternative processes. *Energy* **31**, 425–451 (2006).

9.   Zimmermann, H. & Walzl, R. Ethylene. in *Ullmann's Encyclopedia of Industrial Chemistry* (Wiley-VCH Verlag GmbH & Co. KGaA, Weinheim, Germany, 2009). doi:https://doi.org/10.1002/14356007.a10_045.pub3.

10.   United Nations - Department of Economic and Social Affairs. The 17 goals. https://sdgs.un.org/goals (accessed December 2024).

11.   Monai, M., Gambino, M., Wannakao, S. & Weckhuysen, B. M. Propane to olefins tandem catalysis: a selective route towards light olefins production. *Chem. Soc. Rev.* **50**, 11503–11529 (2021).

12. Ballal, G. Propylene by olefin conversion processes - process economics program report 267C. *IHS Chemical Technical Report* https://cdn.ihs.com/www/pdf/RP267C-toc.pdf (accessed April 2024).

13. Jasper, S. & El-Halwagi, M. A techno-economic comparison between two methanol-to-propylene processes. *Processes* **3**, 684–698 (2015).

14. Ye, M., Tian, P. & Liu, Z. DMTO: A sustainable methanol-to-olefins technology. *Engineering* **7**, 17–21 (2021).

15. Marsh, M. & Wery, J. On-purpose propylene production. https://www.digitalrefining.com/article/1002264/on-purpose-propylene-production (accessed August 2023).

16. Bhasin, M. M., Mccain, J. H., Vora, B. V, Imai, T. & Pujad, P. R. Dehydrogenation and oxydehydrogenation of paraffins to olefins. *Appl. Catal. A: Gen.* **221**, 397–419 (2001).

17. Grasselli, R. K., Stern, D. L. & Tsikoyiannis, J. G. Catalytic dehydrogenation (DH) of light paraffins combined with selective hydrogen combustion (SHC) I . DH → SHC → DH catalysts in series (co-fed process mode). *Appl. Catal. A: Gen.* **189**, 1–8 (1999).

18. Sattler, J. J. H. B., Ruiz-Martinez, J., Santillan-Jimenez, E. & Weckhuysen, B. M. Catalytic dehydrogenation of light alkanes on metals and metal oxides. *Chem. Rev.* **114**, 10613–10653 (2014).

19. Nawaz, Z. Light alkane dehydrogenation to light olefin technologies: A comprehensive review. *Rev. Chem. Eng.* **31**, 413–436 (2015).

20. Polfus, J. M., Xing, W., Fontaine, M. L., Denonville, C., Henriksen, P. P. & Bredesen, R. Hydrogen separation membranes based on dense ceramic composites in the La27W5O55.5-LaCrO3 system. *J. Membr. Sci.* **479**, 39–45 (2015).

21. Gallucci, F., Fernandez, E., Corengia, P. & Sint, M. Van. Recent advances on membranes and membrane reactors for hydrogen production. *Chem. Eng. Sci.* **92**, 40–66 (2013).

22. Norby, T. & Haugsrud, R. Dense ceramic membranes for hydrogen separation. in *Nonporous Inorganic Membranes: for Chemical Processing* (eds. Sammells, A. F. & Mundschau, M. V.) 1–48 (Wiley-VCH Verlag GmbH & Co. KGaA, 2006).

23. Malerød-fjeld, H., Clark, D., Yuste-tirados, I., Zanón, R., Catalán-martinez, D., Beeaff, D., Morejudo, S. H., Vestre, P. K., Norby, T., Haugsrud, R., Serra, J. M. & Kjølseth, C. Thermo-electrochemical production of compressed hydrogen from methane with near-zero energy loss. *Nat. Energy* **2**, 923–931 (2017).

24. Meng, Y., Gao, J., Zhao, Z., Amoroso, J., Tong, J. & Brinkman, K. S. Review : recent progress in low-temperature proton-conducting ceramics. *J. Mater. Sci.* 9291–9312 (2019).

25. Ding, D., Zhang, Y., Wu, W., Chen, D., Liu, M. & He, T. A novel low-thermal-budget approach for the co-production of ethylene and hydrogen via the electrochemical non-oxidative deprotonation of ethane. *Energy Environ. Sci.* **11**, 1710–1716 (2018).

26. Wu, W., Wang, L. C., Hu, H., Bian, W., Gomez, J. Y., Orme, C. J., Ding, H., Dong, Y., He, T., Li, J. & Ding, D. Electrochemically engineered, highly energy-efficient conversion of ethane to ethylene and hydrogen below 550 °C in a protonic ceramic electrochemical cell. *ACS Catal.* **11**, 12194–12202 (2021).

27. Taylor, R. & Kooijman, H. Depropanizer. *ChemSep - Modeling Separation Processes* http://www.chemsep.org/downloads/data/CScasebook_Strigle_depropanizer.pdf (accessed April 2023).

28. O'Brien, J. V. Cryogenic separation process for the recovery of components from the products of a dehydrogenation reactor. (2001).

29. Bijani, P. M. & Sahebdelfar, S. Modeling of a radial-flow moving-bed reactor for dehydrogenation of isobutane. *Kinet. Catal.* **49**, 599–605 (2008).

30. U.S. Department of Energy - Office of Energy Efficiency and Renewable Energy. Effect of intake on compressor performance. *U.S. Department of Energy* https://research-hub.nrel.gov/en/publications/effect-of-intake-on-compressor-performance-industrial-technologie (accessed October 2023).

31. The Linde Group. Hydrogen recovery by pressure swing adsorption. *Technical report* https://assets.linde.com/-/media/global/engineering/engineering/home/products-and-services/process-plants/adsorption-and-membrane-plants/hydrogen-recovery-and-purification/ha_h_1_1_e_09_150dpi_nb.pdf (accessed October 2023).

32. Umo, A. M. & Bassey, E. N. Simulation and performance analysis of propylene-propane splitter in petroleum refinery case study. *Int. J. Chem. Eng. Appl.* **8**, (2017).

33. Chen, Y., Cheng, S., Chen, L., Wei, Y., Ashman, P. J. & Wang, H. Niobium and molybdenum co-doped La5.5WO11.25-d membrane with improved hydrogen permeability. *J. Membr. Sci.* **510**, 155–163 (2016).

34. Magrasó, A. & Haugsrud, R. Effects of the La/W ratio and doping on the structure, defect structure, stability and functional properties of proton-conducting

lanthanum tungstate La28-xW4+xO54+δ. A review. *J. Mater. Chem. A* **2**, 12630–12641 (2014).

35. Amsif, M., Magrasó, A., Marrero-López, D., Ruiz-Morales, J. C., Canales-Vázquez, J. & Núñez, P. Mo-substituted lanthanum tungstate La28-yW4+yO54+δ: A competitive mixed electron-proton conductor for gas separation membrane applications. *Chem. Mat.* **24**, 3868–3877 (2012).

36. Vøllestad, E., Vigen, C. K., Magrasó, A. & Haugsrud, R. Hydrogen permeation characteristics of La27Mo1.5W3.5O55.5. *J. Membr. Sci.* **461**, 81–88 (2014).

37. Cao, Y., Xiong, C., Jian, L., Vøllestad, E., Evans, A. & Haugsrud, R. Enhancement of the electron conductivity of La27(W0.85Nb0.15)5O55.5−δ by Mo doping for hydrogen permeation. *J. Electrochem. Soc.* **163**, F1151–F1156 (2016).

38. Magrasó, A. Transport number measurements and fuel cell testing of undoped and Mo-substituted lanthanum tungstate. *J. Power Sources* **240**, 583–588 (2013).

39. Magrasó, A., Frontera, C., Marrero-López, D. & Núñez, P. New crystal structure and characterization of lanthanum tungstate 'La6WO12' prepared by freeze-drying synthesis. *Dalton Trans.* **46**, 10273–10283 (2009).

40. Sun, S. & Huang, K. Efficient and selective ethane-to-ethylene conversion assisted by a mixed proton and electron conducting membrane. *J. Membr. Sci.* **599**, 117840 (2020).

41. Moon, K. & Kale, G. R. Energy analysis in combined reforming of propane. *J. Eng.* **2013**, 1–10 (2013).

42. Morejudo, S. H., Zanón, R., Escolástico, S., Yuste-Tirados, I., Malerød-Fjeld, H., Vestre, P. K., Coors, W. G., Martínez, A., Norby, T., Serra, J. M. & Kjølseth, C. Direct conversion of methane to aromatics in a catalytic co-ionic membrane reactor. *Science* **353**, 563–566 (2016).

43. Railsback, J., Choi, S. H. & Barnett, S. A. Effectiveness of dense Gd-doped ceria barrier layers for (La,Sr)(Co,Fe)O3 cathodes on yttria-stabilized zirconia electrolytes. *Solid State Ion.* **335**, 74–81 (2019).

44. Clark, D., Malerød-Fjeld, H., Budd, M., Yuste-Tirados, I., Beeaff, D., Aamodt, S., Nguyen, K., Ansaloni, L., Peters, T., Vestre, P. K., Pappas, D. K., Valls, M. I., Remiro-Buenamañana, S., Norby, T., Bjørheim, T. S., Serra, J. M. & Kjølseth, C. Single-step hydrogen production from NH3, CH4, and biogas in stacked proton ceramic reactors. *Science* **376**, 390–393 (2022).

45. Kee, B. L., Curran, D., Zhu, H., Braun, R. J., Decaluwe, S. C., Kee, R. J. & Ricote, S. Thermodynamic insights for electrochemical hydrogen compression with proton-conducting membranes. *Membranes* **9**, 77 (2019).

46.   Maddah, H. A. A comparative study between propane dehydrogenation (PDH) technologies and plants in Saudi Arabia. *American Scientific Research Journal for Engineering, Technology, and Sciences (ASRJETS)* **45**, 49–63 (2018).

47.   Eisele, P. & Killpack, R. Propene. *Ullmann's Encyclopedia of Industrial Chemistry* 281–293 (2012) doi:https://doi.org/10.1002/14356007.a22_211.pub2.

48.   Marsh, M. & Wery, J. Filling the propylene gap – shaping the future with on-purpose technologies. *Technical report.* https://www.hydrocarbonengineering.com/whitepapers/honeywell-uop/filling-the-propylene-gap-shaping-the-future-with-on-purpose-technologies/ (accessed September 2024).

49.   Rambert, O. & Febvre, L. The challenges of hydrogen storage on a large scale. https://www.h2knowledgecentre.com/content/conference3536 (accessed September 2024).

50.   Trading Economics. Propane. https://tradingeconomics.com/commodity/propane (accessed July 2023).

51.   Statista Research Department. Price of propylene worldwide from 2017 to 2022. *Bloomberg; Krungsri Research* https://www.statista.com/statistics/1170576/price-propylene-forecast-globally/ (accessed July 2023).

52.   PricewaterhouseCoopers. The green hydrogen economy - predicting the decarbonisation agenda of tomorrow. https://www.pwc.com/gx/en/industries/energy-utilities-resources/future-energy/green-hydrogen-cost.html (accessed July 2023).

53.   SGH2 Energy Global LLC. Economics - cost comparison. https://www.sgh2energy.com/economics (accessed July 2023).

54.   Worldometer. Natural gas reserves by country. https://www.worldometers.info/gas/gas-reserves-by-country/ (accessed July 2023).

55.   Our World in Data. Natural gas prices. https://ourworldindata.org/grapher/natural-gas-prices (accessed July 2023).

56.   U.S. Energy Information Administration. Maps: oil and gas exploration, resources, and production. https://www.eia.gov/maps/maps.htm (accessed July 2023).

57.   Diener, M. Sizing a cooling system to control process temperature. https://www.process-cooling.com/articles/88572-sizing-a-cooling-system-to-control-process-temperature?v=preview (accessed July 2023).

58. Wattco. The difference between low pressure and high pressure steam systems. https://www.wattco.com/2022/06/low-vs-high-pressure-steam-systems (accessed July 2023).

59. U.S. Department of Energy - Energy Efficiency and Renewable Energy. Benchmark the fuel cost of steam generation. https://www.energy.gov/eere/amo/articles/benchmark-fuel-cost-steam-generation (accessed April 2024).

60. Intratec Solutions LLC. Cooling water costs - cooling water current costs, historical series & forecasts. https://www.intratec.us/products/water-utility-costs/commodity/cooling-water-cost (accessed July 2023).

61. TLV - A Steam Specialist Company. Calculator - steam unit cost. https://www.tlv.com/global/TI/calculator/steam-unit-cost.html?advanced=on (accessed July 2023).

62. U.S. Energy Information Administration. Electric power monthly. https://www.eia.gov/electricity/monthly/epm_table_grapher.php?t=epmt_5_6_a (accessed July 2023).

63. Gómez-Quero, S., Tsoufis, T., Rudolf, P., Makkee, M., Kapteijn, F. & Rothenberg, G. Kinetics of propane dehydrogenation over Pt-Sn/Al2O3. *Catal. Sci. Technol.* **3**, 962–971 (2013).

64. CoorsTek Inc. Proton ceramic membranes for hydrogen production published in 'Science'. https://www.coorstek.com/en/news-events/news/proton-ceramic-membranes-for-hydrogen-production/ (accessed July 2023).

65. Chen, Y., Liao, Q., Li, Z., Wang, H., Wei, Y., Feldhoff, A. & Caro, J. A CO2 stable hollow-fiber membrane with high hydrogen permeation flux. *AIChE Journal* **61**, 1997–2007 (2015).

66. Towler, G. & Sinnott, R. Capital cost estimating. in *Chemical Engineering Design* 307–354 (Butterworth-Heinemann, 2013).

67. Maxwell, C. Cost indices. https://toweringskills.com/financial-analysis/cost-indices/ (accessed August 2023).

68. Towler, G. & Sinnott, R. Estimating revenues and production costs. in *Chemical Engineering Design* 355–387 (Butterworth-Heinemann, 2013).

69. Bray, S. Carbon taxes in Europe. https://taxfoundation.org/data/all/eu/carbon-taxes-in-europe-2022/ (accessed November 2023).

70. Tax Foundation. Corporate income tax. https://taxfoundation.org/taxedu/glossary/corporate-income-tax-cit/ (accessed November 2023).

71.   PricewaterhouseCoopers. United States - corporate - taxes on corporate income. https://taxsummaries.pwc.com/united-states/corporate/taxes-on-corporate-income (accessed November 2023).

72.   U.S. Environmental Protection Agency. eGRID summary tables 2019. https://www.epa.gov/sites/default/files/2021-02/documents/egrid2019_summary_tables.pdf (accessed August 2023).

73.   International Renewable Energy Agency (IRENA). *Renewable Power Generation Costs in 2022*.

74.   Schäfer, R., Noack, M., Kölsch, P., Stöhr, M. & Caro, J. Comparison of different catalysts in the membrane-supported dehydrogenation of propane. *Catal. Today* **82**, 15–23 (2003).

75.   Al-Sheeha, H., Marafi, M., Raghavan, V. & Rana, M. S. Recycling and recovery routes for spent hydroprocessing catalyst waste. *Ind. Eng. Chem. Res.* **52**, 12794–12801 (2013).

76.   Taylor, M., Al-Zoghoul, S. & Ralon, P. Renewable power generation costs in 2022. https://www.irena.org/Publications/2023/Aug/Renewable-power-generation-costs-in-2022 (accessed June 2024).

77.   U.S. Energy Information Administration. EIA projects that renewable generation will supply 44% of U.S. electricity by 2050. https://www.eia.gov/todayinenergy/detail.php?id=51698 (accessed January 2025).

78.   Enerdata. Share of renewables in electricity production. https://yearbook.enerdata.net/renewables/renewable-in-electricity-production-share.html (accessed January 2025).

79.   Oing, A., von Müller, E., Donat, F. & Müller, C. R. Material engineering solutions toward selective redox catalysts for chemical-looping-based olefin production schemes: A review. *Energy & Fuels* **38**, 17326–17342 (2024).

80.   Chauhan, R., Sartape, R., Minocha, N., Goyal, I. & Singh, M. R. Advancements in environmentally sustainable technologies for ethylene production. *Energy & Fuels* **37**, 12589–12622 (2023).

81.   Pappijn, C. A. R., Ruitenbeek, M., Reyniers, M.-F. & Van Geem, K. M. Challenges and opportunities of carbon capture and utilization: electrochemical conversion of CO2 to ethylene. *Front. Energy Res.* **8**, 557466 (2020).

82.   MacWhinney, R. & Klagsbald, O. Inventory of New York City greenhouse gas emissions in 2016. https://www.nyc.gov/assets/sustainability/downloads/pdf/publications/GHG%

20Inventory%20Report%20Emission%20Year%202016.pdf (accessed May 2024).

83.   Knoema. New York - total energy consumption. https://knoema.com/atlas/United-States-of-America/New-York/Energy-consumption (accessed May 2025).

84.   Lide, D. R. Fluid properties. in *CRC Handbook of Chemistry and Physics* 6–103 (Boca Raton, FL, 2005).

85.   Brown, M., Murugan, A. & Foster, S. Hydrogen purity - final report. https://static1.squarespace.com/static/5b8eae345cfd799896a803f4/t/5e58ebfc 9df53f4eb31f7cf8/1582885917781/WP2+Report+final.pdf (accessed March 2023).

86.   Andersson, J. & Grönkvist, S. Large-scale storage of hydrogen. *Int. J. Hydrogen Energy* **44**, 11901–11919 (2019).

87.   Farjoo, A., Khorasheh, F., Niknaddaf, S. & Soltani, M. Kinetic modeling of side reactions in propane dehydrogenation over Pt-Sn/y-Al2O3 catalyst. *Scientia Iranica* **18**, 458–464 (2011).

88.   Li, Q., Sui, Z., Zhou, X. & Chen, D. Kinetics of propane dehydrogenation over Pt–Sn/Al2O3 catalyst. *Appl. Catal. A: Gen.* **398**, 18–26 (2011).

89.   Zhang, Y., Qi, L., Leonhardt, B. & Bell, A. T. Mechanism and kinetics of n-butane dehydrogenation to 1,3-butadiene catalyzed by isolated Pt sites grafted onto SiOZn-OH nests in dealuminated zeolite beta. *ACS Catal.* **12**, 3333–3345 (2022).

90.   van Sint Annaland, M., Kuipers, J. A. M. & van Swaaij, W. P. M. A kinetic rate expression for the time-dependent coke formation rate during propane dehydrogenation over a platinum alumina monolithic catalyst. *Catal. Today* **66**, 427–436 (2001).

91.   Farsi, M. Optimal condition of radial flow moving bed reactors to enhance isobutene production through heat coupling of isobutane dehydrogenation and nitrobenzene hydrogenation. *J. Nat. Gas Sci. Eng.* **19**, 295–302 (2014).

92.   Farsi, M., Jahanmiri, A. & Rahimpour, M. R. Steady state modeling and simulation of the Oleflex process for isobutane dehydrogenation considering reaction network. *Asia-Pac. J. Chem. Eng.* **8**, 862–869 (2013).

93.   Kareeri, A. A., Zughbi, H. D. & Al-Ali, H. H. Simulation of flow distribution in radial flow reactors. *Ind. Eng. Chem. Res.* **45**, 2862–2874 (2006).

94.   MetalMiner. Stainless Steel Price. https://agmetalminer.com/metal-prices/stainless-steel/ (accessed July 2023).

95.   Haugen, A. B., Aguilera, L. M., Kwok, K., Molla, T., Andersen, K. B., Pirou, S., Kaiser, A., Hendriksen, P. V. & Kiebach, R. Exploring the processing of tubular chromite-and zirconia-based oxygen transport membranes. *Ceramics* **1**, 229–245 (2018).

96.   Special Power Sources. A comprehensive comparison of planar and tubular solid oxide fuel cells. https://spsources.com/a-comprehensive-comparison-of-planar-and-tubular-solid-oxide-fuel-cells/ (accessed September 2024).

97.   Gallucci, F., Medrano, J. A., Fernandez, E., Melendez, J., van Sint Annaland, M. & Pacheco-Tanaka, D. A. Advances on high temperature Pd-based membranes and membrane reactors for hydrogen purification and production. *J. Membr. Sci. Res.* **3**, 142–156 (2017).

98.   Institute for Sustainable Process Technology. Amazing – Additive Manufacturing for Zero-Emission Innovative Green Chemistry. https://ispt.eu/projects/amazing/ (accessed July 2023).

99.   Harboe, S., Schreiber, A., Margaritis, N., Blum, L., Guillon, O. & Menzler, N. H. Manufacturing cost model for planar 5 kWel SOFC stacks at Forschungszentrum Jülich. *Int. J. Hydrogen Energ.* **45**, 8015–8030 (2020).

100.   CerPoTech. Barium cerium yttrium zirconate, BZCY. https://www.cerpotech.com/products/barium-cerium-yttrium-zirconate-bzcy (accessed August 2023).

101.   Dagde, K. K. & Puyate, Y. T. Modelling catalyst regeneration in an industrial FCC unit. *Am. J. Sci. Ind. Res.* **4**, 294–305 (2013).

102.   Towler, G. & Sinnott, R. Transport and storage of fluids. in *Chemical Engineering Design* 1207–1265 (Butterworth-Heinemann, 2013).

103.   Perez, R. X. An introduction to compressor selection (part 3 of 4). https://empoweringpumps.com/how-to-select-a-compressor-part3-compressor-selection (accessed August 2023).

104.   Towler, G. & Sinnott, R. Separation columns (distillation, absorption, and extraction). in *Chemical Engineering Design* 807–935 (Butterworth-Heinemann, 2013).

105.   Kolmetz, K. Design guidelines for propylene splitters efficiencies. *Engineering Practice* **4**, 8–19 (2018).

106.   Towler, G. & Sinnott, R. Separation of fluids. in *Chemical Engineering Design* 753–806 (Butterworth-Heinemann, 2013).

107. Zaini, M. S. M., Arshad, M. & Syed-Hassan, S. S. A. Adsorption isotherm and kinetic study of methane on palm kernel shell-derived activated carbon. *J. Bioresour. Bioprod.* **8**, 66–77 (2023).

108. Sorrels, J. L. Chapter 1 Carbon Adsorbers. https://www.epa.gov/sites/default/files/2018-10/documents/final_carbonadsorberschapter_7thedition.pdf (accessed June 2024).

109. Towler, G. & Sinnott, R. Design of pressure vessels. in *Chemical Engineering Design* 563–629 (Butterworth-Heinemann, 2013).

110. Industrial Metal Supply Co. Differences between carbon steel & stainless steel. https://www.industrialmetalsupply.com/blog/carbon-steel-vs-stainless-steel (accessed August 2023).

111. Thekdi, A., Nimbalkar, S., Keiser, J. & Storey, J. Preliminary results from electric arc furnace off-gas enthalpy modeling. 1–15 https://www.osti.gov/servlets/purl/1221728 (accessed February 2024).

112. The Engineering ToolBox. Fuels - higher and lower calorific values. https://www.engineeringtoolbox.com/fuels-higher-calorific-values-d_169.html (accessed February 2024).

113. Trading Economics. Propane. https://tradingeconomics.com/commodity/propane (accessed July 2023).

114. Chemical Catalysis for Bioenergy Consortium (ChemCatBio). CatCost. https://catcost.chemcatbio.org/ (accessed September 2023).

115. Baksh, M., Safdar, A. & Rosinski, A. C. Continuous feed three-bed pressure swing adsorption system. (2005).

116. IndexBox Inc. U.S. - activated carbon - market analysis, forecast, size, trends and insights. https://www.indexbox.io/blog/activated-carbon-price-per-ton-june-2022/ (accessed August 2022).

117. Intratec Solutions LLC. Butane price / current and forecast. https://www.intratec.us/products/energy-price-references/commodity/butane-price (accessed September 2023).

118. Intratec Solutions LLC. Ethane prices / current and forecast. https://www.intratec.us/chemical-markets/ethane-price (accessed September 2023).

119. U.S. Environmental Protection Agency. *Natural Gas Combustion.* https://www.epa.gov/air-emissions-factors-and-quantification/ap-42-fifth-edition-volume-i-chapter-1-external-0 (accessed August 2023).

120.   CO2emissiefactoren. Lijst emissiefactoren. https://www.co2emissiefactoren.nl/lijst-emissiefactoren/ (accessed July 2023).

121.   van der Niet, S. & Bruinsma, M. *Ketenemissies Elektriciteit - Actualisatie Elektriciteitsmix 2019*. https://ce.nl/publicaties/ketenemissies-elektriciteit-actualisatie-elektriciteitsmix-2019/ (accessed August 2024).

122.   Kilkovský, B. & Jegla, Z. Preliminary design and analysis of regenerative heat exchanger. *Chem. Eng. Trans.* **52**, 655–660 (2016).

123.   Nagano, Y. Micro-combustion calorimetry of coronene. *J. Chem. Thermodyn.* **32**, 973–977 (2000).

124.   REMAK. How a rotary regenerative heat exchanger works? https://www.remak.eu/en/how-rotary-regenerative-heat-exchanger-works (accessed July 2023).

Supporting Information

5.A. Feed and product specifications

The specifications of the targeted propylene product (**Supporting Information 5.A1**), the hydrogen product (**Supporting Information 5.A2**), and the fresh propane feed stream (**Supporting Information 5.A3**) are summarized here.

5.A1. Polymer grade propylene

The targeted propylene product was polymer grade propylene, which should satisfy the product specifications listed in **Table 5.A1** [47]. It was produced at 19 bar(a) pressure. Since the vapor pressure of propylene is about 11 bar(a) at 25 °C [84], propylene can be stored in liquid phase at ambient conditions at 19 bar(a).

Table 5.A1: Polymer grade propylene product specifications [47].

Compound:	Concentration:
Propylene (mol%)	99.5-99.8
Acetylene (mol ppm)	<2
Ethylene (mol ppm)	<20
Ethane (mol ppm)	<100
Propyne (mol ppm)	<5
Propadiene (mol ppm)	<5
C_{4+} (mol ppm)	<10
Hydrogen (mol ppm)	<10
Nitrogen (mol ppm)	<50
Oxygen (mol ppm)	<5
Carbon monoxide (mol ppm)	<5
Carbon dioxide (mol ppm)	<5
Sulfur (mass ppm)	<1
Water (mol ppm)	<10
Propane	remainder

5.A2. Internal combustion fuel grade A hydrogen

The targeted hydrogen product was internal combustion fuel grade A hydrogen, which needs to satisfy the specifications listed in **Table 5.A2** [85]. The hydrogen product was in the gas phase in the Oleflex and membrane-assisted processes and was considered to be stored in the gas phase after production. Compressed hydrogen gas is usually stored in aboveground vessels at pressures lower than 100 bar(a) due to vessel material constraints [86]. In spherical storage vessels the storage pressure is typically up to 50 bar(a) [49],

which was therefore taken as hydrogen product pressure in this work. In the MPEC and PCEC processes, the obtained hydrogen product was even more pure than the specifications listed in **Table 5.A2**, as the MPEC and PCEC membranes were assumed to be fully permselective. However, the potential higher value of the hydrogen product in the MPEC and PCEC processes relative to Oleflex was not included in the revenue calculations in this work.

Table 5.A2: Fuel grade A hydrogen specifications [85].

Compound:	Concentration:
H_2 (mol%)	98.0
Total hydrocarbon (mol ppm)	100
Combined water, O_2, N_2, and Ar (mol%)	1.9
Carbon monoxide (mol ppm)	1
Sulfur (mol ppm)	2

5.A3. Fresh propane feed

The fresh propane feed stream was derived from a natural gas processing plant and its typical composition is shown in **Table 5.A3** [46]. Such a stream generally also contains sulfur impurities [46]. However, the removal of these impurities was considered to be beyond the scope of this work, as these sulfur impurities are commonly removed in desulfurization pre-treatment steps. The costs, energy usage, and carbon footprint of these desulfurization units were consequently also excluded from this analysis. The pipeline pressure of the fresh propane stream was 5 bar(a).

Table 5.A3: Fresh propane feed stream specifications [46].

Compound:	Concentration:
Propane (mol%)	95
Ethane (mol%)	2.5
n-butane (mol%)	2.5

5.B. Propane NODH thermodynamic equilibrium

The theoretical influence of hydrogen removal on the thermodynamic equilibrium conversion of propane NODH at 1 bar(a) and 600 °C (**Figure 5.B1**) was constructed based on thermodynamic equilibrium data from Gómez-Quero et al. [63]. The hydrogen removal fraction is defined here as the ratio between the molar flow of H_2 removed divided by the molar flow of H_2 produced in the propane NODH reaction. **Figure 5.B1** shows that at 1 bar(a) and 600 °C the equilibrium conversion is about 50% in absence of any hydrogen removal; industrial propane NODH processes commonly operate around 40%-50% conversion [19]. It also shows that the most pronounced increment in conversion level can be achieved for hydrogen removal degrees of more than 80%. Also, full propane-to-

propylene conversion can theoretically be attained for 100% hydrogen removal under these conditions. In this work, the extent of hydrogen removal in the MPEC and PCEC membranes was set to 95%, corresponding to a propane NODH equilibrium yield of about 88% at 1 bar(a) and 600 °C. In **Supporting Information 5.S1**, it is explained why a single-pass propane NODH yield of 50% was selected in the MPEC and PCEC processes for 95% hydrogen removal, in spite of the theoretically much higher equilibrium yield of 88% that could be attained for this extent of hydrogen removal.
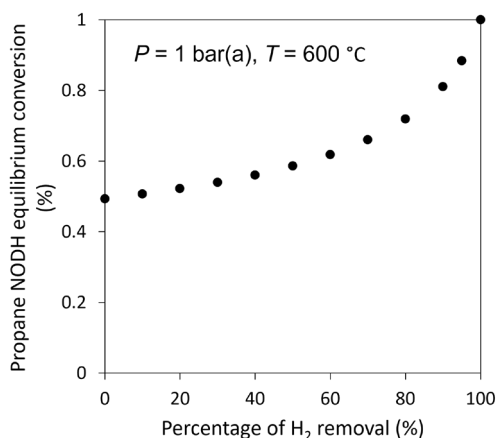
Figure 5.B1: Propane NODH thermodynamic equilibrium conversion as a function of percentage of hydrogen removal.

5.C. Process flow diagrams

The detailed process flow diagrams of the Oleflex process, MPEC-assisted process, and PCEC-assisted process are presented in **Supporting Information 5.C1**, **5.C2**, and **5.C3**, respectively. In all three processes, the coke model compound coronene was effectively separated from the reactor product stream using a component splitter in Aspen Plus (CS-1 in Oleflex and CS-2 in the MPEC and PCEC processes). In the Oleflex process, this step mimics the physical separation of moving bed catalyst particles, whilst for the MPEC and PCEC processes this step mimics the switch from operation mode to regeneration mode of the fixed bed membrane reactors.

The cold box technology that is part of the Oleflex process (**Supporting Information 5.C1**) was simulated in Aspen Plus using a sequence of cooling and expansion steps, as described in a patent about this technology [28]. The costs of the pressure changing, temperature changing, and phase separating unit operations that are part of the cold box were included in the capital investment assessment. However, the corresponding energy duties were not included in the heat integration analysis and energy usage assessment, as this cold box technology is known to be an auto-refrigeration method [5,28]. The pressure swing adsorption (PSA-1) that is applied in the Oleflex process to separate methane

impurities from the H_2 product, was simulated in Aspen Plus using a component splitter and an expander. The expander was used to mimic the pressure decrease of the methane retentate stream after applying the pressure swings between high pressure (methane adsorption) and low pressure (methane desorption).

The MPEC membrane reactor was simulated in Aspen Plus using four heaters, a stoichiometric reactor, two component splitters, and an expander (see **Supporting Information 5.C2**). The fired heater FH-1 heats the hydrocarbon feed stream. A separate heater (H-8) was used to heat the cosupplied H_2O, as this H_2O needs to be evaporated before mixing. The targeted fractional conversions of the MPEC reactor as described in **Section 5.3.3** were specified in the stoichiometric reactor. The two component splitters separate the H_2 from the hydrocarbons (CS-1) and the coronene from the other hydrocarbons (CS-2), respectively. The CS-1 unit represents the H_2 removal function of the MPEC membrane reactor, which was operated with a feed pressure of 4 bar(a) and a permeate side pressure of 1 bar(a). The pressure of the permeated H_2 stream therefore needs to be fictively reduced from 4 bar(a) to 1 bar(a) in an expander after separation in CS-1. As this expansion step is accompanied by a temperature reduction, an additional heater was needed to heat the permeated H_2 stream again to the reaction temperature of 600 °C. The H_2O sweep gas is only added to the permeated H_2 stream to (i) obtain an estimate of the duty for heating this sweep gas, and to (ii) obtain an estimate of the duty for cooling the H_2/H_2O permeate stream, including steam condensation.

In contrast to the MPEC process where the permeate stream is at atmospheric pressure, the permeate stream of the PCEC process is at elevated pressure, due to the *in situ* H_2 compression. To mimic this pressurization step in Aspen Plus, a compressor is used in the PCEC process flow diagram (**Supporting Information 5.C3**).

5.C1. Oleflex process
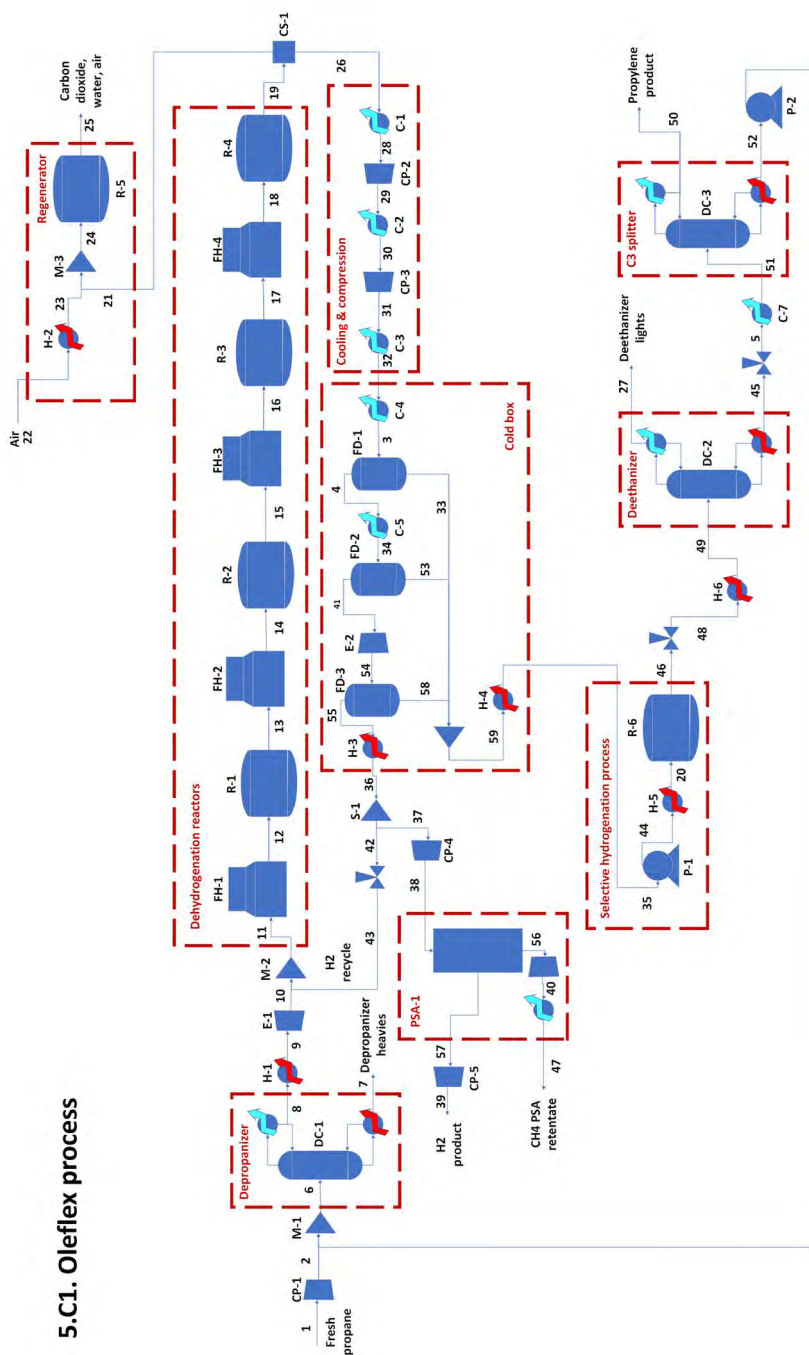
Stream table Oleflex process

Stream number	1	2	3	4	5	6	7	8	9	10	11	12	13	14	15	16	17	18	19	20
Vapor fraction	1	0	0.50	1	0.52	0.06	0	0	1	1	1	1	1	1	1	1	1	1	1	0
Temperature °C	25	40	-80	-80	51	43	56	42	75	39	36	600	532	600	533	600	534	600	535	40
Pressure bar(a)	5	15	14	14	19	15	15	15	15	5	5	5	4	4	3	3	2	2	1	40
Molar flow kmol/h	1642	1642	7395	3683	3536	3906	137	3770	3770	3770	5939	5939	6312	6312	6678	6678	7041	7041	7402	3762
Mole fractions:																				
Propane	0.95	0.95	0.29	0.01	0.61	0.95	0.70	0.96	0.96	0.96	0.61	0.61	0.51	0.51	0.43	0.43	0.36	0.36	0.29	0.58
Ethane	0.03	0.03	0.01	0.00	0.00	0.01	0	0.01	0.01	0.01	0.01	0.01	0.01	0.01	0.01	0.01	0.01	0.01	0.01	0.03
Methane	0	0	0.02	0.04	0	0	0	0.03	0.03	0.03	0.01	0.01	0.02	0.02	0.02	0.02	0.02	0.02	0.02	0.01
Propylene	0	0	0.19	0.01	0.39	0.03	0.00	0	0	0	0.02	0.02	0.07	0.07	0.11	0.11	0.16	0.16	0.19	0.38
Ethylene	0	0	0.00	0.00	0	0	0	0	0	0	0.00	0.00	0.00	0.00	0.00	0.00	0.00	0.00	0.00	0.01
Hydrogen	0	0	0.48	0.95	0	0	0	0	0	0	0.35	0.35	0.39	0.39	0.42	0.42	0.45	0.45	0.47	0.01
Coronene	0	0	0	0	0	0	0	0	0	0	0	0	0.00	0.00	0.00	0.00	0.00	0.00	0.00	0
n-butane	0.03	0.03	0	0	0	0.01	0.30	0.00	0.00	0.00	0.00	0	0	0	0	0	0	0	0	0
1,3-butadiene	0	0	0	0	0	0	0	0	0	0	0	0	0	0	0	0	0	0	0	0.00
Carbon monoxide	0	0	0	0	0	0	0	0	0	0	0	0	0	0	0	0	0	0	0	0
Carbon dioxide	0	0	0	0	0	0	0	0	0	0	0	0	0	0	0	0	0	0	0	0
Water	0	0	0	0	0	0	0	0	0	0	0	0	0	0	0	0	0	0	0	0
Oxygen	0	0	0	0	0	0	0	0	0	0	0	0	0	0	0	0	0	0	0	0
Nitrogen	0	0	0	0	0	0	0	0	0	0	0	0	0	0	0	0	0	0	0	0

Stream number	21	22	23	24	25	26	27	28	29	30	31	32	33	34	35	36	37	38	39	40
Vapor fraction	0	1	1	1	1	1	1	1	1	1	1	1	1	0.99	0.01	1	1	1	1	1
Temperature °C	535	20	600	574	600	535	25	40	57	40	58	40	-80	-110	-20	30	30	40	40	-44
Pressure bar(a)	1	1	1	1	1	1	1	1	1	1	1	1	14	14	6	6	6	20	50	3
Molar flow kmol/h	7	1014	1014	1021	1036	7395	226	7395	7395	7395	7395	7395	3712	3683	3762	3633	1464	1464	1436	28
Propane	0	0	0	0	0	0.29	0.08	0.29	0.29	0.29	0.29	0.29	0.58	0.01	0.58	0	0	0	0	0.00
Ethane	0	0	0	0	0	0.01	0.43	0.01	0.01	0.01	0.01	0.01	0.03	0.00	0.03	0.00	0.00	0.00	0	0.09
Methane	0	0	0	0	0	0.02	0.16	0.02	0.02	0.02	0.02	0.02	0.01	0.04	0.01	0.04	0.04	0.04	0.02	0.85
Propylene	0	0	0	0	0	0.19	0.16	0.19	0.19	0.19	0.19	0.19	0.38	0.01	0.38	0	0	0	0	0.00
Ethylene	0	0	0	0	0	0.00	0.10	0.00	0.00	0.00	0.00	0.00	0.01	0.00	0.01	0.00	0.00	0.00	0	0.06
Hydrogen	0	0	0	0	0	0.48	0.08	0.48	0.48	0.48	0.48	0.48	0.01	0.95	0.01	0.96	0.96	0.96	0.98	0
Coronene	1	0	0	0.01	0	0	0	0	0	0	0	0	0.01	0	0.01	0	0	0	0	0
n-butane	0	0	0	0	0	0	0	0	0	0	0	0	0	0	0	0	0	0	0	0
1,3-butadiene	0	0	0	0	0	0	0	0	0	0	0	0	0.00	0	0.00	0	0	0	0	0
Carbon monoxide	0	0	0	0	0	0	0	0	0	0	0	0	0	0	0	0	0	0	0	0
Carbon dioxide	0	0	0	0	0.02	0	0	0	0	0	0	0	0	0	0	0	0	0	0	0
Water	0	0	0	0	0.17	0	0	0	0	0	0	0	0	0	0	0	0	0	0	0
Oxygen	0	0.21	0.21	0.21	0.04	0	0	0	0	0	0	0	0	0	0	0	0	0	0	0
Nitrogen	0	0.79	0.79	0.79	0.78	0	0	0	0	0	0	0	0	0	0	0	0	0	0	0

Stream number		41	42	43	44	45	46	47	48	49	50	51	52	53	54	55	56	57	58	59	60
Vapor fraction		1	1	1	0	0	0	1	0	0	0	0	0	0	1	1	1	1	0	0	0
Temperature	°C	-110	30	30	-15	86	40	40	40	78	45	50	54	-110	-135	-135	40	40	-135	-80	54
Pressure	bar(a)	14	6	5	40	38	40	3	38	38	19	19	19	14	6	6	20	20	6	6	19
Molar flow	kmol/h	3638	2169	2169	3762	3536	3762	28	3762	3762	1272	3536	2264	44	3638	3633	28	1436	6	3762	2264
Propane		0.00	0	0	0.58	0.61	0.58	0.00	0.58	0.58	0.00	0.61	0.95	0.46	0.00	0	0.00	0	0.26	0.58	0.95
Ethane		0.00	0.00	0.00	0.03	0.00	0.03	0.09	0.03	0.03	0.00	0.00	0	0.09	0.00	0.00	0.09	0	0.30	0.03	0
Methane		0.04	0.04	0.04	0.01	0	0.01	0.85	0.01	0.01	0	0	0	0.02	0.04	0.04	0.85	0.02	0.03	0.01	0
Propylene		0.00	0	0	0.38	0.39	0.38	0.00	0.38	0.38	0.995	0.39	0.05	0.40	0.00	0	0.00	0	0.34	0.38	0.05
Ethylene		0.00	0.00	0.00	0.01	0	0.01	0.06	0.01	0.01	0	0	0	0.02	0.00	0.00	0.06	0	0.07	0.01	0
Hydrogen		0.96	0.96	0.96	0.01	0	0.01	0	0.01	0.01	0	0	0	0.00	0.96	0.96	0	0.98	0.00	0.01	0
Coronene		0	0	0	0	0	0	0	0	0	0	0	0	0	0	0	0	0	0	0	0
n-butane		0	0	0	0	0	0	0	0	0	0	0	0	0	0	0	0	0	0	0	0
1,3-butadiene		0	0	0	0.00	0	0	0	0	0	0	0	0	0	0	0	0	0	0	0.00	0
Carbon monoxide		0	0	0	0	0	0	0	0	0	0	0	0	0	0	0	0	0	0	0	0
Carbon dioxide		0	0	0	0	0	0	0	0	0	0	0	0	0	0	0	0	0	0	0	0
Water		0	0	0	0	0	0	0	0	0	0	0	0	0	0	0	0	0	0	0	0
Oxygen		0	0	0	0	0	0	0	0	0	0	0	0	0	0	0	0	0	0	0	0
Nitrogen		0	0	0	0	0	0	0	0	0	0	0	0	0	0	0	0	0	0	0	0

5.C2. MPEC process

Stream table MPEC process

Stream number		1	2	3	4	5	6	7	8	9	10	11	12	13	14	15	16	17	19	21	22
Vapor fraction		1	0.95	0.04	0	0	1	1	1	1	1	1	1	1	0	1	1	1	0	1	0
Temperature	°C	25	40	42	60	41	75	33	600	600	600	600	40	397	25	600	600	-10	30*	30*	600
Pressure	bar(a)	5	15	15	15	15	15	4	4	4	4	4	50	1	1	1	1	1	1	1	4
Molar flow	kmol/h	1525	1525	2879	98	2781	2781	2781	2781	4308	1350	2958	1350	1350	13701	15051	13701	13699	13699	1350	6
Mole fractions:																					
Propane		0.95	0.95	0.91	0.60	0.92	0.92	0.92	0.92	0.27	0	0.40	0	0	0	0	0	0	0	0	0
Ethane		0.03	0.03	0.01	0	0.01	0.01	0.01	0.01	0.01	0	0.02	0	0	0	0	0	0	0	0	0
Methane		0	0	0	0	0	0	0	0	0.01	0	0.02	0	0	0	0	0	0	0	0	0
Propylene		0	0	0.06	0.01	0.07	0.07	0.07	0.07	0.34	0	0.49	0	0	0	0	0	0	0	0	0
Ethylene		0	0	0	0	0	0	0	0	0.01	0	0.01	0	0	0	0	0	0	0	0	0
Hydrogen		0	0	0	0	0	0	0	0	0.33	1	0.02	1	1	0	0.09	0	0	0	1	0
Coronene		0	0	0	0	0	0	0	0	0.00	0	0.00	0	0	0	0	0	0	0	0	1
n-butane		0.03	0.03	0.01	0.39	0.00	0.00	0.00	0.00	0	0	0.00	0	0	0	0	0	0	0	0	0
1,3-butadiene		0	0	0.00	0.00	0	0	0	0	0	0	0.00	0	0	0	0	0	0	0	0	0
Carbon monoxide		0	0	0	0	0	0	0	0	0	0	0	0	0	0	0	0	0	0	0	0
Carbon dioxide		0	0	0	0	0	0	0	0	0	0	0	0	0	0	0	0	0	0	0	0
Water		0	0	0	0	0	0	0	0	0.02	0	0.03	0	0	1	0.91	1	0	1	0	0
Oxygen		0	0	0	0	0	0	0	0	0	0	0	0	0	0	0	0	1	0	0	0
Nitrogen		0	0	0	0	0	0	0	0	0	0	0	0	0	0	0	0	0	0	0	0

Stream number		23	24	25	26	27	28	29	30	31	32	34	35	36	39	40	41	42	43	44	45
Vapor fraction		1	1	1	1	1	0.72	1	1	1	1	0	1	0	0.51	0	0	0	1	1	1
Temperature	°C	600	20	600	583	600	30*	54	40	97	53	40	38	85	49	49	46	53	20	600	600
Pressure	bar(a)	4	1	1	1	1	4	14	14	38	19	38	38	38	19	19	19	19	4	4	4
Molar flow	kmol/h	2952	897	897	903	916	2952	2852	2852	2852	1354	2852	228	2624	2624	2624	1270	1354	100	100	2881
Mole fractions:																					
Propane		0.40	0	0	0	0	0.40	0.41	0.41	0.41	0.86	0.41	0.01	0.45	0.45	0.45	0.00	0.86	0	0	0.89
Ethane		0.02	0	0	0	0	0.02	0.02	0.02	0.02	0	0.02	0.28	0.00	0.00	0.00	0.00	0	0	0	0.01
Methane		0.02	0	0	0	0	0.02	0.02	0.02	0.02	0	0.02	0.22	0.55	0.55	0.55	0.996	0	0	0	0
Propylene		0.50	0	0	0	0	0.50	0.51	0.51	0.51	0.14	0.51	0.06	0	0	0	0	0.14	0	0	0.06
Ethylene		0.01	0	0	0	0	0.01	0.01	0.01	0.01	0	0.01	0.11	0	0	0	0	0	0	0	0
Hydrogen		0.02	0	0	0	0	0.02	0.02	0.02	0.02	0	0.02	0.31	0	0	0	0	0	0	1	0
Coronene		0	0	0	0.01	0	0	0	0	0	0	0	0	0	0	0	0	0	0	0	0
n-butane		0	0	0	0	0	0	0	0	0	0.00	0	0	0.00	0.00	0.00	0	0.00	0	0	0.00
1,3-butadiene		0.00	0	0	0	0	0.00	0.00	0.00	0.00	0.00	0.00	0	0.00	0.00	0.00	0	0.00	0	0	0
Carbon monoxide		0	0	0	0	0	0	0	0	0	0	0	0	0	0	0	0	0	0	0	0
Carbon dioxide		0	0	0	0	0.17	0.03	0	0	0	0	0	0	0	0	0	0	0	0	0	0
Water		0.03	0	0	0	0.04	0.03	0	0	0	0	0	0	0	0	0	0	0	0	0	0.03
Oxygen		0	0.21	0.21	0.21	0.02	0	0	0	0	0	0	0	0	0	0	0	0	1	0	0
Nitrogen		0	0.79	0.79	0.78	0.77	0	0	0	0	0	0	0	0	0	0	0	0	0	0	0

Stream number		46	47	48	49
Vapor fraction		1	0	1	1
Temperature	°C	40	30*	30*	40
Pressure	bar(a)	1	4	4	4
Molar flow	kmol/h	1350	100	2852	2852
Mole fractions:					
Propane		0	0	0.41	0.41
Ethane		0	0	0.02	0.02
Methane		0	0	0.02	0.02
Propylene		0	0	0.51	0.51
Ethylene		0	0	0.01	0.01
Hydrogen		1	0	0.02	0.02
Coronene		0	0	0	0
n-butane		0	0	0	0
1,3-butadiene		0	0	0.00	0.00
Carbon monoxide		0	0	0	0
Carbon dioxide		0	0	0	0
Water		0	1	0	0
Oxygen		0	0	0	0
Nitrogen		0	0	0	0

The function of flash drums FD-1 and FD-2 is to condense and separate the steam that is cosupplied to the feed side and sweep side of the MPEC membrane, respectively. These flash drums are simulated as component splitters in Aspen Plus operating at 30 °C and are assumed to fully separate the water content. In reality, the sweep side vapor stream (stream 21) and the feed side vapor stream (stream 48) would contain 3 mol% and 0.8 mol% of water, respectively, at 30 °C but these water concentrations are, thus, not included in this process analysis. In practice, industrial dryers could be needed to remove these last traces of water from the membrane effluent streams but this was considered to be beyond the scope of this work.

5.C3. PCEC process
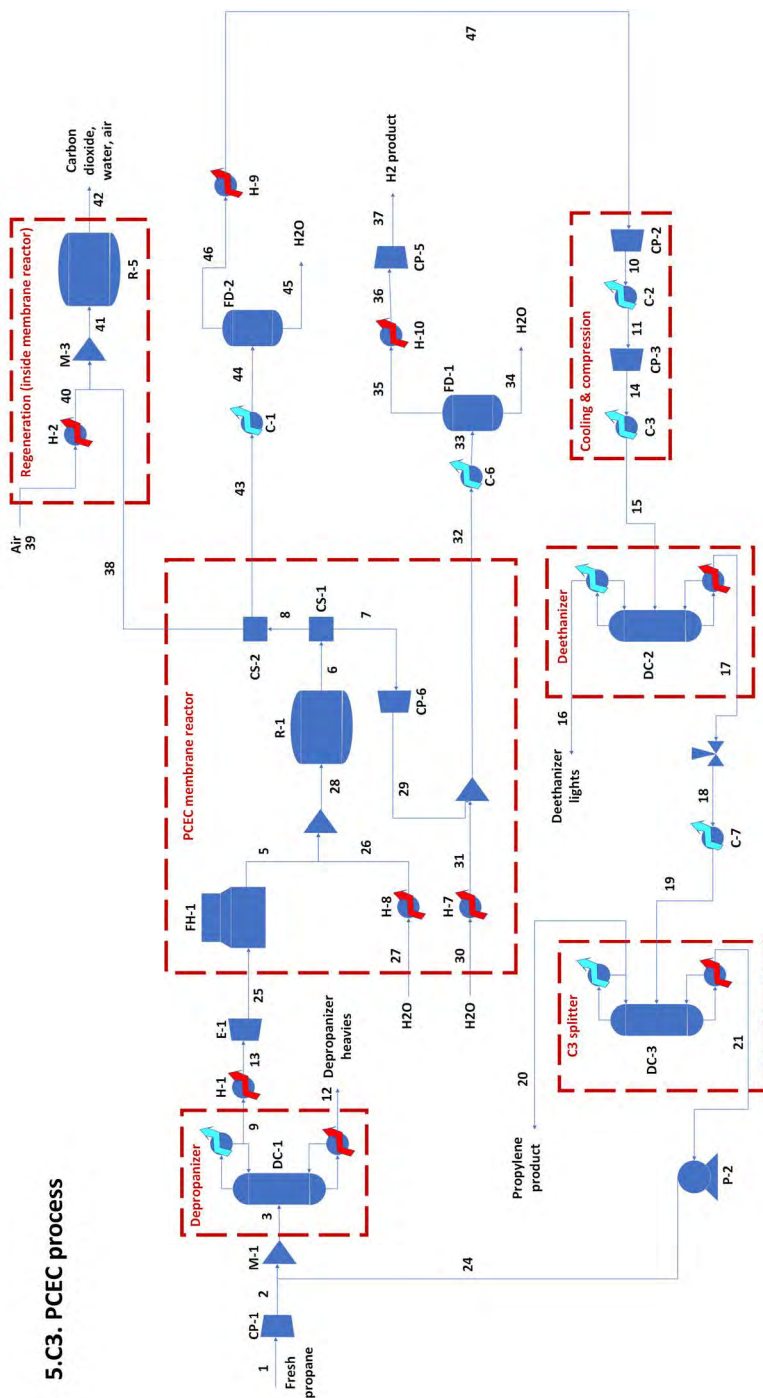
Stream table PCEC process

	1	2	3	4	5	6	7	8	9	10	11	12	13	14	15	16	17	18	19	20
Stream number	1	2	3	4	5	6	7	8	9	10	11	12	13	14	15	16	17	18	19	20
Vapor fraction	1	0	0.05	1	1	1	1	1	0	1	1	0	1	1	0	1	0	0.51	0	0
Temperature °C	25	40	42	600	600	600	600	600	41	54	40	69	75	97	40	45	84	49	49	45
Pressure bar(a)	5	15	15	1	4	4	4	4	15	14	14	15	15	38	38	38	38	19	19	19
Molar flow kmol/h	1473	1473	2908	908	2841	4345	1337	3008	2841	2912	2912	67	2841	2912	2912	204	2708	2708	2708	1273
Mole fractions:																				
Propane	0.95	0.95	0.88	0	0.89	0.27	0	0.39	0.89	0.40	0.40	0.44	0.89	0.40	0.40	0.00	0.43	0.43	0.43	0.00
Ethane	0.03	0.03	0.01	0	0.01	0.01	0	0.02	0.01	0.02	0.02	0	0.01	0.02	0.02	0.28	0.00	0.00	0.00	0.00
Methane	0	0	0	0	0	0.01	0	0.02	0	0.02	0.02	0	0	0.02	0.02	0.25	0	0	0	0
Propylene	0	0	0.09	0	0.09	0.35	0	0.51	0.09	0.53	0.53	0.01	0.09	0.53	0.53	0.01	0.57	0.57	0.57	0.995
Ethylene	0	0	0	0	0	0.01	0	0.01	0	0.01	0.01	0	0	0.01	0.01	0.12	0	0	0	0
Hydrogen	0	0	0	0	0	0.32	1	0.02	0	0.02	0.02	0	0	0.02	0.02	0.35	0	0	0	0
Coronene	0	0	0	0	0	0.00	0	0.00	0	0.00	0.00	0	0	0	0	0	0	0	0	0
n-butane	0.03	0.03	0.01	0	0.00	0	0	0.00	0.00	0.00	0.00	0.55	0.00	0.00	0.00	0	0.00	0.00	0.00	0
1,3-butadiene	0	0	0.00	0	0	0	0	0.00	0	0.00	0.00	0.00	0	0.00	0.00	0	0.00	0.00	0.00	0
Carbon monoxide	0	0	0	0	0	0	0	0	0	0	0	0	0	0	0	0	0	0	0	0
Carbon dioxide	0	0	0	0.17	0	0	0	0	0	0	0	0	0	0	0	0	0	0	0	0
Water	0	0	0	0.04	0	0.02	0	0.03	0	0	0	0	0	0	0	0	0	0	0	0
Oxygen	0	0	0	0.02	0	0	0	0	0	0	0	0	0	0	0	0	0	0	0	0
Nitrogen	0	0	0	0.77	0	0	0	0	0	0	0	0	0	0	0	0	0	0	0	0

	21	22	24	25	26	27	28	29	30	31	32	33	34	35	36	37	38	40	41	43
Stream number	21	22	24	25	26	27	28	29	30	31	32	33	34	35	36	37	38	40	41	43
Vapor fraction	0	1	0	1	1	0	1	1	0	1	0.99	0.96	0	1	1	1	1	1	1	1
Temperature °C	52	20	52	33	600	20	600	600	25	600	600	30*	30*	30*	40	40	600	600	583	600
Pressure bar(a)	19	1	19	4	4	4	4	10	10	10	10	10	10	10	10	50	4	1	1	4
Molar flow kmol/h	1435	889	1435	2841	90	90	2931	1337	55	55	1392	1392	55	1337	1337	1337	6	889	895	3002
Mole fractions:																				
Propane	0.81	0	0.81	0.89	0	0	0.87	0	0	0	0	0	0	0	0	0	0	0	0	0.39
Ethane	0	0	0	0.01	0	0	0.01	0	0	0	0	0	0	0	0	0	0	0	0	0.02
Methane	0	0	0	0	0	0	0	0	0	0	0	0	0	0	0	0	0	0	0	0.02
Propylene	0.19	0	0.19	0.09	0	0	0.09	0	0	0	0	0	0	0	0	0	0	0	0	0.51
Ethylene	0	0	0	0	0	0	0	0	0	0	0	0	0	0	0	0	0	0	0	0.01
Hydrogen	0	0	0	0	1	0	0	1	1	1	0.96	0.96	1	1	1	1	1	0	0	0.02
Coronene	0	0	0	0	0	0	0	0	0	0	0	0	0	0	0	0	0	0	0.01	0
n-butane	0.00	0	0.00	0.00	0	0	0.00	0	0	0	0	0	0	0	0	0	0	0	0	0.00
1,3-butadiene	0.00	0	0.00	0	0	0	0.00	0	0	0	0	0	0	0	0	0	0	0	0	0.00
Carbon monoxide	0	0	0	0	0	0	0	0	0	0	0	0	0	0	0	0	0	0	0	0
Carbon dioxide	0	0	0	0	0	0	0	0	0	0	0	0	0	0	0	0	0	0	0	0
Water	0	0	0	0	0	1	0.03	0	0	0	0.04	0.04	0	0	0	0	0	0	0	0.03
Oxygen	0	0.21	0	0	0	0	0	0	0	0	0	0	0	0	0	0	0	0.21	0.20	0
Nitrogen	0	0.79	0	0	0	0	0	0	0	0	0	0	0	0	0	0	0	0.79	0.79	0

Stream number		44	45	46	47
Vapor fraction		0.75	0	1	1
Temperature	°C	30*	30*	30*	40
Pressure	bar(a)	4	4	4	4
Molar flow	kmol/h	3002	90	2912	2912
Mole fractions:					
Propane		0.39	0	0.40	0.40
Ethane		0.02	0	0.02	0.02
Methane		0.02	0	0.02	0.02
Propylene		0.51	0	0.53	0.53
Ethylene		0.01	0	0.01	0.01
Hydrogen		0.02	0	0.02	0.02
Coronene		0	0	0	0
n-butane		0.00	0	0.00	0.00
1,3-butadiene		0.00	0	0.00	0.00
Carbon monoxide		0	0	0	0
Carbon dioxide		0	0	0	0
Water		0.03	1	0	0
Oxygen		0	0	0	0
Nitrogen		0	0	0	0

The function of flash drums FD-1 and FD-2 is to condense and separate the steam that is cosupplied to the feed side and sweep side of the PCEC membrane, respectively. These flash drums are simulated as component splitters in Aspen Plus operating at 30 °C and are assumed to fully separate the water content. In reality, the water content on the sweep side is fully condensed at 10 bar(a) and 30 °C. However, the feed side vapor stream (stream 46) would contain 0.8 mol% of water at 30 °C but this water concentration is, thus, not included in this process analysis. In practice, industrial dryers could be needed to remove these last traces of water from the membrane effluent streams but this was considered to be beyond the scope of this work.

5.D. Process simulations

5.D1. Oleflex reactors

The Oleflex process is typically equipped with a sequence of four moving bed reactors with interstage fired heaters. In the Aspen Plus simulations, a sequence of four stoichiometric reactors with interstage fired heaters was used to mimic this Oleflex reactor setup. The product distribution specified in the stoichiometric reactors of the Oleflex process was based on previous academic studies [5,19]. The propane conversion per reactor is typically about 10%, leading to a single-pass conversion of about 40% for a sequence of four moving bed reactors. Propylene selectivity is generally about 90% [5,19,47]. The Oleflex process employs a Pt-based catalyst on which the following side reactions take place [87,88]:

Propane cracking: $$C_3H_8 \rightarrow C_2H_4 + CH_4 \qquad (5.D1)$$

Propane hydrogenolysis: $$C_3H_8 + H_2 \rightarrow C_2H_6 + CH_4 \qquad (5.D2)$$
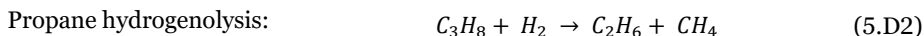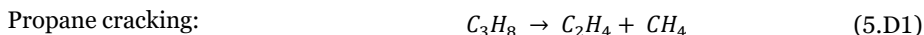
The selectivity of the side reactions were estimated at 4% cracking selectivity, 2% hydrogenolysis selectivity, and 4% coke selectivity (**Equation 5.D5**), based on Agarwal et al. [5]. For a sequence of four Oleflex reactors, this led to the following single-pass yields: propane dehydrogenation (36%), propane cracking (1.6%), propane hydrogenolysis (0.8%), and coking (1.6%). Also, 50% of the ethylene is hydrogenated to ethane via **Equation 5.D3**. Moreover, 50% of the *n*-butane impurity in the propane feed is converted into 1,3-butadiene as presented in **Equation 5.D4** [89].

Ethylene hydrogenation: $$C_2H_4 + H_2 \leftrightharpoons C_2H_6 \qquad (5.D3)$$

n-butane dehydrogenation: $$C_4H_{10} \leftrightarrow C_4H_6 + 2\,H_2 \qquad (5.D4)$$
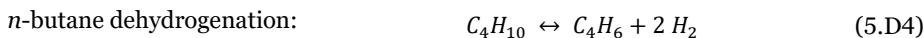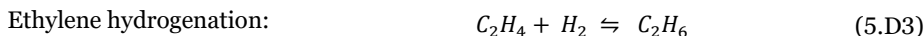
In addition to the side reactions listed in **Equations 5.D1-5.D4**, coke formation takes place on the surface of the Pt catalyst, which is generally believed to be the result of deep dehydrogenation of propylidene surface intermediates [18]. In all three processes, coke formation was specified as fractional conversion of propane. In the process simulations the polycyclic aromatic hydrocarbon coronene, with chemical formula $C_{24}H_{12}$, was employed as coke model compound. Coronene is in the gas phase under reaction conditions ($T = 600\ °C$) and therefore easily transported to a separate regeneration unit in the process simulations. The formation of coronene from propane is presented in **Equation 5.D5**.

Propane coking: $$8\,C_3H_8 \leftrightharpoons C_{24}H_{12} + 26\,H_2 \qquad (5.D5)$$

5.D2. MPEC and PCEC membrane reactors

Similar to the Oleflex simulations, 50% of ethylene was hydrogenated to ethane (**Equation 5.D3**), whilst 50% of the *n*-butane impurity in the propane feed was dehydrogenated to 1,3-butadiene via **Equation 5.D4**. The removal of hydrogen from the reaction zone and the corresponding increase in propylene yield is expected to boost coke formation, since propylene oligomerization is believed to be the initial step of carbon

deposition [90]. In this work, a 2% coke yield was taken as initial estimate for the base case MPEC and PCEC-assisted process simulations.

5.D3. Design specifications

The following design specifications were used in the process simulations in Aspen Plus:

- The propylene production capacity was set to 450 ktpa in all three processes by varying the dimension of the fresh propane feed flow rate.

- The purity of the propylene product stream was set to 99.5 mol% propylene by varying the reflux ratio of the C3 splitter column to ensure the production of polymer grade propylene.

- The H_2 product purity in the Oleflex process was attained by adjusting the amount of methane separated in the upstream pressure swing adsorption (PSA) step, the latter being simulated as component splitter. For the MPEC and PCEC process, a pure H_2 stream was obtained, as the MPEC and PCEC membranes were assumed to be fully permselective, and the present traces of H_2O to hydrate the membrane were nearly fully separated in a flash drum.

- The fresh air flow needed for catalyst regeneration in all three processes was specified in such a way that coronene is fully combusted and that an oxygen amount of 500 kg/hr remained in the regenerator outlet stream.

- The required H_2O sweep gas flow in the MPEC process needed to be set is such a way that the permeate side H_2 partial pressure is below the feed side H_2 partial pressure along the entire membrane, as otherwise H_2 transport would occur in the opposite direction. The H_2 molar fraction near the end of the membrane on the feed side (i.e. after 95% H_2 removal) is about 0.024, which leads to a partial pressure of about 96 mbar(a) for a 4 bar(a) reaction pressure. The H_2O sweep gas flow is varied in such a way that the permeate side H_2 partial pressure is 90 mbar(a).

5.E. Oleflex dehydrogenation reactors

5.E1. Reactor design

A sequence of radial-flow moving-bed reactors is applied in the Honeywell UOP Oleflex process [29]. Such a moving-bed reactor contains two cylinders that are coaxially configured in between which the supported Pt catalyst slowly moves downward due to gravity (**Figure 5.E1**). The propane and hydrogen reactants enter from the bottom inside the inner cylinder and flow radially through the dividing wall between the two cylinders to reach the catalyst. The pressure drop is typically low due to the radial flow principle and the reactors are commonly operated adiabatically.
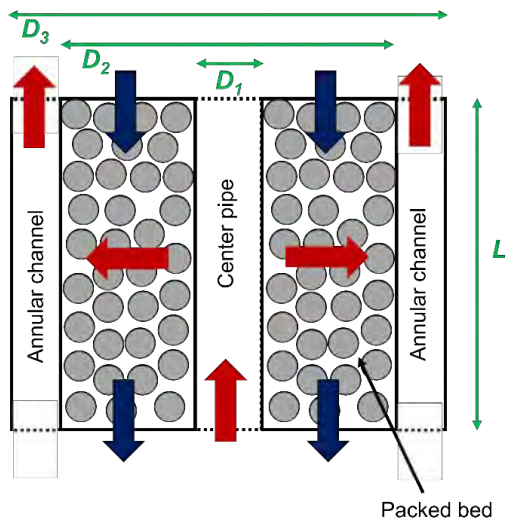
Figure 5.E1: Schematic representation of a radial-flow moving-bed reactor. Red arrows indicate gas flow direction, blue arrows indicate catalyst flow direction.

The dimensions of the Oleflex reactors were determined by using a model for radial-flow moving-bed reactors as developed by Bijani et al. [29] for isobutane dehydrogenation (see **Supporting Information 5.E2** for more details). This model relates the catalyst residence time to the predicted alkane conversion level. Here, it was assumed that the reaction rate constant for isobutane dehydrogenation is representative for propane dehydrogenation. Furthermore, the propane molar feed fraction was considered to be 0.65, whilst the remaining part was comprised of recycled hydrogen [5].

The catalyst residence time was calculated to be about 47 hours per reactor. In total, this led to a reaction cycle time of about 8 days for a sequence of four radial-flow moving-bed reactors. For comparison, the total Oleflex cycle time, including regeneration step, was reported in previous studies to be between 5 to 10 days [18,19,29,46]. The total catalyst holdup per reactor is known to be about 17 ton [91,92]. From the catalyst holdup and catalyst residence time, a catalyst mass flow rate of about 360 kg_{cat}/h was calculated. The length of moving bed reactors for alkane dehydrogenation is typically around 12 m [91,92]. Besides, the ratio between outer catalyst bed and inner catalyst bed diameter is generally about three [93]. With this information, the center pipe diameter (i.e. the inner catalyst bed diameter, D_1), the outer catalyst bed diameter (D_2), and the reactor diameter (D_3) were estimated to be 3.2 m, 10.1 m, and 12.4 m, respectively (**Figure 5.E1**).

5.E2. Reactor dimensioning

Bijani et al. [29] developed a model for a radial-flow moving-bed reactor for isobutane dehydrogenation. Their proposed reaction rate expression for isobutane conversion is shown in **Equation 5.E1**.

$$-r_A = \frac{k_1 a C_{A,0}(X_{A,eq} - X_A)(\alpha + \beta X_A)}{(1 + \varepsilon_A X_A)^2} \tag{5.E1}$$

Where:

$$\alpha = \frac{X_{A,eq} + (\theta_H + \theta_B) + \theta_H \theta_B(1 - \varepsilon_A + \varepsilon_A X_{A,eq})}{(\theta_H + X_{A,eq})(\theta_B + X_{A,eq})} \tag{5.E2}$$

And:

$$\beta = \frac{\left(1 + \varepsilon_A X_{A,eq} - X_{A,eq}\right) + \varepsilon_A X_{A,eq}(\theta_H + \theta_B) + \varepsilon_A \theta_H \theta_B}{(\theta_H + X_{A,eq})(\theta_B + X_{A,eq})} \tag{5.E3}$$

And:

$$C_{A,0} = \frac{n_{A,0}}{V} = \frac{p_{A,0}}{RT} = \frac{P * y_{A,0}}{RT} \tag{5.E4}$$

Equation 5.E1 can be rewritten into the following form [29]:

$$\frac{(\beta - \varepsilon_A \alpha)^2}{\beta(\alpha + \beta X_{A,eq})} \ln\left(\frac{\alpha + \beta X_{A,out}}{\alpha + \beta X_{A,in}}\right) - \left(\frac{\beta\left(1 + \varepsilon_A X_{A,eq}\right)^2}{(\alpha + \beta X_{A,eq})}\right) \ln\left(\frac{X_{A,eq} - X_{A,out}}{X_{A,eq} - X_{A,in}}\right) \tag{5.E5}$$

$$- \varepsilon_A^2 (X_{A,out} - X_{A,in}) = \frac{k_1 a_0 C_{A,0} U_s \beta}{k_d F_{A,0} X_{A,eq}} \left(1 - \exp\left(\frac{-k_d W_c}{U_s}\right)\right)$$

The definition, units, and values used for all parameters in **Equations 5.E1-5.E5** are presented in **Table 5.E1**.

Table 5.E1: Parameters used in the Oleflex radial-flow moving-bed reactor model calculations.

Par.:	Description:	Value:	Unit:	Reference:
k_1	Dehydrogenation rate constant	3.61	[m^3_g/kg$_{cat}$.h]	[29], isobutane NODH constant assumed to be representative for propane NODH
a	Catalyst activity	Depends on k_d	[-]	Calculated in the form of k_d
P	Total pressure	$4 \cdot 10^5$	[Pa]	Assumed Oleflex reactor pressure (ranges between 1-5 bar(a))
R	Universal gas constant	8.314	[J/mol.K]	
T	Reaction temperature	873	[K]	All Oleflex reactors operate with inlet T = 600 °C
$y_{A,0}$	Gas phase molar fraction of propane	0.65	[-]	[29] and own Oleflex simulations → H$_2$ recycle suppresses propane partial pressure

$C_{A,0}$	Propane inlet concentration	35.8	[mol/m³$_g$]	Calculated using **Equation 5.E4**
$X_{A,eq}$	Propane equilibrium conversion	0.493	[-]	Eq. conversion at 1 bar(a), 600 °C, and a pure propane feed, based on [63]
θ_H	Hydrogen/propane molar ratio in the feed	0.538	[-]	Calculated based on $y_{A,0}$, assuming that propane and H_2 are the only components in the feed
θ_B	Propylene/propane ratio in the feed	0	[-]	Propylene concentration is assumed to be 0
ε_A	Volume expansion factor	2	[-]	Assuming propane NODH is the only reaction taking place: propane ⇌ propylene + H_2
α	Dimensionless parameter 1	2.03	[-]	Calculated using **Equation 5.E2**
β	Dimensionless parameter 2	3.98	[-]	Calculated using **Equation 5.E3**
$X_{A,in}$	Propane 'inlet' conversion	0	[-]	Propane conversion of inlet stream of 1st reactor = 0, all reactors dimensioned as if they were the first in sequence
$X_{A,out}$	Propane outlet conversion	0.1	[-]	Propane conversion level per dehydrogenation reactor
W_c	Catalyst mass per dehydrogenation reactor	17,000	[kg$_{cat}$]	[91,92]
U_s	Mass flow rate of catalyst	360	[kg$_{cat}$/h]	This value is used as variable in **Equation 5.E5** → Value is varied until left part of **Equation 5.E5** equals the right part
k_d	Catalyst deactivation rate constant	0.0127	[1/h]	[29]
$F_{propane,0}$	Molar flow rate of propane	4,237,460	[mol/h]	From Aspen Plus simulations Oleflex process

Based on the outcomes of the reactor model calculations, the dimensions of the Oleflex radial-flow moving-bed reactors were determined as explained in **Table 5.E2**.

Table 5.E2: Parameters used in determination of Oleflex reactor dimensions.

Par.:	Description:	Value:	Unit:	Reference:
ρ_c	Catalyst bed density	800	[kg/m³$_R$]	[92]
V_c	Volume needed per dehydrogenation reactor	21.25	[m³$_R$]	Catalyst holdup divided by catalyst bed density
L	Reactor length	12	[m$_R$]	Estimated based on [91,92]
A_c	Cross-sectional area occupied by catalyst particles	1.77	[m²$_R$]	V_c divided by L
D_1	Center pipe diameter	3.21	[m$_R$]	Based on A_c and D_2/D_1, assuming cylindrical tubes
D_2/D_1	Typical D_2/D_1 ratio radial-flow moving-bed reactors	3.15	[-]	Based on [93]
D_3/D_1	Typical D_3/D_1 ratio radial-flow moving-bed reactors	3.85	[-]	Based on [93]
D_2	Outer catalyst bed diameter	10.14	[m$_R$]	
D_3	Outer reactor diameter	12.36	[m$_R$]	

5.E3. CAPEX Oleflex reactors

The purchase equipment costs of the Oleflex reactors were based on the total steel costs, which were calculated using the required wall thickness, as prescribed in **Supporting Information 5.H**. Three walls were considered: (i) the tube wall of the center pipe (D_1), (ii) the outer wall of the catalyst bed (D_2), and (iii) the outer wall of the reactor (D_3) (see **Figure 5.E1**). All compartments were considered to be at 4 bar(a) pressure, corresponding to a design pressure of 4.4 bar(a), including 10% overdesign. These reactors were constructed with stainless steel grade 304 (SS304), with a price of about 2.20 USD/lb (July 2023, equals 4.85 €/kg) [94].

5.F. Membrane reactors

5.F1. Membrane reactor design

For the design and cost estimation of the membrane reactors in the MPEC and PCEC-assisted propane NODH processes, the ceramic membrane reactor design proposed by CoorsTek was considered [44,64]. This design comprises of a modular approach containing tubular ceramic cells. Tubular cells are more tolerant to thermal stresses [95,96] and are mechanically more stable than planar designs under pressure gradients between feed and permeate side [97]. Six ceramic tubes together, separated by sealing and/or interconnects, is referred to as a stack [44]. A single engineering unit (SEU)

represents a shell in which such a stack is positioned [44]. A membrane panel contains twelve of these SEUs and a membrane panel cluster is comprised of eight membrane panels, thus 96 SEUs [44]. When placed inside a hot box, i.e. inside a heating mantle, such a membrane panel cluster is called a membrane pack [44]. The heating principle inside the hot box is normally based on steam circulation. Further specifications of an individual SEU are listed in **Table 5.F1**. The Pt-based catalyst (d_p = 600 μm [92]) was considered to be packed outside the tube cells in order to minimize the pressure drop along the catalyst bed.

Table 5.F1: Specifications of a single engineering unit (SEU).

Parameter:	Value:	Reference:
Ceramic cell diameter (mm)	9.6	[44]
SEU shell inner diameter (mm)	47	[44]
# of parallel cells (-)	6	[44]
Ceramic cell length (mm)	25	[44]
SEU length (m)	5	Estimation

The required stack materials were different for the MPEC and PCEC membranes (see **Table 5.F2** and **5.F3**). The MPEC materials were based on a configuration proposed in the AMAZING project [98] focusing on improving the sustainability of industrial alkane dehydrogenation processes by using MPEC membranes. In this configuration, asymmetric membranes were used with a dense separation layer made of molybdenum-substituted lanthanum tungstate (LWMO) on top of a porous lanthanum tungstate (LWO) layer. On the contrary, the PCEC design was based on a cathode-supported cell design with an anode layer made of $PrBa_{0.5}Sr_{0.5}Co_{1.5}Fe_{0.5}O_{5+\delta}$ (PBSCF) on top of an electrolyte layer of $BaZr_{0.7}Ce_{0.2}Y_{0.05}Yb_{0.05}O_{3-\delta}$ (BZCYYb), which in turn was applied on top of a NiO/BZCYYb cathode support [25]. An additional barrier layer of Gd-doped ceria (GDC) was needed to avoid chemical reactions between PBSCF and the yttrium-containing electrolyte [43].

Table 5.F2: Specifications of MPEC materials.

MPEC membrane design		Reference
Porous membrane layer:		
Material	LWO	[98]
Layer thickness (μm)	500	[98]
Porosity (%)	20	**Table 5.F3**
Dense membrane layer:		
Material	LWMO	[98]
Layer thickness (μm)	30	[98]
Porosity (%)	0	

Table 5.F3: Specifications of PCEC materials.

PCEC membrane design		Reference
Anode:		
Anode material	PBSCF	[25]
Anode layer thickness (μm)	30	[25]
Porosity of anode layer (%)	20	[99]
Anode contact layer material	PBSCF	[25]
Anode contact layer thickness (μm)	100	[99]
Anode contact layer porosity (%)	40	[99]
Barrier layer:		
Barrier layer material	GDC	[43,99]
Barrier layer thickness (μm)	5	[99]
Porosity of barrier layer (%)	5	[99]
Electrolyte:		
Electrolyte material	BZCYYb	[25]
Electrolyte layer thickness (μm)	10	[25]
Porosity of electrolyte (%)	0	
Cathode:		
Cathode material	NiO/BZCYYb	[25]
Cathode layer thickness	300	[25]
Porosity of cathode layer (%)	20	[99]
Cathode contact layer material	8YSZ/NiO	[99]
Cathode contact layer thickness (μm)	7	[99]
Porosity of cathode contact layer (%)	40	[99]

The MPEC and PCEC processes required different surface areas, as both membrane types have different hydrogen permeation fluxes. For PCEC membranes, the flux through BZCY-based electrolytes was estimated at 3.3 Nml/min.cm^2 (ca. 2.3 μmol/s.cm^2), based on the work by Malerød-Fjeld et al. [23], who obtained this flux at 800 °C for a current density of 0.5 A/cm^2. This flux was assumed here to be representative to BZCY electrolytes at 600 °C for 1.0 A/cm^2. Typical hydrogen fluxes through MPEC membranes at temperatures above 600 °C are a factor 100 lower than through PCEC membranes [65], meaning ca. 0.033 μmol/s.cm^2. For a propylene production capacity of 450 ktpa (i.e. 350 mol/s) and 95% hydrogen removal, ca. 330 mol/s of hydrogen needs to be removed in the MPEC and PCEC process. As a result, ca. 10^4 m^2 of PCEC membrane area was needed, whilst ca. 10^6 m^2 of MPEC membrane area was required. One needs to realize that the mentioned hydrogen fluxes were experimentally obtained at higher temperatures (700-900 °C) and in systems where a hydrogen-rich feed stream was supplied [65]. Particularly for MPEC membranes,

these hydrogen fluxes are therefore yet a highly optimistic approximation, as in reality feed side hydrogen partial pressures and thus the driving force for permeation will be much lower.

The calculated membrane areas are the actual areas needed for *in situ* H_2 permeation. However, in practice part of the membrane reactor tubes will be in regeneration mode, as catalyst and membrane regeneration is anticipated to be required, because of continuous carbon deposition. As a consequence, an overdesign on the required membrane area is needed. In industrial propane NODH processes, typically about 15% of the reactor capacity is needed for regeneration [19]. Since hydrogen removal is anticipated to boost coke formation, a larger reactor capacity will be needed for regeneration in both membrane processes. In this work, 40% of the reactor capacity is assumed to be in regeneration mode for the MPEC and PCEC processes, corresponding to a 40% overdesign compared to the required membrane surface areas.

5.F2. Reactor dimensioning MPEC membrane reactors

In **Table 5.F4**, the parameters used for determining the MPEC reactor dimensions are listed for an MPEC membrane area of 10^6 m^2 in total. To this end, the wall thickness of individual single engineering units (SEUs) and hot boxes were required, which were determined using the wall thickness calculations prescribed in **Supporting Information 5.H** using the information listed in **Table 5.F5**.

Table 5.F4: Parameters used in MPEC reactor dimensioning.

Parameter:	Description:	Value:	Unit:	Reference:
d_{cell}	Ceramic cell diameter	0.0096	[m]	
Cell circumference	Ceramic cell circumference	0.0302	[m]	Based on d_{cell}
SEU length	SEU length	5	[m]	
$A_{m.cell}$	Membrane area per ceramic cell	0.15	[m^2]	Based in cell circumference and SEU length
# of cells per SEU	# of cells per SEU	6	[-]	
$A_{m,SEU}$	Membrane area per SEU	0.90	[m^2]	
# of SEUs per membrane panel	# of SEUs per membrane panel	12	[-]	
$A_{m,panel}$	Membrane area per membrane panel	10.86	[m^2]	
# of membrane panels per cluster	# of membrane panels per cluster	8	[-]	
$A_{m,cluster}$	Membrane area per membrane panel cluster	86.86	[m^2]	

# of membrane panel clusters per module	# of membrane panel clusters per module	9	[-]	
$A_{m,module}$	Membrane area per module	781.73	[m²]	
# of membrane modules needed	# of membrane modules needed	1258	[-]	Based on total required membrane area and membrane area per module
# of SEUs needed	# of SEUs needed	1,086,822	[-]	
SEU steel mass estimation	SEU steel mass estimation	34.82	[kg/SEU]	See **Table 5.F5** below
Hot box steel mass estimation	Hot box steel mass estimation	34.30	[kg/SEU]	See **Table 5.F5** below
Total SEU steel mass	Total SEU steel mass	37,839,082	[kg]	
Total hot box steel mass	Total hot box steel mass	37,277,366	[kg]	

Table 5.F5: Steel mass estimation MPEC reactors.

Parameter:	Description:	Value:	Unit:	Reference:
SEU steel mass estimation				
SEU inner diameter	SEU inner diameter	4.7	[cm]	
L	SEU length	5	[m]	
P	Internal pressure	4	[bara]	
P_{design}	Design pressure	4.4	[bara]	10% overdesign
t_{min}	Minimum wall thickness	0.15	[mm]	**Equation 5.H1**
t_{corro}	Corrosion allowance	4	[mm]	
$t_{combined}$	Combined minimum wall thickness	4.15	[mm]	
t_{wall}	Selected wall thickness	5	[mm]	
Mass of steel required per SEU	Mass of steel required per SEU	34.82	[kg]	
Hot box shell steel mass estimation				
D_{hotbox}	Hot box diameter	2	[m]	
L	Hot box length	5	[m]	
P	Internal pressure	4	[bara]	
P_{design}	Design pressure	4.4	[bara]	10% overdesign

t_{min}	Minimum wall thickness	6.2	[mm]	**Equation 5.H1**
t_{corro}	Corrosion allowance	4	[mm]	
$t_{combined}$	Combined minimum wall thickness	10.2	[mm]	
t_{wall}	Selected wall thickness	13	[mm]	
Mass of steel required per hot box	Mass of steel required per hot box	3,292.7	[kg]	
Hot box steel mass required per SEU	Hot box steel mass required per SEU	34.30	[kg]	

5.F3. CAPEX MPEC membrane reactors

The stack material costs were estimated based on a method proposed by Malerød-Fjeld et al. [23], which not only concerned the costs for the bare electrode and electrolyte materials but also included costs for e.g. gas manifolds and sealing rings. The results are shown in **Table 5.F6**. Afterward, the total MPEC reactor purchase equipment costs were determined in **Table 5.F7** and comprised of (i) SEU steel costs, (ii) hot box steel costs, (iii) stack material costs, (iv) tooling costs, and (v) additional costs. The SEUs and hot box were constructed with stainless steel grade 304 (SS304), with a price of about 2.20 USD/lb (July 2023, equals 4.85 €/kg) [94]. The tooling costs represent the depreciation of the equipment needed for manufacturing, and the additional costs contain costs for instrumentation, tubing, fittings, etc. [23].

Table 5.F6: MPEC stack material cost estimation.

Parameter:	Value/description:	Unit:	Reference:
Porous membrane layer			
Material	LWO (lanthanum tungstate)		[98]
Layer thickness	500	[µm]	[98]
Porosity	20	[%]	Estimation based on [99]
Density	6,400	[kg/m³]	Estimation based on [39]
Material costs	100	[€/kg]	Estimated based on material prices reported by [99]
Dense membrane layer			
Electrolyte material	LWMO (molybdenum-substituted lanthanum tungstate)		[98]

Electrolyte layer thickness	30	[μm]	[98]
Porosity	0	[%]	By definition
Density	6,400	[kg/m³]	Estimation based on [39]
Material costs	100	[€/kg]	Estimated based on material prices reported by [99]
Per m² of membrane area:			
Dense volume LWO	0.0005	[m³]	
Dense volume LWMO	0.00003	[m³]	
Actual volume LWO	0.0004	[m³]	
Actual volume LWMO	0.00003	[m³]	
LWO mass	2.56	[kg]	
LWMO mass	0.192	[kg]	
Per SEU:			
$A_{m,SEU}$	0.90	[m²]	
LWO mass	2.32	[kg]	
LWMO mass	0.17	[kg]	
LWO costs	231.62	[€]	
LWMO costs	17.37	[€]	
Interconnect costs	0	[€]	Not needed for MPEC membranes
Gas manifold costs	6.32	[€]	Costs per SEU, based on [23]
Weld connector costs	0	[€]	Not needed for MPEC membranes
Sealing ring costs	0.19	[€]	Costs per SEU, based on [23]
Total material costs per SEU	**255.51**	**[€]**	
	274.74	[USD]	
# of SEUs needed	1,086,822	[-]	
Total stack material costs	**277.7**	**[MMUSD]**	

Table 5.F7: Estimation of purchase equipment costs MPEC reactor.

Parameter:	Value:	Unit:	Reference:
SEU steel costs			
Stainles steel 304 price	2.2	[USD/lb]	[94]
	4.85	[USD/kg]	
Total SEU steel mass	37,839,082	[kg]	
SEU steel costs	**183.52**	**[MMUSD]**	
Hot box steel costs			
Total hot box steel mass	37,277,366	[kg]	
Hot box steel costs	**180.80**	**[MMUSD]**	
Stack material costs			
Total stack material costs	**277.7**	**[MMUSD]**	Table 5.F6
Tooling costs			
Tooling costs per SEU	290.0	[USD/SEU]	[23]
Total tooling costs	**315.18**	**[MMUSD]**	
Additional costs (instrumentation, tubing, fittings, assembly, etc.)	**46.12**	**[MMUSD]**	Assumed to be 10% of stack costs + SEU shell costs, based on [23]
Regeneration/operation ratio	0.4	[-]	40% overdesign considered for MPEC SEUs that are in regeneration mode instead of reaction mode
Total MPEC costs	**1,404.63**	**[MMUSD]**	

5.F4. Reactor dimensioning PCEC membrane reactors

In **Table 5.F8**, the parameters used for determining the PCEC reactor dimensions are listed for a total PCEC membrane area of 10^4 m^2. To this end, the wall thickness of individual single engineering units (SEUs) and hot boxes were required, which were determined using the wall thickness calculations prescribed in **Supporting Information 5.H** using the information listed in **Table 5.F9**. Even though H$_2$ is electrochemically compressed to 10 bar(a) in the base case, a design pressure of 15 bar(a) is taken in the steel mass calculation to allow for possible H$_2$ compression to higher pressures.

Table 5.F8: Parameters used in PCEC reactor dimensioning.

Parameter:	Description:	Value:	Unit:	Reference:
d_{cell}	Ceramic cell diameter	0.0096	[m]	
Cell circumference	Ceramic cell circumference	0.0302	[m]	Based on d_{cell}
SEU length	SEU length	5	[m]	
$A_{m.cell}$	Membrane area per ceramic cell	0.15	[m²]	Based in cell circumference and SEU length
# of cells per SEU	# of cells per SEU	6	[-]	
$A_{m,SEU}$	Membrane area per SEU	0.90	[m²]	
# of SEUs per membrane panel	# of SEUs per membrane panel	12	[-]	
$A_{m,panel}$	Membrane area per membrane panel	10.86	[m²]	
# of membrane panels per cluster	# of membrane panels per cluster	8	[-]	
$A_{m,cluster}$	Membrane area per membrane panel cluster	86.86	[m²]	
# of membrane panel clusters per module	# of membrane panel clusters per module	9	[-]	
$A_{m,module}$	Membrane area per module	796.21	[m²]	
# of membrane modules needed	# of membrane modules needed	13	[-]	Based on total required membrane area and membrane area per module
# of SEUs needed	# of SEUs needed	11,053	[-]	
SEU steel mass estimation	SEU steel mass estimation	38.61	[kg]	See **Table 5.F9** below
Hot box steel mass estimation	Hot box steel mass estimation	39.57	[kg]	See **Table 5.F9** below
Total SEU steel mass	Total SEU steel mass	426,700	[kg]	
Total hot box steel mass	Total hot box steel mass	437,372	[kg]	

Table 5.F91: Steel mass estimation PCEC reactors.

Parameter:	Description:	Value:	Unit:	Reference:
SEU steel mass estimation				
SEU inner diameter	SEU inner diameter	4.7	[cm]	
L	SEU length	5	[m]	
P	Internal pressure	15	[bara]	1.5 times the currently targeted operational pressure of 10 bar(a)
P_{design}	Design pressure	16.5	[bara]	10% overdesign
t_{min}	Minimum wall thickness	0.55	[mm]	**Equation 5.H1**
t_{corro}	Corrosion allowance	4	[mm]	
$t_{combined}$	Combined minimum wall thickness	4.55	[mm]	
t_{wall}	Selected wall thickness	6	[mm]	
Mass of steel required per SEU	Mass of steel required per SEU	38.61	[kg]	
Hot box shell steel mass estimation				
D_{hotbox}	Hot box diameter	2	[m]	
L	Hot box length	5	[m]	
P	Internal pressure	5	[bara]	Assumed pressure inside hot box empty volume
P_{design}	Design pressure	5.5	[bara]	10% overdesign
t_{min}	Minimum wall thickness	7.76	[mm]	**Equation 5.H1**
t_{corro}	Corrosion allowance	4	[mm]	
$t_{combined}$	Combined minimum wall thickness	11.76	[mm]	
t_{wall}	Selected wall thickness	15	[mm]	
Mass of steel required per hot box	Mass of steel required per hot box	3798.96	[kg]	
Hot box steel mass required per SEU	Hot box steel mass required per SEU	39.57	[kg]	

5.F5. CAPEX PCEC membrane reactors

Similar to the capital investment estimation of the MPEC membrane reactor (**Supporting Information 5.F3**), the CAPEX of the PCEC membrane reactor was estimated based on a method proposed by Malerød-Fjeld et al. [23]. The stack material costs are summarized

in **Table 5.F10**, whilst the total PCEC reactor capital expenditures are determined in **Table 5.F11**. The SEUs and hot box were again constructed with stainless steel grade 304 (SS304), with a price of about 2.20 USD/lb (July 2023, equals 4.85 €/kg) [94].

Table 5.F10: PCEC stack material cost estimation.

Parameter:	Value:	Unit:	Reference:
Anode			
Material	PBSCF ($PrBa_{0.5}Sr_{0.5}Co_{1.5}Fe_{0.5}O_{5+\delta}$)		[25]
Layer thickness	30	[μm]	[25]
Porosity	20	[%]	Estimated based on [99]
Anode contact layer material	PBSCF ($PrBa_{0.5}Sr_{0.5}Co_{1.5}Fe_{0.5}O_{5+\delta}$)		[25]
Anode contact layer thickness	100	[μm]	[25]
Anode contact layer porosity	40	[%]	Estimated based on [99]
Density	6,300	[kg/m³]	Estimated based on the density of LSCF, as reported by [99]
Material costs	100	[€/kg]	Estimated based on material prices in [99]
Electrolyte			
Electrolyte material	BZCYYb ($BaZr_{0.1}Ce_{0.7}Y_{0.1}Yb_{0.1}O_{3-\delta}$)		[25]
Electrolyte layer thickness	10	[μm]	[25]
Porosity	0	[%]	By definition
Density	6,180	[kg/m³]	Estimated based on [100]
Material costs	70	[€/kg]	Estimated based on material prices in [99]
Barrier layer			
Material	GDC (Gd-doped ceria)		[25]
Layer thickness	5	[μm]	[25]
Porosity	5	[%]	Estimated based on [99]
Density	7,230	[kg/m³]	Estimated based on [99]

Material costs	800	[€/kg]	Estimated based on prices in [99]
Cathode			
Material	NiO/BZCYYb		[25]
Layer thickness	300	[μm]	[25]
Porosity	20	[%]	Estimated based on [99]
Density	6,180	[kg/m³]	Estimated based on [100]
Material costs	50	[€/kg]	Estimated based on prices in [99]
Cathode contact layer material	8YSZ/NiO		[25]
Cathode contact layer thickness	7	[μm]	[25]
Cathode contact layer porosity	40	[%]	Estimated based on [99]
Cathode contact layer density	6,500	[kg/m³]	Estimated based on [99]
Cathode contact layer material costs	80	[€/kg]	Estimated based on material prices in [99]
Per m² of membrane area:			
Dense volume PBSCF (anode)	0.00003	[m³]	
Dense volume PBSCF (anode contact)	0.0001	[m³]	
Dense volume BZCYYb	0.00001	[m³]	
Dense volume GDC	0.000005	[m³]	
Dense volume NiO/BZCYYb	0.0003	[m³]	
Dense volume 8YSZ/NiO	0.000007	[m³]	
Actual volume PBSCF (anode)	0.000024	[m³]	
Actual volume PBSCF (anode contact)	0.00006	[m³]	
Actual volume BZCYYb	0.00001	[m³]	
Actual volume GDC	0.00000475	[m³]	
Actual volume NiO/BZCYYb	0.00024	[m³]	

Actual volume 8YSZ/NiO	0.0000042	[m³]	
Mass PBSCF (anode)	0.15	[kg]	
Mass PBSCF (anode contact)	0.38	[kg]	
Mass BZCYYb	0.06	[kg]	
Mass GDC	0.03	[kg]	
Mass NiO/BZCYYb	1.48	[kg]	
Mass 8YSZ/NiO	0.03	[kg]	
Per SEU:			
$A_{m,SEU}$	0.90	[m²]	
Mass PBSCF (anode)	0.14	[kg]	
Mass PBSCF (anode contact)	0.34	[kg]	
Mass BZCYYb	0.06	[kg]	
Mass GDC	0.03	[kg]	
Mass NiO/BZCYYb	1.34	[kg]	
Mass 8YSZ/NiO	0.02	[kg]	
Costs PBSCF (anode)	13.68	[€]	
Costs PBSCF (anode contact)	34.20	[€]	
Costs BZCYYb	3.91	[€]	
Costs GDC	24.86	[€]	
Costs NiO/BZCYYb	67.10	[€]	
Costs 8YSZ/NiO	1.98	[€]	
Interconnect costs	6.70	[€]	Costs per SEU, based on [23]
Gas manifold costs	6.32	[€]	Costs per SEU, based on [23]
Weld connector costs	47.99	[€]	Costs per SEU, based on [23]
Sealing ring costs	0.19	[€]	Costs per SEU, based on [23]
Total material costs per SEU	**206.92**	**[€]**	
	222.50	[USD]	
# of SEUs needed	11,053	[-]	
Total stack material costs	**2.29**	**[MMUSD]**	

Table 5.F11: Estimation of purchase equipment costs PCEC reactor.

Parameter:	Value:	Unit:	Reference:
SEU steel costs			
Stainless steel 304 price	2.2	[USD/lb]	[94]
	4.85	[USD/kg]	
Total SEU steel mass	426,670	[kg]	
SEU steel costs	**2.07**	**[MMUSD]**	
Hot box steel costs			
Total hot box steel mass	437,372	[kg]	
Hot box steel costs	**2.12**	**[MMUSD]**	
Stack material costs			
Total stack material costs	**2.29**	**[MMUSD]**	**Table 5.F10**
Tooling costs			
Tooling costs per SEU	290.0	[USD/SEU]	[23]
Total tooling costs	**3.21**	**[MMUSD]**	
Additional costs (instrumentation, tubing, fittings, assembly, etc.)	**0.44**	**[MMUSD]**	Assumed to be 10% of stack costs + SEU shell costs, based on [23]
Regeneration/operation ratio	0.4	[-]	40% overdesign considered for PCEC SEUs that are in regeneration mode instead of reaction mode
Total PCEC costs	**14.17**	**[MMUSD]**	

5.G. Other equipment design

5.G1. Regenerator design

The regeneration unit only had to be designed for the benchmark Oleflex process, as the Pt catalyst is regenerated inside the dehydrogenation reactor equipment in case of the parallel membrane reactors. The dimensions of the Oleflex regenerator were estimated based on available information on industrial regeneration units in fluid catalytic cracking (FCC) processes [101]. The regenerator diameter is typically about 10 m and the height is commonly about 35 m for catalyst flow rates between 300-500 kg/s and air flow between 40-80 m^3/s at the regeneration temperature [101], which were representative values for the Oleflex regenerator specifications in this work. The capital costs of this regenerator were estimated based on the method by Towler and Sinnott considering the regenerator as a jacketed reactor [66].

5.G2. Compressor simulations

All compressors were simulated by specifying the desired discharge pressure and by defining the number of compression stages needed. All compressors were centrifugal compressors, because of the high flow rates in all three processes [102]. The compression ratio per stage is typically about 1.2-1.3 for centrifugal compressors [103]. A value of 1.3 per stage was used in this work.

5.G3. Distillation columns

The distillation columns were designed based on the method by Towler and Sinnott [104]. The diameter of a distillation column (D_c) primarily depends on the vapor flow rate and is approximated by **Equation 5.G1**.

$$D_c = \sqrt{\frac{4\dot{m}_m}{\pi \rho_v u_v}} \qquad (5.G1)$$

Where $\dot{m}_m$ represents the maximum vapor mass flow rate (in kg/s), ρ_v is the vapor density (in kg/m³), and u_v the maximum allowable superficial vapor velocity (in m/s). The latter parameter depends on the vapor and liquid densities and on the distance between trays (l_t, in m), following **Equation 5.G2**. A distance between trays of 0.5 m is taken for all distillation columns in this work.

$$u_v = (-0.171\, l_t^2 + 0.27\, l_t - 0.047) * \left(\frac{\rho_l - \rho_v}{\rho_v}\right)^{1/2} \qquad (5.G2)$$

The height of a distillation column is comprised of vertical space needed for (i) the reboiler, (ii) the condenser, (iii) the skirt (column support), (iv) and the column itself. The reboiler and condenser contributions to the total height were taken as three times and two times the distance between trays (l_t), respectively [104]. Besides, the required height for the skirt was assumed to be two meter. The respective tray efficiencies of depropanizer, deethanizer, and C3 splitter columns are typically 75%, 70%, and 85% [105]. These tray efficiency values were therefore taken for the three different distillation columns in this work to calculate the actual number of trays needed. The actual reflux ratio was assumed to be 1.3 times the minimum reflux ratio in all cases [104].

The capital investment of the distillation columns was comprised of the steel costs for the column itself and the costs for the required number of bubble-cap trays or sieve trays. The column steel costs depended on the column dimensions and wall thickness (**Supporting Information 5.H**). The choice for bubble-cap trays or sieve trays depended on the vapor-to-liquid ratio inside the concerning column. In this case, the depropanizer column contained a relatively low liquid hold-up, making bubble-cap trays more suitable to ensure a liquid level on each tray [104]. For the deethanizer and C3 splitter columns, more standard sieve trays were selected.

The specifications of the distillation columns in the three different processes are presented in **Table 5.G1**. The diameter of the depropanizer column is slightly larger for the Oleflex process compared to both membrane processes, as vapor streams are larger for the Oleflex process due to the bigger recycle. The net amount of lights to be removed in the deethanizer column is fairly similar in all three processes, regardless of the dimension of the propane recycle. Since the diameter of a distillation column is mainly governed by the vapor flow, the dimensions of the deethanizer column are found to be comparable for all three processes. **Table 5.G1** clearly shows that increasing the propane NODH yield from 36% in Oleflex to 50% in the MPEC and PCEC-assisted processes strongly affects the diameter of the C3 splitter column. This can be attributed to the smaller process streams caused by the higher single-pass yields. Interestingly, the required number of C3 splitter column stages becomes somewhat higher for higher single-pass propylene yields. This propane/propylene separation step is complicated because of a small relative volatility. In case of 50% MPEC and PCEC propane dehydrogenation yields, the C3 splitter has a ca. 1:1 ratio of propane/propylene in the feed, whilst its feed ratio is about 2:1 in the Oleflex process. The higher propylene content in the feed makes separation in the C3 splitter column somewhat more complicated.

Table 5.G1: Distillation column specifications. Number of stages represent actual number of stages, reflux ratio is on molar basis.

ID	Description	Parameter	Oleflex	MPEC	PCEC
DC-1	Depropanizer column	# of stages (-)	28	28	28
		Reflux ratio (-)	0.9	0.9	0.9
		Height (m)	19	19	19
		Diameter (m)	6.1	5.3	5.3
DC-2	Deethanizer column	# of stages (-)	56	52	50
		Reflux ratio (-)	27.7	19.0	19.0
		Height (m)	33	31	30
		Diameter (m)	9.1	9.7	9.3
DC-3	C3 splitter column	# of stages (-)	150	156	157
		Reflux ratio (-)	22.6	18.3	22.5
		Height (m)	80	83	84
		Diameter (m)	13.4	10.6	11.1

5.G4. Pressure swing adsorption

The mass of adsorbent needed per pressure swing adsorption (PSA) bed (M_a, in kg) was calculated using **Equation 5.G3** [106].

$$(F_1 y_1 - F_2 y_2) M_w t_a = 1000 (m_1 - m_2) M_a f_L \qquad (5.G3)$$

Where F_1 and F_2 represented the feed and product molar flow rates, respectively, as retrieved from the Aspen simulations. Analogously, y_1 and y_2 are the molar fractions of hydrocarbons to be adsorbed in the feed and product flows. Here, it was considered that all light hydrocarbons needed to be removed from the H_2 product stream, so y_1 and y_2 are the sum of the hydrocarbon molar fractions in those streams. Besides, M_w is the molar weight of the component to be adsorbed. Since methane is the main component to be removed, the molar weight of methane was taken here. Furthermore, t_a represents the time in which the bed is in adsorption mode. This was assumed to be ten minutes here, based on the typical total cycle time of pressure swing adsorption of 5-60 minutes [106]. The maximum and minimum adsorbent loadings (m_1 and m_2) present the amounts of light hydrocarbons that can be adsorbed per g of activated carbon under high pressure (adsorption stage, 20 bar(a) here) and low pressure (desorption stage, 3 bar(a) here), respectively. The difference between both equals the amount of hydrocarbons that can be adsorbed per g of activated carbon per adsorption cycle. The methane loadings on activated carbon at 20 and 3 bar(a) are 0.072 and 0.024 g/g, respectively [107]. Finally, f_L is the fraction of the bed that is loaded, which is close to 1 in case the adsorption system contains four or more adsorption beds [106]. The results are summarized in **Table 5.G2**. The lifetime of the activated carbon adsorbent was estimated to be two years [108].

Table 5.G2: Pressure swing adsorption Oleflex process.

Parameter:	Description:	Value:	Unit:
m_1	High pressure CH_4 loading	0.072	[g CH_4/g AC]*
m_2	Low pressure CH_4 loading	0.024	[g CH_4/g AC]*
$F_1 y_1$	Mole flow adsorbed hydrocarbons	0.016	[mol/s]
$F_2 y_2$	Mole flow adsorbed hydrocarbons	0.008	[mol/s]
M_w	Molar weight adsorbed hydrocarbons	16.04	[g/mol]
t_a	Adsorption mode time	600	[s]
f_L	Loading fraction of bed	1	[-]
M_a (1 bed)	Adsorbent mass per bed	1.55	[kg]
M_a (4 beds)	Total adsorbent mass	6.20	[kg]

AC = activated carbon.

5.H. Wall thickness

The wall thickness of the Oleflex reactors, membrane reactors, and distillation columns was estimated using **Equation 5.H1**, valid for cylindrical pressure vessels [109].

$$t = \frac{P_i D_i}{2J * f - P_i} \tag{5.H1}$$

Where t represents the wall thickness (in mm), P_i the design pressure (in N/mm^2), D_i the internal diameter (in mm), J the joint factor, and f the material design stress (in N/mm^2). The design pressure was 10% above the operational pressure for safety reasons, the joint factor typically ranges between 0 and 1. A value of 0.8 was used in this work, corresponding to a single-welded butt joint [109]. A material design stress of 89 N/mm^2 was used for all pressure vessels in this work [109]. For safety reasons, an additional overdesign of 10-30% was applied on the minimum wall thickness, as determined using **Equation 5.H1**. The resulting wall thickness values were used together with the respective column dimensions to calculate the required steel volume. Subsequently, the required steel mass was estimated by multiplying the concerning steel volume with a steel density of 7850 kg/m^3 [110]. The wall thickness of the Oleflex reactors, membrane reactors, and distillation columns, as calculated using **Equation 5.H1**, are summarized in **Table 5.H1**.

Table 5.H1: Wall thickness (t) of the (membrane) reactors and distillation columns.

Process unit:	Indicator:	Description:	t:	Unit:
Oleflex reactor	D_1	Center pipe wall	18	[mm]
	D_2	Outer catalyst bed wall	46	[mm]
	D_3	Reactor shell wall	55	[mm]
MPEC reactor		SEU shell	5	[mm]
		Hot box shell	13	[mm]
PCEC reactor		SEU shell	6	[mm]
		Hot box shell	15	[mm]
Depropanizer column	DC-1	Oleflex process	82	[mm]
	DC-1	MPEC process	72	[mm]
	DC-1	PCEC process	72	[mm]
Deethanizer column	DC-2	Oleflex process	308	[mm]
	DC-2	MPEC process	327	[mm]
	DC-2	PCEC process	315	[mm]
C3 splitter	DC-3	Oleflex process	178	[mm]
	DC-3	MPEC process	141	[mm]
	DC-3	PCEC process	147	[mm]

5.J. Heat integration

5.J1. Off-gas heat recovery

Part of the energy needed for the process could be generated by burning off-gas streams available within the process. The deethanizer lights, depropanizer heavies, and PSA retention (Oleflex) streams were the three main off-gas streams in the three different processes from which heat could be recovered and the characteristics of these streams are tabulated in **Table 5.J1**. It is assumed that 70% of the available off-gas heat could be recovered for integration within the process [111].

Table 5.J1: Process heat available via off-gas recovery.

Stream		Oleflex	MPEC	PCEC	Note*/ref.
Depropanizer heavies	Mass flow (kg/s)	1.83	1.45	1.04	*n*-butane
	Higher heating value (MJ/kg)	49.10	49.10	49.10	[112]
Energy available (MW):		*89.89*	*71.01*	*50.98*	
Energy recovered, 70% eff. (MW) [111]:		*62.92*	*49.71*	*35.69*	
Deethanizer lights	Mass flow (kg/s)	1.77	1.20	1.32	ethane
	Higher heating value (MJ/kg)	51.9	51.9	51.9	[112]
Energy available (MW):		*91.97*	*62.21*	*68.44*	
Energy recovered, 70% eff. (MW) [111]:		*64.38*	*43.55*	*47.91*	
PSA retention stream	Mass flow (kg/s)	0.14	0	0	methane
	Higher heating value (MJ/kg)	55.5	55.5	55.5	[112]
Energy available (MW):		*7.82*	*0*	*0*	
Energy recovered, 70% eff. (MW) [111]:		*5.47*	*0*	*0*	
Total energy available (MW):		**189.68**	**133.23**	**119.42**	
Total energy recovered, 70% eff. (MW) [111]:		**132.77**	**93.26**	**83.59**	

Indicates the main constituent of the stream. The stream heating value was calculated by assuming that the entire mass flow had the heating value of this constituent.

5.J2. Catalyst regeneration and Joule heating

The amounts of energy generated via catalyst regeneration and Joule heating within the process were yet included in the base case analysis. The Joule heating calculations are presented in **Supporting Information 5.K**.

5.J3. Combining process streams (thermal pinch analysis)

Only the heating/cooling operations with a minimum energy duty of 10 MW were included in the thermal pinch analysis. The source temperature, targeted temperature, and heat duty of all heating/cooling steps that satisfy this requirement were used to construct the hot and cold composite curves of all three processes (**Figure 5.J1**).
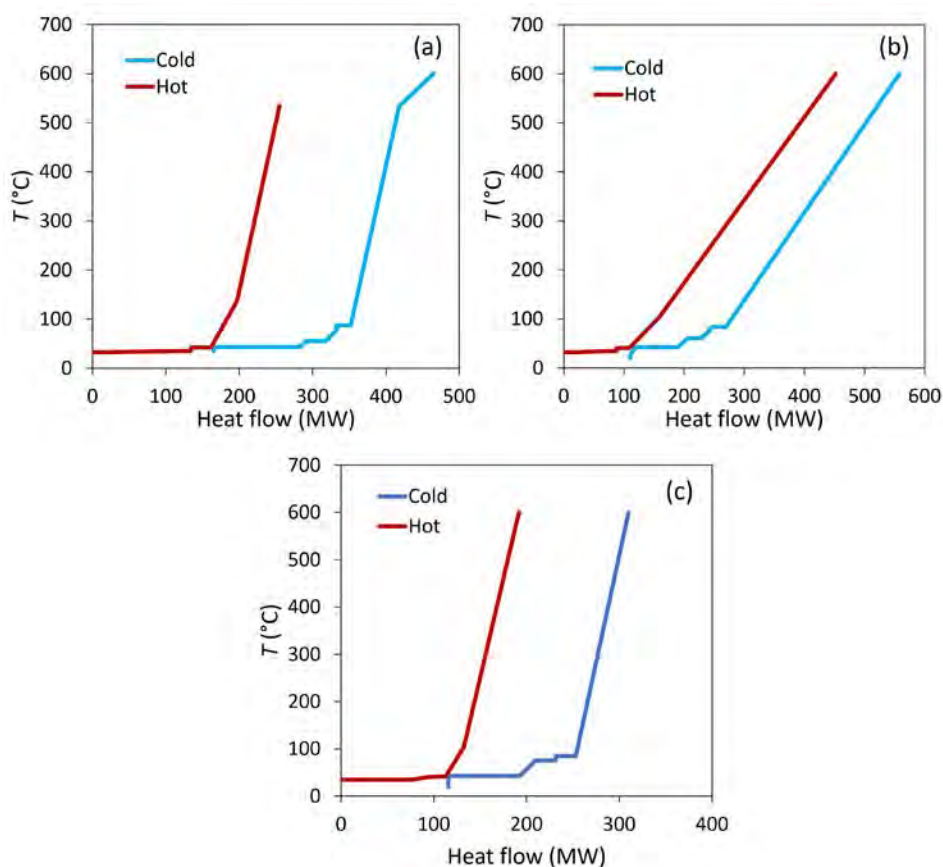
Figure 5.J1: Composite curves of (a) Oleflex process, (b) MPEC-assisted process, and (c) PCEC-assisted process.

The composite curves of the Oleflex and PCEC process are comparable in shape but the total heat flow of the PCEC process is smaller, because of the smaller recycle as a result of a higher single-pass yield. Also, the PCEC membrane reactor was operated isothermally at

600 °C, whilst the Oleflex reactors were operated adiabatically with a temperature gradient along the reactor length. In spite of a smaller recycle stream due to the higher single-pass yield, the total heat flow within the MPEC process is notably even larger than Oleflex. This is attributed to the high heating and cooling demand of the H_2O sweep gas in that process. Note that in the construction of the composite curves of the MPEC process (**Figure 5.J1b**), it was assumed that the sweep gas heating/cooling duties are equally distributed along the corresponding temperature range (room temperature to reaction temperature). However, in reality the steam sweep gas needs to be evaporated and condensed, implying that a considerable amount of energy needs to be exchanged around 100 °C. This issue is further discussed in **Section 5.J5**.

5.J4. Hot utility overview

The total hot utility demand and the distribution with which this total demand is covered in the heat integration for the three different processes is illustrated in **Figure 5.J2**. The flue gas from the fired heaters still contains a substantial amount of energy that could be used for the generation of steam but this is not included in this work.
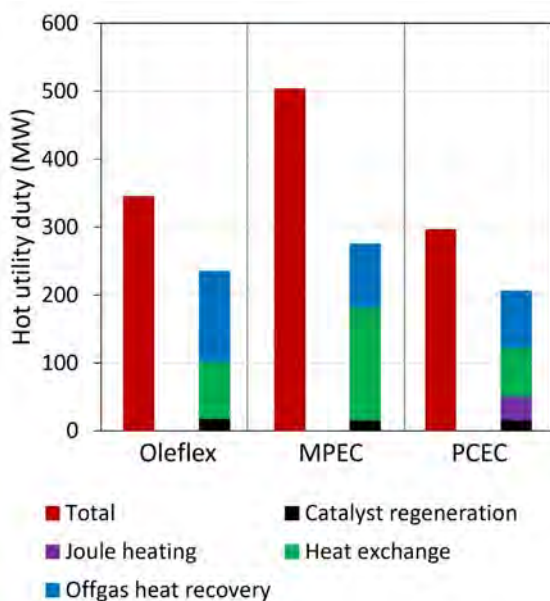
Figure 5.J2: Overview of hot utility distribution.

5.J5. MPEC process – steam sweep gas heat exchanger

In the MPEC process, the hot steam sweep gas outlet of the MPEC reactor that needs to be cooled to condense the water content and isolate the hydrogen product, is integrated with the water stream that needs to be evaporated and recycled as sweep gas to the MPEC reactor. The heat exchanger inlet temperature of the cold stream is 30 °C (i.e. 10 °C above

the cooling water temperature), whilst the heat exchanger inlet temperature of the hot stream is 600 °C (i.e. the reactor temperature). Since a large amount of water needs to be condensed and evaporated in this heat exchanger, a substantial part of the total cooling and heating energy requirement will be covered by the condensation and evaporation duties. For this reason, the expected temperature profile in this heat exchanger needs to be carefully checked. In this analysis, the temperature profile within this heat exchanger was checked by means of a temperature vs. energy duty plot for a targeted outlet temperature of the hot stream of 80 °C (**Figure 5.J3**). The parts in this graph that are about horizontal indicate the energy duty range across which the water condensation and evaporation take place. As condensation and evaporation of the water both occur around 100 °C, these energy duties cannot be exchanged. Instead, only the energy duties associated with cooling and heating the sweep gas can be exchanged, which sums up to 95 MW in total (see **Figure 5.J3**).
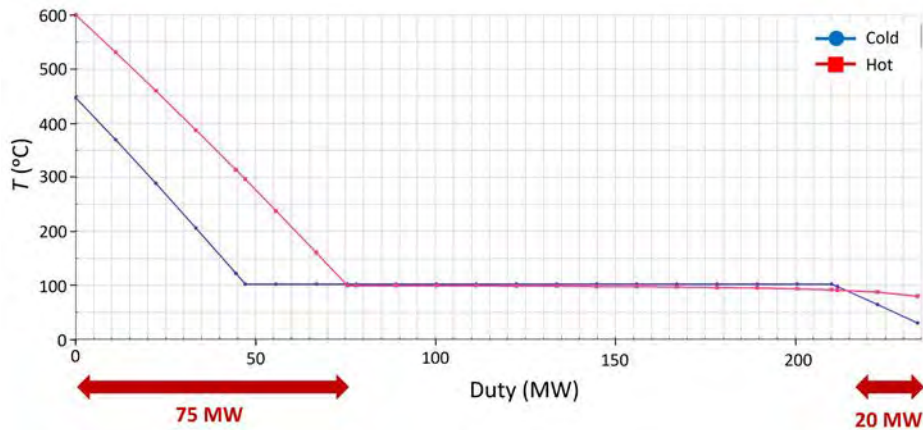
Figure 5.J3: Expected temperature profile inside the sweep gas heat exchanger of the MPEC process.

5.K. Resistive Joule heating

The hydrogen flow through a PCEC membrane is coupled with the electrical current according to **Equation 5.K1** [45].

$$I = \frac{n\dot{m}F}{M_{H_2}} \qquad (5.K1)$$

Where n represents the number of electrons transported per mole of permeated H_2 (i.e. 2), $\dot{m}$ is the mass flow rate of H_2 permeated (in kg/s), F is the Faraday constant (96,485.3 C/mol), and M_{H2} is the molar weight of H_2. The cell voltage of a proton conducting electrochemical cell can be described by [45]:

$$E_{cell} = E_{OCV} + IR \qquad (5.K2)$$

In which the open-circuit voltage (E_{OCV}) is defined by **Equation 5.K3**.

$$E_{OCV} = \frac{R_{gas}T}{nF} \ln\left(\frac{p_{H2,out}}{p_{H2,in}}\right) \qquad (5.K3)$$

The resistance (R) of protons across a PCEC is commonly presented as a function of the area specific resistance (ASR):

$$R = \frac{ASR}{A_{mem}} \qquad (5.K4)$$

The *ASR* of PCEC systems based on BZCY electrolytes was estimated at 0.4 $\Omega.cm^2$ [23]. Besides, the required membrane area (A_{mem}) was calculated to be about 10^4 m^2 in **Section 5.3.4** for the targeted application in this work. Lastly, the power of the electrochemical cell can be evaluated using **Equation 5.K5**.

$$P_{cell} = E_{cell}I = E_{OCV}I + I^2R \qquad (5.K5)$$

Where the first term represents the power for reversible electrochemical compression of H_2, whilst the second term is related to the cell resistance. The latter term represents the power required to overcome the overpotential. This energy is released as thermal energy in the PCEC membrane reactor and is referred to as resistive Joule heating. The inputs and outcomes of the Joule heating calculations are presented in **Table 5.K1**. Note that the Joule heating was assumed to be constant over time here. In reality, the membrane performance will deteriorate over time, leading to a higher resistance, and thus a larger amount of resistive Joule heat generated.

Table 5.K1: Results of the PCEC membrane reactor calculations.

Parameter:	Description:	Value:	Unit:
R_{gas}	Universal gas constant	8.314	[J/mol.K]
T	Operational temperature	600	[°C]
		873	[K]
n	Number of electrons transferred	2	[-]
F	Faraday constant	96,485.3	[C/mol]
p_{out}	Permeate side pressure PCEC	10	[bar(a)]
$y_{H2,out}$	Molar fraction H_2 on permeate side	0.961	[-]
$p_{H2,out}$	H_2 partial pressure permeate side	9.61	[bar(a)]
p_{in}	Feed side pressure PCEC	4	[bar(a)]
$y_{H2,in}$	Molar fraction H_2 on feed side	0.293	[-]
$p_{H2,in}$	H_2 partial pressure feed side	1.172	[bar(a)]
E_{OCV}	Open-circuit voltage	0.079	[V]
M_{H2}	Molar weight H_2	$2.016 \cdot 10^{-3}$	[kg/mol]

$\dot{m}$	Mass flow rate of permeating H_2	0.972	[kg/s]
I	Current	$9.3 \cdot 10^7$	[A]
ASR	Area specific resistance	0.4	[$\Omega.cm^2$]
A_{mem}	Membrane area	10,000	[m^2]
		$1 \cdot 10^8$	[cm^2]
R	Cell resistance	$4 \cdot 10^{-9}$	[Ω]
$P_{compression}$	Power of electrochemical compression	7,366,023	[W]
		7.4	[MW]
P_{Joule}	Power related to resistive heating	34,652,174	[W]
		34.7	[MW]
P_{cell}	Total cell power	42.0	[MW]
E_{cell}	Total cell voltage	0.451	[V]

5.L. Purchased equipment cost calculations

Note: The heaters and coolers of the H_2O cofeed and sweep gas were included in the process economics assessment and in the evaluation of process energy usage and CO_2 emissions. However, corresponding pumps needed to recycle H_2O streams were excluded and were anticipated to have a negligible influence on process economics and energy usage.

The purchased equipment costs (C_e) were calculated using **Equation 5.L1**, which forms the basis for the factor method for quantifying process equipment costs as proposed by Towler and Sinnott [66].

$$C_e = a + b\,S^n \tag{5.L1}$$

In **Equation 5.L1**, a and b are cost constants, applicable to a specific type of process equipment, S is the size parameter corresponding to that process equipment, and n represents the exponent for that type of equipment. The full list of parameters used in the purchased equipment costs calculations are available in **Table 5.L1**. The results of the purchased equipment costs are presented in **Table 5.L2**.

Table 5.L1: Parameters used for calculating purchased equipment costs of common plant equipment [66].

Equipment type	Units for size, S	S_{lower}	S_{upper}	a	b	n
Vertical pressure vessel	kg (shell mass)	160	250,000	11,600	34	0.85
Bubble cap trays (1 tray)	m (diameter)	0.5	5	340	640	1.9
Sieve trays (1 tray)	m (diameter)	0.5	5	130	440	1.8
Reactor, jacketed, agitated	m³ (volume)	0.5	100	61,500	32,500	0.8
Box furnace	MW (duty)	30	120	43,000	111,000	0.8
Pump, single stage, centrifugal	L/s (flow)	0.2	126	8,000	240	1
Centrifugal compressor	kW (driver power)	75	30,000	580,000	20,000	0.6
Compressor blower	m³/h	200	5,000	4,450	57	0.8
Thermosiphon reboiler	m² (area)	10	500	30,400	122	1.1
Floating head shell and tube	m² (area)	10	1,000	32,000	70	1.2
Plate and frame exchanger	m² (area)	1	500	1,600	210	0.95

Table 5.L2: Results of the purchased equipment costs calculations.

ID	Description	Ref.	Equipment type	Size parameter, S	Size value, S			Purchased equipment cost, Cₑ (US$)		
					Oleflex	MPEC	PCEC	Oleflex	MPEC	PCEC
Distillation columns										
DC-1	Depropanizer column	[66]	Vertical pressure vessel	kg (shell mass)	271,073	202,746	202,746	1.42 MM	1.11 MM	1.11 MM
	Depropanizer column trays	[66]	Bubble–cap trays	m (diameter)	6.05	5.26	5.26	0.56 MM (28 trays)	0.43 MM (28 trays)	0.43 MM (28 trays)
DC-2	Deethanizer column	[66]	Vertical pressure vessel	kg (shell mass)	2,598,217	2,794,567	2,518,863	9.65 MM	10.26 MM	9.40 MM
	Deethanizer column trays	[66]	Sieve trays	m (diameter)	9.11	9.68	9.34	1.32 MM (56 trays)	1.37 MM (52 trays)	1.23 MM (50 trays)
DC-3	C3 splitter column	[66]	Vertical pressure vessel	kg (shell mass)	5,094,742	3,242,124	3,566,721	17.09 MM	11.64 MM	12.63 MM
	C3 splitter trays	[66]	Sieve trays	m (diameter)	13.42	10.57	11.05	7.09 MM (150 trays)	4.81 MM (156 trays)	5.24 MM (157 trays)
*Reactors, note that the costs for Oleflex dehydrogenation reactors (**Supporting Information 5.E**) and MPEC and PCEC membrane reactors (**Supporting Information 5.F**) are described elsewhere.*										
R-5	Regenerator oleflex	[66]	Vertical pressure vessel	kg (shell mass)	150,499	-	-	0.87 MM	-	-
R-6	SHP reactor Oleflex	[66]	Reactor, jacketed, agitated	m³ (volume)	35	-	-	0.62 MM	-	-
Fired heaters										
FH-1	Fired heater I	[66]	Box furnace	MW (duty)	83.6	53.9	54.8	3.87 MM	2.74 MM	2.78 MM
FH-2	Fired heater II	[66]	Box furnace	MW (duty)	12.6	-	-	0.89 MM	-	-
FH-3	Fired heater III	[66]	Box furnace	MW (duty)	12.3	-	-	0.87 MM	-	-
FH-4	Fired heater IV	[66]	Box furnace	MW (duty)	12.2	-	-	0.86 MM	-	-
Pumps										
P-1	Reactor effluent pump	[66]	Single stage, centrifugal	L/s (flow)	139.5	-	-	28,432	-	-
P-2	Propane recycle pump	[66]	Single stage, centrifugal	L/s (flow)	67.6	40.1	55.0	18,645	14,653	16,842
Compressors and expanders										
CP-1	Fresh propane feed compressor	[66]	Centrifugal compressor	kW (driver power)	1578.0	1465.2	1415.7	2.24 MM	2.17 MM	2.13 MM
CP-2	Reactor effluent compressor 1	[66]	Centrifugal compressor	kW (driver power)	10437.2	3313.6	3382.5	5.73 MM	3.17 MM	3.20 MM
CP-3	Reactor effluent compressor 2	[66]	Centrifugal compressor	kW (driver power)	9311.3	2322.2	2369.1	5.39 MM	2.67 MM	2.70 MM
CP-4	H2 product compressor 1	[66]	Centrifugal compressor	kW (driver power)	1831.9	0	0	2.39 MM	-	-

Tag	Description	Ref	Type	Units						
CP-5	H₂ product compressor 2	[66]	Centrifugal compressor	kW (driver power)	1389.8	5542.0	2261.6	5.13 MM	13.43 MM	7.14 MM
E-1	Expander to reduce P of depropanizer top	[66]	Compressor blower	m³/h	6092.1	4810.9	4828.8	65,219	54,760	54,910
E-2	Cold box expander	[66]	Compressor blower	m³/h	3545.1	-	-	43,858	-	-
Heat exchangers										
DC-1-R	Depropanizer reboiler	[66]	Thermosiphon reboiler	m² (area)	805	640	712	0.22 MM	0.18 MM	0.20 MM
DC-2-R	Deethanizer reboiler	[66]	Thermosiphon reboiler	m² (area)	1113	1146	926	0.30 MM	0.31 MM	0.25 MM
DC-3-R	C3 splitter reboiler	[66]	Thermosiphon reboiler	m² (area)	4052	2423	2789	1.16 MM	0.67 MM	0.78 MM
DC-1-C	Depropanizer condenser	[66]	Floating head shell and tube	m² (area)	1343	1270	1390	2.57 MM	2.02 MM	2.23 MM
DC-2-C	Deethanizer condenser	[66]	Floating head shell and tube	m² (area)	1328	1317	1399	2.97 MM	2.52 MM	1.35 MM
DC-3-C	C3 splitter condenser	[66]	Floating head shell and tube	m² (area)	1465	1467	1474	10.40 MM	6.15 MM	7.14 MM
H-1	Reactor feed/effluent heat exchanger	[66]	Plate and frame heat exchanger	m² (area)	570	418	430	88,709	66.541	68.345
H-2	Air to regenerator heater	[66]	Box furnace	MW (duty)	4.99	4.41	4.38	0.44 MM	0.41 MM	0.40 MM
H-3	H₂ product heater	[66]	Floating head shell and tube	m² (area)	150	0	0	60,695	0	0
H-4	Cold box hydrocarbon effluent heater I	[66]	Floating head shell and tube	m² (area)	73	0	0	43,977	0	0
H-5	Cold box hydrocarbon effluent heater II	[66]	Floating head shell and tube	m² (area)	124	0	0	54,748	0	0
H-6	Deethanizer feed heater	[66]	Floating head shell and tube	m² (area)	217	0	0	76.615	0	0
H-7	H₂O sweep gas heater	[66]	Box furnace	MW (duty)	0	258.2	1.0	0	9.48 MM	0.16 MM
H-8	H₂O co-feed heater feed side	[66]	Box furnace	MW (duty)	0	1.9	1.7	0	0.23 MM	0.21 MM
H-9	Hydrocarbon heater after H₂O flash drum	[66]	Plate and frame heat exchanger	m² (area)	0	133	132	0	23,505	23,368
H-10	Permeate side H₂ heater	[66]	Plate and frame heat exchanger	m² (area)	0	26	26	0	6,262	6.227
C-1	Reactor effluent cooler I	[66]	Floating head shell and tube	m² (area)	2409	1714	1733	0.83 MM	0.56 MM	0.57 MM
C-2	Reactor effluent cooler II	[66]	Floating head shell and tube	m² (area)	998	481	491	0.31 MM	0.15 MM	0.15 MM
C-3	Reactor effluent cooler III	[66]	Floating head shell and tube	m² (area)	979	1487	1521	0.30 MM	0.48 MM	0.49 MM

C-4	Cold box cooler I	[66]	Plate and frame heat exchanger	m² (area)	2045	0	0	0.30 MM	0	0
C-5	Cold box cooler II	[66]	Plate and frame heat exchanger	m² (area)	259	0	0	42,855	0	0
C-6	H₂ product cooler	[66]	Floating head shell and tube	m² (area)	0	8420	235	0	3.63 MM	81,019
C-7	Cooler in between deethanizer and C3 splitter	[66]	Floating head shell and tube	m² (area)	1248	951	1000	0.40 MM	0.29 MM	0.31 MM
Vessels										
PSA	Pressure Swing Adsorption (Oleflex)	[66]	Vertical pressure vessel	kg (shell mass)	16	0	0	11,966	0	0

5.M. Installation factors

The purchase equipment costs were determined per unit operation in **Supporting Information 5.L**. Additional costs for installation were included to account for the fact that the purchased equipment needs to be installed in the process. This is done by using the installation compensation factor proposed by W.E. Hand [66]. The Hand installation factors applied in this work are summarized in **Table 5.M1**. All (membrane) reactors were taken as pressure vessels, meaning these complex types of process equipment dealt with the largest correction in terms of installation costs.

Table 5.M1: Process cost installation factors proposed by Hand [66].

Equipment type	Installation factor
Compressors	2.5
Distillation columns	4
Fired heaters	2
Heat exchangers	3.5
Instruments	4
Miscellaneous equipment	2.5
Pressure vessels	4
Pumps	4

5.N. Direct investment calculations

The results of the direct investment calculations are summarized in **Table 5.N1**. The corresponding purchase equipment costs for almost all process equipment are available in **Supporting Information 5.L**. Exceptions are the separately evaluated purchase equipment costs for the Oleflex reactors (**Supporting Information 5.E**) and the MPEC and PCEC membrane reactors (**Supporting Information 5.F**).

Table 5.N1: Results of direct investment calculations. S.I. = Supporting Information, ISBL = inside battery limits, OSBL = outside battery limits.

ID	Description	Material	Material factor	Hand factor	Reference year	CEPCI reference year	CEPCI Apr. 2023	Source	Oleflex process (USD) Before + after HI	MPEC process (USD) Before HI	MPEC process (USD) After HI	PCEC process (USD) Before + after HI
Reactors												
R-1, R-2, R-3, R-4	Moving bed reactors (Oleflex)	Stainless steel 304	1.3	4	2022	797.6	803.4	S.I. 5.E	40.07 MM	-	-	-
R-1	Membrane reactor (MPEC + PCEC)	Stainless steel 304	1.3	4	2022	797.6	803.4	S.I. 5.F (MPEC) S.I. 5.F (PCEC)	-	7,386.09 MM	7,386.09 MM	74.20 MM
R-5	Regenerator (Oleflex)	Carbon steel	1	4	2010	532.9	803.4	S.I. 5.L	5.23 MM	-	-	-
R-6	SHP reactor (Oleflex)	Carbon steel	1	4	2010	532.9	803.4	S.I. 5.L	3.77 MM	-	-	-
								Subtotal:	*49.07 MM*	*7,386.09 MM*	*7,386.09 MM*	*74.20 MM*
Distillation columns												
DC-1	Depropanizer column (vessel)	Carbon steel	1	4	2010	532.9	803.4	S.I. 5.L	8.58 MM	6.72 MM	6.72 MM	6.72 MM
	Depropanizer column (bubble-cap trays)	Carbon steel	1	4	2010	532.9	803.4	S.I. 5.L	0.84 MM	0.65 MM	0.65 MM	0.65 MM
DC-2	Deethanizer column (vessel)	Carbon steel	1	4	2010	532.9	803.4	S.I. 5.L	58.19 MM	61.90 MM	61.90 MM	56.67 MM
	Deethanizer column (sieve trays)	Carbon steel	1	4	2010	532.9	803.4	S.I. 5.L	1.99 MM	2.06 MM	2.06 MM	1.86 MM
DC-3	C3 splitter column (vessel)	Carbon steel	1	4	2010	532.9	803.4	S.I. 5.L	103.08 MM	70.22 MM	70.22 MM	76.15 MM
	C3 splitter column (sieve trays)	Carbon steel	1	4	2010	532.9	803.4	S.I. 5.L	10.69 MM	7.25 MM	7.25 MM	7.90 MM
								Subtotal:	*183.37 MM*	*148.80 MM*	*148.80 MM*	*149.95 MM*
Fired heaters												
FH-1	Fired heater I	Carbon steel	1	2	2010	532.9	803.4	S.I. 5.L	11.68 MM	8.26 MM	8.26 MM	8.37 MM
FH-2	Fired heater II	Carbon steel	1	2	2010	532.9	803.4	S.I. 5.L	2.67 MM	-	-	-

Tag	Description	Material										
FH-3	Fired heater III	Carbon steel	1	2	2010	532.9	803.4	S.I. 5.L	2.63 MM	-	-	-
FH-4	Fired heater IV	Carbon steel	1	2	2010	532.9	803.4	S.I. 5.L	2.60 MM	-	-	-
								Subtotal:	19.58 MM	8.26 MM	8.26 MM	8.37 MM
Pumps												
P-1	Reactor effluent pump	Carbon steel	1	4	2010	532.9	803.4	S.I. 5.L	0.17 MM	-	-	-
P-2	Propane recycle pump	Carbon steel	1	4	2010	532.9	803.4	S.I. 5.L	0.11 MM	0.09 MM	0.09 MM	0.10 MM
								Subtotal:	0.28 MM	0.09 MM	0.09 MM	0.10 MM
Compressors and expanders												
CP-1	Fresh propane feed compressor	Carbon steel	1	2.5	2010	532.9	803.4	S.I. 5.L	8.44 MM	8.17 MM	8.17 MM	8.05 MM
CP-2	Reactor effluent compressor I	Carbon steel	1	2.5	2010	532.9	803.4	S.I. 5.L	21.61 MM	11.95 MM	11.95 MM	12.07 MM
CP-3	Reactor effluent compressor II	Carbon steel	1	2.5	2010	532.9	803.4	S.I. 5.L	20.33 MM	10.07 MM	10.07 MM	10.17 MM
CP-4	H2 product compressor I	Carbon steel	1	2.5	2010	532.9	803.4	S.I. 5.L	9.03 MM	-	-	-
CP-5	H2 product compressor II	Carbon steel	1	2.5	2010	532.9	803.4	S.I. 5.L	19.34 MM	50.60 MM	50.60 MM	26.91 MM
E-1	Expander to reduce P of depropanizer top	Carbon steel	1	2.5	2010	532.9	803.4	S.I. 5.L	0.25 MM	0.21 MM	0.21 MM	0.21 MM
E-2	Cold box expander	Carbon steel	1	2.5	2010	532.9	803.4	S.I. 5.L	0.17 MM	-	-	-
								Subtotal:	79.16 MM	80.99 MM	80.99 MM	57.39 MM
Heat exchangers												
DC-1-R	Depropanizer reboiler	Carbon steel	1	3.5	2010	532.9	803.4	S.I. 5.L	1.17 MM	0.95 MM	0.95 MM	1.04 MM
DC-2-R	Deethanizer reboiler	Carbon steel	1	3.5	2010	532.9	803.4	S.I. 5.L	1.61 MM	1.65 MM	1.65 MM	1.34 MM
DC-3-R	C3 splitter reboiler	Carbon steel	1	3.5	2010	532.9	803.4	S.I. 5.L	6.15 MM	3.56 MM	3.56 MM	4.13 MM
DC-1-C	Depropanizer condenser	Carbon steel	1	3.5	2010	532.9	803.4	S.I. 5.L	13.58 MM	10.64 MM	10.64 MM	11.76 MM
DC-2-C	Deethanizer condenser	Carbon steel	1	3.5	2010	532.9	803.4	S.I. 5.L	15.65 MM	13.29 MM	13.29 MM	7.10 MM

Tag	Name	Material							54.85 MM	143.43 MM	114.88 MM	37.66 MM
DC-3-C	C3 splitter condenser	Carbon steel	1	3.5	2010	532.9	803.4	S.I. 5.L	54.85 MM	32.48 MM	32.48 MM	37.66 MM
H-1	Reactor feed heater	Carbon steel	1	3.5	2010	532.9	803.4	S.I. 5.L	0.47 MM	0.35 MM	0.35 MM	0.36 MM
H-2	Air to regenerator heater	Carbon steel	1	3.5	2010	532.9	803.4	S.I. 5.L	2.35 MM	2.15 MM	2.15 MM	2.13 MM
H-3	H_2 product heater	Carbon steel	1	3.5	2010	532.9	803.4	S.I. 5.L	0.32 MM	-	-	-
H-4	Cold box hydrocarbon effluent heater I	Carbon steel	1	3.5	2010	532.9	803.4	S.I. 5.L	0.23 MM	-	-	-
H-5	Cold box hydrocarbon effluent heater II	Carbon steel	1	3.5	2010	532.9	803.4	S.I. 5.L	0.29 MM	-	-	-
H-6	Deethanizer feed heater	Carbon steel	1	3.5	2010	532.9	803.4	S.I. 5.L	0.40 MM	-	-	-
H-7	H_2O sweep gas heater	Carbon steel	1	3.5	2010	532.9	803.4	S.I. 5.L	-	50.03 MM	34.74 MM	0.83 MM
H-8	H_2O co-feed heater feed side	Carbon steel	1	3.5	2010	532.9	803.4	S.I. 5.L	-	1.20 MM	1.20 MM	1.13 MM
H-9	Hydrocarbon heater after H_2O flash drum	Carbon steel	1	3.5	2010	532.9	803.4	S.I. 5.L	-	0.12 MM	0.12 MM	0.12 MM
H-10	Permeate side H_2 heater	Carbon steel	1	3.5	2010	532.9	803.4	S.I. 5.L	-	0.03 MM	0.03 MM	0.03 MM
C-1	Reactor effluent cooler I	Carbon steel	1	3.5	2010	532.9	803.4	S.I. 5.L	4.39 MM	2.98 MM	2.98 MM	3.01 MM
C-2	Reactor effluent cooler II	Carbon steel	1	3.5	2010	532.9	803.4	S.I. 5.L	1.64 MM	0.78 MM	0.78 MM	0.80 MM
C-3	Reactor effluent cooler III	Carbon steel	1	3.5	2010	532.9	803.4	S.I. 5.L	1.60 MM	2.54 MM	2.54 MM	2.60 MM
C-4	Cold box cooler I	Carbon steel	1	3.5	2010	532.9	803.4	S.I. 5.L	1.56 MM	-	-	-
C-5	Cold box cooler II	Carbon steel	1	3.5	2010	532.9	803.4	S.I. 5.L	0.23 MM	-	-	-
C-6	H_2 product cooler	Carbon steel	1	3.5	2010	532.9	803.4	S.I. 5.L	-	19.13 MM	5.88 MM	0.43 MM
C-7	Cooler in between deethanizer and C3 splitter	Carbon steel	1	3.5	2010	532.9	803.4	S.I. 5.L	2.09 MM	1.55 MM	1.55 MM	1.64 MM
								Subtotal:	*108.57 MM*	*143.43 MM*	*114.88 MM*	*76.13 MM*

Vessels

PSA-1	Pressure Swing Adsorption (PSA)	Carbon steel	1	4	2010	532.9	803.4	S.I. 5.L	0.29 MM	- MM	- MM	- MM
								Subtotal:	*0.29 MM*	*- MM*	*- MM*	*- MM*
								Total direct investment (ISBL):	*440.31 MM*	*7,767.66 MM*	*7,739.11 MM*	*366.14 MM*
								Storage and transport (30% of OSBL)	52.84 MM	932.12 MM	928.69 MM	43.94 MM
								Utilities (30% of OSBL)	52.84 MM	932.12 MM	928.69 MM	43.94 MM
								Offsites (30% of OSBL)	52.84 MM	932.12 MM	928.69 MM	43.94 MM
								Environmental provisions (10% of OSBL)	17.61 MM	310.71 MM	309.56 MM	14.65 MM
								Total OSBL (=40% of ISBL) [66]:	*176.13 MM*	*3,107.06 MM*	*3,095.64 MM*	*146.45 MM*
								Engineering costs (10% of ISBL + OSBL) [66]	61.64 MM	1,087.47 MM	1,083.48 MM	51.26 MM
								Contingency charges (15% of ISBL + OSBL) [66]	92.47 MM	1,631.21 MM	1,625.21 MM	76.89 MM
								Engineering costs + contingency charges (= 25% of ISBL + OSBL):	*154.11 MM*	*2,718.68 MM*	*2,708.69 MM*	*128.15 MM*
								Total fixed capital investment:	771 MM	13,593 MM	13,543 MM	641 MM

5.O. Process utilities

The process utilities were quantified for fossil fuel and electrically heated reactors, and for situations before heat integration (BHI) and after heat integration (AHI). The results of fossil fuel heated reactors are summarized in **Table 5.O1** (BHI) and **Table 5.O2** (AHI), whilst the results for electrically heated reactors are summarized in **Table 5.O3** (BHI) and **Table 5.O4** (AHI), respectively.

Table 5.O1: Process utilities for fossil fuel heated reactors, before heat integration.

ID	Description	Oleflex process		MPEC-assisted process		PCEC-assisted process	
		Duty (MW)	Cost (MM$/yr)	Duty (MW)	Cost (MM$/yr)	Duty (MW)	Cost (MM$/yr)
Cooling water							
DC-1	Condenser depropanizer column	26.59	0.81	19.64	0.60	20.06	0.61
DC-2	Condenser deethanizer column	17.24	1.05	14.66	0.89	11.23	0.34
DC-3	Condenser C3 splitter column	133.68	5.09	82.99	3.16	96.19	3.66
C-1	Reactor effluent cooler I	72.28	2.20	56.29	1.71	56.90	1.73
C-2	Reactor effluent cooler II	10.60	0.32	4.16	0.13	4.25	0.13
C-3	Reactor effluent cooler III	9.85	0.30	12.28	0.37	12.56	0.38
C-6	H$_2$ product cooler	0	0	276.50	8.42	7.72	0.23
C-7	Cooler in between deethanizer column and C3 splitter	6.26	0.19	4.52	0.14	4.64	0.14
Subtotal:		*276.50*	*9.96*	*471.04*	*15.42*	*213.55*	*7.23*
LP steam							
DC-1	Reboiler depropanizer column	25.75	4.95	19.19	3.69	19.59	3.77
DC-2	Reboiler deethanizer column	18.92	3.64	20.06	3.86	16.67	3.21
DC-3	Reboiler C3 splitter column	133.71	25.71	83.01	15.61	96.21	18.50
H-1	Reactor feed stream heater (cold box)	17.09	3.29	12.63	2.43	12.91	2.48
H-3	H$_2$ product heater	4.77	0.92	0	0	0	0
H-4	Cold box hydrocarbon effluent heater I	6.11	1.17	0	0	0	0
H-5	Cold box hydrocarbon effluent heater II	6.51	1.25	0	0	0	0
H-6	Deethanizer feed heater	6.42	1.24	0	0	0	0
H-9	Hydrocarbon heater after H$_2$O flash drum	0	0	2.74	0.53	2.73	0.52
H-10	Permeate side H$_2$ heater	0	0	0.54	0.10	0.53	0.10
Subtotal:		*219.29*	*42.17*	*138.18*	*26.22*	*148.64*	*28.58*
Natural gas							
FH-1	Fired heater I	83.60	15.45	53.92	9.96	54.85	10.13
FH-2	Fired heater II	12.60	2.33	0	0	0	0
FH-3	Fired heater III	12.33	2.28	0	0	0	0
FH-4	Fired heater IV	12.19	2.25	0	0	0	0
R-1	Dehydrogenation reactor	0	0	48.79	9.02	48.32	8.93
H-2	Air to regenerator heater	4.99	0.92	4.41	0.82	4.38	0.81
H-8	H$_2$O co-feed heater feed side	0	0	1.90	0.35	1.71	0.32

H-7	H₂O co-feed heater permeate side	0	0	258.23	47.72	1.03	0.19
R-5	*Energy from catalyst regeneration*	*-18.08*	*-3.34*	*-16.07*	*-2.97*	*-15.82*	*-2.92*
R-1	*Resistive Joule heating*	*0*	*0*	*0*	*0*	*-34.70*	*-6.41*
Subtotal:		***107.63***	***19.89***	***351.18***	***64.90***	***59.77***	***11.04***
Electricity							
P-1	Reactor effluent pump	0.52	0.33	0	0	0	0
P-2	Propane recycle pump	0.00	0.00	0.00	0.00	0.00	0.00
CP-1	Fresh propane feed compressor	1.58	1.01	1.47	0.94	1.42	0.90
CP-2	Reactor effluent compressor I	10.44	6.66	3.31	2.12	3.38	2.16
CP-3	Reactor effluent compressor II	9.31	5.94	2.32	1.48	2.37	1.51
CP-4	H₂ product compressor I	1.83	1.17	0	0	0	0
CP-5	H₂ product compressor II	1.39	0.89	5.54	3.54	2.26	1.44
CP-6	H₂ product compressor III	0	0	0	0	0	0
R-1	Dehydrogenation reactor heating	0	0	0	0	0	0
R-1	Dehydrogenation reactor permeation	0	0	0	0	37.10	23.68
Subtotal:		***25.07***	***16.00***	***12.64***	***8.07***	***46.53***	***29.70***
Total utility:		**628.48**	**88.02**	**973.04**	**114.61**	**468.48**	**76.57**

Table 5.O2: Process utilities for fossil fuel heated reactors, after heat integration (AHI). BHI = before heat integration. For more information on the heat integration calculations, see **Supporting Information 5.J.**

Description	Oleflex process		MPEC-assisted process		PCEC-assisted process	
	Duty (MW)	Cost (MM$/yr)	Duty (MW)	Cost (MM$/yr)	Duty (MW)	Cost (MM$/yr)
Cooling water						
Total BHI **(Table 5.O1)**	276.50	9.96	471.04	15.42	213.55	7.23
Duty covered by combining hot and cold process streams	-84.33		-165.73		-71.44	
Subtotal AHI	*192.17*	*6.92*	*305.31*	*9.99*	*142.11*	*4.81*
LP steam						
Total BHI **(Table 5.O1)**	219.29	42.17	138.18	26.22	148.64	28.58
Duty covered by off-gas recovery	-25.14		-0.00		-23.83	
Duty covered by combining hot and cold process streams	-84.33		-0.00		-71.44	
Subtotal AHI:	*109.82*	*21.12*	*138.18*	*26.22*	*53.37*	*10.26*
Natural gas						
Total BHI **(Table 5.O1)**	107.63	19.89	351.18	64.90	59.77	11.04
Duty covered by off-gas recovery	-107.63		-93.26		-59.77	
Duty covered by combining hot and cold process streams	0.00		-165.73		0.00	
Subtotal:	*0.00*	*0.00*	*92.19*	*17.04*	*0.00*	*0.00*
Electricity						
Total BHI **(Table 5.O1)**	25.07	16.00	12.64	8.07	46.53	29.70
Subtotal:	*25.07*	*16.00*	*12.64*	*8.07*	*46.53*	*29.70*
Total utility:	**327.05**	**44.04**	**548.32**	**61.32**	**242.01**	**44.78**

Table 5.O3: Process utilities for electrically heated reactors, before heat integration.

ID	Description	Oleflex process		MPEC-assisted process		PCEC-assisted process	
		Duty (MW)	Cost (MM$/yr)	Duty (MW)	Cost (MM$/yr)	Duty (MW)	Cost (MM$/yr)
Cooling water							
DC-1	Condenser depropanizer column	26.59	0.81	19.64	0.60	20.06	0.61
DC-2	Condenser deethanizer column	17.24	1.05	14.66	0.89	11.23	0.34
DC-3	Condenser C3 splitter column	133.68	5.09	82.99	3.16	96.19	3.66
C-1	Reactor effluent cooler I	72.28	2.20	56.29	1.71	56.90	1.73
C-2	Reactor effluent cooler II	10.60	0.32	4.16	0.13	4.25	0.13
C-3	Reactor effluent cooler III	9.85	0.30	12.28	0.37	12.56	0.38
C-6	H$_2$ product cooler	0	0	276.50	8.42	7.72	0.23
C-7	Cooler in between deethanizer column and C3 splitter	6.26	0.19	4.52	0.14	4.64	0.14
Subtotal:		**276.50**	**9.96**	**471.04**	**15.42**	**213.55**	**7.23**
LP steam							
DC-1	Reboiler depropanizer column	25.75	4.95	19.19	3.69	19.59	3.77
DC-2	Reboiler deethanizer column	18.92	3.64	20.06	3.86	16.67	3.21
DC-3	Reboiler C3 splitter column	133.71	25.71	83.01	15.61	96.21	18.50
H-1	Reactor feed stream heater (cold box)	17.09	3.29	12.63	2.43	12.91	2.48
H-3	H$_2$ product heater	4.77	0.92	0	0	0	0
H-4	Cold box hydrocarbon effluent heater I	6.11	1.17	0	0	0	0
H-5	Cold box hydrocarbon effluent heater II	6.51	1.25	0	0	0	0
H-6	Deethanizer feed heater	6.42	1.24	0	0	0	0
H-9	Hydrocarbon heater after H$_2$O flash drum	0	0	2.74	0.53	2.73	0.52
H-10	Permeate side H$_2$ heater	0	0	0.54	0.10	0.53	0.10
Subtotal:		**219.29**	**42.17**	**138.18**	**26.22**	**148.64**	**28.58**
Natural gas							
FH-1	Fired heater I	0	0	0	0	0	0
FH-2	Fired heater II	0	0	0	0	0	0
FH-3	Fired heater III	0	0	0	0	0	0
FH-4	Fired heater IV	0	0	0	0	0	0
R-1	Dehydrogenation reactor	0	0	0	0	0	0
Subtotal:		**0**	**0**	**0**	**0**	**0**	**0**
Electricity							

P-1	Reactor effluent pump	0.52	0.33	0	0	0	0
P-2	Propane recycle pump	0.00	0.00	0.00	0.00	0.00	0.00
CP-1	Fresh propane feed compressor	1.58	1.01	1.47	0.94	1.42	0.90
CP-2	Reactor effluent compressor I	10.44	6.66	3.31	2.12	3.38	2.16
CP-3	Reactor effluent compressor II	9.31	5.94	2.32	1.48	2.37	1.51
CP-4	H_2 product compressor I	1.83	1.17	0	0	0	0
CP-5	H_2 product compressor II	1.39	0.89	5.54	3.54	2.26	1.44
CP-6	H_2 product compressor III	0	0	0	0	0	0
FH-1	Fired heater I	83.60		53.92		54.85	
FH-2	Fired heater II	12.60					
FH-3	Fired heater III	12.33					
FH-4	Fired heater IV	12.19					
FH-total	*Total fired heater*	*120.72*		*53.92*		*54.85*	
R-5	*Energy from catalyst regeneration*	*-18.08*		*-16.07*		*-15.82*	
R-1	Dehydrogenation reaction heat	0		48.79		48.32	
H-8	H_2O co-feed heater feed side	0		1.90		1.71	
H-7	H_2O co-feed heater permeate side	0		258.23		1.03	
R-1	Total reactor heating	102.64	65.53	346.77	221.38	90.09	57.51
R-1	Dehydrogenation reactor permeation	0	0	0	0	37.10	23.68
R-1	*Resistive Joule heating*	*0*	*0*	*0*	*0*	*-34.70*	*-22.15*
H-2	Air to regenerator heater	4.99	3.18	4.41	2.82	4.38	2.79
Subtotal:		*132.70*	*84.71*	*363.83*	*232.27*	*106.30*	*67.86*
Total utility:		**628.48**	**136.84**	**973.04**	**273.90**	**468.48**	**103.68**

Table 5.O4: Process utilities for electrically heated reactors, after heat integration (AHI). BHI = before heat integration. For more information on the heat integration calculations, see **Supporting Information 5.J**.

ID	Description	Oleflex process		MPEC-assisted process		PCEC-assisted process	
		Duty (MW)	Cost (MM$/yr)	Duty (MW)	Cost (MM$/yr)	Duty (MW)	Cost (MM$/yr)
Cooling water							
Total BHI (**Table 5.O3**)		276.50	9.96	471.04	15.42	213.55	7.23
Duty covered by combining hot and cold process streams		-84.33		-165.73		-71.44	
Subtotal:		*192.17*	*6.92*	*305.31*	*9.99*	*142.11*	*4.81*
LP steam							
Total BHI (**Table 5.O3**)		219.29	42.17	138.18	26.22	148.64	28.58
Duty covered by combining hot and cold process streams		-84.33		-0.00		-48.74	
Subtotal:		*134.96*	*25.94*	*138.18*	*26.22*	*99.90*	*19.21*
Natural gas							
Subtotal:		*0*	*0*	*0*	*0*	*0*	*0*
Electricity							
Total BHI (**Table 5.O3**)		132.70	84.71	363.83	232.27	106.30	67.86
Duty covered by off-gas recovery		-132.70		-93.26		-83.59	
Duty covered by combining hot and cold process streams		-0.00		-165.73		-22.70	
Subtotal:		*0.00*	*0.00*	*104.84*	*66.93*	*0.00*	*0.00*
Total utility:		**327.05**	**32.86**	**548.32**	**103.14**	**242.01**	**24.02**

5.P. OPEX calculations

The operating expenditures (OPEX) of the three processes were calculated in this work using the conventional methodology described by Towler and Sinnott [68]. In this method, the total production costs are the sum of the total variable production costs and the total fixed production costs. The former depend on the plant capacity and contain costs for the (i) raw feedstock, (ii) process utilities, (iii) catalysts and chemicals, (iv) effluent disposal, and (v) packaging and shipping. On the contrary, fixed production costs are independent of production capacity and consist among others of (i) labor costs, (ii) process maintenance costs, (iii) property taxes, and (iv) rent of land.

5.P1. Variable production costs

The only raw material of the process was fresh propane that was derived from a natural gas processing plant. The price of the air needed for catalyst regeneration was assumed to be negligible. Besides, the H_2O cosupplied on both sides of the membrane in the MPEC and PCEC processes was not purchased as it was assumed to be recyclable without further treatment. The fresh propane price was estimated to be about 500 USD/ton based on average global market prices in 2022 [113]. The utilities needed to operate the propane dehydrogenation processes were (i) low pressure (LP) steam, (ii) electricity, (iii) cooling water, and (iv) natural gas. Costs for consumables in the different processes consisted of catalyst, adsorbent, and membrane costs. The catalyst costs were estimated using the CatCost^{TM} software V1.1.0 from the Chemical Catalysis for Bioenergy Consortium (ChemCatBio) [114] for a Pt/Al_2O_3 catalyst containing 1 wt.% of Pt. The catalyst lifetime was estimated to be two years in all three processes, based on the typical lifetime of Pt-based catalysts in the Oleflex process [18]. The amount of catalyst needed in the membrane-assisted processes was assumed to be equal to the Oleflex process for equal production capacities. Besides, an adsorbent was only needed for the pressure swing adsorption (PSA) in the Oleflex process. Activated carbon was used in this adsorption column, as it is known to be a good adsorbent for separating hydrogen and methane [115]. The price for activated carbon adsorbent was about 2,500 USD/ton [116]. For further details regarding the quantification of the amount of activated carbon adsorbent needed, see **Supporting Information 5.G4**. The total membrane reactor costs for MPEC and PCEC-based membranes depend on stack material costs, reactor steel costs, tooling costs, and furnace costs (see **Supporting Information 5.F**). For the OPEX analysis, it is assumed that only the stack material costs have to be replaced periodically. Here, in the base case analysis it was assumed that the lifetime of the membrane materials was equal to the lifetime of the Pt catalyst (two years), such that they can be replaced all at once.

5.P2. Fixed production costs

Labor costs for operation were estimated for five shifts, six operators per shift, and a gross salary of 60,000 USD per year per shift position. The number of personnel needed for operation was assumed to be equal for all three processes. Additional supervision and management labor costs were estimated at 25% of these operator costs [68]. Process

maintenance costs were in all cases estimated to be 3% of the ISBL capital investment (**Supporting Information 5.N**) [68]. In addition to process maintenance costs, equipment replacement costs were included for the MPEC and PCEC processes, as it is expected that regular replacement of the solid oxide membranes will be more complicated and more costly than replacing only the catalyst. These equipment replacement costs were also estimated as 3% of the ISBL capital investment (**Supporting Information 5.N**). Land rental costs and insurance costs were both estimated to be 1% of the ISBL+OSBL capital investment (**Supporting Information 5.N**) [68]. Lastly, company lab and services costs were estimated to be 15% and 50% of labor operation costs, respectively.

5.P3. Revenues

Next to propylene, the produced H_2 was regarded as a valuable product. The purity of the different off-gas streams, i.e. the depropanizer heavies, the deethanizer lights, and the PSA retentate (Oleflex), was too low to be sold as a chemical product. In the before heat integration (BHI) cases, these off-gas streams were considered to be sold at their heating value, leading to an additional contribution to the total revenues. On the contrary, in the after heat integration (AHI) cases, these off-gas streams were incinerated to provide heat within the process and they were in that case, thus, not sold as fuel product. The CO_2 and H_2O generated in catalyst regeneration and in natural gas and off-gas incineration were considered to be valueless. The revenue calculations are summarized in **Table 5.P5**.

5.P4. Profitability assessment

The three different processes were compared to one another in terms of profitability based on the return on investment (*ROI*) and the payback period. The payback period was calculated as the ratio between the total depreciable capital and the net annual profit, according to **Equation 5.P1**. Besides, the *ROI* was calculated based on the net annual profit and the total capital investment using **Equation 5.P2**. First, the gross annual profit was determined by subtracting the depreciation costs and the variable and fixed production costs from the total revenues. Herein, the depreciation costs were determined from the total depreciable capital considering linear depreciation throughout a project duration of 30 years. Afterward, the net annual profit was calculated from the gross annual profit using a corporate income tax rate of 21% for the U.S. Gulf Coast region [70,71].

$$Payback\ period = \frac{Total\ depreciable\ capital}{Net\ annual\ profit} \qquad (5.P1)$$

$$ROI = \frac{Net\ annual\ profit}{Total\ capital\ investment} \bullet 100\% \qquad (5.P2)$$

5.P5. OPEX results

A breakdown of the results of the OPEX calculations is shown in **Table 5.P1** and **Table 5.P3** for situations before and after heat integration, respectively. The calculations of the variable production costs that are part of the OPEX analysis are presented in **Table 5.P2**

and **Table 5.P4** for situations before and after heat integration, respectively. Lastly, the revenue calculations are summarized in **Table 5.P5** and the results of the profitability assessment are presented in **Table 5.P6** and **5.P7**.

Table 5.P1: Breakdown of the outcomes of the OPEX calculations, before heat integration, when green electricity was utilized. S.I. = supporting information. ISBL = inside battery limits, OSBL = outside battery limits, NG = natural gas.

OPEX	Fossil fuel heated reactors (MMUSD/yr)			Electrically heated reactors (MMUSD/yr)		
	Oleflex	**MPEC**	**PCEC**	**Oleflex**	**MPEC**	**PCEC**
Variable production costs (Table 5.P2)						
Raw materials						
NG-derived propane	302.7	281.1	279.5	302.7	281.1	279.5
Catalyst & chemicals						
Pt-Sn catalyst	17.1	17.1	17.1	17.1	17.1	17.1
PSA adsorbent	0.0	-	-	0.0	-	-
LWO membrane	-	138.8	-	-	138.8	-
BZCY membrane	-	-	1.1	-	-	1.1
Total utility (**S.I. 5.O**)	88.0	114.6	76.6	136.8	273.9	103.7
CO_2 tax	15.3	43.9	9.8	6.9	11.1	5.8
Subtotal:	*423.2*	*595.6*	*384.2*	*463.6*	*722.1*	*407.3*
Fixed production costs						
Operations	2.3	2.3	2.3	2.3	2.3	2.3
Maintenance (3% of ISBL)	13.2	233.0	11.0	13.2	233.0	11.0
Replacement costs (3% of ISBL)	0	233.0	11.0	0	233.0	11.0
Company Lab (15% of operations)	0.3	0.3	0.3	0.3	0.3	0.3
Staff and Services (50% of operations)	1.1	1.1	1.1	1.1	1.1	1.1
Ground rent (1% of ISBL+OSBL)	6.2	108.7	5.1	6.2	108.7	5.1
Property tax/insurance (1% of ISBL+OSBL)	6.2	108.7	5.1	6.2	108.7	5.1
Fixed production costs:	*29.3*	*687.3*	*35.9*	*29.3*	*687.3*	*35.9*
Total (variable + fixed):	**452.5**	**1,282.9**	**420.0**	**492.8**	**1,409.4**	**443.1**

Table 5.P2: Calculation of variable production costs, before heat integration. S.I. = supporting information, NG = natural gas.

OPEX	Fossil fuel heated reactors (MMUSD/yr)			Electrically heated reactors (MMUSD/yr)		
	Oleflex	MPEC	PCEC	Oleflex	MPEC	PCEC
Raw materials						
NG-derived propane						
Fresh propane feed flow (ton/hr)	72.37	67.31	66.82	72.37	67.31	66.82
Propylene product flow (kg/hr)	53.43	53.51	53.43	53.43	53.51	53.43
Price NG-derived propane (USD/ton)	496.6	496.6	496.6	496.6	496.6	496.6
# of operating hours (hr/yr)	8,400	8,400	8,400	8,400	8,400	8,400
Total raw material costs (MMUSD/yr)	*302.7*	*281.1*	*279.5*	*302.7*	*281.1*	*279.5*
Catalyst & Chemicals						
Pt-Sn catalyst						
Estimated catalyst costs (USD/ton$_{cat}$)	360,000	360,000	360,000	360,000	360,000	360,000
Catalyst mass per reactor (ton$_{cat}$)	17	17	17	17	17	17
# of dehydrogenation reactors (-)	4	4	4	4	4	4
Total catalyst mass in reactors (ton$_{cat}$)	68	68	68	68	68	68
Regeneration/reaction ratio (-)	0.4	0.4	0.4	0.4	0.4	0.4
Estimated catalyst mass in regenerator (ton$_{cat}$)	27.2	27.2	27.2	27.2	27.2	27.2
Total catalyst mass needed (ton$_{cat}$)	95.2	95.2	95.2	95.2	95.2	95.2
Estimated catalyst lifetime (yr)	2	2	2	2	2	2
Propylene production capacity per catalyst batch (ton$_{propylene}$)	900,000	900,000	900,000	900,000	900,000	900,000

Catalyst mass needed ($ton_{cat}/ton_{propylene}$)	0.000106	0.000106	0.000106	0.000106	0.000106	0.000106
Total catalyst costs (MMUSD/yr)	*17.1*	*17.1*	*17.1*	*17.1*	*17.1*	*17.1*
Adsorbent for PSA (activated carbon)						
Activated carbon (AC) price (USD/ton_{AC})	2,500	-	-	2,500	-	-
Mass of AC needed per bed (kg_{AC}) → **S.I. 5.G4**	1.56	-	-	1.56	-	-
Estimated # of PSA columns needed (-)	4	-	-	4	-	-
Total amount of AC needed (kg_{AC})	6.24	-	-	6.24	-	-
Estimated lifetime of AC (yr)	2			2		
Propylene production capacity per AC batch ($ton_{propylene}$)	900,000	900,000	900,000	900,000	900,000	900,000
AC mass needed (ton_{AC}/ton propylene)	$6.93 \cdot 10^{-9}$	-	-	$6.93 \cdot 10^{-9}$	-	-
Total AC costs (MMUSD)	*$8 \cdot 10^{-6}$*	*-*	*-*	*$8 \cdot 10^{-6}$*	*-*	*-*
LWO membrane						
LWO stack material costs (MMUSD)	-	277.69	-	-	277.69	-
Estimated LWO stack lifetime (yr)	-	2	-	-	2	-
Propylene production capacity per LWO stack ($ton_{propylene}$)	900,000	900,000	900,000	900,000	900,000	900,000
Estimated annual LWO stack material costs (MMUSD/yr)	*-*	*138.85*	*-*	*-*	*138.85*	*-*
BZCY membrane						
BZCY stack material costs (MMUSD)	-	-	2.29	-	-	2.29
Estimated BZCY stack lifetime (yr)	-	-	2	-	-	2

Propylene production capacity per BZCY stack (ton$_{propylene}$)	900,000	900,000	900,000	900,000	900,000	900,000
Estimated annual BZCY stack material costs (MMUSD/yr)	-	-	1.15	-	-	1.15
Utilities						
Total utility costs (MMUSD/yr, see **S.I. 5.O**)	**88.0**	**114.6**	**76.6**	**136.8**	**273.9**	**103.7**
Taxes						
CO_2 tax (USD/ton$_{CO2}$)	65	65	65	65	65	65
Total CO_2 emissions (ktpa), green electricity	236.1	675.8	151.2	105.7	171.4	89.4
CO_2 tax to be paid	15.3	43.9	9.8	6.9	11.1	5.8
Total variable costs (MMUSD/yr), green electricity	*423.2*	*595.6*	*384.2*	*463.6*	*722.1*	*407.3*
Alternatively, when fossil U.S. average electricity is used instead of green electricity:						
Total CO_2 emissions (ktpa), fossil electricity	312.7	714.5	293.3	510.9	1,282.5	414.0
CO_2 tax to be paid	20.3	46.4	19.1	33.2	83.4	26.9
Total variable costs (MMUSD/yr), fossil electricity	**428.2**	**598.1**	**393.4**	**489.9**	**794.3**	**428.4**

Table 5.P3: Breakdown of outcomes of OPEX calculations, after heat integration, when green electricity was utilized. S.I. = supporting information, ISBL = inside battery limits, OSBL = outside battery limits, NG = natural gas.

OPEX	Fossil fuel heated reactors (MMUSD/yr)			Electrically heated reactors (MMUSD/yr)		
	Oleflex	MPEC	PCEC	Oleflex	MPEC	PCEC
Variable production costs (Table 5.P4)						
Raw materials						
NG-derived propane	302.7	281.1	279.5	302.7	281.1	279.5
Catalyst & chemicals						
Pt-Sn catalyst	17.1	17.1	17.1	17.1	17.1	17.1
PSA adsorbent	0.0	-	-	0.0	-	-
LWO membrane	-	138.8	-	-	138.8	-
BZCY membrane	-	-	1.1	-	-	1.1
Total utility (**S.I. 5.O**)	44.0	61.3	44.8	32.9	103.1	24.0
CO_2 tax	26.5	30.1	19.1	26.0	21.5	18.2
Subtotal:	*390.4*	*528.5*	*361.7*	*378.7*	*561.8*	*340.0*
Fixed production costs						
Operations	2.3	2.3	2.3	2.3	2.3	2.3
Maintenance (3% of ISBL)	13.2	233.0	11.0	13.2	233.0	11.0
Replacement costs (3% of ISBL)	0	233.0	11.0	0	233.0	11.0
Company Lab (15% of operations)	0.3	0.3	0.3	0.3	0.3	0.3
Staff and Services (50% of operations)	1.1	1.1	1.1	1.1	1.1	1.1
Ground rent (1% of ISBL+OSBL)	6.2	108.7	5.1	6.2	108.7	5.1
Property tax/insurance (1% of ISBL+OSBL)	6.2	108.7	5.1	6.2	108.7	5.1
Fixed production costs:	*29.3*	*687.3*	*35.9*	*29.3*	*687.3*	*35.9*
Total (variable + fixed):	419.7	1,215.8	397.6	408.0	1,249.0	375.9

The raw material, catalyst, adsorbent, and membrane costs are all the same before and after heat integration and are presented in **Table 5.P2**. Hence, the only differences between the variable production costs before and after heat integration are the utility costs and the carbon taxes, which are shown in **Table 5.P4** for the situation after heat integration.

Table 5.P4: Calculation of variable production costs, after heat integration. S.I. = supporting information.

	Fossil fuel heated reactors (MMUSD/yr)			Electrically heated reactors (MMUSD/yr)		
	Oleflex	**MPEC**	**PCEC**	**Oleflex**	**MPEC**	**PCEC**
Utilities						
Total utility costs (MMUSD/yr, see **S.I. 5.O**)	44.0	61.3	44.8	32.9	103.1	24.0
Taxes						
CO_2 tax (USD/ton$_{CO2}$)	65	65	65	65	65	65
Total CO_2 emissions (ktpa), green electricity	408.2	463.4	294.5	400.3	331.3	279.8
CO_2 tax to be paid	26.5	30.1	19.1	26.0	21.5	18.2
Total variable costs (MMUSD/yr)	*390.4*	*528.5*	*361.7*	*378.7*	*561.8*	*340.0*
Alternatively, when fossil U.S. average electricity is used instead of green electricity:						
Total CO_2 emissions (ktpa), fossil electricity	484.7	502.0	436.6	400.3	651.5	279.8
CO_2 tax to be paid	31.5	32.6	28.4	26.0	42.3	18.2
Total variable costs (MMUSD/yr), fossil electricity	**395.4**	**531.0**	**370.9**	**378.7**	**582.6**	**340.0**

Table 5.P5: Revenue calculations for the three different processes. BHI = before heat integration, AHI = after heat integration, NG = natural gas.

Revenues	Oleflex		MPEC		PCEC	
	BHI	**AHI**	**BHI**	**AHI**	**BHI**	**AHI**
Propylene product flow (ton/hr)	53.43	53.43	53.51	53.51	53.43	53.43
Propylene price (USD/t)	997	997	997	997	997	997
Propylene revenue (USD/hr)	53,268	53,268	53,350	53,350	53,267	53,267
Propylene revenue (MMUSD/yr)	***447.45***	***447.45***	***448.14***	***448.14***	***447.44***	***447.44***
Hydrogen product flow (ton/hr)	3.29	3.29	3.50	3.50	3.74	3.74
Hydrogen price (USD/t)	1,500	1,500	1,500	1,500	1,500	1,500
Hydrogen revenue (USD/hr)	4,936	4,936	5,256	5,256	5,613	5,613
Hydrogen revenue (MMUSD/yr)	***41.46***	***41.46***	***44.16***	***44.16***	***47.15***	***47.15***
Depropanizer heavies						
Energy available (MW), **Table 5.J1**	89.89		71.01		50.98	
Higher heating value (MJ/kg) [112]	49.1		49.1		49.1	
Butane fuel price (USD/t) [117]	400		400		400	
Revenue (MMUSD/yr)	22.14		17.49		12.56	
Deethanizer lights						
Energy available (MW), **Table 5.J1**	91.97		62.21		68.44	
Higher heating value (MJ/kg) [112]	51.9		51.9		51.9	
Ethane fuel price (USD/t) [118]	200		200		200	
Revenue (MMUSD/yr)	10.72		7.25		7.98	
PSA retentate						
Energy available (MW), **Table 5.J1**	7.82		0		0	
Higher heating value (MJ/kg) [112]	55.5		55.5		55.5	

NG fuel price (USD/MWh) [118]	22		22		22
Revenue (MMUSD/yr)	1.44		0		0
Off-gas revenue (MMUSD/yr)	*34.31*		*24.74*		*20.53*
Total revenue (MMUSD/yr):	*523.22*	*488.92*	*517.05*	*492.30*	*515.13*	*494.60*

Table 5.P6: Results of the profitability assessment in case of fossil fuel-based reactor heating using natural gas. BHI = before heat integration, AHI = after heat integration.

	Fossil fuel heated reactors				
	F-Oleflex		F-PCEC		
	BHI	AHI	BHI	AHI	Unit:
U.S. average electricity:					
*Revenues – production costs**	*65.8*	*64.3*	*85.9*	*87.8*	*MMUSD/yr*
Depreciable capital	770.6	770.6	639.3	639.3	MMUSD
Estimated plant lifetime	30	30	30	30	yr
Yearly depreciation	*25.7*	*25.7*	*21.3*	*21.3*	*MMUSD/yr*
Gross profit	*40.1*	*38.6*	*64.5*	*66.5*	*MMUSD/yr*
Corporate income tax rate	21	21	21	21	%
Corporate income tax	8.4	8.1	13.6	14.0	MMUSD/yr
Net profit	*31.7*	*30.5*	*51.0*	*52.5*	*MMUSD/yr*
Payback time	*24*	*25*	*13*	*12*	*yr*
Total fixed capital	886.1	886.1	735.2	735.2	MMUSD
Return on investment (ROI)	*3.6*	*3.4*	*6.9*	*7.1*	*%*
Green electricity:					
*Revenues – production costs**	*70.8*	*69.3*	*95.1*	*97.0*	*MMUSD/yr*
Depreciable capital	770.6	770.6	639.3	639.3	MMUSD
Estimated plant lifetime	30	30	30	30	yr
Yearly depreciation	*25.7*	*25.7*	*21.3*	*21.3*	*MMUSD/yr*
Gross profit	*45.1*	*43.6*	*73.8*	*75.7*	*MMUSD/yr*
Corporate income tax rate	21	21	21	21	%
Corporate income tax	9.5	9.1	15.5	15.9	MMUSD/yr
Net profit	*35.6*	*34.4*	*58.3*	*59.8*	*MMUSD/yr*
Payback time	*22*	*22*	*11*	*11*	*yr*
Total fixed capital	886.1	886.1	735.2	735.2	MMUSD
Return on investment (ROI)	*4.0*	*3.9*	*7.9*	*8.1*	*%*

Note that the financial margin was different for the situations in which relatively fossil U.S. average electricity was utilized instead of fully renewable electricity, despite the fact that the price of green electricity was assumed to be equal to the price of U.S. average electricity. This difference originated from the higher carbon footprint of the cases in which U.S. average electricity was utilized (see **Table 5.P2 and **5.P4**).*

Table 5.P7: Results of the profitability assessment in case of electrical reactor heating. BHI = before heat integration, AHI = after heat integration.

	Fossil fuel heated reactors				
	F-Oleflex		F-PCEC		
	BHI	AHI	BHI	AHI	Unit:
U.S. average electricity:					
Revenues – production costs*	*4.1*	*81.0*	*50.9*	*118.7*	*MMUSD/yr*
Depreciable capital	770.6	770.6	639.3	639.	MMUSD
Estimated plant lifetime	30	30	30	30	yr
Yearly depreciation	*25.7*	*25.7*	*21.3*	*21.3*	*MMUSD/yr*
Gross profit	*-21.6*	*55.3*	*29.6*	*97.4*	*MMUSD/yr*
Corporate income tax rate	21	21	21	21	%
Corporate income tax	-	*11.6*	*6.2*	*20.5*	MMUSD/yr
Net profit	*-21.6*	*43.7*	*23.4*	*77.0*	*MMUSD/yr*
Payback time	*-36*	*18*	*27*	*8*	*yr*
Total fixed capital	886.1	886.1	735.2	735.2	MMUSD
Return on investment (ROI)	*-2.4*	*4.9*	*3.2*	*10.5*	*%*
Green electricity:					
Revenues – production costs*	*30.4*	*81.0*	*72.0*	*118.7*	*MMUSD/yr*
Depreciable capital	770.6	770.6	639.3	639.3	MMUSD
Estimated plant lifetime	30	30	30	30	yr
Yearly depreciation	*25.7*	*25.7*	*21.3*	*21.3*	*MMUSD/yr*
Gross profit	*4.7*	*55.3*	*50.7*	*97.4*	*MMUSD/yr*
Corporate income tax rate	21	21	21	21	%
Corporate income tax	*1.0*	*11.6*	*10.7*	*20.5*	MMUSD/yr
Net profit	*3.7*	*43.67*	*40.1*	*77.0*	*MMUSD/yr*
Payback time	*206*	*18*	*16*	*8*	*yr*
Total fixed capital	886.1	886.1	735.2	735.2	MMUSD
Return on investment (ROI)	*0.4*	*4.9*	*5.5*	*10.5*	*%*

Note that the financial margin was different for the situations in which relatively fossil U.S. average electricity was utilized instead of fully renewable electricity, despite the fact that the price of green electricity was assumed to be equal to the price of U.S. average electricity. This difference originated from the higher carbon footprint of the cases in which U.S. average electricity was utilized (see **Table 5.P2 and **5.P4**).*

5.Q. Specific energy input

The specific energy input of the three different processes was evaluated before and after heat integration. The results are shown in **Table 5.Q1** and **Table 5.Q2**, respectively.

Table 5.Q1: Specific energy input (*SEI*) for the three different processes before heat integration.

ID	Description	Oleflex (MJ/kg$_{propylene}$)	MPEC (MJ/kg$_{propylene}$)	PCEC (MJ/kg$_{propylene}$)
Compression				
CP-1	Fresh propane compressor	0.11	0.10	0.10
CP-2	1st reactor effluent compressor	0.70	0.22	0.23
CP-3	2nd reactor effluent compressor	0.63	0.16	0.16
CP-4	1st H$_2$ product compressor	0.12	0	0
CP-5	2nd H$_2$ product compressor	0.09	0.37	0.15
CP-6	3rd H$_2$ product compressor	0	0	0
Subtotal (MJ/kg$_{propylene}$):		*1.65*	*0.85*	*0.63*
Distillation column reboilers				
DC-1	Depropanizer reboiler	1.73	1.29	1.32
DC-2	Deethanizer reboiler	1.27	1.35	1.12
DC-3	C3 splitter reboiler	8.99	5.58	6.47
Subtotal (MJ/kg$_{propylene}$):		*11.99*	*8.22*	*8.90*
Reactor (pre)heating				
FH-1	Fired heater I	5.62	3.62	3.69
FH-2	Fired heater II	0.85	0	0
FH-3	Fired heater III	0.83	0	0
FH-4	Fired heater IV	0.82	0	0
R-1	Reactor heating	0	3.28	5.74
R-5	Regeneration heat (80% heat recovery)	-1.49	-1.33	-1.32
R-1	Resistive Joule heat	0	0	-2.33
Subtotal (MJ/kg$_{propylene}$):		*6.92*	*5.84*	*6.04*
Additional heating				

H-1	Heater to evaporate depropanizer top	1.15	0.85	0.91
H-2	Air heater for regeneration	0.34	0.30	0.30
H-3	H_2 product heater	0.32	0	0
H-7	H_2O sweep gas heater	0	17.35	0.07
H-4	Hydrocarbon heater after cold box I	0.41	0	0
H-5	Hydrocarbon heater after cold box II	0.44	0	0
H-6	Deethanizer column pre-heater	0.43	0	0
H-8	H_2O cofeed heater feed-side	0	0.13	0.11
H-9	Hydrocarbon heater after H_2O flash drum	0	0.18	0.19
H-10	Permeate side H_2 heater	0	0.04	0.05
Subtotal (MJ/kg$_{propylene}$):		*3.08*	*18.63*	*1.35*
Total (MJ/kg$_{propylene}$):		**23.64**	**33.53**	**16.92**

Table 5.Q2: Specific energy input (*SEI*) for the different processes after heat integration.

Description	Oleflex	MPEC	PCEC
	(MJ/kg$_{propylene}$)	(MJ/kg$_{propylene}$)	(MJ/kg$_{propylene}$)
Heat exchange	5.67	11.14	4.80
Off-gas heat	8.92	6.27	5.62
Compression (**Table 5.Q1**)	1.65	0.85	0.63
External heat	7.40	15.28	5.87
Total:	**23.64**	**33.53**	**16.92**

5.R. Carbon footprint

5.R1. Carbon footprint calculation methods

The only type of greenhouse gas emissions included here are the CO_2 emissions, which were comprised of four contributors, related to: (i) natural gas burning, (ii) electricity generation, (iii) coke burning upon catalyst regeneration, and (iv) off-gas burning. The applied emission factor related to natural gas burning was ca. 1.92 kg/m$^3_{NG}$ (i.e. 120,000 lb/10^6 scf) [119], whilst the emission factor related to the generation of U.S. average grid electricity was ca. 401.1 kg/MWh (i.e. 884.2 lb/MWh) [72]. In addition, emission factors for green electricity were determined by quantifying the CO_2 emissions related to the

construction of wind turbines and solar panels [120]. For a 50%/50% solar/wind ratio in generating green electricity, this gives the emission factors shown in **Table 5.R1**.

Table 5.R1: Emission factors related to the construction of wind turbines and solar panels needed for generating green electricity [120,121].

Electricity source	Emission factor (g_{CO_2}/kWh)
Wind power	14
Solar power	61
50% wind, 50% solar	37.5

In calculating the carbon dioxide emissions associated with coke burning upon catalyst regeneration, the entire carbon content in the coronene model compound was assumed to be fully oxidized to carbon dioxide. This can be established in regenerative heat exchangers. These heat exchangers are suitable for transferring heat between enormous amounts of gases at high temperature via a solid phase transfer agent [122]. Here, the energy generated during coke burning was calculated using the standard heat of combustion of coronene (ca. 11,300 kJ/mol) [123]. A thermodynamic efficiency of 80% was taken for heat transfer in these regenerative heat exchangers [124].

The streams taken into account for the off-gas combustion were: (i) the depropanizer heavies, (ii) the deethanizer lights, and (iii) the PSA retentate. The major constituents in these streams were n-butane, ethane, and methane, respectively. In estimating the carbon dioxide emissions related to burning these off-gas streams, the total stream was considered to be comprised of the major constituent, whilst again full combustion was assumed. The calculations are summarized in **Table 5.R2**.

Table 5.R2: Carbon dioxide emissions related to off-gas combustion upon heat integration.

	Oleflex	MPEC	PCEC	Notes:
Depropanizer heavies molar flow (mol/s)	31.5	24.9	17.9	Major constituent: n-butane
Deethanizer lights molar flow (mol/s)	58.9	39.9	43.9	Major constituent: ethane
PSA retentate molar flow (mol/s)	8.8	0	0	Major constituent: methane
CO_2 emissions from off-gas combustion (mol/s)	252.6	179.3	159.2	Considering major constituents
Molar weight CO_2 (kg/mol)	0.04401	0.04401	0.04401	
CO_2 emissions from off-gas combustion (ktpa)	**336.2**	**238.6**	**211.8**	Considering 8,400 operating hours

5.R2. Carbon footprint results

The three processes were compared to one another for two different situations. In the first case, all reactor (pre-)heating steps were carried out in a fossil manner, i.e. by using natural gas burning (**Table 5.R1**). In the second case, all reactor heating and preheating steps were operated using electricity (**Table 5.R2**). In addition, for every situation a distinction was made between the use of U.S average grid and fully renewable electricity.

Table 5.R1: Carbon footprint of the three different processes in case all reactor heating and preheating steps were operated in a fossil manner.

	Fossil U.S. average electricity (kg CO_2/kg propylene)			Green electricity (kg CO_2/kg propylene)		
	Oleflex	MPEC	PCEC	Oleflex	MPEC	PCEC
Before heat integration (BHI):						
Natural gas burning	0.37	1.37	0.18	0.37	1.37	0.18
Electricity generation	0.19	0.09	0.35	0.02	0.01	0.03
Coke combustion	0.14	0.13	0.12	0.14	0.13	0.12
Total:	***0.69***	***1.59***	***0.65***	***0.52***	***1.50***	***0.34***
After heat integration (AHI):						
Natural gas burning	0.00	0.36	0.00	0.00	0.36	0.00
Electricity generation	0.19	0.09	0.35	0.02	0.01	0.03
Coke combustion	0.14	0.13	0.15	0.14	0.13	0.15
Off-gas combustion	0.75	0.53	0.47	0.75	0.53	0.47
Total:	***1.08***	***1.12***	***0.97***	***0.91***	***1.03***	***0.65***

Table 5.R2: Carbon footprint of the three different processes in case all reactor heating and preheating steps were operated using electricity.

	Fossil U.S. average electricity (kg CO_2/kg propylene)			Green electricity (kg CO_2/kg propylene)		
	Oleflex	MPEC	PCEC	Oleflex	MPEC	PCEC
Before heat integration (BHI):						
Natural gas burning	0.00	0.00	0.00	0.00	0.00	0.00
Electricity generation	0.99	2.72	0.80	0.09	0.25	0.07
Coke combustion	0.14	0.13	0.12	0.14	0.13	0.12
Total:	***1.14***	***2.85***	***0.92***	***0.23***	***0.38***	***0.20***
After heat integration (AHI):						
Natural gas burning	0.00	0.00	0.00	0.00	0.00	0.00
Electricity generation	0.00	0.78	0.00	0.00	0.07	0.00

Coke combustion	0.14	0.13	0.15	0.14	0.13	0.15
Off-gas combustion	0.75	0.53	0.47	0.75	0.53	0.47
Total:	*0.89*	*1.45*	*0.62*	*0.89*	*0.74*	*0.62*

5.S. Sensitivity analysis

5.S1. Specific energy input

The effect of propylene yield on the specific energy input (*SEI*) of the PCEC process is shown in **Figure 5.S1**. The yield was varied up to 80%, as for 95% hydrogen removal the thermodynamic equilibrium yield at 1 bar(a) and 600 °C is about 88% (**Supporting Information 5.B**). The side reaction yields (1% cracking, 1% hydrogenolysis, 2% coking) were maintained constant, leading to an increased propylene selectivity with increasing propylene yield (**Figure 5.S1**). The *SEI* of the PCEC process is slightly higher than the *SEI* of the Oleflex process for 36% propylene yield, due to the additional energy demand for electrically driving hydrogen permeation, despite the energetic advantage of integrated dehydrogenation and hydrogen compression. Besides, the biggest gain in energy usage is attained when the PCEC propylene yield increases from ca. 36% (24.7 MJ/kg$_{propylene}$) to ca. 50% (19.2 MJ/kg$_{propylene}$). Upon further increasing the propylene yield, the energy savings are more marginal. Even for 100% propylene yield there is a minimum amount of energy needed for reaction (2.95 MJ/kg$_{propylene}$), heating, and mass circulation. Upon approaching full conversion, consecutive dehydrogenation and coking reactions are anticipated to be enhanced. Hence, we envision that a 50% propylene yield is the optimal balance between optimized energy savings and minimized consecutive reactions. A 50% propane NODH yield was therefore selected for the base case MPEC and PCEC processes.
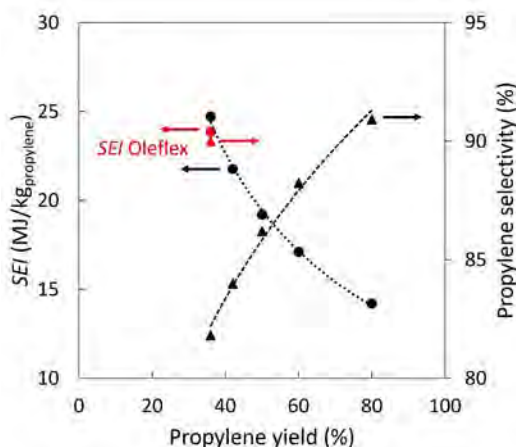
Figure 5.S1: Specific energy input (*SEI*) and propylene selectivity vs. propylene yield for the PCEC-assisted process. The Oleflex data are indicated in red.

5.S2. Electricity price

Low pressure steam and electricity are the major contributors to the total utility costs, particularly for electrically heated reactor systems (see **Supporting Information 5.O**). Especially electricity prices generally slow large fluctuations, thereby potentially strongly impacting process economics. The effect of electricity price on the total annual profit is therefore assessed (**Figure 5.S2**) for situations before and after heat integration. **Figure 5.S2** illustrates that before heat integration the Oleflex and PCEC processes are both more profitable in case of fossil reactor heating for the current electricity price of 76 USD/MWh (**Figure 5.S2a**). This is attributed to the fact that natural gas-based heating (22 USD/MWh) is cheaper than electrical heating (76 USD/MWh). **Figure 5.S2a** also shows that electrification of the Oleflex and PCEC processes only results in higher profits if the electricity price is below the natural gas price of 22 USD/MWh.

Upon heat integration, off-gas heat replaces parts of the natural gas utility for the fossil fuel heated processes, whereas it replaces the total electricity requirement for the electrically heated processes. As a consequence, the electrified processes become independent of the electricity price, whilst the fossil fuel heated processes still become more profitable with decreasing electricity price (**Figure 5.S2b**). Hence, the electrified processes are more profitable in this situation for the current electricity price of 76 USD/MWh. It should be noted that replacing green electricity utility for heating by off-gas heat is accompanied by a considerable increase in carbon emissions (**Figure 5.9**).
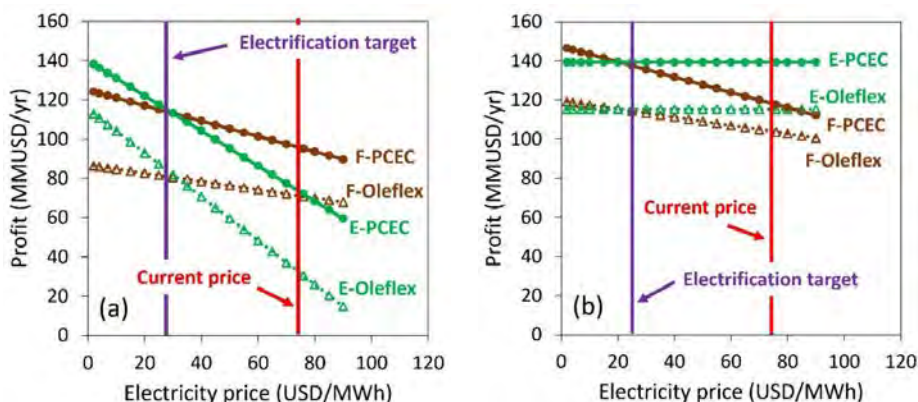
Figure 5.S2: Influence of electricity price on annual profit for fossil fuel heated (F) and electrically heated (E) reactor (pre-)heating steps for the Oleflex and PCEC-assisted processes (a) before heat integration, and (b) after heat integration, for a carbon tax based on the use of green electricity.

5.S3. Membrane replacement frequency

In the comparison made in this work between the techno-economics of membrane-assisted and conventional propane dehydrogenation processes, it was assumed that the

membranes needed to be replaced every two years. This membrane lifetime was thereby set equal to the dehydrogenation catalyst lifetime. However, this membrane lifetime estimation could be too optimistic, as hydrogen removal by the membranes is anticipated to boost coke formation and thereby limit the membrane stability. For this reason, the sensitivity of the membrane replacement frequency on the total profitability of the PCEC process was investigated (see **Figure 5.S3**). The total downtime was kept constant in this analysis and equaled 366 hours per year (i.e. ca. 15 days per year), since the number of operating hours was 8,400 in this work and the total average number of hours per year is 8,766. Possible extensions of total downtimes per year for higher membrane replacement frequencies, and related reductions in total revenues, were disregarded in this analysis. **Figure 5.S3** shows that the profitability of the PCEC process remains more or less unaffected even down to situations where the PCEC membrane needs to be replaced every ca. two months. This is caused by the fact that the major contributor to the operating costs are the costs for raw materials, while the membrane costs have a more marginal impact on the OPEX. If the membrane needs to be replaced multiple times per month, then the membrane costs start to significantly impact the profitability of the PCEC process (see **Figure 5.S3**). Hence, it can be concluded that a PCEC membrane lifetime of at least two months is required to have a profitable PCEC-assisted process.
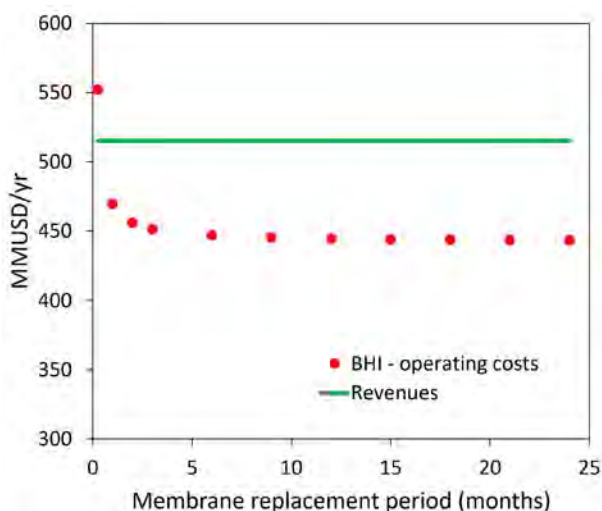
Figure 5.S3: Sensitivity of the operating costs and the revenues of the PCEC process before heat integration (BHI) with respect to the PCEC membrane replacement period.

5.S4. Carbon intensity of electricity

The influence of the carbon intensity of the electricity on the total carbon footprint of the various electrified Oleflex and PCEC process cases is shown in **Figure 5.S4**. Note that the carbon emissions of the electrified process cases after heat integration (AHI) were independent of the electricity carbon intensity, as the full electricity requirement in these

cases was covered by fuel gas combustion (see **Supporting Information 5.R2**). Interestingly, the total carbon footprint of the before heat integration (BHI) cases was higher than their AHI counterparts for a carbon intensity above ca. 300 kg$_{CO2}$/MWh (**Figure 5.S4**). In that situation, it was environmentally beneficial to combust fuel gas streams available within the process for heating instead of using fossil fuel-based electricity. On the contrary, below a electricity carbon intensity of ca. 250 kg$_{CO2}$/MWh the BHI cases had a lower carbon footprint than the AHI cases (**Figure 5.S4**). This implies that in case renewable electricity (e.g solar, wind) is available it was ecologically recommended to utilize electrical heat rather than to combust available off-gas streams for heating. The carbon intensity of the electricity generated using wind and solar power, as indicated in **Figure 5.S4**, represents the carbon emissions related to the construction of wind mills and solar panels, respectively [120]. When using only wind power to generate the electricity needed to operate the electrified Oleflex and PCEC processes, the carbon footprint of propylene production can be reduced to less than 0.2 kg$_{CO2}$/kg$_{propylene}$ (**Figure 5.S4**).
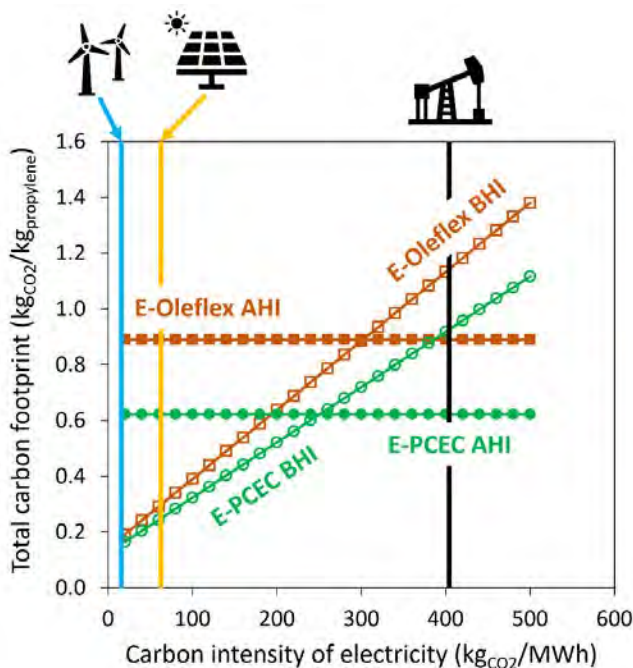
Figure 5.S4: Influence of the carbon intensity of the electricity on the total carbon footprint of the electrified Oleflex and PCEC process cases before heat integration (BHI) and after heat integration (AHI). The carbon intensity of wind and solar energy represent the carbon emissions related to the construction of wind mills and solar panels, respectively [120]. Besides, the fossil fuel based electricity considers U.S. average electricity, dealing with a carbon intensity of ca. 400 kg$_{CO2}$/MWh [72].

5.S5. Carbon taxation

The influence of the imposed carbon tax on the return on investment (*ROI*) of the different Oleflex and PCEC process case before heat integration (BHI) and after heat integration (AHI) was investigated for situations in which U.S. average grid electricity (**Figure 5.S5a**) or fully renewable electricity (**Figure 5.S5b**) was utilized. In case relatively fossil U.S. average electricity was used, all considered process cases suffered from increments in carbon taxation (**Figure 5.S5a**), as all these cases coped with a large carbon footprint (see **Figure 5.8**). Also, the least profitable case was the electrified Oleflex case BHI dealing with a great demand for expensive electricity. On the contrary, the most profitable case was the PCEC case AHI (**Figure 5.S5a**) in which the complete electricity demand was covered by burning off-gas streams (see **Figure 5.8**).

In case fully renewable electricity was utilized (**Figure 5.S5b**), all PCEC cases were more profitable than their Oleflex counterparts, which was ascribed to lower raw material and utility costs for the PCEC process, which was related to the higher single-pass propylene yield (50%) in comparison to the Oleflex process (36%). For marginal carbon taxation (<250 USD/t_{CO2}), the most profitable case was the electrified PCEC process AHI (**Figure 5.S5b**), in which the great and expensive electricity demand was completely covered by incinerating off-gas streams. However, for carbon taxes higher than 250 USD/t_{CO2} the fossil and electrified PCEC cases BHI became more viable than the electrified PCEC case AHI. This indicates that a carbon tax of more than 250 USD/t_{CO2} needs to be levied to make the usage of green electricity more attractive than incineration of off-gas streams in the PCEC process.
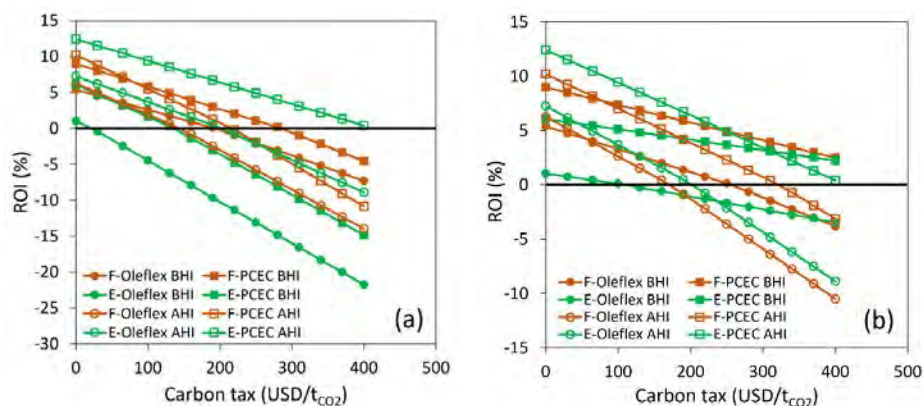
Figure 5.S5: Influence of the imposed carbon tax on the return on investment (*ROI*) of the different Oleflex and PCEC process cases before heat integration (BHI) and after heat integration (AHI) in case of (a) U.S. average electricity, and (b) green electricity.

Chapter 6

Industrial perspective of electrified ethylene production via membrane-assisted ethane dehydrogenation

Summary

The potential of applying proton-conducting electrolysis cell (PCEC) membranes in ethylene production processes was explored in this chapter. To this end, the techno-economics of a PCEC-assisted ethane dehydrogenation process were compared with the conventional ethane steam cracking (SC) process. The PCEC process required four to five times more electricity than the SC process. Consequently, fully renewable electricity needed to be utilized in the PCEC process to outcompete conventional SC in terms of carbon footprint. Notably, the PCEC process was only financially and environmentally competitive with conventional SC when achieving similar ethylene yields (ca. 50%). For an ethylene yield of ca. 25%, which is currently achievable using PCEC technologies, the capital investment and carbon emissions of the PCEC process were too excessive to outcompete electrified SC. The total energy usage, utility demand, and capital investment were substantially higher for the 25% ethylene yield PCEC case as compared to the 50% PCEC one, due to larger process streams and process units as a result of the lower single-pass yield. The results further highlighted that carbon emissions could be reduced from ca. 1.5 $t_{CO2}/t_{ethylene}$ to ca. 0.2 $t_{CO2}/t_{ethylene}$ when employing green electrified SC or PCEC instead of conventional fossil fuel-based SC but only if renewable electricity was utilized. Moreover, a carbon tax of more than 100 USD/t_{CO2} was required to make the green electrified SC and PCEC process more viable than their fossil-based counterparts. Lastly, technological challenges related to attainable ethylene yield, PCEC stability, large-scale sustainable production of PCECs, and the continuous availability of green electricity were identified as the main hurdles for PCEC industrialization and process electrification.

6.1. Introduction

Ethylene is a crucial building block for the chemical industry, as it functions as monomer to produce various plastics (e.g. polyethylene, polyvinylchloride, polyethylene terephthalate) [1]. Due to an ever-increasing demand for commodity chemicals, the ethylene market size is anticipated to grow from ca. 196 billion USD in 2023 to ca. 287 billion USD in 2030 [2]. Most of the commercial ethylene is produced via steam cracking of hydrocarbon reactants ranging from ethane to naphtha [3]. Despite its dominating industrial appearance, steam cracking is a highly energy intensive process, due to the high temperature required (T: >800 °C). This results in significant carbon dioxide emissions (1.0-2.0 t_{CO2}/t_{olefin}), related to the combustion of the natural gas fuel [4]. To reduce global greenhouse gas emissions while expanding the ethylene market, it is therefore crucial to develop more energy efficient ethylene production routes.

An emerging alternative pathway to produce ethylene is the direct dehydrogenation of ethane [5,6]. This reaction can be conducted either in an oxidative or non-oxidative manner. Ethane oxidative dehydrogenation (ODH) is usually operated autothermally, due to the exothermic nature of the reaction but suffers from a poor olefin selectivity (ca. 70%), due to unwanted consecutive oxidation reactions [5,7]. On the contrary, the endothermic non-oxidative dehydrogenation (NODH) of ethane allows for much more selective ethylene formation (>93%) [5,6]. Moreover, ethane NODH allows for the generation of a valuable hydrogen byproduct. Therefore, alkane NODH is generally industrially preferred to alkane ODH [8–10].

Alkane NODH processes have been successfully commercialized to produce propylene and butylenes from propane and butanes, respectively [10,11]. These processes are commonly operated in the temperature range from 550 to 700 °C [11]. In sharp contrast, the more stringent thermodynamic equilibrium of ethane NODH (**Equation 6.1**) limited the application of this approach at commercial scales. Here, exceedingly high reaction temperatures (>700 °C) are needed to attain significant ethylene yields (ca. 40%) via ethane NODH (see **Supporting Information 6.B**).

$$C_2H_6 \leftrightarrows C_2H_4 + H_2 \qquad (\Delta H^0_{298} = +137.0 \text{ kJ/mol}) \qquad (6.1)$$

Ethylene formation is thermodynamically favored at elevated temperatures and reduced pressures. By using hydrogen permeable dense membranes, the ethane NODH equilibrium (**Equation 6.1**) can be shifted toward ethylene, thereby potentially allowing for higher ethylene yields at milder reaction temperatures (550-700 °C). Despite the higher H_2 permeation fluxes through metallic membranes [12], dense ceramic membranes are preferred for integration with high-temperature reactions (T = 550-700 °C), due to their considerably greater stability [13]. The strategy of using hydrogen permeable membranes further offers an opportunity to realize process electrification, and integration of reaction, *in situ* H_2 separation, and H_2 compression.

A membrane configuration that is particularly interesting for improving the energy efficiency of endothermic reactions, while allowing for facile process electrification, is the proton-conducting electrolysis cell (PCEC) configuration [14–16]. In PCECs, only protons are transported through the membrane, whilst electrons are directed via an external circuit by applying a voltage (see **Figure 6.1a**). PCECs thereby offer the possibility to tailor the thermodynamics and kinetics of the targeted reaction and to electrify ethylene production processes. Optimal PCEC hydrogen permeation fluxes are claimed to be attained when wetting both sides of the membrane with ca. 3 wt.% of steam to generate sufficient surface hydroxyl groups that facilitate hydrogen incorporation and recombination [17]. Hydrogen transport through PCEC membranes is driven by a gradient in hydrogen electrochemical potential, i.e. a combination of a gradient in hydrogen partial pressure and a gradient in electrostatic potential under ideal conditions [18]. A PCEC is commonly operated at high voltages, such that the gradient in electrostatic potential dominates the driving force and hydrogen can be transported in a direction opposing the H_2 partial pressure gradient (see **Figure 6.1b**). In other words, a pure hydrogen product stream can be generated in PCECs. Malerød-Fjeld et al. [15] showed that H_2 can be pressurized to 50 bar(a) using this concept.
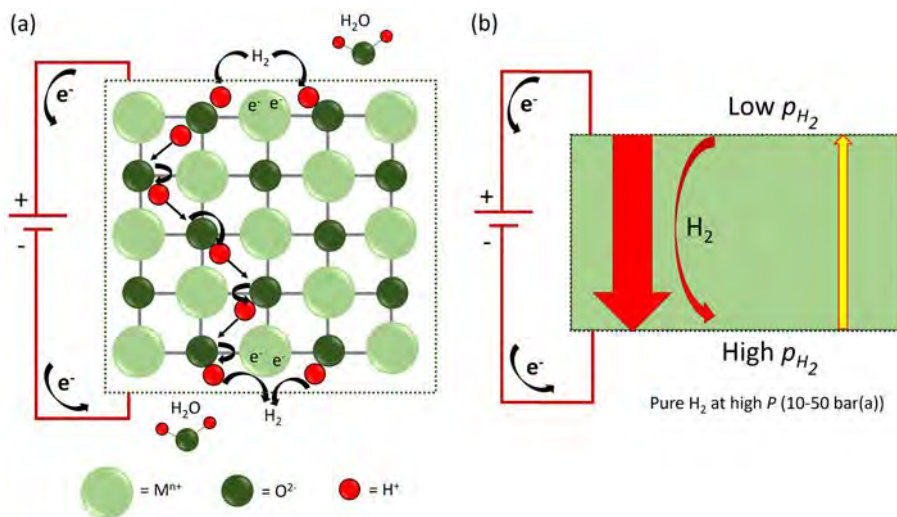
Figure 6.1: (a) Transport mechanism of protons and electrons in proton-conducting electrolysis cell (PCEC) membranes, (b) driving force for hydrogen transport through PCEC membranes. The yellow and red arrows represent the driving forces for H_2 permeation induced by the H_2 partial pressure gradient and electrostatic potential gradient, respectively.

In **Chapter 5**, we compared the techno-economics and carbon footprint of an existing Honeywell UOP Oleflex process for propane NODH to that of a PCEC-assisted process and a process integrated with non-electrically driven mixed proton-electron conducting (MPEC) membranes. There, we showed that the MPEC process is not a financially and

environmentally attractive alternative to conventional Oleflex. The MPEC reactor costs were substantial, since an exceedingly large MPEC membrane area was required, due to the extremely low H_2 permeation rates. Additionally, heating of the sweep gas in the MPEC reactor required a large energy input. We also demonstrated that, in contrast to the MPEC process, the PCEC-assisted propane NODH process could be an attractive alternative to conventional Oleflex. The shift in thermodynamic equilibrium toward propylene induced by the PCEC membranes caused a reduction in the size of process streams and process units, resulting in a lower capital investment and a smaller energy input. The latter only translated into a lower carbon footprint, however, when fully renewable electricity was utilized.

Since the results in **Chapter 5** indicated that the usage of PCEC membranes could lead to substantial financial and environmental benefits for the commercialized propane NODH process, we decided to investigate in this chapter if PCEC membranes could improve the industrial perspective of the non-commercialized ethane NODH technology. We further aim to identify hurdles that could prevent industrial implementation of the PCEC systems. To this end, we benchmarked a PCEC-assisted ethane NODH process against a conventional ethane steam cracking process for ethylene production. We have made a comprehensive assessment of the process economics, energy usage, and carbon dioxide emissions, which included the impact of fossil and electrical heating.

6.2.   Case study

The process flow diagram of the ethane steam cracking (SC) process (**Figure 6.2**) was constructed using information available in literature [3], whilst the methodology proposed by James Douglas [19] for conceptual process design was employed for developing the process flow diagram of the PCEC-assisted process (**Figure 6.3**). For more detailed process flow diagrams as implemented in the process simulations, including the corresponding stream tables, see **Supporting Information 6.C**. Besides, for more details on the process simulations, we refer the reader to **Supporting Information 6.D**.

6.2.1.   Ethane steam cracking process

Ethane steam cracking is conventionally operated in fired tubular furnaces [3]. The residence time of the gas in these furnaces is commonly very short (0.1-0.5 seconds) to optimize the yield toward light olefins, as secondary oligomerization reactions are enhanced for longer residence times. The cracking furnace here was operated at 850 °C and 2 bar(a) and with a steam/hydrocarbon ratio of 0.3 kg/kg [3]. Besides, the ethane steam cracking reaction was simulated with an ethane conversion of 65% in combination with an ethylene selectivity of 80%, resulting in an ethylene yield of ca. 52% [3]. The byproducts comprised hydrogen, carbon monoxide, carbon dioxide, and C1, C2, C3, C4, and C4+ hydrocarbons. The carbon oxides were formed upon steam reforming of coke deposits. For a complete list of side products, see **Supporting Information 6.D1**. The

cracking furnace had to be regenerated periodically in a stream of air to remove coke deposits that were formed inside the furnace coils during the cracking reaction. Steam was cosupplied with the air for heat dilution in an optimized steam/air ratio of 4.67 kg/kg [20]. The design of the ethane steam cracking furnace is further explained in **Supporting Information 6.E**.
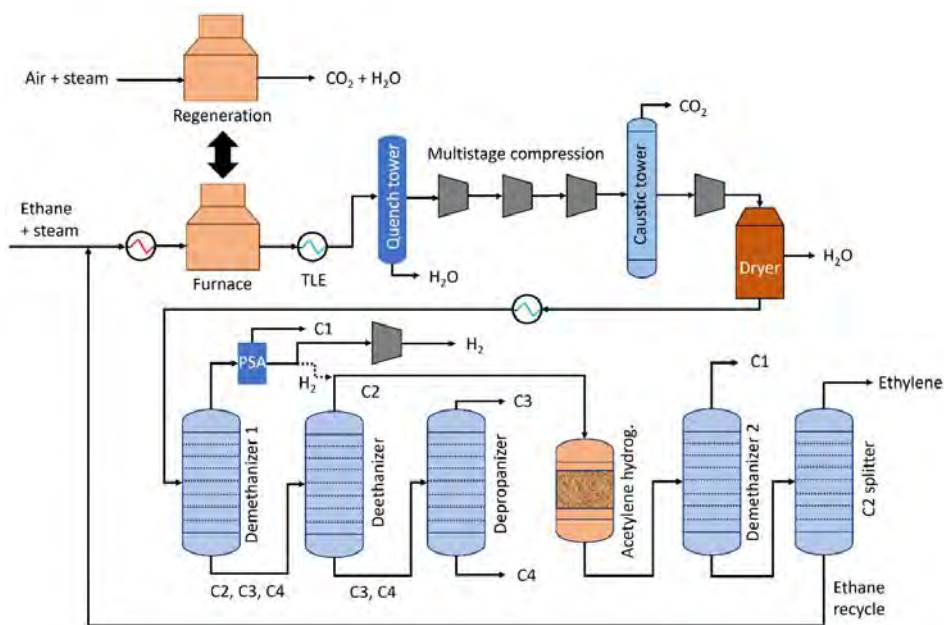
Figure 6.2: Schematic process flow diagram of the ethane steam cracking process. Adapted from Seifzadeh Haghighi et al. [21] with permission from Elsevier.

Downstream the cracking furnace, the hydrocarbon stream was quickly cooled to ca. 300 °C in a transfer line exchanger (TLE) to avoid olefin oligomerization (**Figure 6.2**) [3,22]. In the quench tower, the majority of the water was removed before compression to 17 bar(a) in a multistage compressor system with interstage cooling. After compression, a caustic tower was used to remove carbon dioxide impurities [3]. Succeeding the caustic tower, the hydrocarbon product stream was further pressurized to 32 bar(a). Then, a dryer pressure swing adsorption (PSA) column was applied with pressure swings between 32 and 2 bar(a) to remove the remaining moisture.

The dried and cooled hydrocarbon stream was sent through a sequence of cryogenic distillation columns (**Figure 6.2**) [3]. Light impurities were removed from the process in a demethanizer column. The light impurities were separated into a fuel gas and a hydrogen stream in a pressure swing adsorption (PSA) unit. The fuel gas contained primarily methane and was combusted to generate part of the energy needed for the steam cracking furnace. A major part of the hydrogen stream was sold as a valuable byproduct. The deethanizer column isolated the C2's from the heavy impurities (C3+). The C3 and C4

impurities were separated in a depropanizer column to be sold as byproducts. The C2 stream was sent to an acetylene hydrogenation reactor to selectively hydrogenate the acetylene content to maximize the ethylene yield and to avoid possible detrimental effects to the process induced by the acetylene [22]. The hydrogen needed for this hydrogenation step originated from the PSA (**Figure 6.2**) and was supplied in a hydrogen/acetylene ratio of 1.8 [3]. A second demethanizer was then required to remove the last methane and hydrogen impurities. Lastly, the ethylene product was separated from the unconverted ethane in a C2 splitter. The vapor ethylene product (≥99.9 wt.%) was obtained at 18 bar(a) and 10 °C, while the unconverted liquid ethane was recycled to the cracking furnace. The operating conditions and dimensions of the distillation columns applied in the SC process are summarized in **Supporting Information 6.G3**.

6.2.2.   PCEC membrane-assisted process

Since ceramic membranes are known to function optimally in presence of steam [17], 3 wt.% of steam was cosupplied with the ethane feed stream to the PCEC reactor (**Figure 6.3**) [23,24]. For the same reason, steam was cofed to the PCEC permeate side, in such an amount that the permeate side outlet stream contained 3 wt.% of steam. The PCEC membrane was assumed to be fully permselective, implying that the permeate side effluent stream only contained hydrogen and steam. The steam cosupply on the membrane feed side also helps in suppressing coke formation, thereby improving catalyst stability [25].

The PCEC membrane reactor consisted of parallel-configured tubular membrane cells (see **Supporting Information 6.F**). Continuous operation was achieved by running some of these reactors in dehydrogenation mode (T = 550 °C, P = 5 bar(a)) and other ones in regeneration mode (T = 620 to 830 °C, P = 5 bar(a)) with intermediate flushing runs [3,20]. The PCEC membrane reactor was simulated with 98% hydrogen removal, in which the hydrogen removal fraction was defined as the ratio between the amount of hydrogen extracted and the amount of hydrogen present. This extremely high fraction of hydrogen removal was selected, since more than 95% of the hydrogen needs to be removed to substantially shift the ethane NODH equilibrium yield (**Supporting Information 6.B**). The single-pass ethylene yield in the base case PCEC process was ca. 25%, based on an ethane conversion of 39.5% and an ethylene selectivity of 63.3%, as obtained by Wu et al. [26] in their experimental study on PCEC-assisted ethane NODH. An additional PCEC case was included in which the single-pass ethylene yield was 50%, similar to the SC process. This second PCEC case aimed at evaluating the impact of using PCEC membranes on process economics and sustainability aspects if technological advancements in the field of PCEC research would allow for attaining ethylene yields competitive to conventional SC.

Possible reforming reactions caused by the steam were disregarded in both PCEC process cases. Similar to the ethane steam cracking furnace, the PCEC membrane reactor had to be regenerated periodically because of the anticipated carbon deposition inside the PCEC reactor. This regeneration step was conducted using air at 5 bar(a) and with an inlet

temperature of 620 °C [3,20]. Moreover, steam was again cosupplied in a steam/air ratio of 4.67 kg/kg in the regeneration step for heat dilution [20].
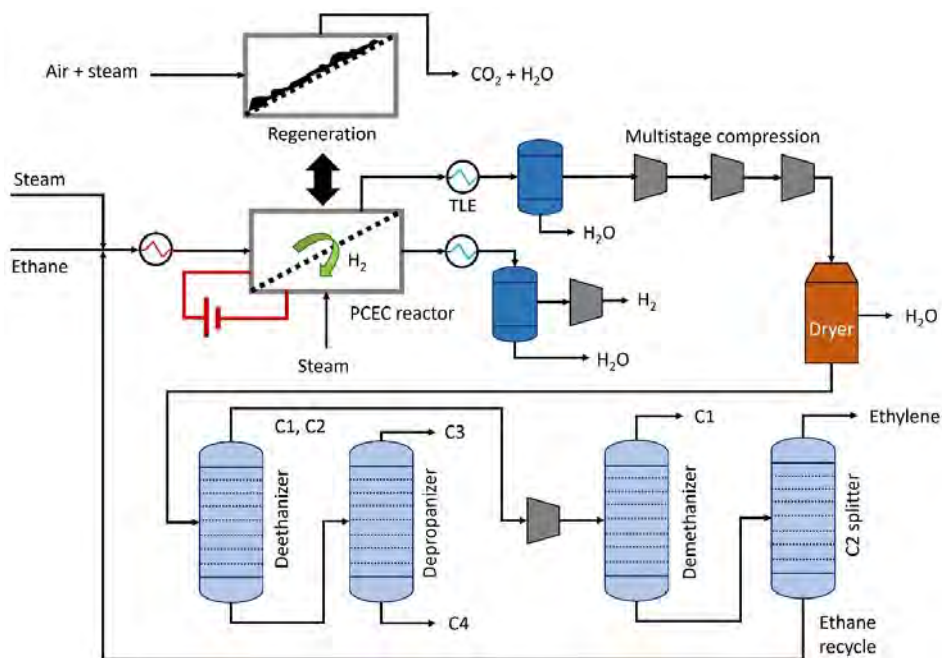
Figure 6.3: Schematic process flow diagram of the PCEC membrane-assisted ethane dehydrogenation process.

The PCEC composition considered in this work equaled the PCEC composition applied by Wu et al. [26] in their experimental work on PCEC-assisted ethane NODH. This concerned a cathode-supported cell in which the cathode consisted of nickel-functionalized barium zirconium cerium yttrium ytterbium oxide (Ni/BZCYYb, $BaZr_{0.1}Ce_{0.7}Y_{0.1}Yb_{0.1}O_{3-\delta}$) with a thickness of 450 μm. The electrolyte was a BZCYYb layer with a thickness of 15 μm. The anode (t = 80 μm) was composed of a praseodymium barium iron molybdenum oxide (PBFM, $PrBa_{0.95}(Fe_{0.9}Mo_{0.1})_2O_{5+\delta}$) impregnated with catalyst phases consisting of platinum and gallium supported on ZSM-5 zeolite (PtGa/ZSM-5). The respective platinum and gallium loadings of this catalyst were 0.175 wt.% and 1.02 wt.%. BZCY-based PCEC systems are known for their outstanding proton conductivity properties in combination with good stability in hydrocarbon atmospheres [14,15].

An external voltage was applied to drive hydrogen (proton) permeation through the PCEC membrane (**Figure 6.3**). It was demonstrated by Malerød-Fjeld et al. [15] for BZCY-based electrochemical cells that hydrogen could be electrochemically compressed to 50 bar(a) using this concept. However, electrochemical compression is most efficient for light compressions [27]. Hydrogen was therefore compressed electrochemically to 20 bar(a) in the PCEC reactor in this work, followed by mechanical compression to 50 bar(a). This 50

bar(a) hydrogen pressure is a typical pressure for hydrogen storage in spherical vessels [28]. The hydrocarbon retentate stream of the PCEC reactor was quickly cooled in a transfer line exchanger (TLE), before separating the water in a flash drum. Afterward, the hydrocarbon stream was compressed to 27 bar(a) in a multistage compression section. The last traces of water were again removed in a dryer PSA column, operated in this case with pressure swings between 27 bar(a) and 2 bar(a).

The hydrocarbon product stream was further purified in a sequence of cryogenic distillation columns (**Figure 6.3**). A front-end deethanizer configuration was selected for the PCEC process, because this configuration had lower operational costs than the possible alternative configurations, as it had the lowest overall heating and cooling duties (see **Supporting Information 6.C**). In the deethanizer column the heavy impurities were removed from the fraction containing C2's and lighter compounds. Subsequently, the depropanizer column further purified the heavy impurities to C3 and C4 fractions, respectively, which were sold as valuable byproducts. Besides, the stream containing C2's and lights was pressurized to 32 bar(a) and then fed to a demethanizer column, in which the light impurities were isolated from the C2's. The remaining lights fraction contained mainly methane and was combusted to generate a fraction of the energy needed to operate the endothermic dehydrogenation reactors. Lastly, the ethylene product (≥99.9 wt.%) was separated from the unconverted ethane in a C2 splitter. The unconverted ethane was recycled to the feed of the PCEC process, similar to the ethane SC process. The operating conditions and dimensions of the distillation columns applied in both PCEC processes are summarized in **Supporting Information 6.G3**.

6.3. Methodology

The ethane steam cracking process and the two PCEC-assisted ethane NODH processes were all simulated in Aspen Plus V12.1 using the Soave-Redlich-Kwong equation of state as the property method and using equal design bases.

6.3.1. Process feed and product specifications

The targeted product was polymer grade ethylene (≥99.9 wt.%, see **Supporting Information 6.A1**) at 18 bar(a), which was within the typical operating range of C2 splitter columns (17-28 bar(a)) [3]. Commercial steam cracking plants generally operate with an ethylene production capacity of more than 1,000 ktpa (**Supporting Information 6.A3**) [29,30]. However, since immediate industrial implementation of the emerging PCEC technology on such a large scale is unrealistic, an ethylene production capacity of 100 ktpa was selected in this work. By doing so, the competitiveness of the PCEC technology on this relatively small scale will provide key insights for the potential scale up approaches in the future. In addition to the ethylene product, high purity fuel grade hydrogen (≥99.95%, **Supporting Information 6.A2**) [31] was targeted as byproduct and was pressurized to 50 bar(a) for transportation and storage [28]. The

ethane feed stream was obtained from a natural gas processing plant and contained 96.16 wt.% of ethane, 1.83 wt.% of methane, and 2.01 wt.% of propane [32]. Possible H_2S impurities were assumed to be removed in desulfurization pre-treatment steps, which were outside the scope of this study. The ethane feed stream was at 31 bar(a) and 11 °C, which was equivalent to the conditions of the ethane stream from the deethanizer column of a natural gas processing plant [33,34]. The number of operating hours per year was set to 8,766.

The two ethylene production processes were considered to be constructed in the Asia-Pacific region, as the financial margin between the ethane and ethylene prices was substantial (see **Table 6.1**), and since the share of renewable resources to the generation of grid electricity is already significant (ca. 30%) in this region [35].

Table 6.1: Feedstock and product prices.

Compound	Price (USD/t)	Ref. year	Location	Reference
Ethane	270	Q1, 2023	Asia-Pacific	Estimated based on [36]
Ethylene	950	Q1, 2023	Asia-Pacific	Estimated based on [37,38]
Hydrogen	1,600	Q1, 2023	Asia-Pacific	Estimated based on [39]

6.3.2.   Utility specifications

The different types of utilities needed, including the corresponding specifications and costs, are available as **Supporting Information 6.A4**. In the utility assessment, the reactors were either heated using fossil fuels via natural gas incineration or using electricity. All heating steps above 285 °C were conducted using fired heaters, while the heating steps at lower temperatures were carried out using either high pressure (80 bar(a)), medium pressure (11 bar(a)), or low pressure (2.3 bar(a)) steam. On the contrary, the cooling steps were executed using cooling water or refrigerants. The cooling water was supplied at 25 °C and discharged at 45 °C [40], whilst the refrigerants were based on methane, ethylene, and propylene cycles. Lastly, pumps and compressors in the process required electricity. Two different types of electricity were considered, namely Asia-Pacific grid electricity and fully renewable electricity. In the base case analysis, green electricity was assumed to be equally expensive as the grid electricity, even though solar and wind-based electricity can already be generated at lower costs than grid electricity [41].

6.3.3.   Reactor simulations

The ethane steam cracking furnace was simulated in Aspen Plus as a stoichiometric reactor. The single-pass ethane conversion was 65% with an ethylene selectivity of 80% (i.e. an ethylene yield of ca. 52%), with mainly light hydrocarbon byproducts (see **Supporting Information 6.D1** for the full product distribution). The PCEC membrane reactor was simulated in Aspen Plus by a combination of a stoichiometric reactor and a component splitter. The stoichiometric reactor defined the fractional conversion of all

reactions taking place inside the PCEC reactor. In the base case PCEC process, dealing with a single-pass ethylene yield of ca. 25% the fractional conversions were retrieved from the work by Wu et al. [26] (see **Supporting Information 6.D2.1**). By contrast, the product distribution of the PCEC target case in which the single-pass ethylene yield was adjusted to 50% is provided in **Supporting Information 6.D2.2**. The component splitter compartment of the PCEC reactor in Aspen Plus specified the fraction of hydrogen that was effectively removed by the PCEC membrane. In this work, a fraction of 98% hydrogen removal was used, theoretically allowing for an ethane dehydrogenation yield increase to ca. 60% at 550 °C (see **Supporting Information 6.B**).

We utilized the polycyclic aromatic hydrocarbon coronene, with chemical formula $C_{24}H_{12}$, as coke model compound in both process simulations. Coronene was in the gas phase under reaction conditions and therefore transportable to a regeneration unit in the Aspen Plus simulations. This regenerator was simulated as a stoichiometric reactor with complete combustion of the coronene content and was used to quantify the amount of energy generated upon regeneration. Based on Wu et al. [26] the amount of coronene formed was set to 2.06 gram per kilogram of ethane converted for the SC as well as the PCEC processes. For more information on the simulations of the (membrane) reactors in both processes, see **Supporting Information 6.D**.

6.3.4. Equipment design

The tubular ceramic membrane reactor design developed by CoorsTek [14,42] was used for dimensioning the PCEC membrane reactor. This tubular design was preferred to a planar design for systems dealing with considerable pressure gradients that arise e.g. upon electrochemical hydrogen compression. The CoorsTek design represents a modular approach in which tubular ceramic PCEC units are stacked together in membrane modules. The total active membrane area per module is about 44 m². For more details on the membrane reactor design and the applied membrane multilayer composition, the reader is referred to **Supporting Information 6.F**. The design of other process equipment, e.g. compressors, and distillation columns, is available in **Supporting Information 6.G**.

The required PCEC membrane area was calculated based on the outcomes of the Aspen Plus simulations. The base case PCEC reactor effluent stream contained 160 mol/s of hydrogen in absence of any hydrogen abstraction. For the assumed 98% hydrogen removal, this means that ca. 157 mol/s of hydrogen had to be removed by the PCEC membrane. The PCEC membrane reactor was operated at a current density of 1 A/cm², estimated based on experimental PCEC studies available in literature [15,16]. With this current density and hydrogen removal rate, the membrane area required for permeation was calculated to be ca. 3,000 m². For industrial propane dehydrogenation processes, typically 17% of the reactor capacity is operating in regeneration mode [11]. Based on this information, the total required PCEC membrane area was determined to be ca. 3,500 m². This corresponds to ca. 80 membrane modules (see **Supporting Information 6.F**). In

the alternative PCEC case targeting a single-pass ethylene yield of 50% the PCEC reactor outlet only contained 129 mol/s of hydrogen. This was ascribed to smaller process stream sizes as compared to the base case PCEC process, as a result of a smaller recycle caused by the higher single-pass ethylene yield. The considered ethane-to-ethylene conversion is also much higher in the target case PCEC process, due to a lower butylene and a higher ethylene selectivity relative to the base case PCEC process, as shown in **Supporting Information 6.D2**. As a consequence, a smaller PCEC membrane area of about 2,800 m^2 was required in the target case PCEC process for 98% hydrogen removal, corresponding to ca. 64 membrane modules.

6.3.5.   Process economics, energy usage, and carbon dioxide emissions

The outcomes of the Aspen Plus simulations (e.g. heating and cooling duties, number of distillation column stages, pump and compressor powers) were used to quantify the capital expenditures (CAPEX), operating expenditures (OPEX), energy usage, and carbon dioxide emissions.

6.3.5.1.   Capital expenditures (CAPEX)

The capital expenditures were estimated based on the factor method proposed by Towler and Sinnott [43]. This method uses a bottom-up approach, in which the capital investment of the process equals a summation of the capital investment per unit operation. The direct capital investment per unit operation in turn is a function of the purchased equipment costs and several compensation factors. The installation factor proposed by W.E. Hand [43] compensated for costs related to the installation of process equipment. Besides, a material factor accounted for possible material constraints and a location factor for the geographic location of the plant in the Asia-Pacific region. In addition, the Chemical Engineering Plant Cost Index (CEPCI) corrected for the inflation. For further information on the applied factor method for the CAPEX estimation, see **Supporting Information 6.K**.

The capital costs of the PCEC membrane reactors were estimated by following a method proposed by Malerød-Fjeld et al. [15] for cost estimation of CoorsTek proton-conducting membrane reactors (**Supporting Information 6.F**). In this method, the investment costs were a summation of (i) membrane reactor steel costs, (ii) hot box steel costs, (iii) stack material costs, (iv) tooling costs, and (v) additional costs. The stack material costs contained the bare costs for the electrode and electrolyte materials, as well as costs for gas manifolds, interconnects, weld connectors, and sealing rings. Besides, the tooling costs represented the depreciation of the equipment needed for manufacturing, in which it was assumed that the equipment was fully depreciated over the process units manufactured in the plant. Lastly, the additional costs contained costs for e.g. instrumentation, tubing, and fittings [15]. The steel costs of the membrane reactor housing and the hot box were estimated based on the process unit dimensions and the required wall thickness.

6.3.5.2. Operating expenditures (OPEX) and revenues

The operating expenditures (OPEX) and revenues were calculated using a method described by Towler and Sinnott [44]. The OPEX consisted of the variable and the fixed production costs. The former contained costs for (i) raw materials, (ii) utilities, (iii) consumables, and (iv) effluent disposal, whereas the latter comprised costs related to (i) labor, (ii) process maintenance, (iii) property taxes, and (iv) rent of land. Besides, the revenues were comprised of contributions from the targeted ethylene product, and the hydrogen, propylene, and butylene byproducts. In case all reactor heating and preheating steps were carried out electrically, then the fuel gas generated in both processes was also sold at fuel value.

The consumables contained costs for catalysts, adsorbents, and membranes. Besides, the effluent disposal expenditures covered costs for flue gas cleaning, spent caustic disposal, and wastewater treatment. The lifetime of the PCEC membranes was set equal to the lifetime of conventional alkane dehydrogenation catalysts (two years) [10], and it was assumed that only the membrane stack materials had to be replaced periodically. In view of the energy transition, it is expected that the carbon tax will become a more dominant factor in evaluating the viability of process alternatives. In the base case economic assessment, no carbon tax was included. Instead, the carbon tax was incorporated in the sensitivity analysis to explore the impact of penalizing carbon emissions on the profitability of the different process cases.

The profitability of the ethane SC and PCEC processes was evaluated by determining the return on investment (*ROI*) and the payback period. In this work, the *ROI* was quantified using the net annual profit and the total capital investment. The net annual profit was calculated from the gross annual profit corrected for an estimated corporate income tax of 18% for the Asia-Pacific region [45]. The gross annual profit was in turn calculated from the difference between the total revenues and the total production costs, including a depreciation contribution for a linear depreciation period of fifteen years of the total depreciable capital. We refer the reader to **Supporting Information 6.L** and **6.P** for more details on the OPEX calculations and the profitability assessment, respectively.

6.3.5.3. Environmental impact

The environmental impact of the different processes was quantified by means of the carbon dioxide emissions, which comprised of contributions from (i) utility natural gas incineration, (ii) fuel gas combustion, (iii) coke combustion, (iv) electricity generation, and (v) natural gas combustion needed for steam generation. Two types of electricity were taken into consideration, namely Asia-Pacific grid electricity and fully renewable electricity. The grid electricity in the Asia-Pacific region has a carbon intensity of 532.1 g_{CO2}/kWh [46], whereas the carbon intensity of fully renewable electricity was estimated at 50 g_{CO2}/kWh [47,48], accounting for emissions related to the construction of windmills and solar panels. Two steam cracking cases were discerned, depending on whether the

reactor feed and the reactor itself were heated by burning a natural gas fuel (SC fossil), or by using electricity (E-cracker, SC full electric). Analogously, for the PCEC processes different cases were assessed in which the reactor feed and the PCEC membrane reactors were both heated by burning natural gas (PCEC fossil) or by using electricity (PCEC full electric). An additional PCEC case was included in which the reactor feed was heated by burning natural gas, whilst the PCEC membrane reactor was heated by operating at thermoneutral voltage (PCEC E_{th}). In the latter case, the heat required for the dehydrogenation reactor was fully delivered by resistive Joule heating inside the PCEC membrane. It should be noted that also in the PCEC fossil cases the reactor heat partially originated from Joule heating effects. Besides, for the SC and PCEC full electric cases the fuel gas streams available within the processes were sold at fuel value and the corresponding carbon emissions were, thus, not included in that situation. More details on the calculations of the carbon dioxide emissions are available in **Supporting Information 6.N**.

6.3.6.   Process heat integration

The heat integration measures implemented in the different processes were related to (i) combustion of carbon deposits, (ii) combustion of the C1-rich off-gas streams, (iii) resistive Joule heating, and (iv) heat exchange between hot and cold process streams. The latter was accomplished by means of a pinch point analysis using the FI^{2}EPI software [49]. In this analysis, a minimum temperature approach of 10 °C between the hot and cold fluids was imposed. Besides, only streams with a duty of more than 1 MW were, in general, included. The only exception comprised of duties of less than 1 MW that had to be covered by one of the expensive refrigerants. Moreover, it was assumed that heat integration with the reactor blocks was practically not possible. The heat integration analysis is discussed in detail in **Supporting Information 6.J**. A detailed heat exchanger network was designed for the SC and PCEC base case processes. The heat exchanger network capital investment was estimated to be equal for the PCEC target case and the PCEC base case. A detailed heat exchanger design for the PCEC target case was considered to be beyond the scope of this work. The influence of heat integration within the PCEC target process on the corresponding energy usage, utility demand, and carbon emissions, was included by assuming that per heating/cooling step the same relative amount of energy could be integrated as for the PCEC base case process.

6.4. Results and discussion

6.4.1.   Utilities

The available heat within the SC and PCEC processes as obtained from (i) resistive Joule heating, (ii) fuel gas combustion, and (iii) high pressure steam was in all cases used to cover part of the heating requirement. Implementation of the heat integration measures by exchanging heat between hot and cold process fluids led to considerable reductions in

the required utilities for the SC and PCEC processes (see **Figure 6.4**). Notably, the utility consumption of the base case PCEC process (ca. 25% ethylene yield) was ca. 25% higher than the base case SC process, regardless of the extent of heat exchange. This was partly attributed to the great electricity demand for electrically driving the hydrogen permeation in the PCEC membrane reactor. Besides, the steam utility demand of the base case PCEC process was higher in comparison with the SC process, particularly due to the heavy C2 splitter reboiler duty. Since the inlet of the C2 splitter in the base case PCEC process contained less ethylene as compared to the SC process, due to the lower single-pass ethylene yield, a larger C2 splitter reboiler capacity was needed to attain the set ethylene product purity (≥99.9 wt.%).
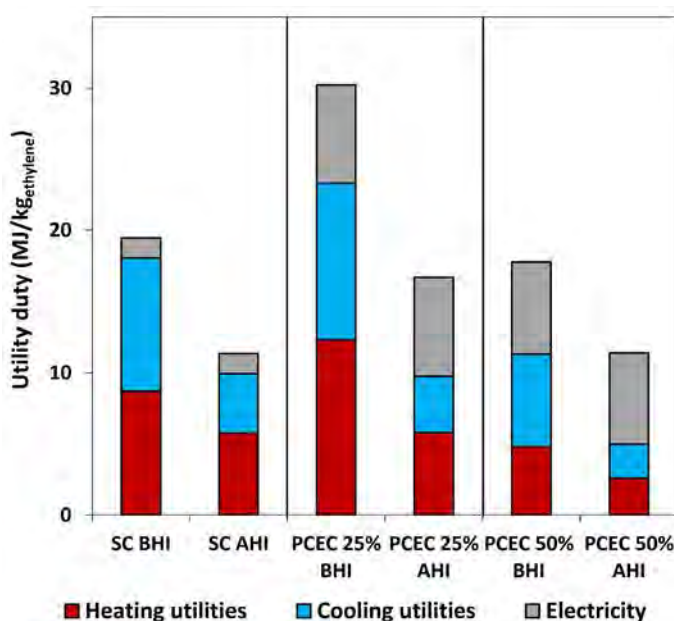
Figure 6.4: Utility duty for the fossil fuel heated ethane steam cracking (SC) and PCEC-assisted processes before heat integration (BHI) and after heat integration (AHI). Herein, heat integration only covers the exchange of heat between hot and cold process fluids; the heating utilities of the BHI cases were already corrected for the heat covered by Joule heating, fuel gas combustion, and high pressure steam. Note that the electricity contribution here contains the electricity needed for compression, pumping, and electrically driven hydrogen permeation but excludes the possibility of electrical heating.

The total utility duty of the target case PCEC process, considering a single-pass ethylene yield of 50%, was similar to the conventional SC process (**Figure 6.4**). The heating and cooling requirements of the PCEC target case were ca. 40% lower as compared to the SC process (**Figure 6.4**), caused by the lower operating temperature of the PCEC reactor (T = 550 °C) relative to the SC furnace (T = 850 °C). By contrast, the PCEC target case

required three to four times more electricity than conventional SC for electrochemical hydrogen separation and compression.

The electricity requirement of the SC process of 1.4 MJ/kg$_{ethylene}$ (**Figure 6.4**) was in line with typical values of about 1 MJ/kg$_{ethylene}$ reported for ethane SC processes [4]. The total energy input, i.e. the sum of the heating and electricity utilities, of the SC process (ca. 10.4 MJ/kg$_{ethylene}$) was below the specific energy input (*SEI*) values typically reported for ethane SC processes (17-21 MJ/kg$_{ethylene}$) [4]. The reason for this is that the utility duty reported here was already corrected for the heat generated from the combustion of fuel gas and the usage of high pressure steam. An overview of the distribution of the different utilities needed and the corresponding costs for the SC and PCEC process cases after heat integration is available in **Supporting Information 6.M**. There it is shown that the total utility costs were about one third higher for the base case PCEC process as compared to the base case SC process, due to high electricity costs for operating the PCEC membrane reactor. By contrast, the total utility costs of the PCEC target case were ca. 10% lower relative to the SC process, due to the lower heating and cooling demand of the PCEC process, caused by the lower operating temperature of the PCEC membrane reactor (*T* = 550 °C) in relation to the SC furnace temperature (*T* = 850 °C). Moreover, it is demonstrated in **Supporting Information 6.M** that the utility costs were dominated by refrigerant costs (SC and PCEC processes) and electricity costs (PCEC processes).

6.4.2.   Environmental impact

The environmental impact of the different process cases was quantified by means of the carbon dioxide emissions (see **Figure 6.5**). The obtained carbon footprint of the fossil fuel heated SC process (ca. 1.5 t$_{CO2}$/t$_{ethylene}$), representing the conventional ethylene production method, was well in line with typical steam cracking emissions (1.0-2.0 t$_{CO2}$/t$_{olefin}$) [4]. This footprint was dominated by contributions from the combustion of natural gas and fuel gas (**Figure 6.5**). By contrast, the carbon footprint of the PCEC process cases was less controlled by natural gas and fuel gas incineration, since for all PCEC cases the required heat was (partially) supplied via Joule heating.

Notably, when grid electricity was utilized in the base case PCEC process (ca. 25% ethylene yield), then the carbon dioxide emissions of fossil fuel heated PCEC were ca. 24% higher compared to the fossil fuel heated SC process (**Figure 6.5**). On the contrary, the carbon emissions were 22% lower for the fossil fuel heated PCEC process compared to the fossil fuel heated SC process when green electricity was used (**Figure 6.5**). This difference was attributed to the contribution of Joule heating to the reactor heat supply. Indirect heat supply via Joule heating was only environmentally beneficial when fully renewable electricity was utilized.

The carbon dioxide emissions of the target case PCEC process (50% ethylene yield) were always lower than the carbon footprint of the base case PCEC process (**Figure 6.5**). The increase in single-pass ethylene yield from ca. 25% to 50% led to a smaller process recycle

and, hence, smaller process streams. Consequently, less utilities were required for the target case PCEC process compared to base case PCEC (see **Figure 6.4**). As a result, the carbon emissions related to these utilities were also lower (**Figure 6.5**). In particular, the smaller ethane recycle stream caused a lower fired heat demand for preheating the reactor feed and a lower steam demand for distillation reboiling. For the case in which the PCEC reactor was operated at thermoneutral voltage, the energy obtained from coke and fuel gas combustion even turned out to be sufficient to cover the natural gas utility demand of target case PCEC (**Figure 6.5**). Similar to base case PCEC, the carbon footprint of the target case PCEC was drastically reduced when using green electricity instead of Asia-Pacific grid electricity. The advantageous effect of using green electricity (50.0 g_{CO2}/kWh) instead of fossil grid electricity (532.1 g_{CO2}/kWh) became even more pronounced when electrifying the respective processes, as the carbon footprint reduced substantially when moving from the fossil fuel heated cases to the fully electrified cases (**Figure 6.5**).
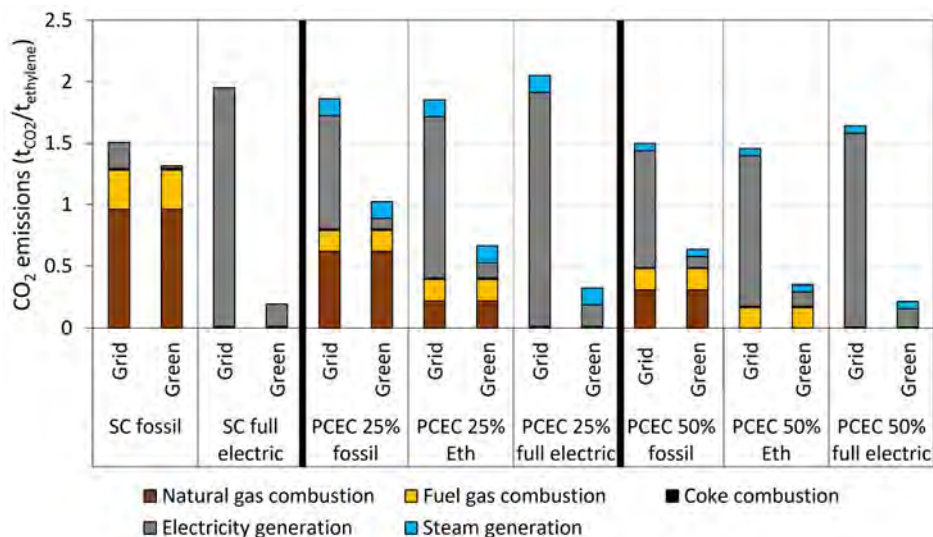
Figure 6.5: Carbon dioxide emissions of the ethane steam cracking (SC) process, the base case PCEC membrane-assisted process (ca. 25% ethylene yield), and the target case PCEC process (50% ethylene yield), in case the reactor feed and the reactor itself were heated by burning natural gas or fuel gas (fossil) or by using electricity (full electric). Additional PCEC cases were included in which the reactor feed was heated by burning natural gas or fuel gas, and in which the reaction heat was fully delivered via resistive Joule heating inside the PCEC membrane reactor (operation at thermoneutral voltage, E_{th}).

Notably, the carbon footprint of the base case SC process electrified using green electricity (ca. 0.2 t_{CO2}/$t_{ethylene}$) was even lower than the green electrified base case PCEC process (ca. 0.3 t_{CO2}/$t_{ethylene}$, **Figure 6.5**). This difference arose from the steam utility requirement of the PCEC process. In the SC process, the amount of high pressure steam generated inside the TLE upon cooling down the hydrocarbon stream from the cracking temperature of 850

°C to ca. 300 °C was sufficient to cover the steam utility demand of the process. On the contrary, the amount of high pressure steam generated in the TLE of the base case PCEC process was more limited, due to a smaller temperature drop from the PCEC reactor temperature of 550 °C to ca. 300 °C. The steam demand of the base case PCEC process could therefore not be fully covered by internally generated steam, leading to an external steam utility demand and related carbon emissions upon generating this external steam (**Figure 6.5**).

The carbon footprint of the green electrified target case PCEC process was similar to that of the green electrified SC process (ca. 0.2 $t_{CO2}/t_{ethylene}$, **Figure 6.5**). This means that green electrification of conventional SC processes had comparable environmental benefits as industrial implementation of green electrified PCEC membrane reactor systems for similar ethylene product yields (ca. 50% in this comparison). It should be emphasized that the target case PCEC process considered an ethylene yield of 50% that hitherto has not been achieved in experimental PCEC research for this application. For currently attainable ethylene yields of ca. 25% [26], the green electrified process could not outcompete green electrified SC in terms of carbon emissions (**Figure 6.5**). An ethylene yield of ca. 50% can, therefore, be regarded as a minimum threshold for industrialization of PCEC-assisted ethane dehydrogenation.

The results in **Figure 6.5** highlight that, irrespective of the type of process case employed, renewable electricity needed to be utilized to outcompete conventional fossil fuel heated SC. For this reason, a sensitivity analysis was applied regarding the influence of the carbon intensity of the electricity on the total carbon dioxide emissions of the various process cases (see **Supporting Information 6.O3**). Recall that the carbon intensity of Asia-Pacific grid electricity was 532.1 g_{CO2}/kWh [46]. The full electric process cases had the lowest carbon footprint for an electricity carbon intensity of less than 200 g_{CO2}/kWh, whilst the fossil fuel heated processes were more sustainable above 350 g_{CO2}/kWh (see **Supporting Information 6.O3**). The carbon emissions related to electricity generation should, thus, be lower than 200 g_{CO2}/kWh to make electrification of SC or PCEC processes environmentally attractive. For more information on the complete carbon footprint assessment, see **Supporting Information 6.N**.

6.4.3. Process economics

6.4.3.1. Capital expenditures

The total investment costs of the base case PCEC process were ca. 15% higher as compared to the conventional ethane SC process (**Table 6.2**). This was particularly attributed to higher reactor costs in the PCEC process. Moreover, the capital investment in distillation columns, heat exchangers, and flash vessels was higher for the base case PCEC process, due to the lower single-pass ethylene yield (ca. 25%) in comparison to the SC process (52%), resulting in a bigger recycle stream and, hence, larger equipment sizes. By contrast, when the PCEC process was operated using an ethylene yield that is similar to the SC

process, as exemplified by the PCEC target case, then the total investment costs were comparable to the SC process (**Table 6.2**). Despite the higher reactor costs for the target case PCEC process relative to SC, the total capital investment of both processes was similar, due to notably lower compressor costs of the PCEC process. The latter was ascribed to the *in situ* hydrogen compression inside the PCEC membrane reactor and the higher operating pressure of the PCEC reactor (5 bar(a)) versus the SC furnace (2 bar(a)), leading to a lower demand for mechanical compression in the PCEC process.

Table 6.2: Comparison of the capital costs between the conventional ethane steam cracking (SC) process and the base case (ca. 25% ethylene yield) and target case (50% ethylene yield) PCEC-assisted ethane NODH processes.

Equipment type	Capital cost (MMUSD, 2023)		
	SC	PCEC base case (25%)	PCEC target (50%)
Reactors	20	32	26
Distillation columns	5	9	7
Compressors and pumps	33	25	21
Heat exchangers	6	7	7
Flash vessels	2	3	2
Other separation equipment	1	0	0
Total direct investment (=ISBL*)	*66*	*76*	*62*
OSBL** costs (=40% of ISBL*)	27	31	25
Design and engineering costs (=30% of ISBL* + OSBL**)	28	32	26
Contingency charges (=10% of ISBL* + OSBL**)	9	11	9
Total fixed capital investment	*130*	*151*	*123*
Working capital	14	16	13
Total capital investment	**144**	**167**	**136**

ISBL = Inside battery limits, **OSBL = outside battery limits.

Table 6.2 shows that the main contributors to the capital investment of the SC and PCEC processes were the reactor and compressor equipment. The compressor costs were independent of whether the reaction and (pre-)heating steps within the processes were operated using electrical heat or heat generated by burning fossil fuels. However, the reactor equipment costs might differ per heating method, as e.g. electrification of cracking equipment could lead to a considerable reduction in the required equipment size [50,51]. On the contrary, electrification is anticipated to be accompanied by additional expenditures on heating elements and power management (transformers, etc.) [50]. Due to this current uncertainty, it was assumed in this work that the CAPEX of the electrically heated processes equals the CAPEX of the corresponding fossil fuel heated process cases.

The capital investment of the distillation columns and heat exchangers in this work (**Table 6.2**) were relatively marginal as compared to values typically reported in literature for alkane dehydrogenation processes [52]. The olefin/paraffin separator (including condenser and reboiler) often even covers 40% of the total direct investment [52]. However, due to the relatively small olefin production capacity selected in this work (100 ktpa) as compared to the typical production capacity of alkane dehydrogenation plants (ca. 400-1,000 ktpa) [53], the distillation column diameters were comparably small here, allowing for relatively thin walls and, hence, relatively low steel costs. Moreover, the cryogenic distillation steps in this ethane dehydrogenation study were carried out using refrigerants at subzero temperatures, whereas distillation columns in propane and butane dehydrogenation plants are commonly operated using cooling water [52]. The use of relatively cheap cooling water for condensation was not possible for the ethane dehydrogenation processes simulated here, as the temperatures of the overhead streams to be condensed were too low (T: -20 to 20 °C). However, the advantage of using more expensive refrigerants (T: -150 to -25 °C) was the large temperature gap between the refrigerant and the overhead stream to be condensed. Consequently, the driving force for condensation was large, leading to low condenser investment costs as compared to typical cooling water-based propane and butane dehydrogenation processes. Analogously, the temperature gap between the low pressure steam utility (T: 125 °C) and the distillate bottom streams to be reboiled (T: -30 to 20 °C) was much larger for the ethane dehydrogenation processes simulated here as compared to typical propane and butane dehydrogenation processes (reboiler T: 50-60 °C). The required reboiler heat exchange areas and corresponding reboiler capital costs were, therefore, also lower in this work as compared to typical propane and butane dehydrogenation processes, even after applying material factors for the operation at subzero temperatures in the distillation section.

6.4.3.2.   Operating expenditures

The operating expenditures (OPEX) of the different processes were quantified for the fossil fuel heated cases. The total OPEX of the base case PCEC process was ca. 30% higher compared to the SC process (**Figure 6.6a**). This was attributed to higher costs for raw materials, utilities, and consumables. The raw material costs were higher for the base case PCEC process, due to the lower ethylene selectivity of that process relative to the SC process (63% versus 80%, respectively). Besides, the utilities were more expensive for the base case PCEC process, since the energy duty to be covered by utilities was higher compared to the SC process (see **Figure 6.4**). Moreover, the costs for consumables were considerably higher for the base case PCEC process than for the SC process, due to the periodic replacement of the membrane stack materials. The membrane lifetime was set equal to the lifetime of the dehydrogenation catalyst of two years in this analysis. Marginal over/underpredictions of the PCEC membrane replacement frequency could strongly impact the total operating costs, as the consumables are a major contributor to the total PCEC OPEX (**Figure 6.6a**).
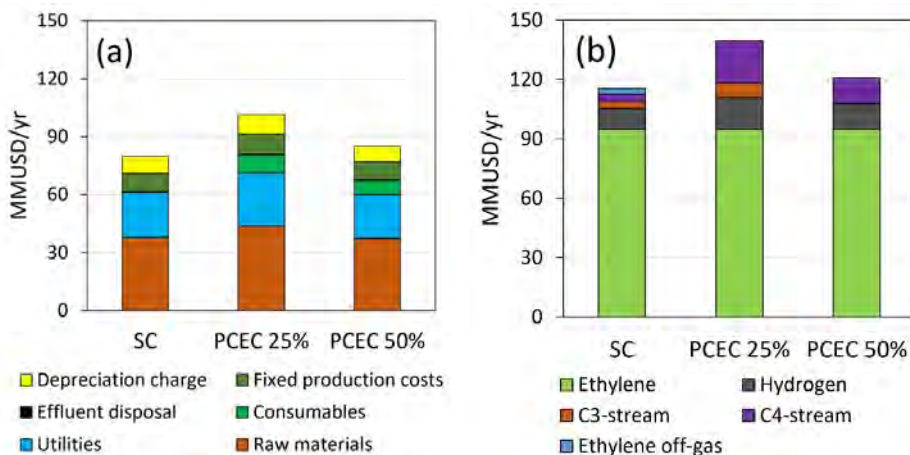
Figure 6.6: (a) the total production costs and (b) the total revenues for the conventional ethane steam cracking (SC) process and the base case (ca. 25% ethylene yield), and target case (50% ethylene yield) PCEC processes.

In contrast to the base case PCEC process, the operating costs of the target case PCEC process were more comparable to conventional SC (**Figure 6.6a**). Solely the expenditures on consumables were significantly higher for the target case PCEC compared to SC, due to periodic replacement of the membranes. It should be noted that the share of raw material costs to the total OPEX of the SC and PCEC processes (ca. 50%, **Figure 6.6a**) was small relative to typical values of bulk chemical production processes (ca. 80%) [44]. This is in agreement with previous ethane steam cracking process simulation studies [54,55]. The lower share of raw material costs to the total OPEX was particularly caused by the high refrigerant utility costs in the different processes, which was associated to the cryogenic operation of the separation train.

Despite the higher OPEX of the PCEC processes compared to the SC process (**Figure 6.6a**), the yearly revenues were also higher for both PCEC process cases (**Figure 6.6b**). This was due to the larger amount of valuable hydrogen, C3, and C4 byproducts generated in the PCEC processes. The *in situ* hydrogen separation inside the PCEC reactor allowed for facile hydrogen isolation. Besides, the simulated PCEC process dealt with a higher C3 and C4 selectivity, as adopted from the work by Wu et al. [26], relative to the simulated SC process. The profitability of the different processes was investigated for situations in which the revenues obtained from selling the C3 and C4 byproducts were included or excluded to evaluate the process viability when aiming at ethylene production (**Table 6.3**, see **Supporting Information 6.P** for more details). When including the C3 and C4 revenues, the profitability of the SC and PCEC processes was comparable in terms of return on investment (*ROI*) and payback time (**Table 6.3**), since the higher operating costs of the PCEC processes (**Figure 6.6a**) were compensated by the higher revenues (**Figure 6.6b**). The profitability of particularly the base case PCEC process declined when only

including the ethylene revenues (**Table 6.3**), as this process case heavily relied on incomes from the C3 and C4 byproducts (**Figure 6.6b**). By contrast, the viability of the SC and target case PCEC processes, which both dealt with similar product distributions, was also comparable when only including ethylene revenues (**Table 6.3**). Note that the results in **Table 6.3** considered a grid electricity price of 60 USD/MWh. However, green electricity is often cheaper than average grid electricity [41]. A sensitivity analysis revealed that, when including C3 and C4 product revenues, the base case PCEC process became more profitable than the SC process if the electricity price was lower than ca. 50 USD/MWh (see **Supporting Information 6.O2**).

Table 6.3: Return on investment (*ROI*) and payback period of the ethane SC process and the base case and target case PCEC-assisted ethane dehydrogenation processes, excluding carbon taxation. A distinction was made between situations in which the revenues obtained from selling C3 and C4 byproducts were included or excluded. See **Supporting Information 6.P** for more details.

	SC	PCEC base case (25%)	PCEC target case (50%)
When including revenues obtained from selling C3 and C4 byproducts:			
ROI	20.3%	18.8%	21.6%
Payback period	4 yr	5 yr	4 yr
When excluding revenues obtained from selling C3 and C4 byproducts:			
ROI	14.7%	4.7%	13.8%
Payback period	6 yr	19 yr	7 yr

In view of resolving the global climate crisis, increased carbon taxes are expected to be levied on the emission of greenhouse gases like carbon dioxide by the chemical industry. For this reason, the potential impact of variations in the carbon tax on the profitability of the SC and PCEC processes was investigated in this work (see **Figure 6.7**). The revenues obtained from selling C3 and C4 byproduct streams, which were particularly significant for the base case PCEC process (**Figure 6.6b**), were excluded from this analysis to highlight the process profitability when aiming at ethylene production.

In the case of Asia-Pacific grid electricity (**Figure 6.7a**), all the considered process cases became substantially less viable with increasing carbon tax, as all these cases coped with considerable carbon dioxide emissions (see **Figure 6.5**). Notably, the SC and PCEC full electric cases that required a substantial amount of relatively expensive electricity (60 USD/MWh), were consistently the least profitable ones (**Figure 6.7a**). Moreover, the base case PCEC process (ca. 25% ethylene yield) was barely profitable, even in absence of carbon taxation and irrespective of the heating method. This is again an indication that higher ethylene yields are needed to make PCEC-assisted ethane NODH industrially attractive. Compared to base case PCEC, the target case PCEC process was significantly

more lucrative, as it dealt with (i) a lower capital investment (**Table 6.2**), (ii) lower utility costs (**Figure 6.6a**), and (iii) lower raw material costs (**Figure 6.6a**). The utility costs were lower, partly due to the lower fired heat and steam demand in preheating and reboiling, and partly due to the lower refrigerant demand in the cryogenic distillation columns. Besides, the raw material costs were lower, due to more efficient usage of the fresh ethane reactant when operating at a higher single-pass ethylene yield.
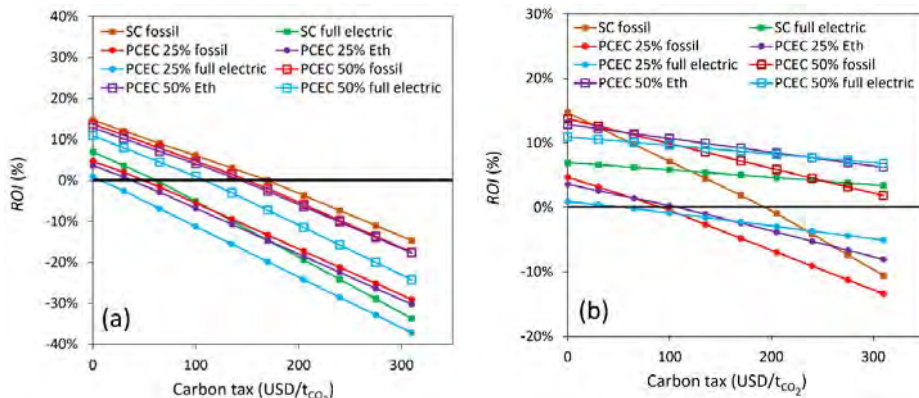
Figure 6.7: Influence of the levied carbon tax on the return on investment (*ROI*) of the different process cases (a) when Asia-Pacific grid electricity was used and (b) when fully renewable electricity was utilized. SC = ethane steam cracking process, PCEC = PCEC-assisted ethane dehydrogenation process, Eth = PCEC operation at thermoneutral voltage. The results presented here excluded the revenues obtained from selling C3 and C4 byproducts.

When fully renewable electricity was used (**Figure 6.7b**), then all full electric cases were significantly less penalized by the imposed carbon tax, as these cases had a considerable smaller carbon footprint (see **Figure 6.5**). The SC and target case PCEC full electric cases remained lucrative up to the highest considered carbon tax and became more profitable than their fossil fuel heated alternatives above a carbon tax of ca. 100 USD/t_{CO2} (**Figure 6.7b**). This thereby illustrates that for the price (60 USD/MWh) and carbon intensity (532.1 g_{CO2}/kWh) of the electricity considered in this work, a carbon tax of more than 100 USD/t_{CO2} is recommended to be levied to stimulate process electrification. Interestingly, the green electrified target case PCEC process was more profitable than the green electrified SC process (**Figure 6.7b**). This difference was ascribed to excessive electricity costs for the green electrified SC process, where in this case expensive electricity was utilized to heat the reactor inlet to the cracking temperature of 850 °C. One needs to note that the *ROI* values of the full electric cases in **Figure 6.7b** are pessimistic estimations, as they were determined using an overestimated electricity price of 60 USD/MWh, i.e. the current grid electricity price. Green electricity can be generated at lower prices than those herein considered [41]. In summary, to environmentally and financially outcompete fossil

fuel-based SC and PCEC processes, fully renewable electricity needs to be utilized and a carbon tax of more than 100 USD/t_{CO2} needs to be imposed (**Figure 6.7b**).

6.4.4.   Perspective and industrial guidelines

The PCEC-assisted ethane dehydrogenation process was simulated in this work based on two distinct product distributions. In the base case, a product distribution was considered that has been obtained in experimental studies on PCEC-assisted ethane NODH [26], which concerned a single-pass ethylene yield of ca. 25%. In the second case, a higher targeted single-pass ethylene yield of 50% was applied to examine the potential impact of industrial usage of PCEC membranes on a process dealing with an equal ethylene yield as conventional SC. In this chapter, we showed that the base case PCEC process had higher capital costs (**Table 6.2**), higher operating costs (**Figure 6.6**), higher energy usage (**Figure 6.4**), and a bigger ecological footprint (**Figure 6.5**) than conventional SC. This was all attributed to the existence of bigger process streams and process units in the base case PCEC process as compared to the SC process, caused by a bigger ethane recycle, due to the lower single-pass ethylene yield (25% vs 52%). As a result, the PCEC process was barely profitable for an ethylene yield of ca. 25% (**Figure 6.7**). On the contrary, the PCEC process could become financially and environmentally competitive with the SC process if it would be operated with an ethylene yield of about 50% (**Figure 6.5** and **6.7**). Moreover, a sensitivity analysis revealed that the biggest energy savings in the PCEC process were achieved when increasing the single-pass ethylene yield from ca. 25% (26.9 MJ/$kg_{ethylene}$) to ca. 50% (19.9 MJ/$kg_{ethylene}$, see **Supporting Information 6.O1**). The energy savings were more marginal upon further increasing the ethane-to-ethylene conversion, as a minimum amount of energy was needed for operating the dehydrogenation reaction, heating, and mass circulation, regardless of the ethylene yield.

Despite the uncertainty in the obtained carbon emission and cost values, it is clear that higher ethylene yields need to be achieved in experimental PCEC research for ethane NODH applications to brighten the industrial perspective of this technology. To this end, a better understanding of the reaction mechanisms taking place under various conditions in PCEC systems for ethylene production would help in steering the product distribution. A key challenge will be to ensure system stability also for higher ethylene yields, as higher olefin and lower hydrogen concentrations generally boost carbon deposition [56]. In particular, the PCEC membrane lifetime needs to be similar or longer than the dehydrogenation catalyst lifetime, as the PCEC membrane replacement was found to be a major contributor to the operating costs for an equal catalyst and membrane lifetime of two years (**Figure 6.6a**).

A possible way to mitigate carbon deposition in PCEC systems is by making use of the co-ionic properties of solid oxide electrolyzer cells. Morejudo et al. [16] demonstrated for the related methane dehydroaromatization reaction that cotransport of O^{2-} ions in the direction opposing proton transport assists in improving PCEC stability, caused by oxidation of carbon deposits induced by well distributed injection of oxygen to the reaction

zone. This counter-current flow of O^{2-} through the solid electrolyte could originate from the steam cosupply that is inevitably needed for optimal membrane operation. Besides, the direct steam cosupply on the PCEC reaction side could help avoiding coke formation, despite possible steam reforming reactions. Additionally, avoiding the use of Ni in PCEC electrode materials could help in improving PCEC stability, as Ni is known to boost carbon deposition [57]. The Ni could e.g. be replaced by other metals (e.g. Cu, Ag) or redox active metal oxides [58]. Also, note that sulfur removal in process pretreatment steps will be essential to avoid possible sulfur poisoning of PCEC materials operating in hydrocarbon-rich atmospheres. Lastly, operation at lower temperatures could minimize issues related to mismatches in thermal expansion coefficients of the different PCEC layers and would thermodynamically be beneficial to diminish coke formation, although this would require higher PCEC voltages to attain certain hydrogen removal rates and ethylene yields.

Another important parameter in PCEC systems is the applied current density. A current density of 1.0 A/cm² was selected in this work as a realistic estimation for industrial PCEC reactors, based on current densities achieved in lab scale PCEC systems [15,16]. Upon increasing the current density, the PCEC reactor capital investment would reduce due to a reduction in required membrane area, whilst the energy consumption would increase for a constant area specific resistance (*ASR*). A sensitivity analysis of the applied current density revealed that the optimum in the trade-off between minimizing membrane area and minimizing energy consumption was obtained for a current density of 1.0 A/cm² (see **Supporting Information 6.O4**). The current density used in this work is therefore also proposed to be used in future PCEC research. Moreover, upon increasing the *ASR*, the required voltage for a given current density and thereby the required energy input will increase, which leads to a less profitable process if electricity is expensive (>50 USD/MWh, see **Supporting Information 6.O5**). If the electricity price would become as low as the natural gas price (ca. 16 USD/MWh), the profitability of the PCEC process was found to become independent of the *ASR*.

In this chapter, we further demonstrated that fully renewable electricity needs to be utilized upon process electrification to potentially reduce the process carbon footprint (**Figure 6.5**). Specifically, the carbon intensity of the electricity needs to be below 200 g_{CO2}/kWh to ecologically justify process electrification (**Supporting Information 6.O3**). Otherwise, the use of direct fossil fuel heat is ecologically friendlier than the use of electrical heat. Moreover, to make electrified processes more profitable than their fossil fuel-based alternative, green electrical heat should become cheaper per MWh than fossil fuel heating, and a carbon tax of more than 100 USD/t_{CO2} should be imposed (**Figure 6.7b**). The latter emphasizes that governments can play a pivotal role in electrifying the chemical industry.

Next to electrochemical ethane NODH, the main alternative routes for green ethylene production encompass (i) electrochemical ethane oxidative dehydrogenation (ODH), (ii) bioethanol dehydration, (iii) electrochemical CO_2 reduction, and (iv) electrical steam cracking. The electrochemical ethane ODH route is technologically undesired, because of

the risk for hydrocarbon overoxidation and the facile generation of explosive atmospheres in ethane ODH conditions [59]. Besides, the bioethanol dehydration route is financially unattractive, as the high costs of the ethanol feedstock raise the ethylene production costs via this route [59].

Ethylene production via CO_2 reduction appears the other most competitive route for green ethylene production. The CO_2-to-ethylene approach has the clear advantage of using CO_2 as feedstock, potentially allowing for net zero emissions. In contrast, electrochemical ethane NODH needs to be combined with depolymerization strategies to establish circular production pathways. However, CO_2 is a highly stable molecule that is hard to convert. Moreover, electrochemical conversion of CO_2 to ethylene is hindered by a limited olefin selectivity of typically less than 60% [59]. Due to this low ethylene selectivity, a lot of energy in the CO_2 reduction process is lost in generating byproducts [60]. Additionally, the CO_2 reduction process suffers from a high capital investment, as only a limited part of the total electrolyzer area is effectively utilized for ethylene production [60]. Therefore, the CO_2 reduction route primarily requires an improvement in ethylene selectivity to become competitive with conventional ethane SC. Without further improvements in ethylene yield in the CO_2 reduction and electrochemical ethane NODH routes, electrification of ethane steam cracking seems the most promising direction for green ethylene production. But, as pointed out in this techno-economic study on ethane NODH and in a previous techno-economic study on CO_2 reduction to produce ethylene [60], a substantial decrease in electricity price is needed to create the incentive for process electrification, regardless of the targeted green ethylene production route.

Apart from the performance requirements and financial constraints of PCECs, several other technological challenges need to be considered before PCEC membrane reactors can be implemented on an industrial scale. Since ethylene is an essential building block for the chemical industry with a market size around 200 billion USD in 2023 [2], possible green alternative production processes need to be scalable to plants with ethylene production capacities in the range 100-1,000 ktpa. For this reason, PCEC systems need to become available in enormous amounts to enable integration with ethylene production facilities. Because of this, non-noble and nonrare elements should be applied in PCEC systems to lower the capital investment of PCEC membrane reactors [59]. Furthermore, a closer look needs to be taken at the synthesis routes of the various PCEC materials. Currently, most of the PCEC electrode and electrolyte materials are obtained from energy and labor intensive lab-scale synthesis methods. Eventually, these synthesis methods need to be scalable to industrial production facilities and the required chemical elements for the PCEC electrode and electrolyte materials need to be abundantly available to satisfy industrial scale ethylene production. An additional challenge lies in the continuous usage of renewable electricity. We confirmed in this work that green electricity needs to be used to minimize carbon emissions in electrified ethylene production processes (**Figure 6.5**). However, it is questionable whether green electricity can be delivered continuously, as e.g. solar and wind power will not be permanently available. Moreover, electrification of large scale

ethylene production processes will put an enormous pressure on the electricity grid. There is a heavy responsibility for governments to facilitate the electrification of the chemical industry by expanding the electricity grid around chemical plants.

Ultimately, electrification of ethylene production processes, whether it is via industrial implementation of PCEC membranes or via electrification of conventional steam crackers, could lead to a reduction in carbon footprint from ca. 1.5 $t_{CO2}/t_{ethylene}$ (SC fossil) to ca. 0.2 $t_{CO2}/t_{ethylene}$ (see **Figure 6.5**). The global ethylene market size was around 200 billion USD in 2023 [2]. For a polymer-grade ethylene price of ca. 950 USD/$t_{ethylene}$, this leads to a global annual production of about 210 million ton of ethylene. A reduction in carbon footprint of ca. 1.3 $t_{CO2}/t_{ethylene}$, thus, corresponds to a saving in carbon dioxide emissions of ca. 270 million tons, which is ca. 0.7% of the global carbon dioxide emissions [61], if all ethylene production processes worldwide would be replaced by these green electrified alternatives.

6.5.   Conclusion

The potential of applying ceramic proton-conducting electrolysis cell (PCEC) membranes in ethylene production processes was explored in this work. To this end, a PCEC-assisted ethane dehydrogenation process was compared to a conventional ethane steam cracking (SC) process in terms of process economics, energy usage, and carbon footprint. The results indicated that the PCEC process could only be financially and environmentally competitive with conventional SC in the case of similar ethylene yields (ca. 50%). For currently achievable ethylene yields using PCEC technologies of ca. 25%, the capital investment and carbon emissions of the PCEC process were too excessive to outcompete electrified ethane SC. The total energy usage, utility demand, and capital investment were substantially higher for the ca. 25% ethylene yield PCEC case as compared to the 50% case, due to larger process streams and process units as a result of the lower single-pass yield. The results further highlighted that carbon emissions could be reduced from ca. 1.5 $t_{CO2}/t_{ethylene}$ to ca. 0.2 $t_{CO2}/t_{ethylene}$ when employing green electrified SC or PCEC (50% yield) processes instead of conventional fossil fuel-based SC but only if fully renewable electricity was utilized. Moreover, a carbon tax of more than 100 USD/t_{CO2} would need to be imposed to make the green electrified SC and PCEC processes more viable than their fossil-based counterparts. Lastly, technological challenges related to the attainable ethylene yield, PCEC stability, large scale sustainable production of PCECs, and the continuous availability of green electricity were identified as hurdles that need to overcome to facilitate industrial implementation of PCECs for green ethylene production.

References

1. Plastics Europe & European Association of Plastics Recycling and Recovery Organisations. Plastics - the facts 2022. https://plasticseurope.org/knowledge-hub/plastics-the-facts-2022/ (accessed October 2024).

2. Bidwai, S. Ethylene market. https://www.precedenceresearch.com/ethylene-market (accessed October 2024).

3. Zimmermann, H. & Walzl, R. Ethylene. in *Ullmann's Encyclopedia of Industrial Chemistry* (Wiley-VCH Verlag GmbH & Co. KGaA, Weinheim, Germany, 2009). doi:https://doi.org/10.1002/14356007.a10_045.pub3.

4. Ren, T., Patel, M. & Blok, K. Olefins from conventional and heavy feedstocks: Energy use in steam cracking and alternative processes. *Energy* **31**, 425–451 (2006).

5. Fairuzov, D., Gerzeliev, I., Maximov, A. & Naranov, E. Catalytic dehydrogenation of ethane: A mini review of recent advances and perspective of chemical looping technology. *Catalysts* **11**, 833 (2021).

6. Saito, H. & Sekine, Y. Catalytic conversion of ethane to valuable products through non-oxidative dehydrogenation and dehydroaromatization. *RSC Adv.* **10**, 21427–21453 (2020).

7. Cavani, F., Ballarini, N. & Cericola, A. Oxidative dehydrogenation of ethane and propane: How far from commercial implementation? *Catal. Today* **127**, 113–131 (2007).

8. Grasselli, R. K., Stern, D. L. & Tsikoyiannis, J. G. Catalytic dehydrogenation (DH) of light paraffins combined with selective hydrogen combustion (SHC) I . DH → SHC → DH catalysts in series (co-fed process mode). *Appl. Catal. A: Gen.* **189**, 1–8 (1999).

9. Bhasin, M. M., Mccain, J. H., Vora, B. V, Imai, T. & Pujad, P. R. Dehydrogenation and oxydehydrogenation of paraffins to olefins. *Appl. Catal. A: Gen.* **221**, 397–419 (2001).

10. Sattler, J. J. H. B., Ruiz-Martinez, J., Santillan-Jimenez, E. & Weckhuysen, B. M. Catalytic dehydrogenation of light alkanes on metals and metal oxides. *Chem. Rev.* **114**, 10613–10653 (2014).

11. Nawaz, Z. Light alkane dehydrogenation to light olefin technologies: A comprehensive review. *Rev. Chem. Eng.* **31**, 413–436 (2015).

12. Gallucci, F., Fernandez, E., Corengia, P. & Sint, M. Van. Recent advances on membranes and membrane reactors for hydrogen production. *Chem. Eng. Sci.* **92**, 40–66 (2013).

13. Polfus, J. M., Xing, W., Fontaine, M. L., Denonville, C., Henriksen, P. P. & Bredesen, R. Hydrogen separation membranes based on dense ceramic composites in the La27W5O55.5-LaCrO3 system. *J. Membr. Sci.* **479**, 39–45 (2015).

14. Clark, D., Malerød-Fjeld, H., Budd, M., Yuste-Tirados, I., Beeaff, D., Aamodt, S., Nguyen, K., Ansaloni, L., Peters, T., Vestre, P. K., Pappas, D. K., Valls, M. I., Remiro-Buenamañana, S., Norby, T., Bjørheim, T. S., Serra, J. M. & Kjølseth, C. Single-step hydrogen production from NH3, CH4, and biogas in stacked proton ceramic reactors. *Science* **376**, 390–393 (2022).

15. Malerød-fjeld, H., Clark, D., Yuste-tirados, I., Zanón, R., Catalán-martinez, D., Beeaff, D., Morejudo, S. H., Vestre, P. K., Norby, T., Haugsrud, R., Serra, J. M. & Kjølseth, C. Thermo-electrochemical production of compressed hydrogen from methane with near-zero energy loss. *Nat. Energy* **2**, 923–931 (2017).

16. Morejudo, S. H., Zanón, R., Escolástico, S., Yuste-Tirados, I., Malerød-Fjeld, H., Vestre, P. K., Coors, W. G., Martínez, A., Norby, T., Serra, J. M. & Kjølseth, C. Direct conversion of methane to aromatics in a catalytic co-ionic membrane reactor. *Science* **353**, 563–566 (2016).

17. Meng, Y., Gao, J., Zhao, Z., Amoroso, J., Tong, J. & Brinkman, K. S. Review : recent progress in low-temperature proton-conducting ceramics. *J. Mater. Sci.* 9291–9312 (2019).

18. Norby, T. & Haugsrud, R. Dense ceramic membranes for hydrogen separation. in *Nonporous Inorganic Membranes: for Chemical Processing* (eds. Sammells, A. F. & Mundschau, M. V.) 1–48 (Wiley-VCH Verlag GmbH & Co. KGaA, 2006).

19. Douglas, J. M. *Conceptual Design of Chemical Processes*. (McGraw-Hill, 1988).

20. Heynderickx, G. J., Schools, E. M. & Marin, G. B. Optimization of the decoking procedure of an ethane cracker with a steam/air mixture. *Ind. Eng. Chem. Res.* **45**, 7520–7529 (2006).

21. Seifzadeh Haghighi, S., Rahimpour, M. R., Raeissi, S. & Dehghani, O. Investigation of ethylene production in naphtha thermal cracking plant in presence of steam and carbon dioxide. *Chem. Eng. J.* **228**, 1158–1167 (2013).

22. Sundaram, K. M., Shreehan, M. M. & Olszewski, E. F. Ethylene. in *Kirk-Othmer Encyclopedia of Chemical Technology* 1–39 (Wiley, 2010). doi:10.1002/0471238961.0520082519211404.a01.pub3.

23. Magrasó, A. Transport number measurements and fuel cell testing of undoped and Mo-substituted lanthanum tungstate. *J. Power Sources* **240**, 583–588 (2013).

24. Magrasó, A., Frontera, C., Marrero-López, D. & Núñez, P. New crystal structure and characterization of lanthanum tungstate 'La6WO12' prepared by freeze-drying synthesis. *Dalton Trans.* **46**, 10273–10283 (2009).

25. Sun, S. & Huang, K. Efficient and selective ethane-to-ethylene conversion assisted by a mixed proton and electron conducting membrane. *J. Membr. Sci.* **599**, 117840 (2020).

26. Wu, W., Wang, L. C., Hu, H., Bian, W., Gomez, J. Y., Orme, C. J., Ding, H., Dong, Y., He, T., Li, J. & Ding, D. Electrochemically engineered, highly energy-efficient conversion of ethane to ethylene and hydrogen below 550 °C in a protonic ceramic electrochemical cell. *ACS Catal.* **11**, 12194–12202 (2021).

27. Kee, B. L., Curran, D., Zhu, H., Braun, R. J., Decaluwe, S. C., Kee, R. J. & Ricote, S. Thermodynamic insights for electrochemical hydrogen compression with proton-conducting membranes. *Membranes* **9**, 77 (2019).

28. Rambert, O. & Febvre, L. The challenges of hydrogen storage on a large scale. https://www.h2knowledgecentre.com/content/conference3536 (accessed September 2024).

29. Petrochemicals Europe. Cracker capacity. https://www.petrochemistry.eu/about-petrochemistry/petrochemicals-facts-and-figures/cracker-capacity/ (accessed May 2024).

30. Middleton, J., Simon, Y., Guillaume, J., Lal, R., Abdin, Z. & Viviano, E. Ethylene - A world leader in the design and construction of ethylene facilities. https://www.ten.com/sites/energies/files/2021-03/Ethylene.pdf (accessed September 2024).

31. Yang, Y., Wang, G., Zhang, L., Zhang, S. & Lin, L. Comparison of Hydrogen Specification in National Standards for China. *E3S Web of Conferences* **118**, 03042 (2019).

32. Cooper, R. Characteristics of Shell Monaca steam cracker, Pittsburgh, PA, U.S.A. *Personal communication, 2023*.

33. Long, N. V. D., Minh, L. Q., Pham, T. N., Bahadori, A. & Lee, M. Novel retrofit designs using a modified coordinate descent methodology for improving energy efficiency of natural gas liquid fractionation process. *J. Nat. Gas Sci. Eng.* **33**, 458–468 (2016).

34. Uwitonze, H., Lee, I. & Hwang, K. S. Alternatives of integrated processes for coproduction of LNG and NGLs recovery. *Chem. Eng. Process.* **107**, 157–167 (2016).

35. Enerdata. Share of renewables in electricity production. https://yearbook.enerdata.net/renewables/renewable-in-electricity-production-share.html (accessed December 2024).

36. International Energy Agency. Simplified levelised cost of petrochemicals for selected feedstocks and regions, 2017. https://www.iea.org/data-and-statistics/charts/simplified-levelised-cost-of-petrochemicals-for-selected-feedstocks-and-regions-2017 (accessed April 2024).

37. ChemAnalyst. Ethylene price trend and forecast. https://www.chemanalyst.com/Pricing-data/ethylene (accessed March 2024).

38. Procurement Resource. Ethylene price trend and forecast. https://www.procurementresource.com/resource-center/ethylene-price-trends (accessed December 2024).

39. PricewaterhouseCoopers. The green hydrogen economy - predicting the decarbonisation agenda of tomorrow. https://www.pwc.com/gx/en/industries/energy-utilities-resources/future-energy/green-hydrogen-cost.html (accessed July 2023).

40. Singapore Statutes Online. Environmental protection and management (trade effluent) regulations, Report number S 160/1999. https://sso.agc.gov.sg/SL/EPMA1999-RG5#pr6- (accessed December 2024).

41. Taylor, M., Al-Zoghoul, S. & Ralon, P. Renewable power generation costs in 2022. https://www.irena.org/Publications/2023/Aug/Renewable-power-generation-costs-in-2022 (accessed June 2024).

42. CoorsTek Inc. Proton ceramic membranes for hydrogen production published in 'Science'. https://www.coorstek.com/en/news-events/news/proton-ceramic-membranes-for-hydrogen-production/ (accessed July 2023).

43. Towler, G. & Sinnott, R. Capital cost estimating. in *Chemical Engineering Design* 307–354 (Butterworth-Heinemann, 2013).

44. Towler, G. & Sinnott, R. Estimating revenues and production costs. in *Chemical Engineering Design* 355–387 (Butterworth-Heinemann, 2013).

45. Crowe Global. Asia-Pacific tax guide 2021/22. https://www.crowe.com/au/insights/asia-pacific-tax-guide-2021-22 (accessed August 2024).

46. Ember and energy institute. Carbon intensity of electricity generation. https://ourworldindata.org/grapher/carbon-intensity-electricity?time=2022 (accessed January 2024).

47. van der Niet, S. & Bruinsma, M. *Ketenemissies Elektriciteit - Actualisatie Elektriciteitsmix 2019*. https://ce.nl/publicaties/ketenemissies-elektriciteit-actualisatie-elektriciteitsmix-2019/ (accessed August 2024).

48. CO2emissiefactoren. Lijst emissiefactoren. https://www.co2emissiefactoren.nl/lijst-emissiefactoren/ (accessed July 2023).

49. Pereira, P. M., Fernandes, M. C. & Matos, H. A. FI2EPI – A freeware tool for performing heat integration based on pinch analysis. in *Proceedings of the 26th European Symposium on Computer Aided Process Engineering – ESCAPE 26* 1815–1820 (2016). doi:10.1016/B978-0-444-63428-3.50307-6.

50. Masuku, C. M., Caulkins, R. S. & Siirola, J. J. Process decarbonization through electrification. *Curr. Opin. Chem. Eng.* **44**, 101011 (2024).

51. Wismann, S. T., Engbaek, J. S., Vendelbo, S. B., Bendixen, F. B., Eriksen, W. L., Aasberg-Petersen, K., Frandsen, C., Chorkendorff, I. & Mortensen, P. M. Electrified methane reforming: a compact approach to greener industrial hydrogen production. *Science* **364**, 756–759 (2019).

52. Agarwal, A., Sengupta, D. & El-halwagi, M. Sustainable process design approach for on-purpose propylene production and intensification. *ACS Sustain. Chem. Eng.* **6**, 2407–2421 (2018).

53. Marsh, M. & Wery, J. Filling the propylene gap – shaping the future with on-purpose technologies. *Technical report*. https://www.hydrocarbonengineering.com/whitepapers/honeywell-uop/filling-the-propylene-gap-shaping-the-future-with-on-purpose-technologies/ (accessed September 2024).

54. Maporti, D., Galli, F., Mocellin, P. & Pauletto, G. Flexible ethylene production: Electrified ethane cracking coupled with oxidative dehydrogenation. *Energy Conv. Manag.* **298**, 117761 (2023).

55. Chen, Y., Kuo, M. J., Lobo, R. & Ierapetritou, M. Ethylene production: process design, technoeconomic and life-cycle assessments. *Green Chem.* **26**, 2903–2911 (2024).

56. van Sint Annaland, M., Kuipers, J. A. M. & van Swaaij, W. P. M. A kinetic rate expression for the time-dependent coke formation rate during propane dehydrogenation over a platinum alumina monolithic catalyst. *Catal. Today* **66**, 427–436 (2001).

57. Nikolla, E., Schwank, J. & Linic, S. Direct electrochemical oxidation of hydrocarbon fuels on SOFCs: improved carbon tolerance of Ni alloy anodes. *J. Electrochem. Soc.* **156**, B1312 (2009).

58. Jang, I., S. A. Carneiro, J., Crawford, J. O., Cho, Y. J., Parvin, S., Gonzalez-Casamachin, D. A., Baltrusaitis, J., Lively, R. P. & Nikolla, E. Electrocatalysis in solid oxide fuel cells and electrolyzers. *Chem. Rev.* **124**, 8233–8306 (2024).

59. Chauhan, R., Sartape, R., Minocha, N., Goyal, I. & Singh, M. R. Advancements in environmentally sustainable technologies for ethylene production. *Energy & Fuels* **37**, 12589–12622 (2023).

60. Pappijn, C. A. R., Ruitenbeek, M., Reyniers, M.-F. & Van Geem, K. M. Challenges and opportunities of carbon capture and utilization: electrochemical conversion of CO2 to ethylene. *Front. Energy Res.* **8**, 557466 (2020).

61. Ritchie, H. & Roser, M. CO2 emissions. https://ourworldindata.org/co2-emissions (accessed August 2024).

62. Andersson, J. & Grönkvist, S. Large-scale storage of hydrogen. *Int. J. Hydrogen Energy* **44**, 11901–11919 (2019).

63. Luyben, W. L. Estimating refrigeration costs at cryogenic temperatures. *Comput. Chem. Eng.* **103**, 144–150 (2017).

64. Tatiana Khanberg. The International Gas Union (IGU) today releases its 2023 global wholesale gas price survey report. https://www.prnewswire.com/news-releases/the-international-gas-union-igu-today-releases-its-2023-global-wholesale-gas-price-survey-report-301934200.html (accessed May 2024).

65. U.S. Department of Energy - Industrial Technologies Program Energy Efficiency and Renewable Energy. How to calculate the true cost of steam. https://www.energy.gov/eere/amo/articles/how-calculate-true-cost-steam (accessed May 2024).

66. Turton, R., Bailie, R. C., Whiting, W. B., Shaeiwitz, J. A. & Bhattacharyya, D. *Analysis, Synthesis, and Design of Chemical Processes*. (Pearson Education, Inc., 2013).

67. International Energy Agency. Electricity market report 2023. https://www.iea.org/reports/electricity-market-report-2023 (accessed June 2024).

68. Champagnie, A. M., Tsotsis, T. T., Minet, R. G. & Wagner, E. The study of ethane dehydrogenation in a catalytic membrane reactor. *J. Catal.* **134**, 713–730 (1992).

69. Allevi, C. & Collodi, G. Hydrogen production in IGCC systems. in *Integrated Gasification Combined Cycle (IGCC) Technologies* 419–443 (Elsevier, 2017). doi:10.1016/B978-0-08-100167-7.00012-3.

70. Cowan, A. Enalysis tip 1.10 - reciprocating compressor limitations. https://www.detechtion.com/learningcenter/enalysis-tip-1.10-reciprocating-compressor-limitations (accessed March 2024).

71. Srivastava, A. Difference between centrifugal and reciprocating compressor. https://whatispiping.com/centrifugal-vs-reciprocating-compressor (accessed September 2024).

72. Delikonstantis, E., Scapinello, M. & Stefanidis, G. D. Process modeling and evaluation of plasma-assisted ethylene production from methane. *Processes* **7**, 68 (2019).

73. Mamrosh, D., McIntosh, K. & Fisher, K. Caustic scrubber designs for H2S removal from refinery gas streams. in *AFPM Annual Meeting; American Fuel & Petrochemical Manufacturers* 1–26 (2014).

74. Geilen, F. M. A., Stochniol, G., Peitz, S. & Schulte-Koerne, E. Butenes. in *Ullmann's Encyclopedia of Industrial Chemistry* 1–13 (Wiley, 2014). doi:10.1002/14356007.a04_483.pub3.

75. Haugen, A. B., Aguilera, L. M., Kwok, K., Molla, T., Andersen, K. B., Pirou, S., Kaiser, A., Hendriksen, P. V. & Kiebach, R. Exploring the processing of tubular chromite-and zirconia-based oxygen transport membranes. *Ceramics* **1**, 229–245 (2018).

76. Special Power Sources. A comprehensive comparison of planar and tubular solid oxide fuel cells. https://spsources.com/a-comprehensive-comparison-of-planar-and-tubular-solid-oxide-fuel-cells/ (accessed September 2024).

77. Gallucci, F., Medrano, J. A., Fernandez, E., Melendez, J., van Sint Annaland, M. & Pacheco-Tanaka, D. A. Advances on high temperature Pd-based membranes and membrane reactors for hydrogen purification and production. *J. Membr. Sci. Res.* **3**, 142–156 (2017).

78. Duan, C., Tong, J., Shang, M., Nikodemski, S., Sanders, M., Ricote, S., Almansoori, A. & O'Hayre, R. Readily processed protonic ceramic fuel cells with high performance at low temperatures. *Science* **349**, 1321–1325 (2015).

79. Made-in-China. Factory price nature BaSO4 TM30 for coil coating. https://shanghaitengmin.en.made-in-china.com/product/CZTQnmHOaAhI/China-Factory-Price-Nature-Baso4-TM30-for-Coil-Coating.html (accessed September 2024).

80. Made-in-China. Rare Earth Oxide Cerium Oxide. https://rst-tech.en.made-in-china.com/product/jFlAsLDOfzrY/China-Rare-Earth-Oxide-Cerium-Oxide-CEO2-CAS-1306-38-3-for-Glass-Ceramic-Polishing.html (accessed September 2024).

81. Made-in-China. Factory high quality zirconium oxide ZrO2 price. https://48bc1abfae09393c.en.made-in-china.com/product/LxIUdqbJZwWk/China-Factory-High-Quality-Zirconium-Oxide-Zro2-Price.html (accessed September 2024).

82. Institut für Seltene Erden und Metalle AG. Current prices of rare earths. https://en.institut-seltene-erden.de/aktuelle-preise-von-seltenen-erden/ (accessed September 2024).

83. Made-in-China. High quality nickel oxide. https://48bc1abfae09393c.en.made-in-china.com/product/hZLApmnxVDrO/China-High-Quality-Nickel-Oxide-CAS-No-1313-99-1-Nickel-Oxide-Nio.html (accessed September 2024).

84. Made-in-China. Alumina toughened zirconia (ATZ). https://hbsuoyi.en.made-in-china.com/product-group/lbMGZEoxhPUC/Alumina-toughened-zirconia-ATZ--1.html (accessed September 2024).

85. Alibaba. High purity 99% ferric nitrate 9H2O iron(III) nitrate nonahydrate. https://www.alibaba.com/product-detail/High-Purity-99-Ferric-Nitrate-9H2O_1600435993377.html?spm=a2700.galleryofferlist.p_offer.d_title.2d662a52KEKCht&s=p (accessed September 2024).

86. Alibaba. Barium nitrate (Ba(NO3)2) fireworks raw material chemical. https://www.alibaba.com/product-detail/Barium-Nitrate-Ba-NO3-2-Fireworks_62543580549.html (accessed September 2024).

87. Alibaba. Ammonium molybdate tetrahydrate 99% Prijs ((NH4)6Mo7O24.4H2O). https://dutch.alibaba.com/product-detail/ammonium-molybdate-tetrahydrate-99-price-NH4-1382943523.html (accessed September 2024).

88. Made-in-China. ZSM-5 zeolite. https://www.made-in-china.com/price/zsm-5-zeolite-price.html (accessed September 2024).

89. BullionVault. BullionVault's Platinum price live chart. https://www.bullionvault.com/platinum-price-chart.do (accessed September 2024).

90. Strategic Metals Invest. Gallium prices. https://strategicmetalsinvest.com/gallium-prices/ (accessed September 2024).

91. Towler, G. & Sinnott, R. Design of pressure vessels. in *Chemical Engineering Design* 563–629 (Butterworth-Heinemann, 2013).

92. Towler, G. & Sinnott, R. Separation columns (distillation, absorption, and extraction). in *Chemical Engineering Design* 807–935 (Butterworth-Heinemann, 2013).

93. Towler, G. & Sinnott, R. Separation of fluids. in *Chemical Engineering Design* 753–806 (Butterworth-Heinemann, 2013).

94. Towler, G. & Sinnott, R. Transport and storage of fluids. in *Chemical Engineering Design* 1207–1265 (Butterworth-Heinemann, 2013).

95. Parks, B. Isentropic efficiency of rotary screw air compressors. https://www.airbestpractices.com/standards/iso-and-cagi/isentropic-efficiency-rotary-screw-air-compressors (accessed June 2024).

96. Perez, R. X. An introduction to compressor selection (part 3 of 4). https://empoweringpumps.com/how-to-select-a-compressor-part3-compressor-selection (accessed August 2023).

97. Jalon Zeolite. 3A Molecular Sieve. https://www.jalonzeolite.com/product-item/zeolite-3a/ (accessed June 2024).

98. Sorrels, J. L. Chapter 1 Carbon Adsorbers. https://www.epa.gov/sites/default/files/2018-10/documents/final_carbonadsorberschapter_7thedition.pdf (accessed June 2024).

99. Chen, Y. & Ahn, H. Optimization strategy for enhancing the product recovery of a pressure swing adsorption through pressure equalization or co-current depressurization: A case study of recovering hydrogen from methane. *Ind. Eng. Chem. Res.* **62**, 5286–5296 (2023).

100. Wang, Y. Measurements and modeling of water adsorption isotherms of zeolite Linde-type A crystals. *Ind. Eng. Chem. Res.* **59**, 8304–8314 (2020).

101. Kolmetz, K. Design guidelines for propylene splitters efficiencies. *Engineering Practice* **4**, 8–19 (2018).

102. Neveril, R. B., Price, J. U. & Engdahl, K. L. Capital and operating costs of selected air pollution control systems - I. *J. Air Pollut. Control Assoc.* **28**, 829–836 (1978).

103. Dehghani, O., Rahimpour, M. & Shariati, A. An experimental approach on industrial Pd-Ag supported α-Al2O3 catalyst used in acetylene hydrogenation process: Mechanism, kinetic and catalyst decay. *Processes* **7**, 136 (2019).

104. Tian, L., Hu, G., Du, W. & Qian, F. Comprehensive CFD simulation of the optimizations of geometric structures and operating parameters for industrial acetylene hydrogenation reactors. *Can. J. Chem. Eng.* **94**, 2427–2435 (2016).

105. Towler, G. & Sinnott, R. Heat-transfer equipment. in *Chemical Engineering Design* 1047–1206 (Butterworth-Heinemann, 2013).

106. Auremo GmbH. Density of structural steel. https://auremo.biz/reference/plotnost-stali-konstruktsionnoy.html (accessed September 2024).

107. Inveno Engineering LLC. Steam system thermal cycle efficiency. https://invenoeng.com/steam-system-thermal-cycle-efficiency-a-important-benchmark-in-the-steam-system/ (accessed June 2024).

108. The Engineering ToolBox. Fuels - higher and lower calorific values. https://www.engineeringtoolbox.com/fuels-higher-calorific-values-d_169.html (accessed February 2024).

109. Intratec Solutions LLC. Process water costs, industrial utilities. https://www.intratec.us/products/water-utility-costs/commodity/process-water-cost. (accessed June 2024).

110. Business Analytiq. Sodium hydroxide price index. https://businessanalytiq.com/procurementanalytics/index/sodium-hydroxide-price-index/ (accessed June 2024).

111. Loh, D., Kawase, K. & Obe, M. Asia's rising interest rates boost banks -- but risks grow for 2023. https://asia.nikkei.com/Business/Business-Spotlight/Asia-s-rising-interest-rates-boost-banks-but-risks-grow-for-2023 (accessed September 2024).

112. U.S. Energy Information Administration. Carbon dioxide emissions coefficients. https://www.eia.gov/environment/emissions/co2_vol_mass.php (accessed December 2024).

113. Seider, W. D., Lewin, D. R., Seader, J. D., Widagdo, S., Gani, R. & Ming Ng, K. Annual costs, earnings, and profitability analysis. in *Product and process design principles: synthesis, analysis and evaluation* 498–550 (John Wiley & Sons, Inc., 2016).

Supporting Information

6.A. Product and utility specifications

The specifications of the targeted ethylene product (**6.A1**), the hydrogen product (**6.A2**), the ethylene product capacity (**6.A3**), and the utilities (**6.A4**) are summarized here.

6.A1. Polymer grade ethylene

The targeted ethylene product was polymer grade ethylene, satisfying the product specifications listed in **Table 6.A1** [3]. It was produced as a vapor at 18 bar(a) and 10 °C.

Table 6.A1: Product specifications of polymer grade ethylene [3].

Compound:	Concentration:
Ethylene (wt.%)	99.90
Water (ml/l)	<2
Oxygen (ml/l)	<5
Methane (ml/l)	<300
Ethane (ml/l)	<500
Propylene (ml/l)	<15
Acetylene (ml/l)	<2
Carbon monoxide (ml/l)	<2
Carbon dioxide (ml/l)	<2
Total sulfur (mg/kg)	<2
Hydrogen (ml/l)	<10

6.A2. Fuel grade hydrogen

High purity fuel grade hydrogen was the targeted hydrogen byproduct in all processes, satisfying the specifications listed in **Table 6.A2** [31]. The hydrogen product was considered to be stored in the gas phase after production. Compressed hydrogen gas is usually stored in aboveground vessels at pressures lower than 100 bar(a) due to vessel material constraints [62]. In spherical storage vessels the storage pressure is typically up to 50 bar(a) [28], which was therefore taken as hydrogen product pressure in this work.

Table 6.A2: Fuel grade hydrogen specifications [31].

Compound:	Concentration:
H_2 (%)	99.95
Total hydrocarbon (μmol/mol)	<2
Water (μmol/mol)	<5
Oxygen (μmol/mol)	<5

Helium (µmol/mol)	<300
Nitrogen, argon (µmol/mol)	<100
Total halogenates (µmol/mol)	0.05
Carbon dioxide (µmol/mol)	<2
Carbon monoxide (µmol/mol)	<0.2
Total sulfur (µmol/mol)	<0.004
Ammonia (µmol/mol)	<0.1

6.A3. Production capacities of steam cracking processes

The typical ethylene production capacities of a selection of industrial steam cracking processes are listed in **Table 6.A3**.

Table 6.A3: Ethylene production capacities of a selection of industrial steam cracking plants.

Description:	Location:	Feedstock:	Capacity:	Unit:	Ref.:
INEOS	Europe	Naphtha	1,155	ktpa	[29]
Shell cracker Moerdijk	Netherlands	Naphtha	910	ktpa	[30]
DOW cracker	USA	Ethane	1,500	ktpa	[30]
Yansab cracker	Saudi Arabia	Ethane and Propane	1,380	ktpa	[30]
PetroRabigh cracker	Saudi Arabia	Ethane	1,500	ktpa	[30]
Etileno XXI cracker	Mexico	Ethane	1,050	ktpa	[30]
Zheijiang Petroleum & Chemical Co.	China	Naphtha and LPG	1,400	ktpa	[30]

6.A4. Utilities

The different types of utilities that were used in all ethylene production processes are listed in **Table 6.A4**. The refrigerant costs were scaled to the respective energy duties transferred [63] and therefore differed for the base case SC and PCEC processes. For sake of simplicity, the refrigerant costs of target case PCEC process were assumed to be equal to those in the base case PCEC process.

Table 6.A4: Utility types and prices.

Utility type	T (ºC)	Cost	Unit	Ref.	Notes
Natural gas	1000	5	USD/GJ	[64]	
High pressure (HP) steam	295	6	USD/GJ	[65]	80 bar(a)
Medium pressure (MP) steam	185	6	USD/GJ	[65]	11 bar(a)
Low pressure (LP) steam	125	6	USD/GJ	[65]	2.3 bar(a)
Cooling water	25	0.35	USD/GJ	[66]	

Electricity	-	0.06	USD/kWh	[67]	
SC process:					
Refrigerant 1	-25	21	USD/GJ	[63]	C3 cycle
Refrigerant 2	-50	37	USD/GJ	[63]	C3 cycle
Refrigerant 3	-125	83	USD/GJ	[63]	C1, C2, and C3 cycle
Refrigerant 4	-150	135	USD/GJ	[63]	C1, C2, and C3 cycle
PCEC process:					
Refrigerant 1	-25	28	USD/GJ	[63]	C3 cycle
Refrigerant 2	-50	36	USD/GJ	[63]	C3 cycle
Refrigerant 3	-125	86	USD/GJ	[63]	C1, C2, and C3 cycle
Refrigerant 4	-150	129	USD/GJ	[63]	C1, C2, and C3 cycle

6.B. Ethane NODH thermodynamic equilibrium

The fractional ethane conversion that can be achieved following thermodynamic equilibrium information obtained by Champagnie et al. [68] is plotted in **Figure 6.B1a** as a function of temperature at 1 bar(a) pressure. Besides, the influence of removing hydrogen from the reaction zone on the thermodynamic equilibrium conversion is presented in **Figure 6.B1b** for a temperature of 550 °C and pressures of 1 bar(a) and 5 bar(a) (i.e. the operating pressure of the PCEC reactor). A hydrogen removal fraction of 98% was selected for the PCEC processes in this work, since substantial hydrogen removal fractions (>95%) were required to significantly shift the ethane dehydrogenation equilibrium toward ethylene (**Figure 6.B1b**).
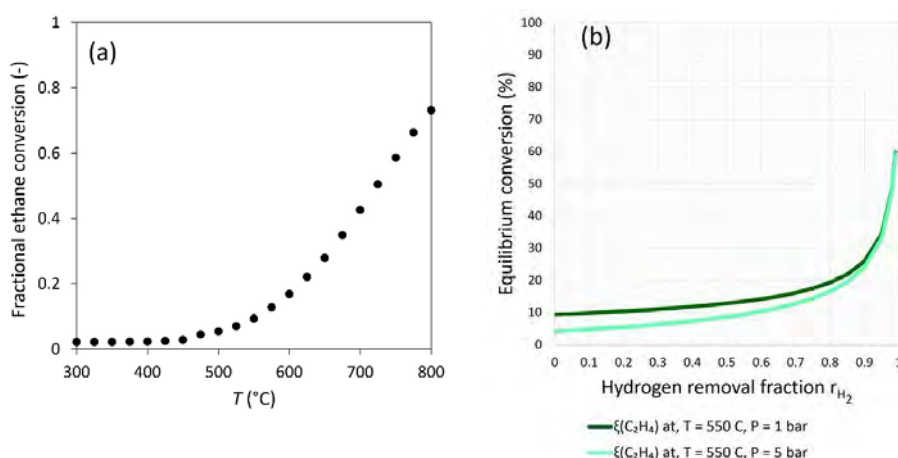
Figure 6.B1: (a) Fractional ethane equilibrium conversion as a function of temperature for a pure ethane feed at 1 bar(a), and (b) as a function of the hydrogen removal fraction at a temperature of 550 °C and at pressures of 1 bar(a) and 5 bar(a), designed based on Champagnie et al. [68].

6.C. Process flow diagrams

The method proposed by James Douglas [19] for the conceptual design of chemical processes was used to design the PCEC-assisted ethane dehydrogenation process. The main considerations playing a role in this process design are explained in **6.C1**. In **6.C2**, several notes relevant to all process simulations are mentioned. Subsequently, the detailed process flow diagrams of the ethane steam cracking (SC), the base case PCEC, and target case PCEC-assisted ethane dehydrogenation processes are presented in **6.C3**, **6.C4**, and **6.C5**, respectively.

6.C1. Conceptual design PCEC-assisted ethane dehydrogenation process

The ultimate conceptual design of the PCEC process contained three distinct process sections: (i) high temperature reaction, (ii) cooling and compression, and (iii) product separation (**Figure 6.C1**), which was in line with a typical ethane SC process. The ethane feed stream originated from a natural gas processing plant. It was assumed that no further pre-treatment steps were needed, as e.g. the removal of sulfur impurities was considered to be beyond the scope of this work. Also, 3 wt.% of steam was cofed to the feed and permeate side of the PCEC membrane [17,23,24].
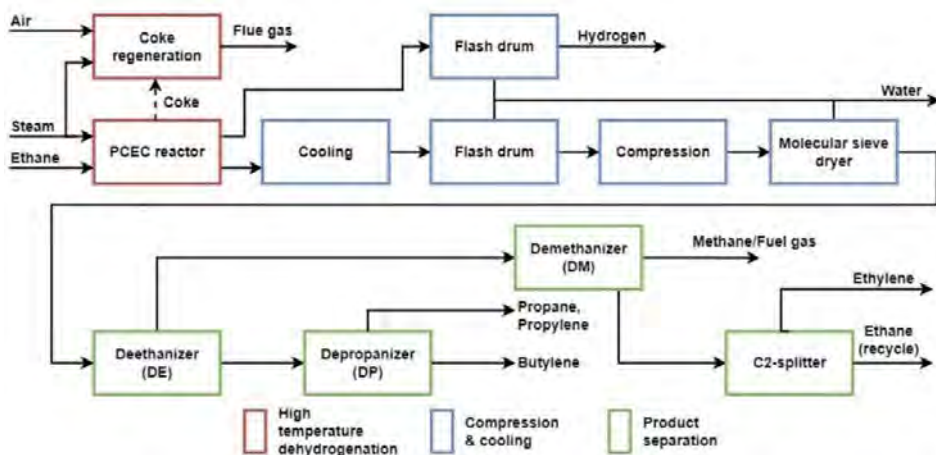
Figure 6.C1: Conceptual design of the PCEC-assisted ethane dehydrogenation process.

Since the ethylene yield in this process was comparably low regardless of the fraction of hydrogen removed (i.e. below 60%, see **Figure 6.B1b**), it was concluded that downstream separation was more effective than upstream separation. Besides, the complete combustion of carbon deposits was selected as the most efficient way of regenerating the PCEC catalyst/membrane system, as the PCEC-assisted ethane dehydrogenation reaction was carried out in parallel-configured tubular membrane cells that could easily switch between reaction and regeneration operating modes. Steam was added in a steam/air ratio of 4.67 kg/kg during regeneration for heat dilution with a stream inlet temperature of 620

°C [20]. Immediate cooling of the hydrocarbon product stream was essential to prevent degradation of the highly reactive olefin products. After cooling, the hydrocarbon mixture still contained H_2, H_2O, CH_4, C_2H_4, C_2H_6, C_3H_6, C_3H_8, and C_4H_8. Water was removed first (**Figure 6.C1**), because the boiling point of water lies far above the boiling point of all other constituents. The remaining hydrocarbons could be separated using either distillation, adsorption, or membrane technologies. Distillation was selected as the best method for product separation, because of its simplicity, cost-effectiveness, and maturity. Distillation of these small hydrocarbons can only be conducted under cryogenic conditions at high pressures (>10 bar(a)). For this reason, the hydrocarbon product stream had to be compressed before distillation. The final traces of water had to be removed using industrial drying methods to avoid possible crystallization in the cryogenic distillation columns. Since high pressures are beneficial for operating these industrial dryers, the hydrocarbon product stream was compressed before drying (**Figure 6.C1**).

The remaining hydrocarbons were further purified using the differences in boiling point. Hydrogen and methane both have a sub -150 °C boiling point and were referred to as lights. Besides, ethane and ethylene have a boiling point between -150 and -50 °C. Lastly, propane, propylene, and butylene all have a boiling temperature above -50 °C and were therefore referred to as heavies. An additional separation step was included to isolate the C3's from the butylene, as a large amount of valuable butylene was produced in the base case PCEC reactor, following the experimental PCEC performance adopted from the work by Wu et al. (ca. 8% butylene yield) [26]. Consequently, four distillation columns were needed: (i) a demethanizer to isolate the lights, (ii) a deethanizer to separate the C2's from the heavies, (iii) a depropanizer to purify the butylene and C3 byproducts, and (iv) a C2 splitter to separate the ethylene product from the unconverted ethane. The optimal distillation column sequence could either be based on a front-end demethanizer, a front-end deethanizer, or a front-end depropanizer [3], depending on the exact conditions of these separations and the composition of the product mixture. All three possible sequences were preliminary and individually simulated in Aspen Plus and compared to one another in terms of utility duties in order to select the optimal configuration (**Table 6.C1**). The front-end deethanizer sequence showed the lowest heating duty as well as the lowest costly refrigerant duty (**Table 6.C1**) for the base case PCEC process, and was therefore selected as the optimal distillation column sequence.

Table 6.C1: Utility duties for the three possible distillation column sequences of the PCEC process.

Sequence	Heating duty (MW)	Cooling water duty (MW)	Refrigerant cooling duty (MW)	Electricity duty (MW)
Front-end demethanizer	22.0	-2.4	-26.7	2.7
Front-end deethanizer	19.7	-4.2	-22.2	2.6
Front-end depropanizer	20.5	-1.8	-25.3	2.4

6.C2. Additional information on the process simulations

- The carbon deposits formed inside the SC furnace and the PCEC membrane reactors were simulated using coronene as a coke model compound. Coronene was separated from the reactor outlet using a component splitter in Aspen Plus.

- All adsorption columns, i.e. the hydrogen-PSA column and the dryer in the SC process and the dryer in the PCEC processes, were simulated as component splitters in Aspen Plus. The complete water content was removed in the dryers, whilst the hydrogen-PSA column was simulated using a hydrogen recovery of 80% [69]. The hydrogen-PSA column was operated with pressure swings from 32 to 0.35 bar(a) at 30 °C (see **Supporting Information 6.G2**), which were effectively included in the SC process simulations using a valve (**Supporting Information 6.C3**). Besides, the dryer pressure swing adsorption (PSA) columns in the SC and PCEC processes were operated with pressure swings between 32 and 2 bar(a) and between 27 and 2 bar(a), respectively, to remove the remaining moisture. Air was used as sweeping gas in the dryer PSA columns. The air stream needed to regenerate the dryer columns was compressed to 2 bar(a) upstream to facilitate water evaporation upon regeneration.

- Hydrogen was removed from the reaction product mixture in the PCEC reactor using a component splitter in Aspen Plus to mimic 98% hydrogen removal via permeation through the PCEC membrane (**Supporting Information 6.C4**). Afterward, a multistage compressor with interstage cooling was used in the Aspen Plus simulations to imitate the electrochemical hydrogen compression from 5 to 20 bar(a) inside the PCEC membrane reactor. The subsequent mechanical compression of the hydrogen product stream from 20 to 50 bar(a) occurred in a separate multistage compressor in Aspen Plus.

- In the multistage compressors, the interstage coolers reduced the temperature of the hydrocarbon product to less than 150 °C to optimize compressor efficiency and to avoid compressor damage and olefin polymerization [3,70,71].

- The caustic tower in the SC process is commonly used to remove carbon dioxide and hydrogen sulfide impurities [3]. In this case, the caustic tower (T = 30 °C, P = 17 bar(a)) was operated using a 22 wt.% sodium hydroxide solution [72]. Moreover, it only removed carbon dioxide, as sulfur removal was considered to be a process pre-treatment step.

- The operating pressures of the distillation columns in the different processes were estimated based on available literature [3], whilst the corresponding reboiler and condenser temperatures were retrieved from the concerning process simulations in Aspen Plus.

- The acetylene hydrogenation reactor of the SC process was operated as an adiabatic reactor at the SC deethanizer pressure of 27 bar(a) and at 70 °C [3].

6.C3. SC Process

Coke regeneration

SC furnace

Cooling and Compression

Product separation

Design specifications

Table 6.C2: Stream table ethane SC process.

Stream number/name		Feed	1	2	3	Water	4	5	6	7	8	9	10	11	12	13	14	15	16	17	18
Vapor fraction		1	1	1	1	0	0	1	1	1	1	1	1	0.77	0	0	1	0	0	0	0
Temperature	°C	11	-40	-54	285	25	25	285	285	850	850	850	306	30	30	30	30	30	30	30	30
Pressure	bar(a)	31	2	2	2	1	2	2	17	2	2	2	2	2	2	2	17	9	5	4	3
Molar flow	kmol/h	533	533	874	874	432	432	432	1306	1306	1787	1786	1786	1786	1377	409	1359	2	3	4	6
Mole fractions:																					
Propane		0.01	0.01	0.01	0.01	0	0	0	0.01	0.01	0.00	0.00	0.00	0.00	0.01	0	0.01	0	0	0	0
Ethane		0.95	0.95	0.89	0.89	0	0	0	0.59	0.59	0.15	0.15	0.15	0.15	0.20	0	0.20	0	0	0	0
Methane		0.03	0.03	0.02	0.02	0	0	0	0.01	0.01	0.04	0.04	0.04	0.04	0.05	0	0.05	0	0	0	0
Propylene		0	0	0	0	0	0	0	0	0	0.00	0.00	0.00	0.00	0.00	0	0.01	0	0	0	0
Ethylene		0	0	0.08	0.08	0	0	0	0.06	0.06	0.28	0.28	0.28	0.28	0.37	0	0.37	0	0	0	0
Hydrogen		0	0	0	0	0	0	0	0	0	0.27	0.27	0.27	0.28	0.35	0	0.35	0	0	0	0
Coronene		0	0	0	0	0	0	0	0	0	0	0	0	0	0	0	0	0	0	0	0
n-butane		0	0	0	0	0	0	0	0	0	0.00	0.00	0.00	0.00	0.00	0	0.00	0	0	0	0
1,3-butadiene		0	0	0	0	0	0	0	0	0	0	0	0	0	0.01	0	0.01	0	0	0	0
Carbon monoxide		0	0	0	0	0	0	0	0	0	0.00	0.00	0.00	0.00	0.00	0	0.00	0	0	0	0
Carbon dioxide		0	0	0	0	0	0	0	0	0	0	0	0	0	0	0	0	0	0	0	0
Water		0	0	0	0	1	1	1	0.33	0.33	0.24	0.24	0.24	0.24	0.02	1	0.00	1	1	1	1
Oxygen		0	0	0	0	0	0	0	0	0	0	0	0	0	0	0	0	0	0	0	0
Nitrogen		0	0	0	0	0	0	0	0	0	0	0	0	0	0	0	0	0	0	0	0
Acetylene		0	0	0	0	0	0	0	0	0	0.00	0.00	0.00	0.00	0.00	0	0.00	0	0	0	0
1-butene		0	0	0	0	0	0	0	0	0	0.00	0.00	0.00	0.00	0.00	0	0	0	0	0	0
Benzene*		0	0	0	0	0	0	0	0	0	0.00	0.00	0.00	0.00	0.00	0	0.00	0	0	0	0
Sodium hydroxide		0	0	0	0	0	0	0	0	0	0	0	0	0	0	0	0	0	0	0	0

Benzene was used in the Aspen Plus simulations as a model compound for all C4+ hydrocarbons, excluding coronene.

Stream number/name		19	20	21	22	Caustics	23	24	Spent-C	25	26	Water-R2	27	28	29	30	31	32	Fuel gas	33	34
Vapor fraction		0	0	1	0	0	0	1	0.01	1	1	0	0.67	1	0	1	1	1	1	1	1
Temperature	°C	30	30	30	30	25	26	30	30	30	30	30	-40	-122	-2	30	30	30	26	30	30
Pressure	bar(a)	7	13	17	17	1	17	17	17	32	32	32	32	32	32	32	32	32	1	32	32
Molar flow	kmol/h	2	1	1358	1	7	7	1358	7	1358	1355	3	1355	554	801	554	381	173	173	7	374
Mole fractions:																					
Propane		0	0	0.01	0	0	0	0.01	0	0.01	0.01	0	0.01	0	0.01	0	0	0	0	0	0
Ethane		0	0	0.20	0	0	0	0.20	0	0.20	0.20	0	0.20	0.00	0.34	0.00	0	0.00	0.00	0	0
Methane		0	0	0.05	0	0	0	0.05	0	0.05	0.05	0	0.05	0.13	0.00	0.13	0	0.42	0.42	0	0
Propylene		0	0	0.01	0	0	0	0.01	0	0.01	0.01	0	0.01	0.01	0.00	0.01	0	0.00	0.00	0	0
Ethylene		0	0	0.37	0	0	0	0.37	0	0.37	0.37	0	0.37	0.01	0.62	0.01	1	0.03	0.03	1	1
Hydrogen		0	0	0.35	0	0	0	0.35	0	0.35	0.35	0	0.35	0.86	0	0.86	1	0.55	0.55	1	1
Coronene		0	0	0	0	0	0	0	0	0	0	0	0	0	0	0	0	0	0	0	0
n-butane		0	0	0.00	0	0	0	0.00	0	0.00	0.00	0	0.00	0	0.00	0	0	0	0	0	0
1,3-butadiene		0	0	0.01	0	0	0	0.01	0	0.01	0.01	0	0.01	0	0.01	0	0	0	0	0	0
Carbon monoxide		0	0	0.00	0	0	0	0.00	0	0.00	0.00	0	0.00	0.00	0	0.00	0	0.00	0.00	0	0
Carbon dioxide		0	0	0	0	0	0	0	0.01	0	0	0	0	0	0	0	0	0	0	0	0
Water		1	1	0.00	1	0.89	0.89	0.00	0.88	0.00	0.00	1	0.00	0.00	0.00	0.00	0	0	0	0	0
Oxygen		0	0	0	0	0	0	0	0	0	0	0	0	0	0	0	0	0	0	0	0
Nitrogen		0	0	0	0	0	0	0	0	0	0	0	0	0	0	0	0	0	0	0	0
Acetylene		0	0	0.00	0	0	0	0.00	0	0.00	0.00	0	0.00	0	0.00	0	0	0	0	0	0
1-butene		0	0	0.00	0	0	0	0.00	0	0.00	0.00	0	0.00	0	0.00	0	0	0	0	0	0
Benzene*		0	0	0.00	0	0	0	0.00	0	0.00	0.00	0	0.00	0	0.00	0	0	0	0	0	0
Sodium hydroxide		0	0	0	0	0.11	0.11	0	0.11	0	0	0	0	0	0	0	0	0	0	0	0

Benzene was used in the Aspen Plus simulations as a model compound for all C4+ hydrocarbons, excluding coronene.

Stream number/name		Hydrogen	35	36	37	38	39	40	41	42	43	44	45	46	47	48	49	50	51	Ethylene	52
Vapor fraction		1	1	1	0.10	1	1	1	0.28	1	0	1	1	1	1	1	0	1	1	1	0
Temperature	°C	30	30	70	-9	-9	83	70	57	30	121	70	91	85	30	-35	-26	10	-33	10	-17
Pressure	bar(a)	50	27	27	27	27	27	27	14	14	14	27	27	18	18	18	18	18	18	18	18
Molar flow	kmol/h	374	7	7	801	770	31	770	31	18	13	777	771	771	771	24	747	24	407	407	340
Mole fractions:																					
Propane		0	0	0	0.01	0	0.25	0	0.25	0.44	0.00	0	0	0	0	0	0	0	0	0	0
Ethane		0	0	0	0.34	0.35	0.09	0.35	0.09	0.16	0	0.34	0.35	0.35	0.35	0.05	0.36	0.05	0.00	0.00	0.78
Methane		0	0	0	0.00	0.00	0	0	0	0	0	0.00	0.00	0.00	0.00	0.03	0	0.03	0	0	0
Propylene		0	0	0	0.01	0	0.22	0	0.22	0.38	0	0	0	0	0	0	0	0	0	0	0.00
Ethylene		0	0	0	0.62	0.65	0.01	0.65	0.01	0.01	0	0.64	0.65	0.65	0.65	0.87	0.64	0.87	0	0	0.22
Hydrogen		1	1	1	0	0	0	0	0	0	0	0.01	0.00	0.00	0.00	0.05	0	0.05	1	1	0
Coronene		0	0	0	0	0	0	0	0	0	0	0	0	0	0	0	0	0	0	0	0
n-butane		0	0	0	0.00	0	0.03	0	0.03	0.00	0.06	0	0	0	0	0	0	0	0	0	0
1,3-butadiene		0	0	0	0.01	0	0.25	0	0.25	0.00	0.59	0	0	0	0	0	0	0	0	0	0
Carbon monoxide		0	0	0	0	0	0	0	0	0	0	0	0	0	0	0	0	0	0	0	0
Carbon dioxide		0	0	0	0	0	0	0	0	0	0	0	0	0	0	0	0	0	0	0	0
Water		0	0	0	0	0	0	0	0	0	0	0	0	0	0	0	0	0	0	0	0
Oxygen		0	0	0	0	0	0	0	0	0	0	0	0	0	0	0	0	0	0	0	0
Nitrogen		0	0	0	0	0	0	0	0	0	0	0	0	0	0	0	0	0	0	0	0
Acetylene		0	0	0	0.00	0.01	0.00	0.01	0.00	0.00	0.06	0.01	0	0	0	0	0	0	0	0	0
1-butene		0	0	0	0.00	0	0.03	0	0.03	0.00	0.28	0	0	0	0	0	0	0	0	0	0
Benzene*		0	0	0	0.00	0	0.12	0	0.12	0	0	0	0	0	0	0	0	0	0	0	0
Sodium hydroxide		0	0	0	0	0	0	0	0	0	0	0	0	0	0	0	0	0	0	0	0

Benzene was used in the Aspen Plus simulations as a model compound for all C4+ hydrocarbons, excluding coronene.

Stream number/name		53	Recycle	54	55	56	57	58	59	60	61	Exhaust	H-flueg	C-flueg	Air	Sweep-g	Water-R
Vapor fraction		0.38	1	1	1	1	0	0	1	1	1	1	1	1	1	1	1
Temperature	°C	-78	-77	850	25	116	25	25	122	135	620	830	310	30	25	116	30
Pressure	bar(a)	2	2	2	1	2	1	2	2	2	2	2	2	2	1	2	2
Molar flow	kmol/h	340	340	0.2	23	23	174	174	174	198	198	198	198	198	726	726	429
Mole fractions:																	
Propane		0.78	0.78	0	0	0	0	0	0	0	0	0	0	0	0	0	0
Ethane		0	0	0	0	0	0	0	0	0.00	0.00	0	0	0	0	0	0
Methane		0.00	0.00	0	0	0	0	0	0	0	0	0	0	0	0	0	0
Propylene		0.22	0.22	0	0	0	0	0	0	0	0	0	0	0	0	0	0
Ethylene		0	0	0	0	0	0	0	0	0	0	0	0	0	0	0	0
Hydrogen		0	0	1	0	0	0	0	0	0	0	0	0	0	0	0	0
Coronene		0	0	0	0	0	0	0	0	0	0	0	0	0	0	0	0
n-butane		0	0	0	0	0	0	0	0	0	0	0	0	0	0	0	0
1,3-butadiene		0	0	0	0	0	0	0	0	0	0	0	0	0	0	0	0
Carbon monoxide		0	0	0	0	0	0	0	0	0	0	0	0	0	0	0	0
Carbon dioxide		0	0	0	0	0	0	0	0	0.00	0.00	0.02	0.02	0.02	0	0	0
Water		0	0	0	0	0	1	1	1	0.88	0.88	0.88	0.88	0.88	0	0	1
Oxygen		0	0	0	0.21	0.21	0	0	0	0.02	0.02	0.00	0.00	0.00	0.21	0.21	0
Nitrogen		0	0	0	0.79	0.79	0	0	0	0.09	0.09	0.09	0.09	0.09	0.79	0.79	0
Acetylene		0	0	0	0	0	0	0	0	0	0	0	0	0	0	0	0
1-butene		0	0	0	0	0	0	0	0	0	0	0	0	0	0	0	0
Benzene*		0	0	0	0	0	0	0	0	0	0	0	0	0	0	0	0
Sodium hydroxide		0	0	0	0	0	0	0	0	0	0	0	0	0	0	0	0

Benzene was used in the Aspen Plus simulations as a model compound for all C4+ hydrocarbons, excluding coronene.

6.C4. base case PCEC process
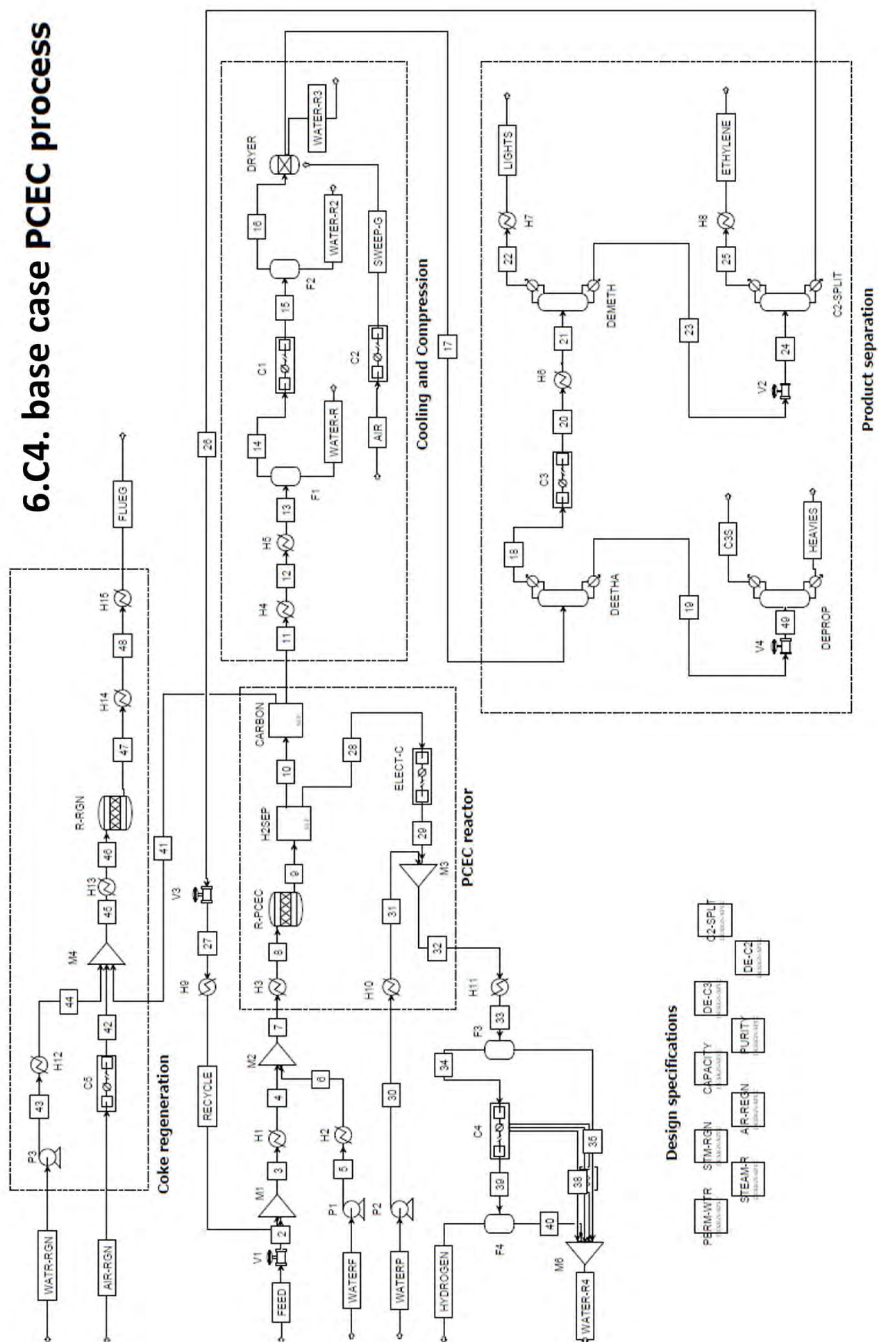
Table 6.C3: Stream table base case PCEC-assisted ethane dehydrogenation process. Single-pass ethylene yield = ca. 25%.

Stream number/name		Feed	2	3	4	WaterF	5	6	7	8	9	10	11	12	13	Water-R	14	15	Water-R2	16	Water-R3
Vapor fraction		1	1	1	1	0	0	1	1	1	1	1	1	1	0.96	0	1	1	0	1	0
Temperature	°C	11	-35	-41	285	25	25	285	285	550	550	550	550	306	30	30	30	45	45	45	45
Pressure	bar(a)	31	5	5	5	5	5	5	5	5	5	5	5	5	5	5	5	27	27	27	27
Molar flow	kmol/h	619	619	1604	1604	83	83	83	1686	1686	2192	1628	1628	1628	1628	72	1556	1556	4	1552	7
Mole fractions:																					
Propane		0.01	0.01	0.01	0.01	0	0	0	0.01	0.01	0.00	0.00	0.00	0.00	0.00	0	0.00	0.00	0	0.00	0
Ethane		0.95	0.95	0.95	0.95	0	0	0	0.91	0.91	0.43	0.58	0.58	0.58	0.58	0	0.60	0.60	0	0.61	0
Methane		0.03	0.03	0.01	0.01	0	0	0	0.01	0.01	0.02	0.03	0.03	0.03	0.03	0	0.03	0.03	0	0.03	0
Propylene		0	0	0.01	0.01	0	0	0	0.01	0.01	0.02	0.03	0.03	0.03	0.03	0	0.03	0.03	0	0.03	0
Ethylene		0	0	0.02	0.02	0	0	0	0.02	0.02	0.20	0.27	0.27	0.27	0.27	0	0.28	0.28	0	0.28	0
Hydrogen		0	0	0	0	0	0	0	0	0	0.26	0.01	0.01	0.01	0.01	0	0.01	0.01	0	0.01	0
Coronene		0	0	0	0	0	0	0	0	0	0	0	0	0	0	0	0	0	0	0	0
n-butane		0	0	0	0	0	0	0	0	0	0	0	0	0	0	0	0	0	0	0	0
1,3-butadiene		0	0	0	0	0	0	0	0	0	0	0	0	0	0	0	0	0	0	0	0
Carbon monoxide		0	0	0	0	0	0	0	0	0	0	0	0	0	0	0	0	0	0	0	0
Carbon dioxide		0	0	0	0	0	0	0	0	0	0	0	0	0	0	0	0	0	0	0	0
Water		0	0	0	0	1	1	1	0.05	0.05	0.04	0.05	0.05	0.05	0.05	1	0.01	0.01	1	0.00	1
Oxygen		0	0	0	0	0	0	0	0	0	0	0	0	0	0	0	0	0	0	0	0
Nitrogen		0	0	0	0	0	0	0	0	0	0	0	0	0	0	0	0	0	0	0	0
Acetylene		0	0	0	0	0	0	0	0	0	0	0	0	0	0	0	0	0	0	0	0
1-butene		0	0	0	0	0	0	0	0	0	0.03	0.04	0.04	0.04	0.04	0	0.04	0.04	0	0.04	0

Stream number/name		Air	Sweep-G	17	18	19	20	21	22	Lights	23	24	25	Ethylene	26	27	Recycle	28	29	WaterP	30
Vapor fraction		1	1	1	1	0	1	0	1	1	0	0.27	1	1	0	0.29	1	1	1	0	0
Temperature	°C	20	111	45	-2	99	10	-15	-98	10	5	-18	-33	10	-12	-53	-51	550	550	25	26
Pressure	bar(a)	1	2	27	27	27	32	32	32	32	32	18	18	18	18	5	5	5	20	1	20
Molar flow	kmol/h	1056	1056	1545	1446	99	1446	1446	54	54	1392	1392	407	407	985	985	985	564	564	2	2
Mole fractions:																					
Propane		0	0	0.00	0.00	0.03	0.00	0.00	0	0	0.00	0.00	0	0	0.00	0.00	0.00	0	0	0	0
Ethane		0	0	0.61	0.65	0	0.65	0.65	0.00	0.00	0.68	0.68	0	0	0.95	0.95	0.95	0	0	0	0
Methane		0	0	0.03	0.03	0	0.03	0.03	0.76	0.76	0.00	0.00	0.00	0.00	0	0	0	0	0	0	0
Propylene		0	0	0.03	0.01	0.29	0.01	0.01	0	0	0.01	0.01	0	0	0.02	0.02	0.02	0	0	0	0
Ethylene		0	0	0.28	0.30	0	0.30	0.30	0.02	0.02	0.31	0.31	1	1	0.03	0.03	0.03	0	0	0	0
Hydrogen		0	0	0.01	0.01	0	0.01	0.01	0.21	0.21	0	0	0	0	0	0	0	1	1	0	0
Coronene		0	0	0	0	0	0	0	0	0	0	0	0	0	0	0	0	0	0	0	0
n-butane		0	0	0	0	0	0	0	0	0	0	0	0	0	0	0	0	0	0	0	0
1,3-butadiene		0	0	0	0	0	0	0	0	0	0	0	0	0	0	0	0	0	0	0	0
Carbon monoxide		0	0	0	0	0	0	0	0	0	0	0	0	0	0	0	0	0	0	0	0
Carbon dioxide		0	0	0	0	0	0	0	0	0	0	0	0	0	0	0	0	0	0	0	0
Water		0	0	0.04	0	0.67	0	0	0	0	0	0	0	0	0	0	0	0	0	1	1
Oxygen		0.21	0.21	0	0	0	0	0	0	0	0	0	0	0	0	0	0	0	0	0	0
Nitrogen		0.79	0.79	0	0	0	0	0	0	0	0	0	0	0	0	0	0	0	0	0	0
Acetylene		0	0	0	0	0	0	0	0	0	0	0	0	0	0	0	0	0	0	0	0
1-butene		0	0	0.04	0	0	0	0	0	0	0	0	0	0	0	0	0	0	0	0	0

Stream number/name		31	32	33	34	35	36	37	38	39	40	Hydrogen	Water-R4	41	Air-RGN	42	Watr-Rgn	43	44	45	46
Vapor fraction		1	1	1	1	0	0	0	0	1	0	1	0	0	1	1	0	0	1	1	1
Temperature	°C	550	550	30	30	30	30	30	30	30	30	30	30	550	25	140	25	25	153	158	620
Pressure	bar(a)	20	20	20	20	20	32	40	25	50	50	50	20	5	1	5	1	5	5	5	5
Molar flow	kmol/h	2	566	566	565	1	0.1	0.1	0.2	565	0.1	564	2	0.1	20	20	152	152	152	172	172
Mole fractions:																					
Propane		0	0	0	0	0	0	0	0	0	0	0	0	0	0	0	0	0	0	0	0
Ethane		0	0	0	0	0	0	0	0	0	0	0	0	0	0	0	0	0	0	0	0
Methane		0	0	0	0	0	0	0	0	0	0	0	0	0	0	0	0	0	0	0	0
Propylene		0	0	0	0	0	0	0	0	0	0	0	0	0	0	0	0	0	0	0	0
Ethylene		0	0	0	0	0	0	0	0	0	0	0	0	0	0	0	0	0	0	0	0
Hydrogen		0	0	1	1	0	0	0	0	1	0	1	0	0	0	0	0	0	0	0	0
Coronene		0	0	0	0	0	0	0	0	0	0	0	0	1	0	0	0	0	0	0.00	0.00
n-butane		0	0	0	0	0	0	0	0	0	0	0	0	0	0	0	0	0	0	0	0
1,3-butadiene		0	0	0	0	0	0	0	0	0	0	0	0	0	0	0	0	0	0	0	0
Carbon monoxide		0	0	0	0	0	0	0	0	0	0	0	0	0	0	0	0	0	0	0	0
Carbon dioxide		0	0	0	0	0	0	0	0	0	0	0	0	0	0	0	0	0	0	0	0
Water		1	0.00	0.00	0.00	1	1	1	1	0.00	1	0.00	1	1	0	0	1	1	1	0	0
Oxygen		0	0	0	0	0	0	0	0	0	0	0	0	0	0.21	0.21	0	0	0	0.88	0.88
Nitrogen		0	0	0	0	0	0	0	0	0	0	0	0	0	0.79	0.79	0	0	0	0.02	0.02
Acetylene		0	0	0	0	0	0	0	0	0	0	0	0	0	0	0	0	0	0	0.09	0.09
1-butene		0	0	0	0	0	0	0	0	0	0	0	0	0	0	0	0	0	0	0	0

| Stream number/name		47	48	C-flueg	49	C3s	Heavies
Vapor fraction		1	1	0.12	0.36	1	0
Temperature	°C	830	306	30	68	33	86
Pressure	bar(a)	5	5	5	14	14	14
Molar flow	kmol/h	172	172	172	99	32	67
Mole fractions:							
Propane		0	0	0	0.03	0.10	0.00
Ethane		0	0	0	0	0	0
Methane		0	0	0	0	0	0
Propylene		0	0	0	0.29	0.90	0.00
Ethylene		0	0	0	0	0	0
Hydrogen		0	0	0	0	0	0
Coronene		0	0	0	0	0	0
n-butane		0	0	0	0	0	0
1,3-butadiene		0	0	0	0	0	0
Carbon monoxide		0.02	0.02	0.02	0	0	0
Carbon dioxide		0.88	0.88	0.88	0	0	0
Water		0.00	0.00	0	0	0	0
Oxygen		0.00	0.00	0	0	0	0
Nitrogen		0.09	0.09	0.09	0	0	0
Acetylene		0	0	0	0	0	0
1-butene		0	0	0	0.67	0.00	0.99

6.C5. target case PCEC process
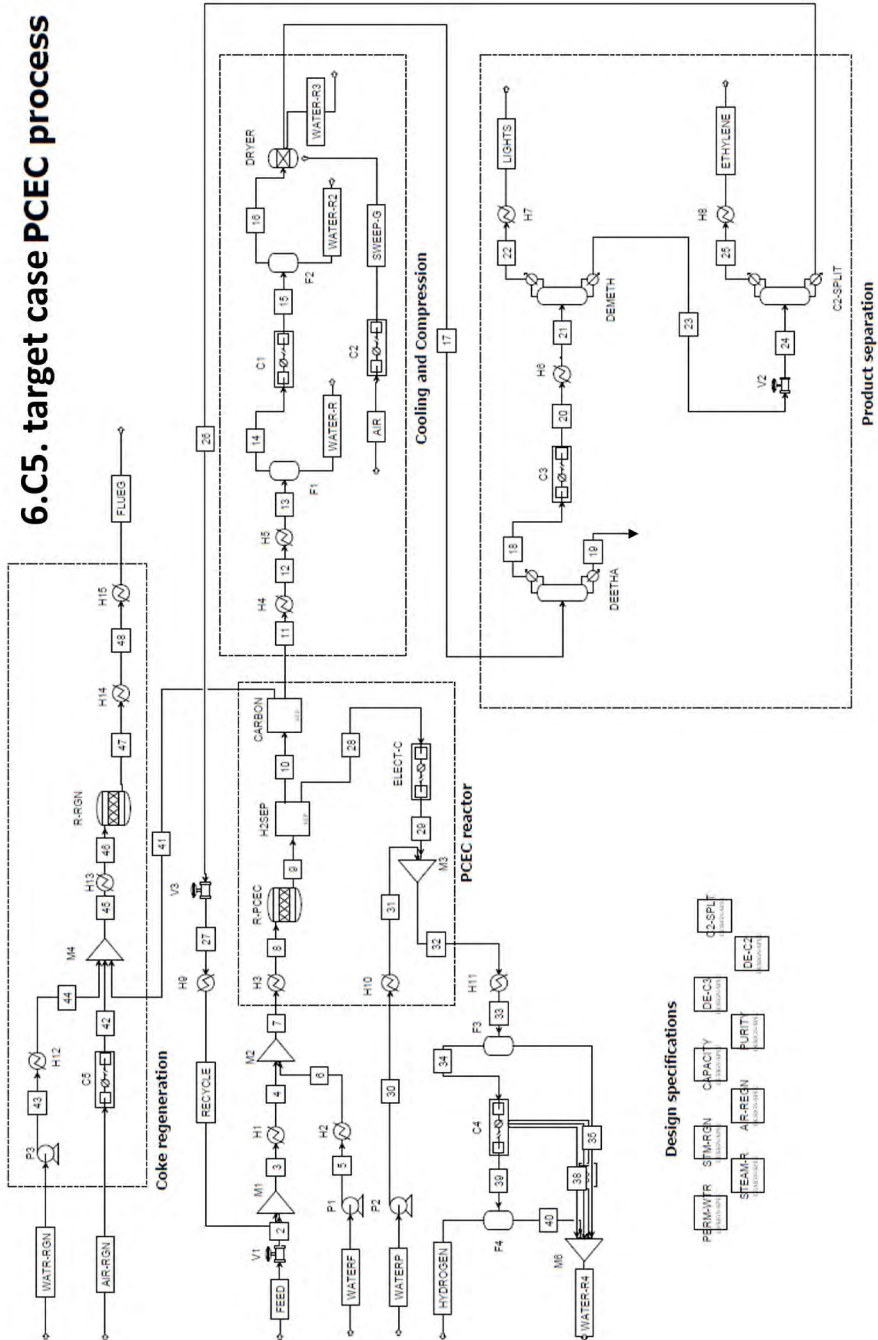
Table 6.C4: Stream table target case PCEC-assisted ethane dehydrogenation process. Single-pass ethylene yield = 50%.

Stream number/name		Feed	2	3	4	WaterF	5	6	7	8	9	10	11	12	13	Water-R	14	15	Water-R2	16	Water-R3
Vapor fraction		1	1	1	1	0	0	1	1	1	1	1	1	1	0.96	0	1	1	0	1	0
Temperature	°C	11	-35	-42	285	25	25	285	285	550	550	550	550	306	30	30	30	45	45	45	45
Pressure	bar(a)	31	5	5	5	1	5	5	5	5	5	5	5	5	5	5	5	27	27	27	27
Molar flow	kmol/h	530	530	938	938	48	48	48	987	987	1443	988	988	988	988	42	946	946	3	943	4
Mole fractions:																					
Propane		0.01	0.01	0.01	0.01	0	0	0	0.01	0.01	0.00	0.00	0.00	0.00	0.00	0	0.00	0.00	0	0.00	0
Ethane		0.95	0.95	0.96	0.96	0	0	0	0.91	0.91	0.30	0.43	0.43	0.43	0.43	0	0.45	0.45	0	0.45	0
Methane		0.03	0.03	0.02	0.02	0	0	0	0.02	0.02	0.02	0.03	0.03	0.03	0.03	0	0.04	0.04	0	0.04	0
Propylene		0	0	0.00	0.00	0	0	0	0.00	0.00	0.02	0.03	0.03	0.03	0.03	0	0.03	0.03	0	0.03	0
Ethylene		0	0	0.01	0.01	0	0	0	0.01	0.01	0.30	0.44	0.44	0.44	0.44	0	0.46	0.46	0	0.46	0
Hydrogen		0	0	0	0	0	0	0	0	0	0.32	0.01	0.01	0.01	0.01	0	0.01	0.01	0	0.01	0
Coronene		0	0	0	0	0	0	0	0	0	0	0	0	0	0	0	0	0	0	0	0
n-butane		0	0	0	0	0	0	0	0	0	0	0	0	0	0	0	0	0	0	0	0
1,3-butadiene		0	0	0	0	0	0	0	0	0	0	0	0	0	0	0	0	0	0	0	0
Carbon monoxide		0	0	0	0	0	0	0	0	0	0	0	0	0	0	0	0	0	0	0	0
Carbon dioxide		0	0	0	0	0	0	0	0	0	0	0	0	0	0	0	0	0	0	0	0
Water		0	0	0	0	1	1	1	0.05	0.05	0.03	0.05	0.05	0.05	0.05	1	0.01	0.01	1	0.00	1
Oxygen		0	0	0	0	0	0	0	0	0	0	0	0	0	0	0	0	0	0	0	0
Nitrogen		0	0	0	0	0	0	0	0	0	0	0	0	0	0	0	0	0	0	0	0
Acetylene		0	0	0	0	0	0	0	0	0	0	0	0	0	0	0	0	0	0	0	0
1-butene		0	0	0	0	0	0	0	0	0	0.00	0.01	0.01	0.01	0.01	0	0.01	0.01	0	0.01	0

Stream number/name		Air	Sweep-G	17	18	19	20	21	22	Lights	23	24	25	26	27	Recycle	28	29	WaterP	30
Vapor fraction		1	1	1	1	0	1	0.14	1	1	0	0.19	1	0	0.29	1	1	1	0	0
Temperature	°C	20	111	45	-8	32	-6	-15	-56	10	-6	-23	-33	-12	-53	-52	550	550	25	26
Pressure	bar(a)	1	2	27	27	27	28	28	28	28	28	18	18	18	5	5	5	20	1	20
Molar flow	kmol/h	1056	1056	940	879	60	879	879	64	64	815	815	407	408	408	408	455	455	2	2
Mole fractions:																				
Propane		0	0	0.00	0.00	0.04	0.00	0.00	0	0	0.00	0.00	0	0	0	0	0	0	0	0
Ethane		0	0	0.45	0.45	0.48	0.45	0.45	0.03	0.03	0.49	0.49	0.00	0.97	0.97	0.97	0	0	0	0
Methane		0	0	0.04	0.04	0	0.04	0.04	0.53	0.53	0.00	0.00	0.00	0	0	0	0	0	0	0
Propylene		0	0	0.03	0.00	0.39	0.00	0.00	0	0	0.00	0.00	0	0.01	0.01	0.01	0	0	0	0
Ethylene		0	0	0.46	0.49	0.00	0.49	0.49	0.14	0.14	0.51	0.51	1	0.02	0.02	0.02	0	0	0	0
Hydrogen		0	0	0.01	0.01	0	0.01	0.01	0.30	0.30	0	0	0	0	0	0	1	1	0	0
Coronene		0	0	0	0	0	0	0	0	0	0	0	0	0	0	0	0	0	0	0
n-butane		0	0	0	0	0	0	0	0	0	0	0	0	0	0	0	0	0	0	0
1,3-butadiene		0	0	0	0	0	0	0	0	0	0	0	0	0	0	0	0	0	0	0
Carbon monoxide		0	0	0	0	0	0	0	0	0	0	0	0	0	0	0	0	0	0	0
Carbon dioxide		0	0	0	0	0	0	0	0	0	0	0	0	0	0	0	0	0	0	0
Water		0	0	0.01	0.01	0	0.01	0.01	0	0	0	0	0	0	0	0	0	0	1	1
Oxygen		0.21	0.21	0	0	0	0	0	0	0	0	0	0	0	0	0	0	0	0	0
Nitrogen		0.79	0.79	0	0	0	0	0	0	0	0	0	0	0	0	0	0	0	0	0
Acetylene		0	0	0	0	0	0	0	0	0	0	0	0	0	0	0	0	0	0	0
1-butene		0	0	0	0	0.09	0	0	0	0	0	0	0	0	0	0	0	0	0	0

Stream number/name		31	32	33	34	35	36	37	38	39	40	Hydrogen	Water-R4	41	Air-RGN	42	Watr-Rgn	43	44	45	46
Vapor fraction		1	1	1	1	0	0	0	0	1	0	1	0	0	1	1	0	0	1	1	1
Temperature	°C	550	550	30	30	30	30	30	30	30	30	30	30	550	25	141	25	25	153	158	620
Pressure	bar(a)	20	20	20	20	20	32	40	25	50	50	50	20	5	1	5	1	5	5	5	5
Molar flow	kmol/h	2	457	457	456	1	0	0	0	456	0	456	1	0	17	17	124	124	124	141	141
Mole fractions:																					
Propane		0	0	0	0	0	0	0	0	0	0	0	0	0	0	0	0	0	0	0	0
Ethane		0	0	0	0	0	0	0	0	0	0	0	0	0	0	0	0	0	0	0	0
Methane		0	0	0	0	0	0	0	0	0	0	0	0	0	0	0	0	0	0	0	0
Propylene		0	0	0	0	0	0	0	0	0	0	0	0	0	0	0	0	0	0	0	0
Ethylene		0	0	0	0	0	0	0	0	0	0	0	0	0	0	0	0	0	0	0	0
Hydrogen		0	1	1	1	1	1	0	0	1	1	1	0	1	0	0	0	0	0	0	0
n-butane		0	0	0	0	0	0	0	0	0	0	0	0	0	0	0	0	0	0	0.00	0.00
Coronene		0	0	0	0	0	0	0	0	0	0	0	0	0	0	0	0	0	0	0	0
1,3-butadiene		0	0	0	0	0	0	0	0	0	0	0	0	0	0	0	0	0	0	0	0
Carbon monoxide		0	0	0	0	0	0	0	0	0	0	0	0	0	0	0	0	0	0	0	0
Carbon dioxide		0	0	0	0	0	0	0	0	0	0	0	0	0	0	0	0	0	0	0	0
Water		1	0.00	0.00	0.00	1	1	1	1	0.00	1	0.00	1	0	0	0	1	1	1	0.88	0.88
Oxygen		0	0	0	0	0	0	0	0	0	0	0	0	0	0.21	0.21	0	0	0	0.02	0.02
Nitrogen		0	0	0	0	0	0	0	0	0	0	0	0	0	0.79	0.79	0	0	0	0.09	0.09
Acetylene		0	0	0	0	0	0	0	0	0	0	0	0	0	0	0	0	0	0	0	0
1-butene		0	0	0	0	0	0	0	0	0	0	0	0	0	0	0	0	0	0	0	0

Stream number/name		47	48	C-flueg
Vapor fraction		1	1	0.11
Temperature	°C	830	306	30
Pressure	bar(a)	5	5	5
Molar flow	kmol/h	141	141	141
Mole fractions:				
Propane		0	0	0
Ethane		0	0	0
Methane		0	0	0
Propylene		0	0	0
Ethylene		0	0	0
Hydrogen		0	0	0
n-butane		0	0	0
Coronene		0	0	0
1,3-butadiene		0	0	0
Carbon monoxide		0.02	0.02	0.02
Carbon dioxide		0.88	0.88	0.88
Water		0.00	0.00	0.00
Oxygen		0.00	0.00	0.00
Nitrogen		0.09	0.09	0.09
Acetylene		0	0	0
1-butene		0	0	0

6.D. Process simulations

6.D1. Ethane steam cracking process

The product distribution of the simulated ethane steam cracking process is shown in **Table 6.D1** and is valid for a residence time of 0.4607 seconds, an ethane conversion of 65%, and a steam dilution of 0.3 kg/kg [3]. The coke model compound coronene was formed directly from ethane, following **Equation 6.D1**. The amount of coke produced in the SC process was assumed to be equal to the amount of coke produced in the PCEC processes, and was therefore estimated based on the work by Wu et al. [26] on PCEC-assisted ethane dehydrogenation.

Table 6.D1: Product distribution of the simulated ethane SC process.

Compound	Wt.%	Reference
H_2	6.22	[3]
CO	0.06	[3]
CO_2	0.02	[3]
CH_4	5.77	[3]
C_2H_2	0.68	[3]
C_2H_4	79.82	[3]
C_3H_4	0.03	[3]
C_3H_6	1.88	[3]
C_3H_8	0.18	[3]
C_4H_4	0.08	[3]
C_4H_6	2.77	[3]
C_4H_8	0.29	[3]
C_4H_{10}	0.32	[3]
C_{4+}	1.89	[3]
Coronene	0.21	[26]

$$12C_2H_6 \leftrightharpoons C_{24}H_{12} + 30H_2 \qquad (6.D1)$$

6.D2. PCEC membrane-assisted process

6.D2.1. PCEC base case: single-pass ethylene yield = ca. 25%

The product distribution of the simulated base case PCEC membrane reactor was based on the product distribution experimentally obtained by Wu et al. [26] for a BZCYYb-based PCEC system and is shown in **Table 6.D2**. These reactions were simulated as serial reactions in a stoichiometric reactor in Aspen Plus. Notably, in the product distribution in **Table 6.D2** a considerable amount of ethylene was consecutively converted to butylene,

which made butylene a major byproduct in the PCEC process. Moreover, coke formation was assumed to take place from methane here, based on Wu et al. [26]. However, coke formation is generally believed to originate from olefin oligomerization in alkane dehydrogenation processes [56]. We utilized the polycyclic aromatic hydrocarbon coronene, with chemical formula $C_{24}H_{12}$, as coke model compound in the process simulations in this work. Coronene was in the gas phase under reaction conditions and therefore transportable to a regeneration unit in the Aspen Plus simulations. For this reason, we simulated the formation of solid carbon as coronene formation from methane (**Equation 6.D8**), which therefore replaced **Equation 6.D7**. A fractional methane conversion of 0.07 leads to the formation of 2.06 gram of coronene per kg of converted ethane. The latter amount of coke was included in all SC and PCEC process simulations.

Table 6.D2: Product distribution of the simulated PCEC-assisted ethane dehydrogenation process, as retrieved from the work by Wu et al. [26].

#	Description:	Reaction:	Fractional conversion:	Limiting reactant:
6.D2	Ethane dehydrogenation	$C_2H_6 \leftrightarrows C_2H_4 + H_2$	0.363	Ethane
6.D3	Ethane metathesis	$2C_2H_6 \leftrightarrows C_3H_8 + CH_4$	0.02	Ethane
6.D4	Propane dehydrogenation	$C_3H_8 \leftrightarrows C_3H_6 + H_2$	0.8	Propane
6.D5	Ethylene oligomerization	$2C_2H_4 \leftrightarrows C_4H_8$	0.23	Ethylene
6.D6	Ethylene metathesis	$C_2H_6 + C_2H_4 \leftrightarrows C_3H_6 + CH_4$	0.032	Ethylene
6.D7	Carbon deposition	$CH_4 \rightarrow C + 2H_2$	0.07	Methane

$$24CH_4 \rightarrow C_{24}H_{12} + 42H_2 \qquad (6.D8)$$

6.D2.2. PCEC target case: single-pass ethylene yield = 50%

In the reactor performance data adopted from Wu et al. [26], 23% of the formed ethylene was consecutively converted to butylene (**Table 6.D2**), resulting in a poor ethylene selectivity. Since ethylene was the targeted product, the butylene yield was adjusted to 2.3% in the ethylene yield variations (**Supporting Information 6.O1**). The fractional conversions of all side reactions were remained constant, implying that the byproduct selectivity changed with varying ethylene yield. The fractional conversions applied in the PCEC target case, which considers a competitive single-pass ethylene yield of 50%, are listed in **Table 6.D3**.

Table 6.D3: Product distribution applied in the PCEC process target case, considering a single-pass ethylene yield of 50% that is competitive with conventional SC processes for ethylene production.

#	Description:	Reaction:	Fractional conversion:	Limiting reactant:
6.D2	Ethane dehydrogenation	$C_2H_6 \leftrightharpoons C_2H_4 + H_2$	0.50	Ethane
6.D3	Ethane metathesis	$2C_2H_6 \leftrightharpoons C_3H_8 + CH_4$	0.02	Ethane
6.D4	Propane dehydrogenation	$C_3H_8 \leftrightharpoons C_3H_6 + H_2$	0.8	Propane
6.D5	Ethylene oligomerization	$2C_2H_4 \leftrightharpoons C_4H_8$	0.023	Ethylene
6.D6	Ethylene metathesis	$C_2H_6 + C_2H_4 \leftrightharpoons C_3H_6 + CH_4$	0.032	Ethylene
6.D7	Carbon deposition	$CH_4 \rightarrow C + 2H_2$	0.07	Methane

6.D3. Regeneration

In the ethane SC and PCEC processes, the regeneration unit in Aspen Plus was operated at 5 bar(a) and with an inlet temperature of 620 °C [20]. Air (21% O_2, 79% N_2) was used as regeneration agent in a 120% molar excess to coronene to ensure complete combustion, following **Equation 6.D9**. Steam was cosupplied with the air for heat dilution in a ratio of 4.67 kilogram of steam per kilogram of air [20]. Under these conditions, the flue gas stream leaving the regenerator is at ca. 800-850 °C.

$$C_{24}H_{12} + 27O_2 \rightarrow 6H_2O + 24CO_2 \tag{6.D9}$$
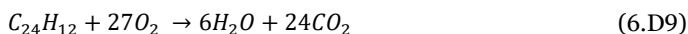
6.D4. Design specifications

The following design specifications were incorporated in the process simulations in Aspen Plus:

- The production capacity of the ethylene product stream (100 ktpa) was attained by varying the size of the fresh ethane feed stream.
- The purity of the ethylene product (99.9%) was ensured by adjusting the molar reflux ratio of the C2 splitter column.
- The amount of hydrogen originating from the hydrogen PSA column that was sent to the acetylene hydrogenation reactor in the SC process was specified based on the acetylene content of stream 40, such that the hydrogen/acetylene ratio equaled 1.8.
- The size of the air stream toward the regenerator was adapted to the amount of coronene produced inside the SC furnace or PCEC reactor. Following **Equation 6.D9**, a stoichiometric O_2/coronene ratio of 27 would be required. In order to

ensure complete combustion, a 20% excess of oxygen was cosupplied to the regeneration unit [3], corresponding to an O_2/coronene ratio of 32.4.

- The amount of steam cosupplied with the air to the regenerator for heat dilution was defined by using an optimal steam/air ratio of 4.67 kg/kg, as proposed by Heynderickx [20].

- The required amount of sodium hydroxide in the SC process was regulated based on the principle that the outlet sodium carbonate concentration should not exceed 4 wt.% [73], i.e. the $NaOH:CO_2$ mass ratio should be around 14:1.

- The mass flow of steam toward the SC furnace was defined by setting the steam/ethane mass ratio entering the SC furnace to 0.3, based on the desired steam dilution of 0.3 kg/kg [3].

- Similarly, the amount of steam cosupplied to the PCEC membrane reactor was adjusted in such a way that the PCEC reactor inlet stream contained 3 wt.% of steam.

- The large amount of 1-butylene byproduct generated in the base case PCEC process was purified to 99.6 wt.%, which is the industrial requirement of high value 1-butylene [74], by varying the molar reflux ratio of the depropanizer column.

- The amount of steam that was effectively cofed to the permeate side of the PCEC membrane was specified to 3 wt.% by setting the mass fraction of steam in the permeated hydrogen stream (stream 32 of the PCEC process) to 0.03.

6.E. Ethane steam cracking furnace

The ethane steam cracking furnace was designed based on a conventional furnace described by Zimmermann and coworkers [3]. This concerns a box furnace that was constructed with stainless steel 304. The total furnace capacity was divided over four furnaces to allow for continuous operation. Since the targeted ethylene production capacity was relatively small in this work (100 ktpa), a relative small furnace tube size of 50 mm was selected here. The length of the coils was about 70 m to ensure a residence time of 0.4607 seconds, corresponding to the product distribution in **Table 6.D1**. This results in the use of 28 coils in total. The regeneration step in ethane steam cracking furnaces is typically required every 2-3 months and takes only a few hours. For this reason, no additional furnace had to be included to compensate for operation in regeneration mode. The steam cracking furnace characteristics are summarized in **Table 6.E1**. The duty of the steam cracking furnaces equaled the sum of the energy needed for heating and reaction, while incorporating a furnace efficiency of 90% [3]. The capital investment of the steam cracking furnaces was estimated by using the method proposed by Towler and Sinnott [43] for calculating the capital investment of individual process equipment, considering that the steam cracking furnaces were box furnaces.

Table 6.E1: Characteristics of the ethane steam cracking furnace.

Parameter	Value	Unit	Reference
Residence time	0.4607	s	[3]
Conversion	65	%	[3]
Inlet temperature	285	°C	[3]
Outlet temperature	850	°C	[3]
Inlet pressure	2	bar(a)	[3]
Total capacity	296	ktpa	Simulations in Aspen Plus
# of furnaces	4		
Per furnace:			
Duty	10.28	MW	
Inlet mass flow	74	ktpa	
Inlet volume flow	2.10	m³/s	
Tube diameter	0.05	m	
Coil length	70.4	m	
Single coil volume	0.14	m³	
Total coil volume	0.97	m³	
# of coils	7		
Hot box length	2	m	
Hot box width	3	m	
Hot box height	15	m	

6.F. PCEC membrane reactors

6.F1. PCEC membrane reactor design

The design of the PCEC membrane reactor was based on the multi-tubular and modular ceramic membrane reactors developed by CoorsTek, as described in Malerød-Fjeld et al. [15]. The hydrocarbon stream was fed on the inner tube side, such that the hydrogen was transported through the electrochemical cell in outward direction. Relative to planar designs, tubular ceramic cells are more tolerant to thermal stresses [75,76] and more stable under pressure gradients between feed and permeate side [77]. The characteristics of a single ceramic cell are summarized in **Table 6.F1**. Eight of these ceramic cells are connected in series in a PCEC tube and ten of these PCEC tubes together, separated by sealing and/or interconnects, is referred to as a stack [14]. A single engineering unit (SEU) represents a shell in which such a stack is positioned [14]. The characteristics of an SEU are presented in **Table 6.F2**.

Table 6.F1: Characteristics of a single ceramic cell.

Parameter:	Value:	Unit:	Reference:
Feed side pressure	5	bar(a)	
Permeate side pressure	20	bar(a)	
Outer diameter	10	mm	[15]
Active electrode length	186	mm	[15]
Active membrane area	55.25	55.25 cm^2	
Current density	1	A/cm^2	
E_{OCV}	0.12	V	
E_{cell}	0.527	V	
Power density	0.527	W/cm^2	

Table 6.F2: Characteristics of a single engineering unit (SEU).

Parameter:	Value:	Unit:	Reference:
Design pressure	32	bar(a)	[15]
Construction material	Alloy 800HT		[15]
Outer diameter	116	mm	[15]
Wall thickness	8	mm	[15]
Height	1.15	m	[15]
# of ceramic cells	80		
Active membrane area	0.44	m^2	

Ten SEUs were positioned inside a membrane panel and ten of those membrane panels together represented a membrane module [15]. Such a membrane module, in turn, was placed inside a hot box, which is a heating mantle in which the heating principle is normally based on steam circulation. The characteristics of a membrane module are summarized in **Table 6.F3**.

Table 6.F3: Characteristics of a membrane module.

Parameter:	Value:	Unit:
# of SEUs	100	
Total active membrane area	44.20	m^2
Width	1.16	
Length	4.64	
Height	2.3	

The Aspen Plus simulations of the base case PCEC process showed that the hydrogen flow in the reactor effluent was 160 mol/s in absence of any hydrogen extraction. For the selected 98% hydrogen removal, this means that 157 mol/s needed to permeate through the base case PCEC membrane. For a current density of 1 A/cm^2 this resulted in a total required membrane area for permeation of ca. 3,000 m^2. It was estimated that 17% of the total reactor capacity had to be available for regeneration cycles, based on information obtained from industrialized propane dehydrogenation processes [11]. As a consequence, ca. 3,500 m^2 of membrane area was needed to operate the base case PCEC reactor. Using the available membrane area per module (**Table 6.F3**), the total required number of membrane modules was calculated to be about 80. Analogous calculations for the target case PCEC process, where the PCEC reactor contained only 129 mol/s of hydrogen, yielded a total requirement of 64 PCEC membrane modules (ca. 2,800 m^2 of PCEC membrane area needed). The hydrogen stream in the reactor outlet was smaller for the target case PCEC process, due to smaller process stream sizes as a result of a smaller recycle caused by the higher single-pass ethylene yield.

The PCEC membrane composition was retrieved from the work by Wu et al. [26] on PCEC-assisted ethane dehydrogenation. The corresponding required PCEC stack materials are summarized in **Table 6.F4**. In addition, the operating parameters of the PCEC reactor stack are summarized in **Table 6.F5**.

Table 6.F4: PCEC stack materials.

Parameter:		Unit:	Reference:
Anode:			
Anode material	$(PrBa)_{0.95}(Fe_{0.9}Mo_{0.1})_2O_{5+\delta}$ (PBFM)		[26]
Anode thickness	80	μm	[26]
Dehydrogenation catalyst	PtGa/ZSM-5		[26]
Catalyst loading	23.7	mg/cm^2	[26]
Pt loading	0.175	%	[26]
Ga loading	1.02	%	[26]
Electrolyte:			
Electrolyte material	$BaZr_{0.1}Ce_{0.7}Y_{0.2-x}Yb_xO_{3-\delta}$ (BZCYYb)		[26]
Electrolyte thickness	15	μm	[26]
Cathode:			
Cathode material	Ni-BZCYYb		[26]
Cathode thickness	450	μm	[26]
Ni loading	351.25	mg/cm^2	[26]

Table 6.F5: Operating parameters of PCEC stack.

Parameter:	Value:	Unit:	Reference:
Temperature	550	°C	[26]
Anode pressure	5	bar(a)	
Cathode pressure	20	bar(a)	
Power	15.92	MW	[26]
Area specific resistance (*ASR*)	0.4	$\Omega.cm^2$	Estimated based on [78]
Ethane conversion	39.5	%	[26]
Ethylene selectivity	63.3	%	[26]
Ethylene yield	25.0	%	[26]

6.F2. PCEC membrane reactor CAPEX

The PCEC stack material costs were estimated based on a method proposed by Malerød-Fjeld et al. [15] in which the stack material costs were calculated using the price of the raw materials and the related amounts of those raw materials needed for the synthesis of one SEU. The anode, electrolyte, and cathode thickness of the PCEC membranes employed by Wu et al. [26] were 80, 15, and 450 μm, respectively (see **Table 6.F4**), whilst the electrolyte and total electrode thickness in the work by Malerød-Fjeld et al. [15] were 30 and 800 μm, respectively. The required amounts of raw materials for the synthesis of one SEU in this work were scaled to the required raw materials per SEU retrieved from Malerød-Fjeld et al. [15], using the electrode and electrolyte thickness from Wu et al. [26], assuming equal electrode porosities. The results are summarized in **Table 6.F6**. The total costs per SEU are summarized in **Table 6.F7**, whilst the total membrane reactor costs are presented in **Table 6.F8**.

Table 6.F6: PCEC stack material costs.

Material	Usage (kg/SEU)	Price (USD/kg)	Cost per SEU (USD)	Reference for price
$BaSO_4$	1.66	0.50	0.83	[79]
CeO_2	0.25	2	0.49	[80]
ZrO_2	0.62	6	3.70	[81]
Y_2O_3	0.08	4	0.31	[82]
NiO	1.55	35	54.34	[83]
Yb_2O_3	0.14	16	2.20	[82]
Zirconia toughened alumina (ZTA)	0.38	15	5.70	[84]
$Pr(NO_3)_3$	0.38	58	22.02	[82]
$Fe(NO_3)_3$	0.44	0.50	0.22	[85]

Ba(NO$_3$)$_2$	0.30	3	0.91	[86]
(NH$_4$)$_6$Mo$_7$O$_{24}$	0.02	10	0.20	[87]
ZSM-5	0.10	4.50	0.47	[88]
Pt	$1.83\cdot10^{-4}$	30,376	5.57	[89]
Ga	$1.07\cdot10^{-3}$	756	0.81	[90]
Total (USD/SEU):			**97.77**	
Total per PCEC tube (80 tubes per SEU)			1.22 USD	
Total per PCEC tube including 10% manufacturing costs			1.34 USD	

Table 6.F7: Costs per single engineering unit (SEU).

Component	# of items per SEU	Price per item (USD)	Cost per SEU (USD)	Reference
PCEC tubes	80	1.34	107.54	**Table 6.F6**
Interconnect	100	0.07	7.20	[15]
Gas Manifolds	10	0.68	6.80	[15]
Weld connectors	20	2.58	51.60	[15]
Sealing rings	240	0.001	0.24	[15]
Pressure tube	1		390	[15]
Pre-heating zone	1		51.60	[15]
Assembly of SEU			22.40	[15]
Tooling costs			290	[15]
Total (USD/SEU):			**927**	

Table 6.F8: Total membrane reactor costs.

Description	Value	Unit	Reference
# of SEUs per membrane module	100		
Total active membrane area per module	44.20	m^2	
Total SEU costs	92,700	USD	**Table 6.F7**
Instrumentation	1,500	USD	[15]
Tubings and fittings	2,000	USD	[15]
Housing	1,500	USD	[15]
Safety system	1,000	USD	[15]
System assembly	3,000	USD	[15]
Total module costs, before markup	**101,700**	**USD**	
Markup (40%)	40,700	USD	
Total module costs, including markup	**142,400**	**USD**	

As highlighted in **Supporting Information 6.F1**, the base case PCEC process requires 80 membrane modules, whilst the target PCEC process requires 64 PCEC membrane modules. Considering the total costs per module (**Table 6.F8**), this results in total PCEC membrane reactor costs of ca. 11.5 MMUSD and ca. 9.1 MMUSD for the base case and target case PCEC processes, respectively.

6.G. Other equipment design

All process equipment was designed and dimensioned based on methods proposed by Towler and Sinnott [91–94], if not stated otherwise.

6.G1. Compressors

The compressors were simulated as multistage isentropic compressors with interstage cooling and a stage efficiency of 72% [95]. All compressors were centrifugal compressors, because of the high flow rates in both processes [94]. A compression ratio of 1.3 per stage was applied, which is within the typical range for centrifugal compressors [96]. Moreover, the upper temperature for all compression steps was 150 °C to avoid compressor damage and possible olefin polymerization, and to optimize the compression efficiency [3,70,71]. Since the steam concentration in the reactor effluent stream was much higher in the ethane SC process compared to the PCEC process, interstage water removal needed to be implemented in the multistage compression sequence of this stream in the SC process.

6.G2. Adsorption columns

The dryer in the SC and PCEC processes was a pressure swing adsorption (PSA) unit. The same holds for the hydrogen/methane separation step in the SC process. The size of the concerning columns was calculated based on the required size of the adsorption bed, in combination with an 80% fraction of the adsorption column that was occupied by the adsorption bed [93]. Besides, the adsorption time per cycle was estimated to be 30 minutes in all cases. Moreover, all adsorption separations were assumed to be perfect, leaving pure adsorbate and desorbate gases. The only operating costs of the adsorption columns were the costs for compressing the sweep gas.

Dryer:

The last traces of water were removed from the hydrocarbon reactor effluent stream in all processes using an industrial dryer, which was a molecular sieve pressure swing adsorption (PSA) step. Water adsorption from the hydrocarbon stream happened at high pressure (ca. 30 bar(a)), whilst water desorption into an air sweep gas stream occurred at near-ambient pressure. Adsorption inside this dryer took place at a temperature between 30 to 50 °C. Besides, the air sweeping gas for the desorption runs was compressed to 2 bar(a), resulting in a sweep gas temperature of ca. 115 °C, which further enhanced water desorption. In the Aspen Plus simulations, a component splitter was used to model this industrial dryer, in which complete removal of the water content was assumed. UOP

molecular sieve Zeolite-3A was used as adsorbent in the dryers with a density of 750 kg/m^3 [97]. Its lifetime was estimated to be five years, based on the typical lifetime of carbon adsorbents [98].

Hydrogen/methane separation:

In this column, 80% of the hydrogen was recovered from the impurity gases methane, ethane, ethylene, and carbon monoxide. It was assumed that all these impurities behave like methane. Activated carbon was applied in this adsorption column with a density of 776 kg/m^3 [99]. Similar to the molecular sieve adsorbent used in the dryers, also the lifetime of the activated carbon adsorbent was estimated to be five years [98].

Column dimensions:

The mass of adsorbent needed per pressure swing adsorption (PSA) bed (M_a, in kg) was calculated using **Equation 6.G1** [93].

$$(F_1 y_1 - F_2 y_2) M_w t_a = 1000 \, (m_1 - m_2) M_a f_L \qquad (6.G1)$$

Where F_1 and F_2 define the respective feed and product molar flow rates, as obtained from the Aspen simulations. Similarly, y_1 and y_2 are the molar fractions of the components to be adsorbed in the feed and product flows. Besides, M_w is the molar weight of the component to be adsorbed. Furthermore, t_a represents the time in which the bed is in adsorption mode, here estimated to be 30 minutes [93]. The maximum and minimum adsorbent loadings (m_1 and m_2) define the adsorbate amount that can be adsorbed per g of adsorbent under the high and low pressure ends of the corresponding pressure swings. The difference between both represents the amount of adsorbent that can be adsorbed per g of adsorbent per adsorption cycle. The amount of zeolite-3A adsorbent required in the dryer columns was estimated based on the adsorption isotherms for water adsorption on zeolite-3A obtained by Yu Wang [100]. Besides, the required amount of activated carbon adsorbent for the hydrogen/methane separation step was retrieved from an adsorption isotherm for methane and hydrogen adsorption on activated carbon [99]. Finally, f_L was the loaded fraction of the bed, which was approximated to be 80% [93]. The results of the dimensions of the PSA columns are summarized in **Table 6.G1**. The dimensions of the dryer in the target case PCEC process were assumed to be equal to those of the dryer in the base case PCEC process.

Table 6.G1: Dimensions of pressure swing adsorption (PSA) columns.

Description:	Dryer PCEC	Dryer SC	H-PSA-SC	Unit:
Temperature	47	30	30	°C
Inlet pressure	27	32	32	bar(a)
Discharge pressure	2	2	1	bar(a)
Adsorbate	H_2O	H_2O	CH_4	

# of beds	4	4	4	
Desorbate recovery	100	100	80	%
Feed flow rate per bed, F_1	388	340	38	mol/s
Product flow rate per bed, F_2	386	339	26	mol/s
Sweep gas flow rate per bed	293	202	0	mol/s
Adsorbate partial pressure in feed	0.12	0.09	4.49	bar(a)
Adsorbate partial pressure in off-gas	0.012	0.009	0.45	bar(a)
Adsorption time, t_a	30	30	30	min
Max. loading (high pressure), m_1	13.90	13.50	1.94	mol/kg
Min. loading (low pressure), m_2	7.40	7.00	0.38	mol/kg
Loaded fraction of bed, f_L	80	80	80	%
Adsorbent weight, M_a	609	314	7798	kg
Adsorbent volume	0.81	0.42	10.05	m³
Adsorption column volume	1.02	0.52	12.56	m³
H/D ratio	4	4	4	
Column diameter	0.69	0.55	1.59	m
Column height	2.75	2.20	6.35	m

6.G3. Distillation columns

All distillation columns were first simulated as DSTWU columns in Aspen Plus to retrieve approximated column dimensions and specifications required to perform the concerning separation steps. Afterward, the DSTWU columns were replaced by RadFrac columns to determine the ultimate required column specifications, where the inputs for the RadFrac column simulations were the outcomes of the DSTWU models.

The distillation columns were designed based on the method by Towler and Sinnott [92]. The diameter of a distillation column (D_c) primarily depends on the vapor flow rate and is approximated by **Equation 6.G2**.

$$D_c = \sqrt{\frac{4\dot{m}_m}{\pi \rho_v u_v}} \qquad (6.G2)$$

Where $\dot{m}_m$ represents the maximum vapor mass flow rate (in kg/s), ρ_v is the vapor density (in kg/m³), and u_v the maximum allowable superficial vapor velocity (in m/s). The latter parameter depends on the vapor and liquid densities and on the distance between trays (l_t, in m), following **Equation 6.G3**.

$$u_v = (-0.171 \, l_t^2 + 0.27 \, l_t - 0.047) \bullet \left(\frac{\rho_l - \rho_v}{\rho_v} \right)^{1/2} \tag{6.G3}$$

The demethanizer, deethanizer, and C2 splitter columns were all designed with a tray spacing of 0.5 meter, while the depropanizer columns had a tray spacing of 0.3 meter.

The approximated height of the distillation columns was comprised of vertical space needed for (i) the reboiler, (ii) the condenser, (iii) the skirt (column support), (iv) and the column itself. The reboiler and condenser contributions to the total height were taken as three times and two times the distance between trays (l_t), respectively [92]. Besides, the required height for the skirt was assumed to be 2 m. A tray efficiency of 80% was taken for all distillation columns in this work, as this is a common tray efficiency for distillation columns dealing with light hydrocarbons [101]. The final dimensions and characteristics of the various distillation columns in both processes are presented in **Table 6.G2**. Note that the C2 splitter column of the base case PCEC process requires more stages and a higher reflux ratio to obtain the purified ethylene product as compared to the C2 splitter of the SC and target case PCEC processes. This is attributed to the relatively low single-pass ethylene yield of the base case PCEC process (ca. 25% vs. ca. 50%), leading to a much lower ethylene concentration in the C2 splitter feed of the base case PCEC process. In contrast to the C3 and C4 impurities of the base case PCEC process, the C3 and C4 impurities in the target case PCEC process were not further purified using a depropanizer column, as the considered yield toward these heavies was much lower in the target case PCEC process compared to the base case PCEC process (see **Supporting Information 6.D2**).

The capital investment of the distillation columns encompassed the column steel costs and the tray costs. The column steel costs depended on the column dimensions and the wall thickness (**Supporting Information 6.H**). The deethanizer and depropanizer columns were equipped with standard sieve trays. By contrast, the demethanizer columns were constructed with valve trays, because of the low liquid holdup. Valve trays were also utilized in the C2 splitters to reduce the sensitivity to plant shutdown.

Table 6.G2: Distillation column specifications. Number of stages represent actual number of stages, reflux ratio is on molar basis.

ID	Description	Parameter	SC	PCEC base case	PCEC 50% case
	Single-pass ethylene yield	$Y_{ethylene}$	52%	25%	50%
Deetha	Deethanizer column	# of actual stages (-)	30	31	31
		Reflux ratio (-)	0.71	1.26	0.92
		Height (m)	19.5	19.0	19.0
		Diameter (m)	1.36	1.71	1.84
		Reboiler utility	LP steam	LP steam	LP steam
		Condenser utility	Refrigerant 1	Refrigerant 1	Refrigerant 1
		Column pressure (bar(a))	27	27	27
		Top temperature (°C)	-10	-2	-8
		Bottom temperature (°C)	83	99	32
Deprop	Depropanizer column	# of actual stages (-)	23	28	-
		Reflux ratio (-)	2.37	4.54	-
		Height (m)	10.4	11.9	-
		Diameter (m)	0.65	1.10	-
		Reboiler utility	MP steam	LP steam	-
		Condenser utility	Cooling water	Cooling water	-
		Column pressure (bar(a))	14	14	-
		Top temperature (°C)	30	33	-
		Bottom temperature (°C)	121	86	-
Demeth-1	Demethanizer column I	# of actual stages (-)	22	32	15
		Reflux ratio (-)	0.77	10.97	12.27
		Height (m)	15.5	20.5	11.0
		Diameter (m)	1.11	1.42	1.47
		Reboiler utility	LP steam	LP steam	LP steam
		Condenser utility	Refrigerant 4	Refrigerant 3	Refrigerant 3
		Column pressure (bar(a))	32	32	28
		Top temperature (°C)	-120	-98	-56
		Bottom temperature (°C)	-2	5	-6

C2-split	C2 splitter column			
	# of actual stages (-)	49	65	49
	Reflux ratio (-)	4.47	9.74	5.11
	Height (m)	29.0	37.0	29.0
	Diameter (m)	2.18	2.94	2.33
	Reboiler utility	LP steam	LP steam	LP steam
	Condenser utility	Refrigerant 2	Refrigerant 2	Refrigerant 2
	Column pressure (bar(a))	18	18	18
	Top temperature (°C)	-33	-33	-33
	Bottom temperature (°C)	-17	-12	-12
Demeth-2	Demethanizer column II			
	# of actual stages (-)	8	-	-
	Reflux ratio (-)	60.35	-	-
	Height (m)	8.5	-	-
	Diameter (m)	1.00	-	-
	Reboiler utility	LP steam	-	-
	Condenser utility	Refrigerant 2	-	-
	Column pressure (bar(a))	18	-	-
	Top temperature (°C)	-35	-	-
	Bottom temperature (°C)	-26	-	-

LP = low pressure, MP = medium pressure, HP = high pressure

6.G4. Caustic scrubber

A caustic scrubber was only required for the SC process to remove the carbon dioxide that was formed during steam reforming reactions inside the steam cracking furnace. A 22 wt.% aqueous sodium hydroxide solution [72] was used to scrub out the carbon dioxide from the steam cracking product mixture conform **Equation 6.G4**. Here, the required amount of sodium hydroxide solution was regulated based on the principle that the outlet sodium carbonate concentration should not exceed 4 wt.% [73], i.e. the $NaOH:CO_2$ mass ratio should be around 14:1.

$$2NaOH + CO_2 \leftrightarrows Na_2CO_3 + H_2O \qquad (6.G4)$$
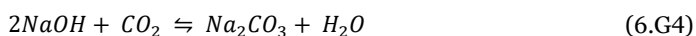
The carbon dioxide recovery was assumed to be 100% and the caustic scrubber was simulated in Aspen Plus as a component splitter. Besides, any possible mass exchange between hydrocarbons in the reactor effluent and the caustic solution were disregarded. Moreover, it was assumed that the carbon monoxide does not interact with the caustic agent and therefore ends up in the lights fraction of the distillation column sequence. The size of the caustic scrubber column was estimated based on an empirical correlation proposed by Neveril and coworkers [102]. The characteristics and dimensions of the caustic scrubber are shown in **Table 6.G3**.

Table 6.G3: Characteristics and dimensions of the caustic scrubber that is part of the SC process.

Parameter	Value	Unit
Temperature	30	°C
Pressure	17	bar(a)
Dirty gas flow	0.544	m³/s
Diameter	1.56	m
Height	2.53	m
Volume	4.84	m³
# of stages	5	

6.G5. Acetylene hydrogenation

In the SC process, an acetylene hydrogenation reactor was applied to selectively hydrogenate acetylene impurities. By doing this, the ethylene yield was maximized and the possible detrimental effects to the process induced by the acetylene were minimized [22]. The hydrogen needed for this hydrogenation step originated from the hydrogen-PSA column and was supplied in low concentrations (ca. 1 vol%). In this work, the acetylene hydrogenation was carried out in an adiabatic reactor operated at the deethanizer pressure of 27 bar(a) and at 70 °C [3]. A hydrogen-to-ethylene ratio of 1.8 was used to ensure complete conversion of acetylene [3], conform **Equation 6.G5**.

$$2C_2H_2 + 3H_2 \leftrightharpoons C_2H_4 + C_2H_6 \tag{6.G5}$$
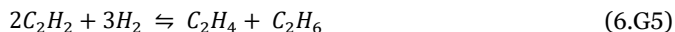
A Pd-Ag/Al$_2$O$_3$ catalyst was used to facilitate the acetylene hydrogenation reaction [103]. Industrially, this catalyst needs to be regenerated periodically to allow for continuous operation. However, regeneration of the acetylene hydrogenation catalyst, including the related costs and carbon dioxide emissions, were not included in this work. This was justified by the low acetylene concentration in the reactor effluent stream of the SC process (ca. 0.2 vol%). On the contrary, the investment costs for the acetylene hydrogenation reactor and the replacement costs of the acetylene hydrogenation catalyst were included in the CAPEX and OPEX calculations. The dimensions of the acetylene hydrogenation reactor (**Table 6.G4**) were estimated based on the work by Tian et al. [104], who designed their reactor for a similar operating pressure, temperature, conversion, and inlet composition. Their reactor dimensions were extrapolated to this work by keeping the reactor length constant to ensure an equal residence time, while changing the reactor diameter. The catalyst loading and properties were retrieved from Dehghani and coworkers [103]. The amount of catalyst needed was calculated from the extrapolated reactor volume and a catalyst density of 720 kg/m^3 [103], while assuming that 80% of the reactor volume was occupied by catalyst particles.

Table 6.G4: Characteristics and dimensions of the acetylene hydrogenation reactor of the SC process.

Parameter	Value	Unit
Inlet temperature	70	°C
Outlet temperature	91	°C
Pressure	27	bar(a)
Inlet volume flow rate	0.20	m^3/s
Mass fraction acetylene in feed	0.46	wt.%
Residence time	36	s
Acetylene conversion	100	%
Reactor diameter	1.55	m
Reactor height	4.88	m
Reactor volume	9.21	m^3
Catalyst	Pd-Ag/Al$_2$O$_3$	
Catalyst density	720	kg/m^3
Pd content	0.03	%
Ag content	0.18	%
Catalyst amount	5262	kg
Catalyst lifetime	4	yr

6.G6. Heat exchangers

The heat exchangers were dimensioned based on the area of heat exchange needed (*A* in m²), which was in turn calculated using **Equation 6.G6** [105].

$$Q = UA\Delta T_{LM} \tag{6.G6}$$

Where *U* represents the overall heat transfer coefficient (in W/m²K), which was estimated based on the nature of the streams involved in the heat exchange operation, and ΔT_{LM} represents the logarithmic mean temperature difference between the streams exchanged (in K), evaluated for counter-current flow. All heat exchangers were assumed to be shell-and-tube heat exchangers, which is a robust design for high pressure operations. Moreover, heat exchangers larger than 1,000 m² were split into multiple exchangers for industrial practicality. The summary of heat exchangers needed for the base case SC and PCEC processes are provided in **Table 6.G5** and **6.G6**, respectively. An explanation about the optimized heat exchanger design for the base case SC and PCEC processes applied in this work is available in **Supporting Information 6.J4**.

The heat exchanger network capital investment was estimated to be equal for the PCEC target case and the PCEC base case. A detailed heat exchanger design for the PCEC target case was considered to be beyond the scope of this work, as the heat exchanger costs were not the most dominant contributor to the total capital investment of the PCEC process (see **Table 6.2**). Nonetheless, the influence of heat integration within the PCEC target process on the corresponding energy usage, utility demand, and carbon emissions, was included by assuming that per heating/cooling step the same relative amount of energy could be integrated as for the PCEC base case process.

Table 6.G5: Heat exchangers of the SC process, see **supporting information 6.J4** for more details on the optimized heat exchanger network.

Identifier	ΔT_{LM} (°C)	Heat exchange area (m²)
HE1	45	25
HE2	18	95
HE3	141	31
HE4	174	23
HE5	250	41
HE6	24	85
HE7	19	1
HE8	112	43
HE9	88	23
HE10	61	15
HE11	202	1

HE12	195	12
HE13	202	35
HE14	134	14
HE15	16.	349
HE16	42	67
HE17	16	366
HE18	23	100
HE19	22	34
HE20	10	28
HE21	22	54
HE22	89	21
HE23	137	196
HE25	97	68
HE27	80	57
HE29	73	0.1
HE30	68	3

Table 6.G6: Heat exchangers of the PCEC process, see **supporting information 6.J4** for more details on the optimized heat exchanger network.

Identifier	ΔT_{LM} (°C)	Heat exchange area (m²)
HE1	11	446
HE2	210	75
HE3	78	28
HE4	157	20
HE5	61	10
HE6	183	14
HE7	110	43
HE8	15	195
HE9	173	14
HE10	197	3
HE11	96	67
HE12	19	1396
HE13	16	682
HE14	22	52
HE15	10	32
HE16	15	224

HE17	40	44
HE18	11	77
HE19	126	12
HE20	77	206
HE21	95	129
HE24	80	11
HE26	38	15
HE27	182	1135

6.G7. Flash vessels

The flash vessels were taken to be vertical vessels and were designed in such a way that the diameter is large enough to slow down the gas below the settling velocity. The latter was calculated using **Equation 6.G7** [93], where the liquid and vapor densities (ρ_L and ρ_v) were retrieved from the Aspen Plus simulations.

$$u_s = 0.07 \left(\frac{\rho_L - \rho_v}{\rho_v} \right)^{0.5} \tag{6.G7}$$

The flash vessel is generally equipped with a demister pad in case of small liquid fractions. In that case, the applied liquid flow velocity equals the settling flow velocity (i.e. $u = u_s$). If a demister pad is not utilized, then $u = 0.15\, u_s$ [93]. The diameter of the flash vessels (D_v) was computed based on the volumetric vapor flow rate (φ_v) and the applied flow velocity of the liquid, according to **Equation 6.G8**.

$$D_v = \sqrt{\frac{4\varphi_v}{\pi u}} \tag{6.G8}$$

The liquid volume inside the flash vessels (V_L) was calculated based on the volumetric liquid flow (φ_L) using **Equation 6.G9**, where the liquid residence time (τ_L) was assumed to be ten minutes.

$$V_L = \tau_L \varphi_L \tag{6.G9}$$

The height of the flash vessels was determined by adding sufficient length on top of the liquid level to ensure continuous gas flow, generally calculated by adding 0.4 m and 1.5 times D_v. The outcomes of the flash vessel design are shown in **Table 6.G7**.

Table 6.G7: Flash vessel characteristics.

Parameter	SC process		Base case PCEC				Target case PCEC				Unit
	F1	F2	F1	F2	F3	F4	F1	F2	F3	F4	
Temperature	30	33	30	47	30	30	30	45	30	30	°C
Pressure	2	17	5	27	20	50	5	27	20	50	bar(a)
Settling velocity, u_s	1.75	0.59	0.86	0.34	1.71	1.09	0.86	0.34	1.71	1.09	m/s
Demister pad	No	No	No	No	No	Yes	No	No	No	Yes	
Vessel diameter, D_v	4.8	2.8	4.5	2.9	1.0	0.3	3.6	2.3	0.9	0.3	m
Liquid height	0.070	0.002	0.014	0.002	0.004	0.004	0.013	0.000	0.004	0.004	m
Vessel height	7.7	4.6	7.2	4.8	2.0	2.0	5.7	3.9	1.9	2.0	m

6.H. Wall thickness

All flash vessels, distillation columns, adsorption columns, and the caustic scrubber were regarded as vertical cylindrical pressure vessels [91]. The corresponding costs of these columns thereby depend on the column steel costs, which in turn depend on the column dimensions and the required minimum wall thickness, the latter being calculated using **Equation 6.H1**.

$$t_{min} = \frac{P_i D_i}{2J \bullet f - P_i} \tag{6.H1}$$

Where t_{min} represents the minimum wall thickness (in mm), P_i the design pressure (in N/mm^2), D_i the internal diameter (in mm), J the joint factor, and f the material design stress (in N/mm^2). The design pressure was 10% above the operating pressure for safety reasons. Besides, a joint factor of 0.85 was taken. A material design stress of 89 N/mm^2 was used for all pressure vessels in this work [91]. The total wall thickness was computed by adding 2 mm thickness for corrosion allowance to the minimum wall thickness calculated with **Equation 6.H1**. The carbon steel density was estimated at 7840 kg/m^3 [106]. The rounded up wall thickness values of the process equipment of the SC, base case PCEC, and target case PCEC processes are summarized in **Table 6.H1**, **6.H2**, and **6.H3**, respectively.

Table 6.H1: Wall thickness (t) calculations of the flash vessels, distillation columns, adsorption columns, and the caustic scrubber of the SC process.

Identifier	Type	D_i (m)	$P_{operating}$ (bar(a))	P_i (bar(a))	t_{min} (mm)	t (mm)
F1	Flash vessel	4.8	2	2.2	7.0	10
F2	Flash vessel	2.8	17	18.7	35.1	38
Demeth-1	Distillation column	1.1	32	35.2	26.6	29
Deetha	Distillation column	1.4	27	29.7	27.4	30
Deprop	Distillation column	0.7	14	15.4	6.7	9
Demeth-2	Distillation column	1.0	32	35.2	23.9	26
C2-split	Distillation column	2.2	18	19.8	28.9	31
Caustic scrubber	Absorption column	1.6	17	18.7	19.6	22
Dryer	PSA* column	0.6	32	35.2	13.1	16
H-PSA	PSA* column	1.6	32	35.2	37.9	40
Ac-hydro	Acetylene hydrogenation reactor	1.6	27	29.7	31.2	34

PSA = pressure swing adsorption

Table 6.H2: Wall thickness (*t*) calculations of the flash vessels, distillation columns, and adsorption column of the base case PCEC process.

Identifier	Type	Diameter (m)	$P_{operating}$ (bar(a))	P_i (bar(a))	t_{min} (mm)	t (mm)
F1	Flash vessel	4.5	5	5.5	16.6	19
F2	Flash vessel	2.9	27	29.7	58.9	61
F3	Flash vessel	1.0	20	22	14.8	17
F4	Flash vessel	0.3	50	55	11.6	14
Deetha	Distillation column	1.7	27	29.7	34.4	37
Demeth	Distillation column	1.4	32	35.2	33.9	36
Deprop	Distillation column	1.1	14	15.4	11.3	14
C2-split	Distillation column	2.9	18	19.8	39.1	42
Dryer	PSA* column	0.7	27	29.7	13.8	16

PSA = pressure swing adsorption

Table 6.H3: Wall thickness (*t*) calculations of the flash vessels, distillation columns, and adsorption column of the target case PCEC process.

Identifier	Type	Diameter (m)	$P_{operating}$ (bar(a))	P_i (bar(a))	t_{min} (mm)	t (mm)
F1	Flash vessel	3.6	5	5.5	13.0	15
F2	Flash vessel	2.3	27	29.7	46.4	49
F3	Flash vessel	0.9	20	22	13.2	16
F4	Flash vessel	0.3	50	55	10.4	13
Deetha	Distillation column	1.8	27	29.7	37.0	39
Demeth	Distillation column	1.5	28	30.8	30.7	33
C2-split	Distillation column	2.3	18	19.8	31.0	33
Dryer	PSA* column	0.7	27	29.7	13.8	16

PSA = pressure swing adsorption

6.J. Heat integration

The heat integration measures implemented in the different processes were related to (i) combustion of carbon deposits, (ii) combustion of the C1-rich off-gas streams (**6.J1**), (iii) resistive Joule heating (**6.J2**), and (iv) heat exchange between hot and cold process streams (**6.J3**). The combustion of carbon deposits was included in the heat integration by considering continuous and complete combustion of the coronene model compound. The energy generated in this way was used for steam generation using a steam boiler efficiency of 81% [107]. The heat exchange between hot and cold process streams was accomplished by means of a pinch point analysis using the FI²EPI software. In this

analysis, a minimum temperature gradient of 10 °C between the hot and cold fluids was imposed. Besides, only streams with a duty of more than 1 MW were, in general, included. The only exception comprised of duties of less than 1 MW that had to be covered by one of the expensive refrigerants. Moreover, it was assumed that heat integration with the reactor blocks was practically not possible. A detailed heat exchanger network was designed for the SC and base case PCEC processes. The heat exchanger network capital investment was estimated to be equal for the PCEC target case and the PCEC base case. A detailed heat exchanger design for the PCEC target case was considered to be beyond the scope of this work, as the heat exchanger costs were not the most dominant contributor to the total capital investment of the PCEC process (see **Table 6.2**). Nonetheless, the influence of heat integration within the PCEC target process on the corresponding energy usage, utility demand, and carbon emissions, was included by assuming that per heating/cooling step the same relative amount of energy could be integrated as for the PCEC base case process.

6.J1. Fuel gas

The first demethanizer column of the SC process and the demethanizer of the PCEC processes yielded a C1-rich off-gas stream that was combusted to generate a fraction of the energy needed to operate the steam cracking furnace and PCEC reactor, respectively. The size of the fuel gas stream was smaller for the PCEC processes in comparison to the SC process (**Table 6.J1**), due to the *in situ* hydrogen separation in the PCEC membrane reactor. The lower heating values included in the calculations were based on a pure methane stream (**Table 6.J1**) [108].

Table 6.J1: Fuel gas streams in the SC and PCEC base case processes.

Parameter	SC	PCEC base case	PCEC target case	Unit
Fuel gas production	0.427	0.200	0.321	kg/s
Lower heating value	50	50	50	MJ/kg
Available energy	21.56	10.01	16.04	MW
Furnace efficiency	90	90	90	%
Net duty	19.40	9.01	14.43	MW

6.J2. Resistive Joule heating

The hydrogen permeation flow is coupled with the electrical current through **Equation 6.J1** [27].

$$I = \frac{n\dot{m}F}{M_{H_2}} \tag{6.J1}$$

Where n represents the number of electrons transported per mole of H_2 permeated (i.e. 2), $\dot{m}$ the permeation mass flow rate of H_2 (in kg/s), F the Faraday constant (96,485.3

C/mol), and M_{H2} the molar weight of H_2. The cell voltage of a proton conducting electrochemical cell can be described by [27]:

$$E_{cell} = E_{OCV} + IR \tag{6.J2}$$

In which the open-circuit voltage (E_{OCV}) is defined by **Equation 6.J3**.

$$E_{OCV} = \frac{R_{gas}T}{nF} \ln\left(\frac{p_{H2,out}}{p_{H2,in}}\right) \tag{6.J3}$$

The resistance of protons across a PCEC is commonly presented as a function of the area specific resistance (*ASR*):

$$R = \frac{ASR}{A_{mem}} \tag{6.J4}$$

The *ASR* of PCEC systems based on BZCY electrolytes was estimated at 0.4 $\Omega.cm^2$ [15]. Besides, the total required PCEC membrane area (A_{mem}) was ca. 3,500 m^2 and ca. 2,800 for the base case and target case PCEC processes, respectively (see **Section 6.3.4**). The power of the electrochemical cell can then be evaluated using **Equation 6.J5**.

$$P_{cell} = E_{cell}I = E_{OCV}I + I^2R \tag{6.J5}$$

The first term in **Equation 6.J5** defines the power for reversible electrochemical H_2 compression, whilst the second term is related to the cell resistance. The latter energy is released as thermal energy in the PCEC membrane reactor and is referred to as resistive Joule heat (see **Table 6.J2**).

Table 6.J2: Results of the PCEC membrane reactor calculations for (i) the PCEC base case considering a single-pass ethylene yield of ca. 25%, and (ii) the PCEC target case considering a single-pass ethylene yield of 50%.

Parameter:	Description:	PCEC base case	PCEC target case	Unit:
$Y_{ethylene}$	Single-pass ethylene yield	25	50	[%]
R_{gas}	Universal gas constant	8.314	8.314	[J/mol.K]
T	Operational temperature	550	550	[°C]
		823	823	[K]
n	Number of electrons transferred	2	2	[-]
F	Faraday constant	96,485.3	96,485.3	[C/mol]
p_{out}	Permeate side pressure PCEC	20	20	[bara]
$y_{H2,out}$	Molar fraction H_2 on permeate side	0.997	0.997	[-]
$p_{H2,out}$	H_2 partial pressure permeate side	19.93	19.93	[bara]

p_{in}	Feed side pressure PCEC	5	5	[bara]
$y_{H2,in}$	Molar fraction H_2 on feed side	0.131	0.131	[-]
$p_{H2,in}$	H_2 partial pressure feed side	0.655	0.655	[bara]
E_{OCV}	Open-circuit voltage	0.120	0.120	[V]
M_{H2}	Molar weight H_2	2.016	2.016	[g/mol]
		$2.016 \cdot 10^{-3}$	$2.016 \cdot 10^{-3}$	[kg/mol]
$\dot{m}$	Mass flow rate of permeating H_2	1.14	0.92	[ton/hr]
		0.317	0.255	[kg/s]
I	Current	$3.3 \cdot 10^7$	$2.5 \cdot 10^7$	[A]
ASR	Area specific resistance	0.4	0.4	[$\Omega.cm^2$]
A_{mem}	Membrane area	3,500	2,800	[m^2]
		$3.5 \cdot 10^7$	$2.8 \cdot 10^7$	[cm^2]
R	Cell resistance	$1.13 \cdot 10^{-8}$	$1.43 \cdot 10^{-8}$	[Ω]
$P_{compression}$	Power of electrochemical compression	4.2	3.0	[MW]
P_{Joule}	Power related to resistive heating	12.3	8.9	[MW]
P_{cell}	Total cell power	16.5	11.9	[MW]
E_{cell}	Total cell voltage	0.527	0.358	[V]

6.J3. Heat exchange between process streams

An overview of the integrated hot and cold process streams is provided in **Table 6.J3** for the SC process and in **Table 6.J4** for the base case PCEC process. The corresponding heat exchanger networks of the SC and base case PCEC processes are schematically presented in **Figure 6.J1** and **6.J2**, respectively.

Table 6.J3: Heat exchanger network of the SC process. Green colored cells indicate heat exchangers in which part of the energy duty was covered by utilities, blue colored cells indicate heat exchangers in which the total energy duty was covered by utilities.

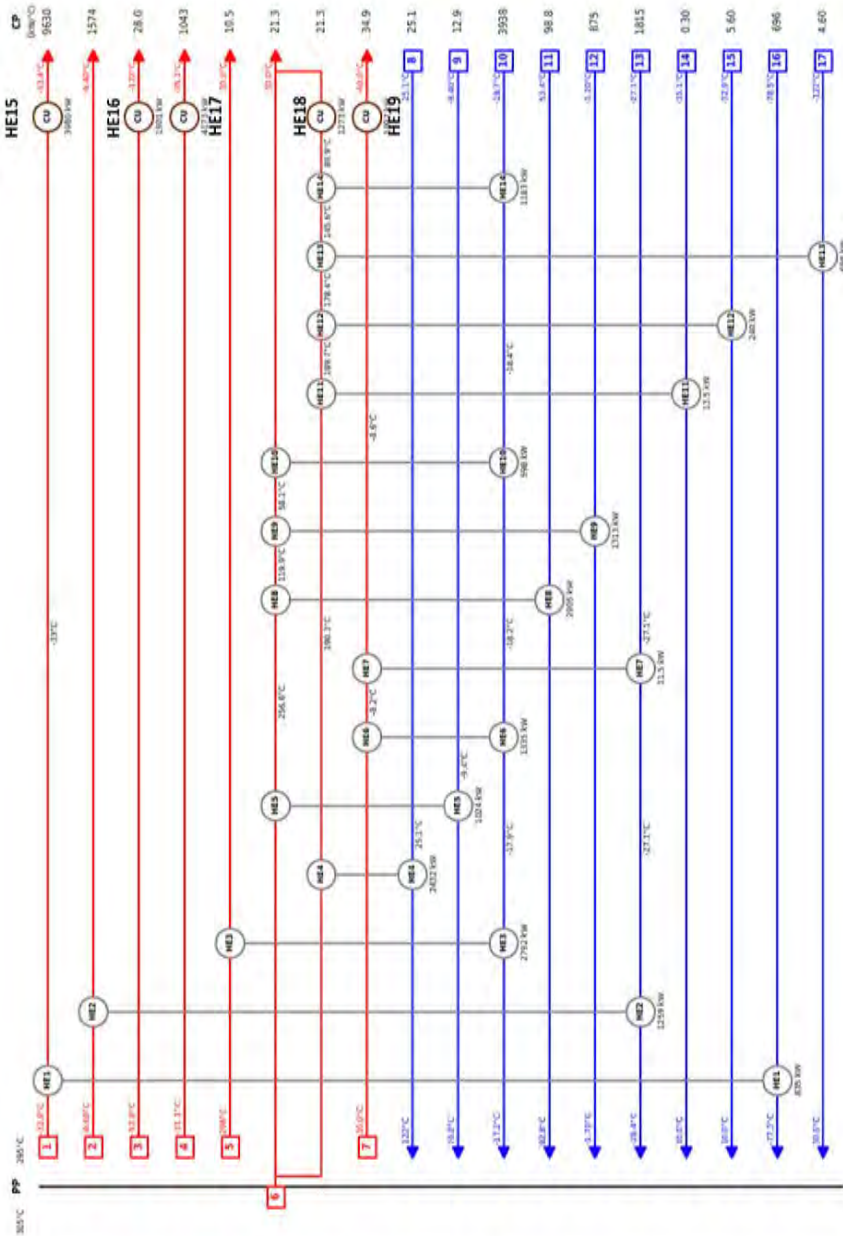| Identifier	Integrated heat?	Hot fluid	Cold fluid	U (kW/m².°C)	$T_{h,in}$ (°C)	$T_{h,out}$ (°C)	$T_{c,in}$ (°C)	$T_{c,out}$ (°C)	Q (MW)
HE1	Yes	C2 splitter condenser	H13	0.75	-32.9	-33.0	-78.5	-77.3	0.84
HE2	Yes	Deethanizer condenser	Demethanizer-2 reboiler	0.75	-8.6	-9.4	-27.1	-26.4	1.26
HE3	Yes	H17	C2 splitter reboiler	0.65	295.9	30.0	-17.9	-17.2	2.79
HE4	Yes	H5	H14	0.65	304.8	190.3	25.1	122.0	2.43
HE5	Yes	H5	H9	0.10	304.8	256.6	-9.4	70.0	1.02
HE6	Yes	H6	C2 splitter reboiler	0.65	30.0	-8.3	-18.3	-17.9	1.33
HE7	Yes	H6	Demethanizer-2 reboiler	0.65	-8.3	-8.6	-27.1	-27.1	0.01
HE8	Yes	H5	Deethanizer reboiler	0.65	256.6	119.9	53.4	82.8	2.90
HE9	Yes	H5	Demethanizer-1 reboiler	0.65	119.9	58.1	-3.2	-1.7	1.31
HE10	Yes	H5	C2 splitter reboiler	0.65	58.1	30.0	-18.4	-18.3	0.60
HE11	Yes	H5	H11	0.10	190.3	189.7	-35.1	10.0	0.01
HE12	Yes	H5	H12	0.10	189.7	178.4	-32.9	10.0	0.24
HE13	Yes	H5	H7	0.10	178.4	145.6	-121.7	30.0	0.70
HE14	Yes	H5	C2 splitter reboiler	0.65	145.6	89.9	-18.7	-18.4	1.18
HE15	Yes	C2 splitter condenser	Refrigerant 2	0.70	-33.0	-33.4	-50.0	-49.0	3.98
HE16	Yes	Demethanizer-1 condenser	Refrigerant 4	0.70	-53.8	-121.7	-140.0	-135.0	1.90
HE17	Yes	Demethanizer-2 condenser	Refrigerant 2	0.70	-31.1	-35.1	-50.0	-49.0	4.17
HE18	Yes	H5	Cooling water	0.55	89.9	30.0	20.0	45.0	1.27
HE19	Yes	H6	Refrigerant 2	1.50	-8.6	-40.0	-50.0	-49.0	1.10
HE20	No	Depropanizer condenser	Cooling tower water	0.65	33.9	30.3	20.0	25.0	0.17
HE21	No	H10	Cooling tower water	0.55	85.2	30.0	20.0	45.0	0.64
HE22	No	H16	Generated steam	0.65	830.1	295.8	294.5	295.5	1.11
HE23	No	H4	Generated steam	0.65	850.0	304.8	294.5	295.5	17.25
HE24	No	Fired heat	Furnace heat exchanger	0.10	1000.0	876.0	850.0	850.5	18.62
HE25	No	HP steam	H1	0.80	295.5	294.5	-54.3	285.0	5.22
HE26	No	Fired heat	H15	0.10	1000.0	400.0	133.5	620.0	0.99
HE27	No	HP steam	H2	1.50	295.5	294.5	25.0	285.0	6.72
HE28	No	Fired heat	H3	0.10	1000.0	400.0	285.0	850.0	17.39
HE29	No	LP steam	H8	0.25	125.0	124.0	30.2	70.0	0.01
HE30	No	MP steam	Depropanizer reboiler	0.95	185.0	184.0	111.9	121.0	0.22

Figure 6.J1: Heat exchanger network of the SC process.

Table 6.J4: Heat exchanger network of the base case PCEC process. Green colored cells indicate heat exchangers in which part of the energy duty was covered by utilities, blue colored cells indicate heat exchangers in which the total energy duty was covered by utilities.

Identifier	Integrated heat?	Hot fluid	Cold fluid	U (kW/m².°C)	$T_{h,in}$ (°C)	$T_{h,out}$ (°C)	$T_{c,in}$ (°C)	$T_{c,out}$ (°C)	Q (MW)
HE1	Yes	Deethanizer condenser	C2 splitter reboiler	0.75	0.3	-1.9	-11.9	-11.7	3.67
HE2	Yes	H11	H12	0.20	550.0	119.1	25.2	152.7	2.15
HE3	Yes	H11	C2 splitter reboiler	0.20	119.1	30.0	-11.9	-11.9	0.45
HE4	Yes	H15	Demethanizer reboiler	0.65	302.6	73.2	3.8	4.6	2.06
HE5	Yes	H15	C2 splitter reboiler	0.65	73.2	30.0	-12.0	-11.9	0.39
HE6	Yes	H5	Demethanizer reboiler	0.65	305.1	255.0	92.2	99.4	1.70
HE7	Yes	H5	Deethanizer reboiler	0.65	255.0	165.9	92.2	99.4	3.03
HE8	Yes	H6	C2 splitter reboiler	0.65	10.3	-2.1	-12.1	-12.0	1.94
HE9	Yes	H5	H8	0.10	165.9	158.9	-33.0	10.0	0.24
HE10	Yes	H5	H7	0.10	158.9	157.0	-97.5	10.0	0.06
HE11	Yes	H5	C2 splitter reboiler	0.65	157.0	35.0	-12.3	-12.1	4.15
HE12	Yes	C2 splitter condenser	H9	0.10	-33.0	-33.0	-52.6	-51.0	2.63
HE13	Yes	C2 splitter condenser	Refrigerant 2	0.70	-33.0	-33.0	-50.0	-49.0	7.87
HE14	Yes	Deethanizer condenser	Refrigerant 3	0.70	-1.9	-2.4	-25.0	-24.0	0.82
HE15	Yes	H5	Cooling water	0.55	35.0	30.0	20.0	25.0	0.17
HE16	Yes	H6	Refrigerant 3	0.60	-2.1	-15.0	-25.0	-24.0	2.02
HE17	Yes	Demethanizer condenser	Refrigerant 1	0.70	-65.2	-97.5	-125.0	-120.0	1.21
HE18	No	Depropanizer condenser	Cooling water	0.65	34.1	33.5	20.0	25.0	0.56
HE19	No	H14	Generated steam	0.65	829.7	302.6	294.5	295.5	0.98
HE20	No	H4	Generated steam	0.65	550.0	305.1	294.5	295.5	10.17
HE21	No	H1	HP steam	0.80	295.5	294.5	-44.9	285.0	9.65
HE22	No	Fired heat	H10	0.10	1000.0	400.0	21.0	550.0	0.04
HE23	No	Fired heat	H13	0.10	1000.0	400.0	156.9	620.0	0.83
HE24	No	HP steam	H2	1.50	295.5	294.5	25.2	285.0	1.28
HE25	No	Fired heat	H3	0.10	1000.0	400.0	285.0	550.0	11.77
HE26	No	LP steam	Depropanizer reboiler	0.95	125.0	124.0	85.9	86.2	0.55
HE27	No	Fired heat	PCEC reactor heat exchanger	0.10	1000.0	600.0	550.0	550.5	20.62

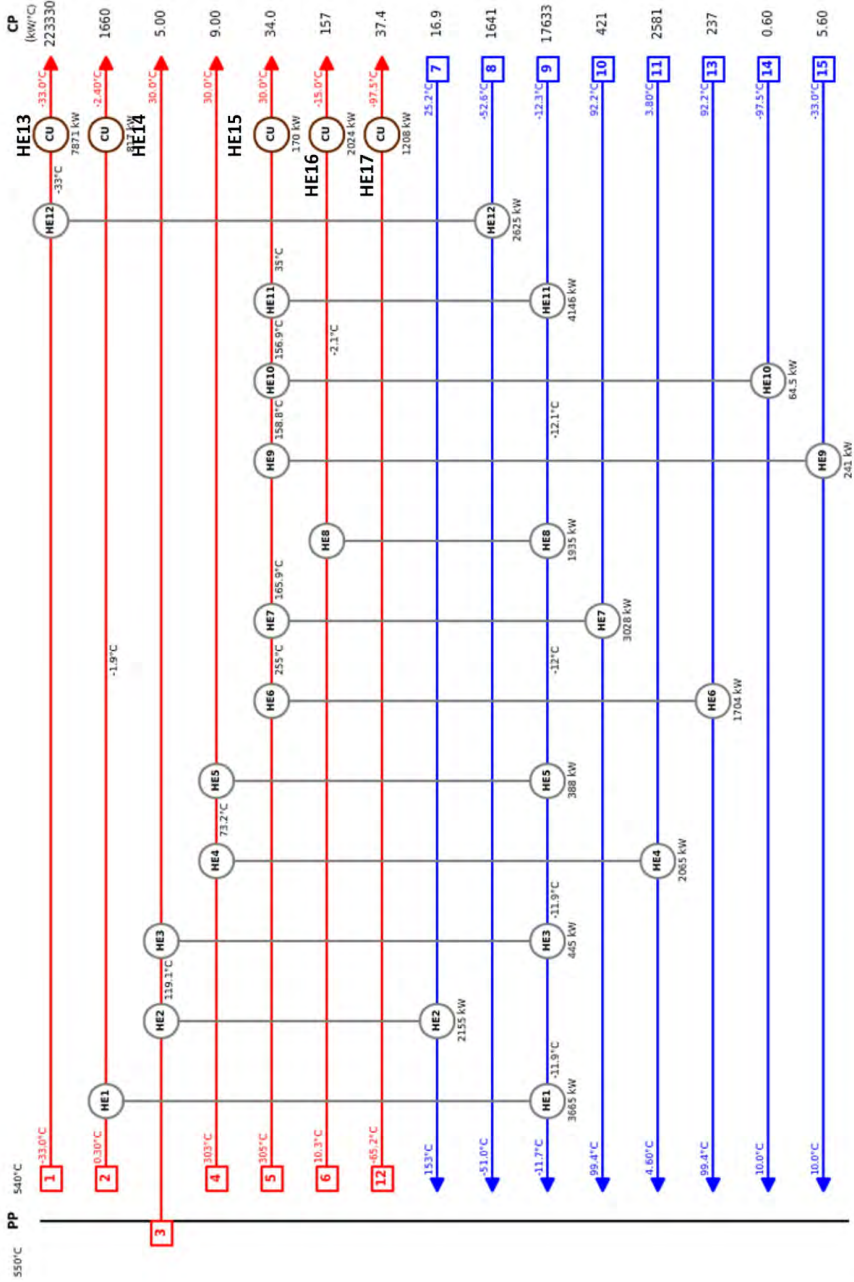**Figure 6.J2**: Heat exchanger network of the base case PCEC process.

6.K. Purchased equipment costs

The purchased equipment costs of the different types of process equipment were calculated here in the same manner as in **Chapter 5** (see **Section 5.L** for more details). The outcomes of the purchased equipment cost calculations are presented in **Table 6.K1** for the ethane SC process and in **Table 6.K2** for the base case and target case PCEC processes. In addition, a summary of the total investment is provided in **Table 6.K3**.

Table 6.K1: Results of the purchased equipment costs calculations of the ethane SC process. Prices valid for the U.S. Gulf Coast, 2010.

Identifier	Type	Size	Units	Design	Equipment costs (kUSD)	Multiplication factor*	ISBL** (kUSD)
F1	Flash vessel	14,874	Shell mass, kg	Vertical vessel, no demister pad	131	3.2	420
F2	Flash vessel	19,709	Shell mass, kg	Vertical vessel, no demister pad	164	3.2	524
DEMETH-1	Distillation column	14,473	Shell mass, kg	Vertical vessel	129	3.2	411
	Trays	1.11	Diameter, m	Sieve tray – 22 stages	15	3.2	47
DEETHA	Distillation column	22,949	Shell mass, kg	Vertical vessel	185	3.2	591
	Trays	1.36	Diameter, m	Sieve tray – 30 stages	23	3.2	74
DEPROP	Distillation column	1,729	Shell mass, kg	Vertical vessel	31	3.2	99
	Trays	0.65	Diameter, m	Sieve tray – 23 stages	5	3.2	15
DEMETH-2	Distillation column	6,438	Shell mass, kg	Vertical vessel	70	3.2	225
	Trays	0.97	Diameter, m	Valve tray – 8 stages	3	3.2	10
C2-SPLIT	Distillation column	54,211	Shell mass, kg	Vertical vessel	371	3.2	1,187
	Trays	2.18	Diameter, m	Valve tray – 47 stages	83	3.2	264
Caustic scrubber	Absorption column	3,519	Shell mass, kg	Vertical vessel	47	3.2	150
	Trays	1.56	Diameter, m	Sieve tray – 5 stages	5	3.2	16
Dryer	PSA column	640	Shell mass, kg	Vertical vessel	20	3.2	64
	Adsorbent	314	Weight, kg	Zeolite-3A			
H-PSA	PSA column	13,250	Shell mass, kg	Vertical vessel	120	3.2	384
	Adsorbent	7,798	Weight, kg	Activated carbon			
Furnace	Furnace 1	10.28	Duty, MW	Box furnace	759	3.74	2,838
	Furnace 2	10.28	Duty, MW	Box furnace	759	3.74	2,838
	Furnace 3	10.28	Duty, MW	Box furnace	759	3.74	2,838
	Furnace 4	10.28	Duty, MW	Box furnace	759	3.74	2,838
AC-HYDRO	Reactor	7,360	Shell mass, kg	Shell mass, kg	77	3.2	248
	Catalyst	5,262	Weight, kg	Weight, kg			
C1	Compressor	2,883	Driver power, kW	Multistage turbo compressor	2,962	3.2	9,478
	Driver	2,883	Driver power, kW	Explosion proof motor	249	3.2	797
C2	Compressor	884	Driver power, kW	Multistage turbo compressor	1,752	3.2	5,605

	Driver	884	Driver power, kW	Explosion proof motor	122	3.2	390
C3	Compressor	17,758	Flow, m³/h	Multistage axial flow blower	148	3.2	472
	Driver	534	Driver power, kW	Explosion proof motor	90	3.2	288
C4	Compressor	171	Driver power, kW	Multistage reciprocating	388	3.2	1,241
	Driver	171	Driver power, kW	Explosion proof motor	45	3.2	143
C5	Compressor	17	Driver power, kW	Multistage reciprocating	283	3.2	905
	Driver	17	Driver power, kW	Explosion proof motor	11	3.2	34
P1	Pump	0.43	Flow, L/s	Radial – multistage	8	3.2	26
	Driver	0.58	Power, kW	Explosion proof motor			
P2	Pump	0.04	Flow, L/s	Positive displacement – multistage	8	3.2	26
	Driver	0.20	Power, kW	Explosion proof motor			
P3	Pump	0.91	Flow, L/s	Radial – single stage	8	3.2	26
	Driver	0.31	Power, kW	Explosion proof motor			
HE1	Heat exchanger	25	Area, m²	Shell & tube, counter-current, U-tube	31	3.2	98
HE2	Heat exchanger	95	Area, m²	Shell & tube, counter-current, U-tube	41	3.2	130
HE3	Heat exchanger	30	Area, m²	Shell & tube, counter-current, U-tube	31	3.2	100
HE4	Heat exchanger	23	Area, m²	Shell & tube, counter-current, U-tube	30	3.2	97
HE5	Heat exchanger	41	Area, m²	Shell & tube, counter-current, U-tube	33	3.2	105
HE6	Heat exchanger	85	Area, m²	Shell & tube, counter-current, U-tube	39	3.2	125
HE7	Heat exchanger	1	Area, m²	Shell & tube, counter-current, U-tube	28	3.2	90
HE8	Heat exchanger	43	Area, m²	Shell & tube, counter-current, U-tube	33	3.2	105
HE9	Heat exchanger	23	Area, m²	Shell & tube, counter-current, U-tube	30	3.2	97
HE10	Heat exchanger	15	Area, m²	Shell & tube, counter-current, U-tube	29	3.2	94

HE11	Heat exchanger	1	Area, m²	Shell & tube, counter-current, U-tube	28	3.2	90
HE12	Heat exchanger	12	Area, m²	Shell & tube, counter-current, U-tube	29	3.2	93
HE13	Heat exchanger	35	Area, m²	Shell & tube, counter-current, U-tube	32	3.2	102
HE14	Heat exchanger	14	Area, m²	Shell & tube, counter-current, U-tube	29	3.2	94
HE15	Heat exchanger	349	Area, m²	Shell & tube, counter-current, U-tube	89	3.2	284
HE16	Heat exchanger	67	Area, m²	Shell & tube, counter-current, U-tube	36	3.2	116
HE17	Heat exchanger	365	Area, m²	Shell & tube, counter-current, U-tube	92	3.2	295
HE18	Heat exchanger	100	Area, m²	Shell & tube, counter-current, U-tube	42	3.2	133
HE19	Heat exchanger	34	Area, m²	Shell & tube, counter-current, U-tube	32	3.2	102
HE20	Heat exchanger	27	Area, m²	Shell & tube, counter-current, U-tube	31	3.2	99
HE21	Heat exchanger	54	Area, m²	Shell & tube, counter-current, U-tube	35	3.2	110
HE22	Heat exchanger	21	Area, m²	Shell & tube, counter-current, U-tube	30	3.2	96
HE23	Heat exchanger	196	Area, m²	Shell & tube, counter-current, U-tube	59	3.2	187
HE25	Heat exchanger	68	Area, m²	Shell & tube, counter-current, U-tube	37	3.2	117
HE27	Heat exchanger	57	Area, m²	Shell & tube, counter-current, U-tube	35	3.2	112
HE29	Heat exchanger	1	Area, m²	Shell & tube, counter-current, U-tube	28	3.2	90
HE30	Heat exchanger	3	Area, m²	Shell & tube, counter-current, U-tube	28	3.2	90
						Total ISBL:	***38.9 MMUSD***

The multiplication factor in this table encompasses cost compensation factors for equipment erection, piping, instrumentation and control, electrical, civil, structures and buildings, and lagging and paint.

**ISBL = inside battery limit*

Table 6.K2: Results of the purchased equipment costs calculations of the base case and target case PCEC processes. Prices valid for the U.S. Gulf Coast, 2010.

Identifier	Type	Size	Units	Design	Equipment costs (kUSD)	Multiplication factor*	ISBL** (kUSD) base case	ISBL** (kUSD) target case ($Y_{ethylene}$ = 50%)
F1	Flash vessel	25,101	Shell mass, kg	Vertical vessel, no demister pad	198	3.2	635	362
F2	Flash vessel	35,032	Shell mass, kg	Vertical vessel, no demister pad	260	3.2	830	483
F3	Flash vessel	1,295	Shell mass, kg	Vertical vessel, no demister pad	27	3.2	85	76
F4	Flash vessel	271	Shell mass, kg	Vertical vessel, with demister pad	16	3.2	50	48
DEETHA	Distillation column	37,439	Shell mass, kg	Vertical vessel	274	3.2	877	976
	Trays	1.71	Diameter, m	Sieve tray – 29 stages	34	3.2	108	123
DEMETH	Distillation column	32,162	Shell mass, kg	Vertical vessel	242	3.2	775	471
	Trays	1.42	Diameter, m	Valve tray – 32 stages	25	3.2	80	35
DEPROP	Distillation column	5,656	Shell mass, kg	Vertical vessel	64	3.2	206	0
	Trays	1.10	Diameter, m	Sieve tray – 28 stages	15	3.2	47	0
C2-SPLIT	Distillation column	139,967	Shell mass, kg	Vertical vessel	816	3.2	2,612	2,014
	Trays	2.94	Diameter, m	Valve tray – 65 stages	203	3.2	648	512
DRYER	PSA column	1,053	Shell mass, kg	Vertical vessel	24	3.2	77	77
	Adsorbent	609.24	Weight, kg	Zeolite-3A				
PCEC REACTOR	Modular membrane reactor	81	# of modules	Modular design	8,238	2.05	16,887	13,343
					3,295	2.05	3,295	2,604
C1	Compressor	2,380	Driver power, kW	Multistage turbo compressor	2,703	3.2	8,650	6,975
	Driver	2,380	Driver power, kW	Explosion proof motor	222	3.2	710	534
C2	Compressor	25,832	Flow, m³/h	Multistage axial flow blower	198	3.2	632	612

Tag	Item	Value	Parameter	Description				
	Driver	0.78	Driver power, kW	Explosion proof motor	1	3.2	2	2
C3	Compressor	147.53	Driver power, kW	Single stage reciprocating	374	3.2	1,198	910
	Driver	147.53	Driver power, kW	Explosion proof motor	41	3.2	131	36
C4	Compressor	528.95	Driver power, kW	Multistage reciprocating	558	3.2	1,785	1,643
	Driver	528.95	Driver power, kW	Explosion proof motor	89	3.2	286	251
C5	Compressor	38.06	Driver power, kW	Multistage reciprocating	301	3.2	964	946
	Driver	38.06	Driver power, kW	Explosion proof motor	18	3.2	56	49
P1	Pump	0.43	Flow, L/s	Radial	8	3.2	26	26
	Driver	0.58	Power, kW	Explosion proof motor		3.2	26	26
P2	Pump	0.01	Flow, L/s	Positive displacement	8	3.2	26	26
	Driver	0.07	Power, kW	Explosion proof motor		3.2	26	26
P3	Pump	0.79	Flow, L/s	Radial	8	3.2	4	4
	Driver	1.07	Power, kW	Explosion proof motor	1	3.2	4	4
HE1	Heat exchanger	446	Area, m²	Shell & tube, counter-current, U-tube	110	3.2	351	351
HE2	Heat exchanger	75	Area, m²	Shell & tube, counter-current, U-tube	38	3.2	120	120
HE3	Heat exchanger	28	Area, m²	Shell & tube, counter-current, U-tube	31	3.2	99	99
HE4	Heat exchanger	20	Area, m²	Shell & tube, counter-current, U-tube	30	3.2	96	96
HE5	Heat exchanger	10	Area, m²	Shell & tube, counter-current, U-tube	29	3.2	92	92
HE6	Heat exchanger	14	Area, m²	Shell & tube, counter-current, U-tube	29	3.2	94	94
HE7	Heat exchanger	43	Area, m²	Shell & tube, counter-current, U-tube	33	3.2	105	105
HE8	Heat exchanger	195	Area, m²	Shell & tube, counter-current, U-tube	58	3.2	186	186
HE9	Heat exchanger	14	Area, m²	Shell & tube, counter-current, U-tube	29	3.2	94	94
HE10	Heat exchanger	3	Area, m²	Shell & tube, counter-current, U-tube	28	3.2	90	90

HE11	Heat exchanger	67	Area, m²	Shell & tube, counter-current, U-tube	36	3.2	116	116
HE12-1	Heat exchanger	698	Area, m²	Shell & tube, counter-current, U-tube	168	3.2	537	537
HE12-2	Heat exchanger	698	Area, m²	Shell & tube, counter-current, U-tube	168	3.2	537	537
HE13	Heat exchanger	637	Area, m²	Shell & tube, counter-current, U-tube	153	3.2	490	490
HE14	Heat exchanger	52	Area, m²	Shell & tube, counter-current, U-tube	34	3.2	110	110
HE15	Heat exchanger	32	Area, m²	Shell & tube, counter-current, U-tube	32	3.2	101	101
HE16	Heat exchanger	224	Area, m²	Shell & tube, counter-current, U-tube	64	3.2	204	204
HE17	Heat exchanger	44	Area, m²	Shell & tube, counter-current, U-tube	33	3.2	106	106
HE18	Heat exchanger	77	Area, m²	Shell & tube, counter-current, U-tube	38	3.2	121	121
HE19	Heat exchanger	12	Area, m²	Shell & tube, counter-current, U-tube	29	3.2	93	93
HE20	Heat exchanger	206	Area, m²	Shell & tube, counter-current, U-tube	60	3.2	193	193
HE21	Heat exchanger	129	Area, m²	Shell & tube, counter-current, U-tube	46	3.2	149	149
HE24	Heat exchanger	11	Area, m²	Shell & tube, counter-current, U-tube	29	3.2	93	93
HE26	Heat exchanger	15	Area, m²	Shell & tube, counter-current, U-tube	29	3.2	94	94
						Total ISBL:	**46.0 MMUSD**	**37.5 MMUSD**

The multiplication factor in this table encompasses cost compensation factors for equipment erection, piping, instrumentation and control, electrical, civil, structures and buildings, and lagging and paint.

**ISBL = inside battery limit*

Table 6.K3: Summary of total investment calculations.

	SC base case	PCEC base case ($Y_{ethylene}$ = 25%)	PCEC case $Y_{ethylene}$ = 50%
Total ISBL* U.S. Gulf Coast, 2010 (**Table 6.K1** and **6.K2**)	38.9 MMUSD	46.0 MMUSD	37.5 MMUSD
CEPCI 2010	532.9	532.9	532.9
CEPCI 2023	813.0	813.0	813.0
CEPCI ratio 2023/2010	1.53	1.53	1.53
Location factor SE Asia/U.S. Gulf Coast	1.12	1.12	1.12
ISBL 2023, Asia-Pacific region	66.3 MMUSD	76.8 MMUSD	62.6 MMUSD
OSBL** (=40% of ISBL)	26.5 MMUSD	30.7 MMUSD	25.0 MMUSD
Design and engineering (=30% of ISBL + OSBL)	27.9 MMUSD	32.3 MMUSD	26.3 MMUSD
Contingency (=10% of ISBL + OSBL)	9.3 MMUSD	10.8 MMUSD	8.8 MMUSD
Total fixed capital cost	*130.0 MMUSD*	*150.5 MMUSD*	*122.7 MMUSD*
Working capital (=15% of ISBL+OSBL)	13.9 MMUSD	16.1 MMUSD	13.1 MMUSD
Total investment cost	*144.0 MMUSD*	*166.7 MMUSD*	*135.8 MMUSD*

ISBL = inside battery limit

**OSBL = outside battery limit*

6.L. OPEX calculations

The operating expenditures (OPEX) of the different processes (**Table 6.L1**) comprised of the variable production costs and the fixed production costs and were calculated based on the method proposed by Towler and Sinnott [44].

6.L1. Variable production costs

The raw material costs were computed using the fresh feed streams retrieved from the Aspen Plus simulations and contained costs for ethane, water, and caustics. The air needed for regeneration was assumed to be available for free. Besides, the costs for utilities and consumables were determined based on information from the heat integration network and the equipment design. The following assumptions were made in the calculations:

- The cooling water price was estimated at 0.378 USD/m^3 [109]. When considering a water density of 998 kg/m^3, this results in a mass-based price of 0.379 USD/tons.

- The price of pure sodium hydroxide needed as a feedstock of the caustic scrubber was estimated at 280 USD/tons [110]. Consequently, the price of the 22 wt.% aqueous caustic water solution was defined at 61.80 USD/tons.
- The costs for effluent disposal were approximated at 2% of the OSBL [44] and covered costs for flue gas cleaning, spent caustic disposal, and wastewater treatment.

6.L2. Fixed production costs

The following assumptions were made in the calculation of the fixed production costs:

- The labor costs were based on five shifts, with five operators per shift, and an annual salary of 56,000 USD for both processes [44]. Besides, the labor costs related to supervision were approximated at 25% of the operator labor costs. Moreover, a direct salary overhead of 40% of the summed operator and supervision labor costs was included.
- Process maintenance costs were estimated at 3% of the ISBL plant costs, and insurance, rent of land, and local property tax costs at 1% of ISBL+OSBL.
- An interest rate of 2% was taken, valid for December 2022 [111].

6.L3. Revenues

In addition to ethylene, the produced and isolated hydrogen was considered as a valuable product (**Table 6.L2**). Besides, the depropanizer product (C3 top and C4 bottoms) streams were sold as products. The prices of these C3 and C4 side streams were estimated at 50% of the pure component prices. Moreover, the SC process contained an ethylene-rich off-gas stream originating from the second demethanizer column that was also sold at 50% of the pure component value. Lastly, the water byproduct (**Table 6.L2**) defines the respective cooled and condensed water streams that were cosupplied as steam to the ethane SC furnace and PCEC reactor. The flue gas from regeneration operations was considered to be valueless.

Table 6.L1: Summary of the operating expenditures of the various ethane steam cracking (SC) and PCEC-assisted ethane dehydrogenation cases.

Variable production costs		SC		PCEC base case			PCEC target case		
		Fossil	Full electric	Fossil	E_{th}	Full electric	Fossil	E_{th}	Full electric
Raw materials	USD/ton								
Ethane	270	37,595	37,595	43,607	43,607	43,607	37,352	37,352	37,352
Water	0.38	36	36	14	14	14	10	10	10
Caustics	62	78	78	-	-	-	-	-	-
Utilities	USD/GJ								
HP steam	6	2,226	2,226	2,039	2,039	2,039	1,186	1,186	1,186
MP steam	6	41	41	-	-	-	-	-	-
LP steam	6	0.4	0.4	102	102	102	-	-	-
Fired heat	5	5,941	-	3,366	1,211	-	2,339	841	-
Cooling water	0.35	23	23	8	8	8	1	1	1
Refrigerant 3	28	-	-	2,538	2,538	2,538	1,179	1,179	1,179
Refrigerant 2	36	10,630	10,630	9,046	9,046	9,046	4,755	4,755	4,755
Refrigerant 1	86	-	-	3,275	3,275	3,275	5,638	5,638	5,638
Refrigerant 4	129	7,732	7,732	-	-	-	-	-	-
Electricity	17	2,368	21,832	10,410	14,796	21,439	10,714	13,738	17,730
Generated HP steam	-6	-2,773	-2,773	-1,684	-1,684	-1,684	-989	-989	-989
Generated fuel gas	-5	-2,708	-2,708	-1,279	-1,279	-1,279	-2,086	-2,086	-2,086
Consumables	USD/kg								
Zeolite-3A	1.50	0.1	0.1	0.2	0.2	0.2	0.2	0.2	0.2
Activated carbon	1.62	3	3	-	-	-	-	-	-
Pd-Ag/Al$_2$O$_3$:									
Pd	39,600	26	26	-	-	-	-	-	-
Ag	773	3	3	-	-	-	-	-	-
Al$_2$O$_3$	1.43	3	3	-	-	-	-	-	-
Membrane	3,215	-	-	9,141	9,141	9,141	7,222	7,222	7,222
Effluent disposal (=2% of OSBL)		531	531	614	614	614	501	501	501
Carbon tax (=0 in base case)		0	0	0	0	0	0	0	0
Variable cost of production (VCOP)		*61,755*	*75,278*	*81,199*	*83,428*	*88,861*	*67,822*	*69,349*	*72,500*

Fixed production costs

Labor cost

Labor wages (LW)	1,400	1,400	1,400	1,400	1,400	1,400	1,400	1,400
Supervision + management (SMC, =25% of LW)	350	350	350	350	350	350	350	350
Direct salary overhead costs (DSOC, =40% of LW+SMC)	700	700	700	700	700	700	700	700
Other fixed production costs								
Maintenance costs (=3% of ISBL)	1,990	1,990	2,304	2,304	2,304	1,878	1,878	1,878
Rent of land (=1% of ISBL+OSBL)	929	929	1,075	1,075	1,075	876	876	876
Local property tax (=1% of ISBL+OSBL)	929	929	1,075	1,075	1,075	876	876	876
Insurance costs (=1% of ISBL+OSBL)	929	929	1,075	1,075	1,075	876	876	876
Interest payments (=2% of working capital)	279	279	323	323	323	263	263	263
General and administrative costs (=65% of LW+SMC+DSOC)	1,593	1,593	1,593	1,593	1,593	1,593	1,593	1,593
Royalties (=0.5% of VCOP)	309	309	406	406	406	339	339	339
Fixed cost of production (FCOP)	*9,407*	*9,407*	*10,301*	*10,301*	*10,301*	*9,152*	*9,152*	*9,152*
Cash cost of production (CCOP)	**71.2 MMUSD/yr**	**84.7 MMUSD/yr**	**91.5 MMUSD/yr**	**93.7 MMUSD/yr**	**99.2 MMUSD/yr**	**77.0 MMUSD/yr**	**78.5 MMUSD/yr**	**81.7 MMUSD/yr**

Table 6.L2: Profitability assessment of the various ethane steam cracking (SC) and PCEC-assisted ethane dehydrogenation cases.

Key products	USD/ton	SC		PCEC base case			PCEC target case		
		Fossil	Full electric	Fossil	E_{th}	Full electric	Fossil	E_{th}	Full electric
Ethylene	950	95,000	95,000	94,999	94,999	94,999	94,999	94,999	94,999
Hydrogen	1,600	10,568	10,568	16,049	16,049	16,049	12,955	12,955	12,955
By-products									
C3-stream	495	3,179	3,179	7,302	7,302	7,302	-	-	-
C4-stream	544	3,839	3,839	21,384	21,384	21,384	12,922	12,922	12,922
Ethylene off-gas	525	2,919	2,919	-	-	-	-	-	-
Water	0.38	36	36	14	14	14	14	14	14
Total revenues:		*115.5 MMUSD/yr*	*115.5 MMUSD/yr*	*139.7 MMUSD/yr*	*139.7 MMUSD/yr*	*139.7 MMUSD/yr*	*120.9 MMUSD/yr*	*120.9 MMUSD/yr*	*120.9 MMUSD/yr*
Cash cost of production (CCOP, **Table 6.L1**)		71.2 MMUSD/yr	84.7 MMUSD/yr	91.5 MMUSD/yr	93.7 MMUSD/yr	99.2 MMUSD/yr	77.0 MMUSD/yr	78.5 MMUSD/yr	81.7 MMUSD/yr
Revenues - CCOP		*44.4 MMUSD/yr*	*30.9 MMUSD/yr*	*48.2 MMUSD/yr*	*46.0 MMUSD/yr*	*40.6 MMUSD/yr*	*43.9 MMUSD/yr*	*42.4 MMUSD/yr*	*39.2 MMUSD/yr*
Depreciation:									
Estimated plant lifetime (yr)		15	15	15	15	15	15	15	15
Depreciable cost (=total fixed capital cost)		130.0 MMUSD*	130.0 MMUSD*	150.5 MMUSD*	150.5 MMUSD*	150.5 MMUSD*	122.7 MMUSD*	122.7 MMUSD*	122.7 MMUSD*
Yearly depreciation		8.7 MMUSD/yr	8.7 MMUSD/yr	10.0 MMUSD/yr	10.0 MMUSD/yr	10.0 MMUSD/yr	8.2 MMUSD/yr	8.2 MMUSD/yr	8.2 MMUSD/yr
Taxation:									
Corporate income tax (=18% of gross profit – yearly depreciation)		6.4 MMUSD/yr	4.0 MMUSD/yr	6.9 MMUSD/yr	6.5 MMUSD/yr	5.5 MMUSD/yr	6.4 MMUSD/yr	6.2 MMUSD/yr	5.6 MMUSD/yr
Net profit		*29.3 MMUSD/yr*	*18.2 MMUSD/yr*	*31.3 MMUSD/yr*	*29.5 MMUSD/yr*	*25.1 MMUSD/yr*	*29.3 MMUSD/yr*	*28.1 MMUSD/yr*	*25.5 MMUSD/yr*
Total fixed capital cost (MMUSD, **Table 6.K3**)		130.0 MMUSD	130.0 MMUSD	150.5 MMUSD	150.5 MMUSD	150.5 MMUSD	122.7 MMUSD	122.7 MMUSD	122.7 MMUSD
Payback period (yr)		**4.4**	**7.2**	**4.8**	**5.1**	**6.0**	**4.2**	**4.4**	**4.8**
ROI		**20.3%**	**12.6%**	**18.8%**	**17.7%**	**15.0%**	**21.6%**	**20.7%**	**18.8%**

*Note that the capital investment of the electrically heated SC and PCEC processes is assumed to be equal to the capital investment of the fossil fuel heated alternatives.

6.M. Utilities

The distribution of utility duties for the ethane SC process and the PCEC-assisted processes after heat integration are presented in **Figure 6.M1**. The net utility duty for the SC process was 10.4 MJ/kg$_{ethylene}$, while it was 16.7 MJ/kg$_{ethylene}$ and 11.4 MJ/kg$_{ethylene}$ for the base case (ca. 25% ethylene yield) and target case (50% ethylene yield) PCEC processes, respectively. The negative duties in **Figure 6.M1** represent the utilities available within the processes that can be used for heat integration, which consisted of fuel gas incineration, high pressure (HP) steam generation, and Joule heating (PCEC process). The negligible medium (MP) steam duties were omitted from **Figure 6.M1**. For the SC process, the amount of HP steam generated was even larger than the amount of HP steam needed. The excess steam was sold in this situation. Besides, for the SC process the fuel gas incineration covered ca. 50% of the fired heat duty, whilst for the base case PCEC process the combination of fuel gas incineration and resistive Joule heat covered ca. 60% of the fired heat duty. Remarkably, in the target case PCEC process the combination of Joule heat and fuel gas incineration covered more than 90% of the fired heat demand (**Figure 6.M1**). In contrast to the SC and base case PCEC processes, the limited amount of C3's are not further purified in the target case PCEC process (**Supporting Information 6.O1**). Instead, the C3's are incinerated, resulting in a larger flue gas stream in the target case PCEC process.
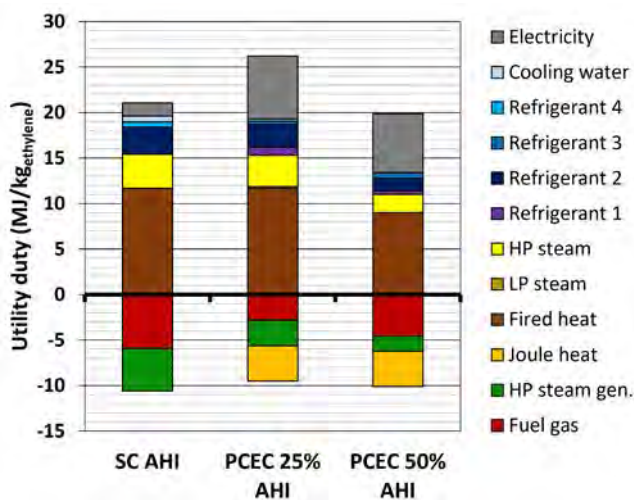
Figure 6.M1: Distribution of utility duties for the ethane steam cracking (SC) and PCEC-assisted processes after heat integration. HP = high pressure, LP = low pressure.

The distribution of the utility costs for the ethane SC process and the PCEC processes after heat integration is shown in **Figure 6.M2**. The total utility costs were about one third higher for the PCEC base case (ca. 25% ethylene yield) as compared to the SC base case. While the cost for heating and cooling utilities were similar for both base cases, the

electricity costs were substantially higher for the PCEC base case (**Figure 6.M2**), due to the electricity demand of the PCEC membrane reactor. Interestingly, the total utility costs of the PCEC target case (50% ethylene yield) were about 10% lower as compared to the SC process (**Figure 6.M2**). Even though the electricity costs were considerably higher for the PCEC target case, the heating and cooling utility costs of the PCEC target case were substantially lower as compared to the SC process. This was caused by the lower heating and cooling demand of the PCEC process, as lower reaction temperatures could be applied in the PCEC process (T = 550 °C) relative to the SC process (T = 850 °C) for similar ethylene product yields. **Figure 6.M2** shows that the costs for refrigerants were a major contributor to the total utility costs in all three process cases. In addition, electricity costs heavily affected the utility costs of the PCEC process, because of the electricity demand for electrochemical hydrogen purification and compression inside the PCEC membrane reactor. The unit operations that were most strongly affecting the utility costs were the demethanizer columns (refrigerants) in both processes and the PCEC reactor (electricity).
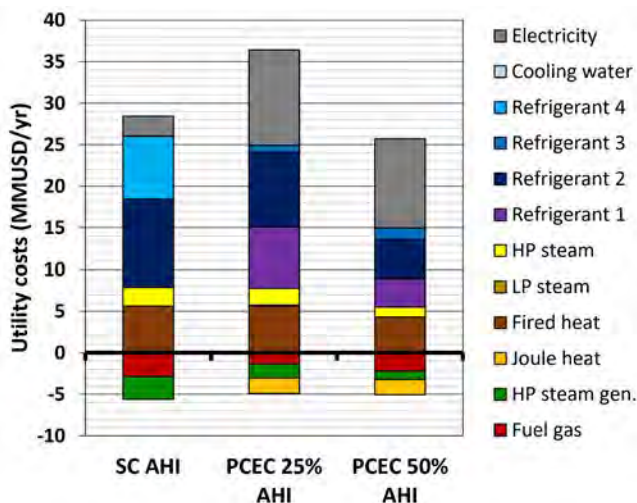
Figure 6.M2: Distribution of utility costs for the ethane steam cracking (SC) and PCEC-assisted processes after heat integration. HP = high pressure, LP = low pressure.

6.N. Carbon footprint

The environmental impact assessment was based on the emissions of the greenhouse gas carbon dioxide. Five different contributors were included, related to (i) natural gas combustion, (ii) fuel gas combustion, (iii) coke combustion, (iv) electricity generation, and (v) steam generation. The natural gas (NG) contribution was determined by using the fired heat duty retrieved from the Aspen Plus process simulations and a carbon intensity of natural gas consumption of 136.1 kg_{CO2}/GJ_{NG} [112]. Besides, the carbon dioxide emissions related to fuel gas combustion were calculated using the available fuel gas energy duties reported in **Table 6.J1**. The coronene coke model compound was considered to be

completely oxidized in quantifying the corresponding carbon footprint. The emission factor associated with generation of Asia-Pacific average grid electricity was 532.1 g_{CO2}/kWh [46]. Besides, the emission factor related to the generation of fully renewable electricity corrected for the carbon dioxide emission related to the construction of windmills and solar panels and was estimated to be ca. 50 g_{CO2}/kWh [47,48]. Lastly, the carbon dioxide emissions from steam generation were calculated using a natural gas consumption of 1.29 GJ per GJ of steam utility, using the carbon intensity of natural gas burning of 136.1 kg_{CO2}/GJ_{NG} [112]. The required amount of natural gas needed for the generation of 1 GJ of steam utility was the result of assuming a steam boiler efficiency of 81% [107]. The carbon footprint of the base case ethane SC and PCEC-assisted ethane NODH processes (**Table 6.N1**) and the target case PCEC process (**Table 6.N2**), were all determined for situations in which either Asia-Pacific grid electricity or fully renewable electricity was utilized.

Table 6.N1: Carbon dioxide emissions of the base case ethane steam cracking (SC) and PCEC-assisted ethane dehydrogenation processes. In case of fossil operation, all reaction and (pre)heating steps were carried out by natural gas burning, whereas they were operated in an electrical way for the full electric cases. In case of operation at thermoneutral voltage (E_{th}), the PCEC reactor was operated electrically, while the preheating steps were operated via natural gas burning.

$t_{CO2}/t_{ethylene}$	SC fossil		SC full electric		PCEC 25% fossil		PCEC 25% E_{th}		PCEC 25% full electric	
	Grid	Green	Grid	Green	Grid	Green	Grid	Green	Grid	Green
Natural gas combustion	0.96	0.96	0.00	0.00	0.62	0.62	0.22	0.22	0.00	0.00
Fuel gas combustion	0.32	0.32	0.00	0.00	0.17	0.17	0.17	0.17	0.00	0.00
Coke combustion	0.01	0.01	0.01	0.01	0.01	0.01	0.01	0.01	0.01	0.01
Electricity generation	0.21	0.02	1.94	0.18	0.92	0.09	1.31	0.12	1.90	0.18
Steam generation	0.00	0.00	0.00	0.00	0.14	0.14	0.14	0.14	0.14	0.14
Total:	*1.51*	*1.31*	*1.95*	*0.20*	*1.86*	*1.02*	*1.85*	*0.66*	*2.05*	*0.33*

Table 6.N2: Carbon dioxide emissions of the target case PCEC-assisted ethane dehydrogenation process. In case of fossil operation, all reaction and (pre)heating steps were carried out by natural gas burning, whereas they were operated in an electrical way for the full electric cases. In case of operation at thermoneutral voltage (E_{th}), the PCEC reactor was operated electrically, while the preheating steps were operated via natural gas burning.

$t_{CO2}/t_{ethylene}$	PCEC 50% fossil		PCEC 50% E_{th}		PCEC 50% full electric	
	Grid	Green	Grid	Green	Grid	Green
Natural gas combustion	0.31	0.31	0.00	0.00	0.00	0.00
Fuel gas combustion	0.17	0.17	0.17	0.17	0.00	0.00
Coke combustion	0.01	0.01	0.01	0.01	0.01	0.01
Electricity generation	0.95	0.09	1.22	0.11	1.57	0.15
Steam generation	0.06	0.06	0.06	0.06	0.06	0.06
Total:	*1.50*	*0.64*	*1.46*	*0.35*	*1.64*	*0.22*

6.O. Sensitivity analysis

6.O1. Ethane-to-ethylene yield

The impact of varying ethane-to-ethylene fractional conversion on the specific energy input (*SEI*), comprising of all heating, reboiling, and compression duties, of the PCEC process is shown in **Figure 6.O1**. It is noted here that the net ethylene yield differed from the fractional ethane-to-ethylene conversion, as part of the produced ethylene was consecutively converted to butylene, propylene, and methane (see **Supporting Information 6.D2**). At the PCEC reactor feed side operating conditions of 5 bar(a) and 550 °C, the ethane dehydrogenation equilibrium conversion could be increased from ca. 5% to ca. 60% by removing hydrogen from the reaction zone (see **Supporting Information 6.B**). The impact of changing the ethylene yield on the process economics and the required energy input of the PCEC process was therefore investigated across an ethylene yield varying from 25 up to 60%. In the reactor performance data adopted from Wu et al. [26], 23% of the formed ethylene was consecutively converted to butylene, resulting in a poor ethylene selectivity. Since ethylene was the targeted product, the ethylene-to-butylene yield was adjusted to 2.3% in the ethylene yield variations. The fractional conversions of all side reactions were remained constant, implying that the byproduct selectivity changed with varying ethylene yield.
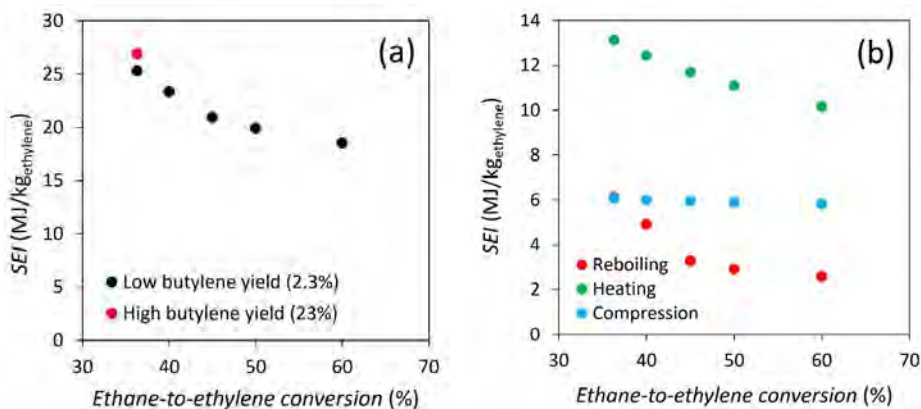
Figure 6.O1: (a) Total specific energy input (*SEI*) as a function of the ethane-to-ethylene conversion for the PCEC-assisted process, and (b) the corresponding distribution in *SEI* for the lower butylene yield data from (a).

Upon reducing the ethylene-to-butylene yield, the *SEI* of the PCEC process reduced from 26.9 (base case) to 25.3 MJ/kg$_{ethylene}$ (see **Figure 6.O1a**). For the lower butylene yield, a larger fraction of the reactor energy input was used for the production of ethylene, as less energy was wasted for butylene formation. Moreover, the ethane feedstock was more efficiently used for the production of ethylene in that case, due to a higher ethylene selectivity, leading to a smaller ethane recycle stream and, hence, smaller process streams.

These two causes ensured a lower *SEI* when reducing the butylene yield. The biggest gain in energy usage was obtained when increasing the ethane-to-ethylene conversion from ca. 36% (25.3 MJ/kg$_{ethylene}$) to ca. 50% (19.9 MJ/kg$_{ethylene}$), as shown in **Figure 6.O1a**. Energy savings were more marginal upon further increasing the ethane-to-ethylene conversion. A minimum amount of energy was needed for operating the dehydrogenation reaction, heating, and mass circulation, regardless of the ethylene yield. Moreover, for high ethylene yields (>70%) the formation of carbon deposits is anticipated to be boosted, as carbon deposition is believed to originate from olefin oligomerization [56]. We therefore envision that an ethane-to-ethylene conversion of ca. 50% represents the optimal balance between energy savings and minimized consecutive reactions. **Figure 6.O1b** shows that particularly reboiling and heating duties were reduced when increasing the ethylene yield.

6.O2. Electricity price

The influence of the electricity price on the return on investment of the ethane SC and base case PCEC-assisted ethane dehydrogenation processes is illustrated in **Figure 6.O2**. Since the base case PCEC process consumed more electricity than the SC process for operating the PCEC reactor, its profitability depended more strongly on the electricity price than the profitability of the SC process. A grid electricity price of 60 USD/MWh was used, corresponding to a price around which the base case SC and PCEC processes were equally profitable (**Figure 6.O2**). However, green electricity is often yet cheaper than grid electricity [41]. **Figure 6.O2** shows that the electricity price should be below ca. 50 USD/MWh to make the base case PCEC process more profitable than the SC process.
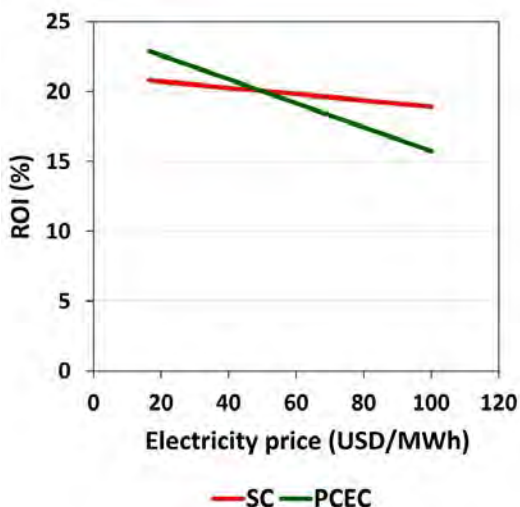
Figure 6.O2: Influence of electricity price on the return on investment (*ROI*) of the ethane steam cracking and base case PCEC-assisted ethane dehydrogenation processes.

6.O3. Carbon intensity of electricity

The carbon dioxide emission results shown in **Figure 6.5** highlighted that renewable electricity needed to be utilized in all electrified ethylene production processes to possibly outcompete conventional fossil fuel based SC. For this reason, the influence of the carbon intensity of the electricity on the total CO_2 emissions of the various base case SC and PCEC process cases was investigated (see **Figure 6.O3**). In the reference situation, a carbon intensity of 532.1 g_{CO_2}/kWh was applied, which is typical for the Asia-Pacific grid electricity [46]. The full electric process cases had the lowest carbon footprint for an electricity carbon intensity of less than 200 g_{CO_2}/kWh, whilst the fossil fuel heated processes were more sustainable above 350 g_{CO_2}/kWh (**Figure 6.O3**). Interestingly, for an electricity carbon intensity between 200-350 g_{CO_2}/kWh, the base case PCEC process operated at thermoneutral voltage was the most sustainable alternative (**Figure 6.O3**).
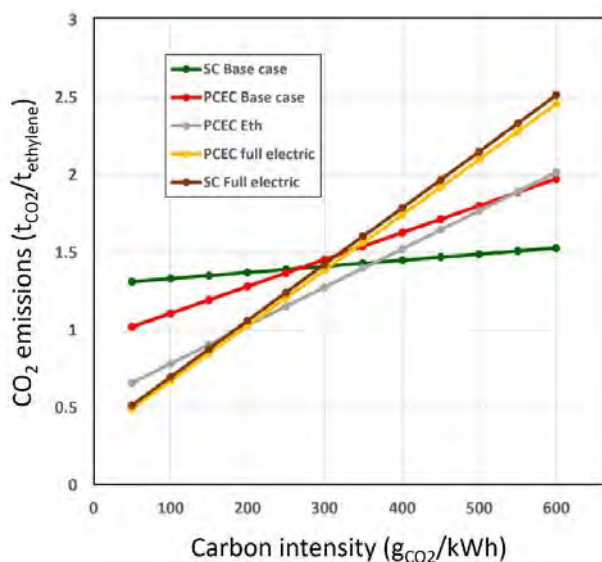
Figure 6.O3: Influence of the carbon intensity of the utilized electricity on the total carbon dioxide emissions of the various base case SC (ca. 52% ethylene yield) and base case PCEC (ca. 25% ethylene yield) processes.

6.O4. Current density

The influence of the applied current density in the PCEC reactors on the profitability of the base case PCEC process is shown in **Figure 6.O4**. Upon increasing the current density, the coupled proton flux through the PCEC membrane increases. As a result, a smaller membrane area is required for a given hydrogen permeation rate, resulting in lower membrane reactor costs. However, when increasing the current density while keeping the area specific resistance constant, then the applied voltage needs to increase, leading to a

higher energy consumption. **Figure 6.O4** shows that the *ROI* increases substantially when moving from a current density of 0.5 A/cm² to 1.0 A/cm², whilst it increases more marginally when moving further to 1.5 A/cm². At the same time, the energy consumption of the PCEC reactor increases linearly from 0.5 A/cm² to 1.5 A/cm² for a given area specific resistance. The optimal current density was therefore selected to be 1.0 A/cm², as this combines a high annual profit to a high return on investment and a moderate energy consumption of the PCEC reactor.
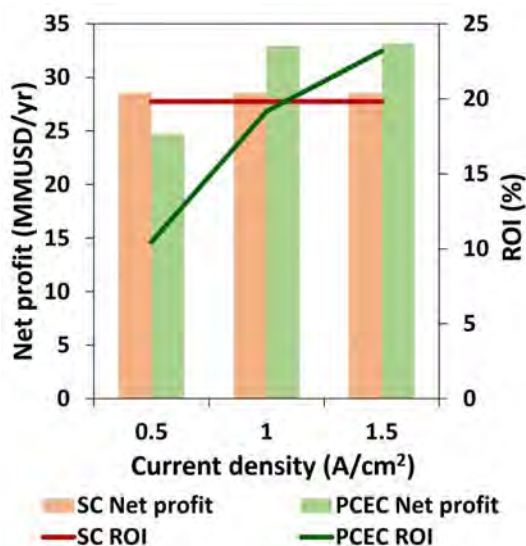
Figure 6.O4: Influence of the current density applied in the PCEC reactors on the net annual profit and the return on investment (*ROI*) of the base case PCEC-assisted ethane dehydrogenation process.

6.O5. Electricity price and area specific resistance

The electricity price was varied in combination with variations in the area specific resistance of the PCEC to get a better view of the cost dynamics of the PCEC reactor (**Figure 6.O5**). In general, when the area specific resistance increases, a higher voltage needs to be applied to attain the same current density. Consequently, a higher energy input in terms of electricity is needed. This particularly had an effect on the process economics in terms of return on investment (*ROI*) for higher electricity prices (**Figure 6.O5**). Interestingly, the profitability of the base case PCEC process became independent of the area specific resistance for an electricity price of 16 USD/MWh. At this value, the electricity was equally expensive as the natural gas price. The result in **Figure 6.O5** also implies that operation at thermoneutral voltage leads to lower *ROI* values compared to the base case scenario.
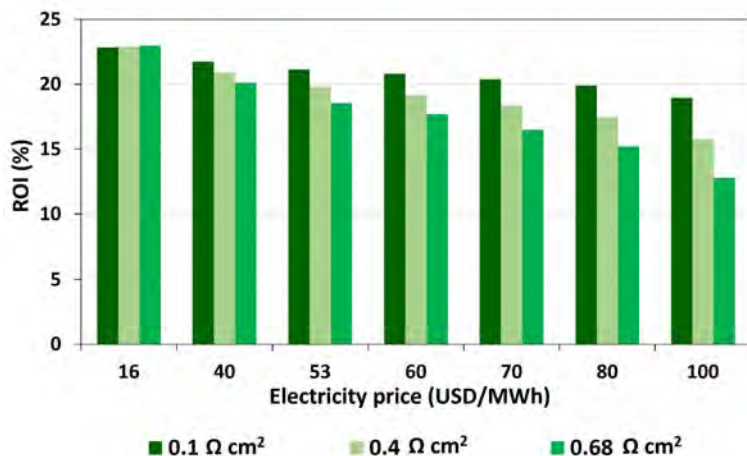
Figure 6.O5: Influence of the electricity price and area specific resistance (*ASR*) on the return on investment (*ROI*) of the base case PCEC-assisted ethane dehydrogenation process.

6.P. Profitability assessment

The profitability of the ethane SC and PCEC processes was further evaluated by determining the return on investment (*ROI*) and the payback period (**Table 6.P2**). The *ROI* was calculated using the net annual profit and the total capital investment (**Equation 6.P1**), while the payback period equaled the ratio between the total depreciable capital, i.e. the total fixed capital investment, and the net annual profit (**Equation 6.P2**) [113]. In this calculation, the gross annual profit was determined by subtracting the yearly depreciation and the cash cost of production (*CCOP*) from the total revenues (see **Table 6.P1**). Subsequently, the gross annual profit was converted into a net annual profit by using a corporate income tax of 18% for the Asia-Pacific region (**Table 6.P1**) [45]. The example calculation of the profitability assessment in **Table 6.P1** included revenues obtained from selling C3 and C4 byproducts.

$$ROI = \frac{Net\ annual\ profit}{Total\ capital\ investment} \cdot 100\% \qquad (6.P1)$$

$$Payback\ period = \frac{Total\ depreciable\ capital}{Net\ annual\ profit} \qquad (6.P2)$$

Table 6.P1: Gross annual profit and net annual profit calculations for the fossil heated process cases, including revenues obtained from selling C3 and C4 byproducts.

Parameter:	SC:	PCEC (25%):	PCEC (50%):	Unit:	Note:
Total revenues	115.5	139.7	120.9	MMUSD/yr	
Cash cost of production (CCOP)	71.2	91.5	77.0	MMUSD/yr	
Revenues – CCOP	*44.4*	*48.2*	*43.9*	*MMUSD/yr*	
Total depreciable capital	130.0	150.5	122.7	MMUSD	Equals the total fixed capital investment
Estimated plant lifetime	15	15	15	yr	
Yearly depreciation	8.7	10.0	8.2	MMUSD/yr	
Taxable income = gross profit	*35.7*	*38.2*	*35.7*	*MMUSD/yr*	
Corporate income tax	*6.4*	*6.9*	*6.4*	*MMUSD/yr*	18% of taxable income [45]
Net annual profit	**29.3**	**31.3**	**29.3**	**MMUSD/yr**	Equals gross profit minus corporate income tax

Table 6.P2: Calculation of the return on investment (*ROI*) and the payback period.

Parameter:	SC:	PCEC (25%):	PCEC (50%):	Unit:	Note:
Net annual profit	29.3	31.3	29.3	MMUSD/yr	**Table 6.P1**
Total fixed capital cost	144.0	166.7	135.8	MMUSD	**Table 6.K3**
ROI	20.3	18.8	21.6	%	**Equation 6.P1**
Total depreciable capital	130.0	150.5	122.7	MMUSD	**Table 6.K3**
Payback period	4.4	4.8	4.2	yr	**Equation 6.P2**

Chapter 7

Conclusion and outlook

Summary

The main conclusions are presented in this chapter by answering the research questions stated in **Chapter 1**. A distinction is made between an evaluation of the technological feasibility and an evaluation of the techno-economic feasibility of applying ceramic membranes in light alkane dehydrogenation processes to produce light olefins. Based on the outcomes of these evaluations, recommendations are proposed for future research in the field of ceramic membrane-assisted alkane dehydrogenation and for industrialization of this technology. Moreover, an industrial perspective is outlined for membrane-assisted alkane dehydrogenation in relation to conventional and possible green alternative olefin production processes.

7.1. Introduction

This dissertation aims to assess the technological and techno-economic feasibility of applying ceramic membranes in light olefin production processes via non-oxidative dehydrogenation (NODH) of light alkanes. The questions central to this dissertation, as stated in **Chapter 1**, were:

- Which technological hurdles need to be overcome to operate ceramic membrane reactors for light alkane NODH?
- Is ceramic membrane-assisted alkane NODH a feasible industrial alternative to produce ethylene and propylene?

The technological feasibility of ceramic membrane-assisted alkane dehydrogenation is evaluated in **Section 7.2**, whilst its techno-economic viability is evaluated in **Section 7.3**. Lastly, recommendations for future research and an outlook on the industrial potential of this technology are provided in **Section 7.4**.

7.2. Technological evaluation

Proton-conducting membranes can potentially be used to shift the thermodynamic equilibrium of light alkane NODH toward the olefins side. When integrating these membranes into membrane reactors, then the traditional dehydrogenation catalysts will be exposed to great variations in alkane, olefin, and hydrogen concentrations. In **Chapter 2** we investigated the influence of varying ethane, ethylene, and hydrogen partial pressures on the reaction rate and mechanism of ethane NODH on a Pt-Sn/ZnAl$_2$O$_4$ catalyst. The results indicated that the ethane surface coverage was negligible under reaction conditions, whilst the surface occupancy of ethylene and hydrogen inhibited the formation of ethylene. The proposed Langmuir-Hinshelwood-Hougen-Watson (LHHW) reaction rate expression (**Equation 7.1**) was based on the following elementary steps: (i) dissociative ethane adsorption, (ii) surface hydrogen removal, (iii) ethylene desorption, and (iv) hydrogen desorption, where step (i) was considered as the rate-determining step.

$$TOF_{app,model} = \frac{k_1 \left(p_{C2H6} - \frac{p_{C2H4} p_{H2}}{K_{eq}} \right)}{\left(1 + K_4\, p_{C2H4} + \sqrt{K_5 p_{H2}}\ \right)^2} \tag{7.1}$$

The adsorption constants for ethylene (K_4) and hydrogen (K_5) were found to be strongly coverage dependent. For ethylene, it was postulated that its adsorption configuration changes with surface coverage. For higher surface coverages at lower temperatures, ethylene possibly adsorbs primarily as weak π-bonded species (**Figure 7.1a**). On the contrary, ethylene expectedly adsorbs to a larger extent as stronger di-σ-bonded species on lower covered surfaces, which are more prevalent at higher temperatures (**Figure 7.1b**). For hydrogen adsorption, the coverage dependency was attributed to lateral

interactions and hydrogen surface mobility. For high surface coverages, likely existing at low temperatures, hydrogen adsorption is possibly hindered by lateral interactions with any adsorbed species and a reduced surface mobility. By contrast, the hindrance to hydrogen adsorption by lateral interactions is mitigated for low coverages at high temperatures. The strong coverage dependency of the ethane NODH reaction indicates that variations in ethane, ethylene, and hydrogen partial pressure inside membrane reactors will strongly modify the ethane NODH reaction mechanism and related dehydrogenation rate on Pt-Sn/ZnAl$_2$O$_4$.
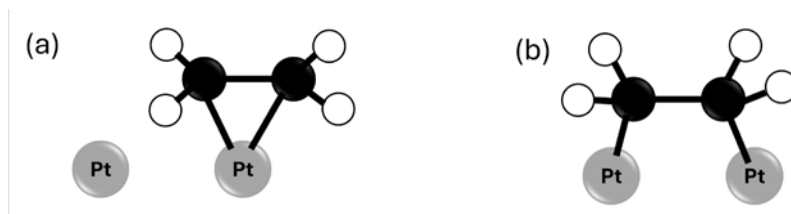
Figure 7.1: Schematic representation of (a) π-bonded ethylene, and (b) di-σ-bonded ethylene adsorbed on Pt, based on Watwe et al. [1].

In ceramic membrane-assisted alkane NODH systems, the Pt-based dehydrogenation catalyst will be exposed to moistened gas phase atmospheres, as dense ceramic membranes are known to function optimally in the presence of steam [2]. In **Chapter 3**, it was demonstrated that cofeeding 3 vol% of steam enhances ethane NODH rates on Pt/ZnAl$_2$O$_4$ and Pt-Sn/ZnAl$_2$O$_4$. The Pt/ZnAl$_2$O$_4$ catalyst was not physicochemically modified by the steam and the related increase in ethylene formation rate was therefore attributed to mechanistic effects induced by the steam. Supposedly, steam functions as surface cleaning agent in Pt/ZnAl$_2$O$_4$. In contrast to Pt/ZnAl$_2$O$_4$, the Pt-Sn/ZnAl$_2$O$_4$ catalyst was physicochemically modified by the steam. The XRD results indicated PtSn dealloying under steam exposure and the XPS results showed that the Pt in steam treated PtSn was significantly more oxidized than the Pt in reduced Pt and PtSn and in steam treated Pt. Hydrocarbon attraction and ethane dissociation are possibly boosted on the more oxidized Pt species in Pt-Sn/ZnAl$_2$O$_4$ exposed to steam. The stability of particularly Pt-Sn/ZnAl$_2$O$_4$ under moistened alkane NODH conditions needs to be investigated in more detail. If the stability of PtSn in steam remains worse than that of Pt, then the use of Sn-free catalysts is recommended for future ceramic membrane reactor applications.

Traditional packed bed membrane reactors face issues related to heat management and mass transport from the catalyst to the membrane [3,4]. In an alternative configuration, the catalyst can be deposited directly in the porous layer of an asymmetric membrane to minimize mass transfer limitations and better distribute the heat across the reaction zone. If the catalyst-functionalized membrane configuration is applied for alkane dehydrogenation systems, then the reaction will take place in the immediate vicinity of the membrane, as the Pt dehydrogenation catalyst is in intimate contact with the membrane material. To assess the potential of the catalyst-functionalized membrane strategy for

alkane NODH, Pt catalyst active phases were deposited onto a promising MPEC material (i.e. LWO, lanthanum tungsten oxide) and a promising PCEC material (i.e. BZCY, barium zirconium cerium yttrium oxide) and the corresponding performances were compared to a conventional $Pt/ZnAl_2O_4$ dehydrogenation catalyst in **Chapter 4**. Relative to $Pt/ZnAl_2O_4$, the ethylene selectivity was significantly lower for Pt/LWO and Pt/BZCY, due to enhanced methane formation on these proton-conducting supports. The methane formation in Pt/LWO and Pt/BZCY was attributed to Lewis acid sites present in LWO and BZCY, caused by intrinsic oxygen vacancies. The metal cations in LWO and BZCY are less shielded when adjacent oxygens are missing. These acid sites located on the LWO and BZCY supports can accelerate undesired C-C cleavage [5,6]. Next to this, the ethylene formation activity of Pt/LWO declined rapidly over time compared to a stable $Pt/ZnAl_2O_4$ catalyst. This deactivation on the proton-conducting supports was ascribed to Pt sintering. Surprisingly, this Pt sintering was suppressed when cofeeding steam. Pt sintered to a lesser extent on BZCY as compared to LWO, possibly due to stronger interactions of the Pt with the Ba in BZCY. As a result, ethylene formation was comparably stable on Pt/BZCY relative to Pt/LWO. If the stability and ethylene selectivity of these catalyst-functionalized membranes cannot be improved, then the traditional packed bed membrane reactor designs are recommended for PCEC-assisted light alkane NODH.

7.3. Techno-economic evaluation

A techno-economic assessment of the usage of ceramic membranes in light olefin production processes was conducted for two different cases in **Chapter 5** and **6**, respectively. In the first one (**Chapter 5**), the potential impact of applying MPEC and PCEC membranes on the corresponding process economics, energy usage, and carbon footprint was evaluated for the commercialized propane dehydrogenation process. To this end, the techno-economics of an MPEC-assisted and a PCEC-assisted process were compared to a benchmark Honeywell UOP Oleflex process for propane dehydrogenation with a commercial plant capacity of 450 ktpa. A main conclusion from **Chapter 5** was that the MPEC-assisted process was ca. 18 times more expensive and had a ca. 40% higher energy demand than the conventional Oleflex process. The extremely high capital investment of the MPEC process was attributed to the large MPEC membrane area required for *in situ* hydrogen separation. This was caused by the weak driving force for hydrogen permeation through MPECs when operating with low H_2 partial pressures on the feed side of the membrane. Besides, the large energy input of the MPEC process was ascribed to the high energy demand of membrane sweep gas heating. High sweeping rates were needed to minimize the hydrogen partial pressure on the permeate side to maximize the driving force for H_2 permeation. MPEC membranes are therefore not suitable for hydrogen extraction configurations, such as in alkane NODH applications. **Chapter 5** also showed that the PCEC process, in contrast to the MPEC process, could be an attractive alternative to traditional Oleflex. Compared to Oleflex, the capital investment of the PCEC process was ca. 20% lower and the total energy demand was ca. 30% lower. A higher single-

pass propylene yield was considered in the PCEC process (50%) than in the traditional Oleflex process (ca. 36%) to mimic the shift in propane NODH equilibrium induced by hydrogen removal. Due to this higher single-pass propylene yield, the process recycle stream and all connected process streams and process units were smaller in size for the PCEC process as compared to the Oleflex process, leading to a lower capital investment and process energy demand.

In the second techno-economic study (**Chapter 6**), the potential impact of applying ceramic membranes on the industrial viability of the ethane dehydrogenation process was investigated. The focus in **Chapter 6** was on PCEC membranes, as **Chapter 5** demonstrated that MPEC membranes are financially and energetically not competitive for integration into high temperature alkane dehydrogenation processes. The PCEC-assisted ethane dehydrogenation process was benchmarked against a conventional ethane steam cracking process for ethylene production with a plant capacity of 100 ktpa. For ethylene yields of about 25% that have been achieved so far in PCEC-assisted ethane NODH research [7], the total energy demand was found to be 25% higher and the total capital investment 15% higher as compared to ethane steam cracking. The considered 25% PCEC ethylene yield at 550 °C was insufficient to compete with typical ethane steam cracker yields of ca. 50% at 850 °C, leading to relatively big process streams and process units in the PCEC process. If single-pass ethylene yields of about 50% could also be achieved using PCEC technologies, then the PCEC process was found to be competitive with ethane steam crackers in terms of process energy demand, capital investment, and profitability.

In both techno-economic studies (**Chapter 5** and **6**), we demonstrated that the PCEC-assisted alkane dehydrogenation process can be financially and energetically competitive to the conventional alternative olefin production process. The shift in alkane dehydrogenation equilibrium induced by the PCEC membrane resulted in a smaller process recycle. Consequently, the equipment sizes and the heating, cooling, and compression duties were all lower as compared to alkane dehydrogenation processes operated without membranes. The lower total process energy demand of the PCEC process, however, only translated into a lower carbon footprint, as compared to conventional olefin production, when fully renewable electricity was utilized. The reason for this is the large electricity requirement for electrically driven hydrogen permeation in PCECs, which was heavily carbon penalized when the applied electricity was predominantly non-renewable. Moreover, green electrification of the respective conventional olefin production routes, i.e. the Honeywell UOP Oleflex process and the ethane steam cracking process, led to similar savings in carbon dioxide emissions as industrial implementation of green electrified PCEC membrane reactors.

7.4.   Outlook

7.4.1.   Recommendations for future research

The reaction model for ethane NODH on Pt-Sn/ZnAl$_2$O$_4$, as proposed in **Chapter 2**, was developed using a wide range in ethane, hydrogen, and ethylene partial pressures. However, the operational conditions that would be needed to make ethane NODH industrially feasible were not attained in these kinetic tests. In **Chapter 6** it was demonstrated that more than 95% of the hydrogen needs to be removed to substantially shift the ethane NODH equilibrium, which is needed to provide the related benefits in energy usage and investment reductions. Under those hydrogen-poor and ethylene-rich conditions, the Pt-Sn/ZnAl$_2$O$_4$ catalyst deactivated during catalytic testing, as shown in **Chapter 2**. The validity of the proposed reaction model for ethane NODH therefore also needs to be verified under these extreme membrane reactor conditions to fully understand the membrane reactor performance for this application. To this end, coke suppressing agents, like H$_2$O or CO$_2$ could be cosupplied in the kinetic tests to improve the stability of Pt-Sn/ZnAl$_2$O$_4$ [8,9].

In **Chapter 3**, it was demonstrated that the Pt-Sn/ZnAl$_2$O$_4$ catalyst was physicochemically modified by the presence of steam. However, in the commercial steam active reforming process by Uhde (i.e. the STAR® process), a Pt-Sn/ZnAl$_2$O$_4$ catalyst is employed [8]. This commercial catalyst contains calcium-magnesium aluminate as a binder [8], which possibly prevents Sn leaching or PtSn dealloying. Adaptations to the Pt-Sn/ZnAl$_2$O$_4$ catalyst used in this work could, therefore, also be considered for improving the stability of PtSn-based catalysts in wet atmospheres. **Chapter 3** further showed that the apparent activation barriers and the hydrogen reactions orders for ethane NODH on Pt/ZnAl$_2$O$_4$ and Pt-Sn/ZnAl$_2$O$_4$ changed under dry and wet atmospheres. Ideally, one would compare the activation barrier between the various cases for equal ethane, ethylene, and hydrogen reaction orders to confirm the uniformity of the reaction mechanism. In that situation, it would be valuable to quantify the actual activation barrier and the enthalpies and entropies of ethylene and hydrogen adsorption under moistened conditions and compare the outcomes to the kinetic and thermodynamic parameters retrieved under dry conditions, as reported in **Chapter 2**. This would allow for a quantitative assessment of the possible role of steam on the activation and adsorption barriers for both catalysts.

Chapter 4 showed that Pt sintered on the surface of the LWO support upon performing the ethane dehydrogenation reaction under dry conditions. The Pt-support interactions appeared to be too weak to anchor the Pt on LWO. For alumina-based supports it is known that ZnAl$_2$O$_4$ and MgAl$_2$O$_4$ spinels bind Pt more strongly than e.g. more traditional γ-Al$_2$O$_3$ or θ-Al$_2$O$_3$ [10]. This is caused by strong interactions between the Pt and the Zn or Mg in the support. For this reason, incorporation of Zn, Mg, or alkali metals in the LWO support could assist in anchoring Pt. Moreover, this could help with improving the olefin selectivity by suppressing C-C cleavage on support acid sites [10–13]. Another potential strategy that

could help in strengthening metal-support interactions is based on exsolution methods [14,15]. In recent years, for instance the exsolution of Ni [14,16–19] and Co [19,20] from various metal oxides has been studied for fuel cell applications. Exsolution of the bulkier platinum is more challenging but has been demonstrated from lanthanum titanates by Kothari et al. [21]. Exsolution of Pt from proton conducting supports could allow for the generation of anchored and isolated Pt sites. Note that the suggestions for future research described here focus on improving the catalytic performance but could at the same time (negatively) affect the performance of the LWO membrane.

In both process simulation studies (**Chapter 5** and **6**), important assumptions were made regarding the stability and achievable olefin yield of PCEC systems. For this reason, the activity, selectivity, and stability of PCEC systems in the non-oxidative dehydrogenation of light alkanes must be studied experimentally on lab and pilot scale to demonstrate the potential of this technology. In **Chapter 5** and **6** it was demonstrated that the largest savings in energy usage were attained when shifting the respective propane NODH and ethane NODH equilibrium yields to ca. 50%. Even higher single-pass olefin yields increase the chance of deactivation due to coke formation with only marginal further savings in energy usage. For this reason, single-pass olefin yields of ca. 50% are recommended as target for future experimental PCEC research and for upscaling of PCEC systems for light alkane NODH.

In terms of stability, the lifetime of the PCECs was assumed to be equal to the lifetime of a typical dehydrogenation catalyst (i.e. two years) in both simulation studies. However, upon removing H_2 from the reaction zone and shifting the dehydrogenation equilibrium toward the olefins side, carbon deposition is anticipated to be accelerated [22–24]. Consequently, the stability of PCEC systems could be considerably worse than that of standard dehydrogenation catalysts, requiring more frequent regeneration cycles. A sensitivity analysis in **Chapter 5** illustrated that the influence of PCEC membrane replacement on the process profitability was only marginal for replacement frequencies lower than six times per year. In that case, raw material and utility costs had a more pronounced impact on profitability than membrane replacement. However, it should be noted that possible fluctuations in the prices of the different PCEC compartments and the uncertainty over the required production downtime for membrane replacement make predictions about the impact of PCEC replacement on process profitability complex at this stage. Future research into the possible required regeneration and replacement methods of PCEC systems is therefore essential for industrialization of this technology.

If severe deactivation of PCEC systems would be encountered in future stability tests, then several research directions can be explored. A possible way to mitigate coke-induced PCEC deactivation is to use the co-ionic character of solid oxide electrolyzer cells to oxidize carbon deposits. Morejudo et al. [25] demonstrated for the related methane dehydroaromatization reaction that cotransport of O^{2-} ions in the direction opposing proton transport assists in improving PCEC stability, caused by oxidation of carbon deposits induced by well distributed injection of oxygen to the reaction zone. This counter-

current flow of O^{2-} through the solid electrolyte could originate from the steam cofeed on the permeate side of the membrane. Besides, the direct steam cofeed on the PCEC reaction side supposedly helps avoiding coke formation. Additionally, avoiding the use of Ni in PCEC electrode materials is recommendable when aiming at coke minimization, as Ni is known to boost carbon deposition [26]. The Ni could be replaced by other metals (e.g. Cu, Ag) or by redox metal active oxides [27]. Lastly, PCEC operation at lower temperatures would thermodynamically be beneficial to diminish coke formation.

In addition to the PCEC stability, the hydrogen permeation flux through PCECs for a given combination of temperature, current density, area specific resistance (*ASR*), and feed-to-permeate side pressure ratio needs to be proven. In **Chapter 5**, the PCEC hydrogen permeation flux through a BZCY-based PCEC at 600 °C at a current density of 1 A/cm^2 and an *ASR* of 0.4 Ω.cm^2 was estimated at 3.3 µmol.s.cm^2. This estimation was based on experimental work by Malerød-Fjeld et al. [28] on a BZCY-based PCEC system operated at 800 °C using a current density of 0.4 A/cm^2 and an *ASR* of 0.4 Ω.cm^2. Experimental evidence of PCEC performance at temperatures suitable for integration with alkane dehydrogenation reactions (i.e. 500-700 °C) is required to confirm the potential of PCEC systems in this field.

A final aspect that could assist in understanding the performance of ceramic membrane reactors for light alkane dehydrogenation, and that could allow for predicting the performance of membrane reactors in this field, would be a multi-scale steady state membrane reactor model. This model should include (i) the axial performance of the catalyst packed bed, as well as (ii) the radial transport of H$_2$ through the dense ceramic membrane. Ideally, the membrane transport contains an electrostatic potential contribution as well, such that the influence of an applied voltage on the membrane reactor performance could also be evaluated. A cotransport of O^{2-} ions through the PCEC membrane in a direction opposing proton transport, driven by a gradient in oxygen-containing gas phase molecules on both sides of the membrane, can improve the stability of PCECs, as demonstrated by Morejudo et al. [25] for the related methane dehydroaromatization reaction. It would be valuable to also include this O^{2-} cotransport in the model.

7.4.2. Industrial potential

The simulation studies in **Chapter 5** and **6** demonstrated that PCEC-assisted processes for light alkane NODH can be financially and environmentally competitive to conventional olefin production routes. The envisaged shift in thermodynamic equilibrium toward higher single-pass olefin yields resulted in smaller process streams and process units and, thereby, a lower capital investment, utility demand, and carbon emissions. However, in both studies it was also found that green electrification of the conventional light olefin production routes, i.e. the Oleflex and ethane steam cracking processes, led to similar savings in carbon dioxide emissions as industrial implementation of PCEC systems. From

an industrial perspective, electrification of more mature conventional olefin production pathways is anticipated to be preferred to commercialization of electrified processes containing innovative PCEC systems. Still, based on the outcomes of this dissertation a set of guidelines can be outlined where one should adhere to when targeting for process electrification:

- To financially stimulate process electrification, electrical heat should become cheaper than fossil fuel-based heat. Grid electricity prices are typically still higher (50-80 USD/MWh) than e.g. natural gas prices (ca. 20 USD/MWh) [29,30], while for instance wind powered electricity can already be generated for a competitive price [31].
- To ecologically justify process electrification, the carbon intensity of the used electricity should be below 200 kg_{CO_2}/MWh. The carbon footprint of fully electrified process cases was found to be smaller than that of alternative cases heated by burning natural gas or off-gas resources below this threshold value.
- As long as fossil fuel-based heat is cheaper than electrical heat, carbon taxes can be levied to stimulate process electrification. The suggested taxation levels found in this dissertation depended on the targeted reaction and production capacity, and the suggested minimum carbon tax was 250 USD/t_{CO_2} for propane NODH (**Chapter 5**) and 100 USD/t_{CO_2} for ethane NODH (**Chapter 6**).

The PCEC technology also faces several challenges for light alkane NODH applications that need to be tackled before PCECs could be industrially implemented. A first challenge is related to the large scale of the olefin production processes to which these PCEC systems have to be integrated. Commercial propane dehydrogenation plants have typical production capacities between 450 to 750 ktpa [32] and commercial ethane steam cracking facilities of more than 1,000 ktpa [33,34]. For this reason, PCECs need to become available in substantial amounts to meet the potential industrial demand. This introduces a restriction to the applicable PCEC compositions, as the PCECs should contain abundantly available elements. Moreover, in case it turns out that PCECs are not fully regeneratable by coke removing gas treatments, then periodic membrane replacement would be required. In that situation, an additional research field on the recyclability and recovery of PCEC elements at the end of lifetime needs to be explored. One also needs to keep in mind that the methods for assembling the PCEC systems and for synthesizing the PCEC electrolyte and electrode materials have to be sustainable and scalable.

One of the main conclusions from the process simulations studies in **Chapter 5** and **6** was that fully renewable electricity needs to be utilized in PCEC-assisted processes to ever outcompete conventional olefin production routes in terms of carbon dioxide emissions. For this reason, renewable electricity needs to become continuously available around olefin production sites, which presents a challenge if e.g. intermittent wind or solar power is targeted as renewable electricity source. Also, the capacity of electricity grids around olefin production plants have to be drastically expanded to meet the great electricity

demand of these processes. These infrastructural prerequisites are essential not only for PCEC integrated chemical reactors but also for other electrified chemical production facilities.

Apart from alkane NODH, green production of light olefins could be accomplished via (i) alkane oxidative dehydrogenation (ODH), (ii) methanol-to-olefins, (iii) or electrochemical CO_2 reduction routes. Alkane ODH can be employed using an oxidant cofeed [13] or via chemical looping systems with redox catalysts [35]. When using an oxidant cofeed there is a high risk of over-oxidizing the olefin product and of creating explosive atmospheres, which makes this route industrially unattractive [13]. Besides, the chemical looping route suffers from limitations related to the mechanical stability of the redox catalysts and the complexity of the reactor design [35]. The drawback of the methanol-to-olefins route is the limited financial margin between reactant and product prices to develop a profitable process, especially in comparison to e.g. alkane dehydrogenation [36]. Electrochemical CO_2 reduction therefore seems to be the most promising alternative for green olefin production, as it has the clear advantage of having CO_2 as feedstock, potentially allowing for net zero emissions. However, electrochemical CO_2 reduction suffers from a low activity and selectivity, in combination with high reactor costs [37,38], and significant performance improvements are needed for this route to justify industrialization. Electrochemical CO_2 reduction is thereby in a similar technological development stage as membrane-assisted alkane NODH.

All in all, **Chapter 5** and **6** showed that the green electrified PCEC processes had a 60-80% smaller carbon footprint than the conventional fossil fuel heated alternatives. Industrial implementation of green electrified PCEC processes for light olefin production could, therefore, potentially have a great contribution to the targeted reduction in global greenhouse gas emissions, following the Paris Agreement. These carbon emission savings, however, can only be attained if stable, active, and selective performance of the PCEC membrane as well as the PtSn dehydrogenation catalyst is guaranteed. In **Chapter 1**, it was demonstrated that the reaction mechanism and the catalyst activity, selectivity, and stability varied significantly with varying hydrogen, ethane, and ethylene concentrations. Afterward, **Chapter 2** illustrated that cofeeding steam negatively impacted the stability of PtSn, despite signs of improved dehydrogenation activity under moistened atmospheres. Besides, **Chapter 3** showed that proton-conducting supports can distort the performance of Pt catalysts and can interfere in the dehydrogenation reaction. These technological challenges, in combination with the infrastructural requirements related to PCEC manufacturing, present a major barrier to industrial implementation of PCEC-based membrane reactors. Instead, electrifying existing and more mature propane dehydrogenation and ethane steam cracking facilities using renewable electricity, which offers similar savings in carbon emissions (see **Chapter 5** and **6**), appears to be a better option to reach net zero emissions in 2050.

References

1. Watwe, R. M., Cortright, R. D., Mavrikakis, M., Nørskov, J. K. & Dumesic, J. A. Density functional theory studies of the adsorption of ethylene and oxygen on Pt(111) and Pt3Sn(111). *J. Chem. Phys.* **114**, 4663–4668 (2001).

2. Meng, Y., Gao, J., Zhao, Z., Amoroso, J., Tong, J. & Brinkman, K. S. Review : recent progress in low-temperature proton-conducting ceramics. *J. Mater. Sci.* 9291–9312 (2019).

3. Gallucci, F., Fernandez, E., Corengia, P. & Sint, M. Van. Recent advances on membranes and membrane reactors for hydrogen production. *Chem. Eng. Sci.* **92**, 40–66 (2013).

4. Deshmukh, S. A. R. K., Heinrich, S., Mörl, L., van Sint Annaland, M. & Kuipers, J. A. M. Membrane assisted fluidized bed reactors: Potentials and hurdles. *Chem. Eng. Sci.* **62**, 416–436 (2007).

5. Galvita, V., Siddiqi, G., Sun, P. & Bell, A. T. Ethane dehydrogenation on Pt/Mg(Al)O and PtSn/Mg(Al)O catalysts. *J. Catal.* **271**, 209–219 (2010).

6. Sheintuch, M., Liron, O., Ricca, A. & Palma, V. Propane dehydrogenation kinetics on supported Pt catalyst. *Appl. Catal. A: Gen.* **516**, 17–29 (2016).

7. Wu, W., Wang, L. C., Hu, H., Bian, W., Gomez, J. Y., Orme, C. J., Ding, H., Dong, Y., He, T., Li, J. & Ding, D. Electrochemically engineered, highly energy-efficient conversion of ethane to ethylene and hydrogen below 550 °C in a protonic ceramic electrochemical cell. *ACS Catal.* **11**, 12194–12202 (2021).

8. Sattler, J. J. H. B., Ruiz-Martinez, J., Santillan-Jimenez, E. & Weckhuysen, B. M. Catalytic dehydrogenation of light alkanes on metals and metal oxides. *Chem. Rev.* **114**, 10613–10653 (2014).

9. Nawaz, Z. Light alkane dehydrogenation to light olefin technologies: A comprehensive review. *Rev. Chem. Eng.* **31**, 413–436 (2015).

10. Aguilar-rios, G., Valenzuela, M. A., Salas, P., Armendariz, H., Bosch, P., Del Toro, G., Silva, R., Bertín, V., Castillo, S., Ramírez-Solís, A. & Schifter, I. Hydrogen interactions and catalytic properties of platinum-tin supported on zinc aluminate. *Appl. Catal. A: Gen.* **127**, 65–75 (1995).

11. Lai, Y., He, S., Li, X., Sun, C. & Seshan, K. Dehydrogenation of n-dodecane over PtSn/MgAlO catalysts: Investigating the catalyst performance while monitoring the products. *Appl. Catal. A: Gen.* **469**, 74–80 (2014).

12. Pakhomov, N. A., Buyanov, R. A., Moroz, E. M., Kotelnikov, G. R. & Patanov, V. A. Medium Effect in Thermal Pretreatment on the State and Catalytic Properties of Platinum Supported on Zinc-aluminium Spinel. *React. Kinet. Catal. Lett.* **9**, 257–263 (1978).

13. Bhasin, M. M., Mccain, J. H., Vora, B. V, Imai, T. & Pujad, P. R. Dehydrogenation and oxydehydrogenation of paraffins to olefins. *Appl. Catal. A: Gen.* **221**, 397–419 (2001).

14. Neagu, D., Oh, T.-S., Miller, D. N., Ménard, H., Bukhari, S. M., Gamble, S. R., Gorte, R. J., Vohs, J. M. & Irvine, J. T. S. Nano-socketed nickel particles with enhanced coking resistance grown in situ by redox exsolution. *Nat. Commun.* **6**, 8120 (2015).

15. Neagu, D., Tsekouras, G., Miller, D. N., Ménard, H. & Irvine, J. T. S. In situ growth of nanoparticles through control of non-stoichiometry. *Nat. Chem.* **5**, 916–923 (2013).

16. Li, H., Song, Y., Xu, M., Wang, W., Ran, R., Zhou, W. & Shao, Z. Exsolved alloy nanoparticles decorated Ruddlesden–Popper perovskite as sulfur-tolerant anodes for solid oxide fuel cells. *Energy Fuels* **34**, 11449–11457 (2020).

17. Toscani, L. M., Giangiordano, F. V., Nichio, N., Pompeo, F. & Larrondo, S. A. In-situ Ni exsolution from NiTiO3 as potential anode for solid oxide fuel cells. *Int. J. Hydrog. Energy* **45**, 23433–23443 (2020).

18. Yang, X., Wei, T., Chi, B., Pu, J. & Li, J. Lanthanum manganite-based perovskite as a catalyst for co-production of ethylene and hydrogen by ethane dehydrogenation. *J. Catal.* **377**, 629–637 (2019).

19. Fan, Y., Xi, X., Medvedev, D., Wang, Q., Li, J., Luo, J.-L. & Fu, X.-Z. Emerging anode materials architectured with NiCoFe ternary alloy nanoparticles for ethane-fueled protonic ceramic fuel cells. *J. Power Sources* **515**, 230634 (2021).

20. Liu, S., Liu, Q., Fu, X.-Z. & Luo, J.-L. Cogeneration of ethylene and energy in protonic fuel cell with an efficient and stable anode anchored with in-situ exsolved functional metal nanoparticles. *Appl. Catal. B: Environ.* **220**, 283–289 (2018).

21. Kothari, M., Jeon, Y., Miller, D. N., Pascui, A. E., Kilmartin, J., Wails, D., Ramos, S., Chadwick, A. & Irvine, J. T. S. Platinum incorporation into titanate perovskites to deliver emergent active and stable platinum nanoparticles. *Nat. Chem.* **13**, 677–682 (2021).

22. Schäfer, R., Noack, M., Kölsch, P., Stöhr, M. & Caro, J. Comparison of different catalysts in the membrane-supported dehydrogenation of propane. *Catal. Today* **82**, 15–23 (2003).

23. Peters, T. A., Liron, O., Tschentscher, R., Sheintuch, M. & Bredesen, R. Investigation of Pd-based membranes in propane dehydrogenation (PDH) processes. *Chem. Eng. J.* **305**, 191–200 (2016).

24. Gimeno, M. P., Wu, Z. T., Soler, J., Herguido, J., Li, K. & Menéndez, M. Combination of a two-zone fluidized bed reactor with a Pd hollow fibre membrane for catalytic alkane dehydrogenation. *Chem. Eng. J.* **155**, 298–303 (2009).

25. Morejudo, S. H., Zanón, R., Escolástico, S., Yuste-Tirados, I., Malerød-Fjeld, H., Vestre, P. K., Coors, W. G., Martínez, A., Norby, T., Serra, J. M. & Kjølseth, C. Direct conversion of methane to aromatics in a catalytic co-ionic membrane reactor. *Science* **353**, 563–566 (2016).

26. Nikolla, E., Schwank, J. & Linic, S. Direct electrochemical oxidation of hydrocarbon fuels on SOFCs: improved carbon tolerance of Ni alloy anodes. *J. Electrochem. Soc.* **156**, B1312 (2009).

27. Jang, I., S. A. Carneiro, J., Crawford, J. O., Cho, Y. J., Parvin, S., Gonzalez-Casamachin, D. A., Baltrusaitis, J., Lively, R. P. & Nikolla, E. Electrocatalysis in solid oxide fuel cells and electrolyzers. *Chem. Rev.* **124**, 8233–8306 (2024).

28. Malerød-fjeld, H., Clark, D., Yuste-tirados, I., Zanón, R., Catalán-martinez, D., Beeaff, D., Morejudo, S. H., Vestre, P. K., Norby, T., Haugsrud, R., Serra, J. M. & Kjølseth, C. Thermo-electrochemical production of compressed hydrogen from methane with near-zero energy loss. *Nat. Energy* **2**, 923–931 (2017).

29. International Energy Agency. Electricity market report 2023. https://www.iea.org/reports/electricity-market-report-2023 (accessed June 2024).

30. U.S. Energy Information Administration. Electric power monthly. https://www.eia.gov/electricity/monthly/epm_table_grapher.php?t=epmt_5_6_a (accessed July 2023).

31. CO2emissiefactoren. Lijst emissiefactoren. https://www.co2emissiefactoren.nl/lijst-emissiefactoren/ (accessed July 2023).

32. Marsh, M. & Wery, J. On-purpose propylene production. https://www.digitalrefining.com/article/1002264/on-purpose-propylene-production (accessed August 2023).

33. Petrochemicals Europe. Cracker capacity. https://www.petrochemistry.eu/about-petrochemistry/petrochemicals-facts-and-figures/cracker-capacity/ (accessed May 2024).

34. Middleton, J., Simon, Y., Guillaume, J., Lal, R., Abdin, Z. & Viviano, E. Ethylene - A world leader in the design and construction of ethylene facilities.

https://www.ten.com/sites/energies/files/2021-03/Ethylene.pdf (accessed September 2024).

35. Oing, A., von Müller, E., Donat, F. & Müller, C. R. Material engineering solutions toward selective redox catalysts for chemical-looping-based olefin production schemes: A review. *Energy & Fuels* **38**, 17326–17342 (2024).

36. Agarwal, A., Sengupta, D. & El-halwagi, M. Sustainable process design approach for on-purpose propylene production and intensification. *ACS Sustain. Chem. Eng.* **6**, 2407–2421 (2018).

37. Chauhan, R., Sartape, R., Minocha, N., Goyal, I. & Singh, M. R. Advancements in environmentally sustainable technologies for ethylene production. *Energy & Fuels* **37**, 12589–12622 (2023).

38. Pappijn, C. A. R., Ruitenbeek, M., Reyniers, M.-F. & Van Geem, K. M. Challenges and opportunities of carbon capture and utilization: electrochemical conversion of CO2 to ethylene. *Front. Energy Res.* **8**, 557466 (2020).

Summary

This dissertation presents a technological and techno-economic assessment of applying ceramic proton-conducting membranes in light alkane dehydrogenation processes. The corresponding light olefin (e.g. ethylene, propylene) products are widely used to produce e.g. plastics, oxygenates, and chemical intermediates. Light olefins are traditionally obtained from carbon and energy intensive steam cracking and fluid catalytic cracking processes. The non-oxidative dehydrogenation (NODH) of C2-C3 alkanes to olefins represents a more direct alternative production pathway. However, light alkane NODH is limited by thermodynamic equilibrium, requiring high temperatures (500-700 °C) for restricted olefin yields (30-40%).

The alkane NODH equilibrium limitation can potentially be overcome by using ceramic hydrogen permeable membranes that can shift the equilibrium toward the olefin side. The use of membranes could thereby substantially reduce the required energy input and carbon footprint of olefin production processes. Two different types of ceramic membranes could be utilized, namely (i) mixed proton-electron conducting (MPEC), and (ii) proton-conducting electrolysis cell (PCEC) membranes. Protons as well as electrons are conducted through MPEC membranes, where transport is fully driven by a gradient in hydrogen chemical potential. On the contrary, PCEC membranes are commonly operated using an external voltage, such that only protons are transported through the membrane, whilst electrons are directed via an external circuit. In that case, transport is driven by a gradient in hydrogen electrochemical potential. While MPECs only offer the opportunity for shifting the alkane NODH equilibrium, the PCEC systems have the additional advantages of process electrification and tailoring the reaction thermodynamics and kinetics through the applied potential. Moreover, part of the PCEC power is converted into Joule heat, because of the electrical resistance across the PCEC membrane. The challenge of integrating ceramic membranes into large scale olefin production facilities is the delicate balance between the optimal operating conditions of the dehydrogenation catalyst and the proton-conducting membrane. This dissertation assesses the main technological hurdles and the potential techno-economic benefits and barriers of membrane-assisted light alkane NODH, as introduced in **Chapter 1**.

The alkane, olefin, and hydrogen concentrations will vary drastically in membrane reactors for alkane NODH, wherein olefin yields are targeted to be maximized by removing hydrogen. The influence of changing ethane, ethylene, and hydrogen concentrations on the kinetics and mechanism of the ethane NODH reaction over a traditional Pt-Sn dehydrogenation catalyst is investigated in **Chapter 2**. The results indicate that the ethane surface coverage is negligible under reaction conditions, whilst the surface occupancy of ethylene and hydrogen inhibit ethylene formation. The proposed Langmuir-Hinshelwood-Hougen-Watson (LHHW) reaction model comprises of four elementary

steps: (i) dissociative ethane adsorption, (ii) surface hydrogen removal, (iii) ethylene desorption, and (iv) hydrogen desorption, where step (i) is identified as the rate-determining step. Ethylene and hydrogen adsorption are strongly coverage dependent in this model. For high surface coverages, likely existing at low temperatures, hydrogen adsorption is hindered by lateral interactions and a reduced hydrogen surface mobility. In addition, ethylene is claimed to adsorb as a weak π-bonded species for high surface coverages and as a stronger di-σ-bonded species for lower surface coverages.

Dense ceramic membranes for proton conduction function optimally under moistened atmospheres. Alkane dehydrogenation catalysts will, therefore, inevitably be exposed to steam rich conditions in ceramic membrane reactors. The influence of steam on the structure and performance of Pt-based dehydrogenation catalysts in the ethane NODH reaction is explored in **Chapter 3**. There, it is demonstrated that steam enhances the ethylene formation rate on $Pt-Sn/ZnAl_2O_4$ and $Pt/ZnAl_2O_4$. The tin-free $Pt/ZnAl_2O_4$ catalyst is not physicochemically modified by the steam. The corresponding increase in ethylene formation rate under wet conditions is, therefore, attributed to the surface cleaning role of steam in $Pt/ZnAl_2O_4$. By contrast, the $Pt-Sn/ZnAl_2O_4$ catalyst is physicochemically modified by steam, as XRD indicates PtSn dealloying in presence of steam and XPS shows a more oxidized Pt species in the Pt-Sn catalyst after steam treatment as compared to dry reduced Pt and PtSn and steam treated Pt. Hydrocarbon attraction and ethane dissociation are possibly boosted on the more oxidized Pt species in steam treated $Pt-Sn/ZnAl_2O_4$, which increases the corresponding ethylene formation rate.

In established membrane reactor configurations, the membrane is usually physically separated from the catalyst. In an alternative configuration, the Pt dehydrogenation catalyst could be deposited directly onto the ceramic membrane material. The potential advantage of that configuration is that the reaction takes place in the immediate vicinity of the membrane, which would optimize the mass transfer from catalyst to membrane. To assess the potential of this strategy, Pt is deposited on promising MPEC (lanthanum tungstate, LWO) and PCEC (barium zirconium cerium yttrium oxide, BZCY) membrane materials and the performance of the concerning catalyst powders is compared with the conventional $Pt/ZnAl_2O_4$ catalyst in **Chapter 4**. Relative to $Pt/ZnAl_2O_4$, a higher methane selectivity and a lower ethylene selectivity are observed for both proton-conducting supports. The enhanced methane formation for Pt/LWO and Pt/BZCY is ascribed to Lewis acid centers in LWO and BZCY. Additionally, the Pt/LWO and Pt/BZCY catalysts deactivate over time as compared to a stable $Pt/ZnAl_2O_4$ catalyst, caused by Pt sintering. Metal-support interactions are supposedly stronger in $Pt/ZnAl_2O_4$ than in Pt/LWO and Pt/BZCY. Nevertheless, cofeeding steam appears to facilitate Pt redispersion and thereby suppresses Pt sintering in Pt/LWO and Pt/BZCY.

The potential techno-economic benefits and challenges of the membrane-assisted alkane NODH concept are explored in two different process simulation studies in **Chapter 5** and **6**. In **Chapter 5**, it is investigated whether membrane-assisted propane NODH could be a feasible alternative to the already commercialized Honeywell/UOP Oleflex process for

propane NODH. The results indicate that the MPEC-assisted propane NODH process is not an attractive alternative, as it is ca. 18 times more expensive and has a ca. 40% higher energy demand than the Oleflex process. This is attributed to high MPEC membrane reactor equipment costs and an enormous sweep gas heating demand, both related to the weak driving force for hydrogen permeation through MPECs. By contrast, the capital investment of the PCEC-assisted process is ca. 20% lower and the total energy demand ca. 30% lower as compared to Oleflex, making the PCEC process a suitable industrial alternative. These financial and energetic benefits are related to the reduction in process stream and unit operation sizes as a result of the higher single-pass propylene yield of the PCEC process (ca. 50%) relative to Oleflex (ca. 36%).

In **Chapter 6**, it is explored whether the use of PCEC membranes could brighten the industrial perspective of the non-commercialized ethane NODH process. To this end, the techno-economics of PCEC-assisted ethane NODH are compared to a conventional ethane steam cracking (SC) process for ethylene production. The results indicate that ethylene yields of ca. 25%, which have been achieved so far in experimental PCEC-assisted ethane NODH studies, are insufficient to financially and environmentally compete with ethane SC. Single-pass ethylene yields of ca. 50% would be required to possibly outcompete ethane SC in terms of carbon footprint, capital investment, and profitability.

In **Chapter 7**, it is concluded that variations in gas phase composition along the length of ceramic membrane reactors strongly modify the ethane NODH reaction mechanism and related dehydrogenation rate on PtSn catalysts. Besides, it is suggested that the stability of PtSn catalysts under wet conditions needs to be further investigated to conclude whether tin-free or tin-rich dehydrogenation catalysts would be preferred in membrane reactor configurations. Also, if the stability and ethylene selectivity of systems in which Pt is deposited on proton-conducting supports cannot be improved, then the traditional packed bed membrane reactor designs are recommended for membrane-assisted light alkane NODH. Lastly, both techno-economic studies highlight that the targeted savings in carbon dioxide emissions can only be attained if fully renewable electricity is utilized in the PCEC-assisted alkane NODH processes. Moreover, green electrification of the respective conventional olefin production routes leads to similar savings in carbon dioxide emissions as industrial implementation of green electrified PCEC membrane reactors. All in all, the combination of the technological hurdles related to the reaction rate and catalyst stability under membrane reactor conditions and the limited techno-economic benefits of PCEC industrialization make green electrification of more mature conventional olefin production processes the preferred option to reach net zero emissions in 2050.

Samenvatting

Dit proefschrift beschrijft een onderzoek naar de technologische en techno-economische haalbaarheid van het toepassen van proton-geleidende membranen in processen voor de dehydrogenering van lichte alkanen. De lichte olefinen (bv. ethyleen, propyleen), die hierbij gevormd worden, worden grootschalig toegepast als grondstof voor de productie van o.a. plastics. Lichte olefinen worden traditioneel geproduceerd via koolstof- en energie-intensieve processen gebaseerd op het stoomkraken en katalytisch kraken van nafta of alkanen. De niet-oxidatieve dehydrogenering (NODH) van C2-C3 alkanen naar olefinen vormt een directer alternatief. Alkaan NODH wordt echter geremd door het thermodynamisch evenwicht, waardoor hoge temperaturen (500-700 °C) benodigd zijn, zelfs voor een beperkte olefineopbrengst (30-40%).

Het alkaan NODH evenwicht kan potentieel verlegd worden d.m.v. keramische waterstofdoorlatende membranen. Dit kan leiden tot een substantiële reductie van het energieverbruik en de CO_2-uitstoot van processen voor de productie van olefinen. Twee verschillende typen keramische membranen kunnen gebruikt worden: (i) mixed proton-electron conducting (MPEC) en (ii) proton-conducting electrolysis cell (PCEC) membranen. Zowel protonen als elektronen worden door MPEC membranen getransporteerd, waarbij het transport volledig gedreven is door een gradiënt in de chemische potentiaal van de waterstof. PCEC membranen worden daarentegen over het algemeen toegepast middels een extern voltage. Hierdoor worden alleen protonen door PCECs getransporteerd, terwijl de elektronen door een extern circuit geleid worden. Het transport wordt hierbij gedreven door een gradiënt in de elektrochemische potentiaal van de waterstof. Waar MPECs alleen het alkaan NODH evenwicht verschuiven, hebben PCECs de bijkomende voordelen van proceselektrificatie en het afstellen van de reactie thermodynamica en kinetiek middels de toegepaste elektrische potentiaal. Een deel van het elektrisch vermogen van de PCEC wordt bovendien omgezet in Joule warmte, vanwege de elektrische weerstand over de PCEC. De uitdaging van het integreren van keramische membranen in grootschalige olefin productieprocessen zit hem in de delicate balans tussen de optimale gebruiksomstandigheden van de dehydrogeneringskatalysator en het proton-geleidende membraan. In dit proefschrift worden de grootste technologische uitdagingen en potentiële techno-economische voordelen en obstakels onderzocht van membraan-gedreven alkaan NODH, zoals geïntroduceerd in **Hoofdstuk 1**.

De alkaan-, olefine- en waterstofconcentraties zullen sterk variëren in membraanreactoren voor alkaan NODH. De invloed van veranderingen in de ethaan-, ethyleen- en waterstofconcentraties op de kinetiek en het mechanisme van de ethaan NODH reactie over een Pt-Sn dehydrogeneringskatalysator is daarom onderzocht in **Hoofdstuk 2**. De resultaten laten zien dat de oppervlaktebezettingsgraad van ethaan verwaarloosbaar is onder reactieomstandigheden, terwijl de oppervlaktebezettingen van

ethyleen en waterstof de vorming van ethyleen belemmeren. Het voorgestelde Langmuir-Hinshelwood-Hougen-Watson (LHHW) reactiemodel is gebaseerd op de volgende vier elementaire reactiestappen: (i) dissociatieve adsorptie van ethaan, (ii) waterstof eliminatie op het katalysatoroppervlak, (iii) ethyleen desorptie en (iv) waterstof desorptie, waarbij stap (i) is vastgesteld als snelheidsbepalende stap. De adsorptie van ethyleen en waterstof is sterk afhankelijk van de oppervlaktebezettingsgraad. Bij een hoge bezettingsgraad, die zich voordoet bij lage temperaturen, wordt waterstofadsorptie gehinderd door laterale oppervlakte-interacties en een beperkte oppervlaktemobiliteit van de waterstof. Daarnaast adsorbeert ethyleen voornamelijk in een π-gebonden configuratie bij een hoge bezettingsgraad en in een di-σ-gebonden configuratie bij lagere bezettingsgraden.

Dichte keramische membranen voor proton-geleiding functioneren het beste in een vochtige atmosfeer. Katalysatoren voor alkaandehydrogenering worden daardoor onvermijdelijk blootgesteld aan stoomrijke omstandigheden in keramische membraanreactoren. De invloed van stoom op de structuur en werking van Pt-gebaseerde katalysatoren in de ethaan NODH reactie is onderzocht in **Hoofdstuk 3**. Daarin is aangetoond dat stoom de vorming van ethyleen bevorderd over zowel $Pt-Sn/ZnAl_2O_4$ als $Pt/ZnAl_2O_4$. De fysisch-chemische eigenschappen van $Pt/ZnAl_2O_4$ zijn daarbij niet aangepast door de stoom. De bijbehorende toename in de reactiesnelheid onder vochtige omstandigheden wordt daarom toegeschreven aan het leegmaken van het $Pt/ZnAl_2O_4$ katalysatoroppervlak door de stoom. In tegenstelling tot $Pt/ZnAl_2O_4$ worden de fysisch-chemische eigenschappen van $Pt-Sn/ZnAl_2O_4$ wel veranderd door de stoom. De XRD resultaten wijzen op het verbreken van de PtSn legering door stoom en de XPS resultaten laten een meer geoxideerd Pt zien in de Pt-Sn katalysator na behandeling met stoom in vergelijking met gereduceerd Pt en Pt-Sn en stoombehandeld Pt. De adsorptie van koolwaterstoffen en de dissociatie van ethaan worden mogelijkerwijs bevorderd op het meer geoxideerde Pt in stoombehandeld $Pt-Sn/ZnAl_2O_4$, wat de reactiesnelheid verhoogd.

In reeds ontwikkelde membraanreactoren is het membraan doorgaans fysiek gescheiden van de katalysator. In een alternatieve configuratie kan de Pt katalysator direct worden aangebracht op het membraanmateriaal. Het potentiële voordeel daarvan is dat de reactie kan plaatsvinden in de directe nabijheid van het membraan, wat het massatransport vanaf de katalysator naar het membraan bevorderd. Om het potentieel van deze strategie te onderzoeken is Pt aangebracht op het oppervlak van een veelbelovend MPEC (lanthaan wolframaat, LWO) en PCEC (barium zirconium cerium yttrium oxide, BZCY) materiaal. De werking van deze twee katalysatoren is vergeleken met die van de traditionele $Pt/ZnAl_2O_4$ katalysator in **Hoofdstuk 4**. In vergelijking met $Pt/ZnAl_2O_4$ lieten Pt/LWO en Pt/BZCY allebei een hogere methaanselectiviteit en een lagere ethyleenselectiviteit zien. De versterkte methaanproductie over Pt/LWO en Pt/BZCY kan worden toegeschreven aan Lewiszuurposities in LWO en BZCY. Daarnaast deactiveerden Pt/LWO en Pt/BZCY door het sinteren van Pt, terwijl $Pt/ZnAl_2O_4$ stabiel bleef. De interacties tussen Pt en het dragermateriaal zijn vermoedelijk sterker in $Pt/ZnAl_2O_4$ dan in Pt/LWO en Pt/BZCY.

Desalniettemin kan een co-toevoer van stoom de herverspreiding van het Pt over het drageroppervlak bevorderen en daarmee het sinteren van Pt tegengaan.

De potentiële techno-economische voordelen en uitdagingen van het membraan-gedreven alkaan NODH concept zijn onderzocht in twee verschillende processimulatiestudies in **Hoofdstuk 5** en **6**. In **Hoofdstuk 5** is er bekeken of membraan-gedreven propaan NODH een haalbaar alternatief is voor het reeds gecommercialiseerde Honeywell/UOP Oleflex proces. De resultaten tonen dat het MPEC-gedreven proces financieel en energetisch niet kan wedijveren met het Oleflex proces, aangezien de investeringskosten 18 keer hoger zijn en het energieverbruik 40% groter is dan het Oleflex proces. Dit is toe te schrijven aan de hoge kosten voor de MPEC membraanreactor en aan de grote hoeveelheid energie die benodigd is voor het verwarmen van de toevoerstromen van de membraanreactor. Beide aspecten worden veroorzaakt door de beperkte drijvende kracht voor waterstofpermeatie door MPECs. In tegenstelling tot het MPEC proces is het PCEC-gedreven proces wel een geschikt industrieel alternatief voor Oleflex met ca. 20% lagere investeringskosten en een ca. 30% lager energieverbruik. Deze financiële en energetische voordelen zijn te danken aan kleinere processtromen en kleinere procesinstallaties als gevolg van een hogere single-pass olefineopbrengst in het PCEC proces (ca. 50%) in vergelijking met het Oleflex proces (ca. 36%).

In **Hoofdstuk 6** is onderzocht of het gebruik van PCEC membranen ook het industriële perspectief van het niet-gecommercialiseerde ethaan NODH proces kan verbeteren. Daartoe zijn de techno-economische aspecten van het ethaan NODH proces vergeleken met die van een conventioneel ethaan stoomkraakproces voor ethyleenproductie. De resultaten laten zien dat een ethyleenopbrengst van ca. 25%, welke tot op heden gehaald is in experimentele studies, onvoldoende is om financieel en ecologisch te kunnen concurreren met het stoomkraakproces. Een PCEC single-pass ethyleenobrengst van ca. 50% is benodigd om in de toekomst met het stoomkraakproces te kunnen concurreren op het gebied van CO_2-emissies, investeringen en winstgevendheid.

In **Hoofdstuk 7** is er geconcludeerd dat veranderingen in de gasfasecompositie in membraanreactoren het mechanisme en de reactiesnelheid van ethaan NODH over PtSn katalysatoren sterk doen veranderen. Daarnaast is er aangegeven dat de stabiliteit van de PtSn katalysator in de aanwezigheid van stoom verder onderzocht moet worden. Ook is er geconcludeerd dat er een voorkeur is voor traditionele packed bed membraanreactoren als de stabiliteit en ethyleenselectiviteit van Pt op proton-geleidende dragermaterialen niet verbeterd kan worden. Tot slot is er uitgelicht dat beide techno-economische studies laten zien dat reducties in CO_2-emissies alleen verwezenlijkt kunnen worden als er volledig duurzame elektriciteit gebruikt wordt in de PCEC-gedreven alkaan NODH processen. Bovendien leidt groene elektrificatie van conventionele olefine productieprocessen tot vergelijkbare besparingen in CO_2-emissies. Al met al zorgt een combinatie van technologische uitdagingen op het gebied van de katalysatorstabiliteit en de beperkte techno-economische voordelen van het PCEC-gedreven proces ervoor dat er een voorkeur bestaat voor het elektrificeren van reeds bestaande olefine productieprocessen.

Acknowledgments

I started my PhD journey in 2020, which was a somewhat extraordinary year, due to the COVID-19 pandemic. Being allowed to go to the campus of the University of Twente only one or two days per week was not easy in the beginning, although it helped that I was already familiar with the way of working within CPM after performing my MSc thesis work in the group in 2019. What followed was a four year roller coaster period covering work activities in the fields of heterogeneous catalysis, process design and simulation, techno-economic analyses, and reactor setup development, combined with self-development opportunities related to e.g. soft-skill and content-focused courses, teaching, student supervision, and conference participations. In this chapter I will try to look back at my PhD journey from my new home in Valencia.

First of all, I would like to thank my two promotors, Jimmy Faria and Leon Lefferts, who allowed me to pursue this PhD adventure. Jimmy, I will always remember the creative ideas and seemingly limitless enthusiasm, which brought me new motivation even in the most frustrating moments. Besides, I am very thankful for the opportunities you gave me regarding teaching, supervising students in practicals and thesis studies, and presenting research work at conferences. Leon, your knowledgeable and at the same time critical view on the applied experimental research frequently provided useful new insights and new steering directions to further finetune the outcomes.

Apart from my promotors I would like to acknowledge the contributions from a few other professors employed by the University of Twente. My PhD work was carried out in the context of a Dutch-German research consortium and Arian Nijmeijer played a crucial role in acquiring the financial support for this AMAZING project. Also, Arian thank you very much for your industrially relevant inputs and for your consistently fair and highly pragmatic assessment of the various process analyses. Next to Arian, Louis van der Ham provided key insights about the process simulation studies in **Chapter 5** and **6**. I really appreciated the fruitful discussions we had about these topics and the impressively detailed examinations you performed on these very comprehensive studies. Additionally, Aayan Banerjee shared very useful knowledge about the functionality of proton-conducting ceramics, especially in the beginning of my PhD, which provided solid background information for many aspects of this dissertation.

None of the doctoral studies could be carried out without the help of technical and supporting staff members. I therefore want to express my gratitude to Bert, Karin, Tom, Ties, Amelia, Maaike, Dorothy, and Anne. Special thanks to Bert for his essential practical support during my PhD, and before during my MSc thesis work. Who would have ever thought that the scrapheap GC would survive five years of catalytic testing! Besides, Bert thanks for the relieving conversations during coffee breaks about our (sometimes roller coaster) personal lives in the last few years. I would like to thank Karin, Tom, Ties, and

Amelia obviously for their important practical assistance, but maybe even more for their down-to-earth mentality, expressed during work activities and coffee breaks, in which I do of course recognize myself as a "Tukker". A personal note here to Maaike, because even though we both hoped that life would take a different turn, I absolutely still cherish the warm and shared memories. Lastly, I would like to mention my appreciation to office managers Dorothy, for the warm welcoming period at CPM, and Anne, for being the social and always approachable "Manusje-van-alles" within the group during the rest of my PhD.

I would further like to acknowledge the role of several other former colleagues on my development within CPM. I received the introduction to the experimental facilities from Rolf, who was my supervisor during my MSc period in the group. Even though organic and inorganic experiments are part of the Chemical Engineering curriculum, it was Rolf who trained me in (re)building and operating catalytic testing setups, in addition to his help in shaping the MSc thesis. Besides, by being one of the only other Dutch researchers within the group, I think I can definitely call you a catalytic father figure, although you probably will not like that nickname. Besides, I would like to thank Kevin and Harm for the great year when we were sharing offices and for all the nice, relieving, and refreshing lunch walks. Also, Maria, Pengyu, Nuria, Guido, Rolf, and Shahab, thank you for continuously creating a social and enthusiastic atmosphere in my beginning period at CPM, which obviously positively influenced my decision on staying for a PhD. Special note here to Shahab, who performed his PhD at SPT in parallel with my PhD at CPM: with your working hours and your straight and open character you absolutely deserve the Dutch nationality!

When moving a bit further in time, I remember several more recent CPM colleagues. I shared my 4 (and a half) year PhD period within CPM almost entirely with Fernando. Being together in online CAIA courses during COVID-19 creates a bond, in addition to my appreciation for your social, calm, and analyzing character. Some South-European vividness was added to the group when Lola arrived for her PostDoc. I had the honor to share the office with Lola for a major part of my PhD, in which I think I learned as much about the Spanish language and culture as she did about the Dutch standards and habits. I promise I will visit Sevilla in the near future, as our relocations have made this somewhat more realistic! Rem and Janek joined CPM right before our group trip to Munich. This was thereby a perfect opportunity to integrate and to demonstrate their social addition to the group. Rem, you are a friendlier and more talented person than you would ever admit. From a social perspective, it was/is therefore a loss that your research period in Spain was/is ultimately more extensive than initially anticipated. Then I move on with my holiday mate, running coach, and, by now, good friend (if he agrees on this at least) Janek. Without any doubt I can say that I will never forget the interrail trip through central Europe and the unique 10-day stay in Paris during the Olympic Games in 2024. Besides, thank you for sharing all your running knowledge, which transformed me from an uninformed amateur runner into a well-trained, carefully monitoring, and physically caring... amateur. Oh, and before I forget, I also really appreciated your scientific attitude within the group.

Next, I would like to thank Martim and Xinming for being valuable additions to the group. If Martim and Xinming are present you know that in every situation something funny and unexpected can happen, which unconsciously creates a pleasantly awkward atmosphere. In recent years, the Indian ladies Preethi and Suman have been very good and close colleagues. Seemingly on the background, but with a lot of know-how and with very social characters, they are an important part of the glue within the recent CPM organization. Last year, Fienie joined the "ladies office" with Suman and Preethi, which was characterological a very good match. Fienie, I am convinced that you will become a collaborative, motivated, and successful researcher, irrespective of the corresponding topic or research group. Lastly, I hope that Shivan, Jab, and other newcomers in the group can take over the leading role in the CPM embodiment of scientific, social, and independent researchers.

In addition to my fellow CPM colleagues, I will also remember several colleagues from the Inorganic Membranes group. In particular, I would like to thank Michel for being my AMAZING collaborator for four years. In addition to the content related discussions, I want to thank you for the nice trips to consortium meetings and conferences, for co-supervising three MSc students, and for relieving conversations about the collective PhD struggles we dealt with. Additionally, I would like to express my gratitude to Julian, Shaur, Wisse, Michel, and Jan for the nice autumn school period in Valencia.

Finally, I would like to acknowledge two persons who both were part of CPM for only three months. Raquel performed a three month research stay within CPM in collaboration with me. Despite the disappointing research outcomes, I think that your short stay in the Netherlands was a successful adventure. When you arrived in the Netherlands, you mentioned that you wanted to become friends with your Dutch colleagues. Back then, I mentioned that you cannot force those things, but regarding the fact that I wanted to attend your defence in Zaragoza at all costs, I dare to say that we have indeed become very good friends. In a similar construction as Raquel's research collaboration with me, Ilaria came to CPM for a collaboration with Janek. Ilaria, I really appreciated your pleasant contribution to the group during your research stay, but here I would particularly like to thank you for introducing me to ITQ and for facilitating my move to Valencia.

During my PhD period I had the opportunity to supervise several students in catalyst synthesis practicals, process design projects, and BSc and MSc thesis projects. The students of the catalyst synthesis and characterization practicals not only provided me new batches of catalyst, but also provided a fresh look on the applied synthesis procedures. Besides, the group of students working on the design of an electrified alkane dehydrogenation process in the context of the MSc course on Process Plant Design provided key initial insights into how such a process should look like and what the potential benefits could be. It is noteworthy to mention that the starting point set by the Process Plant Design group formed the basis of the journal article that was included in this thesis as **Chapter 5**. I would further like to thank former BSc student Akintunde and former MSc students Ruben, Wisse, Koen, Hua, and Simon for their valuable contributions to the AMAZING project, and for all fruitful meetings and social conversations. Ruben

initiated a critical analysis on the working principles of MPEC membranes and started a model for permeation through those membranes, which was later on further developed by Wisse. I am sure that both of them will succeed in sharing their innovative and critical views in their new respective roles as consultant and PhD candidate. Koen set the cornerstone of a research field focusing on modelling of membrane reactors equipped with ceramic membranes, which is still an area to be developed further. Hua contributed to the support comparison study presented in **Chapter 4** of this dissertation. Besides, she opened a research line on exsolution of Pt nanoparticles from MPEC supports, which is also an area that needs to be explored in more detail. Lastly, Simon's process simulations efforts and comprehensive techno-economic analysis of the electrified ethane dehydrogenation process contributed substantially to **Chapter 6** of this dissertation.

From a personal side it was not easy to start the PhD during the COVID-19 pandemic, as the restricted number of office days also strongly reduced social connections. For this reason, I would particularly like to thank my former housemates Harm and Erik. Despite the unpleasant COVID period, I think we managed to keep life entertaining and comfortable with our down-to-earth mentalities. Thanks as well for absorbing my frequent PhD frustrations haha. I will always associate my PhD period with the fun years that we shared in our house in the Bloemendaalstraat. In addition, I would like to thank Harm, Erik, and Sterre for all board game days and nice dinners, and for the holidays to Scandinavia, Rome, and Athens. These spare time activities and trips were all very pleasant and important moments to distract the mind from any work related struggle. I further cherish the friendship with the former group of BSc and MSc study friends, including Harm, Erik, Koen, Jonne, Barend, and Sybe, with whom we are still organizing a barbecue and gourmet activity every half year "om oude koeien uit de sloot te halen".

For the last part of the acknowledgment I will switch to Dutch... Want gedurende mijn hele opgroeiperiode, zowel werk als privé, heeft mijn familie altijd voor mij klaar gestaan, waar ik jullie uiteraard zeer dankbaar voor ben. Die stabiele basis heeft zeker geholpen in mijn ontwikkeling. Daar wil ik met name mijn ouders, Peter en Karin, voor bedanken, bij wie ik altijd goed met mijn emoties terecht kon. Daarnaast waren de gezamenlijke reizen, met in het bijzonder de marathonreizen naar Valencia en Budapest, onvergetelijk. Na alles wat er vorig jaar gebeurd is, besef ik me maar al te goed hoe onbelangrijk dit boekje (oké misschien is het wel een beetje een flink boekwerk geworden) in werkelijkheid is en hoe belangrijk het is om iedere dag van zoveel mogelijk dingen te proberen te genieten. Danique en Bert, ik heb diep respect voor hoe snel jullie het leven weer opgepakt hebben en hoe positief jullie altijd in de situatie gestaan hebben. En de oppassessies met Milou en Sef waren niet alleen leuk, maar met enige regelmaat ook een prettige afleiding van enige vorm van werkstress. Ook nu ik voor langere tijd in Spanje woon, hoop ik dat we die sterke binding kunnen behouden.

Jord

List of publications

Per May 2025

Journal articles

1. **J.P. Haven**, L. Lefferts, J.A. Faria Albanese. Deviations from ideal Langmuir adsorption govern surface coverages in ethane dehydrogenation on Pt-Sn/ZnAl2O4. Submitted to J. Catal., *under revision*.

2. **J.P. Haven**, L. Lefferts, N. García Moncada, J.A. Faria Albanese. Steam impacts catalyst chemistry and enhances product desorption in ethane dehydrogenation over Pt catalysts. *In preparation*.

3. **J.P. Haven**, L. Lefferts, J.A. Faria Albanese. Proton-conducting supports for Pt-catalyzed ethane dehydrogenation. *In preparation*.

4. **J.P. Haven**, L. Lefferts, A. Nijmeijer, A.G.J. van der Ham, J.A. Faria Albanese. Leveraging green electricity to drive propylene production in membrane reactors. Renew. Sustain. Energy Rev. **212**, 115448 (2025), doi: 10.1016/j.rser.2025.115448

5. **J.P. Haven**, S. Haanschoten, L. Lefferts, A. Nijmeijer, A.G.J. van der Ham, J.A. Faria Albanese. Industrial perspective of electrified ethylene production via membrane-assisted non-oxidative dehydrogenation of ethane. ACS Sustain. Chem. Eng., **13**, 7, 2759-2773 (2025), doi: 10.1021/acssuschemeng.4c08549

Oral presentations

1. **J.P. Haven** (2023). Reaction kinetics of ethane dehydrogenation for membrane reactor applications. *2nd University of Twente – Forschungszentrum Jülich summit*, 14 November 2023, Enschede (The Netherlands).

2. **J.P. Haven** (2023). Industrial production of propylene via electrochemical non-oxidative dehydrogenation of propane: A techno-economic assessment. *Autumn School on Inorganic Chemical Reactors for Sustainable Chemicals, Fuels and Power Production*, 25 October 2023, Valencia (Spain).

3. **J.P. Haven** (2023). Industrial production of propylene using dense ceramic membranes (keynote presentation). *16th International Conference on Catalysis in Membrane Reactors (ICCMR16)*, 17 October 2023, Donostia-San Sebastián (Spain).

4. **J.P. Haven** (2023). Industrial production of propylene using dense ceramic membranes. *18th Netherlands' Process Technology Symposium (NPS18)*, 6 July 2023, Enschede (The Netherlands).

5. **J.P. Haven** (2023). Taming the energetics of the transition state by leveraging the water-catalyst interactions during alkane dehydrogenation. *28th North American catalysis society Meeting (NAM28)*, 21 June 2023, Providence, RI (United States of America).

6. **J.P. Haven** (2023). Reaction kinetics of ethane dehydrogenation for membrane reactor applications. *24th Netherlands' Catalysis and Chemistry Conference (NCCC24)*, 6 March 2023, Noordwijkerhout (The Netherlands).

Poster presentations

1. **J.P. Haven** (2024), Proton-conducting supports for Pt-catalyzed ethane dehydrogenation. *18th International Congress on Catalysis (ICC18)*, July 2024, Lyon (France).

2. **J.P. Haven** (2024), Catalysis guidelines for membrane-driven industrial propylene production via non-oxidative dehydrogenation of propane. *25th Netherlands' Catalysis and Chemistry Conference (NCCC25)*, March 2024, Noordwijkerhout (The Netherlands). Awarded VIRAN best poster prize.

3. **J.P. Haven** (2023). Reaction kinetics of ethane dehydrogenation for membrane reactor applications. *15th European Congress on Catalysis (EuropaCat15)*, August 2023, Prague (Czech Republic).

4. **J.P. Haven** (2022). Light paraffin dehydrogenation in catalyst-functionalized membrane reactors. *23rd Netherlands' Catalysis and Chemistry Conference (NCCC23)*, May 2022, Noordwijkerhout (The Netherlands).

5. **J.P. Haven** (2022). Light paraffin dehydrogenation in catalyst-functionalized membrane reactors. *17th Netherlands' Process Technology Symposium (NPS17)*, April 2022, Delft (The Netherlands).

6. **J.P. Haven** (2022). Light paraffin dehydrogenation in catalytic membrane reactors: A modelling study. *6th international conference on Prospects of Proton Ceramic Cells (PPCC6)*, June 2022, Dijon (France).

Other contributions

1. Supervision of 1 BSc and 5 MSc students during their graduation projects, October 2020-February 2024.

2. Supervision of a group of students working in the context of the MSc course Process Plant Design on the design of a process for membrane-driven propane dehydrogenation, February 2022-July 2022.

3. Supervision of various groups during their practical on catalyst synthesis and characterization in the context of the MSc course Project Materials and Molecular S&T, May 2021-April 2023.

4. Development, organization, teaching, and lab supervision in a course on Advanced Reaction Kinetics, March 2023-July 2024.

5. Chairman of the session on Modelling and Simulation at the *16th International Conference on Catalysis in Membrane Reactors (ICCMR16)*, 17 October 2023, Donostia-San Sebastián (Spain).

Jord Peter Haven was born on 7 July 1996 in Oldenzaal, the Netherlands. After obtaining his vwo diploma at the Twents Carmel College De Thij in Oldenzaal in 2014, he started studying Scheikundige Technologie (BSc) at the University of Twente, the Netherlands. His BSc thesis work focused on polyelectrolyte-based membranes for water purification. During the summer of 2017, he received a scholarship to participate in the Future Chemist International Summer Camp (FCISC) at the University of Science and Technology (USTC) in Hefei, China. In September 2017, Jord continued studying at the University of Twente with the MSc Chemical and Process Engineering programme. In addition, he was chairman of the Travel Subcommittee of study association C.T.S.G. Alembic (2017-2018), organizing a 3-week study tour to Argentina in the summer of 2018. His MSc research was about heterogeneous catalysts for selective dehydrogenation of fatty acids. In parallel with his MSc research, Jord worked part-time as a detailed design engineer at Zeton B.V. (2018-2019), collaborating to the design and functional testing of a chemical pilot plant. After obtaining his MSc degree in spring 2020, he received a Bridging Grant from the Twente Graduate School to continue his MSc research for six months. In October 2020, Jord decided to pursue his PhD on catalytic membranes for alkane dehydrogenation under supervision of prof.dr.ir. Leon Lefferts and prof.dr. Jimmy Faria Albanese in the Catalytic Processes and Materials (CPM) research group at the University of Twente. In his PhD, Jord combined his background in heterogeneous catalysis, membranes, and process design. This PhD dissertation is the result thereof.